UNIVERSITY OF CALGARY

CO_2 Sequestration Site Characterization and Time-lapse Monitoring Using Reflection Seismic Methods

by

Abdullah A. Alshuhail

A THESIS

SUBMITTED TO THE FACULTY OF GRADUATE STUDIES

IN PARTIAL FULFILMENT OF THE REQUIREMENTS FOR THE

DEGREE OF DOCTOR OF PHILOSOPHY

DEPARTMENT OF GEOSCIENCE

CALGARY, ALBERTA

MAY, 2011

Abstract

Of the various disciplines involved in carbon capture and storage, seismic methods are critically important. In this dissertation, two case studies in west-central Alberta were investigated by employing reflection seismic methods, rock physics and numerical modelling. In the first case study, regional and local seismic site characterization was undertaken as part of the Wabamun Area CO_2 Sequestration Project. The results show that P-wave reflection seismology can be an effective tool in regional and local mapping of the continuity of the carbonate Nisku aquifer as well as in delineating geologic discontinuities, such as karsting, that may compromise storage integrity. Furthermore, the information provided by the seismic data was valuable when integrated with petrophysical data in order to reduce the ambiguity in identifying CO_2 injection "sweet spots". Results from the fluid substitution and numerical forward seismic modelling suggest that CO_2 anomalies in stiff carbonate aquifers like the Nisku Formation are small and so is the change in seismic response. For instance, the maximum change in reflection time and NRMS amplitude in time-lapse P-wave reflection surface seismic data was found to be ~ 1.5 ms and ~ 24%, respectively. Detection of these small changes depends on a number of factors, including data repeatability, frequency bandwidth and CO_2 saturation scheme. The change in the S-wave properties is much smaller than in the acoustic properties suggesting that it is unlikely that PS-wave would be successful in identifying CO_2 anomaly.

The second case study pertains to 4-D seismic monitoring at the Pembina-Cardium CO_2 Pilot Project site where multi-component surface seismic and walk-away vertical seismic profile methods were implemented as part of the monitoring program. The quality of these data, in particular, was compromised by interference caused by infrastructure development which resulted in the loss of ~ 20% of the seismic shot locations. The 4-D information contributed by the PS-wave surface seismic data was also limited due to the small change in the S-wave properties. Although the magnitude of the predicted change in the acoustic properties was within the detection range, unambiguous identification and mapping of the injected CO_2 in the Cardium sandstone reservoir could not be achieved due, primarily, to the CO_2 confinement to a thin layer within the reservoir. However, the lack of CO_2 anomaly above the reservoir indicates that no upward migration of the CO_2 plume was taking place during the injection program. This observation was supported by the results from fluid substitution and forward seismic modelling which show that the P-wave seismic response would be quite sensitive to upward migration of the plume. The dissertation concludes by outlining some of the recommendations, considerations and challenges involved in the implementation of seismic and rock physics methods in CO_2 sequestration.

Acknowledgements

I thank Allah (Subhanahu Wa Ta'ala) for all the blessings he bestows upon me among which was the ability and strength to undertake and complete this dissertation (Alhamdu-le-Allah).

Of course, completing this dissertation would not have been possible without the instruction and discussion by the various individuals as well as the support and assistance by a number of institutions, whom I would like to acknowledge according to the following categories:

1. Academic:
   1.1. First and most importantly my supervisor Dr. Don Lawton. He agreed to take me on as a graduate student and has been supportive and encouraging throughout my Ph.D. program. His teaching through the highest standard of academia, constructive criticism and critical thinking has had a tremendous influence on elevating my knowledge and the scientific content of this dissertation. I would like to thank him for his dedication toward his students, including myself, and in making available time and resources.
   1.2. My supervisory committee: Dr. Gary Margrave and Dr. Kris Innanen as well as Dr. Michael Wieser ("internal" external examiner), Dr. Mirko van der Baan (external examiner) for taking the time to be onboard my doctoral committee and for their intellectual feedback. Many thanks to the neutral chair Dr. Larry Bentley.
   1.3. The Consortium for Research in Elastic Wave Exploration Seismology (CREWES) project sponsors, faculty, staff and students. Especially, Dr. Don Lawton (the only remaining CREWES co-founder), Dr. Gary Margrave (CREWES director), Dr. Larry Lines (CREWES associate director), Dr. Rob Ferguson (CREWES associate director), Dr. John Bancroft (CREWES associate director), Dr. Rob Stewart (CREWES co-founder; now at the University of Houston), Dr. Brian Russell for their instructions as well as the interesting discussions and useful advices. Special thanks to our outstanding Technical Manager Mr. Kevin Hall and the System Geoscientist Dr. Rolf Maier for their help and support with all the technical issues. Also, I would like to thank the

CREWES project Administrator Manager Ms. Laura Braid for her help with all the administrative issues.

1.4. Department of Geoscience faculty and staff: I have been privileged to be among the faculties, staffs, and colleagues at the Department of Geoscience. Staffs at the main office and Gallagher Library are better than what one would hope for; they made feel as I'm being surrounded by family.

1.5. Special thanks to Ms. Cathy Hubbell (Graduate Program Administrator), Ms. Susan Moisik (Administrative Manager), Ms. Laurie Vaughan (Accounts Administrator), Claudette Cloutier (Gallagher Library Interim Head Science and Technology Liaison Services Manager) and Mr. Irfan Syed (Systems Administrator) for their help and support in issues related to their corresponding specialty.

1.6. Also, I would like to thank Dr. Bernhard Mayer, Mr. Maurice Shevalier, Mr. Gareth Johnson and Mr. Michael Nightingale from the Applied Geochemistry Group (AGg) for the many interesting information and discussions; especially Dr. Mayer for his involvement in my Candidacy Examination Committee.

1.7. Dr. Kris Vasudevan (Solid Earth Processes research team) for making available the regional LITHOPROBE® seismic lines which were interpreted as part of Wabamun Area CO_2 Sequestration Project (WASP).

1.8. Special thanks to Dr. Helen Isaac for her so appreciated help when she taught the ProMAX™ data processing short course as well as with the interpretation of the WASP seismic data.

1.9. The spectral ratio computation was made using a FORTRAN code by Dr. Arnim Hasse and I would like to thank him for helping me with that.

1.10. My friends and colleagues at the Department of Geoscience specifically and the University of Calgary in general: Dr. Saleh Al-Saleh, Salman Bu Bshait, Dr. Taher Sodagar, Faranak Mahmoudian, Rob Taerum, Kelly Classen, Jason McCrank, Louis Chabot, Mahdi Al-Mutlaq, Abdallah Al-Zahrani, Ali Al-Ghamdi, Hussain Hammad and all of my colleagues (for the interesting and useful discussions).

2. Sponsor:

2.1. King Fahd University of Petroleum and Minerals (KFUPM) for the M.Sc. and Ph.D. scholarships. Special thanks to Mr. Mohammed Al-Shehri, Mr. Farhan Al-Enizi, and Mr. Mamdouh Al-Orabi from the Deanship of Faculty and Personnel Affairs.

2.2. In addition, I would like to thank my professors and colleagues at the Earth Sciences Department for their continuous support, especially my respected professors including the department head Dr. Abdulaziz Al-Shaibani, Dr. Mustafa Harriri, Dr. Abdullatif Al-Shuhail, Dr. Mohamad Makkawi, Dr. Abdullatif Qahwash, Dr. Abdulwahab Abokhodair, Dr. Adly Saffin. Also, the department staff Mr. Moushabbab Assiri, Mr. Ahamd Muhammad, Mr. Ahmad Al-Saif, Mr. Shahul Hameed, Mr. Azizulla Khan, and Mr. Khalid Khan.

2.3. Many special thanks to my uncle Dr. Abdullatif Al-Shuhail for being a mentor and a colleague in addition to being a relative, and for the infinite advices and intellectual discussions.

2.4. I would, also, like to thank the current and previous Saudi cultural attaché in Canada Dr. Faisal Abaalkhail, Dr. Ghazi Al-Makk, and Ahmed Al-Metwally; the bureau employee Mr. Habib Bouagada, and my bureau advisors throughout my scholarship Mrs. Nuha Nasser, Miss. Reem Sleiman, Mrs. Saly Michael, Mrs. Soha Nasser for making available the right environment, for their support and effective communication with my sponsor in regard to many scholarship issues.

3. Projects Sponsors:

3.1. Pembina-Cardium CO_2-EOR Pilot Project (PCEP): the Natural Sciences and Engineering Research Council of Canada (NSERC), Alberta Energy Research Institute (AERI; now Alberta Innovates), Natural Resources Canada (NRCan), Western Economic Diversification (WED), PennWest Exploration, and the CREWES project.

3.2. Wabamun Area CO_2 Sequestration Project (WASP): the Natural Sciences and Engineering Research Council of Canada (NSERC), and AERI (now Alberta Innovates), the CREWES project and all the other industrial partners.

3.3. Also, I would like to thank the WASP technical and administrative team, especially, Dr. Rob Lavoie, Dr. David Keith, Dr. Stefan Bachu, Dr. Don Lawton, Dr. Frank Stoakes, Dr. Yuri Leonenko, Dr. Runar Nygaard, Dr. Jerry Jensen, Mr. Chris Eisinger, Ms. Hollie Roberts, and Ms. Michelle Bradford.

4. Industry:
    4.1. PennWest Exploration: for its collaboration in the Pembina-Cardium CO_2-EOR Project. Special thanks to Mr. Louis Chabot for the interesting discussions in various topics, especially those related to the project.
    4.2. EnCana Corporation (now Cenovus Energy): for making available their seismic and well logs database for the Wabamun Area CO_2 Sequestration Project (WASP). Special thanks to Jimmy Haszard, Jay LeBlanc, and Ian Reglar (formerly EnCana) for their help in setting up the database, workstation and getting me started with seismic analysis.
    4.3. Hampson-Russell (a CGG Veritas Company): for donating their software (GeoView™), the applications that come with it. Special thanks to Dr. Brian Russell, Mr. Dan Hampson and Mr. Graham Carter.
    4.4. Zokero: for the SeisWare™ seismic interpretation software and the outstanding technical support.
    4.5. Geophysical Exploration and Development Company (GEDCO): for donating VISTA® seismic processing software and for the technical support. Special thanks to Mr. Mingyu Zhang, Mr. Rick Kuzmiski, and Mr. Gary Engler for their assistance in various issues with VISTA™ Processing.
    4.6. Seismic Micro-Technology (SMT): for donating the Kingdom Suite™ seismic interpretation software and for the excellent technical support.
    4.7. Halliburton: for donating the 2-D and 3-D processing software ProMAX™.
    4.8. GX Technology: now part of ION Solutions for the EarthWave™ modelling and imaging package.
    4.9. Dr. Karl-Josef Sandmeier for providing technical support with the software package (Reflexw™).
5. Family and Friends (*last but not least*):
    5.1. My dear parents (Abdulaziz Alshuhail and Wedad Alshuhail) whom I can't thank enough; my brother (Waleed) and sisters (Nesreen, Muneerah, Hessa and Nora)

who have been of great support and inspiration though they are thousands of miles away.

5.2. My beloved wife Dr. Hathami Almubarak (M.D.) for her support and encouragement. She kept “pushing” me whenever I was losing momentum. I keep asking myself, what would I do if she was not in my life? She took good care of our daughter Lulwa (whom I would like also to thank) and made available the right environment for me to complete my M.Sc. and Ph.D. degrees.

5.3. Many thanks to my uncle Dr. Abdullatif Alshuhail for the useful advices and guidance in many situations. Also, I would like to thanks my aunt Noriyah.

5.4. Also, I would like to thank my friend Dr. Saleh Al-Saleh for the endless interesting discussions, and a friendship of a lifetime.

5.5. The rest of my family; especially my father and mother in-law (Mr. Ahamd Al-Mubarak and Mrs. Fatema Al-Musa), my brother in-law (Abdullah Al-Mubarak)

5.6. My friends in Canada and Saudi Arabia including Eng. Abdulmohsen Al-Mohsen and Eng. Saad Al-Afaleq.

Dedication

Dedicated to my parents, my wife, my daughter, my brother and sisters.

Table of Contents

List of Tables

List of Figures and Illustrations

List of Symbols, Abbreviations and Nomenclature

Symbol	Definition
1-D	One dimensional in space (*x*) or time (*t*)
2-D	Two dimensional in space (*x*, *z*)
3-D	Three dimensional in space (*x*, *y*, *z*)
4-D	Four dimensional, where the fourth dimension is time
A	Amplitude of compressional wavefield (dimensionless)
A	Area in m^2
a	Absorption function in the time domain Intercept An empirical parameter used in the Batzle and Wang relations (1992) An empirical parameter used in the Peng-Robinson EOS (1976)
AERI	**A**lberta **E**nergy **R**esearch **I**nstitute; now Alberta Innovates
AGS	**A**lberta **G**eologic **S**urvey
AI	**A**lberta **I**nnovates **A**coustic **I**mpedance in $kg/m^2.s$
ARC	**A**lberta **R**esearch **C**ouncil
AVO	**A**mplitude **V**ariations with **O**ffset
Al_2O_3	Aluminum oxide
$Al_2Si_2O_5(OH)_4$	Kaolinite (clay mineral)
AWE	**A**coustic **W**ave **E**quation
ARC	**A**lberta **R**esearch **C**ouncil
ART	**A**symptotic **R**ay **T**heory
AWE	**A**coustic **W**ave **E**quation
α	Compressional wave (P-wave speed) speed in m/s An empirical parameter used in the Peng-Robinson EOS (1976)
α/β	Compressional-wavespeed/shear-wavespeed ratio (dimensionless)
B	Amplitude of shear wavefield (dimensionless) Amplitude of the real part of the seismic signal An empirical parameter used in the Batzle and Wang relations (1992)
b	Amplitude of the real part of the seismic signal Window length Slope An empirical parameter used in the Batzle and Wang relations (1992) An empirical parameter used in the Peng-Robinson EOS (1976)
β	Shear wavespeed (S-wave speed) in m/s
C	**C**elsius
C	Amplitude of the imaginary part of the seismic signal
c	Amplitude of the imaginary part of the seismic signal An empirical parameter used in the Batzle and Wang relations (1992)
$CaCO_3$	Calcium carbonate (limestone)
CDP	**C**ommon **D**epth **P**oint
$CaMg(CO_3)_2$	Dolostone
CaO	Calcium oxide

CH_4	Methane
CO_2	Carbon dioxide
CO_3	Carbonate
CREWES	**C**onsortium of **R**esearch on **E**lastic **W**ave **E**xploration **S**eismology
CRG	**C**ommon **R**eceiver **G**ather
CSG	**C**ommon **S**hot **G**ather
CTA	**C**omplex **T**race **A**nalysis
χ	Dimensionless coefficient in the finite-difference modelling formulation
$\mathbf{d}$	Vector of observed data or model response
d	A sample within the observed data or model response vector **d** An empirical parameter used in the Batzle and Wang relations (1992)
d	Difference between adjacent seismic traces in the difference method
$\mathbf{d}^0$	Vector of initial model response
d^0	A sample within the initial model response vector
DM	**D**ifference **M**ethod
DFT	**D**iscrete **F**ourier **T**ransform
DHT	**D**iscrete **H**ilbert **T**ransform
DT	Sonic log in us/m
Δt	Temporal sampling interval in ms
Δx	Spatial sampling interval in the horizontal (x) direction in m
Δy	Spatial sampling interval in the horizontal (y) direction in m
Δz	Spatial sampling interval in the vertical (z) direction in m
E	An empirical parameter used in the Batzle and Wang relations (1992) Acentric coefficient in Peng-Robinson EOS (dimensionless)
$\mathbf{e}$	Error vector
e	A sample within the error vector **e**
e	Exponential function as in $exp(x) = e^x$ An empirical coefficient used in the Brie et al. (1995) relations
$\Vert e \Vert_1$	l_1-norm
$\Vert e \Vert_2$	l_2-norm
ED	**E**dge **D**etection
EHR	**E**nhanced **H**ydrocarbon **R**ecovery
EGR	**E**nhanced **G**as **R**ecovery
EOR	**E**nhanced **O**il **R**ecovery
EOS	**E**quation **o**f **S**tate
ERCB	**E**nergy **R**esources **C**onservation **B**oard
ERFD	**E**xploding **R**eflector **F**inite-**D**ifference
ERM	**E**xploding **R**eflector **M**odel
EUB	**E**nergy and **U**tilities **B**oard
EWE	**E**lastic **W**ave-**E**quation
η	Viscosity in centipoise (cPs); 1 cPs = 10^{-3} Pa.s
FSM	**F**luid **S**ubstitution **M**odelling
FRM	**F**luid **R**eplacement **M**odelling
f	Temporal frequency in hertz (Hz)

	Filter operator $f(t)$
f	Vector source term in the elastic wave equation
F	Mathematical transformation operator which describes the physical process relating the model parameters and the model response
FFT	**F**ast **F**ourier **T**ransform
FM	**F**orward **M**odelling
FT	**F**ourier **T**ransform
$FeCO_3$	Siderite (iron carbonate)
F-D	**F**inite-**D**ifference
f-k	Frequency-wavenumber
ν	Minerals volume fraction (dimensionless)
g	Discrepancy vector
g	A sample within the discrepancy vector **g**
G	**G**iga (1×10^9)
G	Gas gravity or specific gravity of gas (dimensionless)
GEDCO	**G**eophysical **E**xploration and **D**evelopment **Co**mpany
GHG	**G**reen-**H**ouse **G**as
GLI	**G**eneralized **L**inear **I**nversion
GOR	**G**as-**O**il **R**atio (dimensionless)
GPa	**G**iga **Pa**scal
GR	Gamma ray log in API
GRT	**G**eometric **R**ay **T**heory
Gt	Giga tonne
GWR	**G**as-**W**ater **R**atio (dimensionless)
Γ	Factor for computing the minimum or maximum bulk modulus in the Hashin-Shtrikman formulation
γ	Gamma ray log in American Petroleum Institute (API) unit An empirical parameter used in the Batzle and Wang relations (1992)
h	Thickness in m
HT	**H**ilbert **T**ransform
HR	**H**ampson-**R**ussell software services
H^+	Hydrogen ion
HCO_3^-	Bicarbonate
HS^+	**H**ashin-**S**htrikman upper bound of elastic moduli (GPa)
HS^-	**H**ashin-**S**htrikman lower bound of elastic moduli (GPa)
$HS^\pm$	**H**ashin-**S**htrikman average of elastic moduli (GPa)
Hz	**H**ertz
H_2O	Water
H_2S	Hydrogen sulfide
IPCC	**I**ntergovernmental **P**anel on **C**limate **C**hange
I	Identity matrix
I	An empirical parameter used in the Batzle and Wang relations (1992)
IM	**I**nverse **M**odelling
Im	Imaginary part of a signal
I_p	Acoustic impedance in kg/m^2.s

I_s	Shear impedance in $kg/m^2.s$
i	Normal script: imaginary unit $i = \sqrt{-1}$ Subscript or superscript: positive integer number corresponding to sample index; layer or interface number
j	Normal script: imaginary unit $j = \sqrt{-1}$ Subscript or superscript: positive integer number corresponding to sample index; layer or interface number
Im	Imaginary part of a signal
J	Jacobian matrix, i.e. matrix of first partial derivatives.
J	A sample within the Jacobian matrix **J**
K	Kelvin (absolute temperature) **K**ilo (1×10^3)
K	Bulk (incompressibility) modulus in GPa
k	Permeability in Darcy
kg	**K**ilo**g**ram
k	Wavenumber in cycle/m
Kt	Kilo ton
$K_{0.8}Al_{2.8}\ Si_{3.2}O_{10}OH_2$	Illite (clay mineral)
$KAlSi_3O_8$	Potassium(K)-feldspars
$KAl_3Si_3O_{10}OH_2$	Muscovite
l	Water salinity in g/litre
LAI	**L**east-**A**bsolute **I**nversion
LMR	**L**ambda-**M**u-**R**ho
LSI	**L**east-**S**quares **I**nversion
Λ	Factor for computing the minimum or maximum shear modulus in the Hashin-Shtrikman formulation
λ	Lamé constant GPa Damping factor (dimensionless)
λ	Wavelength in m
μ	Shear (rigidity) modulus in GPa
M	**M**ega (1×10^6)
M	**M**eter
M	Function of multiples in the time domain Subscript or superscript: positive integer representing sample index An empirical parameter used in the Batzle and Wang relations (1992)
MBI	**M**odel-**B**ased **I**nversion
MgO	Magnesium oxide
MMV	**M**onitoring **M**easurements and **V**erification
MPa	**M**ega **Pa**scal
Mt	Mega tonne
N	Nitrogen
N	Normal script: noise function in the time domain Subscript or superscript: positive integer representing the length of an operator or number of observations or measurements Number of moles of substance

N	Normal script: Noise function in the frequency domain Subscript or superscript: positive integer representing the number of samples within a given window or design gate
NI	**N**ormal **I**ncidence
NSERC	**N**ational **S**cience and **E**nginee**r**ing **C**ouncil of Canada
NRMS	**N**ormalized **R**oot-**M**ean **S**quares
NOAA	**N**ational **O**ceanic and **A**tmospheric **A**dministration
$\lvert N \rvert$	Amplitude spectrum of the noise function
ODR	**O**ffset **D**ependent **R**eflectivity
Ω	Temporal window function (ms)
ω	Angular frequency in radians/s
OECD	**O**rganisation for **E**conomic **C**o-operation and **D**evelopment
OOIP	**O**riginal **O**il **i**n **P**lace
P	Pressure in MPa
P	Matrix of model parameters Kernel matrix used in inversion
p	Normal script: - horizontal component of slowness (ray parameter) in s/m - a sample within the model parameters vector Subscript or superscript: positive integer representing the power of solution
Pa	**Pa**scal (1 Pa = 10 bars)
PCEP	**P**embina **C**ardium CO_2-**E**nhanced Oil Recovery Pilot **P**roject
PDE	**P**artial **D**ifferential **E**quation
POF	**P**embina **O**il **F**ield
ppm	**P**arts **P**er **M**illion
PS-wave	Converted wave; i.e. incident as P-wave and reflected as vertical S-wave
P-wave	Compressional wave, ; i.e. incident as P-wave and reflected as P-wave
π	Pi = 3.14
ϕ	Porosity (dimensionless)
φ	Phase (Phase spectrum) of the seismic trace in radians Angle in degrees
Φ	Crosscorrelation function
PRED	**Pred**ictability (dimensionless)
ψ	Wavefunction (or seismic trace) in the space-time domain
ψ_1	Wavefunction travelling in the positive direction
ψ_2	Wavefunction travelling in the negative direction
ψ_{im}	Imaginary, or quadrature, part of wavefunction (or seismic trace)
ψ_{re}	Real part of wavefunction (or seismic trace)
$\underline{\psi}$	Complex wavefunction (or seismic trace)
Ψ	Wavefunction (or seismic trace) in the frequency domain
$\lvert \psi \rvert$	Amplitude spectrum of the seismic trace
q	Subscript or superscript: positive integer representing number of model parameters
Q	Quality factor in decibel (dB)

r	Normal script: reflectivity function in the time domain radius or distance between two points in m Subscript: receiver
R	Reflection coefficient (dimensionless) Seismic reflectivity in the frequency domain Universal gas constant 8.31441 in Joule/mole.Kelvin
RC	**R**eflection **C**oefficient
Re	Real part of a signal
RI	**R**ecursive **I**nversion
RT	**R**ay **T**heory; **R**ay **T**racing
$\|R\|$	Amplitude spectrum of the reflectivity function
ρ	Density in kg/m^3
s	**S**econds
s	Normal script: seismic trace in the time domain Subscript: source
S	Seismic trace in the frequency domain Volume fraction of fluid saturation (dimensionless) Brine salinity fraction (dimensionless)
SACS	**S**aline **A**quifer **C**O_2 **S**torage
SC	**S**uper**C**ritical
SCG	**S**toakes **C**onsulting **G**roup
SD	**S**pectral **D**ecomposition
SiO_4	Quartz
SWE	**S**calar **W**ave-**E**quation
SiO_2	Silicon oxide
SR	**S**pectral **R**atio
SWDFT	**S**hort **W**indow **D**iscrete **F**ourier **T**ransform (SWDFT)
STP	**St**andard **T**emperature and **P**ressure (0 C^o and 101 KPa)
S-wave	Shear wave
S/N	**S**ignal to **N**oise ratio
$\|S\|$	Amplitude spectrum of the seismic trace
σ	Poisson's ratio (dimensionless)
T	Normal script: Temperature in C^o Superscript: transpose of a matrix
T	Traveltime in unit time (e.g. s) Transmission coefficient (dimensionless) Period in s
τ	Crosscorrelation lag in s Dummy time variable for integration
t	Two-way traveltime in s; time coordinate in s
θ	Angle of propagation or incidence or refraction Shooting angle in degrees
UNEP	**U**nited **N**ations **E**nvironment **P**rogramme
USDOE	**U**nited **S**tates **D**epartment **o**f **E**nergy
V	Volume (m^3)

V	Vector of model values **v**
v	A sample within the model values vector **v** Absorption coefficient in decibel (dB)/m
$\mathbf{v}^0$	Vector of initial model parameters
v^0	A sample within the initial model parameters vector
VRH	**V**oigt-**R**euss-**H**ill
VSP	**V**ertical **S**eismic **P**rofile
w	Seismic source wavelet in the time domain Volume fraction of constituent (dimensionless)
W	Seismic source wavelet in the frequency domain
WMO	**W**orld **M**eteorological **O**rganization
WT	**W**ave **T**heory
$\lvert W \rvert$	Amplitude spectrum of the seismic source wavelet
x	Distance along the x-axis in m; coordinate along the x-axis in m Arbitrary function of time $x(t)$
X	Offset along the x-axis in m
y	Distance along the y-axis in m; coordinate along the y-axis in m Arbitrary function of time $y(t)$ An empirical parameter used in the Batzle and Wang relations (1992)
VSP	**V**erical **S**eismic **P**rofile
WASP	**W**abamun **A**rea CO_2 **S**equestration **P**roject
WCSB	**W**estern **C**anadian **S**edimentary **B**asin
Z	An empirical parameter used in the Batzle and Wang relations (1992)
z	Distance along the z-axis in m; coordinate along the z-axis in m Arbitrary function of time $z(t)$
ZOS	**Z**ero **O**ffset **S**ection
ZRD	**Z**one of **R**eliable **D**ata
ξ	Taper length
$^{\circ}$	Degrees
$\hat{\ }$	Estimate of function or variable
$\bar{\ }$	Average of function or variable
$\underline{\ }$	Complex representation
$\bullet$	Dot product
$\otimes$	Crosscorrelation operator
$*$	Convolution operator
d	Ordinary derivative operator
∂	Partial derivative operator
∇^2	Laplacian operator
$\sum$	Summation operator
$\lvert \ \rvert$	Absolute value Amplitude spectrum
$\lVert \ \rVert$	Measure of the length of a solution, i.e. norm
$\prod$	Geometrical mean

CHAPTER 1: INTRODUCTION

1.1 Dissertation Premises

This dissertation is devoted to seismic site characterization and time-lapse analysis using field data, rock physics and numerical modelling at a proposed and an established CO_2 sequestration sites in the Western Canada Sedimentary Basin (WCSB) in west-central Alberta. The proposed site is in the Wabamun area, which hosts the Wabamun Area CO_2 Sequestration Project (WASP). This is a University of Calgary lead multi-disciplinary project funded by the National Science and Engineering Research Council (NSERC) and Alberta Energy Research Institute[1] (AERI) with industrial partnership that has investigated the feasibility of 1 megaton (Mt) per year CO_2 sequestration into a deep saline aquifer, namely the Devonian dolomitic Nisku Formation. The established[2] site is in the Violet Grove area, in which the Pembina Cardium CO_2-EOR Pilot Project (PCEP) was undertaken in the period between 2004 and 2009. This is, also, a multi-disciplinary pilot project initiated by Alberta Government and administered by AERI and Alberta Research Council[3] (ARC) that has studied CO_2 sequestration for both enhanced oil recovery (EOR) and long-term storage in the oil-producing Cretaceous siliclastic Cardium Formation in the Pembina Oil Field (POF).

1.2 Anthropogenic CO_2 Emissions and Climate Change

Greenhouse gases (GHG) play an important role in regulating our planet temperature. Under normal GHG concentration, there exists a balance between the amount of energy (heat) transmitted into the earth through the atmosphere and the amount of energy (heat) reflected back into space from the earth's surface (IPCC, 2005). However, the climate change problem arises when the concentration of those GHG

---

[1] Now part of Alberta Innovates.
[2] Although CO_2 was still being injected up until when this dissertation was written, PCEP was officially wrapped-up at the end of 2009. The second (and last) time-lapse seismic survey was acquired in March 2007 after the injection of more than 50,000 tons of CO_2. This research took place during the third (i.e. final) phase of the project, and therefore it focuses on the time-lapse aspect of the project by analyzing the second monitoring survey (acquired in March 2007) with respect to the baseline survey (acquired in December 2005).
[3] Now part of Alberta Innovates.

increase at an accelerated level causing more heat to be trapped in the earth's atmosphere. More specifically, increasing emissions of anthropogenic carbon dioxide (CO_2), primarily due to fossil fuel burning, have caused the atmospheric concentration of this GHG to increase from 280 parts per million (ppm) to 385 ppm (Figure 1-1), i.e. by approximately 32%, in the period between the pre-industrial time (1880) and 2000 (NOAA, 2010). Note the strong correlation between the increasing CO_2 concentration and increasing temperature after the onset of the industrial revolution in1850 (Figure 1-1). Moreover, recent studies by independent establishments like the Intergovernmental Panel on Climate Change (IPCC, 2007) concluded that increasing atmospheric concentration of anthropogenic CO_2 is the major driving mechanism behind climate change, also known as global warming. For instance, CO_2 constituted more than 77% of the total GHG emitted in 2000 (del Pino et al., 2006).

Of particular interest to this dissertation is Canada's net CO_2 emission, which was approximately 740 megaton (Mt) in 2004 (USDOE, 2009). This amounts to approximately 2.2% of the world's total (28 Gt) anthropogenic CO_2 emission in 2004 (USDOE, 2009). This is very significant given that Canada's population makes up only 0.5% of world's total population and therefore the emissions per gross domestic product (GDP) is relatively high (OECD, 2007). In addition, the country's net CO_2 emission in 2005 has put it at 112% over its 1996 Kyoto protocol emission target of 563 Mt (OECD, 2007). Figure 1-2 shows Canada's historical and projected CO_2 emission in the period between 1990 and 2010 (UNEP, 2008) while Figure 1-3 shows Alberta GHG emissions in CO_2 equivalent with respect to the other provinces in 2004 (see Appendix A.1 for contribution by sectors in Alberta). It is obvious that some measures should to be taken if Canada as a nation, and Alberta in particular, are determined to reduce their CO_2 emissions and meet the Kyoto protocol target.

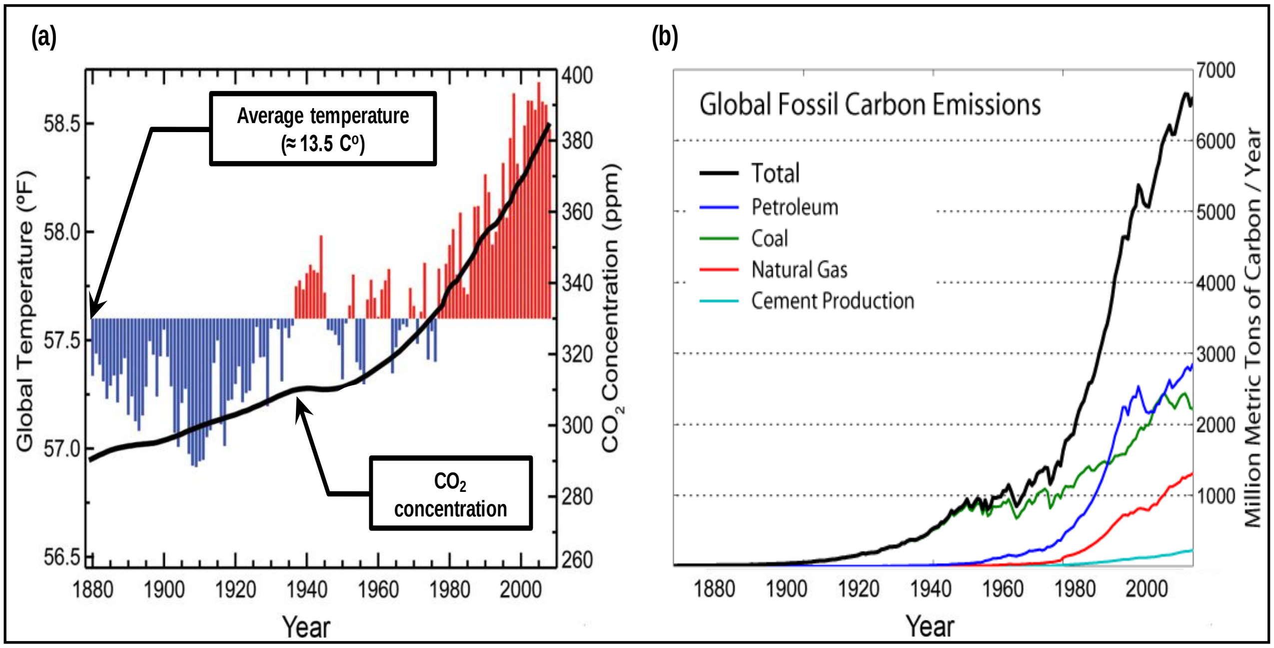

Figure 1-1: (a) average annual global temperature (F^o) and CO_2 concentration (parts per million) in the period between 1880 and 2000. The blue bars indicate temperature below average while red bars represent temperature above average (NOAA, 2010), (b) global CO_2 emissions from fossil fuel consumption between 1800 and 2000 in CO_2 equivalence (UNEP, 2008).

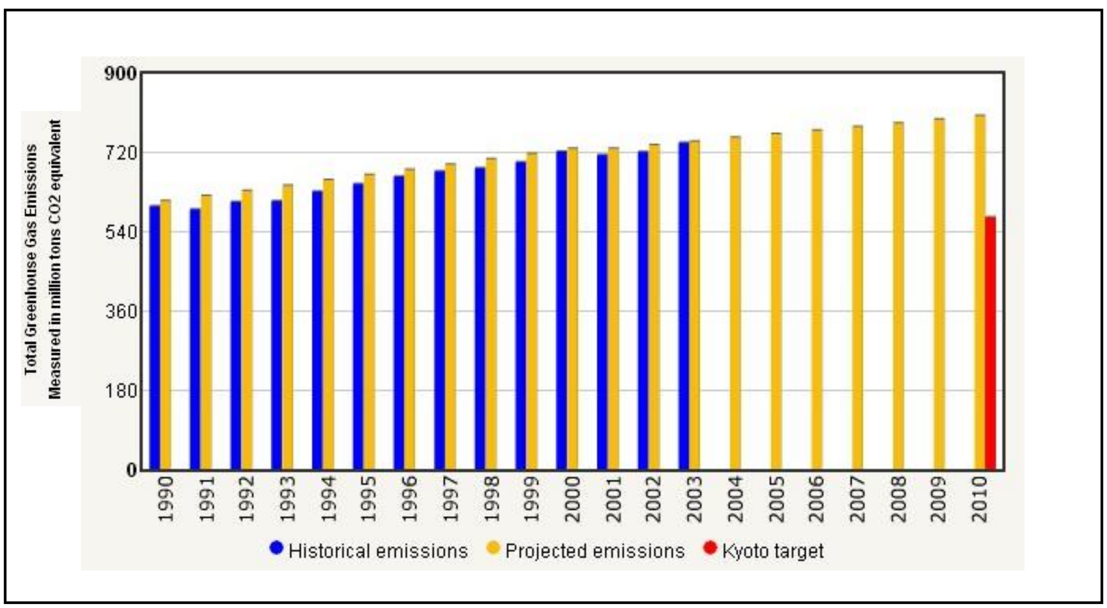

Figure 1-2: Canada's total GHG emissions measured (1990-2003) and projected (1990-2010) in million tons CO_2 equivalent between 1990 and 2010 (UNEP, 2008). The latest published data show that Canada's GHG emissions were 747 Mt in 2007 (Environment Canada, 2009). See Appendix A.1 for contributions by sector in Canada.

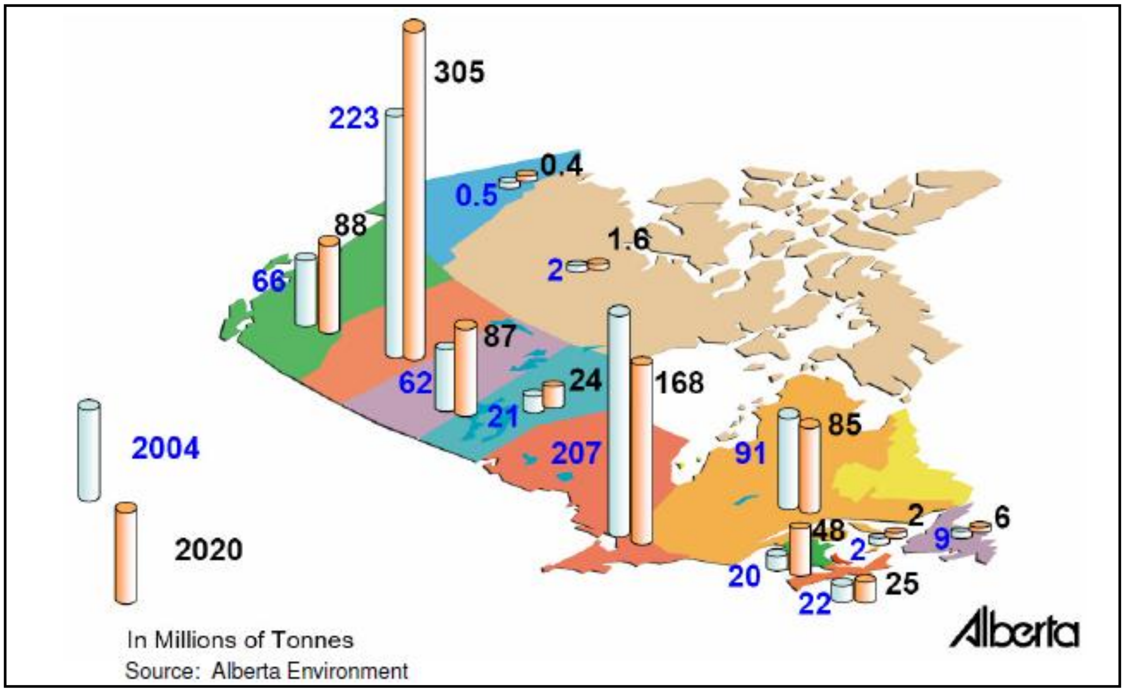

Figure 1-3: Historical and projected Alberta GHG emissions in CO_2 equivalent with respect to the other provinces. CO_2 constituted more than 90% of the total GHG. The latest published data show that Alberta's GHG emissions were ~ 320 Mt in 2007 (Environment Canada, 2009). See Appendix A.2 for contribution by sectors in Alberta.

1.3 Geologic Sequestration of CO_2

1.3.1 Overview

CO_2 sequestration, also known as carbon capture and storage (CCS) in deep geological formations, is a multi-disciplinary technology that consists of three main steps: CO_2 capture, compression and transport, and storage (Figure 1-4). In the first step, CO_2 is captured from a point source either prior to or after combustion via different capturing techniques (IPCC, 2005). Then, it is compressed and transported into the storage site where it is injected into the subsurface aquifer or reservoir, typically in supercritical phase, for long-term storage and/or for enhanced hydrocarbon recovery (EHR).

The viability of the CCS technology has been studied by many including the IPCC, which was established in 1988 by the World Meteorological Organization (WMO) and the United Nations Environment Programme (UNEP). After extensive research involving hundreds of scientists for over a decade, the IPCC published a series of reports one of them entitled Carbon Dioxide Capture and Storage (IPCC, 2005), which substantiates that geological sequestration of CO_2 is feasible and is probably one of the best means available for reducing anthropogenic CO_2 concentration in the atmosphere and, therefore, mitigating climate change. Furthermore, studies have shown that the technology can assist in enhanced oil recovery (EOR) by increasing the amount of recoverable reserve of the original oil in place (OOIP) by 50% as compared to an average of 30% achieved by secondary recovery, commonly using water injection (Lake, 2006; USDOE, 2010).

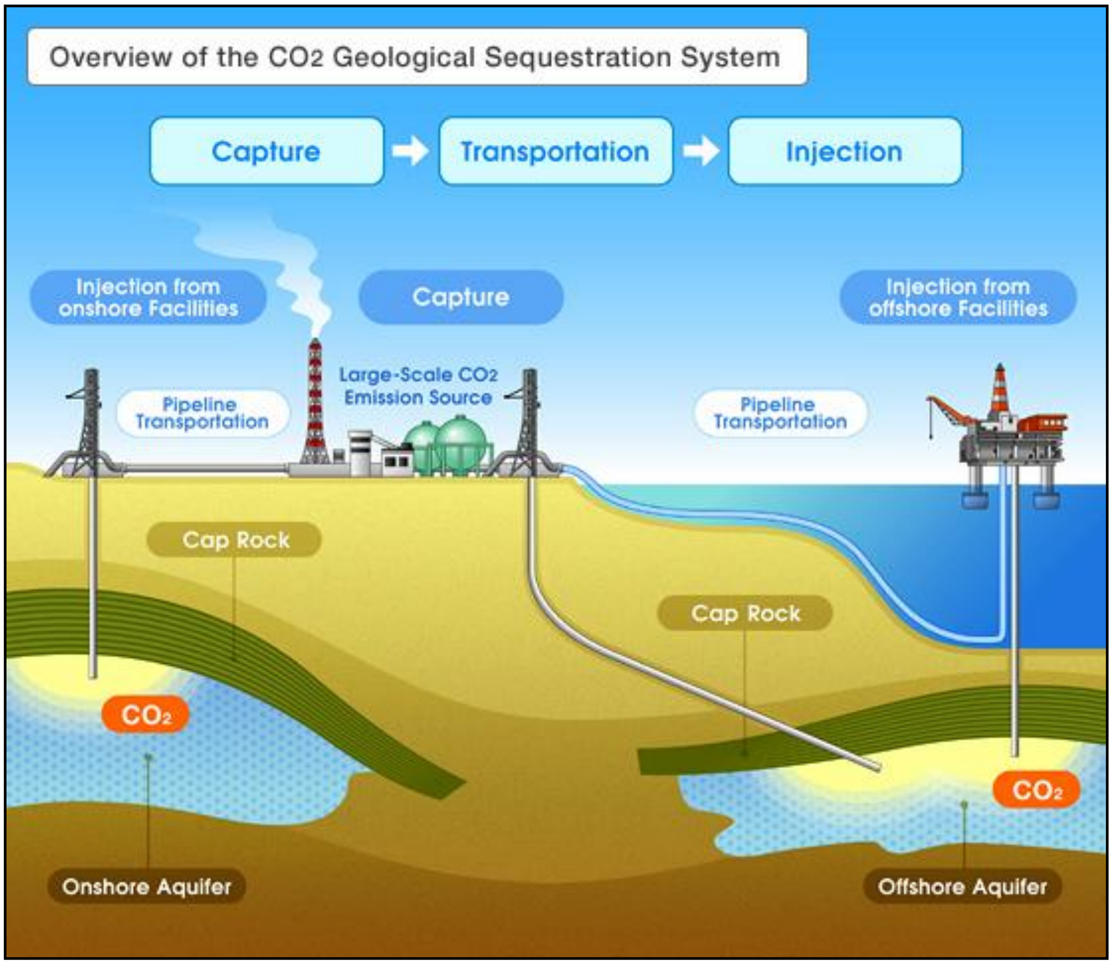

Figure 1-4: Display showing the main steps involved in the CO_2 geological sequestration technology (Japan Petroleum Exploration Co. Ltd., 2008).

There are a number of criteria that dictate whether the implementation of the CCS technology is feasible or not:

(1) Capacity: the volume of pore space available for storage should be sufficient enough to contribute to the reduction of CO_2 concentration in the atmosphere.

The volume is a function of various parameters, such as depth, pressure, temperature, porosity, and permeability (IPCC, 2005).

(2) Injectivity: the rate of CO_2 intake by the reservoir should also be sufficient to accommodate the rate at which it is being captured and transported from the source. Also, care must be taken not to exceed the fracturing pressure (Bachu, 2002).

(3) Confinement: the sequestered CO_2 has to be contained in the storage reservoir. For instance, the reservoir has to have a good and multiple impermeable layers in the stratigraphic column above it. In addition, the injected CO_2 should not cause the reservoir to have a negative effect on neighbouring geologic formations, especially in areas of active hydrocarbon resources (IPCC, 2005).

(4) Safety: the technology implementation, whether in terms of operation or storage integrity, must not pose any health, safety and environmental risks (Benson, 2005).

(5) Cost: a CCS project has to be cost effective (Benson, 2005).

Figure 1-5 shows a simplified depiction of the major disciplines typically involved in the implementation of the CCS technology, with emphasis on geoscience. The role of geophysics, and seismic methods in particular, in the implementation of the CCS technology arises at two different phases: (1) in selecting an appropriate site prior to the commencement of the CO_2 sequestration, and (2) during and after sequestration by providing a mean to monitor the injected CO_2 for environmental (e.g. confinement) and economical (e.g. carbon royalty credit) assessment purposes (Wang, 1997; Benson, 2005; IPCC, 2005; Lumley et al., 2010; Sayers and Wilson, 2010). For instance, multi-component seismic data play an important in site characterization, e.g. anisotropy and fracture detection (Leany, 1994; Schoenberg, 2002; Zhang et al, 2010). In addition, the 4-D information provided by the multi-component data pertaining to the differentiation between pore pressure and CO_2 saturation may be substantial (Liu et al., 2001; Davis et al., 2003). Note that seismic monitoring is only one of the many monitoring, measurement and verification (MMV) techniques, such as atmospheric, geochemical and geomechanical monitoring (Benson, 2005; IPCC, 2005).

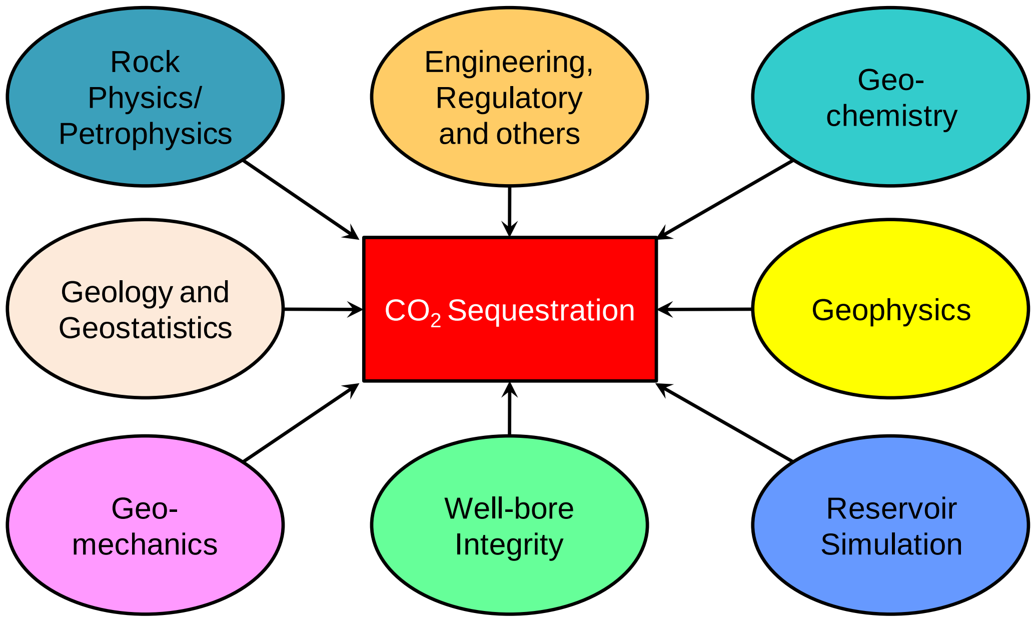

Figure 1-5: A simplified depiction of the various disciplines involved in the CO_2 sequestration technology with emphasis on geoscience.

1.3.2 CO_2 Properties

Carbon dioxide (CO_2) is a chemical compound consisting of two elements: carbon and oxygen. CO_2 is one of many greenhouse gases (GHG) including methane, nitrous oxide and water vapour. The present concentration of CO_2 in the earth's atmosphere is approximately 385 parts per million (ppm), i.e. 0.038% (NOAA, 2010). It is an essential GHG that affects the entire elements making up the earth system: biosphere, hydrosphere atmosphere and lithosphere. For instance, it is a vital ingredient in photosynthesis both in land and in the oceans.

Under standard atmospheric pressure and temperature, CO_2 exists in the gaseous phase and is colorless, relatively odourless, and slightly acidic with density higher than that of air. However, as the pressure and/or temperature vary, the CO_2 undergoes fundamental changes in its state accordingly. The relationship between the various phases as a function of pressure and temperature is illustrated by the phase diagram (Figure 1-6). Table 1-1 summarizes some of the CO_2 properties. Of particular interest to CO_2 sequestration is the supercritical (SC) phase due to the desired properties of carbon dioxide in this phase. Past the critical point (31.1°C and 73.9 bars), the equilibrium between the vapour and liquid phases no longer exists, which results in some interesting behaviour. For instance, CO_2 will have a density closer to that of liquid but its viscosity is more like a gas.

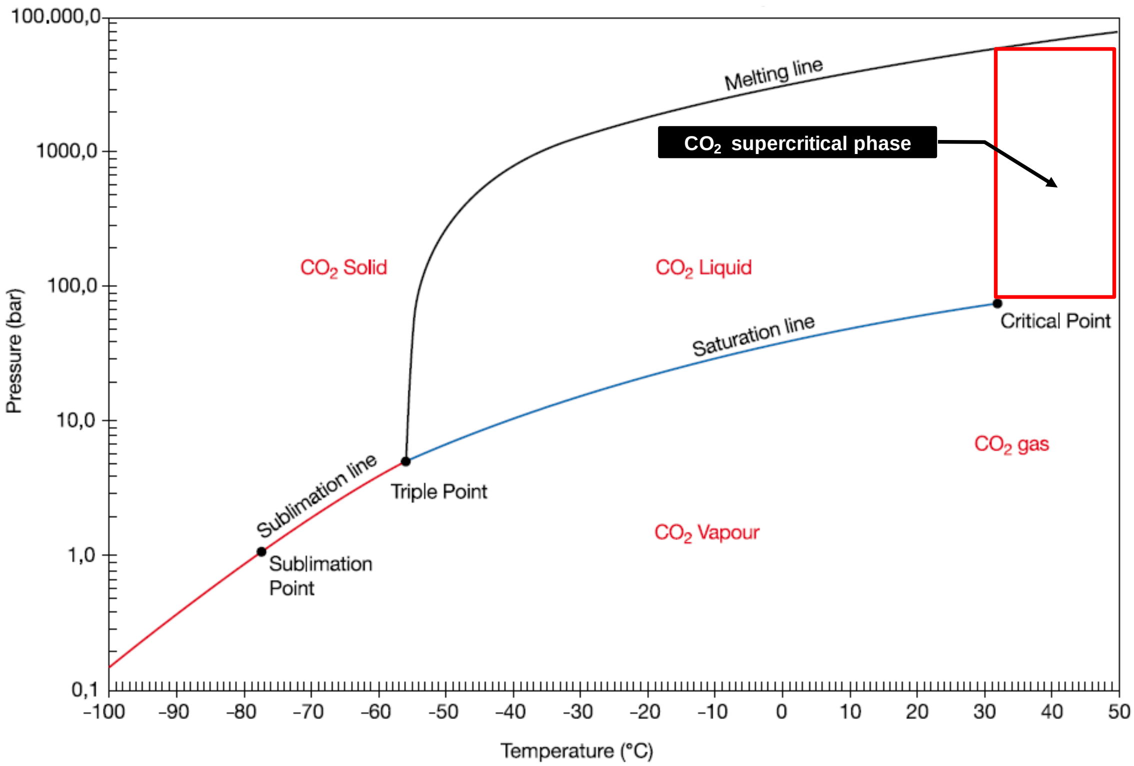

Figure 1-6: CO_2 phase diagram in terms of pressure and temperature (IPCC, 2005). The supercritical region is shown by the red rectangle. 1 bar = 0.1 MPa.

Table 1-1: Compilation of some of the physical and chemical properties of CO_2 (IPCC, 2005; Ursenbach, 2009). STP is standard temperature and pressure. 1 mega Pascal (MPa) = 10 bars.

Substance	Carbon dioxide
Chemical Formula	CO_2
Concentration in the Atmosphere	0.038%
Gas Phase (at STP): Density Incompressibility Viscosity	T = 0^o C; *P* = 0.101 MPa 1.976 kg/m^3 0.132 MPa 13.72×10^{-6} Pa.s
Liquid Phase: Density Incompressibility Viscosity	T = -20^o C; *P* = 5.0 MPa 1073 kg/ m^3 384 MPa 99×10^{-6} Pa.s
Supercritical Phase: Density Incompressibility Viscosity	T = 31.1^o C; *P* = 7.39 MPa 467 kg/m^3 21.8 MPa 13.72×10^{-6} Pa.s
Triple Point Temperature	56.5^o C
Triple Point Pressure	0.517 MPa
Sublimation Point (at P = 0.101MPa)	-78.5^o C
Specific Gravity (at STP)	1.53

1.3.3 CO_2 Trapping Mechanisms

CO_2 interaction and reactivity in the SC phase with the reservoir and the in-situ fluids stimulate different trapping mechanisms (Figure 1-7) which reflect on the storage efficiency. Thus, once CO_2 is injected into the reservoir, the efficiency of the storage depends on a combination of physical and chemical trapping mechanisms. Below is a summary of these various trapping mechanisms:

I. Physical trapping:

I.1. Structural and stratigraphic: this is similar to the way hydrocarbons (HC) are locked in their reservoir. So, once supercritical CO_2 is injected into the host reservoir, it is a free-phase fluid and due to its density, it moves upward due to buoyancy until it reaches the impermeable cap rock (IPCC, 2005). This is an effective and proven closed trap system since hydrocarbons have sustained in such traps for millions of years. In developed fields, induced fractures due to enhanced recovery and surface conduits through improperly completed wells should be taken into consideration.

I.2. Residual: when CO_2 is injected into a reservoir, it displaces some of the in-situ fluids but as the plume moves, some of the CO_2 at the tail of the plume becomes trapped in the pore spaces by capillary forces in what is called non-wetting phase (Bachu, 2002). This means that CO_2 mobility is substantially restricted due to it is being trapped in residual or irreducible saturation, which is analogous to how water is held in a sponge. Over time, this residually trapped CO_2 can dissolve into the formation water.

I.3. Hydrodynamic: this occurs in deep saline formation with no closed trap where, due to its buoyancy, CO_2 migrates along the formation top until it becomes residually trapped or, in the long-term, dissolves in the formation water and becomes part of the saline aquifer system. For the remaining free-phase CO_2, it is estimated that it will take millions of years for it to reach the surface unless it is immobilized by a secondary trapping system. The plume migration is influenced by heterogeneity, temperature and rate of chemical reactions (Bachu et al., 1994).

I.4. Adsorption: This is common in coal seams where injected CO_2 becomes preferentially adsorbed to the coal matrix whereas methane, for instance, is released. This is accompanied by coal surface swelling (Gale and Freund, 2001).

II. Chemical trapping:

II.1. Solubility: this is analogous to the way through which salt, or sugar, dissolves in water. When CO_2 is injected into a water-bearing reservoir, it dissolves in the formation water according to the following chemical reaction (Shevalier et al., 2009):

$$CO_2 + H_2O \rightarrow H^+ + HCO_3^-$$

Thus, CO_2 reacts with the formation water to produce a hydrogen and bicarbonate ions, which causes a small increase in the acidity of the formation water. Solubility dominates at the beginning but it eventually slows down as the reservoir fluids become saturated and the process is then governed by the diffusion and convection rates (IPCC, 2005).

II.2. Ionic: this follows the solubility of CO_2 in the host formation where CO_2 becomes trapped in the aqueous phase. For instance, the dominant CO_2 reaction with carbonate minerals, calcite for instance, is given by the following net reaction (Gunter at al., 1993):

$$CO_2 + H_2O + CaCO_3 \rightarrow Ca^{2+} + 2HCO_3^-$$

Here, in addition to the formation water, CO_2 reacts with the calcite minerals present in the reservoir to produce a calcium ion and two bicarbonate ions (Gunter at al., 1993).

II.3. Mineral: this is analogous to the way shellfish use calcium and carbon from seawater to form their shells. So, in the reservoir, CO_2 reacts with siliclastic minerals, such as feldspar and clay, present in the formation to precipitate calcite and other minerals according to the following net reaction (Gunter at al., 1993):

$$\text{Feldspars} + \text{Clays} + CO_2 \rightarrow \text{Kaolinite} + \text{Calcite} + \text{Dolomite} + \text{Quartz}$$

For example, the reaction of calcium feldspars with CO_2 and water which yields clay and calcite minerals (Gunter at al., 2000):

$$\begin{array}{llll} CaAl_2Si_2O_8 + CO_2 + 2H_2O & \rightarrow Al_2Si_2O_5(OH)_4 & + CaCO_3 \\ [\text{Calcium feldspars}] & \rightarrow [\text{Kaolinite}] & + [\text{Calcite}] \end{array}$$

The main advantage of chemical trapping is that CO_2 no longer exists as a separate phase, which eliminates the buoyancy force driving it toward the surface. However, as can be seen in Figure 1-7 it takes hundreds to thousands of years for chemical trapping to dominate where the rate of dissolution, ionic and mineral trapping is affected by many factors, such as the composition of the reservoir, the water/rock contact area and the rate of fluid flow through the rock. Furthermore, these chemical trapping mechanisms are directly proportional to pressure and inversely proportional to temperature and salinity (IPCC, 2005).

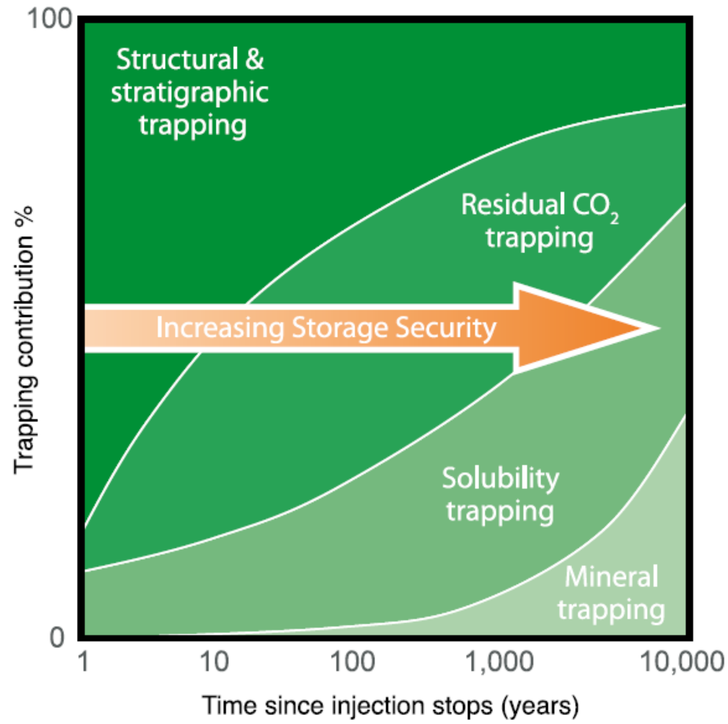

Figure 1-7: Contribution as a function of time of the major CO_2 physical and chemical trapping mechanisms. Initially, mechanical trapping dominates but chemical trapping will increase over with time (IPCC, 2005).

1.3.4 *Supercritical CO_2 Injection and the Time-lapse Seismic Response*

In general and under ideal circumstances in oil reservoirs and saline aquifers, the injection of supercritical CO_2 should result in a number of effects. Below is categorized summary of some of these effects:

I. Effects on the Elastic Properties:

- Supercritical CO_2, typically, has lower density (ρ) than in-situ fluids, e.g. oil or water, which causes the density to slightly decrease with increasing CO_2 saturation (Avseth et al., 2005).
- P-wave speed (α) decreases with CO_2 injection since CO_2 reduces the reservoir incompressibility and slightly reduces its density (Wang, 2001). Thus, causing the P-wave interval traveltime through the reservoir/aquifer to

increase. Depending on the associated magnitude, this 4-D change can be captured by P-wave seismic data.

- The effect associated with S-wave speed (β) is opposite and of smaller magnitude since the rigidity of the reservoir remains unchanged while the density decreases (Mavko et al., 2003).
- The coupled effect of wavespeed (P or S) and density through the acoustic and shear impedances should decrease as CO_2 saturation increases. However, the acoustic impedance decreases at higher rate, typically one order of magnitude higher due to the higher P-wave speed sensitivity to fluid change (Liu et al., 2001).

II. Saturation Effects:

- Under uniform CO_2 saturation, the fluid replacement effect on the elastic properties is most prominent at low CO_2 saturation and tends to reach a plateau at intermediate/high saturation (Vanorio et al., 2010).
- The effect associated with patchy-like saturation tends to be linear and, therefore, the effect may not be significant until intermediate CO_2 saturation (Vanorio et al., 2010).

III. Seismic Wave Attenuation Effects:

- The CO_2 injection should increase seismic wave attenuation in the reservoir and, thus, should incite a shift in the amplitude spectrum towards lower frequencies (Toksöz et al., 1979; Hilterman, 2001).
- The change in the attenuation can be ultimately used in estimating a more desired measure of the reservoir characteristics, namely the quality factor (Q) (Tonn, 1991).

IV. Effects of Rock Stiffness and Micro-structure:

- The ability to detecting changes in CO_2 saturation decreases significantly as the stiffness of the rock increases, e.g. in carbonates and tight sandstones (Avseth et al., 2005).
- The existence of pore space, micro-cracks and their geometry has great influence on the magnitude of the seismic response. In cracked media for

example, the magnitude of the 4-D seismic response tends to increase with CO_2 injection due to the opening of the cracks (Chapman et al., 2000).

V. Effects of Pore Pressure:

- CO_2 injection causes the pore pressure ($P_{\text{pore-pressure}}$) to increase. Thus, decreasing the differential pressure ($P_{\text{differential}}$) if the confining pressure remains unchanged ($P_{\text{confining}}$) (Todd and Simmons, 1972; Hofmann et al., 2005):

$$P_{\text{differential}} = P_{\text{confining}} - P_{\text{pore-pressure}}$$

- Under laboratory measurements and using different pore pressure, Wang and Nur (2001) reported that P-wave speed decreased significantly with CO_2 injection whereas S-wave speed decreased at high pore pressure and increased at low pore pressures in sandstone samples.
- In carbonate, Wang et al. (1998) observed that both P-wave and S-wave speeds decreased with CO_2 injection at pore pressures from 8 to 18 MPa. They indicated that observed changes in P-wave and S-wave speeds could not described by the Gassmann (1951) fluid substitution and that pore pressure must have increased due to the CO_2 injection.
- Since α is sensitive to changes in CO_2 saturation and pore pressure whereas β is sensitive to change in pore pressure only, the latter is considered to be a good indicator of CO_2-saturation/pore-pressure discriminator. Therefore, 4-D multi-component seismic data can be a valuable tool in monitoring the effects of the CO_2 flooding by separating the effects of CO_2 saturation and pore pressure changes (Wang et al., 1998).

VI. Effects of Anisotropy:

- The existence of anisotropy, e.g. azimuthal anisotropy like fractures, and their alignments may have a profound effect on the CO_2 movement as they provide a preferential flow path (MacBeth and Lynn, 2000).
- It has been observed by some authors (Angerer et al., 2000; Davis et al., 2003) that CO_2 injection can cause a considerable change in anisotropy. For example, Angerer et al. (2000) reported about 10% change in anisotropy in the

4-D shear-wave data before and after the CO_2 injection in the Vacuum field, New Mexico, which is higher than the change in the 4-D P-wave. This indicates that multi-component seismic data is very useful in monitoring pressure changes associated with CO_2 injection in fractured reservoirs.

- Similarly, the existence of anisotropy in the overburden, e.g. layering anisotropy like shale, may have a strong effect on the seismic wave propagation and may affect how the reservoir and, eventually, the CO_2 plume are imaged (Vestrum et al., 1999).

VII. Other Effects:

- Include geophysical (data acquisition and processing), geochemical (rock-fluid and fluid-fluid interaction), geomechanical (stress regime) as well as reservoir characteristics, such as depth and temperature, effects.

1.3.5 Industrial Examples

Even before the IPCC report was published in 2005, a large industrial-scale saline aquifer CCS project had already been successfully implemented in the Sleipner field in Norway (Zweigel et al., 2001; Arts et al., 2002; Trop and Gale, 2002; Chadwick et al., 2009). The technology and its seismic component, in the form of site characterization and time-lapse monitoring, has also being implemented in different parts of the world, e.g. in the Weyburn field in Canada for EOR (Brown et al., 2002; Herawati, 2002; Terrell et al., 2002; Davis et al., 2003; Li, 2003; White, 2009), in the In Salah field in Algeria for enhanced gas recovery (EGR) (Riddiford et al., 2003), in the Frio site in the United States for long-term storage in brine formation (Daley et al., 2005), in Ketzin, Germany as part of the CO2SINK project (Wuerdemann et al., 2010) and in China for enhanced coalbed methane recovery (ECBMR) (Yu et al., 2006).

Two of the CCS projects are considered global models in term of the implementation of the CCS technology and, therefore, it is relevant to present an example of the seismic component from each of those two projects. The first is the Sleipner saline aquifer CO_2 storage (SACS) project in Norway while the other is the Weyburn CO_2-EOR project in Canada. Even though the primary incentives behind the two projects are different (i.e. avoiding high CO_2 emission tax versus EOR), they have set industrial scale examples of how the seismic characterization and time-lapse monitoring can be successfully implemented as part of CCS technology and. Figure 1-8 and Figure 1-9 illustrate how surface seismic has aided in the regional site characterization as well as in time-lapse monitoring of the injected CO_2 at the Sleipner field. Similarly, Figure 1-10 shows how time-lapse seismic has been used at the Weyburn field to track the injected CO_2. It is projected that the incremental increase in recoverable oil, due to CO_2 injection, associated with the Weyburn CO_2-EOR project will approximately be 11%, thus increasing the lifespan of the oil field by about 20 years (Petroleum Technology Research Centre, 2008; White, 2009). Table 1-2 summarizes some of the key information pertaining to these two projects.

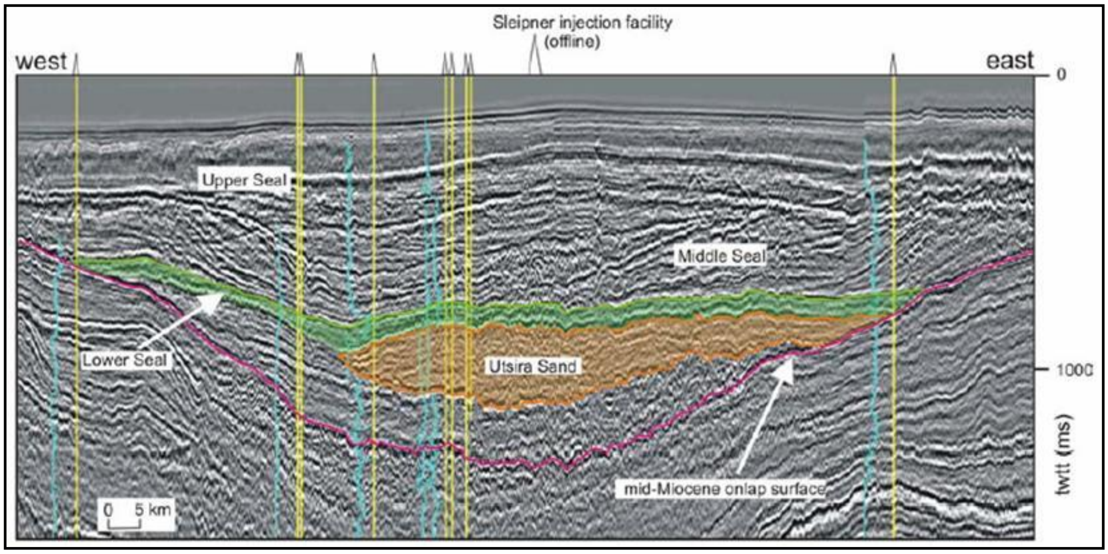

Figure 1-8: Regional P-wave surface seismic reflection section showing the Utsira sand and the various seals (Holloway et al., 2004).

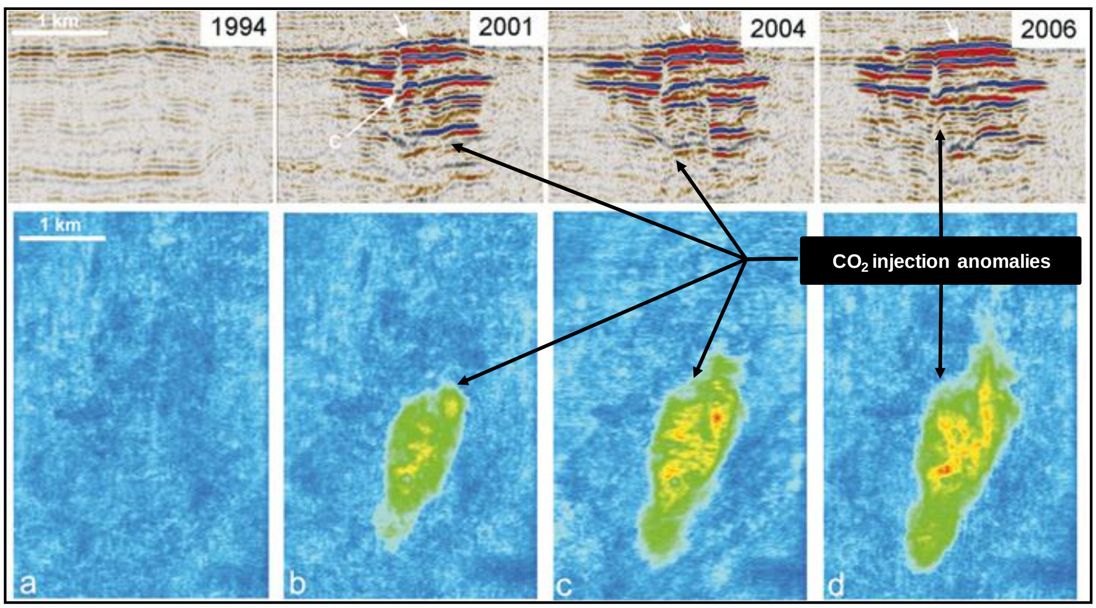

Figure 1-9: P-wave surface seismic reflection data from (a) the baseline survey in 1994 (prior o CO_2 injection), (b) the 2001 monitoring survey, (c) the 2004 monitoring survey, and (d) the 2006 monitoring survey. The CO_2 injection rate was approximately 1 Mt/year. One can clearly see the CO_2-induced amplitude anomaly and time shift. Red: high seismic amplitude; blue: low seismic amplitude. After Chadwick et al. (2009).

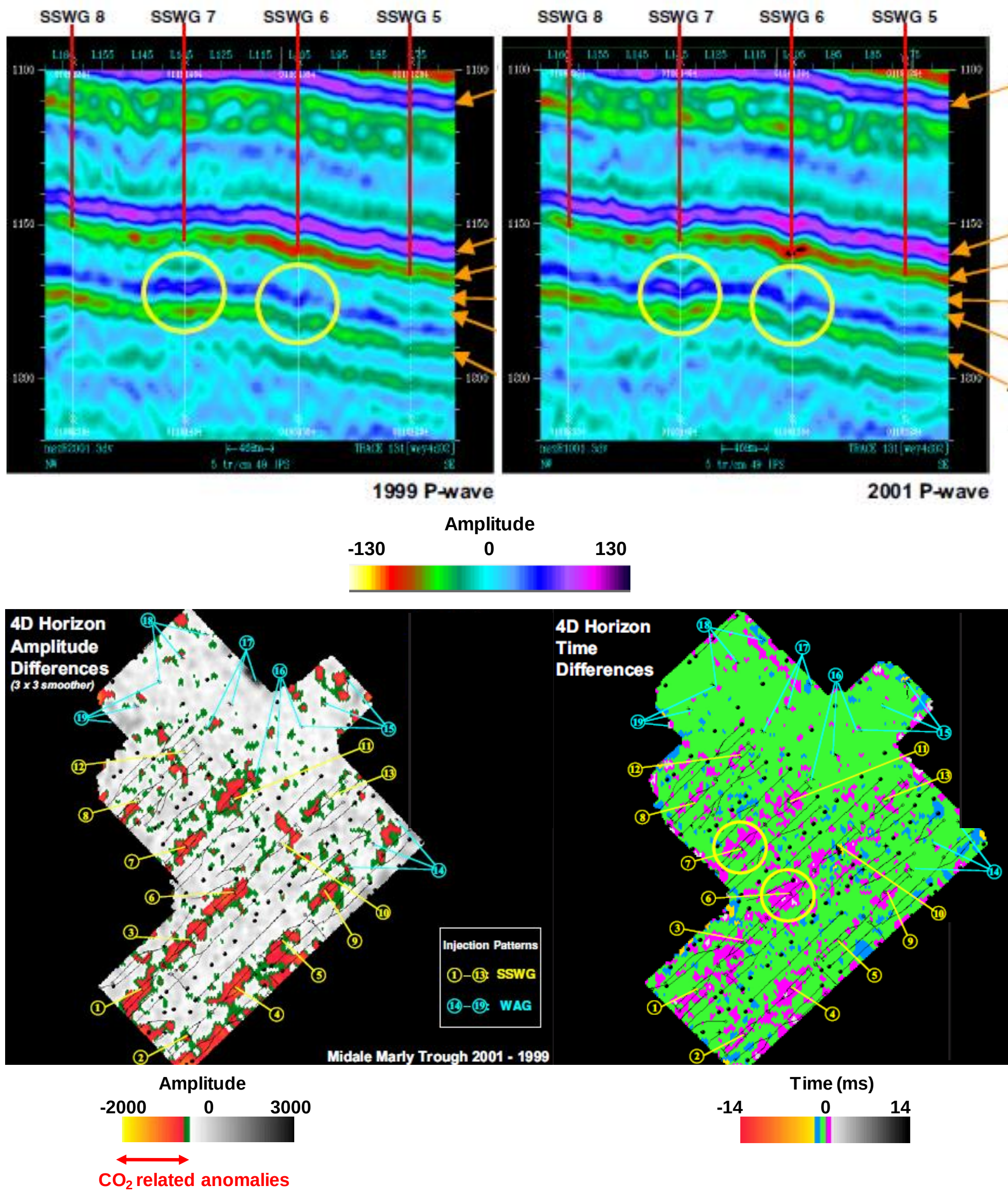

Figure 1-10: Example from the Weyburn field CO_2-EOR project showing a NW-SE oriented P-wave seismic section from the baseline (1999) and monitoring (2001) surveys between which approximately 2 Mt of CO_2 were injected. The extracted section traverses several simultaneous but separate water and gas (SSWG) injection wells. The location of targets, i.e. the Marly dolomite and Vuggy limestone, are shown on the seismic sections. The yellow circles show the locations of some of the anomalies induced by the CO_2 injection. After Li (2003).

Table 1-2: Some of the information and estimated statistics pertaining to the Sleipner and Weyburn projects. 1 Source: Zweigel et al. (2001). 2 Sources: Li (2003); and Petroleum Technology Research Centre (2008). 3 Parts of the activities are continued under the CO2STORE project.

	Sleipner Project[1]	Weyburn Project[2]
Operator	StatoilHydro (now Statoil)	Cenovus (formerly ENCANA; PanCanadian)
Location	North Sea, Offshore Norway	Saskatchewan, Canada
Target Formation	Utsira Sand, saline aquifer	Midale, oil-bearing carbonate (Marly dolomite and Vuggy limestone)
Large-scale Study Area	400 × 65 km	200 × 200 km
Formation Depth	1000 m	1500 m
Formation Thickness	200 – 300 m	3 – 30 m
Pore & Storage Volume	5.5×10^{11} m^3, 6.6×10^8 m^3	-
Temperature & Pressure	37^oC; 9 MPa	60^oC; 14.6 MPa
Storage Capacity of CO_2	42 Gigaton (Gt)	-
Motivations	Long-term CO_2 storage	EOR and long-term CO_2 storage
CO_2 Source	Natural gas	Coal plant
CO_2 Transport	Pipelines (Sleipner Treatment Plant)	325 km pipelines (from Dakota Gasification Plant)
CO_2 Injection Rate	1 Megaton (Mt)/year	1.7 Megaton (Mt)/year
CO_2 Purity	> 90%	95%
Amount of Injected CO_2	~ 10 Mt	~ 26 Mt (by the end of the project)
Commencement	1996	2000
Termination	2002[3]	2011
Average Porosity	27 – 42%	Marly Dolomite: 26% Vuggy Limestone: 15%
Average Permeability	1 – 3 Darcy	Marly Dolomite: 0.01 Darcy Vuggy Limestone: 0.02 Darcy
Original Oil In Place (OOIP)	-	1.4 billion barrel
CO_2 Incremented Oil Recovery	-	155 million barrel (1300 bpd)
Increase in Reservoir Lifespan	-	~ 20 years

1.4 Motivation

CO_2 sequestration is an emerging multi-disciplinary technology, which is suggested to have a big role to play, in addition to green energy technology, in mitigating the excessive emissions of anthropogenic CO_2 (Davison et al., 2001; Chadwick et al., 2001; Benson, 2005; IPCC, 2005). Furthermore, it is suggested that the CCS technology will enable us to significantly reduce CO_2 emissions into the atmosphere, and in some cases recover more fossil fuel from hydrocarbon reservoirs as well, by capturing and injecting CO_2 into producing and/or depleted hydrocarbon reservoir and saline aquifers. Thus, partially achieving the sought after sustainability between the economy and the environment (Benson, 2005; IPCC, 2005; Lumley, 2010). This is of great importance as demand for energy is projected to increase in the coming decades (USDOE, 2009) and given the fact that Canada has the second largest oil reserve in the world, mainly in the form of oil sand that is normally associated with high CO_2 emissions (Environment Canada, 2009; Lakeman, 2009; USDOE, 2009).

In particular, feasibility studies such as those by Bachu, (2001; 2002; 2003), Bachu et al. (2000); Bachu and Shaw (2005), and Michael et al. (2008) advocate that the Western Canada Sedimentary Basin (WCSB) in west-central Alberta holds excellent potential for CO_2 sequestration in depleted hydrocarbon reservoirs for EHR and long-term storage, and even greater potential for long-term CO_2 storage in deep saline aquifers[4]. One aspect of the CCS technology, which constitutes the core of this dissertation, is geological site characterization and time-lapse monitoring using surface seismic and vertical seismic profile (VSP) techniques. These are well-established geophysical methods that have been used for decades in hydrocarbon exploration and reservoir characterization (Kennett et al., 1980; Sheriff and Geldart 1995; Schneider et al., 2000; Lumley, 2004). Furthermore, and as illustrated by the industrial examples in Section 1.3.5, seismic methods will be key element in CCS site selection as well as in the success of a given MMV program as they will provide a mean to monitor the reservoir

---

[4] It is suggested that CO_2 storage capacity in saline aquifers in Alberta is in the order of ~1000 Gt (Bachu and Adams, 2003).

and storage integrity (Benson, 2005; Lumley, 2010; Sayers and Wilson, 2010). Therefore, providing a mean of assessing whether the environmental and economical targets are achieved.

1.5 Objectives

The global objective behind this dissertation is to improve our understanding of the role that seismic methods have to play in CCS site characterization and time-lapse monitoring in the WCSB, in west-central Alberta by using reflection seismic techniques, as part of the CCS multi-disciplinary framework, at the Pembina Cardium CO_2-EOR Project (PCEP) and the Wabamun Area CO_2 Sequestration Project (WASP) study areas.

In the PCEP context, interpretation of the surface seismic (Chen, 2006) and VSP (Couëslan, 2007) datasets from the second[5] phase of the project did not exhibit a clear time-lapse signature nor did it reveal any conclusive information about the CO_2 plume distribution and migration in the reservoir (i.e. Cardium Formation). One of the conclusions emerging from those studies suggests that the time-lapse seismic monitoring program might be more successful in delineating the CO_2 plume during the third[6] (and final) phase of the project. The following summarizes the two main objectives pertaining to the PCEP:

- Analyze the dataset from the second monitoring survey (Phase III) in reference to the baseline survey (Phase I) in an effort to detect the CO_2 plume. The current work aims at estimating the time-lapse response using rock physics with more rigorous choice of parameters that takes into consideration not only the petrophysical but the geochemical data as well. This is followed by numerical modelling, using acoustic finite-difference (F-D) and ray tracing (RT) modelling schemes, to assess whether the surface seismic and VSP methods are capable of detecting and mapping the CO_2 plume.
- The second primary objective is to demonstrate confinement of the injected CO_2 to Cardium Formation and evaluate the methods sensitivity to CO_2

[5] The phase II data was acquired after the injection of approximately 20 kiloton (Kt) of CO_2.
[6] By the time of phase III, more than 50 Kt of CO_2 had been injected in the reservoir.

detection above the reservoir. Furthermore, independent information from other monitoring activities, primarily reservoir fluids composition analysis, would be compared with the seismic interpretation in order to draw more concrete conclusions about the CO_2 plume movement and distribution.

The objectives in the case of WASP are fairly different[7] as this is an assessment study and therefore no CO_2 sequestration has commenced yet. So, instead the objectives are mainly focused on the aspects of seismic site characterization and time-lapse feasibility analysis, which can be summarized as follows:

- Use P-wave reflection surface seismic data to thoroughly map the target saline aquifer (i.e. Nisku Formation) and evaluate its suitability for 1 Mt per year CO_2 sequestration project by delineating zones with favourable qualitative and quantitative attributes, such as low acoustic impedance. This involves identifying geologic discontinuities, such as faults and sinkholes, that might compromise the integrity of the Nisku Formation and the overlying cap rock.
- Time-lapse feasibility modelling, using rock physics and numerical methods, are undertaken to predict how the acoustic response of the Nisku Formation would be affected by a hypothetical CO_2 injection, and therefore determine whether a time-lapse seismic program would be capable of delineating the corresponding CO_2 plume.

Numerical modelling, rock physics as well as qualitative and quantitative interpretation form the key assets employed in achieving these objectives. It should be noted that the numerical modelling schemes employed in this dissertation invokes only the acoustic or compressional wavefield.

[7] Even though some of the tools used are analogous to those used in PCEP,

1.6 Data

The dataset utilized in this dissertation can be divided into two main categories: seismic data and borehole data. No particular seismic data was acquired as part of WASP. Instead, access to enormous compressional wave (P-wave) surface seismic database available from hydrocarbon exploration in and around the area was provided through the generous contribution of EnCana Corporation® (now Cenovus Energy®) which is also one of the industry partners of WASP. Also, four regional 2-D seismic sections were kindly provided by Canada's LITHOPROBE® Geoscience Project[8]. In PCEP, on the other hand, an elaborate survey design was undertaken as part of the project using two multi-component seismic methods, namely surface seismic and walkaway VSP (Lawton, 2005; Lawton et al., 2005). The acquisition and processing of the surface seismic data was outsourced to CGGVeritas® while the processing of the walkaway VSP data was assigned to Schlumberger® Geophysical Services. Brief generic description of the means of acquiring seismic data using the two formerly mentioned methods is given in Chapter 3 whereas specific information pertaining to the WASP and PCEP seismic datasets are found in the corresponding chapters, i.e. Chapters 5 and 7, respectively.

In the context of this dissertation, borehole data provides supplementary information, in terms of wireline logs, petrophysical and geochemical properties, that complemented the seismic data. In general, wireline logging is based on making a detailed log of physical properties, such as transient time and bulk density, of geologic formations by taking measurements at small increments, typically 10 cm, along the borehole (Sheriff, 2002). Therefore, given the appropriate borehole data in the study areas, such data was mainly exploited in: (1) correlating the seismic with the geology, (2) rock physics modelling, and (3) numerical modelling. The major source of the borehole data in this dissertation is public database available through AccuMap™ and GeoSCOUT™ (see the next section, i.e. Section 1.7). However, some additional analyses

[8] This is a collaborative national earth science research project that investigates "the structure and evolution of Canada's landmass and continental margins" (LITHOPROBE, 2010).

were conducted as part of WASP and PCEP, such as core analysis and fluid sampling, which were occasionally exploited in this dissertation.

1.7 Software and Hardware

The work undertaken in this accessed the following software:

- NORSAR-2D™: is a 2-D seismic modelling system based on ray-tracing algorithms. The software is developed by NORSAR®. It operates on a Linux platform and is ran using one of CREWES Linux servers.
- Reflexw™: is a small, yet impressive, Windows™ based software package for 2-D and 3-D seismic data processing and interpretation with a modelling module. The software is developed by Sandmeier Scientific Software®.
- Hampson-Russell™: is a powerful 2-D and 3-D seismic interpretation software suite specializing in AVO analysis, seismic inversion, and reservoir characterization. The package runs on both Windows™ and Linux based operating systems. The suite is developed by Hampson-Russell®, a CGGVeritas Company®. The primary software interface is called GeoView© and it has nine modules. The four modules used in this dissertation are:
    - eLOG™: a well log editing and modelling tool, e.g. well-to-seismic correlation.
    - AVO™: as the name implies, this module is used for amplitude-variation with offset modelling.
    - STRATA™: an inversion module used in the process of estimating the underlying geology from seismic data.
    - PROMC™ and PRO4D™: two modules where multi-component and time-lapse seismic interpretation is facilitated. The modules have a library of functions for the display, comparison, calibration, interpretation and inversion of multiple vintage 3-D seismic data. It, also, incorporates many of the toolkits in the other modules, e.g. well log, fluid replacement and rock physics modeling, synthetic seismic generation.

- VISTA™ Seismic Processing: a Windows™ based software package for quality control and processing of 2-D and 3-D seismic data developed by Geophysical Exploration and Development Company (GEDCO®).
- SeisWare™: a well-built Windows™ based seismic interpretation solutions system developed by SeisWare International Incorporation®.
- KINGDOM™: a geological and seismic interpretation Windows™ based suite by Seismic Micro-Technology® (SMT). The software comes with a number of packs and modules.
- MATLAB™: a technical computing software developed by MathWorks® and runs on both Windows™ and Linux based operating systems. The software is used in conjunction with an outstanding library of functions written by CREWES director Professor Gary Margrave.
- Microsoft Office™: a suite of office interrelated applications by Microsoft Corporation® that operates on both Windows™ and Linux platforms. The key applications used are:
    - Microsoft Word: for word processing and dissertation write-up.
    - Microsoft Excel: for simple computation and some data organization and tabulation aspects.
    - Microsoft PowerPoint: to prepare illustrations.
- Windows Vista™: software operating system by Microsoft Corporation®.
- Linux: a free open-source Unix-like graphical user interface (GUI) based computer operating systems distributed by Free Software Foundation Incorporation© under the GNU General Public License.
- AccuMap™: a Windows™ based application by Information Handling Services® (IHS) that provides access to up-to-date geo-information databases, including land, wells, well logs, production data and many other information pertaining to the oil and gas industry in the Western Canadian Sedimentary Basin.
- GeoSCOUT™: a Windows® based database system by geoLOGIC Systems Limited® that integrates public and proprietary data on wells, well logs, land,

fields and many other geo-information in the Western Canadian Sedimentary Basin.

- Utilities: the following applications were used to allow for remote access to the Linux servers and facilitate data transfer:
  - PuTTY©: a free implementation of Teletype Network (Telnet) and Secure Shell (SSH) for Windows and Unix platforms written and maintained primarily by Simon Tatham.
  - TightVNC Viewer©: a free remote control, i.e. Virtual Network Computing (VNC), software package developed by the TightVNC Group®.
  - WinSCP©: a free open source Shell File Transfer Protocol (SFTP) Client, secure File Transfer Protocol (FTP), and Secure Copy (SCP) client for Windows™ operating system using SSH. WinSCP© is developed primarily by Martin Prikryl.
  - All of three applications described above are distributed under the GNU General Public License (Free Software Foundation Incorporation©).

All the work encompassed in this dissertation, including analysis and writing, was performed on a personal computer (PC) workstation with Windows Vista™ operating system. However, access to Linux servers and clusters was necessary for the numerical modelling and seismic data processing. This was facilitated through the use of the utilities software described above.

1.8 Thesis Structure

The dissertation is comprised of 8 chapters and 3 appendices. Chapter 1 establishes the motivations of this dissertation by briefly reviewing the relationship between increasing anthropogenic CO_2 emissions and climate change. In addition, a brief discussion of the CO_2 sequestration technology is given. Then, the motivations and objectives of the research, data and software/hardware implemented are, also, introduced. The location and geology corresponding to the WASP and PCEP study areas are discussed in Chapter 2. In addition, some of the petrophysical and geochemical properties of the geologic formations of interest in these study areas are introduced as well.

Rather than introducing the various methods implemented in this dissertation at the first encounters, it is deemed appropriate to dedicate a chapter, namely Chapter 3, to give a brief review of these methods. This is due in reason to the diversity of the methods, which include seismic methods, forward and inverse numerical modelling methods, rock physics modelling methods, and numerous quantitative interpretation techniques. This departure, also, serves another purpose that is to avoid over-saturating the analyses and interpretation chapters (4, 5, 6 and 7) by laying down the foundation such that the focus can instead be drawn to the approach adopted in implementing these methods and the achieved results.

The detailed seismic characterization in the WASP study area using 2-D and 3-D surface seismic data is presented in Chapter 4. This involves, data analysis, which consists of data calibration and normalization, as well as qualitative and quantitative interpretation including seismic attributes, such as the difference method and post-stack acoustic impedance inversion.

Chapter 5 is a continuation of Chapter 4 in which the seismic characterization from the field data is reassessed using rock physics and numerical modelling. First, information compiled from Chapters 2 and 4 is used to build a model representing the major geology within the study area. Following that, a fluid substitution modelling (FSM) approach is developed based on petrophysical and geochemical data and using rock physics models that are well–established in the literature. The FSM offers quantitative estimate of changes in the elastic moduli as a result of introducing supercritical CO_2 into the in-situ fluid(s). Then, finite-difference (F-D) acoustic wave-equation (AWE) modelling is performed to determine the feasibility of time-lapse seismology in detecting and mapping the prospective CO_2 plume as part of monitoring measurements and verification (MMV) program.

Chapter 6 describes the time-lapse analysis of the field seismic data from the established PCEP study area. In this chapter, qualitative and quantitative interpretations of the surface seismic and vertical seismic profile (VSP) data are undertaken. In the case of the VSP data, the analysis is extended to the raw data in which attributes, such as spectral ratio, are investigated. The post-stack analysis includes statistical, such as NRMS repeatability and predictability, as well as other seismic attributes, e.g. spectral decomposition.

The analysis in Chapter 6 is then complemented by the FSM and numerical seismic modelling using F-D and ray tracing (RT) methods in Chapter 7. Similar approach to that of Chapter 4 is pursued, i.e. first a geologic model is adopted followed by the rock physics and F-D modelling. In addition, ray trace modelling is invoked to understand the VSP response to the injection of supercritical CO_2. The primary objective behind the modelling therein is to explain the lack of discernible time-lapse signature in the field seismic data from Phase II of the project and assess whether the surface seismic and VSP methods are capable of detecting and mapping the injected CO_2 conclusively at the PCEP study area.

Chapter 8, provides conclusions and recommendations pertaining to the seismic component of WASP and PCEP are assembled. Furthermore, observations are drawn in regard to the seismic performance and suitability for site characterization and MMV for carbon capture and storage (CCS) in the WCSB in Alberta based on the concurrent experience at those two sites. Context for potential future research is also speculated upon.

Appendices, A, B, and C are repository for complementary materials to chapters 1, 5 and 6, respectively, and will be referred to in the appropriate context throughout the dissertation. Appendix A contains supplementary materials to some of the topics covered in Chapter 1. Complementary materials to the WASP numerical modelling are found in Appendix B. Processing flowcharts and acquisition parameters table among other PCEP field data related information are found in Appendix C.

CHAPTER 2: STUDY AREAS AND GEOLOGY

2.1 Introduction

The Wabamun Area CO_2 Sequestration Project (WASP) and the Pembina Cardium CO_2-EOR Project (PCEP) study areas are both located within the province of Alberta south-west of the capital Edmonton (Figure 2-1). They also coexist within the Western Canada Sedimentary Basin (WCSB), which is a large sedimentary basin extending underneath Alberta, southern Saskatchewan, south-western Manitoba, north-eastern British Columbia and the south-west corner of the Northwest Territories (Figure 2-2). The WCSB is an immense wedge, approximately 1.4×10^5 km^2, of Phanerozoic sedimentary strata overlying Precambrian crystalline basement rock (Figure 2-3). It extends from the eastern edge of the Canadian Rocky Mountain in the west to the south-western margin of the Canadian Shield in the east (Mossop and Shetsen, 1994; Wright et al., 1994). It is thickest, about 5 km, under the Rocky Mountains and it thins toward the east until it terminates at its eastern margins (Figure 2-2 (b)). The principle horizontal stress in the WCSB is usually in a north-east south-west direction (Bell and Bachu, 2003). In addition to its potential for large-scale CO_2 geological sequestration (Bachu, 2001), the WCSB within Alberta has one of the world's largest hydrocarbon reserves (ERCB, 2009; USDOE, 2010).

Like other sedimentary basins, the WCSB was formed under the influence of three primary factors (Mossop and Shetsen, 1994): eustasy (i.e. relative change in sea level), tectonic activity (e.g. uplift and subsidence), and sedimentation (i.e. weathering, transportation and deposition of sediments). Most of the sedimentary strata within the WSCB were deposited above sea level or in shallow seas but due to tectonic activity and sedimentation-induced subsidence, they are now found at the currently observed depth (Vigrass, 2010). Rocks within the WCSB range in geologic age from Cambrian (about 550 million years before present) to late Tertiary (about 2 mybp). Tertiary consolidated rocks are covered by blanket of unconsolidated glacial drift that accompanied continental ice sheets during the Pleistocene Epoch (about 2 mybp to 11,000 years before present).

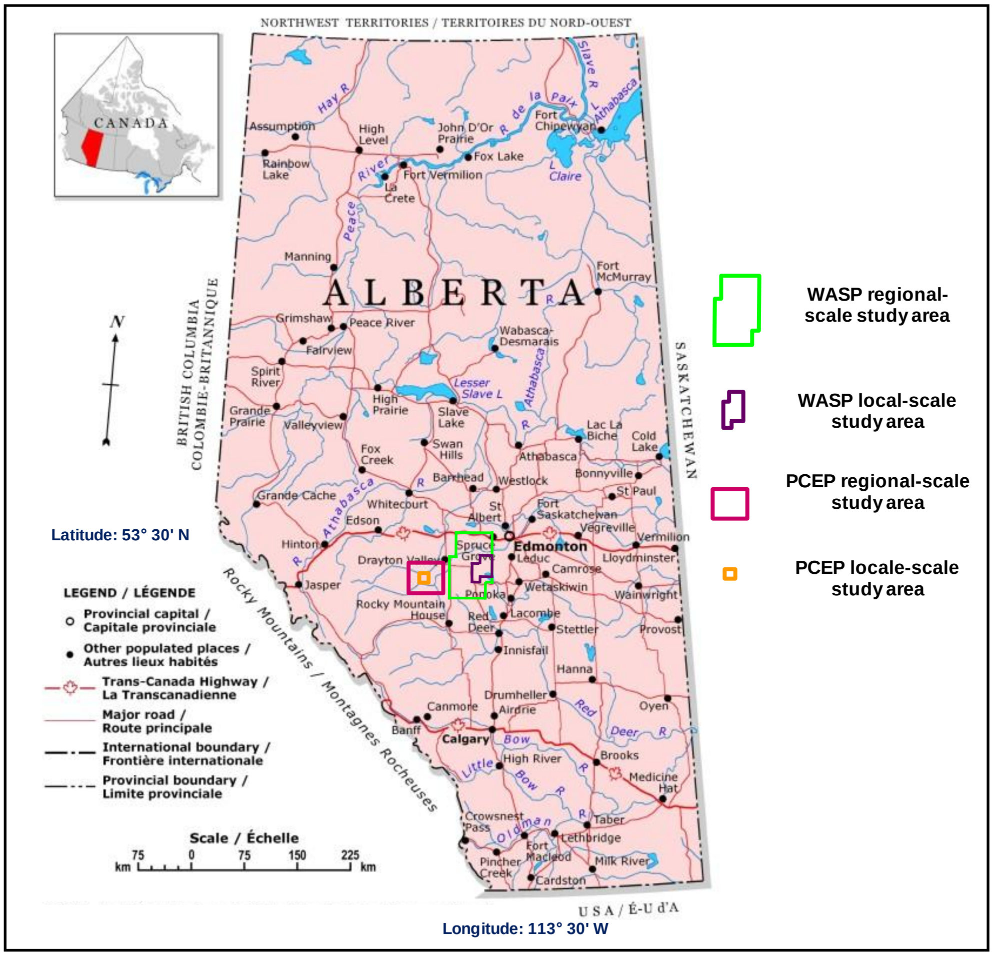

Figure 2-1: Alberta map with the locations of the WASP and PCEP study areas (Natural Resources Canada, 2009).

Based on geologic conditions, strata within the WCSB can be divided into two main categories (Mossop and Shetsen, 1994):

i. Lower succession, which consists mainly of carbonate rocks (limestone and dolostone) with some evaporite (e.g. anhydrite) and siliclastic (mainly shale) rocks. This succession is characterized by long period of passive margin deposition that preceded the major uplift of the Canadian Cordillera. It ranges in geologic age from Cambrian (about 550 mybp) to Jurassic (about 150 mybp).

ii. Upper succession, which is composed primarily of coarse to fine siliclastics (shale, sandstone, and siltstone). This succession was formed after the major mountain building and uplift in the Canadian Cordillera and is associated with the formation of deep foreland basin. It ranges in geologic age from Cretaceous (about 150 mybp) to late Tertiary (about 2 mybp).

Bachu (2003) and IPCC (2005) among others have investigated the suitability of geologic media for CO_2 sequestration. For instance, Bachu (2003) compiled a list of criteria according to which a sedimentary basin is given a class between 1 and 5 based on its suitability for CO_2 sequestration, where 1 indicates poor medium and 5 designates good medium (Table 2-1). In particular, the feasibility of CO_2 sequestration in hydrocarbon and saline aquifers within the WCSB in Alberta has been extensively investigated by many including Bachu (2001), Bachu et al. (2000), Bachu and Shaw (2005), and Michael et al. (2008). Bachu and Shaw (2005) predict that approximately 3.3 Gigaton (Gt) of CO_2 could be sequestrated in the WCSB hydrocarbon reservoirs while much more than that could be stored in saline aquifers (Bachu et al., 1994). Furthermore, Bachu and Stewart (2002) divided the WCSB into several regions (Figure 2-4) based on the basin sustainability for CO_2 sequestration, which is dictated by criteria like those given by Bachu (2003). The WASP and PCEP study areas are both located within a “very good” basin sustainability zone (Figure 2-4).

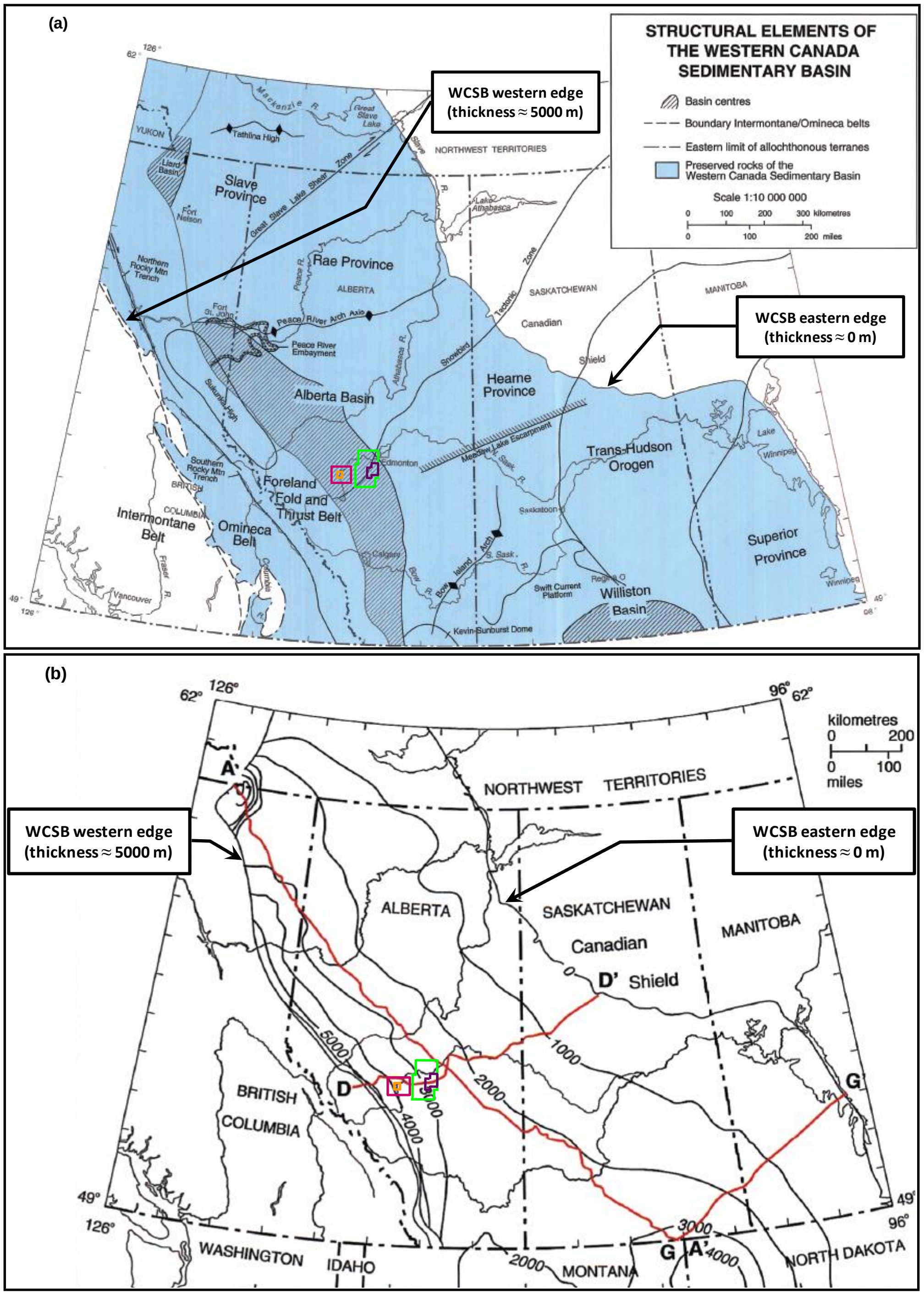

Figure 2-2: (a) Map of the Western Canada Sedimentary Basin. (b): Isopach map of the WCSB showing the thickness of the Phanerozoic sedimentary strata. The WCSB is thickest along the western edge (~ 5000 m). The red line (D-D’) shows the location of the geologic cross-section in Figure 2-3. The approximate locations of the two study areas are shown by the corresponding polygons and colors (see Figure 2-1). After Wright et al. (1994).

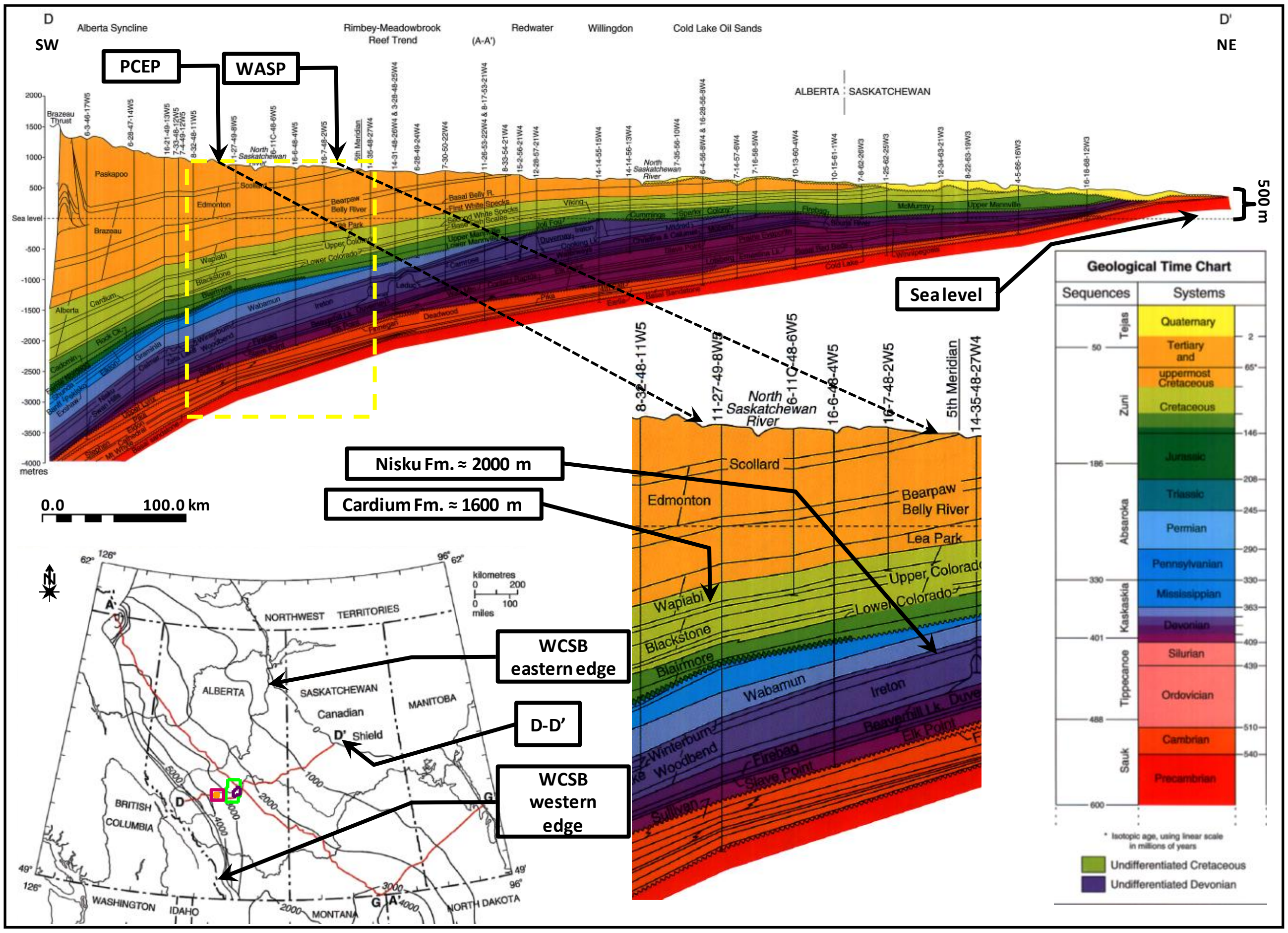

Figure 2-3: Geologic section across the Western Canada Sedimentary Basin (WCSB) in the northeast-southwest (i.e. dip parallel) direction. The dashed yellow rectangle shows the stratigraphic subdivisions (represented by colors) in the WASP and PCEP study areas. The locations of the Upper Devonian Nisku Formation and the Upper Cretaceous Cardium Formation are indicated in the enlarged segment of the cross-section. After Wright et al. (1994).

Table 2-1: Criteria for assessing sedimentary basins for CO_2 geological sequestration. Class 1 indicates poor basin whereas class 5 indicates good basin (Bachu, 2003).

	Criterion	Classes				
		1	2	3	4	5
1	Tectonic setting	Convergent oceanic	Convergent intramontane	Divergent continental shelf	Divergent foredeep	Divergent cratonic
2	Size	Small	Medium	Large	Giant	
3	Depth	Shallow (<1,500 m)	Intermediate (1,500–3,500 m)	Deep (>3,500 m)		
4	Geology	Extensively faulted and fractured	Moderately faulted and fractured	Limited faulting and fracturing, extensive shales		
5	Hydrogeology	Shallow, short flow systems, or compaction flow	Intermediate flow systems	Regional, long-range flow systems; topography or erosional flow		
6	Geothermal	Warm basin	Moderate	Cold basin		
7	Hydrocarbon potential	None	Small	Medium	Large	Giant
8	Maturity	Unexplored	Exploration	Developing	Mature	Over mature
9	Coal and CBM	None	Deep (>800 m)	Shallow (200–800 m)		
10	Salts	None	Domes	Beds		
11	On/Off Shore	Deep offshore	Shallow offshore	Onshore		
12	Climate	Arctic	Sub-Arctic	Desert	Tropical	Temperate
13	Accessibility	Inaccessible	Difficult	Acceptable	Easy	
14	Infrastructure	None	Minor	Moderate	Extensive	
15	CO_2 Sources	None	Few	Moderate	Major	

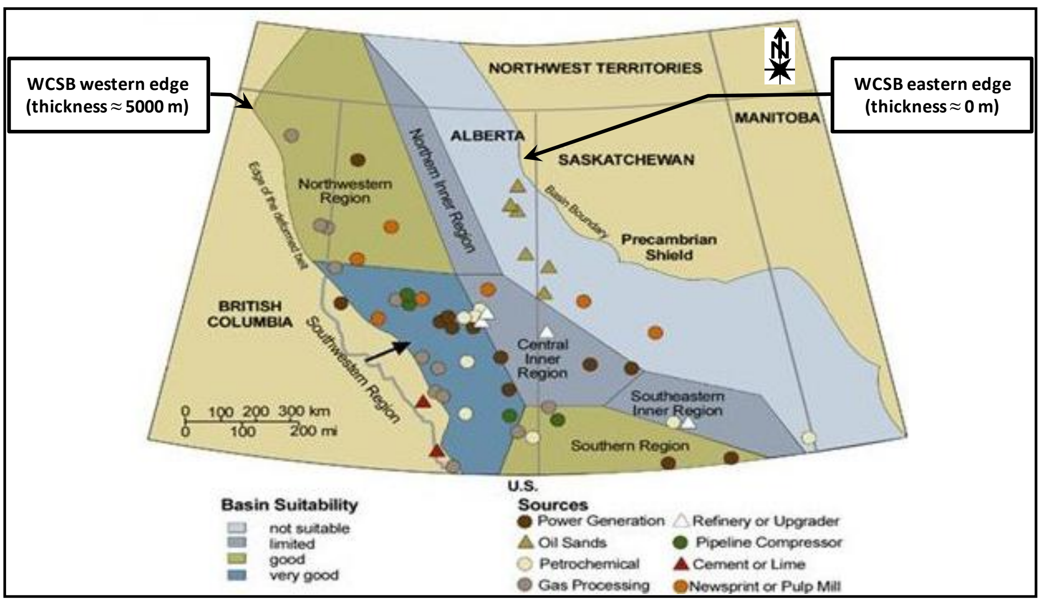

Rank	Region	Characteristics	Score
1	SW Alberta	Deep; cold basin; regional and erosional flow; oil, gas, coal and salts; major CO_2 sources and infrastructure	1.00
2	SE Alberta	Intermediate depth; cold basin; regional flow; oil, gas and coal; major CO_2 sources and infrastructure	0.71
3	Eastern Alberta	Intermediate-to-shallow depth; cold-to-warm basin; regional and local flow; oil, gas and salts; major CO_2 sources and infrastructure	0.53
4	NW Alberta	Deep; high geothermal gradients; regional flow; oil, gas and coal; less accessible; few CO_2 sources and infrastructure	0.40
5	NE Alberta	Shallow; warm basin; local flow; bitumen, gas and salts; a few very large sources and limited infrastructure	0.30

Figure 2-4: Map of the WCSB with the locations of major CO_2 point source emitters. The WASP and PCEP study areas (see Figure 2-1) are located in the SW Alberta region and therefore according to the classification by Bachu (2003), they exist within the "very good" basin sustainability zone (rank 1 and score 1) as indicated by the black arrow (Bachu and Stewart, 2002).

2.2 Wabamun Area CO_2 Sequestration Project (WASP) Study Area

The WASP study area is located approximately 50 km southwest of Edmonton in the vicinity of the Wabamun Area (Figure 2-1). Figure 2-5 shows a map of the WASP study area while a regional cross-section through the WCSB that illustrates the general stratigraphic setting of the strata across the WASP study area is shown in Figure 2-3. The CO_2 sequestration target is the Upper Devonian dolomitic Nisku Formation, which attains a thickness and depth range of 40-100 m and 1700-2200 m, respectively (Watts, 1987; Switzer et al., 1994).

In the regional-scale WASP study area (Figure 2-5), the Nisku Formation can be divided into three distinct regions (Watts, 1987; Switzer et al., 1994; Michael et al., 2008; SCG, 2009):

i. Nisku evaporite basin (to the east), which is composed primarily of anhydrite lithofacies with mixture of dolomite and mudstone and is interbedded with shale.

ii. Nisku shelf (in the middle), which consists mainly of fossil-bearing open marine dolomitized carbonate lithofacies.

iii. Nisku shale basin (to the northwest), this is dominated by shale lithofacies but contains some reef build-ups such as those observed in the Moon Lake reef play area. The Nisku shelf and shale basin are separated by the Nisku ramp, which is characterized by clastic carbonate lithofacies.

Figure 2-6 and Figure 2-7 show two geologic cross-sections in the study area that depict some of the Nisku Formation stratigraphic setting as well as some of its lithofacies variations. The sedimentary strata dip toward the southwest with a fairly gentle slope of 9 m/km and no sign of faulting is observed in the area (Michael et al, 2008). Figure 2-8 shows a rather conceptual model of the Nisku Formation lithofacies in the study area.

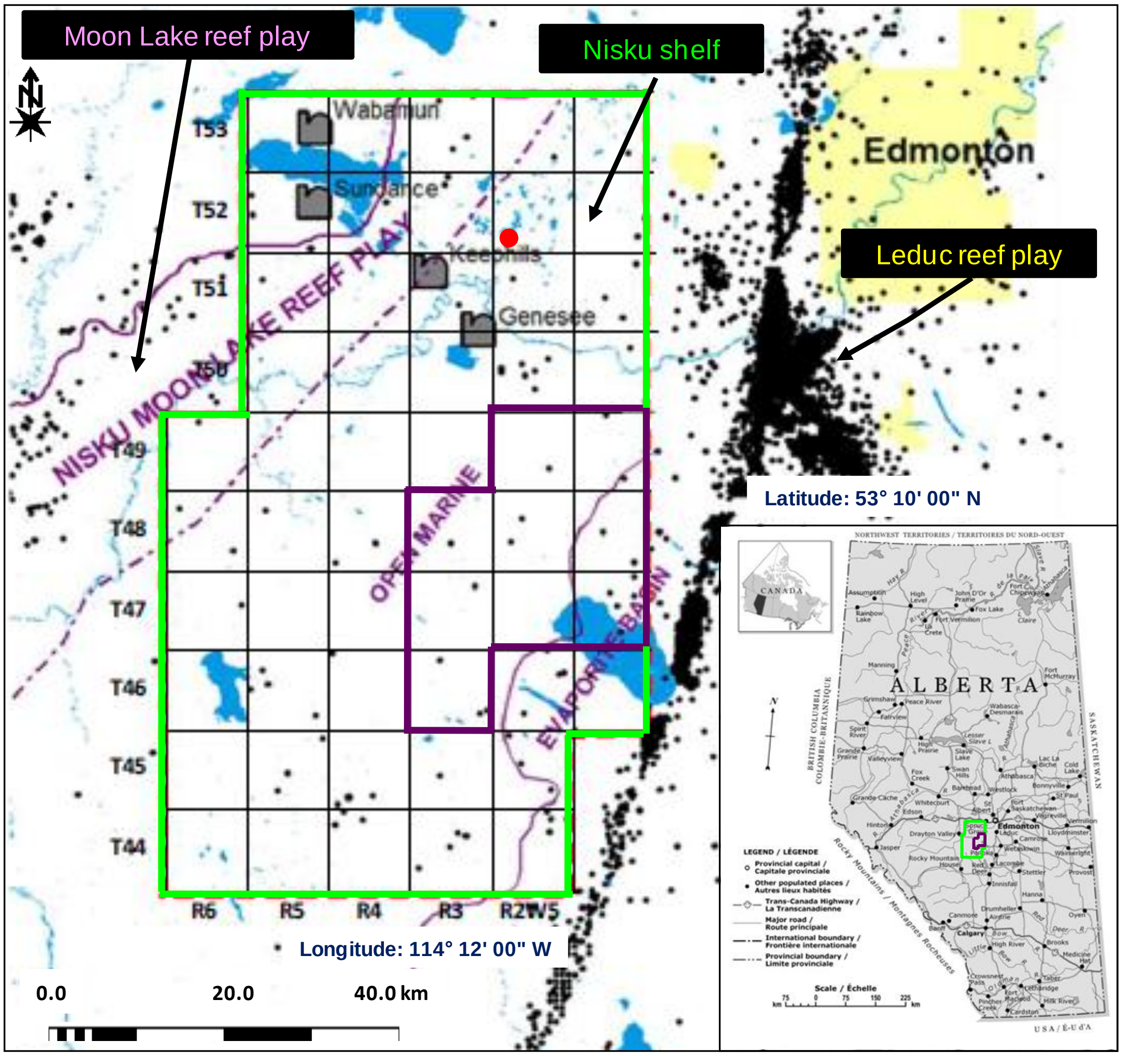

Figure 2-5: Regional (green polygon) and locale-scale (violet polygon) WASP study area. Gray shapes indicate the locations of four large power plants (i.e. major CO_2 point source emissions). Black dots show wells that penetrate the Nisku Formation. Purple curves show the boundaries separating different Nisku lithofacies (evaporite and open marine). Blue polygons and lines indicate the location of bodies of water and rivers, respectively. The red dot shows the location of the well used in constructing the stratigraphic model in Figure 2-9. The approximate areal extent of the regional-scale study area is 5000 km^2. The main map is after Eisinger and Jensen (2009). The Alberta map (see also Figure 2-1) in the lower-right corner is courtesy of Natural Resources Canada (2009). Note that the study area is chosen such that to avoid interference with active hydrocarbon resources. T: township, R: range and W: west of reference meridian. Coordinate system: North American Datum 1927; Ellipsoid: Clarke 1866.

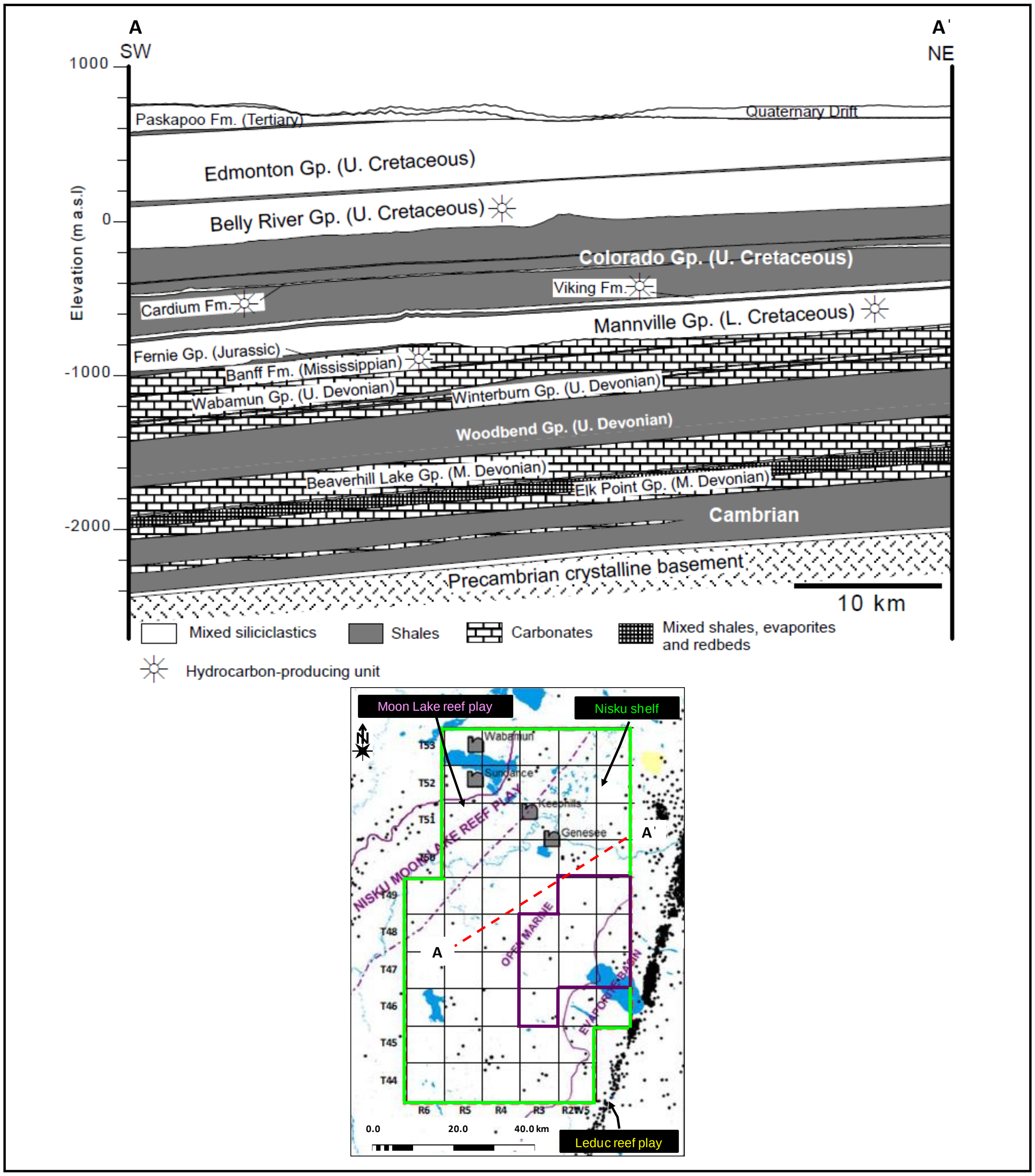

Figure 2-6: Regional geologic section across part of the WASP study area in the northeast-southwest (i.e. dip-parallel) direction. The dashed line (A-A') in the bottom map indicates the location of the cross-section (Michael et al., 2008).

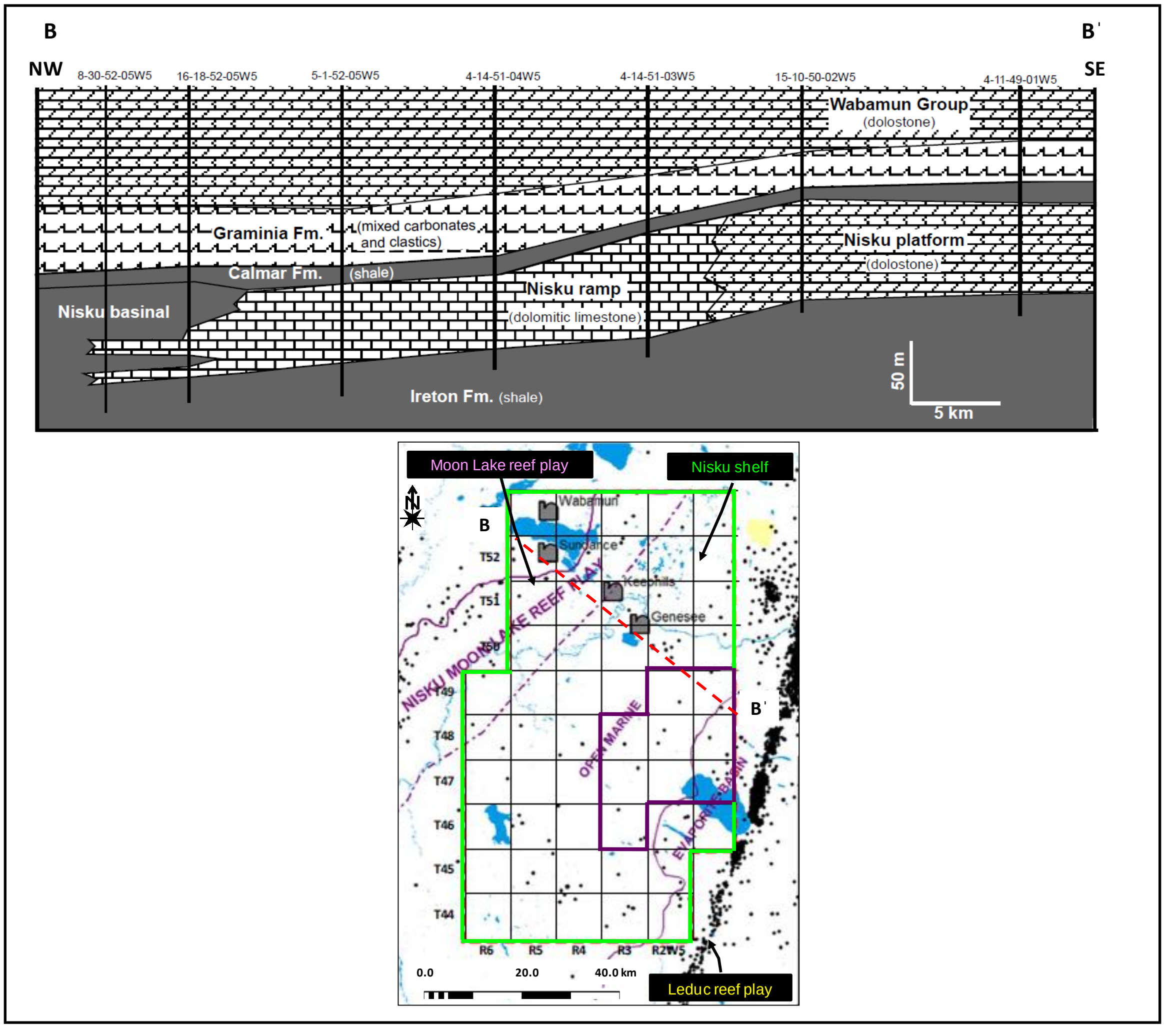

Figure 2-7: Southeast-northwest geologic section across part of the WASP study area in the strike-parallel direction showing some of the different lithofacies of the Nisku Formation. The dashed line (B-B') in the bottom map indicates the location of the cross-section. The seismic characterization is focused on the Nisku platform (Michael et al., 2008).

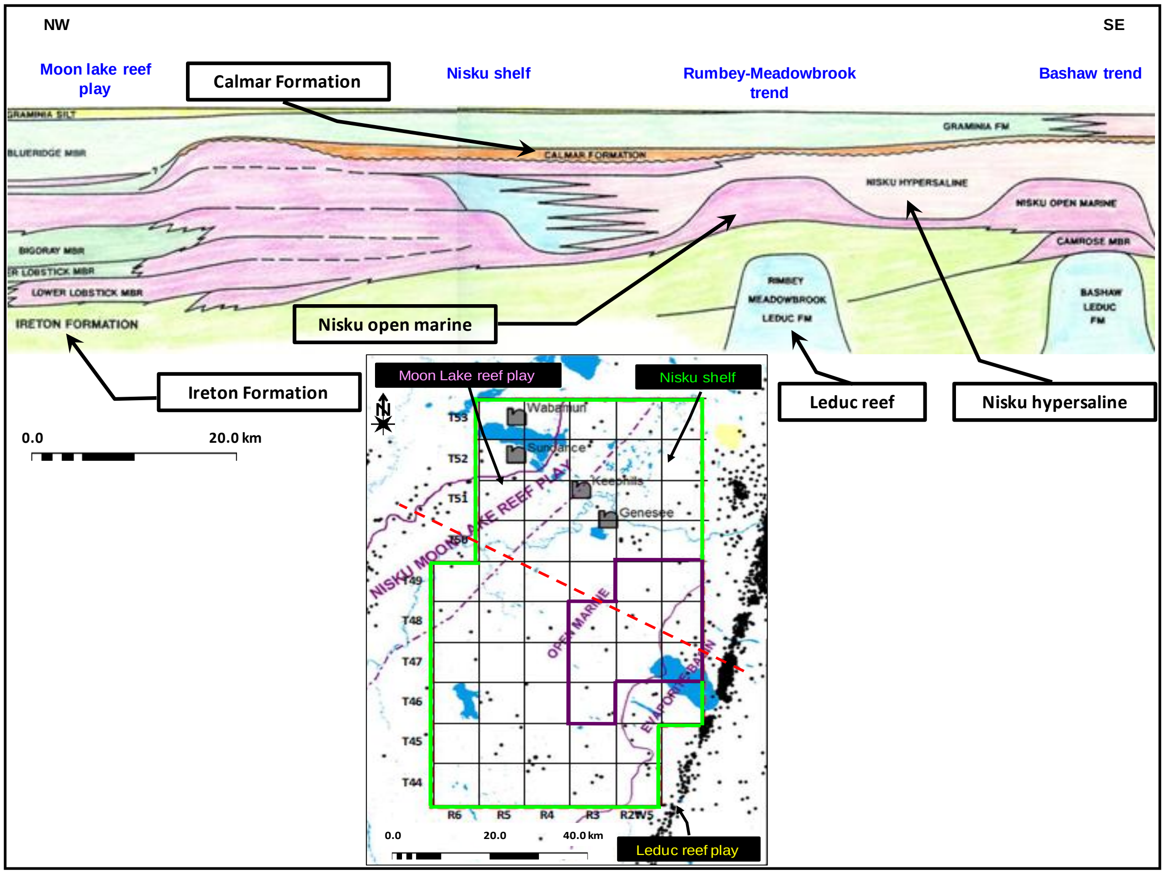

Figure 2-8: A conceptual cross-section through the Nisku Formation showing the different lithofacies, i.e. open marine facies (generally good porosity) and hypersaline facies (poor porosity). The location of the cross-section is indicated by the dashed red line in the inset map (bottom map). Courtesy of SCG (2009).

The eastern boundary of the study area (Figure 2-5) coincides with the transition from the open marine carbonate lithofacies of the Nisku shelf into the low-permeability, low-porosity hypersaline lithofacies of the Nisku evaporite basin. The two lithofacies can be identified based on core samples but are difficult to distinguish based on wireline data (Eisinger and Jensen, 2009; Shevalier et al., 2009). The north-western boundary (Figure 2-5) corresponds to the basin-ward transition into the Nisku shale basin, along which the Nisku becomes inter-bedded with limestone and shale until it becomes shale dominant (Figure 2-7). This region contains hydrocarbon-bearing reef build-ups (i.e. Moon Lake reef play) near the shelf margin. The area of interest to the current study lies along the middle and eastern regions of Nisku shelf (Figure 2-5), which is also referred to as the Nisku platform or Nisku bank. In this region, west of the Leduc reefs, the open marine carbonate lithofacies dominates the Nisku Formation. In addition to its favourable aquifer properties, such as porosity and permeability, this part of the Nisku Formation has no hydrocarbon potential (Michael et al., 2008). One of the principle criteria in selecting the Nisku Formation in this part of the WCSB was to avoid interference with active hydrocarbon resources, namely the Moon Lake reef play (in the north-west) and the Leduc reef play (in the east).

In the local-scale WASP study area, the Nisku Formation corresponds to transgressive system tract in which carbonate ramp deposition is dominant (Switzer et al., 1994). It can be described as carbonate member of the Winterburn Group (Figure 2-9) that is conformably overlain by the Calmar Formation of the Winterburn Group and is underlain by the Ireton Formation of the Woodbend Group (Watts, 1987; Switzer et al., 1994; SCG, 2009). The overlaying low-permeability relatively-thick (~ 15 m) Calmar shale makes a good cap rock which should prevent injected CO_2 from migrating into the surface or shallow aquifers (Michael et al., 2008). From a hydro-stratigraphic perspective, the Nisku Formation can be regarded as deep carbonate saline aquifer that is confined between two shale aquitards, namely the Calmar and Ireton formations.

Figure 2-10 shows photos of three core samples from the study area corresponding to the various lithofacies present within the Nisku shelf. One of the objectives of the seismic characterization was to delineate those areas of the Nisku shelf that exhibit high quality reservoir characteristics (Figure 2-10 (b)). Furthermore, the seismic characterization was focused on the local-scale study area (Figure 2-11) where favourable conditions in terms of seismic coverage and other factors exist, e.g. aquifer properties and absence of hydrocarbon resources. Table 2-2 summarizes of some of the information related to WASP study area and the Nisku Formation in particular.

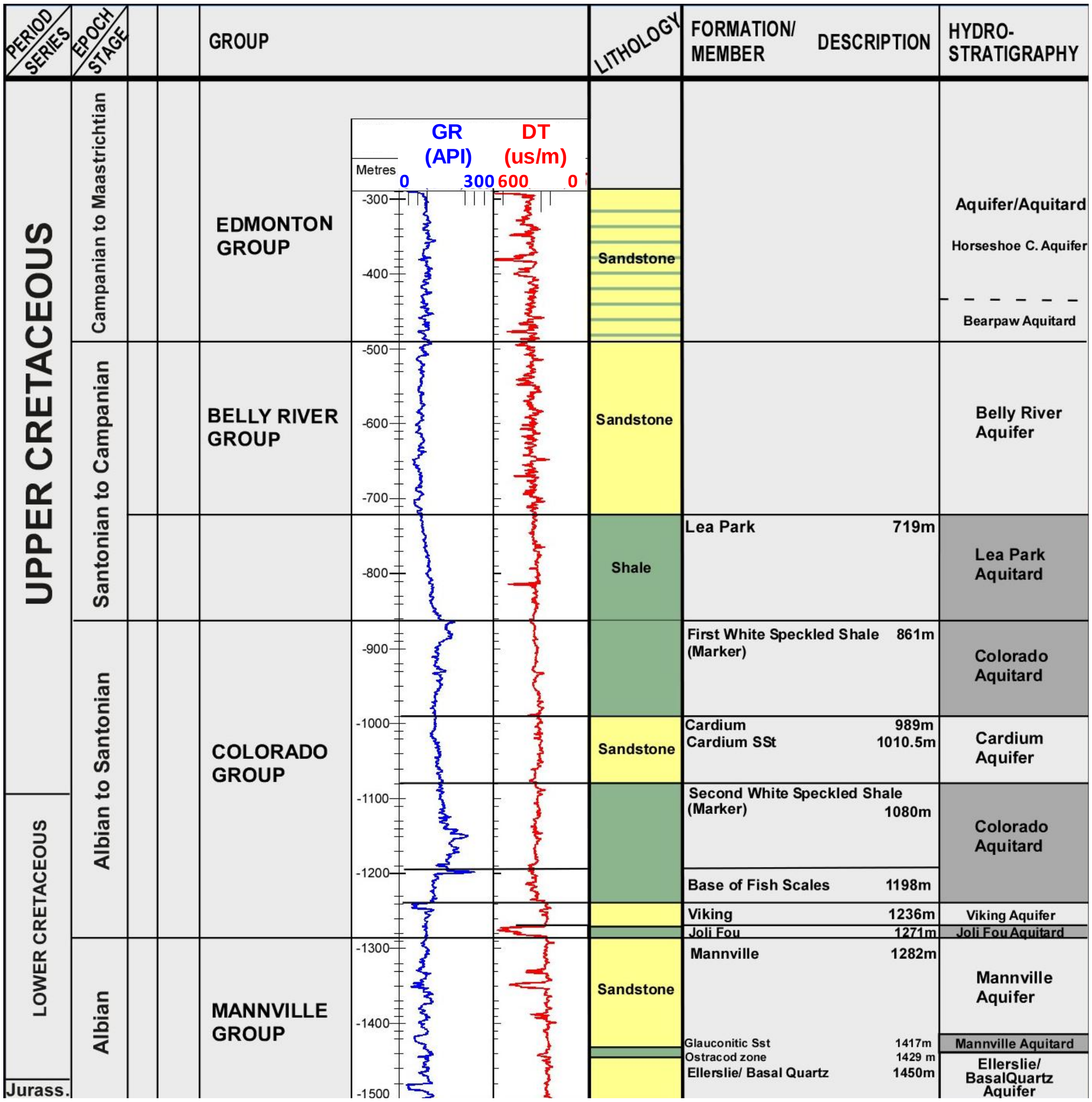

Continued next page

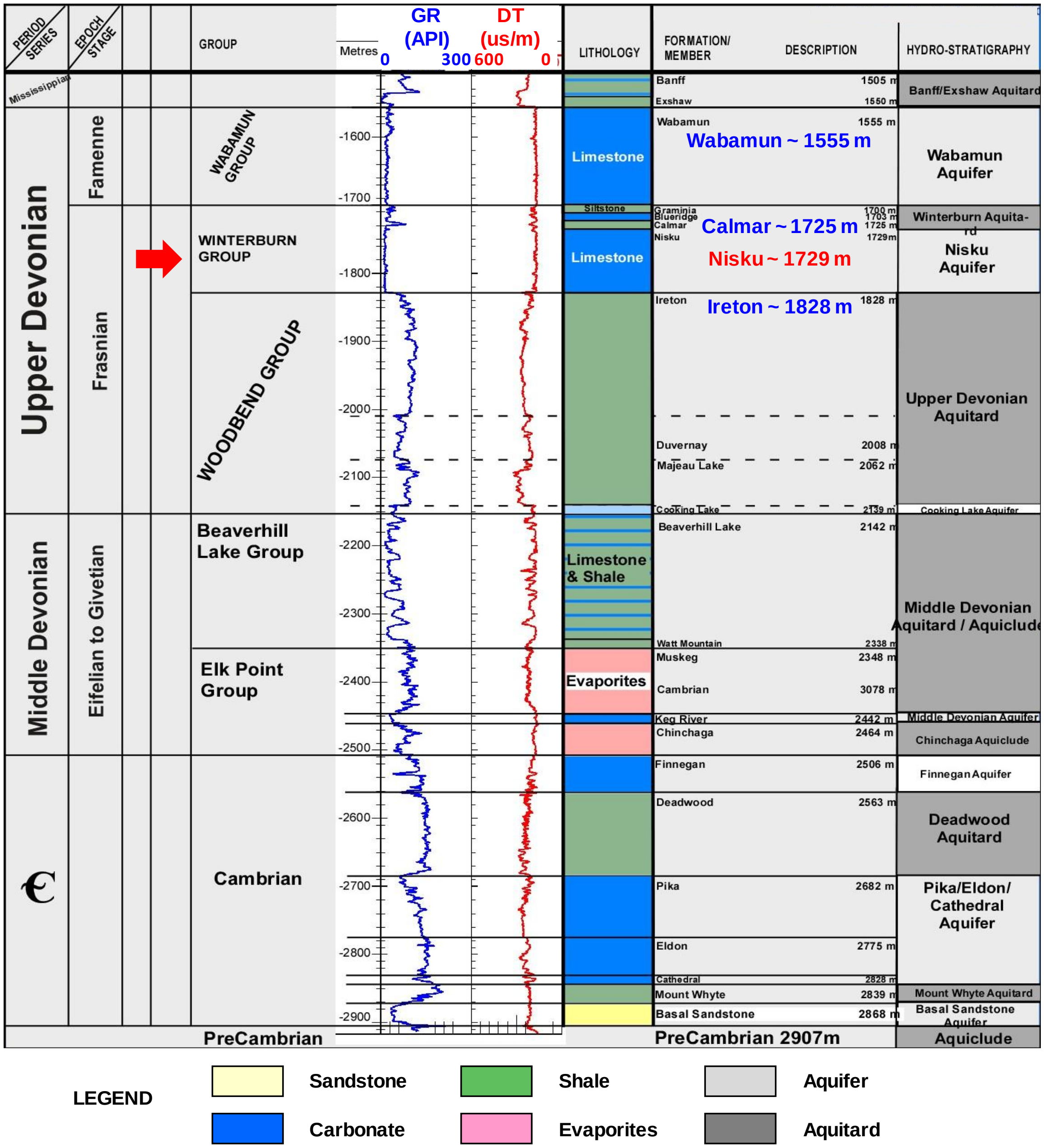

Figure 2-9: Stratigraphic model from the WASP study area. The well (100-10-05-052-2W5) location is shown by the red dot in the inset map in Figure 2-5. The red arrow shows the location of the Nisku Formation (aquifer), which is confined between two aquitards, i.e. Calmar and Ireton formations. The gamma ray and sonic logs are shown by the blue and red curves, respectively. The stratigraphic model is constructed by Maja Buschkuehle (Bachu and Bennion, 2009).

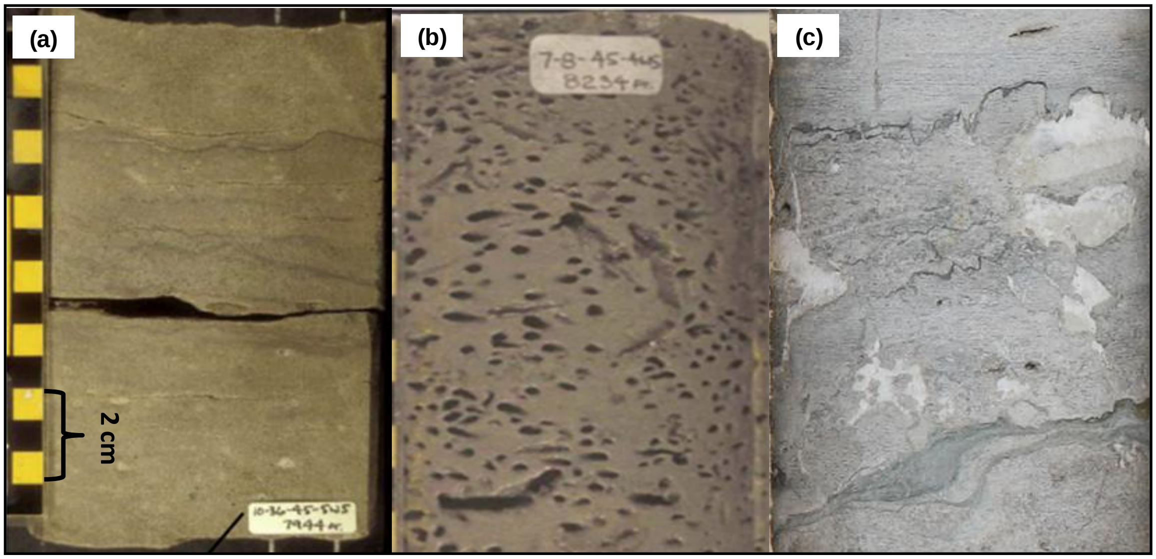

Figure 2-10: Photos showing the character of three core samples from the Nisku Formation in the study area. (a) is a typical carbonate sample showing the open marine lithofacies (within the Nisku shelf) with an average porosity and permeability of 4% and 10 mD (well: 100-10-36-045-5W5); (b) is another carbonate sample showing the open marine lithofacies but with enhanced porosity (~14%) and permeability (~10,000 mD) as a result of diagenetic processes and the abundance of a fossil known as Amphipora (well: 100-07-08-045-4W5); (c) is a carbonate sample showing the hypersaline dolomitic mudstone lithofacies with anhydrite plugging, which dominate the eastern part of the study area and exhibit poor reservoir quality (porosity~1.7% and permeability~3 mD). Photos are courtesy of SCG (2009).

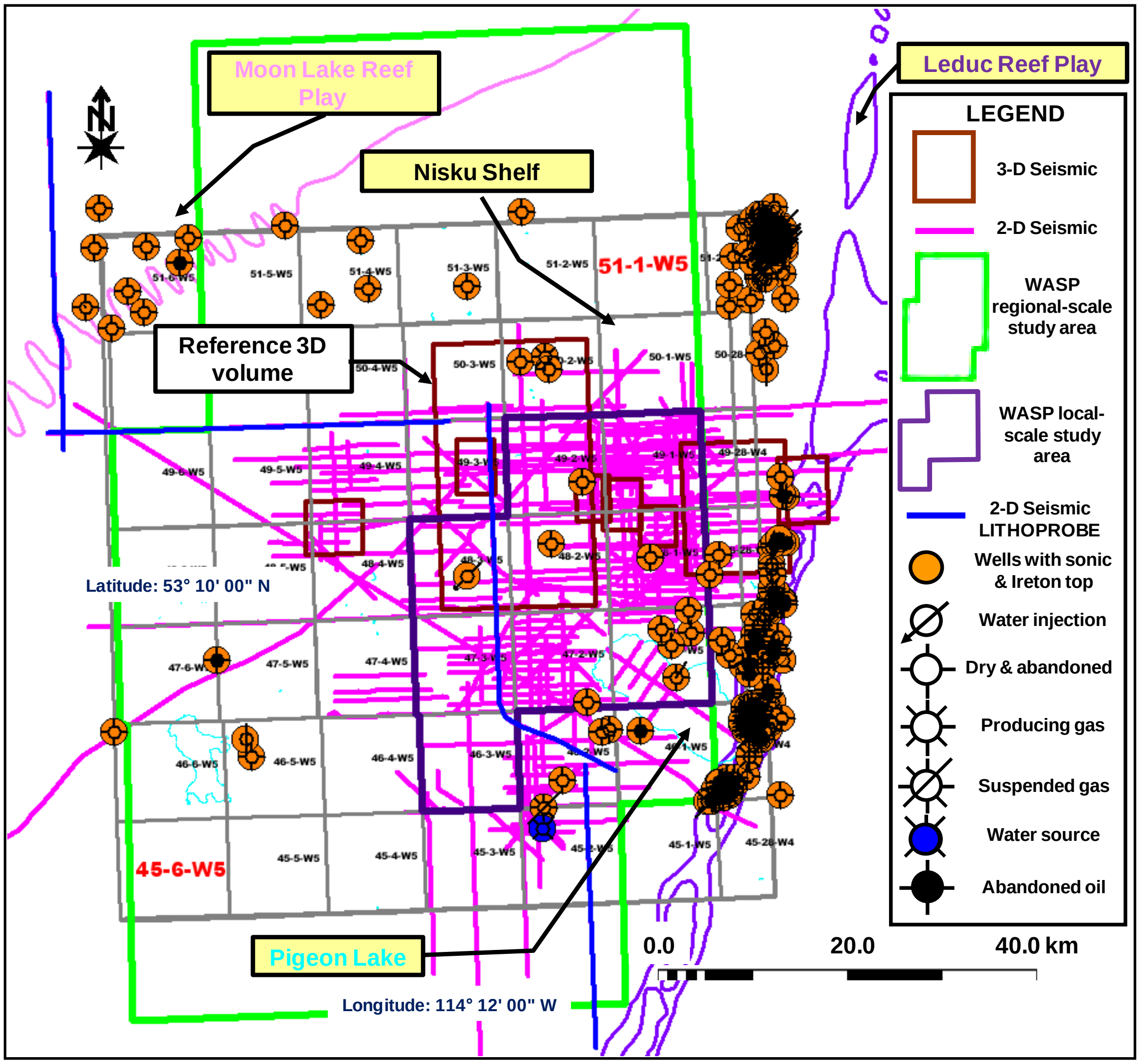

Figure 2-11: Seismic base map showing the distribution of the 2-D and 3-D seismic data as well as the borehole data with respect to the regional and local-scale study areas. Data courtesy of ENCANA (now Cenovus) Corporation®. The red characters refer to the township, range and the meridian reference to the west (e.g., 45-6-W5 is township 45, range 6, west of meridian 5).

Table 2-2: Compilation of information pertaining to the WASP study area and the Nisku Formation. Sources: Michael et al. (2008) and Shevalier et al. (2009).

Motivations	Long-term CO_2 storage
Project Status	Assessment (Phase I)
Commencement	2008
Location	Wabamun Area, Alberta, Canada
Target Formation	Nisku
Bounding (Shale) Aquitards	Calmar (above) and Ireton (below)
Geologic Age	Upper Devonian
Primary Lithology	Dolostone
Reservoir Bearing Fluid	Brine
Other Reservoir Fluid	Gases
Large-scale Study Area	~ 5000 km^2
Local-scale Study Area	~ 900 km^2
Formation Depth	~ 2000 m
Formation Thickness	~ 40-100 m
Reservoir Pressure	~ 15 MPa
Reservoir Temperature	~ 50 C^o
Average Porosity	~ 9%
Average Permeability	~ 0.17 Darcy
Average Water Salinity	~ 115 g/l
Gas-Water Ratio (GWR)	~ 5
Water Density	~ 1117 kg/m^3
Primary Reservoir Mineral(s)	$CaMg(CO_3)_2$ (dolostone ~ 80%)
Other Reservoir Mineral(s)	$CaCO_3$ (calcite), $K_{0.8}Al_{2.8}$ $Si_{3.2}O_{10}OH_2$ (illite), $KAl_3Si_3O_{10}OH_2$ (muscovite), $KAlSi_3O_8$ (K-feldspars), SiO_4 (quartz)
Primary Reservoir Gas(es)	CH_4 (methane), H_2S (hydrogen sulphide)
CO_2 Phase at the Reservoir	Supercritical

2.3 Pembina Cardium CO_2-EOR Project (PCEP) Study Area

The PCEP pilot site is located in the Violet Grove area in the central plains of Alberta, approximately 120 km southwest of the capital Edmonton (Figure 2-1). The large and local-scale PCEP study areas are shown in Figure 2-12 while a regional cross-section through the WCSB in the area was shown in Figure 2-3. The time-lapse seismic program is confined to a small part within the local-scale study area over the Pembina Oil Field (POF), which is the largest conventional oil field in North America with an areal extent of about 4000 km^2 and estimated 7.4 billion barrels of original oil in place (OOIP) (Krause et al., 1987). The CO_2 injection target is the major oil producer[9] Lower Cretaceous sandstone Cardium Formation. Krause et al. (1987) describe the Cardium Formation as a siliclastic sedimentary wedge which was deposited during a relative change in sea level cycle during the Cretaceous Period about 88.5 million years before present. It is thickest and deepest in the foothills and it thins and becomes shallower, as with the WCSB itself, in the east and north-east direction (Dashtgard et al., 2006). The Cardium Formation is, respectively, overlain and underlain by the Wapiabi and Blackstone shale formations (Figure 2-3).

Figure 2-14 shows a geologic cross-section that illustrates the sedimentary succession within the local-scale study area, which is fairly horizontal with no geologic discontinuities present. The Cardium Formation (Figure 2-15) exhibits an average thickness and depth of 40 m and 1600 m, respectively. It is characterized by its fine-grained marine sandstone as illustrated by the hydro-stratigraphic model in Figure 2-15. The Cardium Formation consists of two lithostratigraphic members (Patterson and Anderson, 1957; Krause et al., 1987): Cardium Zone Member and Pembina River Member (Figure 2-17 (b)). The Cardium Zone Member is composed primarily of shale. The Pembina River Member is subdivided into four reservoir units: conglomerate in addition to, upper, middle and lower sandstone units (Figure 2-17 (b)). The conglomerate is separated from the upper sandstone by an erosional surface and each of the sandstone

[9] See Krause and Collins (1984), Krause et al. (1987), Dahstgard (2006), and Hitchon (2009) for information on the reservoir history and production data.

units are underlain by an intervening shale subunit (Figure 2-17 (b)). The maximum thickness of the Cardium Zone and Pembina River Members of the Cardium Formation in the local-scale study area are 18 m and 24 m, respectively. Hydrostratigraphically, the Cardium aquifer is conformed between the Wapiabi and the Blackstone shale aquitards and they are all members of the Colorado Group (Dashtgard et al., 2006).

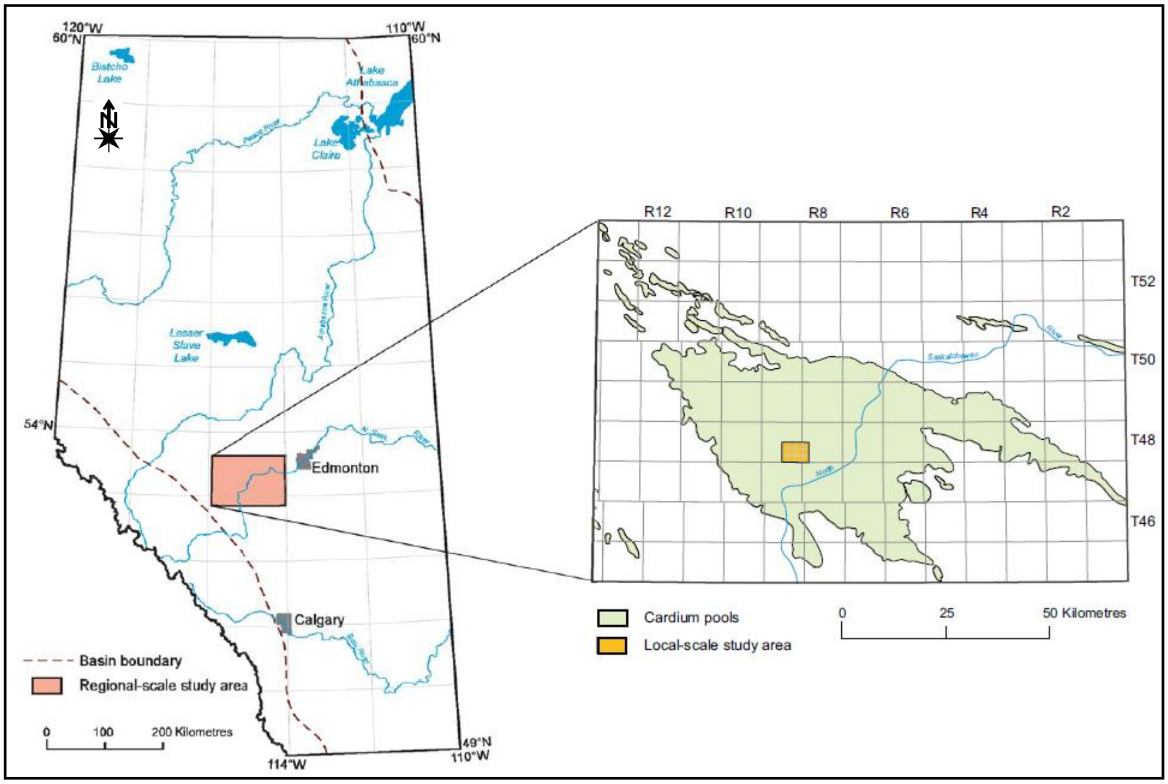

Figure 2-12: Location map of the Pembina Oil Field. The Pembina Cardium CO_2-EOR Project local-scale study area is indicated by the orange rectangle, which is shown in detail in Figure 2-13. Coordinate system: North American Datum 1927; Ellipsoid: Clarke 1866.

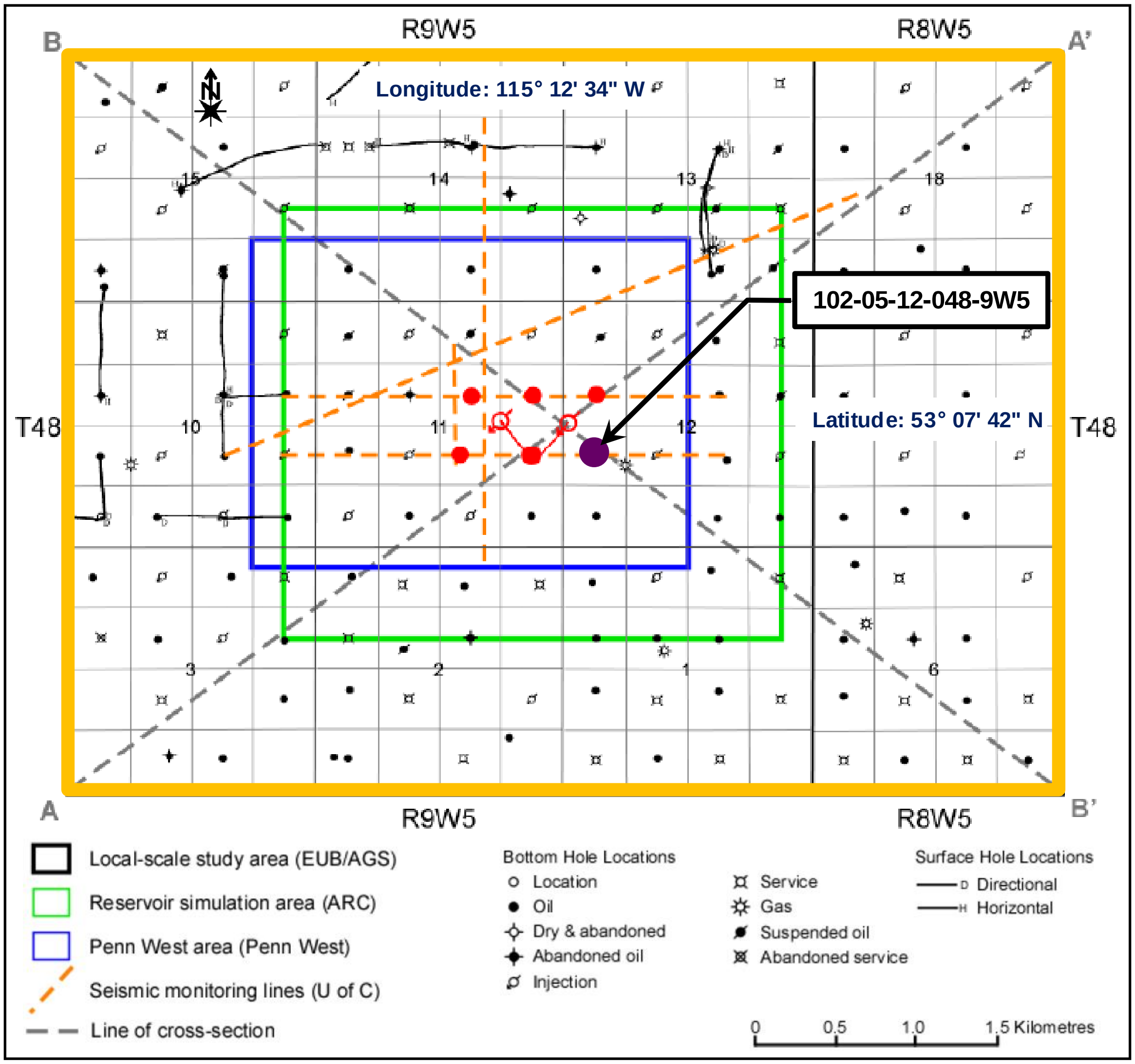

Figure 2-13: Base map showing the location of the producers and injectors, which are highlighted in red. The dashed line (A-A') shows the location of the cross-section that will be shown in Figure 2-14 while the violet dot indicates the location of the well used to construct the stratigraphic model in Figure 2-16. Note that the location of the seismic lines is not accurately represented on the map. T: township, R: range and W: west of reference meridian. ARC: Alberta research Council; AGS: Alberta Geological Survey; EUB: Energy and Utilities Board; U of C: University of Calgary. After Dashtgard et al. (2006).

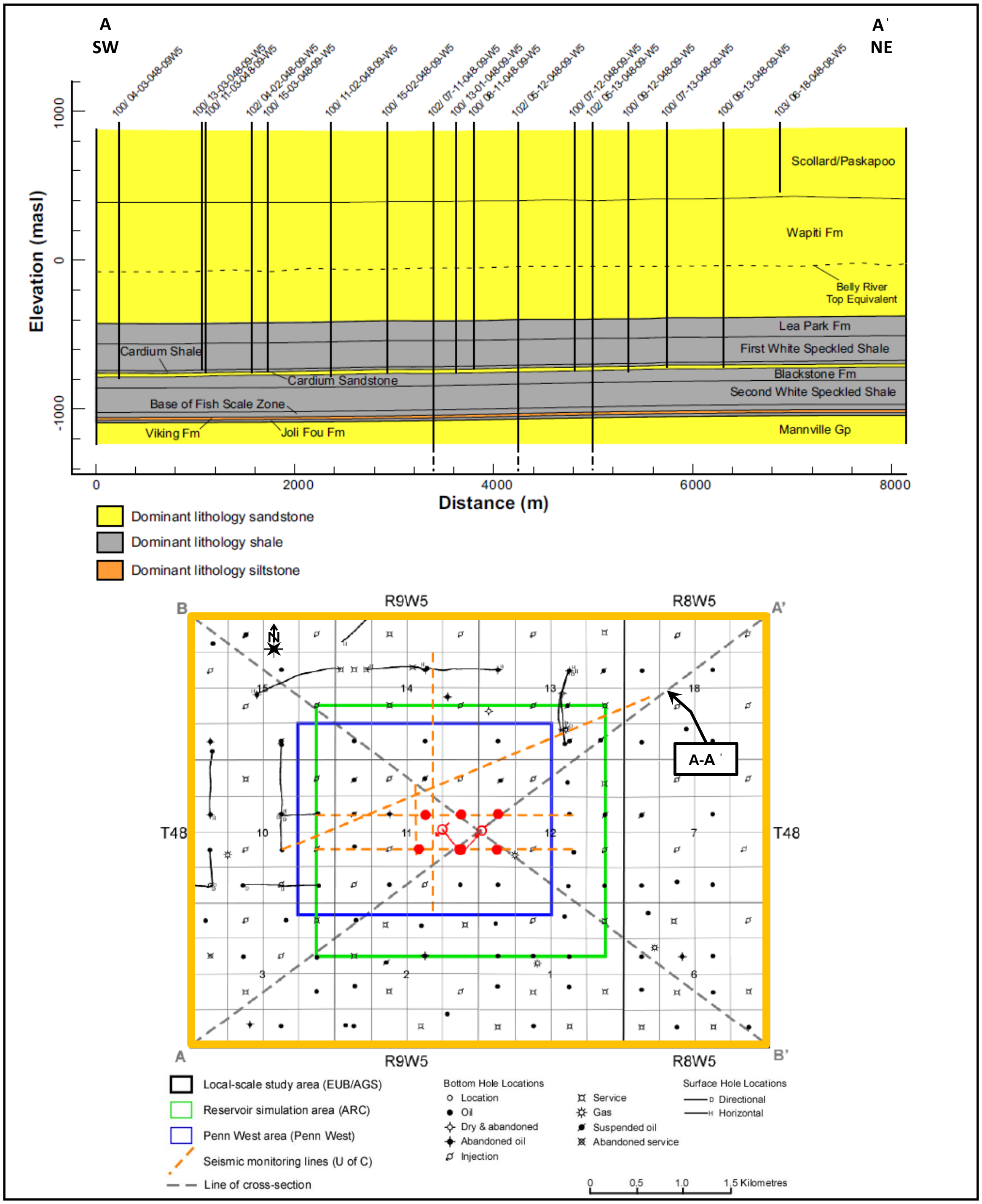

Figure 2-14: Geologic section across the PCEP local-scale study area in the northeast-southwest (i.e. dip parallel) direction. The dashed line (A-A') in the bottom map refers to the location of the cross-section (Dashtgard et al., 2006).

The target of the CO_2-EOR program is the upper sandstone unit of the Pembina River Member of the Cardium Formation, which is also the oil producing unit (Figure 2-17 (b)). Figure 2-18 shows a photo of the Cardium sandstone reservoir, i.e. the upper sandstone unit. The reservoir reaches a maximum thickness of 4 m in the local-scale study area and is confined between the Cardium conglomerate on top and the upper Cardium shale from below. Table 2-3 gives an overview of the depth, thickness, average porosity and permeability of the various units/subunits of the Pembina River Member. The upper shale is considerably thin in the local-scale study area and, therefore, it is not an effective permeability barrier between the upper and middle sandstone units. Furthermore, the overlying Cardium conglomerate may act as a thief zone in parts of the study area. Nonetheless, geologic characterization seems to suggest that fluids preferentially flow along the upper sandstone unit (Dashtgard et al., 2006).

The location of the injection, production and observation wells and, also, the position of the 2-D and 3-D seismic surveys are presented in Figure 2-19. In selecting the site, several criteria were considered including those given by Bachu (2003) (see Section 2.1), e.g. absence of faults, well-developed stratigraphic trap in relevance to storage integrity, in addition to logistical aspects (Hitchon, 2009). Table 2-4 summarizes of some of the information related to PCEP study area and the Cardium Formation in particular.

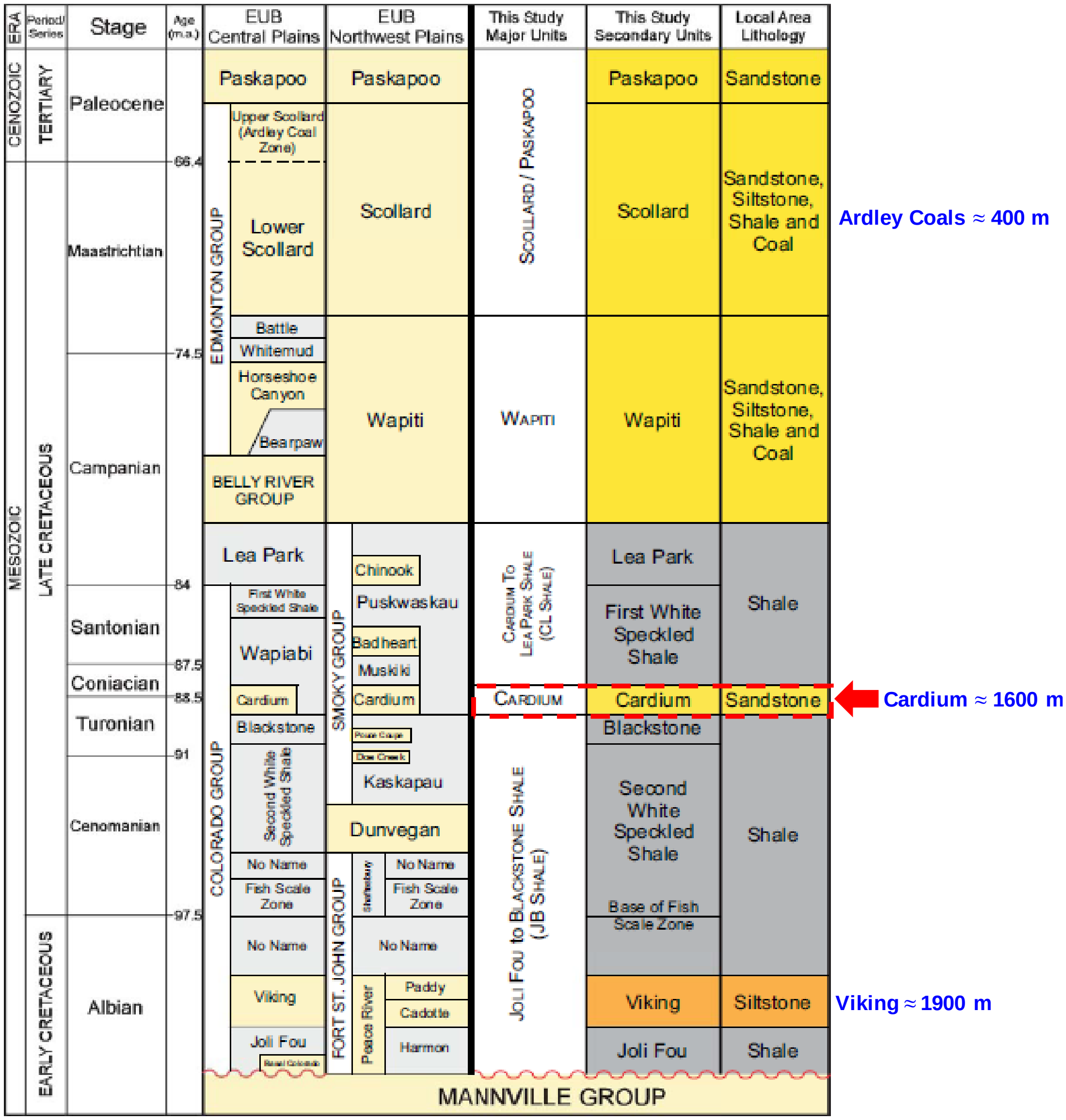

Figure 2-15: Table of formation showing stratigraphic chart from the Early Cretaceous (Mannville) to the Tertiary (Psaskapoo). Courtesy of the AEUB (2009). See Figure 2-16 for the corresponding hydrostratigraphy.

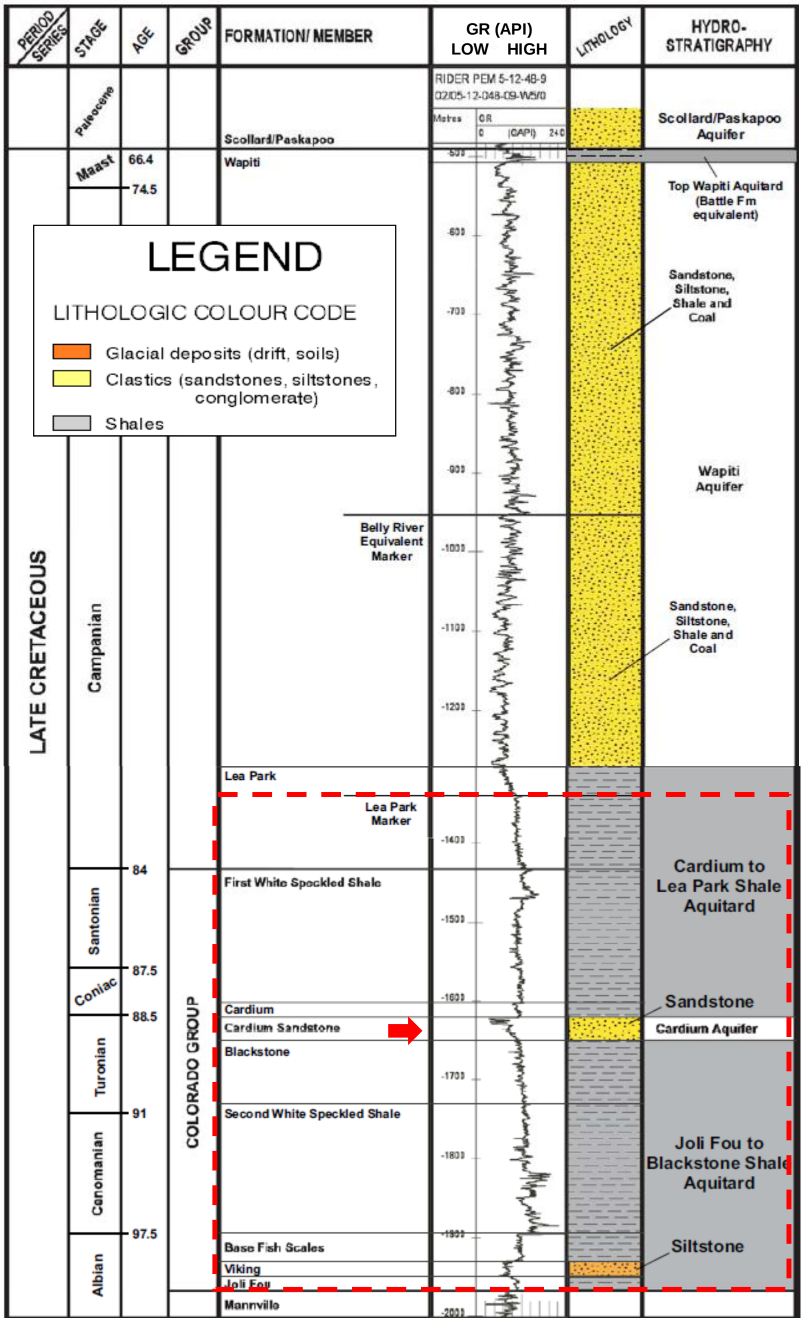

Figure 2-16: Stratigraphic and hydro-stratigraphic model from the PCEP study area (well 102-05-12-048-9W5; see Figure 2-13). The red rectangle enclosing the zone of interest, i.e. the Cardium Formation, is displayed in more detail in Figure 2-17 (Dashtgard et al., 2006).

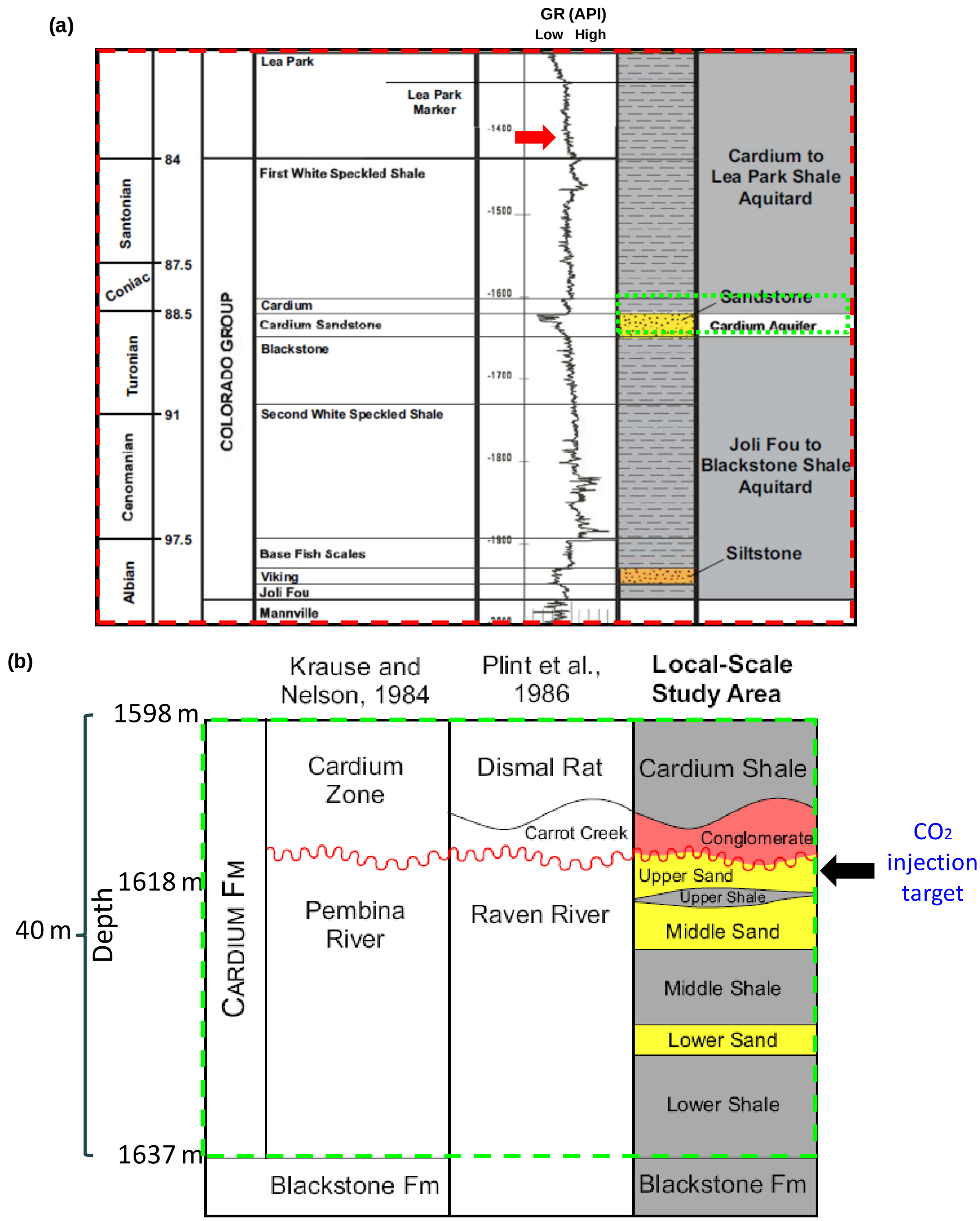

Figure 2-17: (a) The Cardium Formation (aquifer) and the two bounding aquitards (namely the Lea Park and Blackstone formations) that has been enlarged from Figure 2-16. The gamma ray log is shown by the black curve. (b) Stratigraphic classification of the Cardium Formation as outlined by the green dashed rectangle in (a). The red curve above the upper sandstone unit marks the erosional surface separating it from the overlying conglomerate. The well location is shown by the violet dot in the bottom map in Figure 2-13 (Dashtgard et al., 2006).

Table 2-3: Some characteristics of the Cardium Formation at the PCEP study area. Porosity and permeability values represent the average values observed within the local scale study area (Shevalier et al., 2007; Dashtgard et al., 2009).

Unit/Subunit	Thickness (m)	Porosity (%)	Permeability (D)	Comments
Conglomerate	0-5.4	7.4	0.033	Pebble mudstone; sand matrix (85.6 % quartz)
Upper Sandstone	0-4.0	16.4	0.020	Fine-grained (86.4% quartz)
Upper Shale	0.1-4.0	-	-	Interbedded fine-grained shale and sandstone
Middle Sandstone	0.3-6.5	16.2	0.021	Fine-grained (86.2% quartz)
Middle Shale	3.5-8.0	-	-	Shale with sandstone Interbeds
Lower Sandstone	0.5-3.5	14.8	0.010	Fine-grained with shale interbeds (86.8% quartz)
Lower Shale	NA	-	-	Shale with sandstone Interbeds

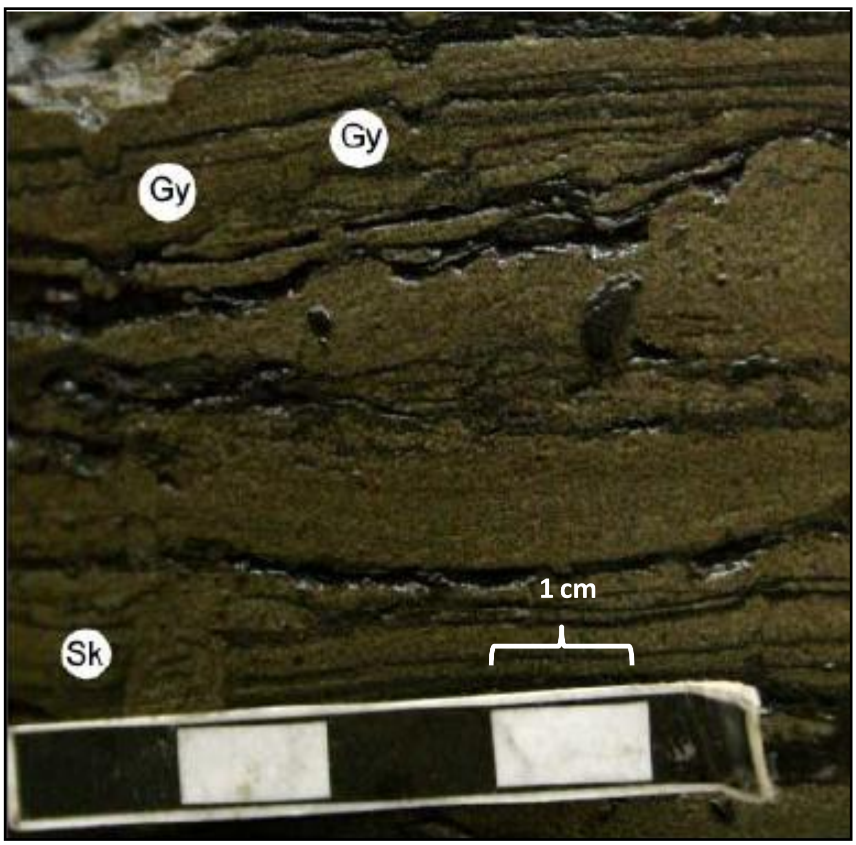

Figure 2-18: Photo of a core sample form the Cardium reservoir (well: 100-03-07-048-08W5) showing burrows in the very-fined upper sandstone unit and the thin mud interbeds. Gy: Gyrochorte; Sk: Skolithos (Dashtgard et al., 2006).

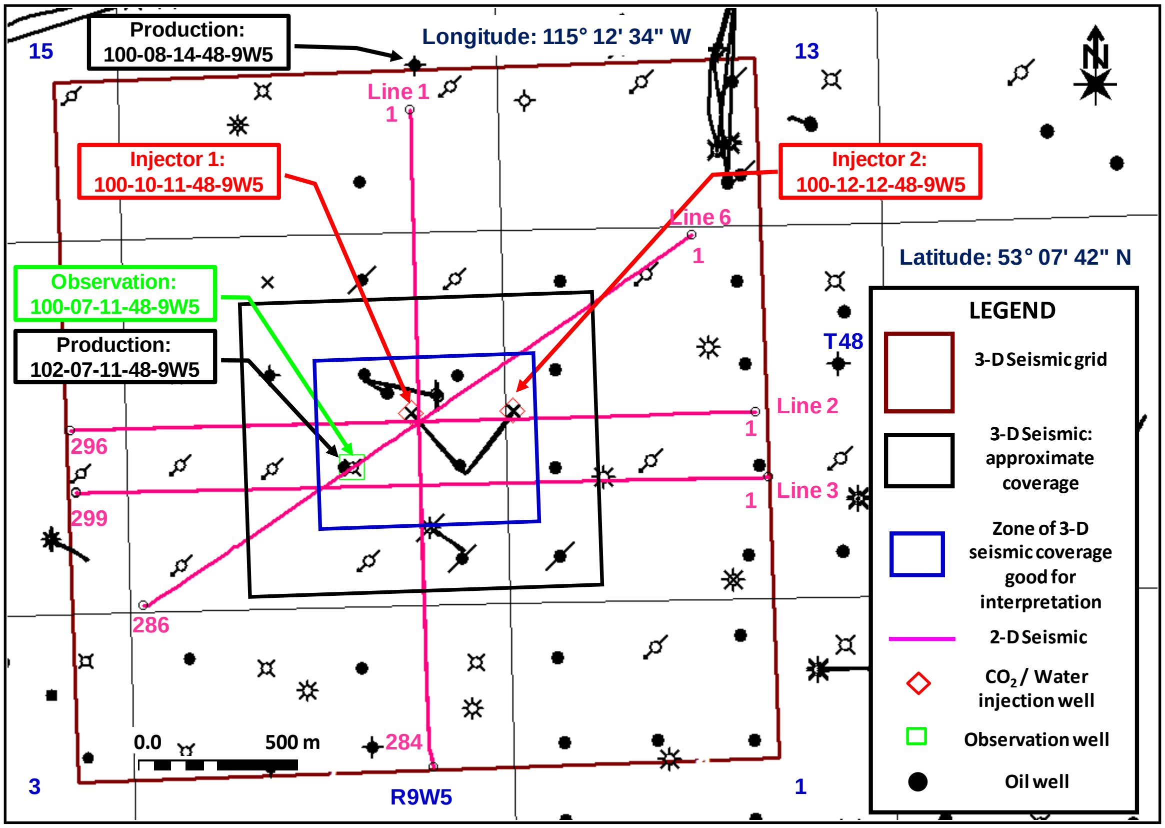

Figure 2-19: Seismic base map showing the distribution of the 2-D and 3-D seismic data as well as the injection and observation wells in the local-scale study areas. T: township, R: range, W: west of the meridian reference. The numbers within each grid represents the section number within the corresponding township and range. See Figure 2-13 for description of the rest of the well symbols.

Table 2-4: Compilation of information pertaining to the PCEP study area and the Cardium Formation. Sources: Krause et al. (1987), Dashtgard et al. (2009) and Shevalier et al. (2007).

Motivation	CO_2-EOR and long-term CO_2 storage
Project Status	Completed
Commencement	2004
Termination	2009
Location	Violet Grove, Alberta, Canada
Target Formation	Cardium (upper sandstone unit)
Bounding (Shale) Aquitards	Wapabi (above) and Blackstone (below)
Geologic Age	Upper Cretaceous
Primary Lithology	Sandstone
Reservoir Primary Fluid	Oil
Other Reservoir Fluid	Water and gases
Large-scale Study Area	~ 11000 km^2
Local-scale Study Area	~ 50 km^2
Pilot Site Area	~ 10 km^2
Formation Depth	~ 1600 m
Formation Thickness	~ 40 m
Reservoir Depth (upper sandstone unit)	~ 1616 m
Reservoir Thickness (upper sandstone unit)	~ 0-4 m
Reservoir Pressure	~ 19 MPa
Reservoir Temperature	~ 50 C^o
Average Porosity	~ 16.4 %
Average Permeability	~ 0.02 Darcy
Average Water Salinity	~ 7.5 g/l
Water Density	~ 1032 kg/m^3

Continued next page

Oil Gravity	~ 40 API
Gas-Oil Ratio (GOR)	~ 4
Primary Reservoir Mineral	SiO_4 (quartz ~ 87%)
Other Reservoir Mineral(s)	$K_{0.8}Al_{2.8}Si_{3.2}O_{10}OH_2$ (illite), $KAl_3Si_3O_{10}OH_2$ (muscovite), $KAlSi_3O_8$ (K-feldspars), $Al_2Si_2O_5OH_4$ (kaolinite) , $CaCO_3$ (calcite)
Primary Reservoir Gas(es)	CH_4 (methane), N (nitrogen)
CO_2 Phase at the Reservoir	Supercritical
CO_2 Injection Rate	~ 20,000 tons/year
Amount of Sequestered CO_2 (end of 2009)	~ 60,000 tons
Operator	Penn West Energy Trust®

2.4 Summary

- In this chapter, the geology of the WASP and PCEP study areas, which are both located within the Western Canada Sedimentary Basin (WCSB), has been reviewed.
- The chapter begun by first offering a brief review of the WCSB and its sustainability for CO_2 sequestration (Section 2.1). According to the basin sustainability criteria by Bachu (2003) and Bach and Stewart (2002), both WASP and PCEP are located within a good sustainability zone of the WCSB.
- The WASP regional-scale study area (Section 2.2) covers approximately 5000 km^2. The target is the Upper Devonian dolomitic Nisku Formation; a saline aquifer that lies within the lower succession of the WCSB.
- In the regional-scale context, the Nisku Formation can be divided into three zones (from east to west): hypersaline basin, shelf and shale basins.
- The local-scale study area, which covers about 900 km^2, is limited to the Nisku shelf due to favourable petrophysical and chemical properties.
- The Nisku Formation is confined between two shale aquitards: Calmar Formation (above) and Ireton Formation (below). The Nisku has an average thickness of 60

m and attain an average porosity and permeability of 9% and 170 mD, respectively.

- For the PCEP study area (Section 2.3), the areal extent of the regional-scale and local-scale are approximately 11,000 km^2 and 50 km^2, respectively.
- The extent of the pilot-site scale is about 10 km^2 and is located in the Pembina Oil Field.
- The target is the Lower Cretaceous siliclastic Cardium Formation, which is confined between two shale aquitards. In contrast to the Nisku Formation, this is an oil reservoir that lies within the upper succession of the WCSB.
- The Cardium Formation consists of two members and four units. The exact target is the upper sandstone unit, which is very thin (0-4 m) and exhibit an average porosity and permeability of 16.4% and 20 mD, respectively.

CHAPTER 3: METHODS

3.1 The Seismic Experiment

Consider a 3-D earth model consisting of a number of homogenous isotropic layers that are distinct based on their elastic moduli[10]. In general, the seismic experiment can be described as using an impulse point-source to propagate mechanical energy through the model in the form of seismic waves[11] and record the ground motion associated with such disturbance at the earth surface or in a borehole using discrete receivers, or array of receivers. The experiment is repeated several times using different source-receivers configurations as well as different locations (coordinates) over the model in order to gather sufficient information about it. The data collected is then processed, analyzed and interpreted in order to construct an image of this earth model and delineate what distribution of the elastic properties within the model is giving rise to the observed data.

Seismic wave propagation through the model is a function of the magnitude and the distribution of the elastic moduli within the earth model as well as some source and media characteristics. The elastic moduli are related to the compressional wave (P-wave) speed, shear wave (S-wave) speed, and density of the media through the following relations:

$$\alpha = \sqrt{\frac{\lambda + 2\mu}{\rho}} \tag{3.1}$$

$$\beta = \sqrt{\frac{\mu}{\rho}} \tag{3.2}$$

$$\lambda = K + \frac{2}{3}\mu \tag{3.3}$$

---

[10] Elastic moduli are mathematical expressions used to describe how an object would deform under the influence of an external force according to fundamental laws of physics, e.g. Hooke's law of elasticity and Newton's second law of motion (Telford et al., 1990).

[11] Seismic waves are harmonic "disturbances that are propagated through the body of a medium without involving net movement of material" (Sherriff, 2002). Waves are characterized by their velocity, amplitude and phase.

where λ and μ are called Lamé parameters where μ is the shear modulus (modulus of rigidity) in force per unit area, K is the bulk modulus (modulus of incompressibility) in force per unit area, ρ is density in mass per unit volume, α is P-wave speed in length per unit time, and β is S-wave speed in length per unit time. The quantities obtained by multiplying the P-wave speed by density and S-wave speed by density, respectively, are called acoustic impedance (I_p) and shear impedance (I_s) of the medium:

$$I_p = \alpha\rho \tag{3.4}$$

$$I_s = \beta\rho \tag{3.5}$$

Media characteristics that affect the propagation of seismic energy include absorption, dispersion and energy partitioning (Sheriff and Geldart, 1995). Energy associated with seismic waves will reflect and/or refract (or in complex media diffract and/or reverberate) upon encountering impedance contrasts in the media. In the case of normal-incidence acoustic wave, the energy partitioning at an interface i separating two distinct layers can be described by the reflection (R_p) and transmission (T_p) coefficients:

$$R_p^i = \frac{I_p^{i+1} - I_p^i}{I_p^{i+1} + I_p^i} \tag{3.6}$$

$$T_p^i = \frac{2I_p^i}{I_p^{i+1} + I_p^i} \tag{3.7}$$

$$R_p^i + T_p^i = 1 \tag{3.8}$$

the subscript i is a positive integer representing the layer number, R_p and T_p are the reflection from and transmission through the interface i separating the layers i and i+1, respectively.

As a physical phenomenon, seismic wave propagation can be described using two fundamental laws of physics: Newton's second law of motion and Hooke's law of elasticity. Based on these laws, two classes of theories each with its own mathematical formulation exist: wave theory (WT) and ray theory (RT). The former is more physically and mathematically comprehensive[12] than the latter, which is rather an approximation of

---

[12] For instance, it better describes wave propagation when multi-pathing is encountered.

the seismic wavefield, but they both play an important role in understanding, describing, as well as in modelling the propagation of seismic waves. Both theories assume that particle displacements are small compared with the propagating wavelengths (Chapman, 2004).

The WT describes the total wavefield associated with seismic wave propagation and the result is the wave-equation (WE), or equation of motion (EOM). The WE can be derived using Newton's and Hooke's laws (Sheriff and Geldart, 1995) and it can be expressed in the following form (Telford et al., 1990):

$$\nabla^2\psi = \frac{\partial^2\psi}{\partial x^2} + \frac{\partial^2\psi}{\partial y^2} + \frac{\partial^2\psi}{\partial z^2} = \left(\frac{1}{\alpha^2}\right)\frac{\partial^2\psi}{\partial t^2} \tag{3.9}$$

where $\psi(x,y,z,t)$ represents a wavefunction (disturbance), x, y, z are the Cartesian coordinates in unit length along the x-axis, y-axis and z-axis, respectively; t is the traveltime in unit time, ∇ is the del operator, and ∂ denotes the partial derivative operator. Equation (3.9) is called the acoustic wave-equation, or scalar wave-equation (SWE), in 3-D and it describes the propagation of pressure wavefield only in homogenous isotropic media. Using Equation (3.9), the WE can be identified as a hyperbolic second-order partial differential equation that "relates the spatial and temporal dependence of a disturbance which can propagate as a wave through a medium" (Sheriff, 2002). The general plane-wave solution to Equation (3.9), in the case of a 1-D wave travelling along the x-axis, can be written in the following form:

$$\psi = \psi_1(x-\alpha t) + \psi_2(x+\alpha t) \tag{3.10}$$

here, $\psi_1(x,t)$ and $\psi_2(x,t)$ represent pressure wavefield travelling in the positive and negative x direction, respectively, x is the distance travelled, t is the traveltime, and α is the P-wave speed of the wave in the medium. Furthermore, the plane-wave solution ψ could be represented by combination of functions, ψ_1 and ψ_2, that satisfy Equation (3.10) and some boundary conditions (Telford et al., 1990). For instance, in the case of a wave travelling along the positive x direction (one-way WE), the solution could be expressed in term of a complex exponential:

$$\psi = \psi_1 = Ae^{j(x-\alpha t)} = Ae^{j\varphi} \tag{3.11}$$

where A is the amplitude and the argument φ is the phase in unit angle, j is the imaginary unit (√-1), α (P-wave speed) is also called the phase wave speed and can be expressed as follows:

$$\alpha = \lambda f = \frac{\omega}{k} \tag{3.12}$$

the symbol f is the temporal frequency in cycles per unit time, λ is the wavelength in unit length, ω is the angular frequency in unit angle per unit time, and k is the wavenumber in cycles per unit length. Elaborate discussions of the WT can be found in Berkhout (1987), Morgan (1983), Lay and Wallace (1995), Shearer (1999), Udías (1999), Aki and Richards (2002), and Slawinski (2003).

The other mean of describing the seismic wavefield is through the ray theory (RT) using either the geometric ray theory[13] (GRT) or asymptotic ray theory (ART). All ray methods are based on approximation to the WE on the premises of high frequency[14] (Červený, 2001). In principle, RT is based on the postulate that the seismic wavefield can be approximated by rays travelling along infinitesimal raypaths, which are governed by Fermat's principle and obey Snell's law (Červený, 2001). Furthermore, these rays travel in direction perpendicular to the wavefornts described by Huygens's principle. This implies, therefore, that only the effect of materials encountered by the infinitesimal rays is taken into consideration, at least in the general RT.

Ray tracing can be divided into two categories: kinetic or dynamic. In kinetic ray tracing, the traveltime along a raypath between a source and receiver is calculated by solving the nonlinear partial differential equation known as the eikonal equation (Krebes, 2004):

$$\nabla^2 T = \frac{\partial^2 T}{\partial x^2} + \frac{\partial^2 T}{\partial y^2} + \frac{\partial^2 T}{\partial z^2} = \frac{1}{\alpha^2} \tag{3.13}$$

---

[13] Due to its relevance to the numerical modeling in this dissertation, GRT is introduced in Section 3.5.4
[14] This means that the elastic properties "should not change very much over distances of the order of the dominant wavelength" (Krebes, 2004). In other words, the elastic parameters are assumed to be slowly changing.

where $T(x,y,z)$ is the traveltime, and α is the P-wave speed, ∇^2 is the Laplacian, and ∂ denotes the partial derivative operator. In addition to computing the traveltime, dynamic ray tracing estimates some of the waveform characteristics, e.g. amplitude, using another differential equation known as the transport equation (Carcione et al., 2002):

$$2\nabla A \cdot \nabla T + A\nabla^2 T = 0 \tag{3.14}$$

where $A(x,y,z)$ is the wave amplitude, and $T(x,y,z)$ is the traveltime computed by solving the eikonal equation. In general, solutions to ray equations are expressed as polynomial series in inverse powers of frequency (Chapman, 2004). For instance, in ART, an ansatz[15] is sought such that it fits the WE asymptotically, i.e. in the limit of high frequency (Červený, 2001):

$$\Psi(x,\omega) \approx \sum_{i=0}^{\infty} \frac{A_i(x)}{(j\omega)^i} e^{j\omega T(x)} \tag{3.15}$$

$\Psi(x,\omega)$ is the wavefunction, ω is the angular frequency, $T(x)$ is the traveltime, $\omega t\ (x)$ is the phase, $A^{(n)}\ (x)$ is the amplitude coefficients of the ray series, and i is a positive integer corresponding to the layer number. Equation (3.15) is an asymptotic series and, in general, is non-convergent (Červený, 2001). In practice, only the 0th order term in Equation (3.15) is retained and the solution is approximated by:

$$\Psi(x,\omega) \sim A_0(x) e^{j\omega T(x)} \tag{3.16}$$

Equations (3.15) and (3.16) describe a progressing wavefield with wavefronts at surfaces of equal $T(x)$ but they are merely ansatze. The final solution would require multiplication by a frequency dependent factor representing finite bandwidth waveform and summation of similar contributions according the external force field (Červený, 2001).

It should be noted that traveltime calculated through ray tracing methods will usually produce accurate results if the rate of change of velocity in the earth is small relative to the wavelength. The calculated waveform, however, is only an approximation to that achieved by the solving the WE and the level of accuracy will depend on a number of factors, for instance the model complexity. More information about the RT can be

[15] An ansatz is an intelligent guess of a mathematical form of a solution to an equation (Chapman, 2004).

found in Bullen (1987), Lay and Wallace (1995), Červený (2001), Aki and Richards (2002), Gjøystdal et al. (2002), Slawinski (2003), and Chapman (2004).

3.2 Seismic Methods

The two types of the seismic experiment employed in this dissertation are the reflection surface seismic and vertical seismic profile (VSP) techniques. To illustrate the basic concept underlying the reflection surface seismic experiment, consider a 2-D section through a 3-D earth model as depicted in Figure 3-1. In this context, the experiment is based on measurements of the waveform associated with seismic waves emitted from a surface source and reflected back, upon encountering impedance contrast in the subsurface, to the surface where they are recorded using a number of receivers. The experiment is repeated using different source-receivers arrangements and locations along the model and the data acquired are then processed and analyzed to describe the model.

VSP differs from the surface seismic in the fact that the receivers are deployed in the borehole instead of the earth's surface (Figure 3-2). Therefore, in addition to measuring the traveltime-depth relationship, the VSP technique may offer better information about the total seismic wavefield, i.e. downgoing and upgoing wavefields. In addition, VSP data are characterized by higher frequency bandwidth than surface seismic data and, therefore, yield better resolution. However, VSP data lack the broad areal coverage attained by surface seismic data. So, in a sense, VSP and surface seismic complement one another. More information about surface seismic and VSP among other seismic techniques can be found in Waters (1978), Kennett et al. (1980), Telford et al. (1990), Sheriff and Geldart (1995), Shearer (1999), Graebner et al. (2001), Hardage (2000), and Hinds et al. (1996).

The previous discussions (Sections 3.1 and 3.2) are intended to give a brief, short and rather simple introduction of some of the concepts involved in the seismic experiment in a simple horizontally stratified media. Discussion of these and other related topics can be found in many references in the literature including Bullen and Bolt (1985), Sheriff and Geldart (1995), Dahlen and Tromp (1998), Shearer (1999), Červený (2001), Graebner et al. (2001), Kennett (2001), Yilmaz (2001), Aki and Richards (2002), Brown (2004), and Stark (2008).

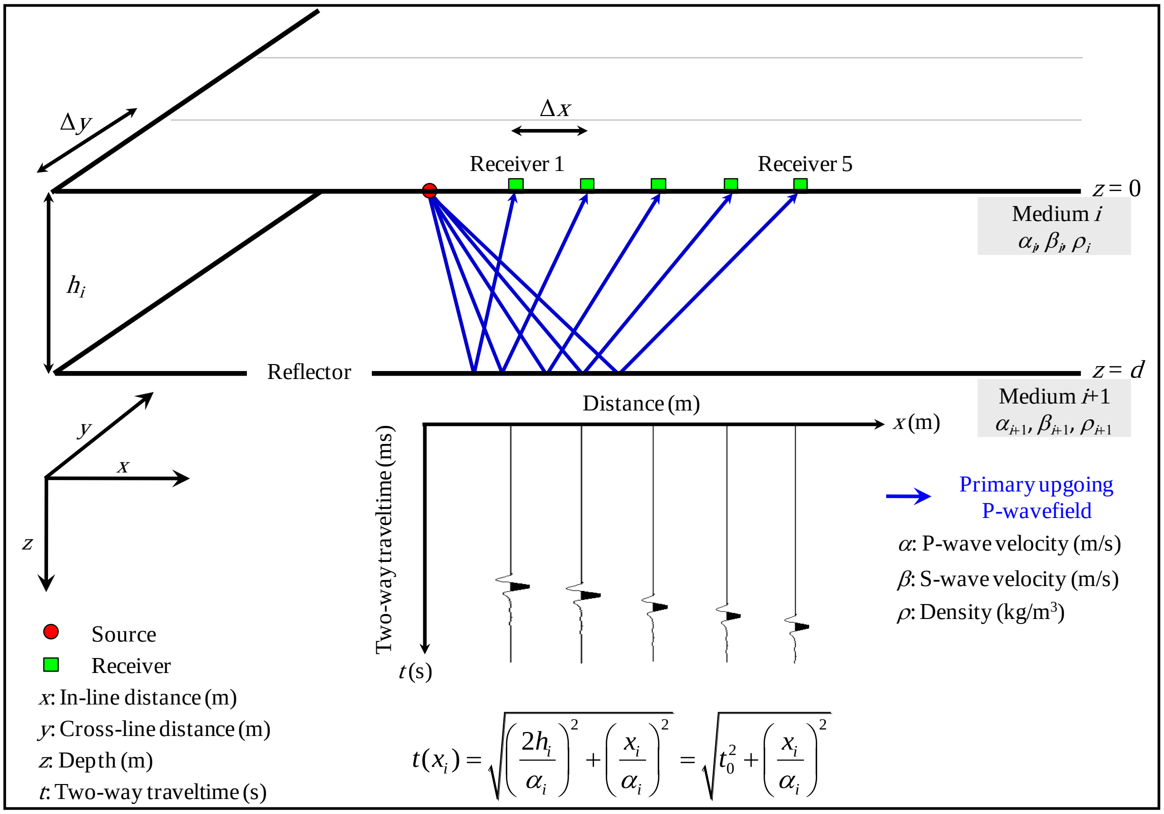

Figure 3-1: Depiction of the seismic experiment[16] in the case of the reflection surface seismic technique showing the primary upgoing P-wavefiled in a simple horizontally stratified media. The response[17] associated with such experiment is shown at the bottom by the noise-free common-shot gather (seismogram). This is oversimplified as the schematic and seismogram do not show other types of seismic energy, such as direct-wave, head-wave, converted-wave, and multiples, which were omitted for simplicity and to avoid cluttering. Note that the seismic energy is represented by rays rather than total wavefield and that the traveltime is described by hyperbolic relation at the bottom.

[16] Using arbitrary setup.

[17] Assuming zero-phase, normal-polarity source wavelet and that P-wave, S-wave and density are increasing with depth.

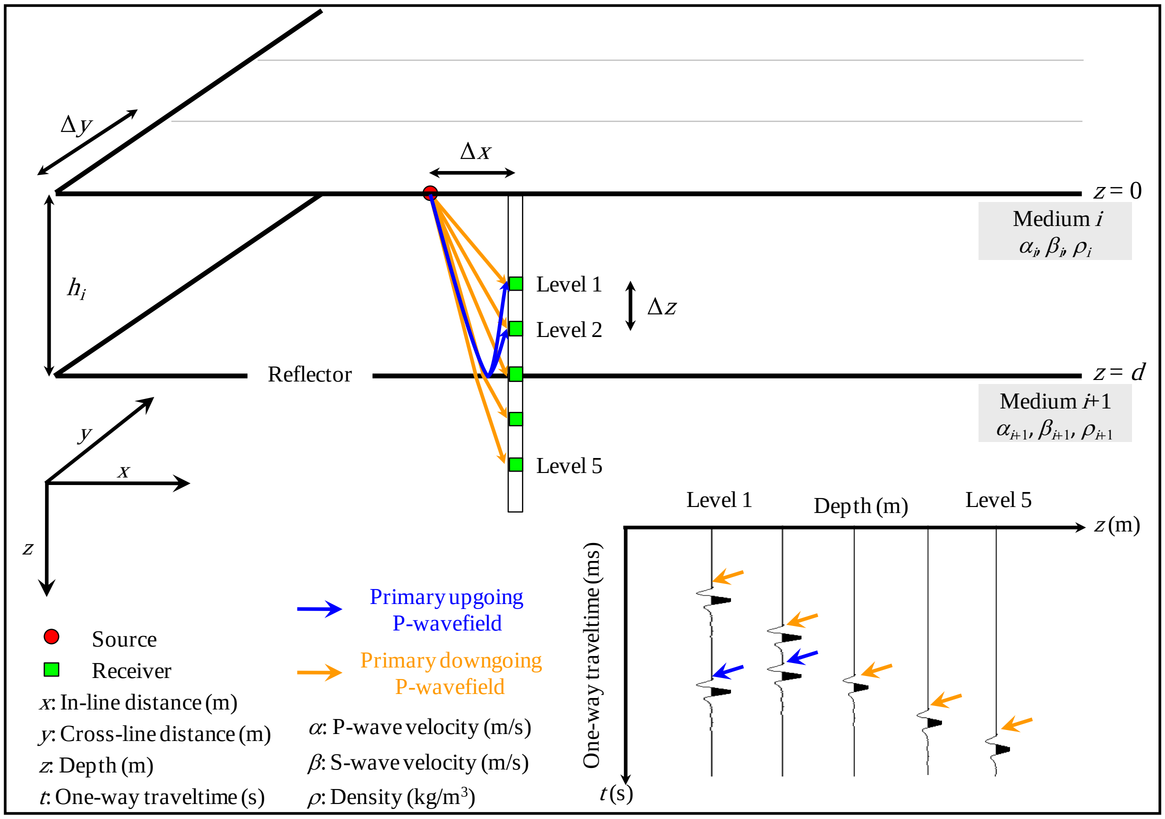

Figure 3-2: Depiction of the seismic experiment[18] in the case of the vertical seismic profile (VSP) technique showing the primary downgoing and primary upgoing P-wavefields in a simple horizontally stratified media. The response[19] associated with such experiment is shown at the bottom right-corner by the noise-free common-shot gather (seismogram). This is an oversimplified illustration as the schematic and seismogram do not show other types of seismic energy, such as converted-wave and multiples, which were omitted for simplicity and to avoid cluttering. Note that the seimsic energy is represented by rays rather than total wavefield.

[18] Using arbitrary setup.

[19] Assuming zero-phase, normal-polarity source wavelet and that P-wave, S-wave and density are increasing with depth.

3.3 Amplitude Variation with Offset (AVO)

In Section 3.1, the magnitude of the reflection coefficient associated with the partitioning of compressional wave seismic energy at an interface separating media with different elastic moduli was described by the normal incidence expression, i.e. Equation (3.6). However, seismic energy also impinges at non-normal angle of incidence (Figure 3-3). In this case, the partitioning of seismic energy is described by more comprehensive, yet more complicated, system of equations known as the Knott-Zoeppritz[20] equations (Knott, 1899; Zoeppritz, 1919). The equations are obtained by solving for the normal and tangential stress and displacement at an interface. Aki and Richards (2002) present neat expressions of these equations and the underlying assumptions.

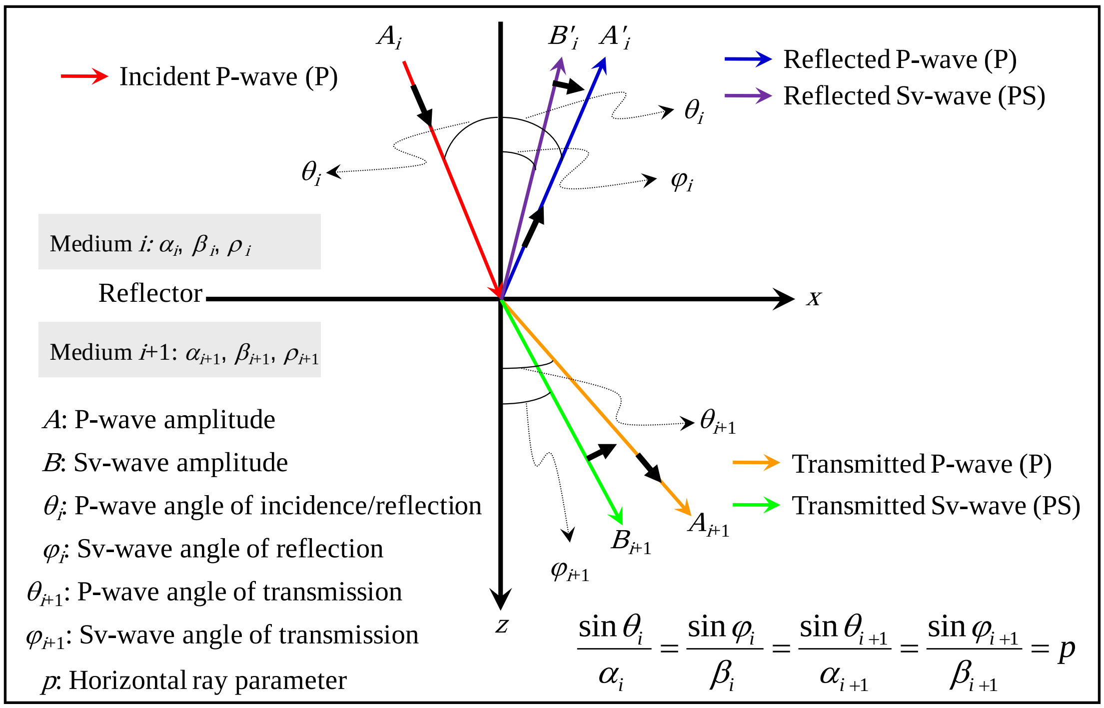

Figure 3-3: Partitioning of an incident P-wave into four components upon encountering a horizontal interface separating two media with different elastic properties. Sv is the vertical shear wavefield component. The black bold arrows indicate the direction of particle displacement. Angles (θ and φ) are in radians; wavespeeds (α and β) are in m/s; slowness (p) is in s/m.

---

[20] Knott derived his equations prior to Zoeppritz. However, his equations are expressed in terms of displacement potential.

The premise of AVO is that the magnitude of the reflection coefficient corresponding to an interface separating two media varies as a function of the source-receiver separation (offset, or more precisely angle) as well as the P-wave speed, S-wave speed and density of the individual media. Thus, AVO attributes can provide a mean of discerning variations in lithology and/or fluid present in an area of interest, e.g. CO_2 plume. Forward AVO modelling involves computing the response, for instance reflectivity, of a given model whereas AVO inversion involves estimating the acoustic/elastic parameters which would give rise to an observed AVO anomaly.

In order to compute the AVO response of a given model, one has to solve for the seismic reflectivity using, for instance, the Zoeppritz equations (Aki and Richards, 2002). In practice, it is customary to seek approximations to the Zoeppritz equations, such as the Aki and Richards approximation (Aki and Richards, 2002), which for an incident and reflected P-wave can be written as:

$$R_p(\theta_i) \approx \left[\frac{1}{2}\left(1-4p^2\bar{\beta}^2\right)\frac{\Delta\rho}{\bar{\rho}}\right]+\left[\frac{1}{2\cos^2\bar{\theta}}\frac{\Delta\alpha}{\bar{\alpha}}\right]-\left[4p^2\bar{\beta}^2\frac{\Delta\beta}{\bar{\beta}}\right] \tag{3.17}$$

where R_p is P-wave reflection coefficient, p is the ray parameter or horizontal slowness described by Snell's law, $\Delta\alpha$ is the difference between the P-wave speed of the two media ($\Delta\alpha=\alpha_{i+1}-\alpha_i$), $\Delta\beta$ is the difference between the S-wave speed of the two media ($\Delta\beta=\beta_{i+1}-\beta_i$), $\Delta\rho$ is the difference between the bulk density of the two media ($\Delta\rho=\rho_{i+1}-\rho_i$), $\bar{\alpha}$, $\bar{\beta}$, and $\bar{\theta}$ are the average P-wave speed, S-wave speed and angle, respectively. Another widely used approximation, mostly in AVO inversion, is the Shuey approximation (Shuey, 1985):

$$R_p(\theta_i) \approx R_p(0)+G\sin^2\bar{\theta}+F\left[\tan^2\bar{\theta}-\sin^2\bar{\theta}\right] \tag{3.18}$$

where

$$
\begin{aligned}
R_p(0) &= \frac{1}{2}\left(\frac{\Delta\alpha}{\bar{\alpha}} + \frac{\Delta\rho}{\bar{\rho}}\right) \\
G &= \frac{1}{2}\frac{\Delta\alpha}{\bar{\alpha}} - 2\left(\frac{\bar{\beta}}{\bar{\alpha}}\right)^2\left(\frac{\Delta\rho}{\bar{\rho}} + 2\frac{\Delta\beta}{\bar{\beta}}\right) \\
F &= \frac{1}{2}\frac{\Delta\alpha}{\bar{\alpha}}
\end{aligned}
\tag{3.19}
$$

$R_p(0)$ is normal-incidence reflection coefficient ($\theta = 0^o$, see Equation (3.6)), also called the intercept, G is the known as the gradient which describes the variation in reflectivity at intermediate angles ($0 < \theta < 40^o$), and F is the far angle term which dominates at far offsets ($40^o < \theta < \theta_c$), θ_c is the critical angle. Since the range of angles available for AVO analysis typically fall below 30^o-40^o (Avseth et al., 2005), only the first two-terms are retained. In such cases, Equation (3.18) can be viewed as a linearization of the Zoeppritz equation for P-wave reflectivity. Furthermore, Equation (3.18) can be further approximated using the Hilterman approximation (Hilterman et al., 1989) in which a Poisson's ratio of 0.3 is assumed; where the Poisson's ratio (σ) is given by:

$$
\sigma = \frac{(\alpha/\beta)^2 - 2}{2\left[(\alpha/\beta)^2 - 1\right]} \tag{3.20}
$$

This implies that the α/β equals to 2, which follows from the mudrock line relation given by Castagna et al. (1985). In AVO inversion, one tries to estimate the AVO parameters, e.g. the intercept ($R_p(0)$) and the gradient (G) using a common-depth point (CDP) gather, or super-gather, encompassing the zone of interest using least-squares optimization methods. These AVO parameters, or entities derived from them, are then visualized in different ways, e.g. using AVO classifications (Castagna et al., 1998), to extract relevant information about the lithology and fluids present in the reservoir. Excellent comprehensive review of AVO history, theory and applications can be found in Castagna and Backus (1993), Ross (1985), Castagna (1993), Russell et al. (2003), and Downton (2005) provide a good discussion of the topic as well. In the premises of this dissertation, forward AVO modelling is employed in predicting time-lapse changes due to actual and hypothetical CO_2 injection in PCEP (Chapter 5) and WASP (Chapter 7), respectively.

3.4 Notes on Sections 3.1, 3.2 and 3.3

The previous discussions (Sections 3.1 through 3.3) are intended to give a brief, short and rather simple introduction of some of the concepts involved in the seismic experiment in a simple horizontally stratified media. Furthermore, fundamental building blocks involved in the theory of seismic wave propagation, such as Hooke's law of elasticity, Newton's second law of motion, the scattering theory, Snell's law, Fermat's principle, Huygen's principle, and the Zoeppritz's equations are not discussed. Important topics like the geometry of seismic wavepaths, types of seismic waves, partitioning of energy at an interface, anisotropy, characteristics of seismic events, equipments used, data acquisition, data analysis and data interpretation methods are not mentioned as well. For instance, only the scalar wave-equation was introduced in Section 3.1. However, more complete form of the wave-equations known as the vector or elastic wave-equation (EWE), that describes both P-wave and S-wave propagation in homogenous isotropic media and includes the term accounting for the force source (**f**) of the wave is given by (Sheriff and Geldart, 1995):

$$\rho \frac{\partial^2 \psi}{\partial t^2} = \mathbf{f} + (2\mu + \lambda)\nabla(\nabla \cdot \psi) - \mu \nabla \times (\nabla \times \psi) \qquad (3.21)$$

Discussion of these and other related topics can be found in many references in the literature including Bullen and Bolt (1985), Sheriff and Geldart (1995), Dahlen and Tromp (1998), Shearer (1999), Červený (2001), Graebner et al. (2001), Kennett (2001), Yilmaz (2001), Aki and Richards (2002), Brown (2004), and Stark (2008).

3.5 Modelling

3.5.1 Introduction

Modelling is an invaluable tool that is invoked during the various stages of the seismic experiment. For instance, it plays an important role in understanding as well as in predicting seismic wave propagation and estimating distribution/magnitude of the physical properties governing such propagation in geologic media (Wason et al., 1984; Carcione et al., 2002). Modelling can be conceptual, physical or mathematical (Lines and Newrick, 2004). Of particular interest in this dissertation is the mathematical, or numerical, modelling as it provides a mean to achieving some of the objectives outlined in Section 1.5. According to the input and the objective, modelling can be divided into:

i. Forward modelling (FM).

ii. Inverse modelling (IM).

Figure 3-4 illustrates the relationship between forward and inverse modelling. In the forward problem, one tries to compute the effect or response of a geologic model with prescribed distribution of physical properties. In the inverse problem, on the other hand, one tries to reconstruct the geologic model and the distribution/magnitude of the physical properties associated with such model from the model response, or observations. The bridge between the model and the model response is given by the model parameters.

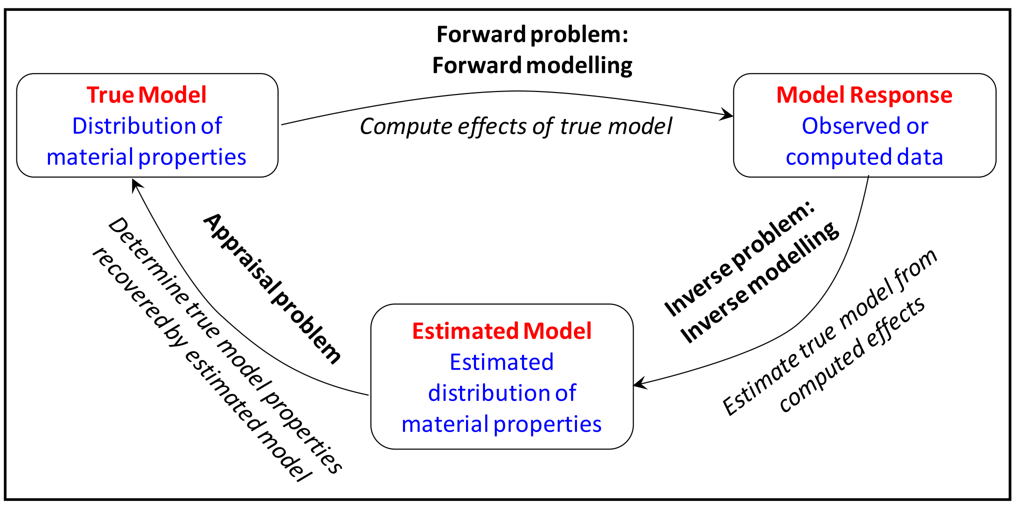

Figure 3-4: General relationship between the various modelling problems. Scheme adopted from Snieder and Trampert (1999), and Sheriff (2002).

To further illustrate the relationship between forward and inverse modelling, consider a distribution of values, or causes, **m** which produces a set of measurements **d** that depends on a system of parameters **P**. The forward problem can be written in the following form (Lines and Newrick, 2004):

$$\mathbf{d} = \mathrm{F}(\mathbf{m}) \tag{3.22}$$

where **d** is a column vector of the model response (d_i,..., d_n), **m** is a column vector of the physical properties values, or geologic model parameters, (m_j,...,m_q), i and j are positive integers corresponding to the sample number, n and q represent the number of measurements and parameters, respectively, F is a mathematical transformation operator, which describes the physical process and transforms from model space into data space. Alternatively, if a linear relationship is assumed between **d** and **m**, then Equation (3.22) can be written as (Sheriff, 2002):

$$\mathbf{d} = \mathbf{P}\mathbf{m} \tag{3.23}$$

where **P** is a matrix of the model parameters (p_{ij},..., p_{nq}). Equation (3.23) represents a linear mathematical model relating distribution of the physical properties values to a set of measurements (model response) through a system of model parameters (Figure 3-4). Solving the equation for m_i transforms from the model space into the data space (Lines and Newrick, 2004). Solving for m_j, on the other hand, is the inverse problem which transforms from the model space into the data space:

$$\mathbf{m} = \left(\mathbf{P}^{\mathrm{T}}\mathbf{P}\right)^{-1}\mathbf{P}^{\mathrm{T}}\mathbf{d} \tag{3.24}$$

where $\mathbf{P}^{\mathrm{T}}$ is the matrix transpose of the matrix **P**, and $(\mathbf{P}^{\mathrm{T}}\mathbf{P})^{-1}$ is the inverse of the multiplication matrix $\mathbf{P}^{\mathrm{T}}\mathbf{P}$. Equation (3.24) is a simple linear inversion formulation and, in practice, it is rather optimized by introducing some constraints[21] to avoid problems, such as singularity[22], and to better estimate the physical properties values (Lines and Treitel, 1984). Discussion of constraints, singularity and other related topics can be found in Tarantola and Valette (1982), Menke (1989), Parker (1995) and Kirsch (1996).

In practice, inverse modelling results are not perfect even if a rigorous mathematical model is developed and employed. This is due to three main reasons: (1) trying to reconstruct a continuous media from finite observations, (2) noise contamination of the observations, and most importantly (3) non-uniqueness; the fact that more than one model may adequately fit the observations (Snieder and Trampert, 1999). Instead, it is more realistic to seek an estimate ($\hat{\mathbf{m}}$) of the true model (**m**) such that the model responses from the estimated and true models satisfy some predefined conditions or criteria. Characterizing the level of agreement between the two is part of the appraisal

[21] For example, constraint on the sum of the squares to be bounded by a finite quantity (Lines and Treitel, 1984). See discussion under Equation 3.58 in Section 3.5.7.
[22] Singularity is an inverse modelling problem arising when a function is not differentiable.

problem[23] (Snieder and Trampert, 1999). Usually, certain indications such as solution convergence and misfit (or error) are invoked in the appraisal process but the scope is much larger than that and is beyond the perimeter of this dissertation.

The choice of the mathematical model and the corresponding model parameters usually depends on the nature of the geologic media to be simulated or reconstructed. In forward modelling, for instance, the simulation of seismic wavefield associated with a complex geologic model would require more rigorous mathematical model, with more model parameters, than that corresponding to a simple earth model (Lines and Newrick. 2004). Similarly, solving an inverse problem with under-determined systems[24] would produce many possible solutions and, therefore, would require imposing additional constraint on the inversion, e.g. by adding a prior information (Snieder and Trampert, 1994; Scales et al., 2001). Finally, it should be noted that there is an inherent interrelationship between forward and inverse modelling as expressed in Equation (3.24), which could also be non-linear. Detailed discussion of forward and inverse seismic modelling can be found in Wason et al., (1984), Russell (1988), Kelly and Marfurt (1990), Snieder and Trampert, (1999), Scales et al. (2001), Yilmaz (2001), Carcione et al. (2002), Gjøystdal et al. (2002), Margrave (2003), and Krebes (2004).

3.5.2 Modelling Methods

In Section 3.1, two categories of mathematical models used in describing the seismic wavefield were introduced: those based on the wave theory and those based on the ray theory. When performing numerical modelling, one is interested in solutions to those mathematical models. Analytical solutions would be ideal but, unfortunately, they are either unknown or difficult to implement in case of realistic earth model (Červený, 2001). As a result, one has to resort to approximate methods. The two principal numerical modelling methods utilized in this dissertation are:

i. Finite-difference (F-D) method.

---

[23] The appraisal problem is a process by which the properties of the true model are retrieved from the estimated model along with the associated error (Snieder and Trampert, 1999).
[24] In inverse problem, under-determined corresponds to a system of equations where there are more equations than unknowns resulting an ill-posed inverse problem.

ii. Ray tracing method.

These are among the most commonly used and, more importantly, highly developed[25] seismic modelling methods (Carcione et al., 2002). Furthermore, depending on the objective and algorithm, these methods can be manipulated to solve the forward or the inverse problem (Figure 3-4). Good discussion of these and other modelling methods are given in Wason et al. (1984), Carcione et al. (2002), and Gjøystdal et al., (2002).

In the framework of this dissertation, forward modelling methods are used to simulate the seismic response, of synthetic geologic models, associated with the surface seismic and VSP experiments as well as offset-dependent reflectivity (Chapters 4 and 6). In addition to F-D and ray tracing, the convolutional modelling method is often used in generating zero-offset synthetic seismograms (ZOS), which aid in interpretation as they provide a mean of identifying and correlating seismic horizons to the geology through seismic-to-well tie (Chapters 4 and 6). When it comes to inverse modelling, two deterministic inversion schemes are employed: recursive inversion (RI) and model-based inversion (MBI). These are, primarily, utilized in estimating the distribution and magnitude of acoustic impedance (AI) corresponding to the field data (Chapters 3 and 5). Besides forward and inverse modelling, it is of profound interest to understand and predict changes in the physical properties[26] that govern seismic wave propagation using rock physics, or fluid substitution, modelling.

Table 3-1 outlines the various modelling methods exploited in this dissertation. In the following sections, a rather short, general and simple introduction of these modelling methods is given. However, it should be noted that it is beyond the scope of this dissertation neither to review the theoretical aspects of these methods nor to discuss the specifics of the mathematical models and computer algorithms implemented. Instead, the focus is rather on employing those established methods using well-developed commercial computer algorithms (Section 1.8) to achieve the objectives discussed in Section 1.5. Nonetheless, references are given, in the appropriate context, where thorough discussions can be found.

---

[25] In terms of both theory and computer algorithms.
[26] Namely, P-wave speed, S-wave speed and bulk density.

Table 3-1: List of the various modelling methods employed in this dissertation.

Modelling Category			Methods	Comment
Numerical	Forward Modelling	I.	Finite-difference	See Section 3.5.3
		II.	Ray tracing	See Section 3.5.4
		III.	Convolutional	See Section 3.5.5
	Inverse Modelling	I.	Recursive	See Section 3.5.6
		II.	Model-based	See Section 3.5.7
Rock Physics			Gassmann fluid substitution	See Section 3.5.9

3.5.3 Forward Modelling I: Finite-difference (F-D) Methods

In order to solve the WE numerically, F-D methods approximate the derivatives in the WE (see Section 3.1) by finite differences in a space-time grid and then evaluate the seismic wavefield recursively using spatial and temporal steps. Recall that the 1-D SWE for a pressure wave travelling along the *x*-axis is given by:

$$\frac{\partial^2\psi}{\partial x^2} = \left(\frac{1}{\alpha^2}\right)\frac{\partial^2\psi}{\partial t^2} \tag{3.25}$$

where $\psi(x,t)$ is a wavefunction (see discussion in Section 3.1). Recall the definition of the first derivative (Smith, 1985):

$$\frac{d\psi(x)}{dx} = \lim_{\Delta x \to 0}\frac{\psi(x+\Delta x)-\psi(x)}{\Delta x} \tag{3.26}$$

In F-D methods, the derivative approximation is expressed in the following form (Margrave, 2003):

$$\frac{d\psi}{dx} \approx \frac{d^{+1}\psi}{dx} = \frac{\psi(x+\Delta x)-\psi(x)}{\Delta x} \tag{3.27}$$

where Δx is an infinitesimal change in space, i.e. grid spatial step value; the time dependence is omitted for shortness. Equation (3.27) computes the forward difference or quotient. Similarly, the backward difference is given by:

$$\frac{d^{-1}\psi}{dx} = \frac{\psi(x)-\psi(x-\Delta x)}{\Delta x} \tag{3.28}$$

A better approximation of the first derivative is given by the centered difference, which is attained by taking the average of the right-hand side of Equations (3.27) and (3.28):

$$\frac{d^1\psi}{dx} \approx \frac{\psi(x+\Delta x)-\psi(x-\Delta x)}{2\Delta x} \tag{3.29}$$

In solving the WE, the interest is actually on approximating the second derivative, which in term of the centered difference can write as (Margrave, 2003):

$$\frac{d^2\psi}{dx^2} \approx \frac{\psi(x+\Delta x)-2\psi(x)+\psi(x-\Delta x)}{\Delta x^2} \tag{3.30}$$

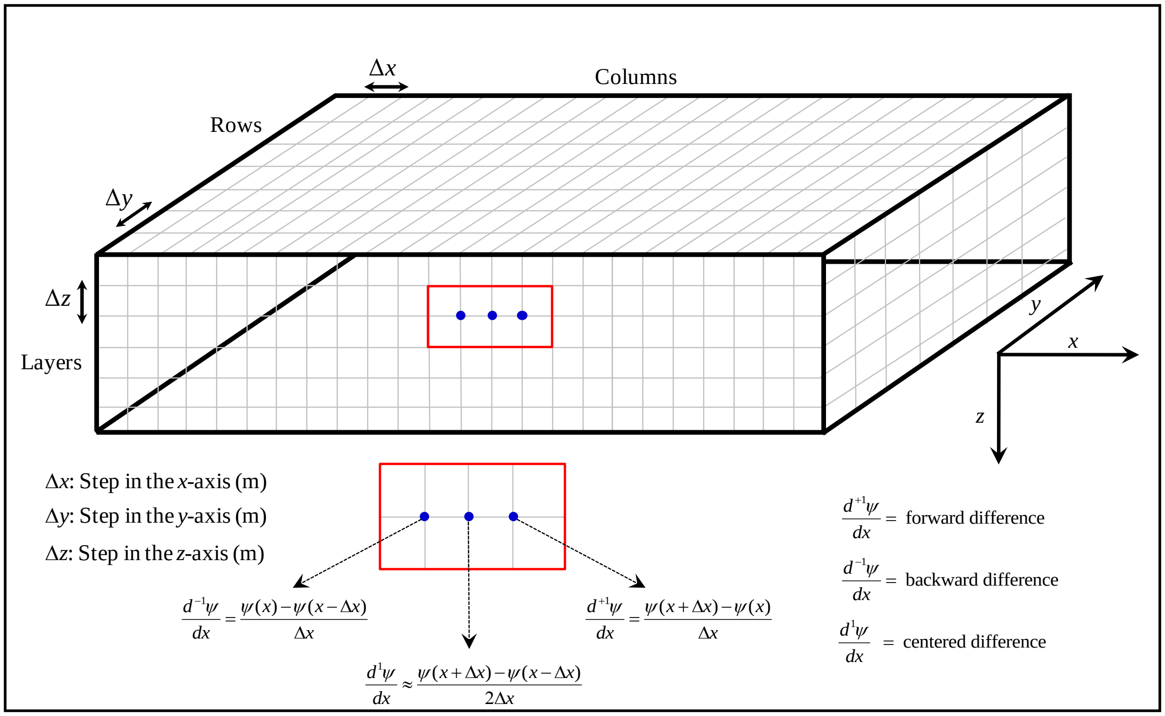

Figure 3-5: Simple illustration of the finite-difference (F-D) method. The first step, following the development of a mathematical model to be used, is to construct and discretize the model by assigning physical and dimensional parameters to the grids. Then, the wavefield snapshot is calculated recursively as shown by the red rectangle, which demonstrates how the wavefield is calculated in 1-D along the *x*-axis using three nodes only. Of course, there is a node at each intersection but those were omitted for the sake of simplicity. Also, only the first derivative approximation is used in this illustration.

The time dependence can be expressed in similar form to Equation (3.30). Then, the space and time derivatives approximations can be plugged back into the 1-D SWE:

$$\frac{\psi(x+\Delta x)-2\psi(x)-\psi(x-\Delta x)}{\Delta x^2} = \left(\frac{1}{\alpha^2}\right)\frac{\psi(t+\Delta t)-2\psi(t)-\psi(t-\Delta t)}{\Delta t^2} \tag{3.31}$$

where Δt is the grid temporal step value. Re-arranging Equation (3.31) to solve for the next snapshot of the wavefield (Wason et al., 1984):

$$\psi(x,t+\Delta t)=2\left(1-\chi^2\right)\left[\psi(x,t)\right]-\left(\chi^2\right)\left[\psi(x+\Delta x,t)+\psi(x-\Delta x,t)\right]-\left[\psi(x,t-\Delta t)\right] \quad (3.32)$$

where

$$\chi=\left(\frac{\Delta t^2\alpha^2}{\Delta x^2}\right) \quad (3.33)$$

Equation (3.32) can be solved recursively, i.e. calculating the wavefield snapshot at the next time step from the current and previous ones given the appropriate boundary conditions (Carcione et al., 2002). The former is a very short and general introduction of the explicit F-D methods. Actual implementation, using computer algorithms, requires taking into consideration many aspects like model source implementation, stability, accuracy, convergence, free surface effect, model discritization, computational cost and boundary problems. Good review and discussion of the F-D methods and how to deal with the earlier mentioned considerations can be found in Mitchell (1969), Boore (1972), Kelly et al. (1976), Smith (1985), Kelly and Marfurt (1990), Ames (1992), Aki and Richards (2002), Carcione et al. (2002), and Krebes (2004).

In this dissertation, a F-D time-domain modelling code is exploited which is part of the software package Reflexw© (see Section 1.8). The F-D code is based on forward computation of the seismic wavefield (synthetic seismogram) using explicit F-D solution to the acoustic WE (Sandmeier, 2009). This computer algorithm is primarily invoked in the modelling of the surface seismic experiment in Chapters 5 and 7.

3.5.4 Forward Modelling II: Ray Tracing Methods

The other mean of simulating the seismic experiment in this dissertation is achieved through the geometric ray tracing (GRT). In a simple horizontally stratified media consisting of homogenous isotropic layers, the time travelled by a pressure wave through the media between two points (i.e. source and receiver) located on the earth surface can, in general, be calculated using simple algebraic formulations. First[27], the

---

[27] The process described herein is intended as an illustration but in practice the approach is fairly different. For instance, instead of defining the offset first, a trial and error approach is implemented in which an array of shooting angle is attempted from the source and only the ray parameter observed at the receiver is retained.

distance travelled (X) between the source and receiver is defined (Figure 3-6) and the ray parameter (p) associated with the ray travelling between them is calculated using the equation (Krebes, 2004):

$$X(p) = \sum_{i=1}^{n} \frac{p\alpha_i h_i}{\sqrt{1-\alpha_i^2 p^2}} \tag{3.34}$$

where h and α are the layer thickness and P-wave speed, i is a positive integer representing the ray segment in the i^{th} layer, n is a positive integer representing the number of ray segments (and layers). Recall that p is the horizontal slowness given by Snell's law:

$$\frac{\sin\theta_i}{\alpha_i} = \frac{\sin\theta_{i+1}}{\alpha_{i+1}} = p \tag{3.35}$$

where θi is the take-off angle which is also in this case the angle of incidence on the i^{th} interface (i.e. the interface separating layers i and i+1), θ_{i+1} is the angle of transmission through the i^{th} interface,. Note that Snell's law states that p is constant for a given raypath. Following the calculation of p, the traveltime (T) can be computed using the following relation (Krebes, 2004):

$$T(p) = \sum_{i=1}^{n} \frac{h_i}{\alpha_i} \frac{1}{\sqrt{1-\alpha_i^2 p^2}} = pX + \sum_{i=1}^{n} \frac{h_i}{\alpha_i}\sqrt{1-\alpha_i^2 p^2} \tag{3.36}$$

Furthermore, the amplitude (A) associated with the pressure wave at the receiver located at X is given by (Krebes, 2004):

$$A(\omega) = \left(\frac{Y}{L}\right) e^{jT} \tag{3.37}$$

where Y is the product of the reflection and transmission coefficients along the raypath, L is the geometrical spreading factor, T is the traveltime and j is the imaginary unit. Equation (3.37) gives the amplitude for a single frequency ω. If the source wavelet is known, then the amplitude of the waveform for all frequencies at the receiver can be computed and therefore the displacement (Krebes, 2004):

$$\psi(x,t) = \int_{-\infty}^{+\infty} W(\omega) A(\omega) e^{-j\omega T} d\omega \tag{3.38}$$

where $W(\omega)$ is the amplitude spectrum of the source wavelet $w(t)$, and $\psi(x,t)$ is the displacement.

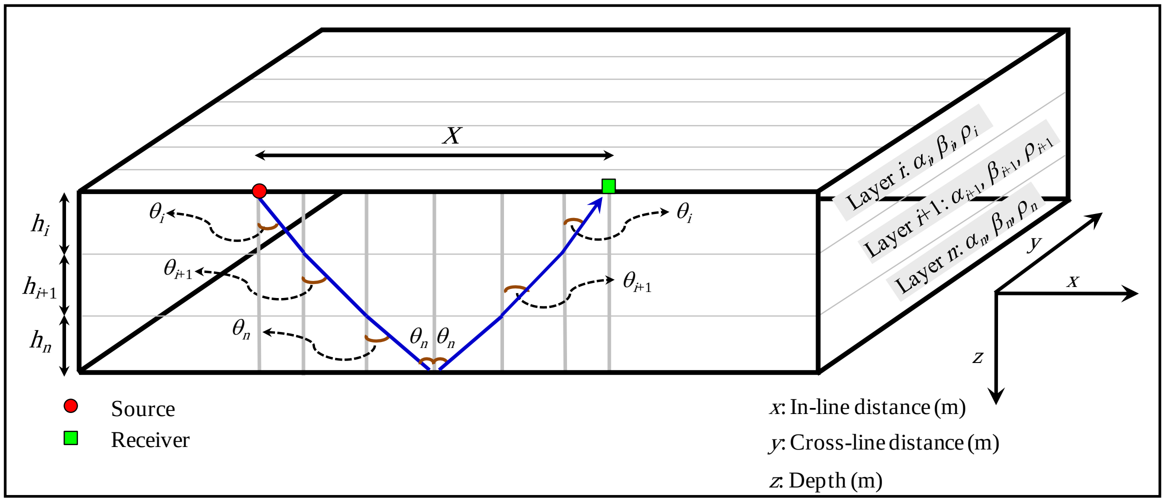

Figure 3-6: Depiction of ray tracing between a source and receiver in a simple horizontally stratified media, where the P-wave velocity increases with depth. The raypath travels according to Fermat's principle and obeys Snell's' law at interfaces separating layers with different elastic properties. The total traveltime observed at the receiver is the cumulative contribution of time travelled by each raypath segment in the individual layers.

It should be noted that traveltime calculated through ray tracing will usually yield accurate results if the rate of change of velocity is small relative to the wavelength[28]. The calculated waveform, however, is only an approximation to that achieved by solving the WE and the level of accuracy will depend on the model complexity. The above discussion assumes very simple, probably the simplest, scenario. Practical implementation of ray tracing, however, in more realistic cases is more complicated and takes a different approach. For instance, in computer modelling one need to take into consideration many issues, e.g. take-off angle, wavefronts construction, free surface effect, caustics, and smoothness of the model among other things. More discussion of ray methods can be found in Bullen (1987), Červený, (2001), Aki and Richards (2002), Carcione et al. (2002), Gjøystdal et al. (2002), and Krebes (2004).

---

[28] Therefore, it is a standard procedure to smooth the velocity.

There are two ray tracing modelling codes that are employed in this dissertation: NORSAR-2-D© and AVO© (see Section 1.8). The first calculates synthetic seismograms utilizing approximate solutions to the WE through the mean of the GRT. AVO© calculates offset-dependent reflectivity using solutions to the Zoeppritz equations or approximations (Dahl and Ursin, 1991; Hampson-Russell, 2009). The implementation of these forward modelling algorithms is presented in Chapters 5 and 7.

3.5.5 Forward Modelling III: Convolutional Methods

In addition to the two former methods, it is customary to use convolutional methods as well at various instances during forward seismic modelling. Figure 3-7 shows an illustration of the convolutional modelling concept. In general, the convolutional model in the time domain can be expressed as (Sheriff and Geldart, 1995):

$$\psi(t) = r(t) * w(t) + n(t) \tag{3.39}$$

$\psi(t)$ is the seismic trace, $r(t)$ is the reflectivity series, $w(t)$ is the seismic wavelet, $n(t)$ is a noise function, and $*$ denotes the convolution operator. Equation (3.39) is a rather simplified expression as it does not include time-variant processes, such as multiples and absorption. In broader context, seismograms, i.e. seismic trace, can be described as the convolution of the medium impulse response, i.e. Green's function, with an embedded wavelet plus a noise function (Sheriff, 2002). For more information on the convolutional model, see Wason et al. (1984), Sheriff and Geldart (1995), Yilmaz (2001) and Margrave (2003). Synthetic seismograms generated using the convolutional model are exploited in Chapters 4 through 7.

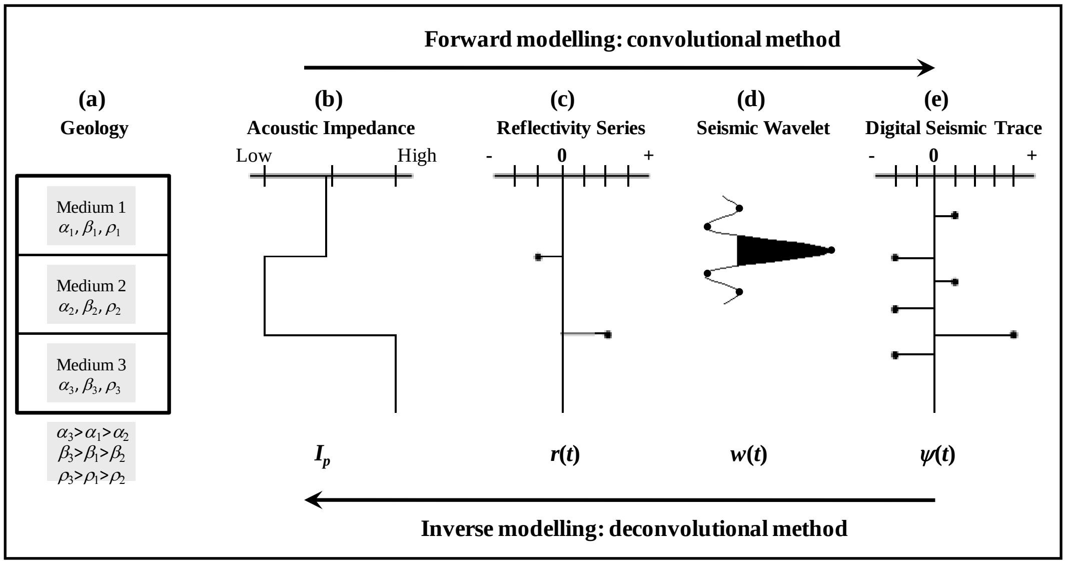

Figure 3-7: Illustration of forward and inverse modelling using the convolutional and deconvolutional methods, respectively. (a) Simple three layers 1-D geologic model with arbitrary P-wave speed, S-wave speed and density, (b) the acoustic impedance (I_p) contrast corresponding to the model, (c) the P-wave reflection coefficient (R_p), (d) seismic wavelet (consisting of 5 samples), and (e) the digital seismic trace (model response) attained by convolving the seismic wavelet in (d) with the reflectivity series in (c). Note that the digital seismogram has 6 samples, i.e. length of $\psi(t)$ = length of $r(t)$ + length of $w(t)$ - 1. Modified after Russell (2007).

3.5.6 Inverse Modelling I: Recursive Methods

Recursive inversion (RI), also known as band-limited inversion[29], estimates the acoustic impedance (AI) recursively by first extracting an approximation of the reflection coefficient from the post-stack seismic data and then re-arranging the normal incidence (NI) reflection coefficient (RC) equation to solve for the acoustic impedance explicitly (Russell, 1988). RI can be thought of as a direct inversion method. Recall that the RC in case of NI seismogram is given by:

$$R_i = \frac{I_p^{i+1} - I_p^i}{I_p^{i+1} + I_p^i} \tag{3.40}$$

Re-arranging Equation (3.40) to solve for the acoustic impedance of the i^{th}+1 layer:

[29] Since it is mainly constrained by the bandwidth of the seismic data, which typically falls between 6 and 60 Hz for surface seismic.

$$I_p^{i+1} = \frac{I_p^i(1+R_i)}{1-R_i} \tag{3.41}$$

where R is the reflection coefficient, I_p is the acoustic impedance (kg/m^2.s), and i is a positive integer representing the layer (or interface) number. Recall that the acoustic impedance is given by multiplying the P-wave speed (m/s) and density (kg/m^3). Thus, starting at the first layer i, the AI of successive layers can be recursively calculated:

$$I_p^n = I_p^1 \prod_{i=2}^{n} \left[\frac{1+R_p^i}{1-R_p^i}\right]^{1/n} \tag{3.42}$$

where $\prod$ is the geometric mean. Equations (3.40) and (3.42) give the discrete form of the NI reflection coefficient and the corresponding acoustic impedance. Assuming that $r(t) \ll |0.3|$, which is typically a valid assumption, the continuous analogue of Equations (3.40) and (3.42) can be written as (Russell, 1988):

$$R_p(t) = \frac{1}{2}\frac{d \ln I_p(t)}{dt} \tag{3.43}$$

$$I_p(t) = I_p^1 \exp\left[2\int_0^t R_p(\tau)d\tau\right] \tag{3.44}$$

where ln is the natural logarithm and τ is a dummy time variable for integration.

In practice, implementation of RI requires constraint provided by primarily by well control (sonic and density logs) and seismic data (horizons). In addition, since RI relies vastly on seismic wavelet deconvolution (Figure 3-7), having a good estimation of the seismic wavelet is probably one of the most crucial steps in achieving reliable results using this inversion scheme. This can be accomplished by trial and error or by using model-based methods (Section 3.5.7). Also, proper seismic amplitude scaling (see Section 3.5.8) and high signal-to-noise ratio is required for useful results. Furthermore, given that seismic data is band-limited, it is important to add low, and occasionally high, frequency components to attain better estimate of the acoustic impedance (Lines and Newrick, 2004). Additional information on RI can be found in Waters (1978), Bamberger et al. (1982), Cooke and Schneider (1983), and Russell (1988).

The RI algorithm exploited in this dissertation is part of the inversion module STRATA© within the Hampson-Russell software suite (see Section 1.8; STRATA, 2009).

Figure 3-8 shows the major steps involved in the implementation of such algorithm whereas actual implementation of RI in this dissertation is presented in Chapters 4 and 6.

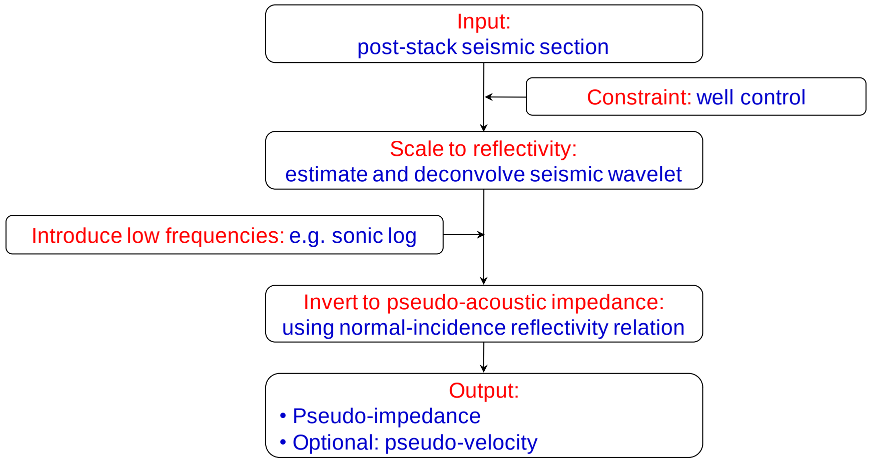

Figure 3-8: Overview of the major steps involved in recursive inversion. Modified after Russell (1988).

3.5.7 Inverse Modelling II: Model-based Methods

Model-based inversion (MBI) uses a different approach than recursive inversion and it can be viewed as an indirect inversion method. First, well control and seismic data are used to build an initial low-frequency model which is essentially an estimate of the acoustic impedance distribution. Then, using an approximation of the seismic wavelet, the model is perturbed by solving the wave-equation, for instance using one of the methods discussed in Section 3.5.2. The computed model response, or synthetic seismogram, is then compared to the actual seismogram, usually by means of cross-correlation and misfit error. The objective is to find a set of model parameters that minimizes the difference between the observed data and the model response. So, the process is iterated until the model converges, i.e. the model response becomes within a predefined acceptable range from the actual observations. The acceptable range is usually quantified in terms of the misfit error between the observed and computed model responses. One of the most commonly used measures is the sum of the squared differences, hence known as least-squares (Russell and Lines, 2007).

To illustrate the basic theory underlying MBI, recall the general mathematical model introduced in Section 3.5.1 which relates the model response and the values of the physical properties:

$$\mathbf{d} = \mathrm{F}(\mathbf{m}) \tag{3.45}$$

where **d** is a column vector of the model response (d_i,...,d_n), **m** is a column vector of the model parameters, for instance acoustic impedance, (m_j,...,m_q), i is a positive integer representing the sample number, n and q are positive integers referring to the number of observations and model parameters, respectively, F is a mathematical transformation operator[30] which describes the physical process and transforms from model space into data space. In generalized linear inversion (GLI), the mathematical relationship can be written as (Russell, 1988):

$$\mathrm{F}(\mathbf{m}) = \mathrm{F}(\mathbf{m}^0) + \left(\frac{\partial \mathrm{F}(\mathbf{m}^0)}{\partial m_j}\right)\Delta\mathbf{m} \tag{3.46}$$

where F(**m**) is vector of the model response, F($\mathbf{m}^0$) is a vector of the initial model response, the term with the partial derivative (∂) inside the parenthesis represents change in calculated values F($\mathbf{m}^0$) with respect to the model parameters (m_j), and $\Delta\mathbf{m}$ is the model parameters change vector with respect to some initial estimate of the parameters $\mathbf{m}^0$:

$$\Delta\mathbf{m} = \mathbf{m} - \mathbf{m}^0 \tag{3.47}$$

If the relationship between the model response and the model parameters is linear, the model response perturbation in Equation (3.46) can be re-written using first-order approximation of Taylor's series expansion about the initial estimate $\mathbf{m}^0$ (Lines and Treitel, 1984):

$$\mathbf{d} = \mathbf{d}^0 + \mathbf{J}\boldsymbol{\delta} \tag{3.48}$$

where **J** is $n \times q$ matrix of partial derivatives known as the Jacobian:

$$\mathbf{J} = J_{ij} = \frac{\partial d_i}{\partial m_j} \tag{3.49}$$

---

[30] In seismic modelling, F yields the model response using solution to the wave-equation.

and $\boldsymbol{\delta}$ is the model parameters change vector given in Equation (3.47):

$$\boldsymbol{\delta} = \Delta\mathbf{m} = \mathbf{m} - \mathbf{m}^0 \tag{3.50}$$

The difference between the observed data and the model response is given by the error vector (**e**):

$$\mathbf{e} = \mathbf{d}^{\text{observed}} - \mathbf{d} \tag{3.51}$$

where $\mathbf{d}^{\text{observed}}$ is the observed or measured data (d_i,...,d_n), and **d** is the model response; **e** is also known as the prediction or misfit error. Similarly, the difference between the observed data ($\mathbf{d}^{\text{observed}}$) and the initial model response ($\mathbf{d}^0$) is defined by the discrepancy vector (**g**):

$$\mathbf{g} = \mathbf{d}^{\text{observed}} - \mathbf{d}^0 \tag{3.52}$$

In linear inverse problem, the solution is based on the length of the model response **m** or norm. The most commonly used norms are those based on the sum of some power (p) of the elements of the vector **e**:

$$l_p - \text{norm}: \; \|\mathrm{e}\|_p = \left[\sum_{i=1}^{n} |\mathrm{e}_i|^p \right]^{1/p} \tag{3.53}$$

where e_i is the difference between the i^{th} measurement ($d_i^{\text{ observed}}$) and the i^{th} model response (d_i):

$$\mathrm{e}_i = d_i^{\text{observed}} - d_i \tag{3.54}$$

Normally, it is only useful to seek as solution in terms of the sum of the absolute error difference (l_1-norm) or the sum of the squared error difference (l_2-norm):

$$l_1 - \text{norm}: \|\mathrm{e}\|_1 = \left[\sum_{i=1}^{n} |\mathrm{e}_i|^1 \right]^1 \tag{3.55}$$

$$l_2 - \text{norm}: \|\mathrm{e}\|_2 = \left[\sum_{i=1}^{n} |\mathrm{e}_i|^2 \right]^{1/2} \tag{3.56}$$

Recall that in GLI, the objective is to find a set of model parameters that minimizes the difference between the model response, i.e. estimated or predicted data, and the measured or observed data without the need for trial and error (Russell, 1988). For instance, in the least-squares scheme the objective is to minimize the sum of the cumulative squares of the errors (***E***), with respect to the model parameters change vector

$\boldsymbol{\delta}$, between the model response **m** and the observed data **d** which implies (Lines and Treitel, 1984):

$$\frac{\partial \boldsymbol{E}}{\partial \boldsymbol{\delta}} = 0 \tag{3.57}$$

where is $\boldsymbol{E}$ is the cumulative least-squares error or cost function:

$$\boldsymbol{E} = \mathbf{e}^{\mathrm{T}}\mathbf{e} = \left(\mathbf{g} - \mathbf{J}\boldsymbol{\delta}\right)^{\mathrm{T}} \left(\mathbf{g} - \mathbf{J}\boldsymbol{\delta}\right) \tag{3.58}$$

In the above equation, the error vector **e** has been re-expressed by substituting Equations (3.48) and (3.52) into Equation (3.51). Performing the multiplication between the entities in the right-hand side of (3.58) and plugging the outcome into Equation (3.57) and undertaking the differentiation yields the normal equations (Parker, 1994; Kirsch, 1996):

$$\mathbf{J}^{\mathrm{T}}\mathbf{J}\boldsymbol{\delta} = \mathbf{J}^{\mathrm{T}}\mathbf{g} \tag{3.59}$$

Since the interest is in estimating the model parameters giving rise to the observed data, Equation (3.60) is re-arranged to solve for the model parameters change vector $\boldsymbol{\delta}$ which yields the objective function:

$$\boldsymbol{\delta} = \left(\mathbf{J}^{\mathrm{T}}\mathbf{J}\right)^{-1} \mathbf{J}^{\mathrm{T}}\mathbf{g} \tag{3.60}$$

This is frequently referred to as Gauss-Newton or unconstrained least-squares solution (Lines and Treitel, 1984). Substituting this solution into Equation (3.58) and performing some matrix manipulation (Kirsch, 1996) yields the actual cumulative squared error ($\hat{\boldsymbol{E}}$):

$$\hat{\boldsymbol{E}} = \mathbf{g}^{\mathrm{T}} \left(\mathbf{I} - \mathbf{J}\mathbf{J}_{\mathrm{G}}^{-1}\right)^{\mathrm{T}} \mathbf{g} \tag{3.61}$$

where **I** is the identity matrix, and $\mathbf{J}_{\mathrm{G}}^{-1}$ is the generalized least-squares inverse matrix of **J**:

$$\mathbf{J}_{\mathrm{G}}^{-1} = \left(\mathbf{J}^{\mathrm{T}}\mathbf{J}\right)^{-1} \mathbf{J}^{\mathrm{T}} \tag{3.62}$$

As outlined in Section 3.5.1, the inverse problem in this context is not always well-posed and, therefore, there are many numerical problems that could arise when solving for $\boldsymbol{\delta}$. For example, singularity, i.e. non-existence of the inverse of $\mathbf{J}^{\mathrm{T}}\mathbf{J}$ and non-convergence of the solution. Another problem is the existence of many possible solutions due to the geophysics inverse problem, in general, being overdetermined meaning that there are more data or measurements ($\mathbf{d}^{\text{observed}}$ or **d**) than model parameters (**m**), or in other words more equations than unknowns (n>q). This leads to the situation where more than one model may adequately fit the observations. Further discussion of the inverse problem and on how to deal with aforementioned problems as well as extension to non-linear case can, for instance, be found in Bamberger et al. (1982), Tarantola and Valette (1982), Cooke and Schneider (1983), Menke (1989), Parker (1994), Kirsch, (1996), Snieder and Trampert (1999), Scales et al. (2001), Aki and Richards (2002), Gubbins (2004), and Pujol (2007).

The MBI scheme used in this dissertation is based on constrained iterative least-squares algorithm which is part of the STRATA© module within the Hamspon-Russell software suite (see Section 1.8; STRATA, 2009). The mathematical model that forms the basis for the computer code is the Marquardt-Levenberg method (Levenberg, 1944; Marquardt, 1963) with the following objective function:

$$\boldsymbol{\delta} = \left(\mathbf{J}^{\mathrm{T}}\mathbf{J} + \lambda\mathbf{I}\right)^{-1}\mathbf{J}^{\mathrm{T}}\mathbf{g} \tag{3.63}$$

here, the so-called damping factor[31] λ is introduced, which alleviates the singularity problem by imposing bounds on the solution through the smoothness of the parameters change vector $\boldsymbol{\delta}$. Figure 3-9 shows the principle steps involved in the implementation of MBI while the actual exploitation is demonstrated in Chapters 4 and 6.

---

[31] For estimation of and other related discussion, see the references under Section 3.5.1.

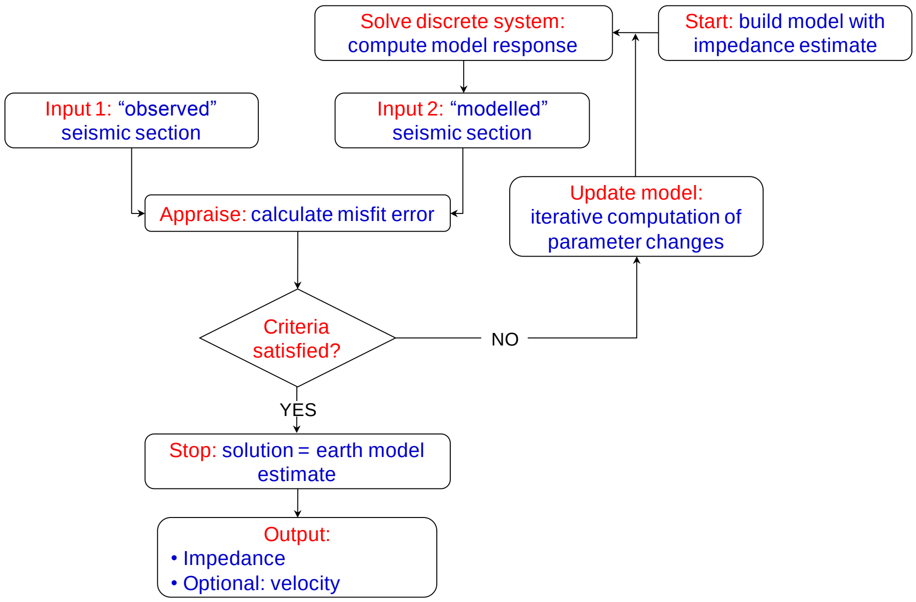

Figure 3-9: Workflow outlining the operation principle of model-based inversion. Modified after Lines and Treitel (1984) and Russell (1988).

3.5.8 Comments on Sections 3.5.6 and 3.5.7

From the application perspective, there are many elements that can degrade the reliability of the inversion results, some of which can not be averted, such as noise. Others might not be precisely reconstructed, such as the seismic wavelet. Furthermore, inversion results are sensitive to the data processing scheme applied and, therefore, care has to be taken to preserve crucial information, such as true amplitude, and to eliminate undesired entities like noise. Figure 3-10 outlines the major seismic data processing steps that should be adhered to, whenever possible, in order to obtain optimal inversion results. Finally, each of the inversion methods employed in this dissertation has its own advantages and disadvantages in regard to the limitations of inverse modelling and it is suggested that by using both methods some of the ambiguities associated with the inversion results could be minimized (Russell, 1988).

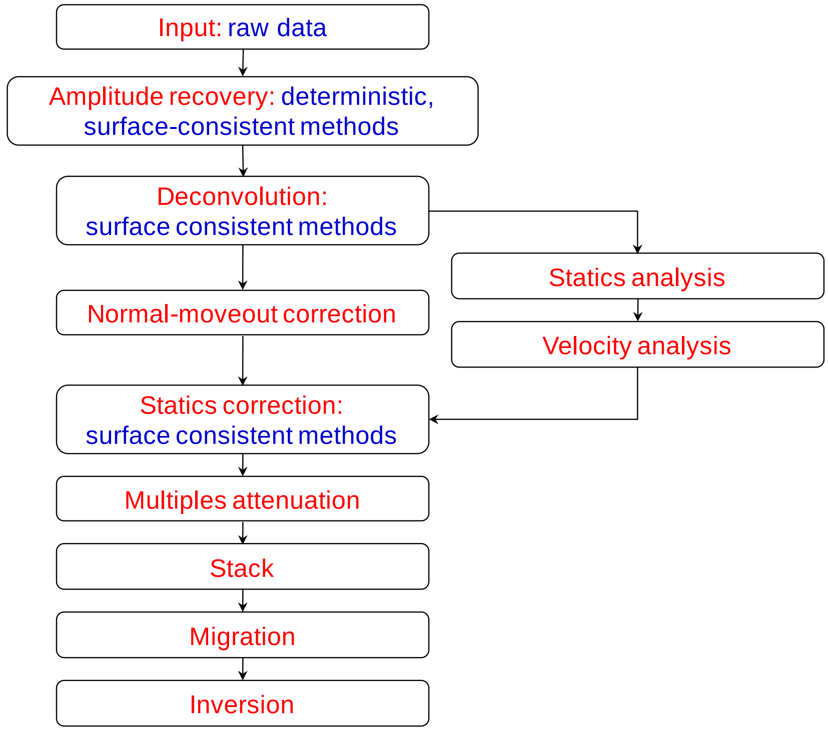

Figure 3-10: Major steps that should be included in seismic data processing flow for optimal post-stack inversion results. Modified after Russell (1988).

3.5.9 Rock Physics Methods

The rock physics modelling approach adopted in this dissertation is based on the well-known Gassmann method (Gassmann, 1951). The Gassmann equations can be derived using Hooke's law of elasticity (Berryman, 1999). In their original form, the Gassmann equations relate the bulk and shear moduli of a saturated homogenous isotropic poroelastic medium, consisting of single mineralogy, to the bulk and shear moduli of the same medium in the unsaturated, or drained, case:

$$K_{\text{saturated}} = K_{\phi} + \frac{\left(1 - \dfrac{K_{\phi}}{K_{\text{mineral}}}\right)^2}{\left(\dfrac{\phi}{K_{\text{fluid}}} + \dfrac{(1-\phi)}{K_{\text{mineral}}} - \dfrac{K_{\phi}}{(K_{\text{mineral}})^2}\right)} \tag{3.64}$$

where $K_{\text{saturated}}$ is the bulk modulus of the saturated medium, K_{ϕ} is the bulk modulus of the porous medium drained of any fluids, K_{mineral} is the bulk modulus of the mineral comprising the medium matrix, K_{fluid} is the bulk modulus of the fluid present in the medium, and ϕ is porosity. Figure 3-11 illustrates the relationship between these parameters. Note that Equation (3.64) is independent of the shear modulus (μ) as it is assumed to be mechanically independent of the fluid present in the medium:

$$\mu_{\text{saturated}} = \mu_\phi \tag{3.65}$$

$\mu_{\text{saturated}}$ is the shear modulus of the saturated medium, and μ_ϕ is the shear modulus of the porous medium drained of any fluids. K and μ are usually measured in GPa. The mathematical relationship between the elastic moduli (K and μ) and seismic velocities (α and β) and density (ρ) were introduced in Section 3.1.

Although the Gassmann equation assumes single mineralogy, it actually can be extended to multi-mineral case by using Voigt-Reuss-Hill or Hashin-Shtrikman averages of effective moduli (Mavko et al., 2003). More discussion of the Gassmann method can be found in Gassmann (1951), Berryman and Milton (1991), Berryman (1999), Mavko et al. (2003), Smith et al. (2003), and Han and Batzle (2004). The first encounter with the Gassmann method in this dissertation is in Chapter 5 where the approach adopted in this study is presented.

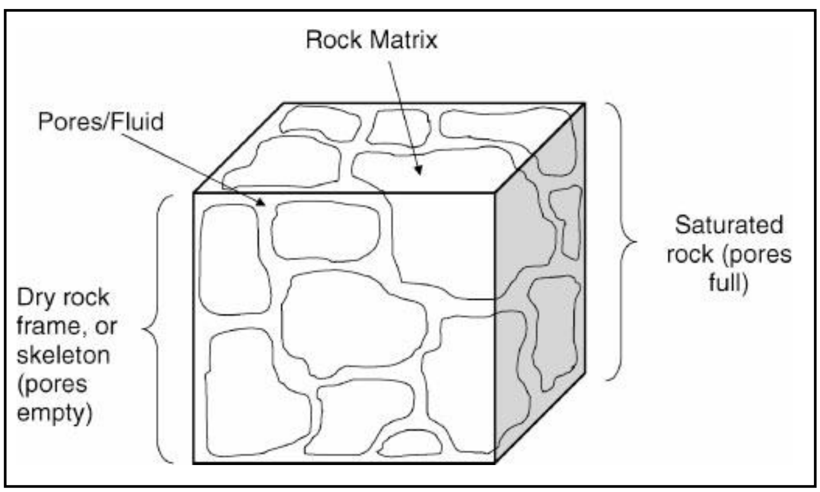

Figure 3-11: Depiction of the major entities characterizing a geologic medium according to the Gassmann equation. (Russell et al, 2003).

3.6 Quantitative Seismic Interpretation

Quantitative seismic interpretation, when used in conjunction with qualitative seismic interpretation, provides an invaluable tool in site characterization and reservoir delineation. Qualitative interpretation is based on conventional interpretation techniques, e.g. horizon mapping and qualitatively identifying zones in seismograms where the seismic signal undergoes characteristics (or attribute) change. These include time shift, amplitude variation, and phase rotation. These changes are then associated with variations in the physical properties of the geologic media, such as changes in pore fluids and lithology. Quantitative interpretation is in fact complementary to the qualitative counterparts. They provide another mean of delineating characteristics (or attribute) change in the physical properties of the media using mathematical models. For instance, the Gassmann method introduced in the previous section (Section 3.5.7) can actually be viewed as one variety of quantitative seismic interpretation.

From time-lapse monitoring perspective, all qualitative and quantitative interpretation methods rely on the presumption that injecting CO_2 alters the physical properties of the rock, thus giving rise to different seismic anomalies. The aim of the seismic experiment is to delineate these anomalies. However, the level of success depends primarily on whether or not the induced anomalies are sufficient enough to be detected by the seismic experiment. In this section, a brief review of the principal quantitative seismic interpretation tools and methods is provided. These are outlined in Table 3-2.

Table 3-2: List of the primary quantitative interpretation tools and methods employed in this dissertation and reviewed in this section.

Method	Attribute Category	Comment
Impedance Inversion	Acoustic and elastic properties	See Sections 3.5.6 and 3.5.7
Calibration	Statistical coherency	See Section 3.6.1
Lambda-Mu-Rho (LMR)	Elastic properties	See Section 3.6.2
Repeatability	Statistical coherency	See Section 3.6.3
Spectral Decomposition (SD)	Frequency	See Section 3.6.4
Complex Trace	Amplitude, frequency & phase	See Section 3.6.5
Spectral Ratio (SR)	Amplitude & Frequency	See Section 3.6.6
Edge Detection (ED)	Structural coherency	See Section 3.6.7
Others	-	See Section 3.6.8

3.6.1 Calibration

Although calibration is not technically a quantitative interpretation technique, it is discussed here as it plays a significant role when working with legacy or time-lapse data. Calibration of seismic data can take various forms. Of relevance to this study is the matching or shaping filter. The basic premise underlying the shaping filter is that given two signals, one as an input and another being the desired output, find a filter that when applied to the input minimizes the difference between the two. Shaping filters are widely used in seismic data processing, such as in deconvolution. Shaping filters are, also, used in minimizing variations between time-lapse surveys, which are not related to the changes within the reservoir, such as CO_2 injection. In general, one can write:

$$\text{Output} = \text{Filter} * \text{Input}$$

The above logic expression can be re-written using the following mathematical model:

$$y(t)=\sum_{ij}^{n} f\left(t_{i-j}\right) * x\left(t_{j}\right) \tag{3.66}$$

where $x(t)$ is the input signal, $y(t)$ is the actual output signal, $f(t)$ is the filter, i is the sample index, n is the number of samples, and $*$ is the convolution operator. The approach sought is such to minimize the sum of the error squares and, thus, the process is known as least-squares filtering:

$$\frac{\partial}{\partial f_i}\sum_{i=1}^{n}\left[z_i(t)-y_i(t)\right]^2=\frac{\partial}{\partial f_i}\sum_{i=1}^{n}\left[z_i(t)-f_i(t)*x_i(t)\right]^2=0 \tag{3.67}$$

where $z(t)$ is the desired output (this is similar to least-squares minimization discussed in Section 3.5.7). Mathematical manipulation yields the normal equations (Robinson and Treitel, 1967; Sheriff and Geldart, 1995):

$$\sum_{j=1}^{n}\Phi_{xx}(t_{i-j})f(t_j)=\Phi_{xz}(t_i) \tag{3.68}$$

where Φ_{xx} is the auto-correlation[32] of the input signal and Φ_{xz} is the cross-correlation of the input and desired output. Since both $x(t)$ and $z(t)$ are known, Equation (3.68) can be solved for $f(t)$, where $f(t)$ is occasionally referred to as Wiener optimum filter (Robinson and Treitel, 1967). Obviously, similar problems to those discussed in Section 3.5.7 may arise and, therefore, a stability factor or pre-whitening noise is typically added to the diagonal of the auto-correlation matrix of the input signal (Yilmaz, 2001). The recursive computer algorithm used in solving the normal equations arising when designing Wiener optimum filter is known as Wiener-Levinson algorithm (Sheriff, 2002). It is important to note that data calibration does not substitute for a rigorous time-lapse processing and is in fact complementary to the latter. In this dissertation, shaping filter was invoked primarily in calibrating: (1) the vintage seismic data in WASP (Chapter 5), and (2) the time-lapse data in PCEP (Chapter 7).

---

[32] See next section for mathematical expressions of auto-correlation and cross-correlation.

3.6.2 Lambda-Mu-Rho (LMR)

LMR obtained its name from the initials of the Greek alphabets of Lamé elastic parameters (λ, μ)[33] and density (ρ). Goodway et al. (1997) advocates the use of λ-μ-ρ as an AVO attribute and have shown in their paper that λ-μ-ρ exhibits an improved sensitivity toward fluids over traditional AVO attributes. Furthermore, since CO_2 has lower incompressibility (K) and density than typical reservoir fluids, it should give rise to a detectable anomaly given that there is sufficient contrast between the in-situ fluids and the injected CO_2.

Goodway et al. (1997) proceed by first extracting the P-wave and S-wave reflectivity from a given P-wave seismic volume using the following approximation:

$$R_p(\theta_i) \approx \left(\frac{\Delta I_p}{2\bar{I}_p}\right)\left[1+\tan^2\bar{\theta}\right] - 8\left(\frac{\bar{\beta}}{\bar{\alpha}}\right)^2\left(\frac{\Delta I_s}{2\bar{I}_s}\right)\sin^2\bar{\theta} - \left(\frac{\Delta\rho}{\bar{\rho}}\right)\left[\frac{1}{2}\left(\tan^2\bar{\theta}\right) - 2\left(\frac{\bar{\beta}}{\bar{\alpha}}\right)^2\left(\sin^2\bar{\theta}\right)\right] \quad (3.69)$$

where $\bar{\alpha}$, $\bar{\beta}$, $\bar{\rho}$, $\bar{\theta}$, $\bar{I}_p$, and $\bar{I}_s$ are the average P-wave velocity, S-wave velocity, density, angle, P-wave impedance and S-wave impedance at the interface, respectively. Recall that:

$$\bar{I}_p^i = \bar{\rho}_i\bar{\alpha}_i;\ \Delta I_p = I_p^{i+1} - I_p^i \quad (3.70)$$

$$\bar{I}_s^i = \bar{\rho}_i\bar{\beta}_i;\ \Delta I_s = I_s^{i+1} - I_s^i \quad (3.71)$$

Then, the reflection coefficient estimates are used to invert for the average P-wave impedance and S-wave impedance. Finally, $\bar{I}_p$, and $\bar{I}_s$ are transformed into $\lambda\rho$ (LR) and $\mu\rho$ (MR) using the following expressions:

$$\mu\rho = \left(\bar{I}_s\right)^2 \quad (3.72)$$

$$\lambda\rho = \left(\bar{I}_s\right)^2 - 2\left(\bar{I}_p\right)^2 \quad (3.73)$$

The LMR transformation described by Equations (3.72) and (3.73) can, also, be achieved following the extraction of the acoustic and shear impedances from seismic volume, as

---

[33] These parameters were defined in Section 3.1.

illustrated in Chapter 4. More discussion of LMR, including real data examples, can be found in Goodway et al. (1997) and Avseth et al. (2005).

3.6.3 Repeatability

From CO_2 monitoring perspective, deviations in seismic signal between seismic surveys, say a baseline and monitor, can in general be attributed to two causes: (1) changes in or above the reservoir due, for instance, to CO_2 injection, or (2) other causes, such as variations in survey geometry or noise. Depending on their respective magnitude, these deviations can affect the seismic signal. Therefore, it is valuable to numerically deduce these deviations to quantify the repeatability of the data and, ultimately, delineate those we are interested in from what is considered as noise. Two repeatability metrics that are invoked in this dissertation to achieve such objectives are normalized root-mean squares (NRMS) (Kragh and Christie, 2002) and predictability (PRED) (White, 1980). These metrics are used in combination with cross-equalization operators to ensure optimum results.

NRMS measures the difference in the root-mean squares (RMS) of the seismic signal between two surveys, say a baseline and monitor, and normalize this difference by the average of the RMS of the two signals (Kragh and Christie, 2002):

$$NRMS = 200 \times \left\{ \frac{\sqrt{\dfrac{\sum_{i=1}^{N} \left[\psi_{monitor}(t_i) - \psi_{baseline}(t_i) \right]^2}{N}}}{\sqrt{\dfrac{\sum_{i=1}^{N} \left[\psi_{baseline}(t_i) \right]^2}{N}} + \sqrt{\dfrac{\sum_{i=1}^{N} \left[\psi_{monitor}(t_i) \right]^2}{N}}} \right\} \tag{3.74}$$

Or in more concise notation:

$$NRMS = 200 \times \left\{ \frac{RMS\left[\psi_{monitor}(t_i) - \psi_{baseline}(t_i) \right]}{RMS\left[\psi_{monitor}(t_i) \right] + RMS\left[\psi_{baseline}(t_i) \right]} \right\} \tag{3.75}$$

where RMS is the root-mean squares operator:

$$RMS = \sqrt{\frac{\sum_{i=1}^{N}\left[\psi\left(t_i\right)\right]^2}{N}} \tag{3.76}$$

where $\psi_{baseline}(t)$ and $\psi_{monitor}(t)$ are the seismic signals from the baseline and monitor surveys, respectively, and N is the number of samples within the window or gate over which the NRMS attribute is measured. Typically, the window is centered at the reservoir. NRMS is sensitive to time shift as well as to changes in amplitude and phase. In general, a small NRMS value indicates good repeatability whereas large magnitude signifies poor repeatability. If the seismic signals from a time-lapse survey, i.e. a baseline and a monitor, are perfectly repeatable, then the NRMS = 0%; if the they contain random uncorrelated noise, then NRMS = 140%,; if they are identical but their polarity is reversed, then NRMS = 200%. Typically, NRMS values of about 40–60% are considered to be good whereas NRMS values less than 20% are considered to be excellent. Kragh and Christie (2002) present more detailed discussion of NRMS and show both numerical and field data examples.

The other repeatability metric is predictability (PRED), which is based on measuring the cross-correlation of the seismic signal from the baseline and monitor surveys and normalize the output by the product of the auto-correlation of the signal from the individual surveys (White, 1980):

$$PRED = 100 \times \left\{ \frac{\sum_{i=1}^{N}\left[\Phi_{baseline-monitor}\left(\tau\right)\right]^2}{\sum_{i=1}^{N}\left[\Phi_{baseline-baseline}\left(\tau\right) \times \Phi_{monitor-monitor}\left(\tau\right)\right]} \right\} \tag{3.77}$$

where τ is the correlation lag ($\tau = 0, 1, \ldots n$), $\Phi_{baseline}$ and $\Phi_{monitor}$ are the auto-correlation of the seismic signal from the baseline and monitor surveys, respectively:

$$\Phi_{baseline-baseline}\left(\tau\right) = \sum_{i=1}^{N}\psi_{baseline}\left(t_i\right)\psi_{baseline}\left(t_i + \tau\right) \tag{3.78}$$

$$\Phi_{monitor-monitor}\left(\tau\right) = \sum_{i=1}^{N}\psi_{monitor}\left(t_i\right)\psi_{monitor}\left(t_i + \tau\right) \tag{3.79}$$

and $\Phi_{baseline\text{-}monitor}$ is the cross-correlation between the baseline and monitor surveys:

$$\Phi_{baseline-monitor}\left(\tau\right)=\sum_{i=1}^{N}\psi_{baseline}\left(t_i\right)\psi_{monitor}\left(t_i+\tau\right) \tag{3.80}$$

PRED is rather sensitive to the amount of noise present in the signal. In contrast to NRMS, a small PRED value means low repeatability whereas large value designates high repeatability. A PRED magnitude of 100% indicates that the time-lapse signals are perfectly repeatable; if both signals are uncorrelated, then PRED = 0%; if they are anti-correlated (polarity-reversed) then PRED = 100%. More discussion of PRED and examples of its utility using both numerical and field data can be found in Kragh and Christie (2002) among others. Both NRMS and PRED are used in this dissertation to quantify the repeatability of the field time-lapse seismic data in Chapter 6 and the synthetic time-lapse data associated with the numerical modelling in Chapters 5 and 7. However, NRMS is more frequently exploited as it has been observed to show better sensitivity towards quantifying the repeatability of 4-D seismic surveys.

3.6.4 Spectral Decomposition (SD)

Spectral decomposition (SD) belongs to a family of seismic data processing and interpretation methods that are based on spectral analysis (Chopra and Marfurt, 2007). SD as an interpretation technique was first introduced by Partyka et al. (1990) who used short window discrete Fourier transform (SWDFT) to construct frequency volume (or slices) from a conventional seismic volume. The approach has proven to be useful in delineating changes associated with lithology and bed thickness (Chopra and Marfurt, 2007). Since bed thickness is an issue at the PCEP study area (Chapter 7), SD was used in an attempt to attain a better image of the reservoir. Figure 3-12 illustrates the main concept underlying SD.

As a periodic[34] time series, the seismic signal can be expressed in terms of sinusoids using Fourier series (Sheriff and Geldart, 1995):

$$\psi(t)=\frac{1}{2}b_0+\sum_{i=1}^{\infty}b_i\cos(i\,\omega_0 t)+\sum_{i=1}^{\infty}c_i\sin(i\,\omega_0 t) \tag{3.81}$$

[34] This means that the function repeats itself after some period, e.g. $\psi(t+2\pi) = \psi(t)$.

where $\psi(t)$ is the seismic signal, i is a positive integer, and ω_0 is discrete angular frequency:

$$\omega_0 = 2\pi f_0 \tag{3.82}$$

Recall that:

$$f_0 = \frac{1}{T} \tag{3.83}$$

where f_0 is known as the fundamental frequency in Hertz, and T is the period in seconds. The Fourier coefficients (or simply the peak amplitudes) b_i and c_i of the i^{th} harmonic can be computed using the following relations:

$$\begin{aligned} b_i &= \frac{2}{T}\sum_{k=0}^{T}\psi_k \cos(\omega_i t) \\ c_i &= \frac{2}{T}\sum_{k=1}^{T}\psi_k \sin(\omega_i t) \end{aligned} \tag{3.84}$$

where ψ_k corresponds to the k^{th} time sample ($\psi_k = k\Delta t$), Δt is the sampling interval. The amplitude spectrum, $|\Psi(\omega)|$, and the phase spectrum, $\varphi(\omega)$, at a given frequency (ω_i) can be found by coordinate transformation from Cartesian to polar coordinates:

$$A(\omega) = |\Psi(\omega)| = \sqrt{a_i^2 + b_i^2} \tag{3.85}$$

$$\varphi(\omega) = \tan^{-1}\left(\frac{b_i}{a_i}\right) \tag{3.86}$$

So, the previous discussion illustrates that the amplitude and phase of the seismic trace can be found by decomposing $\psi(t)$ into its Fourier components by cross-correlating the seismic trace with sines and cosines at predetermined set of frequencies. This is known as Fourier analysis and is achieved through the forward discrete Fourier transform (DFT) (Gubbins, 2004):

$$\Psi(\omega) = \sum_{i=1}^{\infty}\psi(t_i)e^{-j(\omega t_i)} = |\Psi(\omega)|e^{-j(\varphi)} \tag{3.87}$$

where $\psi(t)$ is the seismic signal in the time domain, and $\Psi(\omega)$ is the complex representation of the seismic signal in the Fourier domain. Once in the Fourier domain, the seismic signal can be analyzed using the power spectra, i.e. amplitude and phase spectra, which is simply a plot of $A(\omega)$ and $\varphi(\omega)$ as a function of frequency. Conversely, an inverse DFT exists that transforms the data from the Fourier domain into the time domain and the process is known as Fourier synthesis:

$$\psi(t) = \sum_{i=1}^{n} \Psi(\omega_i) e^{j(\omega_i t)} \tag{3.88}$$

The two functions, i.e. $\psi(t)$ and $\Psi(\omega)$, form a Fourier transform pair:

$$\psi(t) \Leftrightarrow \Psi(\omega) \tag{3.89}$$

Good discussion of the Fourier transform including its properties and application can be found in Bracewell, (1986). Yilmaz, (2001) gives a good review with focus on seismic signal processing applications.

The complex exponential, or the sines and cosines, in the previous discussion form the basis function through which the seismic signal can be Fourier analyzed [$\psi(t) \rightarrow \Psi(\omega)$] or Fourier synthesized [$\psi(t) \leftarrow \Psi(\omega)$]. In SWDFT, the basis function is tapered using the following analysis window (Chopra and Marfurt, 2007):

$$\Omega(i\Delta t) = \Omega_i = \begin{cases} \dfrac{1}{2}\left[1 + \cos\left(\pi \dfrac{|i\Delta t| - b + \xi}{\xi}\right)\right] & ; \text{if } b - \xi \le |i\Delta t| \le b \\ 1 & ; \text{if } |i\Delta t| \le b - \xi \\ 0 & ; \text{if } |i\Delta t| > b \end{cases} \tag{3.90}$$

where Ω_i is the window function centered at the analysis point (i.e. i^{th} time sample ($t_i = i\Delta t$) where Δt is the sampling interval), b is the window length and ξ is the taper length in seconds (ξ is typically 20% the length of b). The analysis is performed for a prescribed set of frequencies over the zone of interest centered at the i^{th} time sample and the results are displayed in the form of frequency slices. More discussion of SD can be found in Partyka et al. (1990). Chopra and Marfurt (2007) provide additional review including a compilation of many examples from variety of published papers on seismic interpretation using SD. In the context of this dissertation, SD constitutes one of the various quantitative seismic attributes utilized in the interpretation of the PCEP time-lapse field data in Chapter 6.

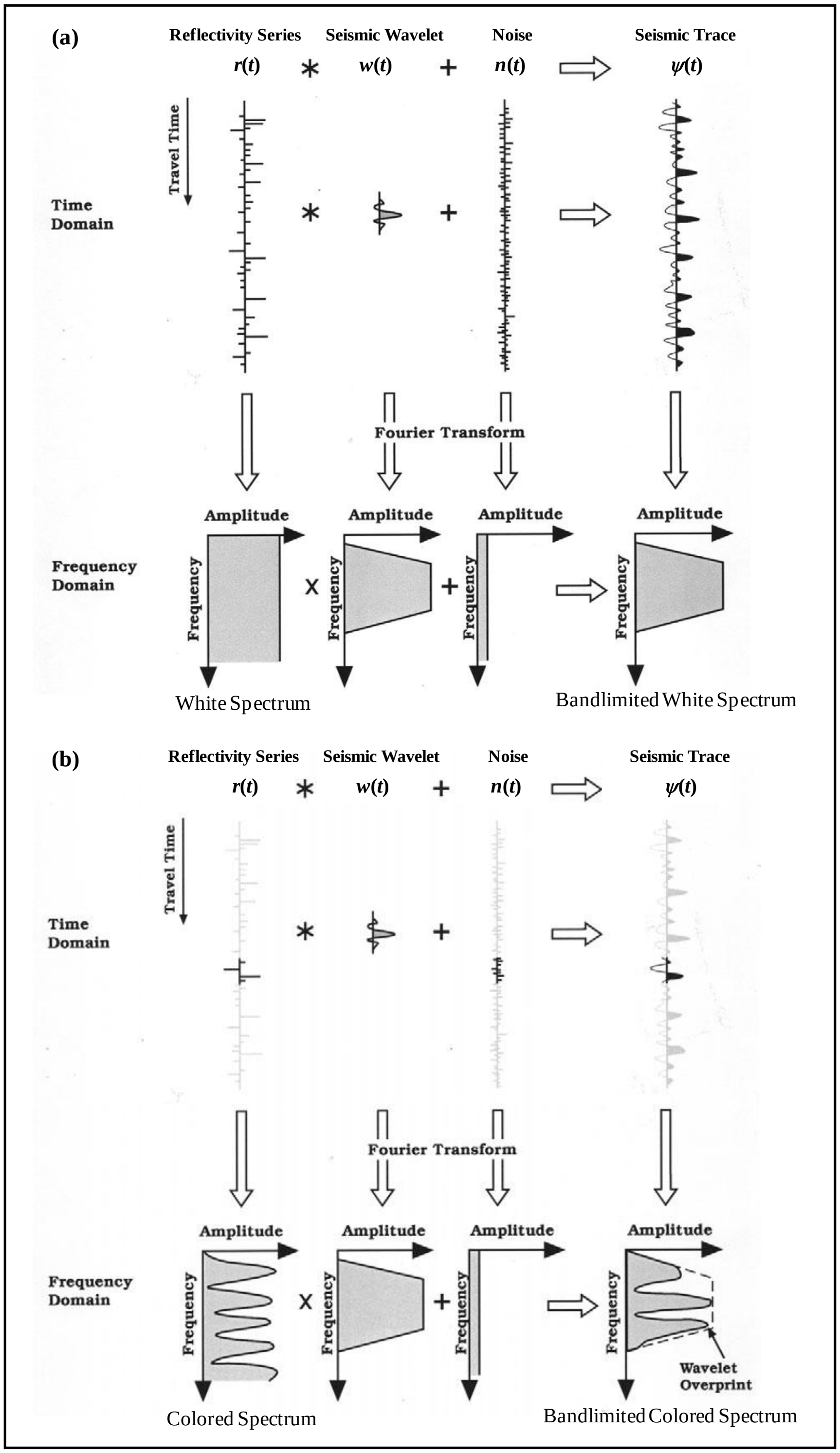

Figure 3-12: (a) conventional, long-windowed or un-windowed, spectral decomposition and the convolutional model, (b) short-windowed spectral decomposition and the convolutional model. Note how using a short window in (b) results in a colored spectrum which ultimately aids in the interpretation of lithology and thing beds. After Partyka et al. (1999).

3.6.5 Complex Trace Analysis (CTA)

The seismic trace represents the real component of an analytic signal (Bracewell, 1986):

$$\begin{aligned} \underline{\psi}(t) &= \mathrm{Re}\left[\underline{\psi}(t)\right] + j\ \mathrm{Im}\left[\underline{\psi}(t)\right] \\ &= \psi_{re}(t) + j\,\psi_{im}(t) \\ &= A\left\{\cos\left[\varphi(t)\right] + j\ \sin\left[\varphi(t)\right]\right\} \\ &= A(t)e^{j\varphi(t)} \end{aligned} \tag{3.91}$$

where $\underline{\psi}(t)$ is the complex representation of the seismic trace, $\psi_{re}(t)$[35] and $\psi_{im}(t)$ are the real ($\mathrm{Re}[\underline{\psi}(t)]$) and imaginary ($\mathrm{Im}[\underline{\psi}(t)]$) components of the complex seismic trace, respectively, A is the amplitude, φ is the phase in radians, $e^{i\varphi}$ is the complex exponential function, and j is the imaginary unit ($j = \sqrt{-1}$). $\psi_{im}(t)$ is also known as the as the quadrature component since it corresponds to the real part of the signal ($\psi_{re}(t)$) with 90^{o} phase shift. The amplitude (A) and phase (φ) of such analytic signal are given by:

$$A(t) = \left|\underline{\psi}(t)\right| = \sqrt{\mathrm{Re}\left[\underline{\psi}(t)\right]^2 + \mathrm{Im}\left[\underline{\psi}(t)\right]^2} \tag{3.92}$$

$$\varphi(t) = \tan^{-1}\left\{\mathrm{Im}\left[\underline{\psi}(t)\right] / \mathrm{Re}\left[\underline{\psi}(t)\right]\right\} \tag{3.93}$$

where in the CTA context, A is often called the amplitude of the envelope, or reflection strength; and φ is referred to as the instantaneous phase. Additionally, it is possible to define another attribute, namely the instantaneous frequency (ω):

$$\omega(t) = \frac{d\varphi(t)}{dt} = \frac{d}{dt}\left[\tan^{-1}\left\{\mathrm{Im}\left[\psi(t)\right] / \mathrm{Re}\left[\psi(t)\right]\right\}\right] \tag{3.94}$$

Carrying out the differentiating yields (Barnes, 2007):

$$\omega(t) = \frac{\psi_{re}(t)\left[\dfrac{d\psi_{im}(t)}{dt}\right] - \psi_{im}(t)\left[\dfrac{d\psi_{re}(t)}{dt}\right]}{\psi_{re}^2(t) + \psi_{im}^2(t)} \tag{3.95}$$

where the derivatives of $\psi_{re}(t)$ and $\psi_{im}(t)$ can be computed in a convolutional form (Taner et al., 1979) or by using a finite-difference scheme (Barnes, 2007). Although only the real

---

[35] Throughout this dissertation, $\psi_{re}(t) = \psi(t)$, unless otherwise noted.

component of analytic signal in Equation (3.91) is actually recorded, it is feasible to determine the quadrature component by the means of the Hilbert transform (HT) using the convolutional method (Taner et al., 1979). Alternatively, the imaginary part can be computed using the Fourier method (Taner et al., 1979; Sheriff and Geldart, 1995):

$$\psi_{re}(t) = \sum_{-\infty}^{\infty} b_i(\omega) e^{j\omega t_i} \tag{3.96}$$

where b is the amplitude. Since the seismic signal is real, the analysis is restricted to positive frequencies ($\omega \geq 0$):

$$\psi_{re}(t) = \sum_{i=0}^{\infty} A_i(\omega) \cos\left[\omega t_i + \phi(\omega)\right] \tag{3.97}$$

where:

$$A(\omega) = 2\left|b(\omega)\right| \tag{3.98}$$

$$\phi(\omega) = \arg\left[b(\omega)\right] \tag{3.99}$$

Then, the imaginary component can by calculated using the following:

$$\psi_{im}(t) = \sum_{i=0}^{\infty} A_i(\omega) \sin\left[\omega t + \phi(\omega)\right] \tag{3.100}$$

and the complex signal can be written as:

$$\underline{\psi}(t) = \sum_{i=0}^{\infty} A_i(\omega) e^{j[\omega t + \phi(\omega)]} \tag{3.101}$$

Analogous to the Fourier transform, $\psi_{re}(t)$ and $\psi_{im}(t)$ form a Hilbert transform pair. Expressing the seismic signal in a complex form and analyzing the emerging attributes (A, φ and $d\varphi/dt$) can sometimes yield certain advantages from an interpretation perspective. For instance, the envelope amplitude can serve as an indicator of lithology and fluid changes whereas the instantaneous phase can help in determining the shape of geologic boundaries (e.g. reflectors). Furthermore, media characteristics, such as absorption and bed thickness associated with seismic events can be emphasized using the instantaneous frequency. The exploitation of these complex trace attributes in this dissertation is presented in Chapter 6. Further discussion of CTA can be found in Bracewell (1986). Taner et al. (1979), Roberston and Nogami, (1984), Roberston and

Fisher (1988), White (1991), and Barnes (2007) give a good review of the topic and present many examples.

3.6.6 Spectral Ratio (SR)

Spectral ratio is a Q-estimation technique used in obtaining compressional wave attenuation by comparing the waveforms (spectra) of a reference signal with that of a non-reference signal[36] (Bath, 1974; Toksöz et al., 1979). The premise on which the SR technique relies is based on the fact that signal amplitude decreases with increasing frequency more rapidly for a lossy medium than for an elastic medium. Following the linear equation given by Tonn (1991), one can write:

$$\ln\left[\frac{|A(\omega)_{i+1}|}{|A(\omega)_i|}\right] = \ln\left[\frac{|A_0(\omega)_{i+1}|}{|A_0(\omega)_i|}\right] - b\omega \tag{3.102}$$

where $|A_0(\omega)|$ and $|A(\omega)|$ are the amplitude spectra of the reference and non-reference signals measured at two levels: z_i (at the reservoir top) and z_{i+1} (at the reservoir bottom). The slope (b) can be computed from a line fitted to the cross-plot of the natural logarithm of the ratio of the two spectra versus frequency. Then, the quality factor can be estimated using the following relation (Tonn, 1991):

$$Q = -\frac{1}{2b}\left(\frac{z_{i+1} - z_i}{\alpha}\right) = -\frac{\Delta t}{2b} \tag{3.103}$$

where α is the P-wave speed in m/s and Δt is the time difference in s between the signal at the top and bottom of the reservoir. One of the most important assumptions underlying the SR is that the recorded waveform will be modified slightly by the decrease in higher-frequency energy due to attenuation. If there is scattering caused by heterogeneities or there are multiple paths of arrivals, the waveforms will be altered dramatically and the method breaks down (Stephen, 2002). Also, Tonn (1991) reports that the method is unreliable and might ultimately fail in case of thin layers. Since SR gives a measure of

---

[36] In the current context, “reference signal” refers to the VSP signal measured from the baseline survey (before CO_2 injection) whereas “non-reference signal” corresponds to that of a monitor survey (after CO_2 injection). Hence, the ratio of the amplitude spectra of a reference signal at depth z_i (reservoir top) and a signal at depth z_{i+1} (reservoir bottom) is computed for each survey and the two ratios are compared.

the relative attenuation, Equation (3.102) was exploited in Chapter 6 as one of many quantitative seismic interpretation techniques invoked in delineating the CO_2 plume for the PCEP.

3.6.7 Edge Detection (ED)

Geologic discontinuities express certain characteristics which can be revealed using coherency-sensitive interpretation techniques, such as edge detection (ED). The ED technique invoked in this dissertation is based on the difference method (DM) introduced by Luo et al. (1996). The mathematical premise on which the technique is based on is rather simple, i.e. taking the difference between adjacent seismic traces and dividing by their sum (Luo et al., 1996):

$$\mathrm{d} = \frac{\|\mathbf{A}-\mathbf{B}\|}{\|\mathbf{A}\|+\|\mathbf{B}\|} \tag{3.104}$$

where **A** is the seismic signal on the target trace, **B** is the seismic signal on the neighbouring trace, and d is the difference of the center sample of the window at the target trace. Recall that the double bars $\| \ \|$ represent the norm of a vector (see Section 3.5.7). The DM was invoked in the seismic site characterization for the Wabamun Area CO_2 Sequestration Project (WASP) in Chapter 4 where it proved to be very useful in delineating geologic discontinuities, such as karsting and sinkholes.

3.6.8 Others

In addition to the previously discussed quantitative interpretation methods, several more conventional and rather simple means were also investigated when appropriate. Those include seismic zone attributes (SZA) and P/S (α/β) wavespeeds ratio. The former is based on computing simple statistics, such as average and RMS amplitude over the zone of interest. This is suggested to alleviate uncertainties involved in picking horizons. Another attribute that falls under the same categories is the amplitude thickness of the peak (ATP), which calculates the length in milliseconds over which positive or negative amplitude samples are observed. Since the injection of CO_2 causes a decrease in the P-wave speed but a small increase in the S-wave speed, the change in α/β ratio between successive surveys is suggested to be a useful metric in capturing such variation (Lumley, 2010):

$$\frac{\alpha}{\beta}=\frac{2t_p-t_{ps}}{t_{ps}} \tag{3.105}$$

where is the t_p and t_{ps} are the two-way P-wave and PS-wave traveltime in s, respectively. Therefore, α/β ratio was incorporated as one of the quantitative interpretation methods in the time-lapse seismic monitoring in Chapter 6.

3.7 Summary

- In this chapter, the modelling and quantitative interpretation tools and methods were reviewed.
- As numerical modelling constitutes an integral part of this dissertation, some of the principals underlying the forward and inverse numerical modelling methods adopted in this research were reviewed in Section 3.3.
- In terms of forward modelling, these include finite-difference, ray tracing and convolutional methods.
- In the context of inverse modelling, the methods reviewed were recursive and model-based methods.
- All of these methods were associated with the algorithms (software) invoked in performing the numerical modelling and the upcoming chapters in which they are implemented.
- In addition to forward and inverse modelling, a brief introduction of the rock physics modelling method, namely the Gassmann method, was given in Section 3.3.
- Then, the assets belonging to the other integral part of the dissertation, namely quantitative seismic interpretation, were introduced in Section 0. These include amplitude variation with offset (AVO), lambda-mu-rho (LMR), repeatability, complex trace analysis (CTA), spectral decomposition (SD), spectral ratio (SR), and edge detection (ED) in addition to other more conventional methods. This suite of quantitative interpretation methods covers a wide spectrum of seismic

attributes: statistical, structural, and those pertaining to physical properties of the subsurface.

CHAPTER 4: WASP SEISMIC SITE CHARACTERIZATION I - FIELD DATA

4.1 Introduction

The Wabamun Area CO_2 Sequestration Project (WASP) was first introduced in Chapter 1, in which the motivations and objectives underlying the seismic characterization of WASP were outlined in Sections 1.4 and 1.5, respectively. The geology of the WASP study area was discussed in detail in Section 2.2. To recap, the primary objectives were:

1. To map the Nisku Formation within the WASP regional and local-scale study area using available seismic data.
2. To interpret the seismic character of the Nisku Formation in terms of porosity and/or lithology.
3. To identify geologic features, e.g., sinkholes and karsting, that may compromise the integrity of the Nisku aquifer and/or its caprock, i.e. Calmar Formation.
4. To undertake a time-lapse feasibility analysis using rock physics and numerical modelling methods to predict how the seismic response of the Nisku Formation would be affected by CO_2 injection, and whether a time-lapse seismic program would be capable of delineating the resultant CO_2 plume.

In this chapter, the discussion is focused on achieving the objectives (1-3) through the seismic analysis of the field data whereas objective 4 along with other modelling aspects of WASP is discussed in Chapter 5. Table 4-1 gives an overview of WASP and the various disciplines involved as well as the completed and prospective phases. Detailed background about the project and the various disciplines involved is given by Keith and Lavoie (2009). The overall project encompasses the geology and geostatistics (Eisinger and Jensen, 2009), geochemistry (Shevalier et al., 2009), geomechanics (Nygaard, 2009a; Goodarzi and Settari, 2009), well-bore integrity (Nygaard, 2009b), reservoir simulation

(Ghaderi and Leonenko, 2009). These papers and regulatory components are available on the project official website[37].

Table 4-1: WASP overview.

Motivation	CO_2 storage (~1 Mt/year)
Location	Wabamun Area, Alberta
Target Formation	Upper Devonian Nisku dolostone
Formation Type	Saline aquifer
Disciplines Involved	Geology, geostatistics, geophysics, geochemistry, geomechanics (and wellbore integrity), reservoir simulation, legal/regulatory
Phases	Phase I (2008-2009): • Site characterization and feasibility analysis • Recommendation: favourable Phase II (renamed Project Pioneer; in progress): • Selection of a pilot site and drilling of an exploratory well • Design and construction of pilot facilities and MMV program
Project Status	Phase I: completed; Phase II: in progress

4.2 Data and Site Characterization Approach

The study area is flanked by two major hydrocarbon zones in Alberta; the Leduc reef play (east) and the Moon Lake reef play (northwest)[38]. Thus, part of the study area was mapped using legacy surface seismic data that had been acquired as part of hydrocarbon exploration in the area. The seismic characterization of the Nisku Formation in WASP was based on analyzing and interpreting these legacy post-stack P-wave seismic datasets comprising more than two hundred 2-D seismic lines and seven 3-D volumes[39]. n Table 3-2.

[37] http://www.ucalgary.ca/wasp /. Since websites are occasionally moved without the option to be redirected to the new web address, the reader may resolve by going to a search engine and use the words corresponding to the project acronyms as a query if the provided link is broken.
[38] See Chapter 2, Section 2.2 for detailed discussion of the geology.
[39] The seismic and borehole data analyzed in this dissertation were generously made available as an in-kind contribution by EnCana™ Corporation (now Cenovus Energy).

Table 3-2 gives an outline of the volume and approximate areal coverage of the analyzed seismic data in addition to wells with appropriate log curves and formation tops that were available for integration into the seismic data analysis. The spatial distribution of the available seismic data is illustrated in Figure 3-1, and shows that the data coverage is not distributed uniformly. Furthermore, no new seismic data were acquired nor has any well being drilled as part of the characterization and feasibility analysis phase of the project. Thus, the characterization was constrained to those areas with good coverage. The 2-D seismic data were used primarily for identifying long-wavelength structures, whereas the high-quality 3-D seismic data near the northern part of the local-scale study area were used for detailed mapping and quantitative interpretation using a suite of relevant seismic attributes. Figure 4-2 gives an overview of the data calibration and normalization approach.

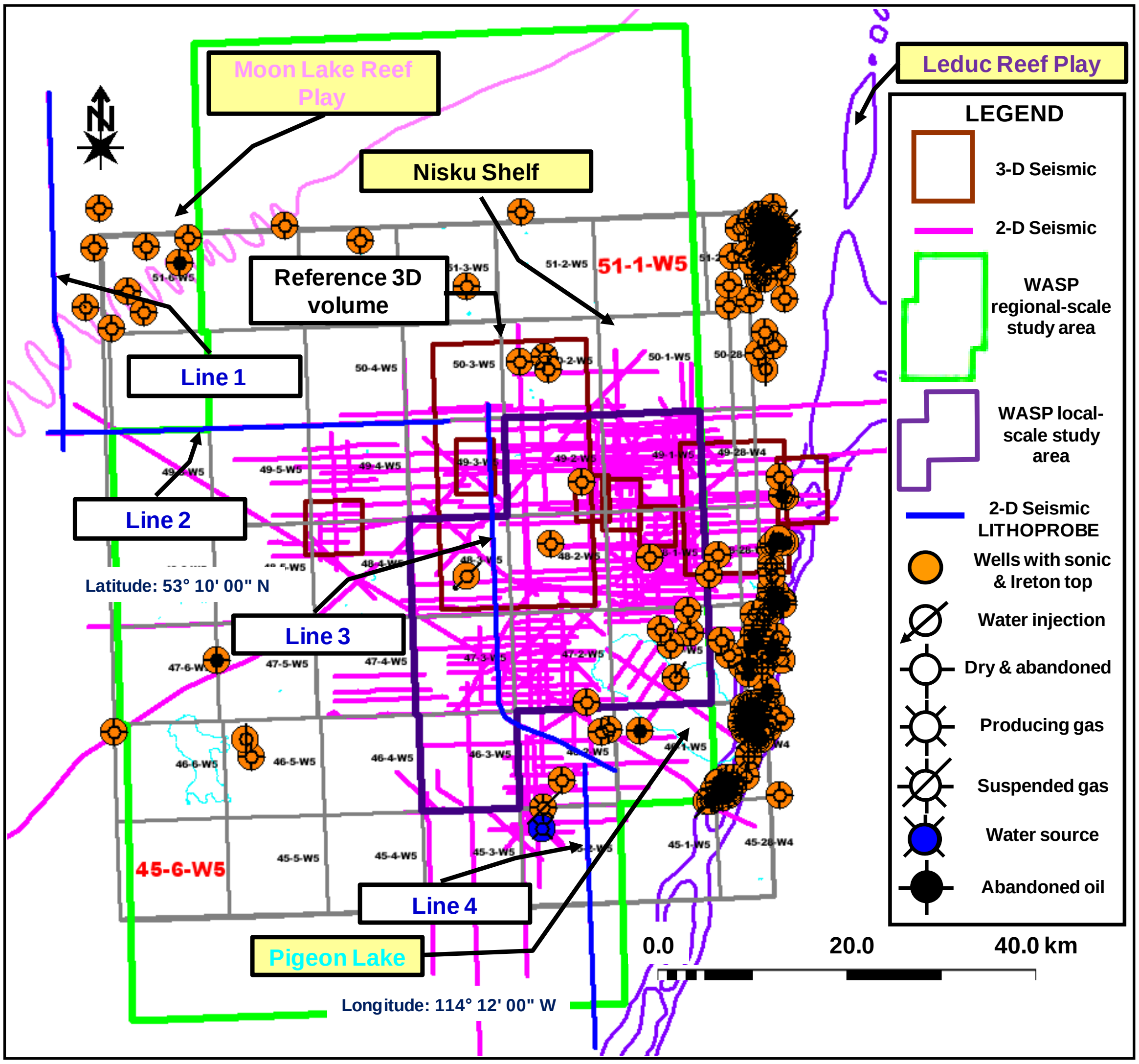

Figure 4-1: Base map showing the distribution of the seismic and well data. Violet contours represent the Leduc Reef trend while cyan shapes indicate bodies of water.

Table 4-2: Summary of the seismic and well data within the regional and local-scale study areas. The well data referred to here are wells that penetrate the Nisku Formation and have a sonic log.

Seismic data	2-D	200 seismic lines, approximately 2432 km in total length
	3-D	7 seismic volumes covering an area of about 419 km^2
Well data	Local-scale	7 wells; only 2 coincide with seismic coverage
	Regional-scale	> than 20 wells; only 6 coincide with seismic coverage

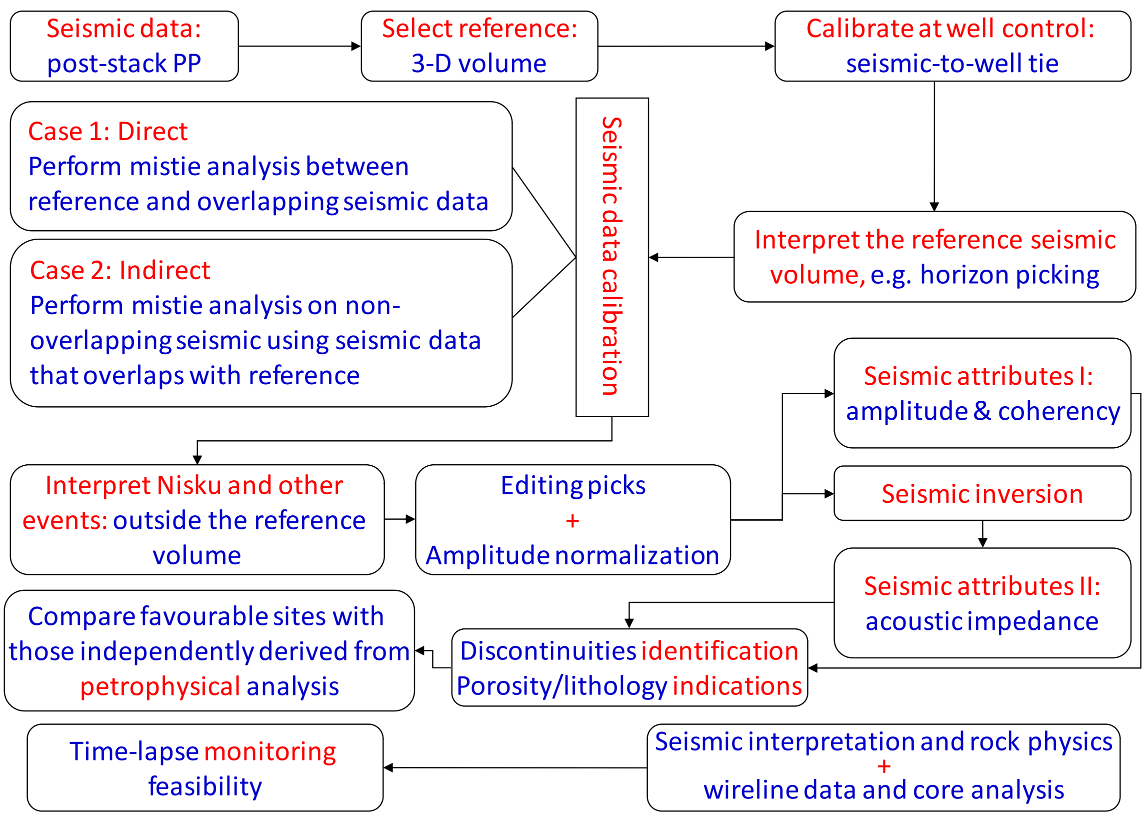

Figure 4-2: Flowchart outlining the major steps followed in the seismic site characterization of WASP.

4.3 Data Calibration and Normalization

The 2-D and 3-D seismic datasets analyzed in this project are legacy datasets and, therefore, have different acquisition and processing parameters, and were acquired over many years prior to this project being embarked upon (1970-2000). Therefore, prior to qualitative and quantitative interpretation, two primary steps were undertaken: data calibration and amplitude normalization. These steps were necessary to account for the processing and datum differences within the data.

Starting with the reference 3-D volume, which is the largest brown rectangle in the middle of Figure 3-1, the majority of the seismic events were identified and picked following the seismic-to-well tie which was made at various locations using available borehole data. The seismic-to-well tie aids in identifying geologic formations by correlating the seismic data with synthetic traces generated by convolving a theoretical wavelet with a reflectivity model based on density and sonic logs from available wells convolutional model (see Section 3.5.5). The reference gamma-ray, P-wave speed and density logs as well as an extracted wavelet (from nearby seismic data) for the case of water source well is illustrated in Figure 4-3. The Nisku event is visible at about 1320 ms (~ 2250 m) with the increase in wavespeed (in Figure 4-4 as well) and decrease in density and gamma-ray responses. Overall, the seismic data exhibit good ties to the synthetic seismograms, with the correlation coefficient ranging from 0.7 to 0.9. Figure 4-3 shows an example of the seismic-to-well tie near the water source well (1F1-11-29-45-2W5), at which a high correlation is obtained (0.92).

Following the seismic-to-well tie and identification of seismic events within the reference 3-D volume, data calibration was begun by first applying a time and phase[40] cross-correlation shift followed by amplitude adjustments to those 3-D volumes and 2-D seismic lines overlapping the reference 3-D volume. The calibration was designed over a wide window that was constrained by the data quality at the shallowest and deepest parts of the input seismic section. Different time and phase shifts were applied to the input sections and only those corresponding to the maximum cross-correlation between the reference and the input were retained. The calibrated overlapping lines were then used to calibrate those that do not overlap the reference 3-D volume using the same approach. The process was repeated until all data were calibrated with respect to the reference 3-D volume.

[40] After the calibration, all the data are interpreted assuming normal polarity.

Once the data were calibrated, seismic amplitudes were normalized[41] to a root-mean squares (RMS) value of 1.0 using a time window designed to include the zone of interest, i.e. Nisku Formation (1000-1500 ms). The normalization process consists of two steps: (1) for each dataset, a scalar was computed for the input based on the desired output statistical value, i.e. RMS = 1.0, over the zone of interest, then (2) the scalar was applied to the input dataset. The combination of calibration and amplitude normalization has performed well in reconciling the legacy dataset.

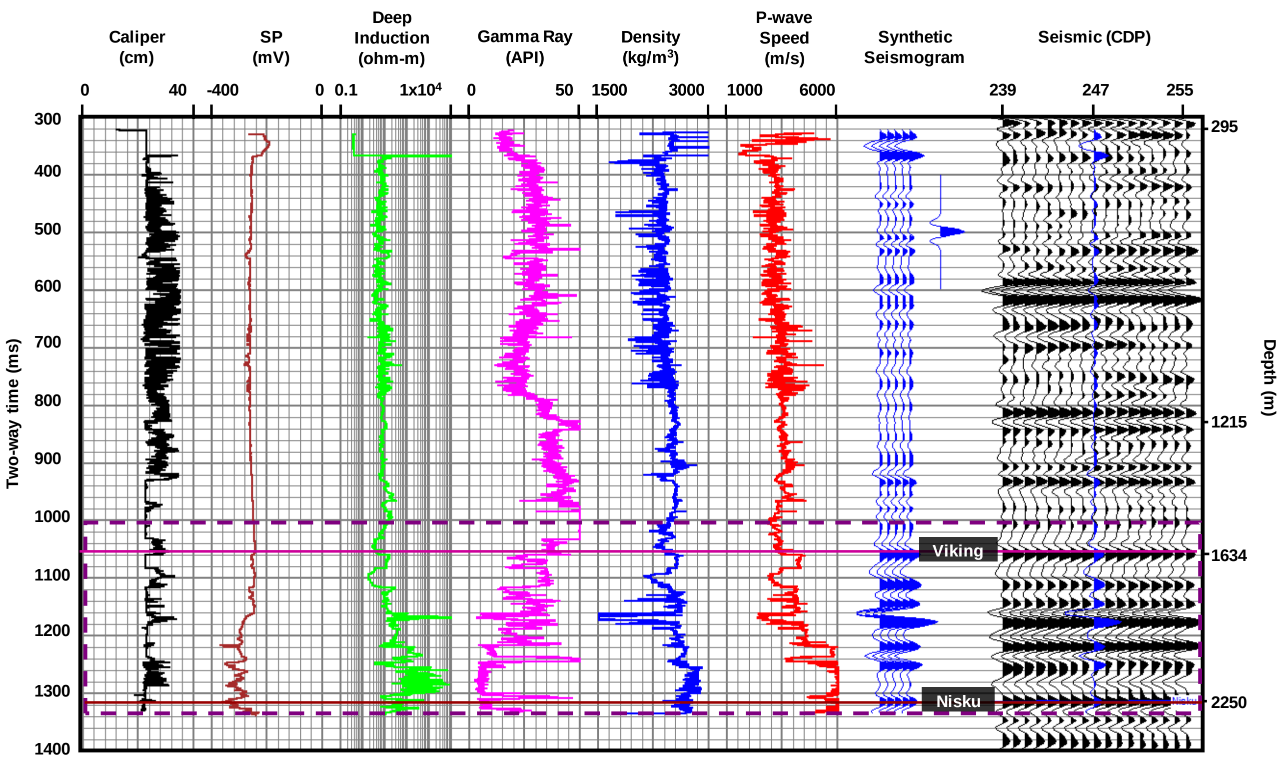

Figure 4-3: Seismic-to-well tie at the water source well (1F1-11-29-45-2W5). The blue traces represent the zero-offset synthetic seismogram whereas the black traces show the field data that ties the well. The correlation coefficient is 0.92 over the outlined zone (dashed rectangle) in the bottom image (enlarged in the next figure).

---

[41] The normalization approach here is slightly different from the one discussed in Section 3.6.3. For instance, there is no baseline here and the data was normalized with respect to a zone of interest, i.e. the Nisku Formation, in the reference 3-D volume. The resultant amplitude is referred to as NRMS throughout Chapter 4.

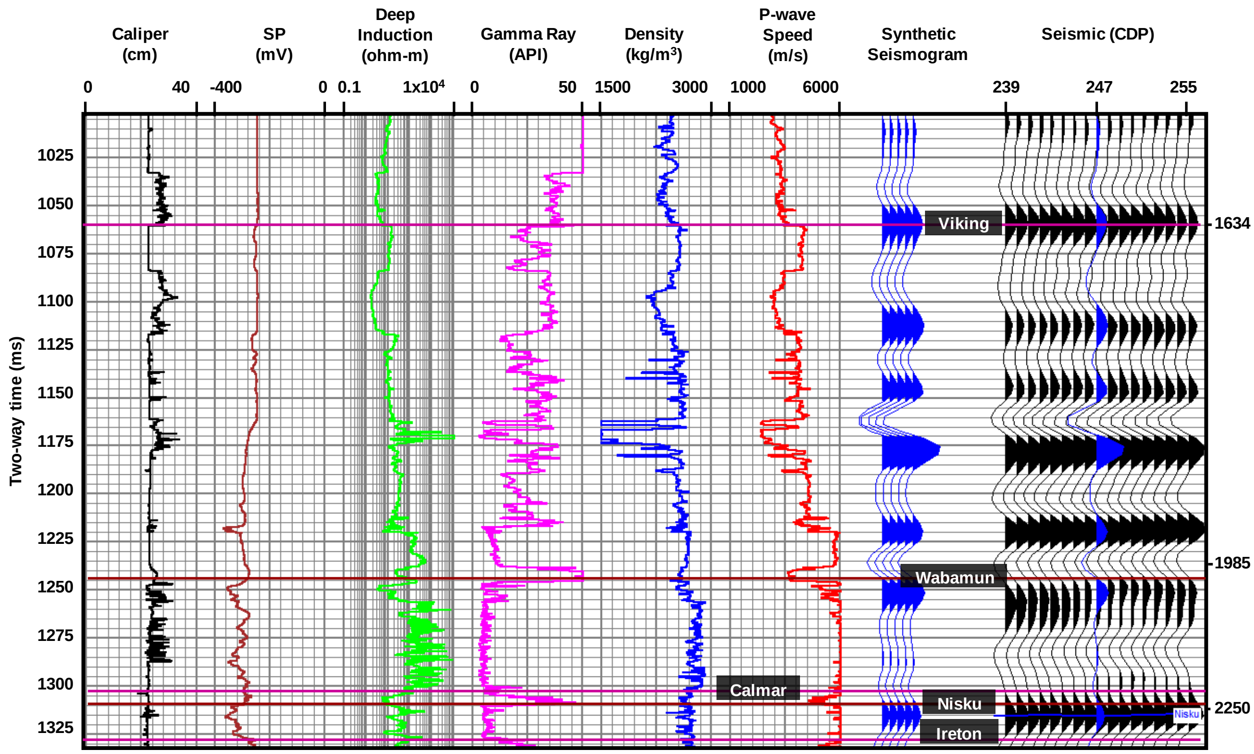

Figure 4-4: Enlarged display of the well logs and seismic-to-well tie shown in Figure 4-3. The Nisku Formation thickness in this well is approximately 60 m.

4.4 Regional Trend and Interpretation

The regional seismic expression encountered in the study area is depicted in four of the regional LITHOPROBE[42] 2-D seismic lines (Figure 4-5 through Figure 4-8). Several seismic events were identified throughout these regional lines, including: the Viking, the Wabamun, the Nisku, and the Beaverhill Lake events, as well as a Cambrian marker[43]. The Viking Formation is composed of sandstone and is part of the Lower Cretaceous series. The Wabamun Formation, on the other hand, is mainly dolostone and it is the shallowest formation in the Upper Devonian strata that include the underlying dolomitized Nisku Formation[44]. The reflection from the Beaverhill Lake Formation marks the transition between the Upper and Middle Devonian. The Cambrian marker

[42] This is a collaborative national earth science research project that investigates "the structure and evolution of Canada's landmass and continental margins" (LITHOPROBE, 2010).
[43] See the stratigraphic model in Figure 2-9.
[44] To facilitate better identification, the Wabamun event was picked using the peak amplitude in the calibrated seismic data which is different from the zero-crossing in Figure 4-4.

represents the reflection from what it is thought to be the Basal Sandstone Formation. In all the seismic lines the Nisku and underlying top Ireton events are represented by one period (one frequency cycle) of the seismic data, meaning that the Nisku is a tuned event.

In Line 1 (Figure 4-5) there is a small change in the Nisku time structure as the line turns southward at trace 950 (within the dashed rectangle). This occurs near the Moon Lake reef boundary but it also coincides with a change in the survey orientation (Figure 3-1). A more interesting anomaly is outlined by the dashed rectangle in Line 2 (Figure 4-6), which marks the interpreted transition between the Nisku bank and the Nisku shale basin to the northwest. The regional dip, which is toward the southwest, is seen clearly on both Lines 1 and 2. In Line 3 (Figure 4-7), which traverses the WASP local-scale study area in the north-south direction, the Nisku event is identified at approximately 1.37 s and is fairly flat. On Line 4 (Figure 4-8), the Nisku event is also flat and no major anomalous features can be identified on this event. A sudden traveltime increase in the overlying Wabamun event is observed between traces 850 and 1100 but this does not seem to affect the Nisku event reflection.

The variation in the Nisku event time and amplitude as observed in these regional 2-D sections can also be seen in the time structure and NRMS amplitude maps, which will be presented in the next section (Figure 4-11). But as far as these regional 2-D lines are concerned, neither the integrity of the Nisku aquifer nor that of the caprock (Calmar Formation) seems to be compromised in the focus area. Furthermore, none of the regional seismic lines exhibits any sign of major faulting. However, the dashed ellipse in Line 3 (Figure 4-7) indicates the location of a local discontinuity in the Wabamun event. This and similar anomalies are more clearly imaged by the 3-D seismic data and will be discussed in later sections.

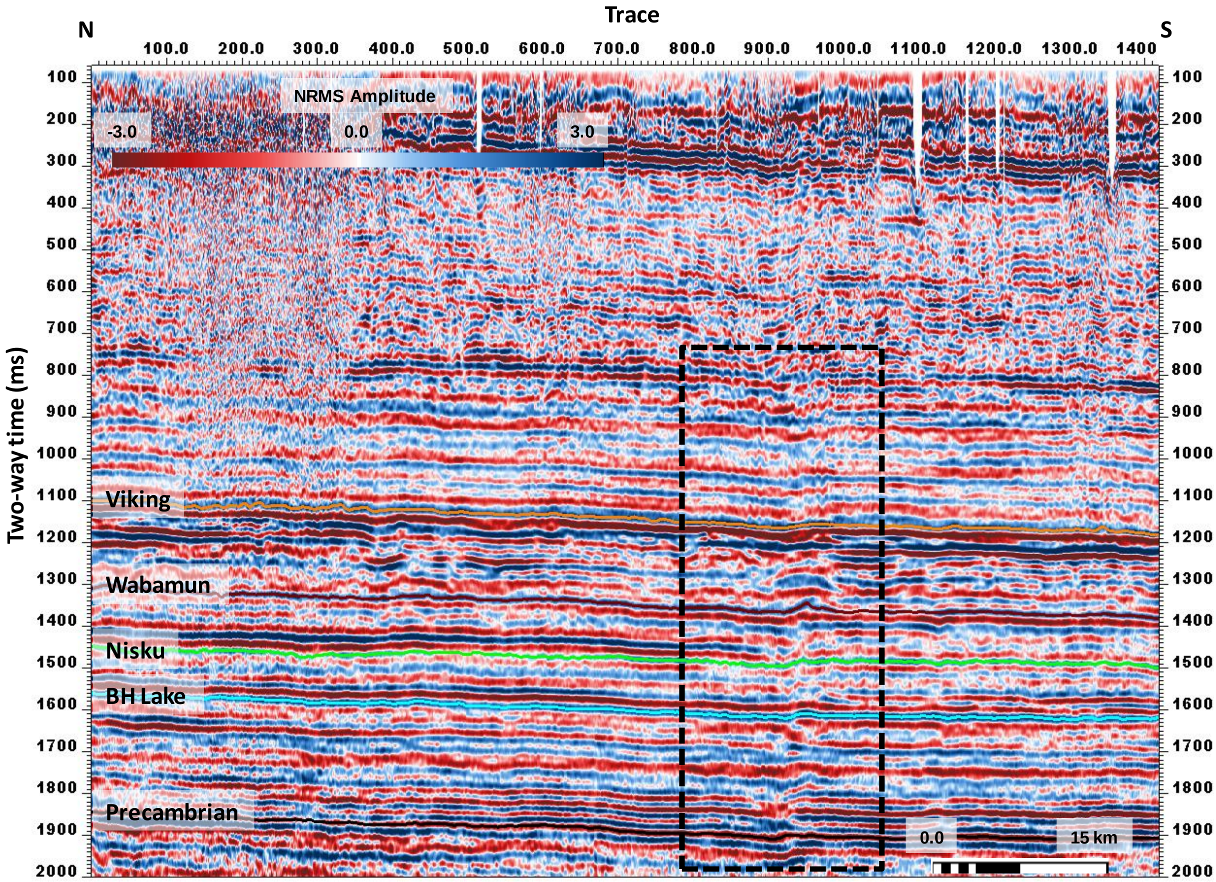

Figure 4-5: Line 1 of the LITHOPROBE regional 2-D seismic data with some of the major seismic events identified, including the Nisku event. The location of Line 1 is shown in the base map (Figure 3-1). The dashed rectangle shows a zone of a sudden change in the time structure, which could be associated with the Moon Lake reef boundary or simply a result of Line 1 turning into the updip direction as can be seen in the base map. BH Lake is the Beaverhill Lake event.

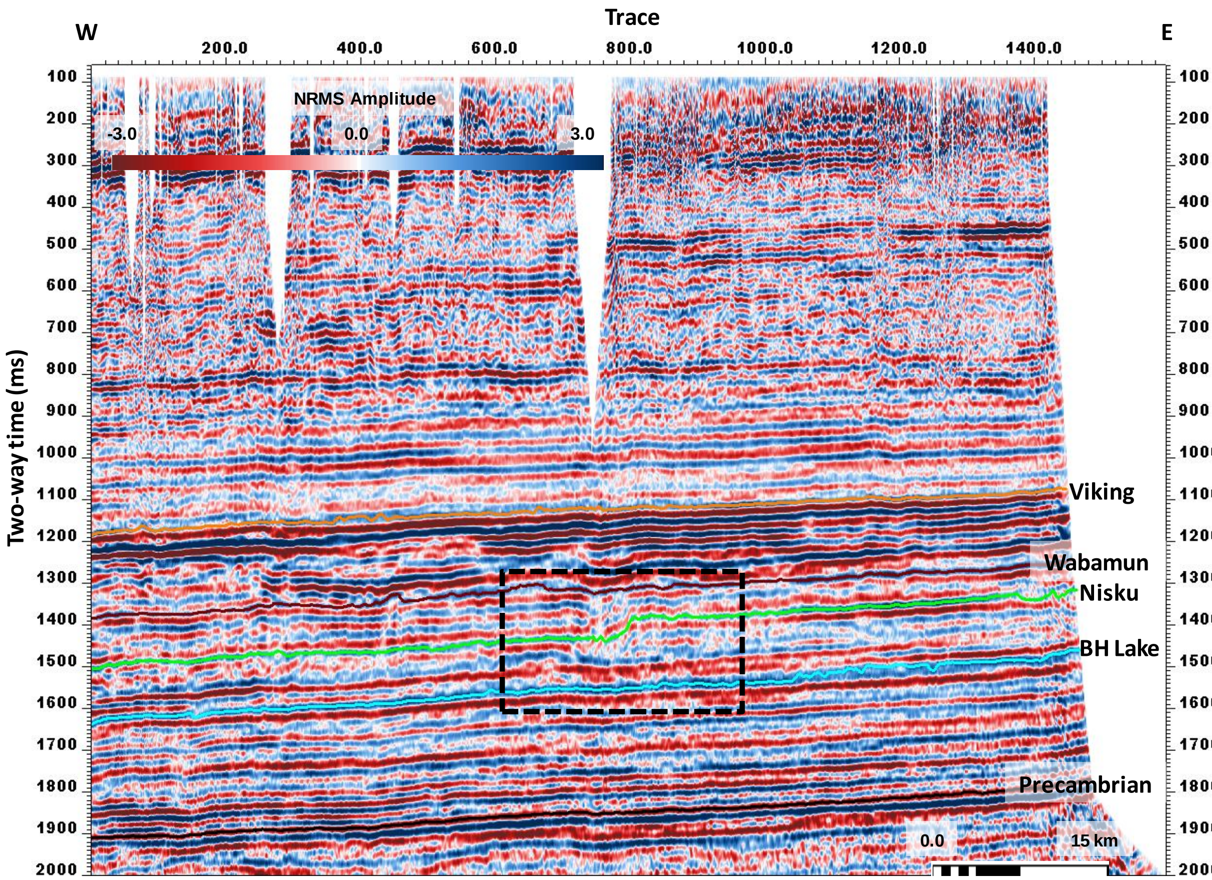

Figure 4-6: Line 2 of the LITHOPROBE regional 2-D seismic data with some of the major seismic events identified, including the Nisku event. The location of Line 2 is shown in the base map (Figure 3-1). The dashed rectangle points to the location of the *transition* between the Nisku bank and Nisku shale basin; see the geologic cross-section in Figure 2-8. BH Lake is the Beaverhill Lake event.

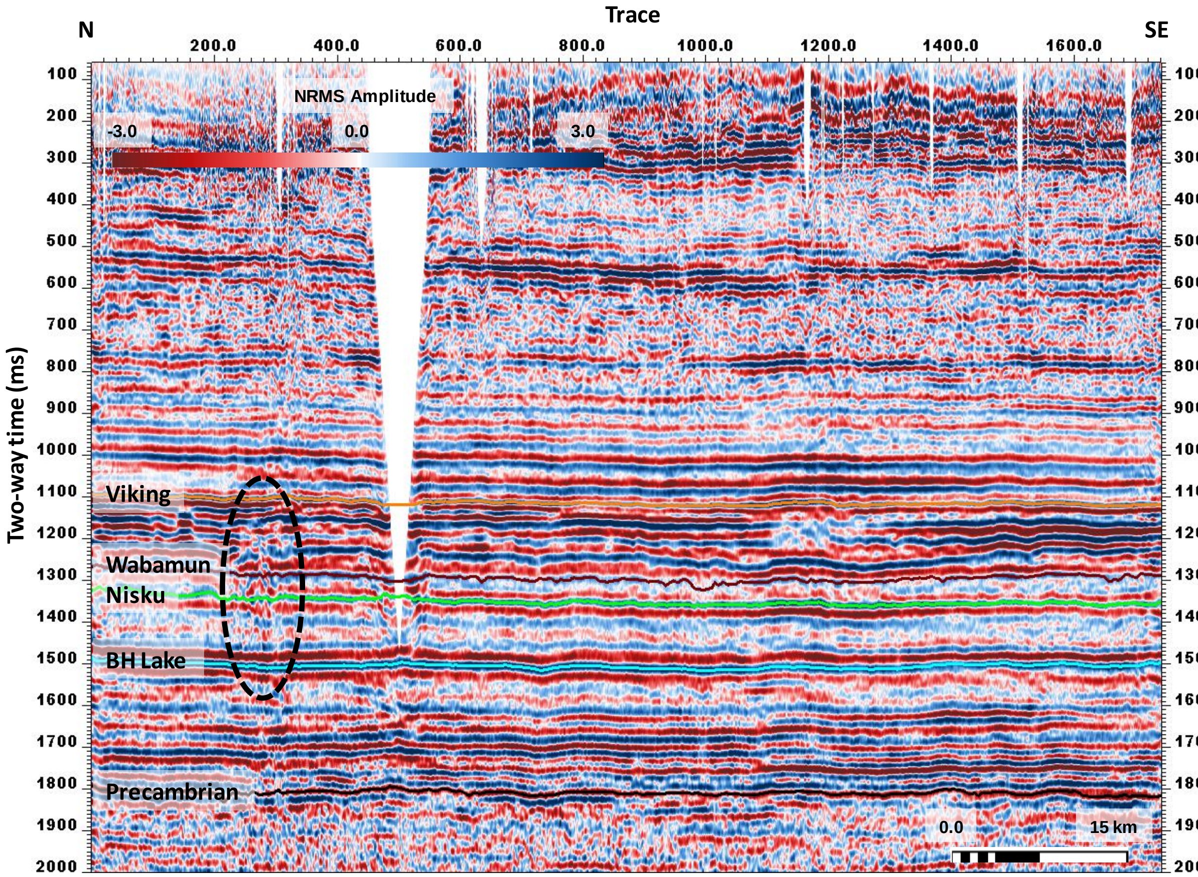

Figure 4-7: Line 3 of the LITHOPROBE regional 2-D seismic data with some of the major seismic events identified, including the Nisku event. The location of Line 3 is shown in the base map (Figure 3-1). The dashed ellipse marks a local anomaly interpreted to be caused by a discontinuity in the Wabamun event. BH Lake is the Beaverhill Lake event.

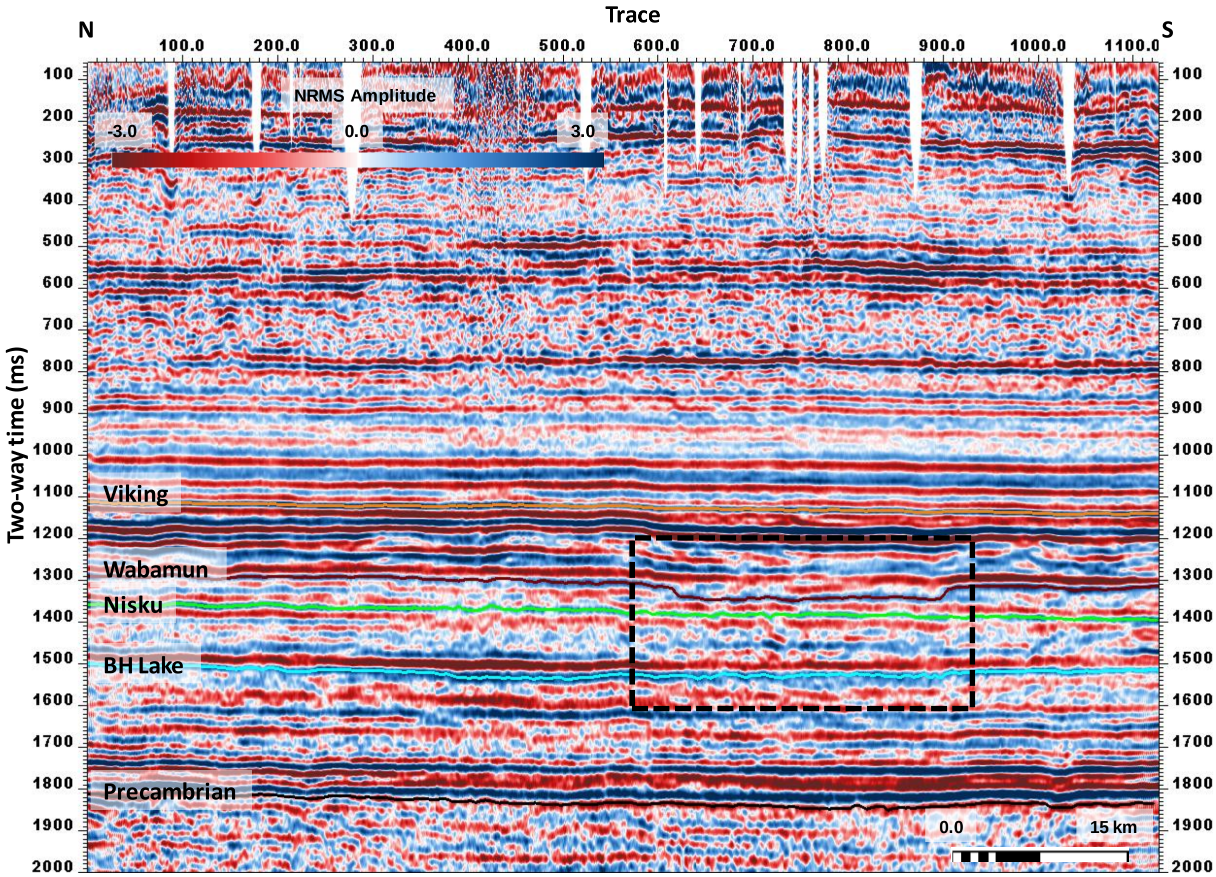

Figure 4-8: Line 4 of the LITHOPROBE regional 2-D seismic data with some of the major seismic events identified, including the Nisku event. The location of Line 4 is shown in the base map (Figure 3-1). The dashed rectangle shows a local depression in the Wabamun event and its induced footprint on the Nisku event. BH Lake is the Beaverhill Lake event.

4.5 Local Trend and Interpretation

4.5.1 Nisku Time, Amplitude and Depth Maps

The time structure of the Nisku event (Figure 4-9 and Figure 4-10) is rather smooth and does not exhibit any significant variations within the WASP study area except for following the regional dip in the northeast-southwest direction. There are a few subtle anomalies, such as the depression to east of the reference 3-D volume in Figure 4-10, which are believed to be footprints associated with discontinuities or irregularities taking place above the Nisku event, primarily in the Wabamun Formation. Conversely, far more information is revealed by the Nisku NRMS amplitude map (Figure 4-11 and

Figure 4-12), which was more robust in identifying anomalies driven by both discontinuities footprints and variations in lithology or porosity in the Nisku Formation[45]. The locations of some of these anomalies are identified in Figure 4-12. These and other features are discussed in detail in Section 4.5.2 where the Nisku character in the local-scale study area is investigated more thoroughly. Moreover, it is evident from Figure 4-12 that only the amplitudes extracted from the 3-D seismic data are reliable as the 2-D seismic data are generally of poorer quality and do not exhibit a consistent areal pattern (as in 3-D) from which useful information could be extracted.

Analogous to the time structure, a depth structure map of the Nisku Formation was constructed as well. In some circumstances, the domain conversion could provide useful information toward understanding whether an observed anomaly is an actual structure or an apparent structure caused by, for instance, velocity pull-up or pull-down. In order to do so, first the time structure map was interpolated using a kriging[46] technique with a grid size of 50×50 m. Both 2-D and 3-D Nisku horizons were used in the interpolation and the result is shown in Figure 4-13. Following the time structure interpolation, a time-to-depth conversion was performed to generate the depth structure map in Figure 4-14. The conversion algorithm utilized the Nisku time structure from picked horizons and the Nisku depths from borehole data[47] within the study area. It should be indicated that no meaningful results were obtained by the interpolation of the NRMS amplitude map and therefore it is not included in the discussion.

---

[45] Throughout this chapter, the reader may presume that discontinuities and variations in lithology or porosity are the primary factors shaping the seismic character of the Nisku Formation in the local-scale study area. In other words, it is assumed that the tuning effect is negligible in the focus area. Such observation is actually verified through numerical modeling, which is discussed in the next chapter (Chapter 5). In particular, the reader may refer to Section 5.2.

[46] Kriging is a linear spatial interpolation method that determines the best linear unbiased estimate (BLUE) of a random variable (Goovaerts, 1997).

[47] The location of the wells used in the time-to-depth conversion can be seen in Figure 4-10.

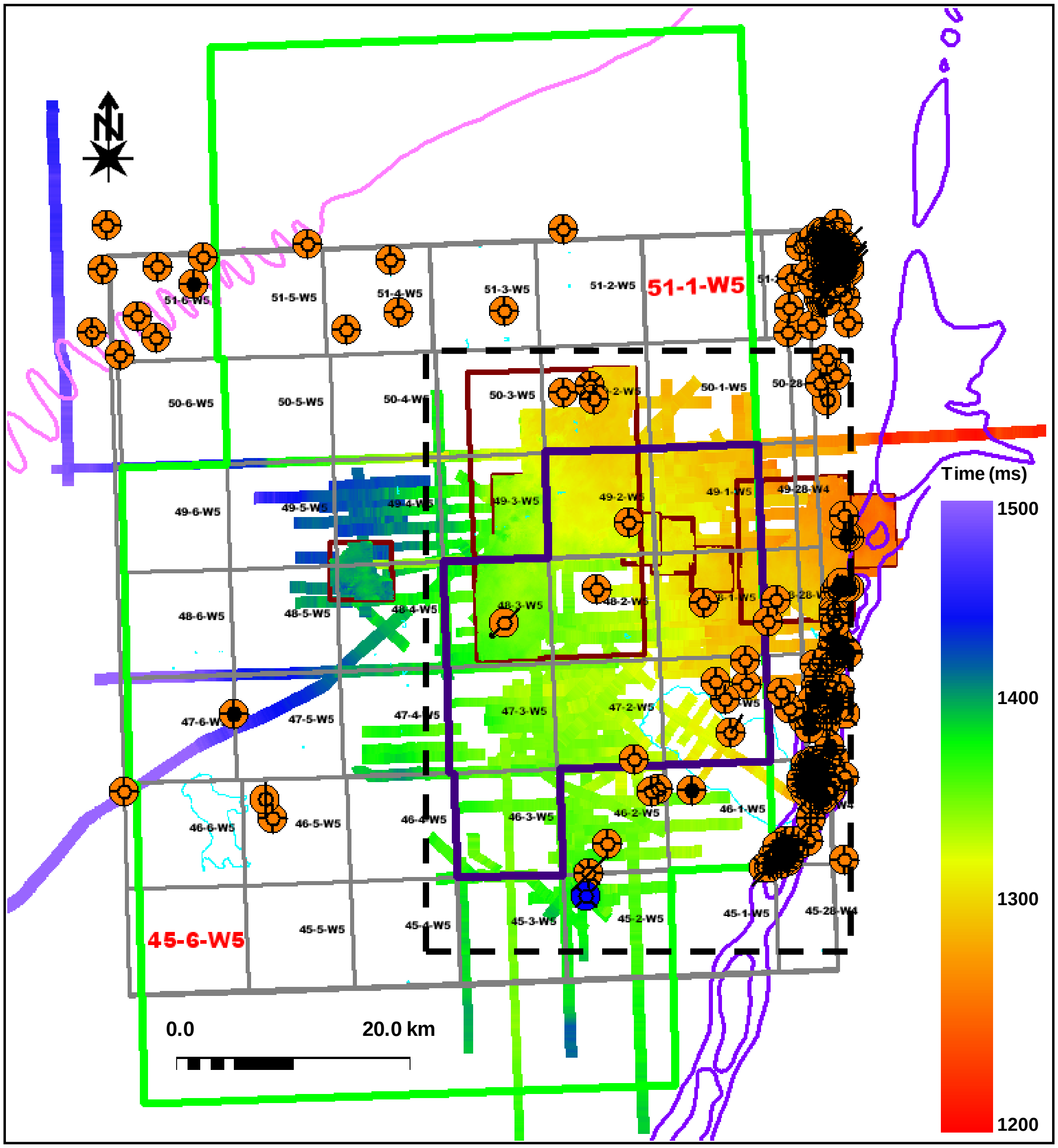

Figure 4-9: The time structure of the Nisku event after data calibration. The dashed black rectangle shows the extent of the detailed display over the study area shown in Figure 4-10.

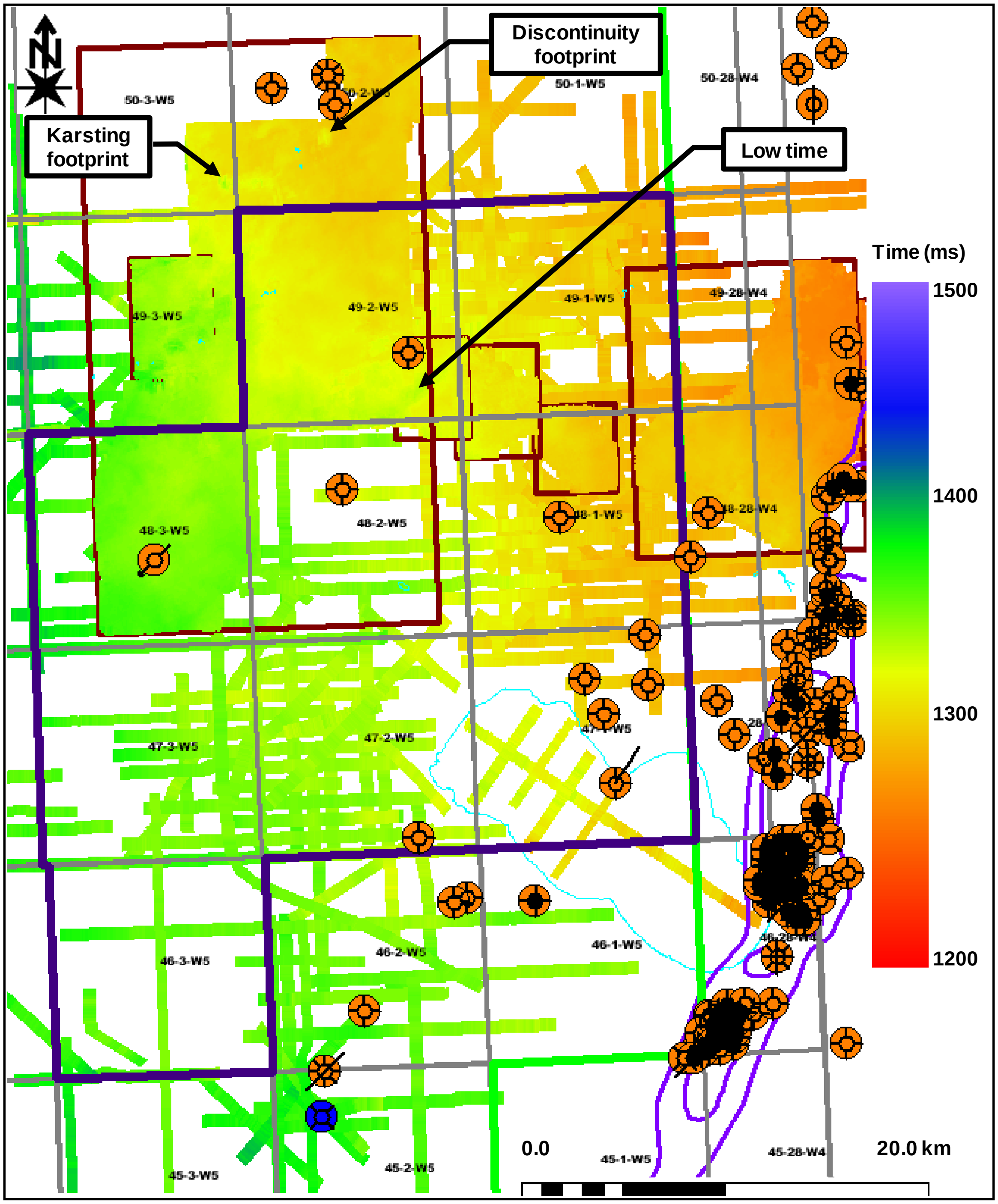

Figure 4-10: Zoom-in display of the Nisku time structure map in Figure 4-9. The locations of some of the major anomalies are specified: Wabamun karsting, Wabamun discontinuities, and the Nisku local depression (see Figure 4-15). It should be emphasized that the karsting and discontinuity effects shown here are the footprints of these anomalies and do not indicate that the Nisku has necessarily been physically affected (see discussion under Section 4.5.2).

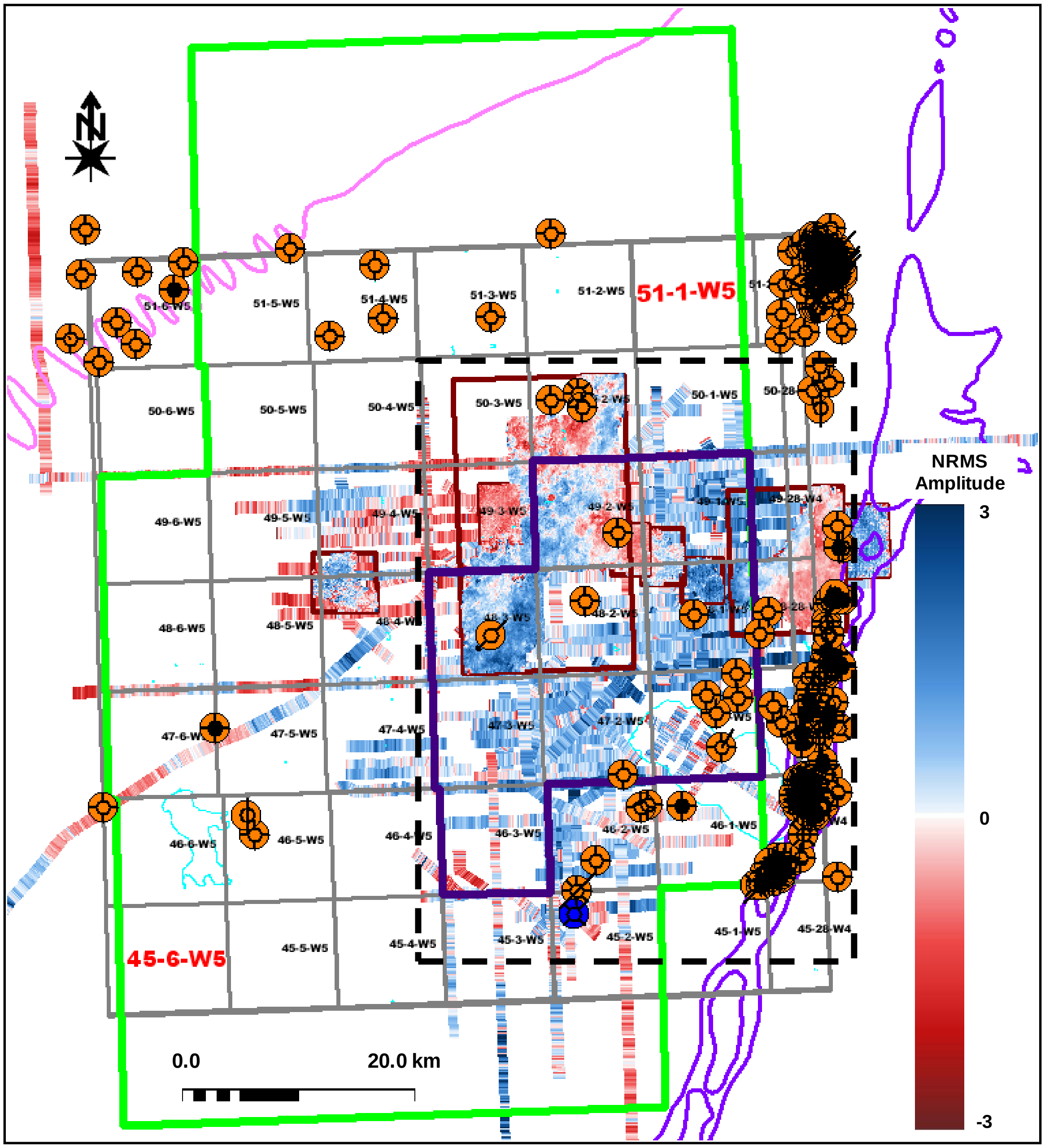

Figure 4-11: NRMS amplitude map of the Nisku event after data calibration and RMS amplitude normalization. Note the strong variations in the Nisku amplitude map compared to the time structure map (Figure 4-9). The dashed black rectangle shows the extent of the detailed display over the study area in Figure 4-12.

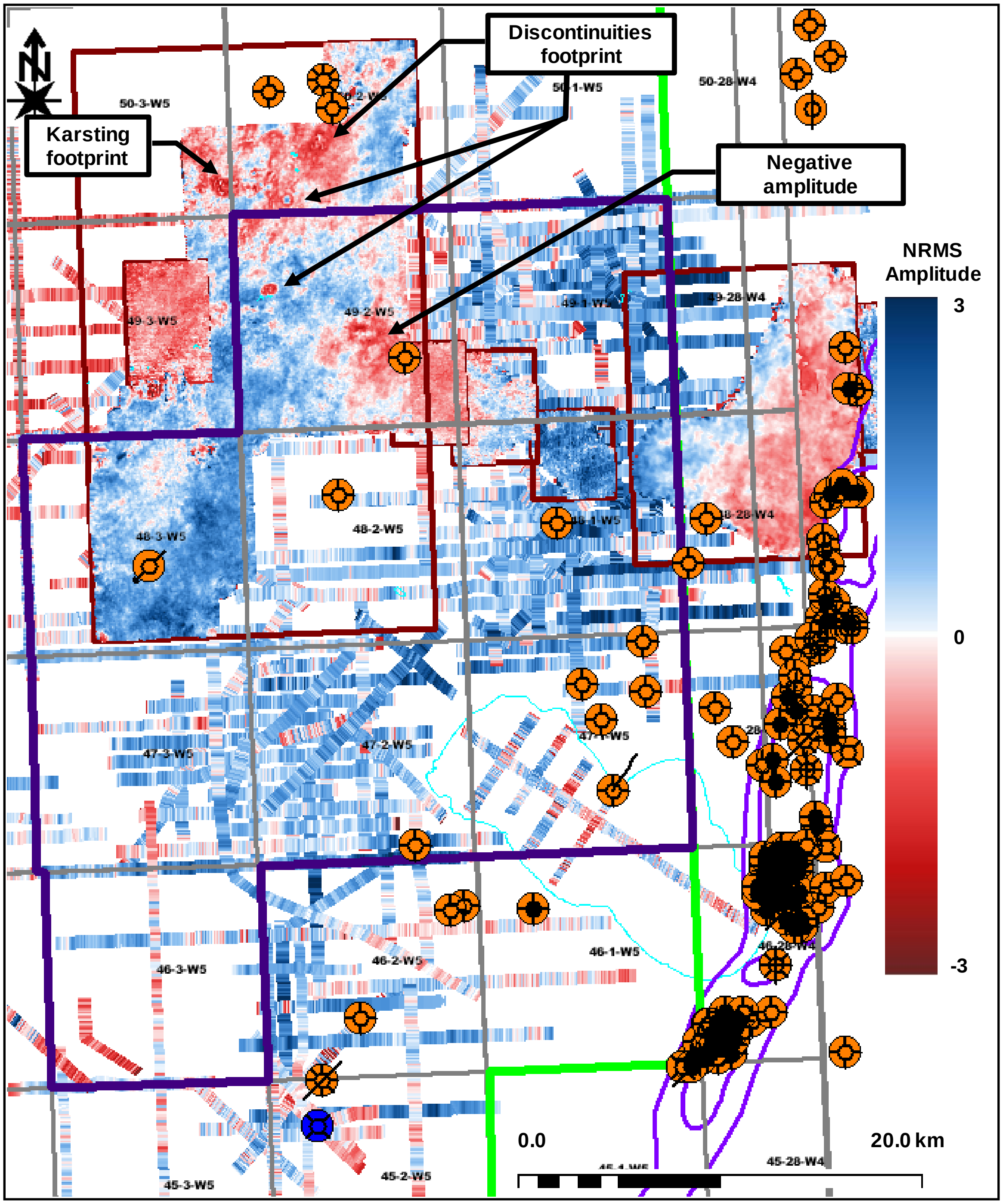

Figure 4-12: Zoom-in display of the Nisku NRMS amplitude map in Figure 4-11. Some of the major amplitude anomalies are specified: Wabamun karsting, Wabamun discontinuities, and the Nisku negative amplitude (see Figure 4-15). It should be emphasized that the karsting and discontinuity effects shown here are the footprints of those anomalies and do not indicate that the Nisku has necessarily been physically affected.

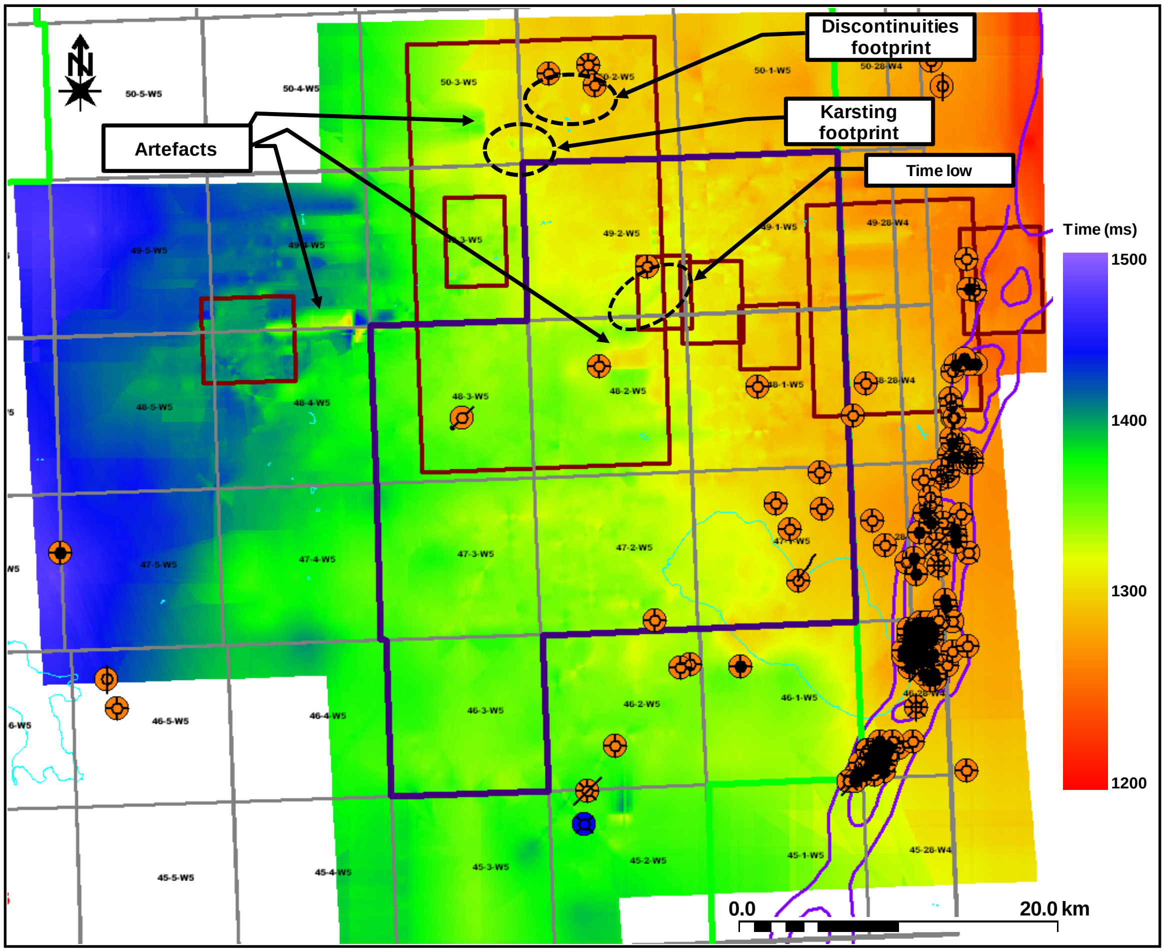

Figure 4-13: Interpolated Nisku event time structure map using a kriging algorithm with a grid size of 50×50 m. Note how some of the details associated with overlying karsting and discontinuities are still preserved after the interpolation. The reference map is shown in Figure 4-9.

In general, the interpolated time and depth structure maps (Figure 4-13 and Figure 4-14) honour the original data, as illustrated in the case of the depth interpolation in Table 4-3, in which the actual and estimated depth values are compared. However, the interpolation seems to produce inaccurate results in areas where there is a large gap in data coverage or where there is a relatively large difference between neighbouring picks (Figure 4-13). An additional cause of inaccuracy in the interpolated depth structure map is the absence of Nisku Formation picked depths in some of the borehole data (Figure 4-14). However, despite the few artefacts, the results suggest that the kriging interpolation algorithm has performed well within the WASP local-scale study area. In addition to providing a more continuous maps of the Nisku Formation, the interpolated depth structure maps (Figure 4-14) gives an insight into the subtle depth variations in the Nisku Formation within the WASP study area. While the discontinuities footprints seem to have faded, they have not been completely diminished by the domain conversion (Figure 4-14). The karsting footprint, in particular, seems to persist. This is, probably, due to the complexity, intensity and chaotic nature of karsting, which would still leave an imprint even after the depth conversion. In order to properly convert from time to depth at the karsting areas, a local velocity function $\alpha(x,z)$ is needed. The karsting among other discontinuities footprints will be examined closer in the next section (Section 4.5.2).

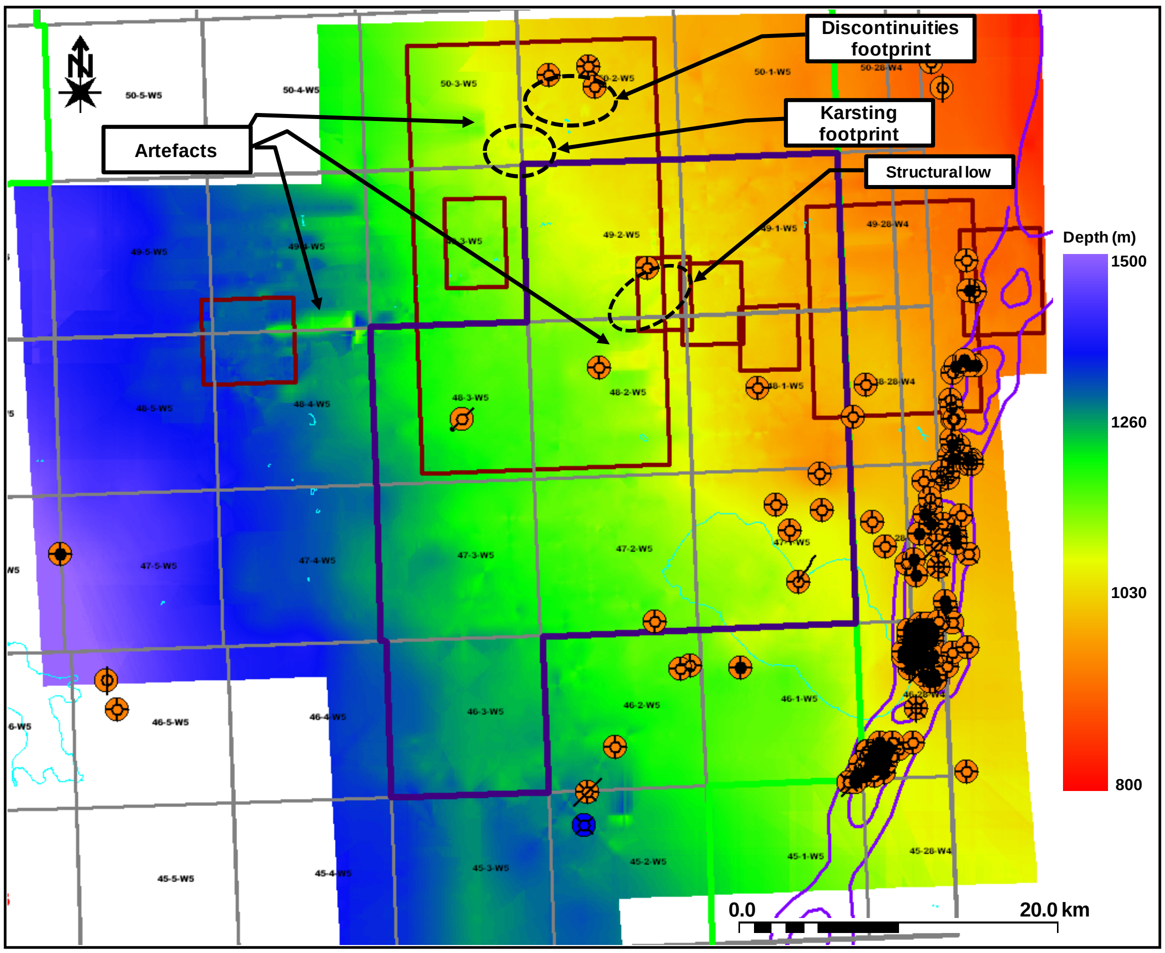

Figure 4-14: Interpolated Nisku event *depth* structure map using a kriging algorithm with a grid size of 50×50 m. Note how some of the footprint anomalies associated with the discontinuities in Figure 4-10 and Figure 4-13 have largely disappeared but not the karsting effects. Depth values are with respect to sea level, i.e. sub-sea.

Table 4-3: Comparison between the measured and estimated depth values (sub-sea) using kriging technique. The difference between the two is also shown. The interpolation algorithm seems to honour the actual data, except at well 100163504701W500.

Well	Measured Depth (m)	Estimated Depth (m)	Difference (m)
100/01-01-046-01W5	1111.6	1111.6	0.0
100/02-01-046-01W5	1114.9	1114.9	0.0
100/02-21-048-01W5	1178.6	1178.6	0.0
100/02-23-04828W4	1038.1	1038.1	0.0
100/02-28-048-02W5	1148.1	1148.1	0.0
100/02-28-048-02W5	1148.1	1148.1	0.0
100/05-20-050-02W5	1075.1	1075.1	0.0
100/06-02-047-02W5	1198.8	1198.8	0.0
100/06-02-047-02W5	1198.8	1198.8	0.0
100/06-15-048-03W5	1219.5	1219.5	0.0
100/06-29-046-01W5	1170.6	1170.6	0.0
100/08-26-047-01W5	1082.7	1082.7	-0.7
100/09-01-046-01W5	1104.8	1106.4	-1.6
100/09-10-047-01W5	1107.9	1101.1	6.8
100/09-24-047-06W5	1488.5	1488.5	0.0
100/10-09-046-02W5	1257.9	1257.9	0.0
100/10-21-050-02W5	1063.3	1063.3	0.0
100/10-22-047-01W5	1098.2	1098.2	0.0
100/10-25-046-02W5	1200.5	1200.5	0.0
100/12-27-047-01W5	1098.8	1099	-0.2
100/13-11-048-28W4	1042.0	1042.4	-0.4
100/13-13-047-28W4	1066.8	1066.8	0.0
100/14-29-046-05W5	1502.2	1502.2	0.0
100/14-32-045-02W5	1285.3	1285.3	0.0
100/15-11-049-02W5	1092.1	1093	-0.9
100/15-23-047-28W4	1069.8	1069.8	0.0
100/16-16-050-02W5	1063.5	1062.9	0.6
100/16-35-047-01W5	1292.1	957.9	334.2
102/12-25-046-02W5	1197.9	1197.9	0.0
1F1/11-29-045-02W5	1297.5	1297.5	0.0

4.5.2 Nisku Seismic Character

In order to delineate the Nisku seismic character and examine the anomalies outlined in the previous sections (see Figure 4-10 and Figure 4-12), an arbitrary multi-segment seismic line was extracted from the seismic data in the focus area (Figure 4-15). This multi-segment traverses various types of anomalies including: karsting “k” and discontinuities “d” originating above the Nisku Formation, low “l” and high “h” amplitude, and peak amplitude thinning “t” in the Nisku Formation itself. Thus, it provides a good comprehensive example of the variety of anomalies observed in the study area.

The first and most prominent anomaly is the karsting associated with dissolution in the overlying Wabamun Formation during Pre-Cretaceous aerial exposure (“k” in Figure 4-16). The seismic data indicate that the karsting covers an area of approximately 7 km^2 north-northwest of the WASP local-scale study area. Other anomalies are more localized, such as the discontinuities “d” in Figure 4-16. The data suggests that they are either originating within the Wabamun Formation or within the Pre-Cretaceous unconformity immediately above the Wabamun event. The amplitude map reveals significant variations within the Nisku Formation lithology or porosity as indicated by the undulation from low “l” to high “h” amplitude as well as interpreted peak amplitude thinning “t”, especially within the northern and eastern regions of the reference 3-D volume (Figure 4-16). Some of the anomalies will be discussed again later in this chapter using seismic attributes (Section 4.6).

As for the Wabamun discontinuities, it is uncertain as to what they represent and what process might have caused them, but there are two suggested explanations: the first is a mechanical process while the second is a chemical process. The mechanical process suggests that these discontinuities are actually rhombo-chasms, a phenomenon associated with strike-slip faults in which a vertical fault surface bends in the fault plane direction (Allen and Allen, 2005). However the lack of spatial (Figure 4-12) and temporal[48] (Figure 4-16) continuity does not seem to support this explanation, as the observed

[48] Other than what seems to be footprint effect, e.g. velocity pull-down.

discontinuities tend to be isolated and exhibit circular patterns. The other explanation is that chemical processes, namely dissolution, such as those responsible for producing karsting, are accountable for those discontinuities. A dissolution agent, i.e. water, would travel along conduits, such as sub-seismic fractures, and thus dissolve parts of the Wabamun strata even at such a small scale where there is an increased concentration in sodium chloride (NaCl). In any case, it is believed that those discontinuities may pose a risk due to fracturing in the Calmar Formation caprock and, therefore, should be taken into consideration[49] for the location of a future CO_2 injection program.

In Section 2.2, it was revealed that the Nisku Formation in the local-scale study area coincides with the Nisku shelf and is dominated by the open marine lithofacies, which exhibits both good and poor reservoir characteristics throughout the focus area based on whether or not the enhanced (moldic) porosity is destroyed by anhydrite plugging. Furthermore, since the distinction between the two open marine lithofacies is ambiguous in the wireline data (Eisinger and Jensen, 2009; Shevalier et al., 2009), it is only fair to presume that such distinction is even more ambiguous in the seismic data. In fact, only through core analysis could the two open marine lithofacies be explicitly discriminated from one another (Eisinger and Jensen, 2009). This observation suggests that anomalies observed in the NRSM amplitude map (and in the subsequent attribute maps), aside from those associated with discontinuities footprints, could be ascribed to variations in lithology or porosity, in general, but not to a particular lithofacies.

There exists a part of the Nisku aquifer in the study area that exhibits excellent reservoir characteristics in terms of porosity and permeability. Figure 4-17 shows a 2-D seismic section near the so-called water source well, which displays a variation in NRMS amplitude. This could be used as an indication of the Nisku trend from a poor to good aquifer. The seismic character from this region, in terms of seismic amplitude and acoustic impedance, will be examined later in this chapter (Section 4.6.4) as a guide toward delineating favourable injection zones in the Nisku Formation.

---

[49] For instance, by avoiding CO_2 injection nearby these discontinuities.

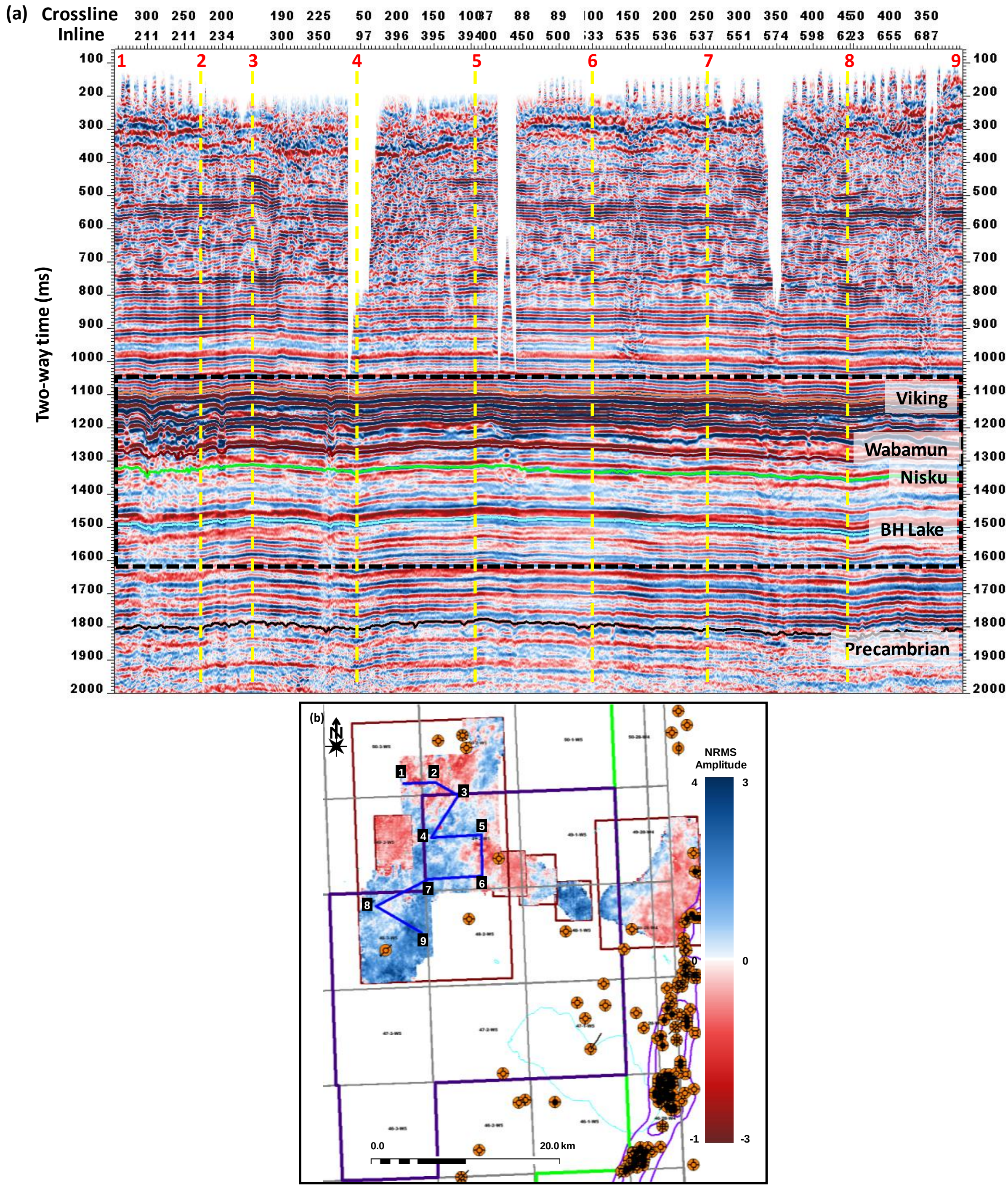

Figure 4-15: (a) multi-segment seismic section traversing some of the geological features within the reference 3-D volume; (b) base map showing the location, length and orientation of the multi-segment section. The nodes are shown at their corresponding location along the horizontal axis. The right side of the colour scale in the base map represents the amplitude within the section (-3 to 3) whereas the left side represents that of the NRMS amplitude map (-1 to 4). The dashed rectangle indicates the extent of the zoom-in display in Figure 4-16.

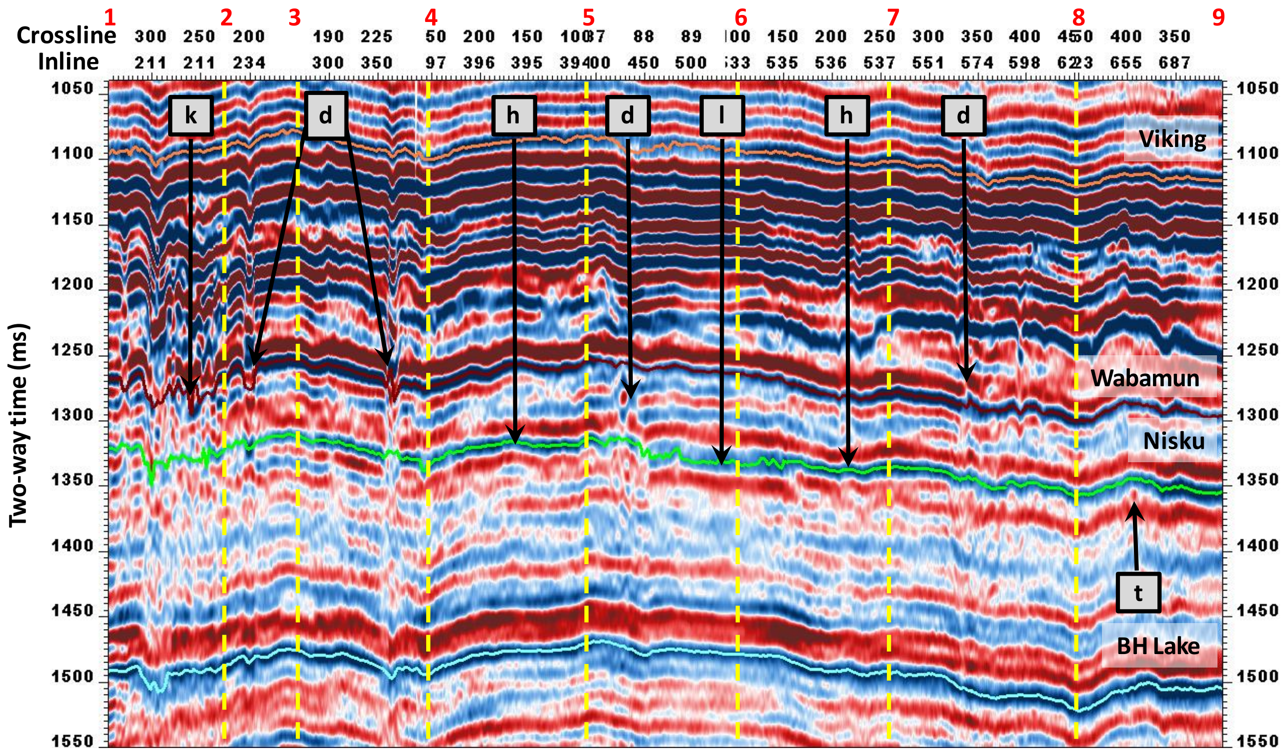

Segment	Feature	Description
1-2	k: karsting	Dissolution associated feature in the Wabamun event
2-3	d: discontinuity	Local amplitude anomaly within the Wabamun event
3-4	d: discontinuity	Local amplitude anomaly within the Wabamun event
4-5	h: high amplitude	High amplitude within the Nisku event
5-6	d: discontinuity	Local amplitude anomaly within the Wabamun event
	l: low amplitude	low amplitude within the Nisku event
6-7	h: high amplitude	High amplitude within the Nisku event
7-8	d: discontinuity	Local amplitude anomaly within the Wabamun event
8-9	t: amplitude thinning	Decreasing duration of the Nisku event

Figure 4-16: Detailed display of the multi-segment line through the reference 3-D volume in Figure 4-15. Segment 1-2 passes through the karsting “k” originating in the Wabamun event. Segments 2-3 and 3-4 cross local Wabamun discontinuities “d”. Segments 4-5, 5-6, and 6-7 show an example of the Nisku amplitude changing from high “h” to low “l” to high “h” again. Note the broadening in the Nisku cycle in segment 5-6. Segment 7-8 shows some amplitude anomalies between 1150 and 1200 ms, which are interpreted to be associated with the Pre-Cretaceous unconformity. The change from moderate to high Nisku amplitude is illustrated in segment 8-9. Segment 8-9 also traverses an area of local Nisku amplitude thinning “t”, which is mapped by the seismic attribute amplitude thickness of the peak (ATP).

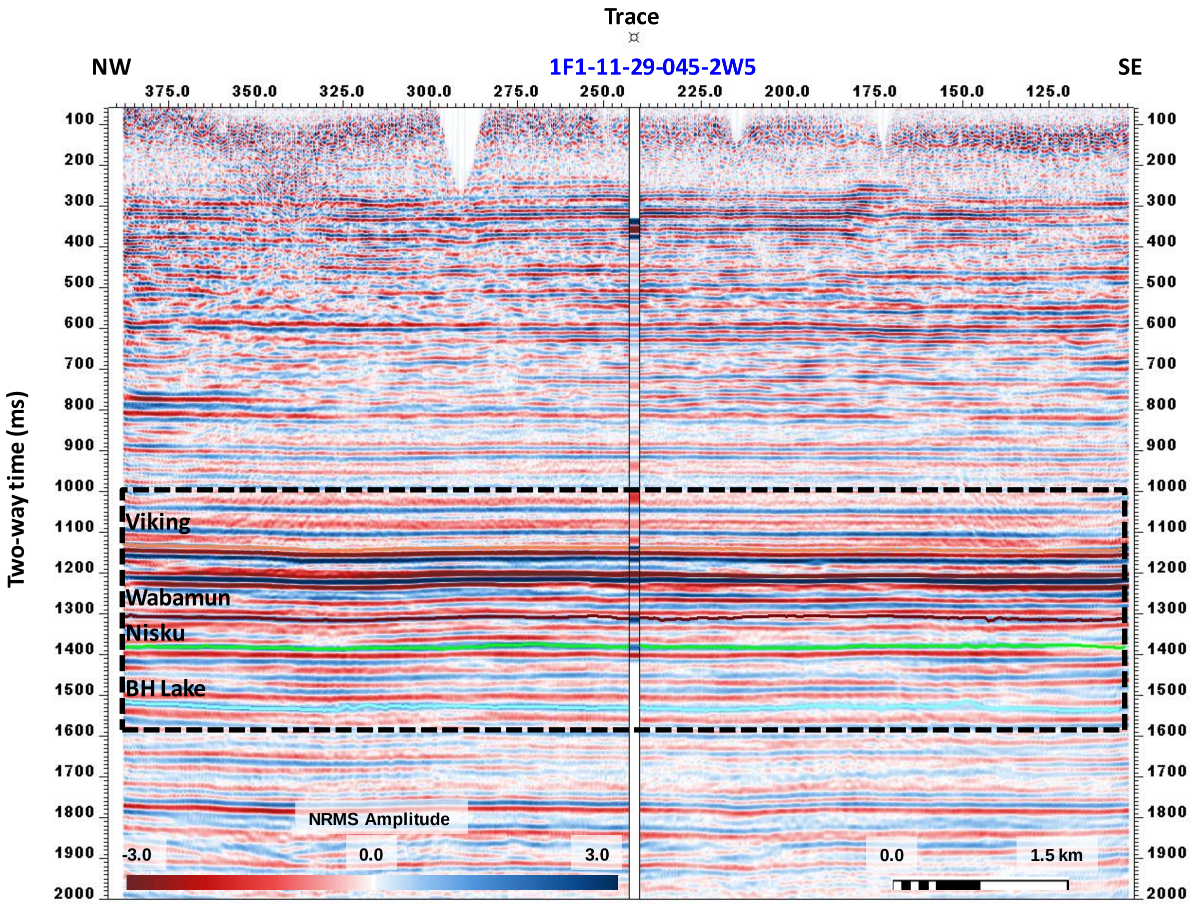

Figure 4-17: The 2-D seismic line near the water source well which is shown by the blue line in the base map (Figure 4-3) with the synthetic seismogram inserted at the well location (1F1-11-29-45-2W5). The seismic character over the zone of interest enclosing the Nisku event (dashed rectangle) is enlarged in Figure 4-18.

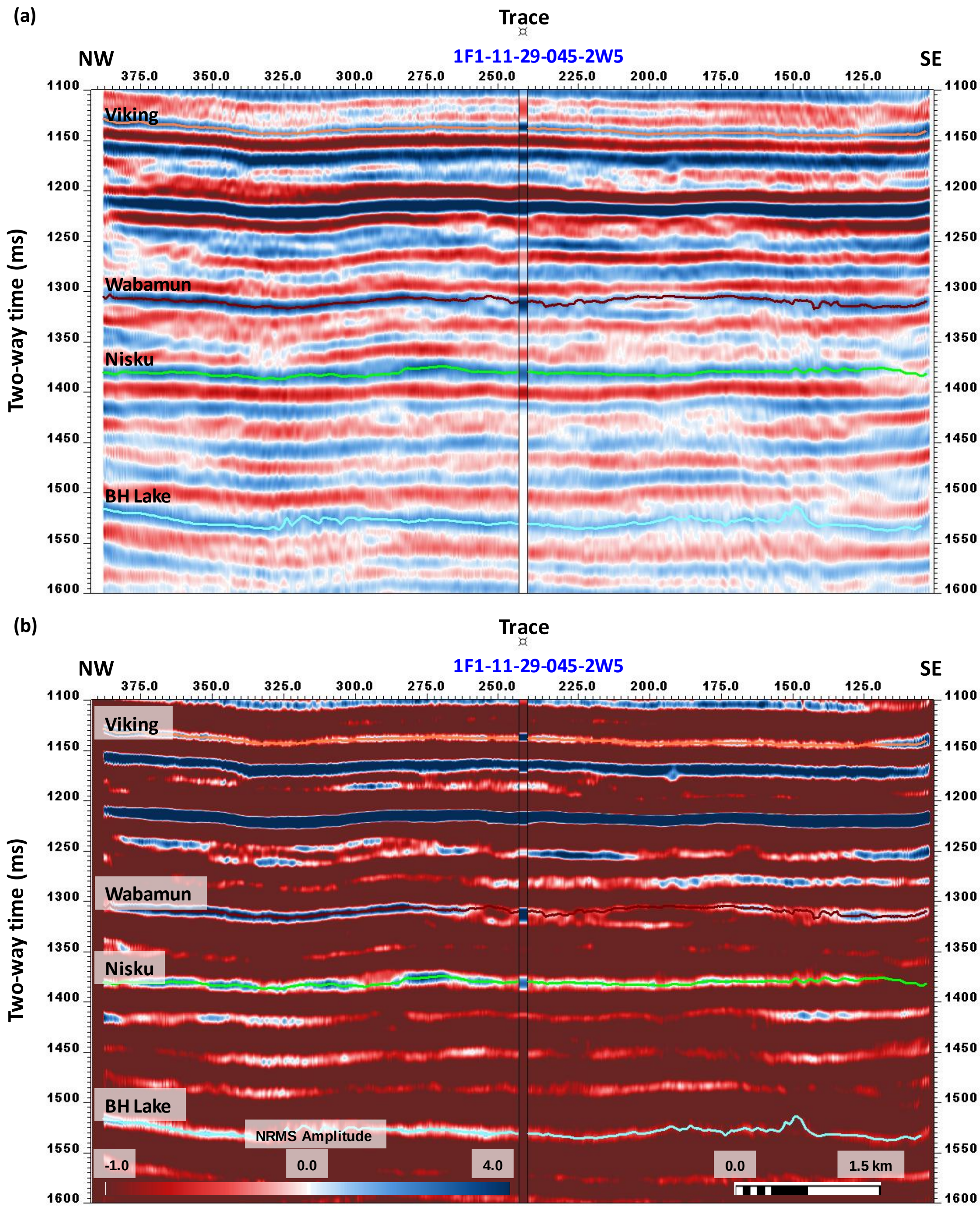

Figure 4-18: Enlarged display of the zone of interest from the 2-D seismic line near the water source well (zone outlined by the dashed rectangle in Figure 4-17) with the synthetic seismogram inserted at the well location (1F1-11-29-45-2W5). The bottom image is identical to the one on top with the dynamic range modified to emphasize lithology or porosity variations within the Nisku event NRMS amplitude. Note the change in the amplitude strength, i.e. increase in the NRMS amplitude in the NW direction.

4.6 Seismic Attributes

In addition to amplitude, several seismic attributes including the average NRMS amplitude, the amplitude thickness of the peak (ATP) of the Nisku reflection, edge detection (ED), and acoustic impedance (AI) attributes were generated to strengthen the interpretation of the lithology changes and geologic discontinuities in the study area. For these attributes, only 3-D seismic data were exploited as such attributes require, in addition to time and amplitude, continuous and dense two-dimensional spatial sampling, both of which are lacking in the 2-D seismic data.

4.6.1 Average NRMS Amplitude

The average NRMS amplitude of the Nisku event (Figure 4-19) was calculated over a window of 10 ms (centred on the Nisku horizon pick). The purpose behind this averaging is to generate another representation of the Nisku event amplitude that captures the amplitude envelope around the event rather than a single value, thus minimizing errors due to picking ambiguities. The computed average NRMS amplitude map is quite similar to the original NRMS amplitude map in Figure 4-12, which is an indication that the representation of the amplitude variations within the Nisku Formation in Figure 4-12 is appropriate. The only difference is that a new pattern emerges from the average NRMS amplitude map, as indicated in Figure 4-19. This pattern is better captured by the attribute called amplitude thickness of the peak (ATP).

4.6.2 Amplitude Thickness of the Peak (ATP)

The ATP calculates the time duration of the Nisku peak from zero-crossing to zero-crossing; the peak being defined as amplitude value larger than zero value (see Section 3.6.8). One of the most interesting features associated with ATP (Figure 4-20) is that it accounts well for the transition between the various seismic volumes, something that was not fully achieved with conventional amplitude maps (Figure 4-12 and Figure 4-19). The low ATP values indicate areas where the Nisku amplitude peak thins. Such zones can also be seen in the seismic sections as indicated by the symbol “t” in the multi-segment line in Figure 4-16. The thinning appears to mainly occur at the base of the

Nisku event and there are two explanations proposed for its cause. The first is that there might be change in the thickness of the Nisku Formation. The second is that the thinning might be associated with a change in acoustic impedance, primarily P-wave speed, resulting from either a lithofacies change, e.g. shale content, or porosity variations within the Nisku Formation, which could be attributed to depositional or digenetic processes, respectively. Unfortunately, there is no well penetration through the Nisku Formation within the 3-D seismic volume that could be used to better calibrate this attribute. Nonetheless, it is possible to reduce the non-uniqueness by integrating high ATP values with optimum values of other attributes, e.g., low impedance, which are used as indicators for favourable site conditions in the study area.

4.6.3 Edge Detection (ED)

Although the NRMS amplitude was successful in outlining discontinuities within the seismic data, it was deemed appropriate to invoke a designated edge detection attribute, namely the difference method (Luo et al., 1996). This method is a member of another class of attributes which, in contrast to the other attributes presented in this section, is sensitive to discontinuities in seismic data. The method is based on a simple algorithm that subtracts a given seismic trace from its neighbouring trace and divides by their average (see Section 3.6.7). The method has proven robust in detecting the various types of discontinuity footprints encountered in the seismic data, as seen in Figure 4-21 and Figure 4-22. To account for preferential direction, the difference attribute was computed in both the in-line direction (Figure 4-21) and in the cross-line direction (Figure 4-22). The former is more robust in identifying geologic discontinuity footprints within the reference 3-D, such as the Wabamun karsting footprint on the Nisku event. The cross-line difference, on the other hand, is more sensitive to variations associated with some of the other seismic volumes, for instance the local time low just east of the reference volume, as shown in Figure 4-10.

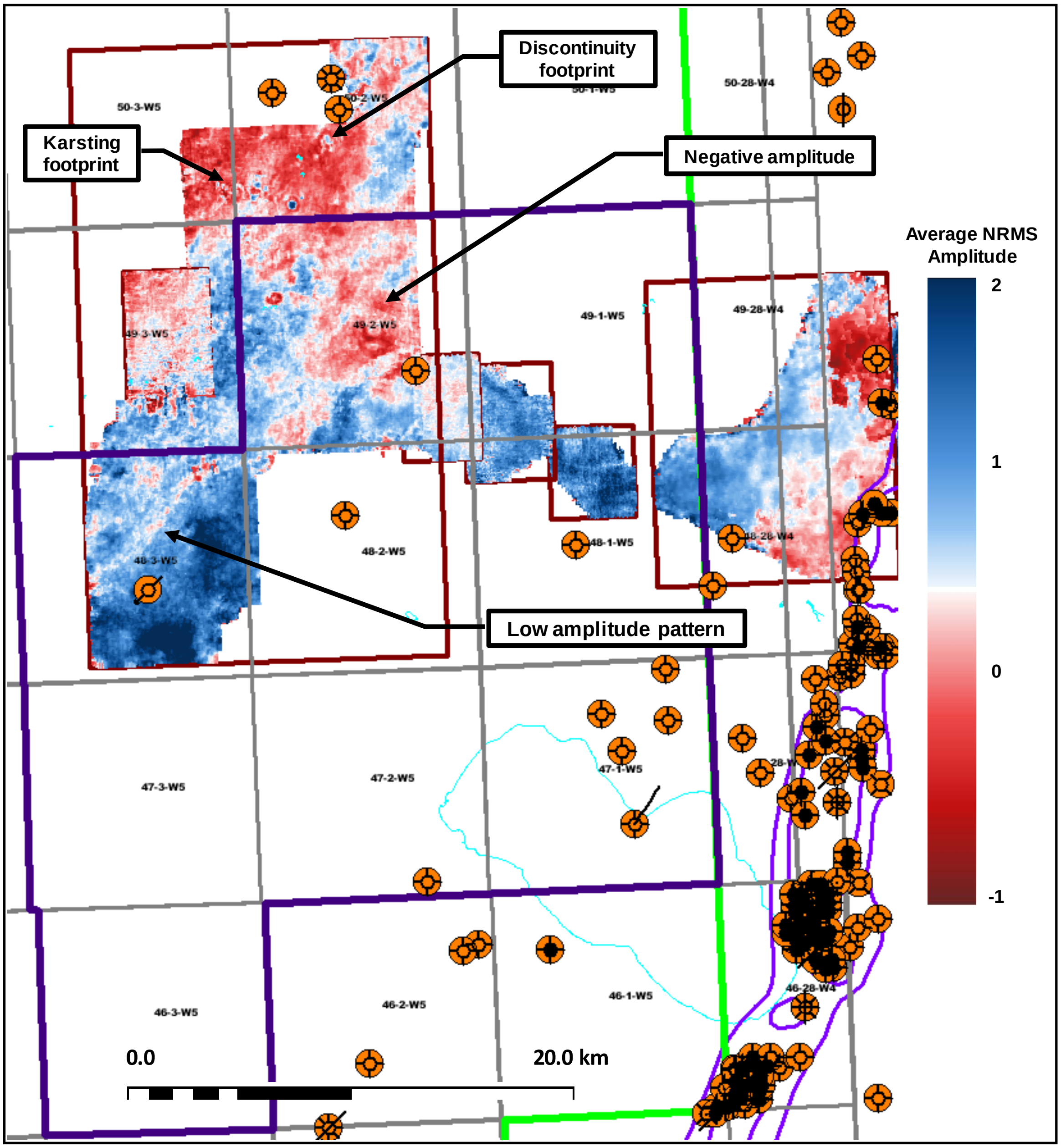

Figure 4-19: Average NRMS Nisku amplitude over a 10 ms window (centred on the Nisku horizon pick). In addition to the patterns already defined in the NRMS Nisku amplitude map (Figure 4-16), another low amplitude pattern emerges from the map. The NRMS amplitude averaging window of 10 ms seems appropriate except within the north-eastern region of the easternmost 3-D volume, which coincides with the Leduc reef trend. The relative position to the large study area is shown by the dashed rectangle in the base map in Figure 4-9.

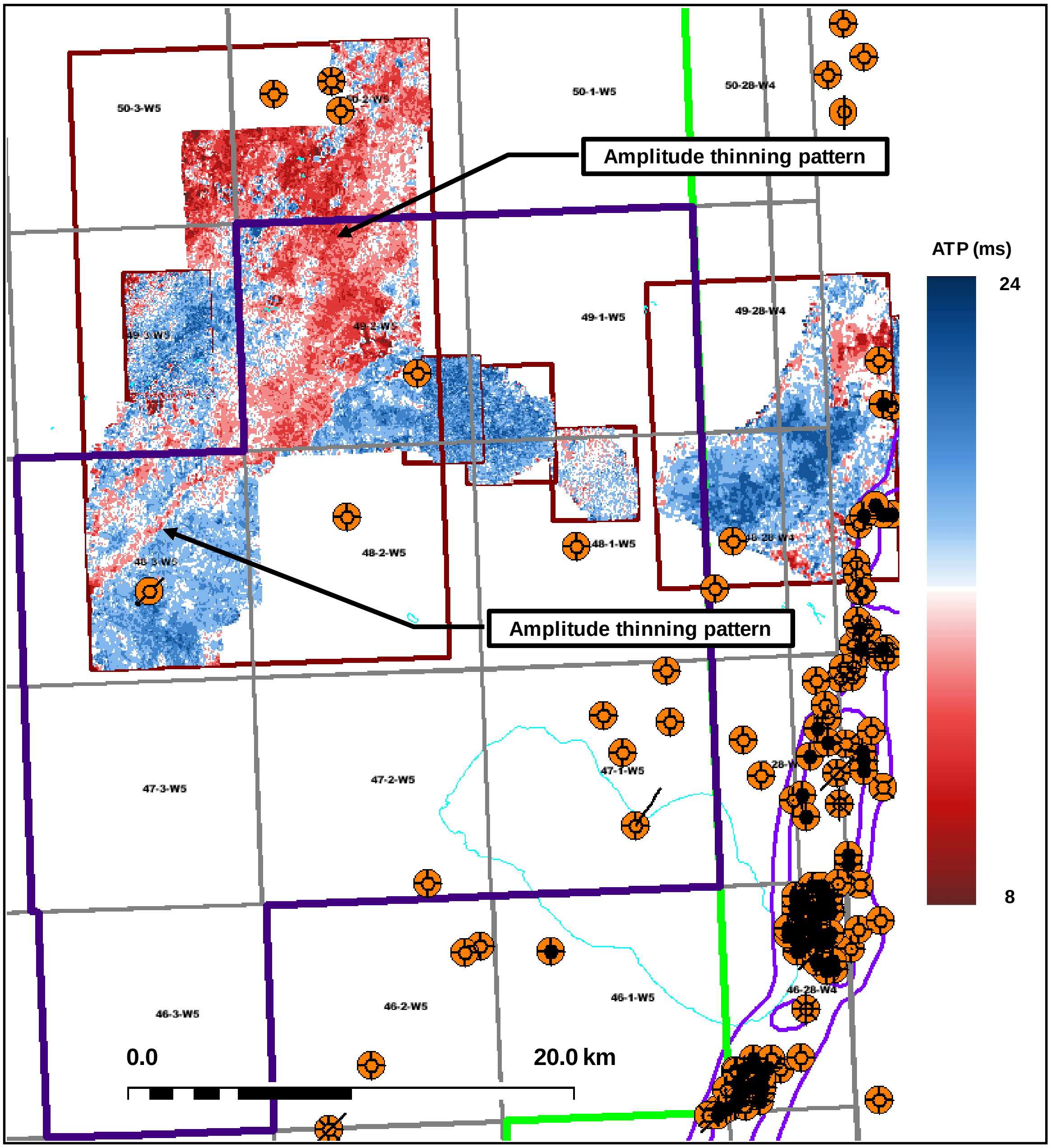

Figure 4-20: Amplitude thickness of the Nisku peak (ATP) in ms computed over a 30 ms window. Note the elongated (NE-SW) thinning pattern that is not captured by the NRMS amplitude map. See the multi-segment line in Figure 4-16 for a cross-sectional view of those anomalies. The relative position to the large study area is shown by the dashed rectangle in the base map in Figure 4-9.

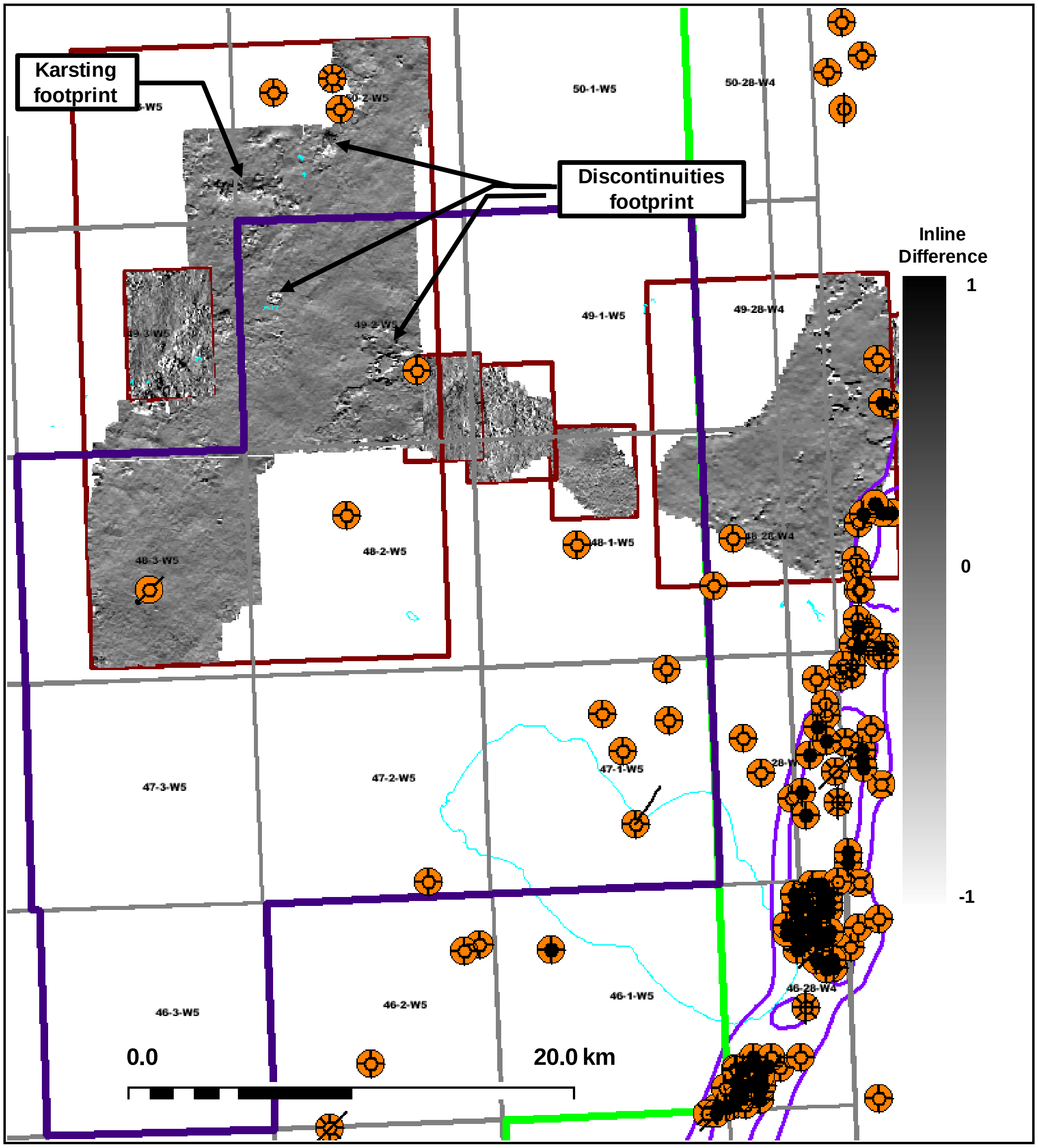

Figure 4-21: In-line difference (coherency) attribute of the Nisku event. The difference method shows more sensitivity toward discontinuity footprints within the Nisku compared with other seismic attributes as can be seen, for instance, with the Wabamun karsting effect on the Nisku event. See the multi-segment line in Figure 4-16 for a cross-sectional view of those anomalies. The relative position to the large study area is shown by the dashed rectangle in the base map in Figure 4-9.

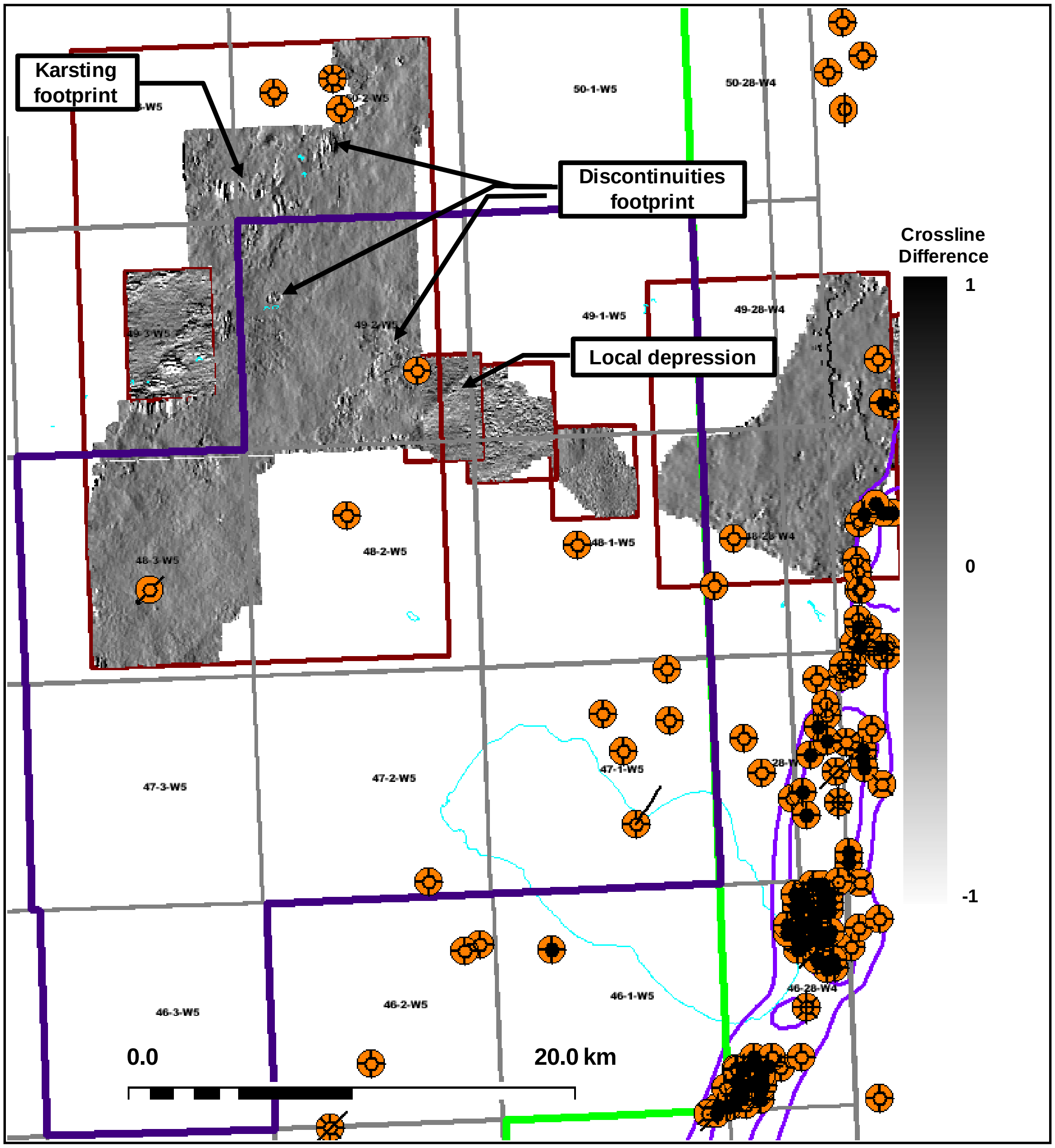

Figure 4-22: Cross-line difference (coherency) attribute of the Nisku event. Note the sensitivity to the direction in which the difference is measured compared to the in-line difference in Figure 4-21. The cross-line difference was not as robust as the in-line difference in defining geologic features within the reference 3-D volume, e.g. the Wabamun karsting effect. However, it performed better in defining some of the features associated with other seismic volumes, such as the local time low (also shown in the time structure map in Figure 4-10). See the multi-segment line in Figure 4-16 for a cross-sectional view of those anomalies. The relative position to the large study area is shown by the dashed rectangle in the base map in Figure 4-9.

4.6.4 Acoustic Impedance (AI)

Acoustic impedance is one of the most useful seismic attributes as it yields distribution of pseudo-physical properties rather than a set of observations pertaining to the physical properties distribution. However, acoustic impedance is more difficult to determine as it requires seismic inversion, which calls for good estimation of parameters as well as high quality seismic data and a good distribution of well control. Furthermore, inversion suffers from non-uniqueness[50]. In estimating the acoustic impedance of the Nisku Formation, various post-stack acoustic impedance inversion techniques were tested and only two were found to produce useful results: recursive inversion (RI) and model-based inversion (MBI).

RI, also known as band-limited inversion, is constrained by the bandwidth of the seismic data, which typically falls between 7 and 60 Hz. The method estimates the acoustic impedance recursively by first extracting an estimate of the reflection coefficient from the seismic data and then re-arranging the normal incidence reflection coefficient relation to solve for the acoustic impedance of the next layer (Russell, 1988). MBI uses a different approach. First, the well control and the seismic data (horizons) are used to build an initial low-frequency model of the acoustic impedance distribution. Using an estimate of the source wavelet, the model is then perturbed and the model response, in the form of synthetic seismogram, is measured. The model responses are then compared to the actual seismic traces, usually by means of cross-correlation, and misfit error is computed. The most commonly used approach is to minimize the sum of the squared difference between the actual and estimated seismograms, hence known as least-squares. The process is iterated until the model converges, i.e. the model response becomes within a predefined acceptable range from the actual observation (Lines and Treitel, 1984).

There are many elements that degrade the reliability of the inversion results, some of which can not be controlled, such as noise, whereas others could not be precisely calculated, such as the source wavelet. However, each method has its own advantages and disadvantages in regard to those limitations and it is suggested that by using both

---

[50] See Section 3.5 and Sections 3.5.6 and 3.5.7 for a brief review of inverse modelling.

methods some of the ambiguities associated with the inversion results could be minimized. Succinct discussions of RI and MBI were presented in Section 3.5.6 and Section 3.5.7, respectively.

Figure 4-23 depicts some of the major steps adopted in the acoustic impedance inversion framework. An important element in achieving good inversion results is the seismic-to-well tie. The correlation coefficients associated with the wells used in the inversion are shown in Figure 4-24. All wells have sonic and density logs but not dipole sonic log which is needed to perform the inversion. Thus, an α/β ratio of 1.9 was used in deriving the S-wave speed from the P-wave speed to perform the inversion. Prior to showing the Nisku acoustic impedance map, two examples were selected to illustrate the performance of each of the inversion methods. The first example is from the 2-D seismic line near the water source well (Figure 4-25). Figure 4-26 show the initial estimated model while the inversion results using RI and MBI for this section are illustrated in Figure 4-27. The other example is from an in-line extracted from the reference 3-D volume (Figure 4-28). The initial model and the estimated acoustic impedance associated with this section are shown in Figure 4-29 and Figure 4-30, respectively.

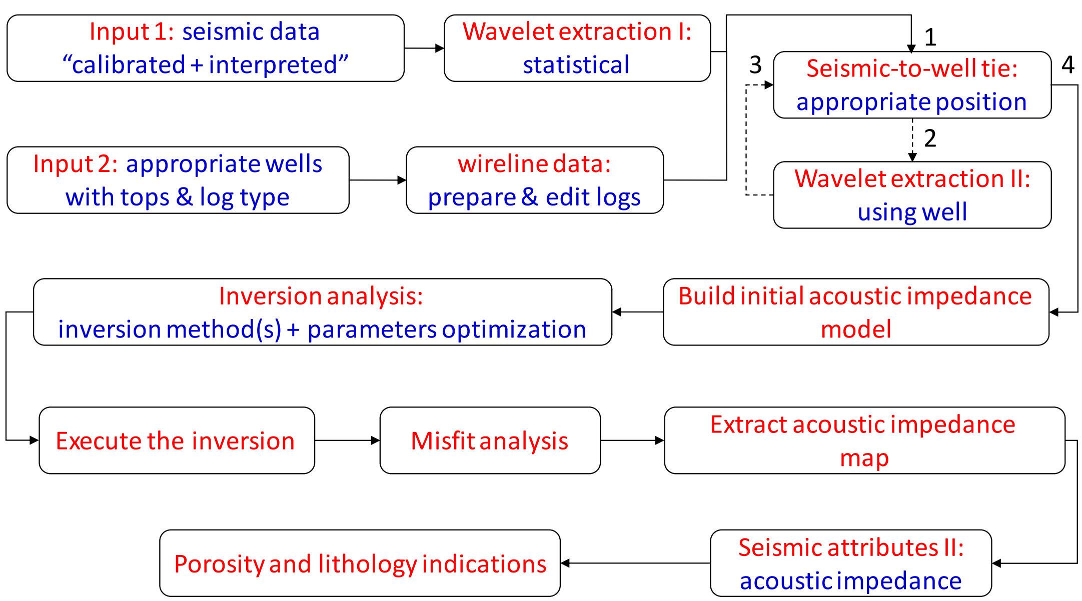

Figure 4-23: Flowchart outlining the major steps followed in the seismic inversion to extract the acoustic impedance of the Nisku event. The dashed arrows (2 and 3) refer to an additional step that is sometime required to achieve a better inversion result if the processed seismic wavelet cannot be represented or approximated by zero-phase wavelet.

The RI appears to produce a more detailed acoustic impedance model than the MBI (Figure 4-27 and Figure 4-30). For instance, the Wabamun and the Nisku formations are clearly separated by low impedance in the RI whereas they are hardly separated in the MBI results. However, for the acoustic impedance of the Nisku Formation, both methods yield similar results, the only apparent difference being in the magnitude of the impedance. This is probably due to scaling differences. Furthermore, because there is a lack of well control, it is crucial that the impedance maps are interpreted only in terms of relative rather than absolute changes in acoustic impedance.

Several interesting low impedance zones are highlighted in Figure 4-31 and Figure 4-32. The impedance determination from the 2-D seismic line near the water source well is also shown for comparison. By examining those maps, there seems to be two categories of low impedance: one that is associated with lithological changes in the Nisku Formation and another which is associated with discontinuity footprints in the overlying strata. A useful way to differentiate between those two classes is to use the difference attribute in Figure 4-21 and Figure 4-22. Any low acoustic impedance (Figure 4-31 and Figure 4-32) that correlates with discontinuities footprints in the difference attribute maps (Figure 4-21 and Figure 4-22) is likely to be associated with Wabamun or Pre-Cretaceous discontinuities. With respect to the lithological changes, low acoustic impedance (Figure 4-31 and Figure 4-32) appears to normally correspond to low NRMS and low average NRMS amplitude (Figure 4-12 and Figure 4-19).

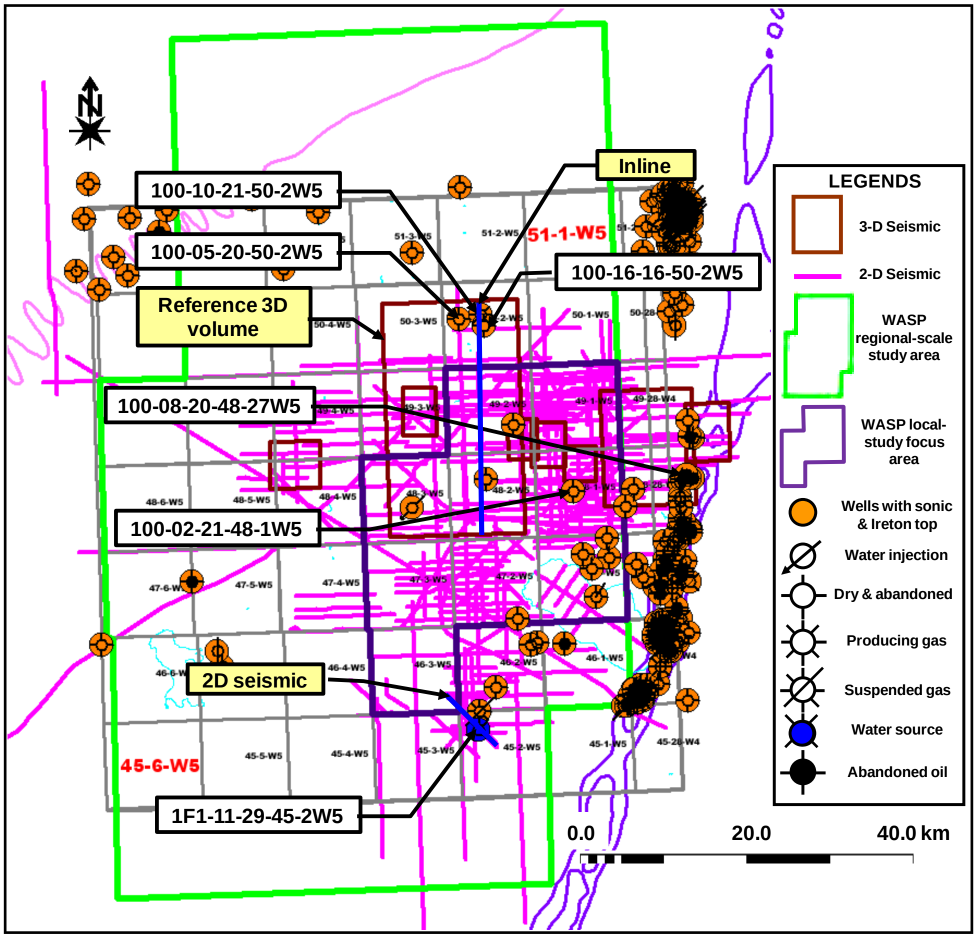

Well	Seismic Reference	Correlation Coefficient
1F1-11-29-45-2W5	2-D	0.92
100-10-21-50-2W5	3-D	0.80
100-16-16-50-2W5	3-D	0.83
100-05-20-50-2W5	3-D	0.72
100-02-21-48-1W5	3-D	0.63
100-08-20-48-27W4	3-D	0.80

Figure 4-24: Well control used in the inversion and the corresponding correlation coefficient between seismic data and synthetic seismogram at these wells. The blue lines show the location of the 2-D seismic line near the water source well (Figure 4-18) and an in-line within the reference 3-D volume.

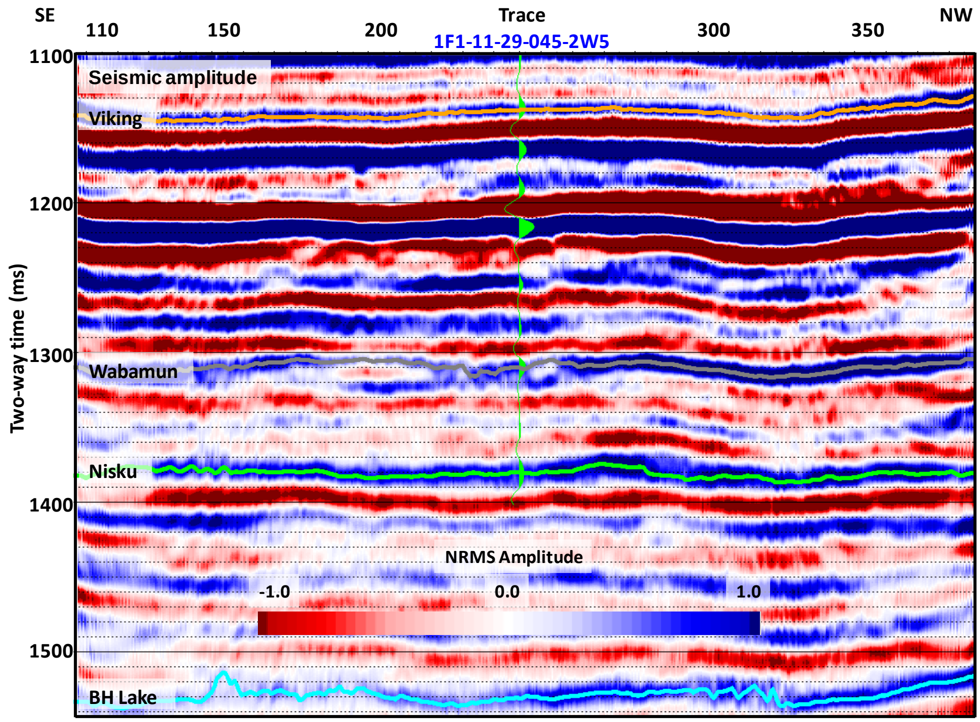

Figure 4-25: Seismic section near the water source well (Figure 4-24). The green curve at the well location is the correlated synthetic seismic trace. The correlation coefficient with the actual seismic trace is 0.92.

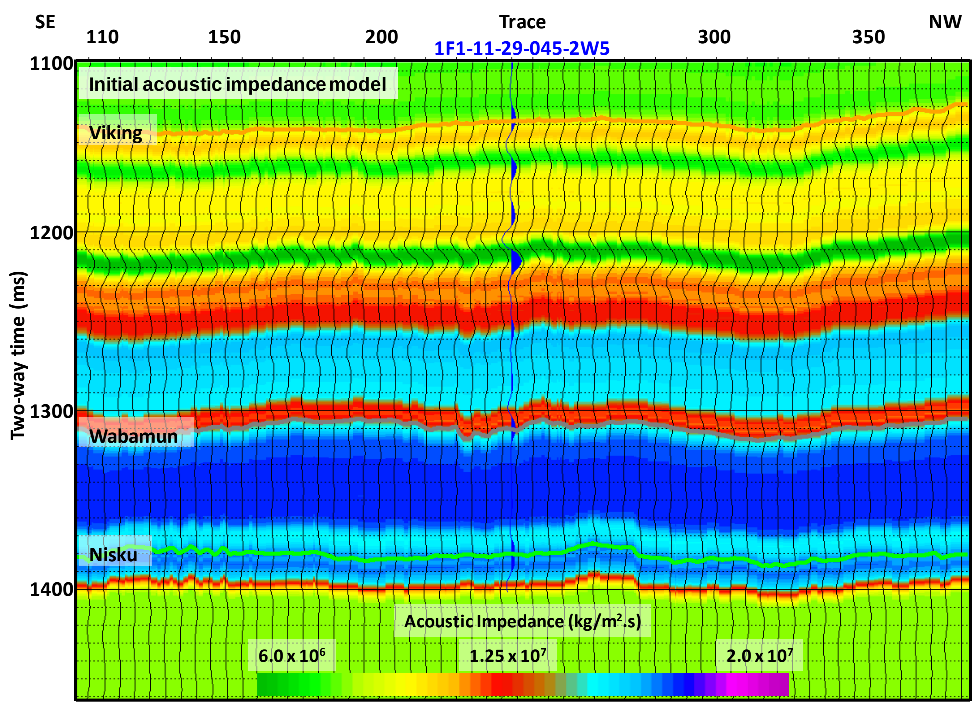

Figure 4-26: The initial acoustic impedance model. The blue curve at the well location is the correlated synthetic seismic trace while the black curves are the actual seismic traces.

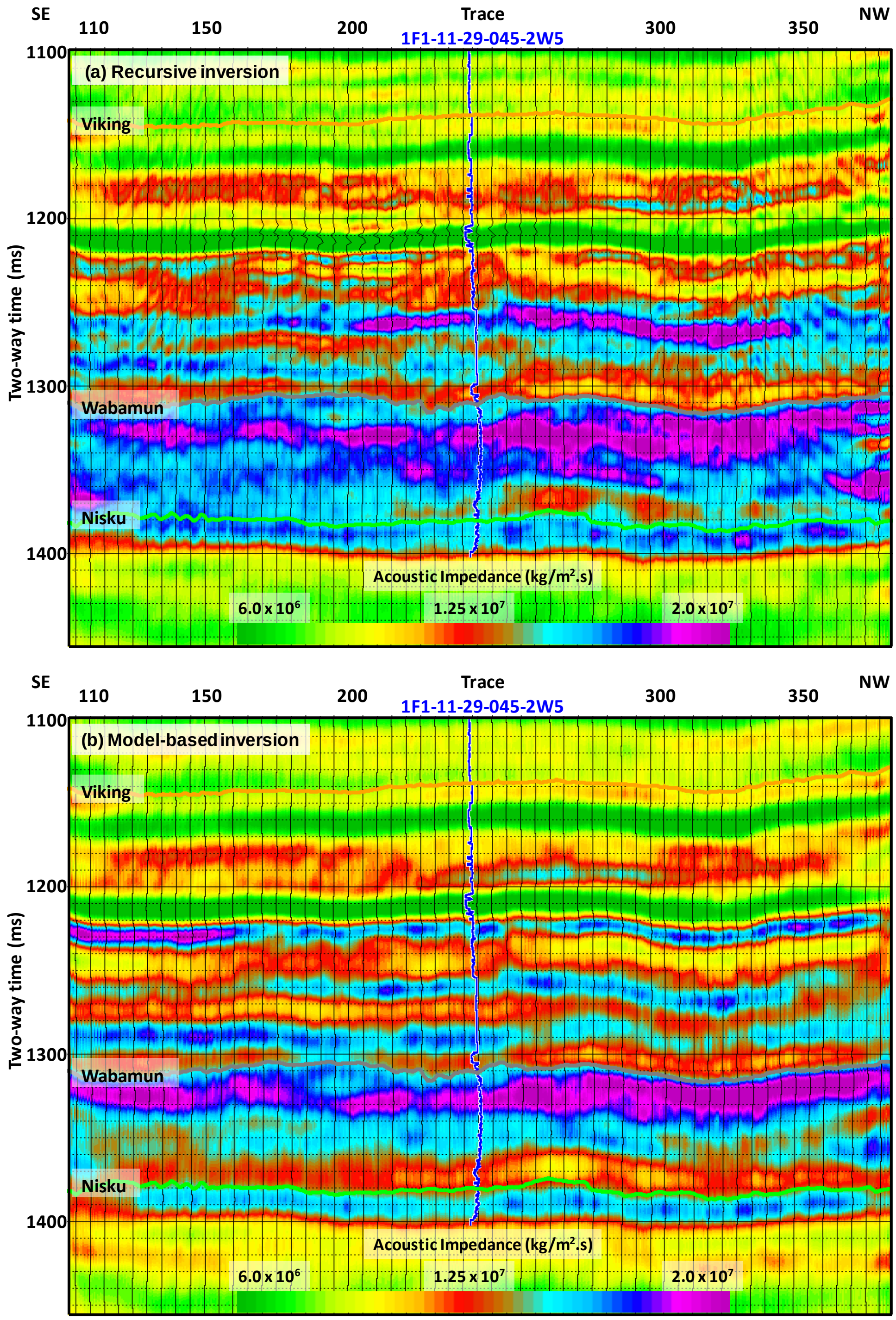

Figure 4-27: Estimated acoustic impedance along the 2-D seismic line near the water source well (Figure 4-24) using (a) recursive and (b) model-based inversion schemes. The inserted blue curve at the well location represents the computed acoustic impedance from the sonic and density logs. The black curves represent the acoustic impedance from the recursive inversion whereas in the model-based inversion they represent the misfit error.

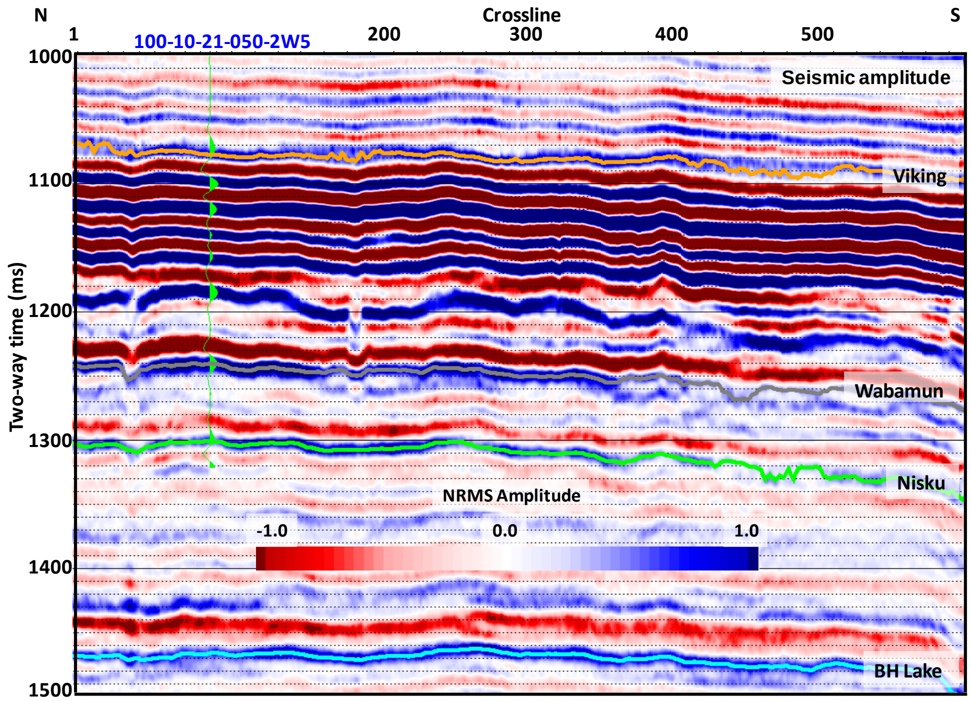

Figure 4-28: In-line extracted from the reference 3-D seismic volume (Figure 4-24). The green curve at the well location is the correlated synthetic seismic trace. The correlation coefficient with the actual seismic trace is 0.8.

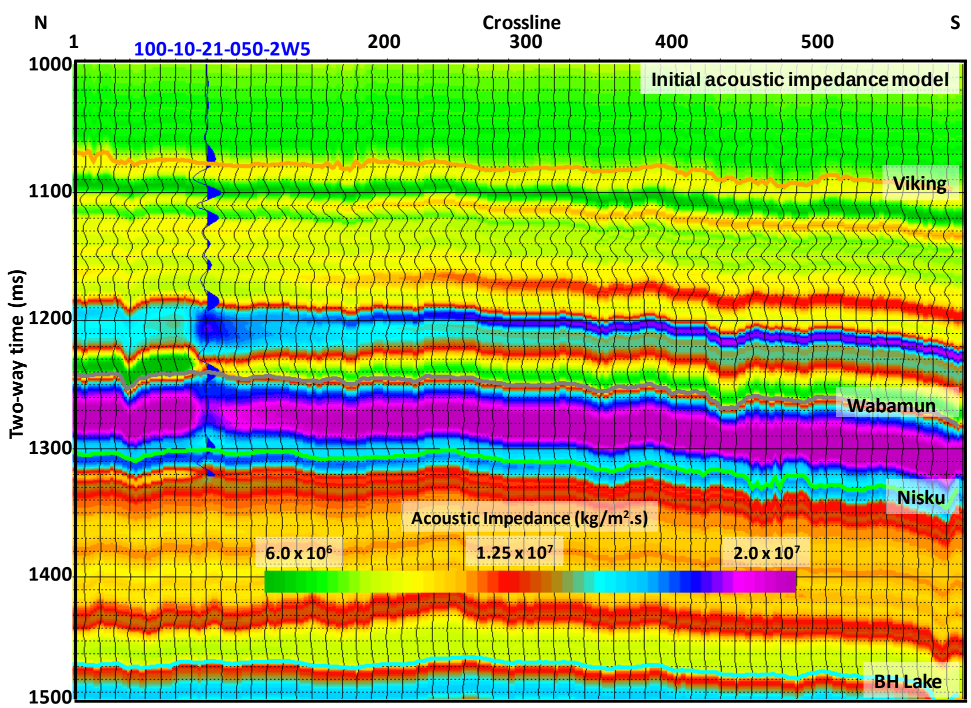

Figure 4-29: The initial acoustic impedance model. The blue curve at the well location is the correlated synthetic seismic trace while the black curves are the actual seismic traces.

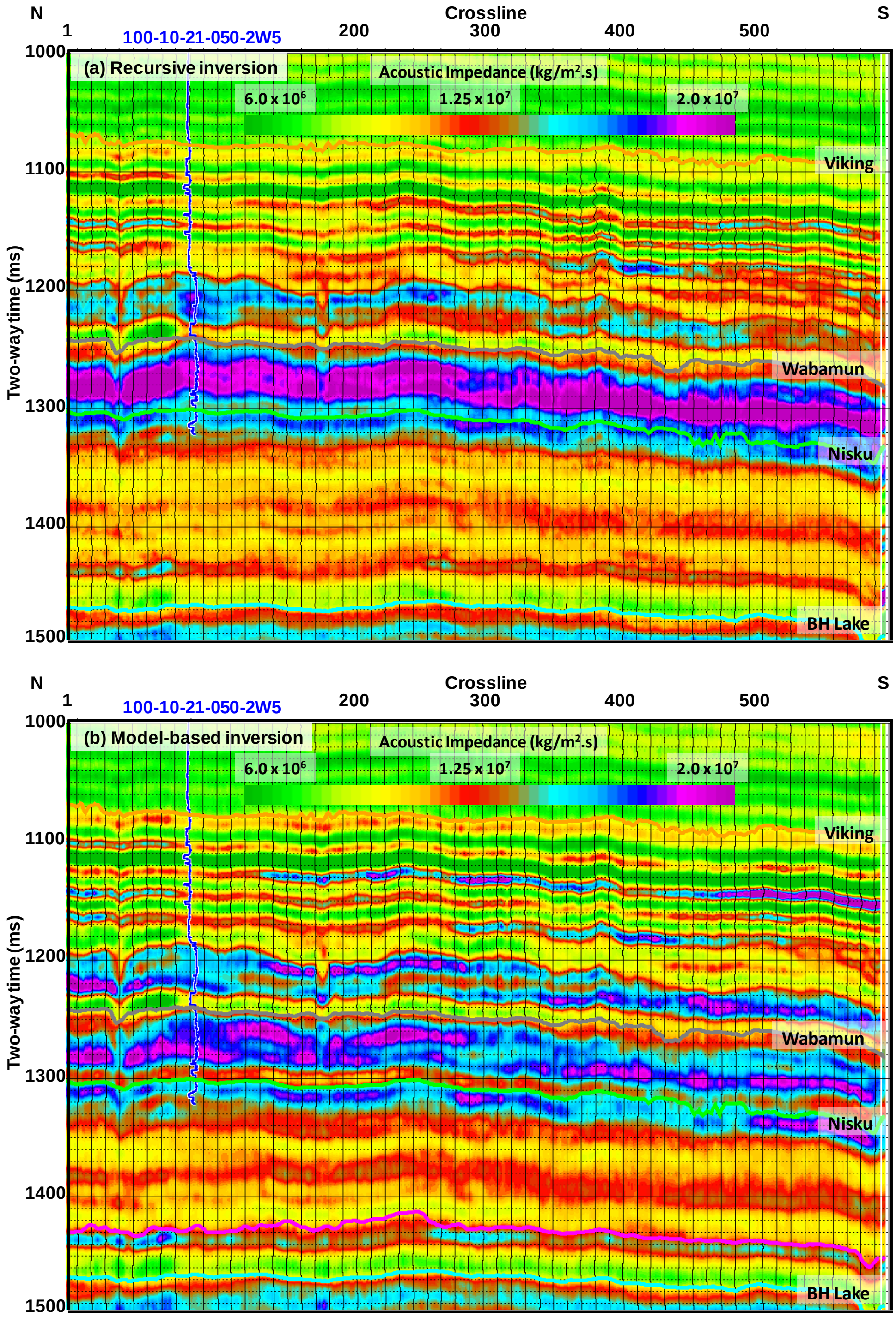

Figure 4-30: Estimated acoustic impedance corresponding to the in-line in Figure 4-28 and Figure 4-29 using (a) recursive and (b) model-based inversion methods. The inserted blue curve at the well location represents the computed acoustic impedance from the sonic and density logs. The black curves refer to the acoustic impedance from the recursive inversion whereas in the model-based inversion they represent the misfit error.

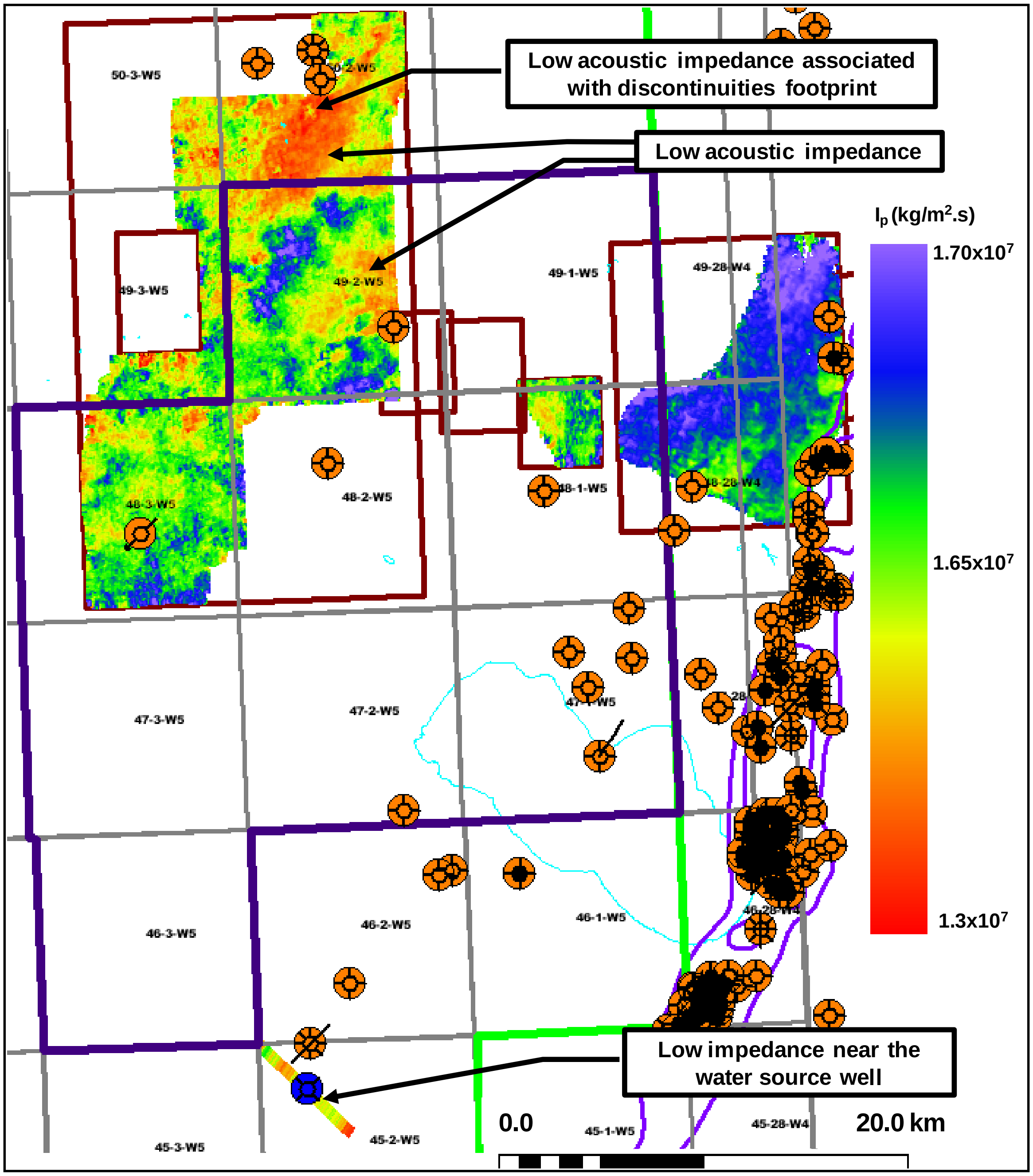

Figure 4-31: Estimated acoustic impedance (I_p) map of the Nisku Formation using recursive inversion. Due to lack of well control, the inversion was performed only on selected 3-D datasets. The relative position to the large study area is shown by the dashed rectangle in the base map in Figure 4-9.

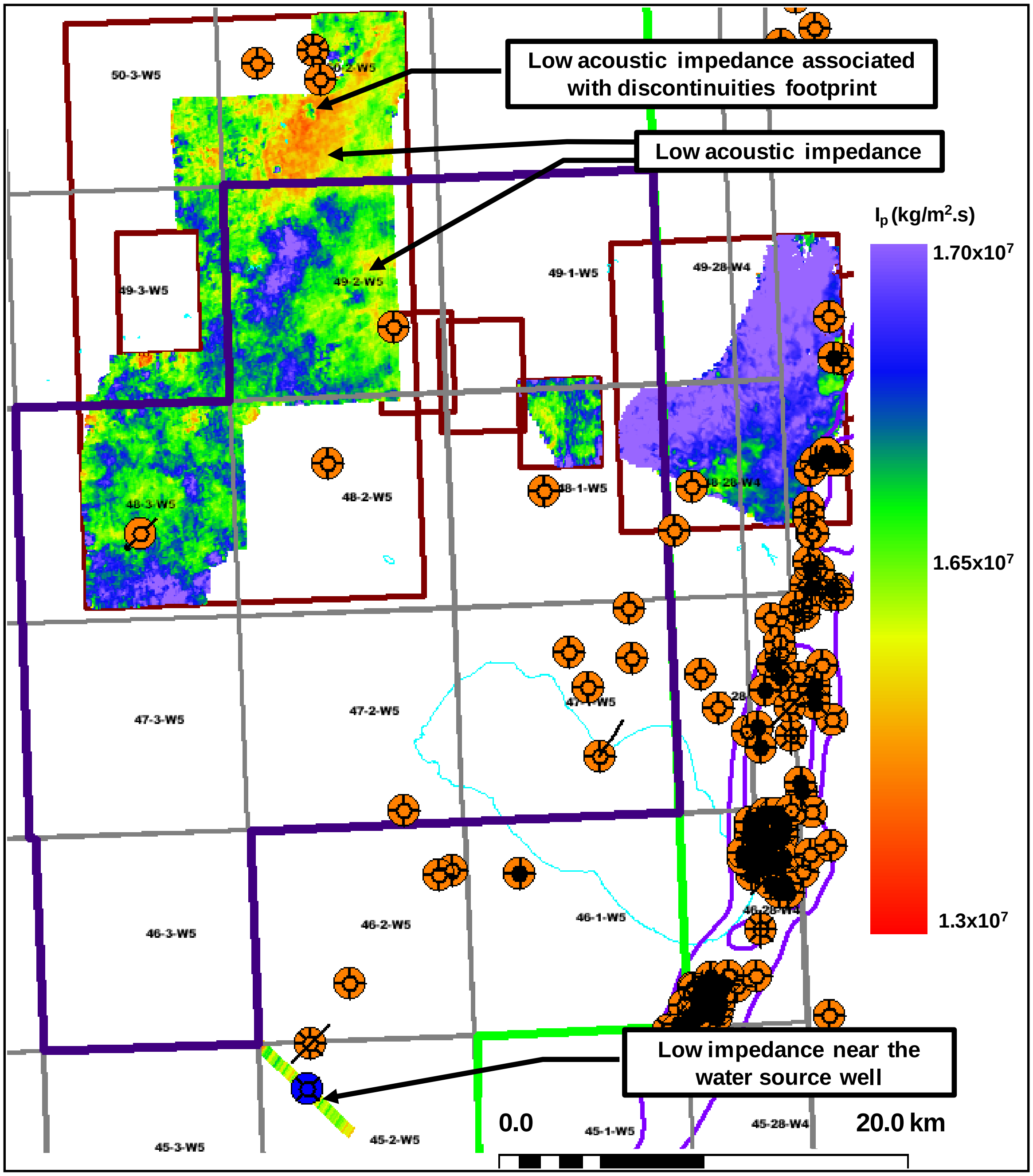

Figure 4-32: Estimated acoustic impedance (I_p) map of the Nisku Formation using model-based inversion. Due to lack of well control, the inversion was not performed on the entire dataset. The relative position to the large study area is shown by the dashed rectangle in the base map in Figure 4-9.

4.6.5 Bulk Porosity

Using the compressional (P) wavespeed derived from acoustic impedance inversion, the bulk porosity of the Nisku Formation was estimated by invoking Wyllie et al. (1956) time-average equation, which relates the P-wave speed and the bulk porosity through the following:

$$\frac{1}{\alpha_{\text{bulk}}} = \frac{1-\phi}{\alpha_{\text{matrix}}} + \frac{\phi}{\alpha_{\text{fluid}}} \tag{4.1}$$

where ϕ is the bulk porosity (dimensionless), α_{matrix} is P-wave speed of the mineral comprising the Nisku matrix (assumed to be 6800 m/s), α_{fluid} is the P-wave speed of the Nisku pore-filling fluid (i.e. $\alpha_{\text{fluid}} = \alpha_{\text{brine}} = 1600$ m/s), and α_{bulk} is the Nisku bulk P-wave speed (m/s) derived from the band-limited acoustic impedance inversion. Re-arranging Equation (4.1) and solving for bulk porosity (ϕ):

$$\phi = \frac{\alpha_{\text{fluid}}\left[\alpha_{\text{matrix}} - \alpha_{\text{bulk}}\right]}{\alpha_{\text{bulk}}\left[\alpha_{\text{matrix}} - \alpha_{\text{fluid}}\right]} \tag{4.2}$$

The resultant pseudo-porosity map in Figure 4-33 correlates well with the low impedance zones in Figure 4-31 and Figure 4-32 which is expected since the bulk speed (α_{bulk}) used in estimating the porosity is derived from the acoustic impedance itself. Although Wyllie et al. (1956) time-average equation assumes clean consolidated formations with uniformly distributed pores (Sherriff, 1991), the estimated porosity values seem to fall within the expected range based on wireline data and core analysis. In fact, the results obtained here agrees well with the bulk porosity (Figure 4-34 (a)) estimated by Eisinger and Jensen (2009) from sonic logs in the study area using the same time-average equation and the rock matrix and formation water parameters (i.e. α_{matrix} and α_{brine}). It, also, shows a good agreement with the porosity values they have, independently, estimated from resistivity logs (Figure 4-34 (b)) in the area by the means of Archie's law (Archie, 1942):

$$\phi^{-m} = \left(\frac{\rho_{\text{rock}}}{\rho_{\text{water}}}\right) \tag{4.3}$$

where ϕ is the formation porosity, ρ_{rock} and ρ_{water} are the resistivity of the formation rock and formation water in ohm-m, respectively, and m is the cementation factor. In their calculation, they assumed a cementation factor of 2 and that the Nisku Formation is 100% brine-saturated. The resistivity values were estimated from deep-induction resistivity logs in the study area to minimize the effect of the invaded zone. In general, there seems to be a fair correlation between some of the high porosity zones in Figure 4-33 and Figure 4-34 and the high permeability zones shown in Figure 4-35 outlined by the dashed ellipse.

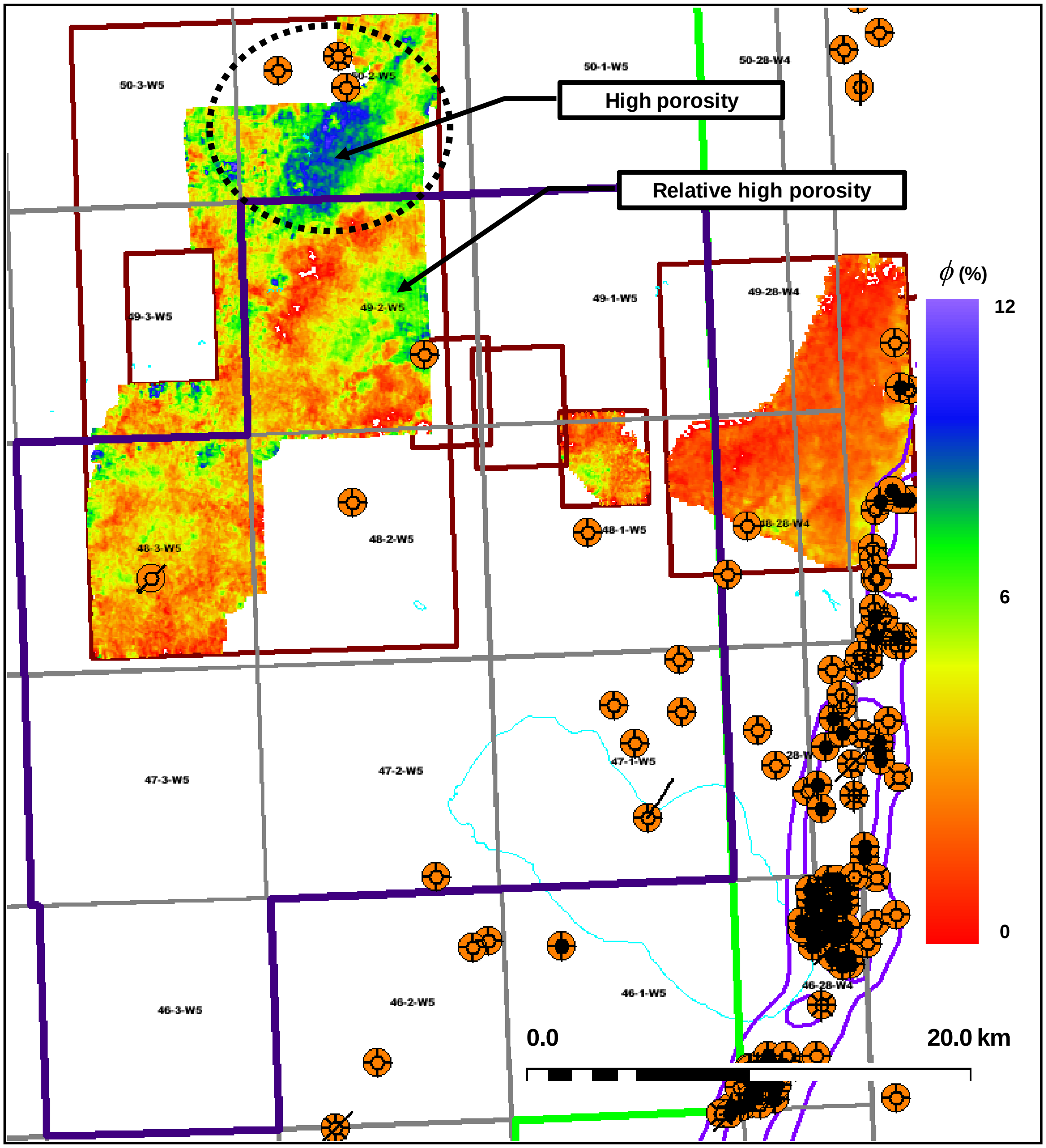

Figure 4-33: Estimated bulk porosity of the Nisku event using Wyllie et al. (1956) time-average equation with bulk speed derived from the acoustic impedance inversion. The relative position to the large study area is shown by the dashed rectangle in the base map in Figure 4-9. The dashed ellipse outlines a zone of high porosity and permeability shown in the next two figures (Figure 4-34 and Figure 4-35).

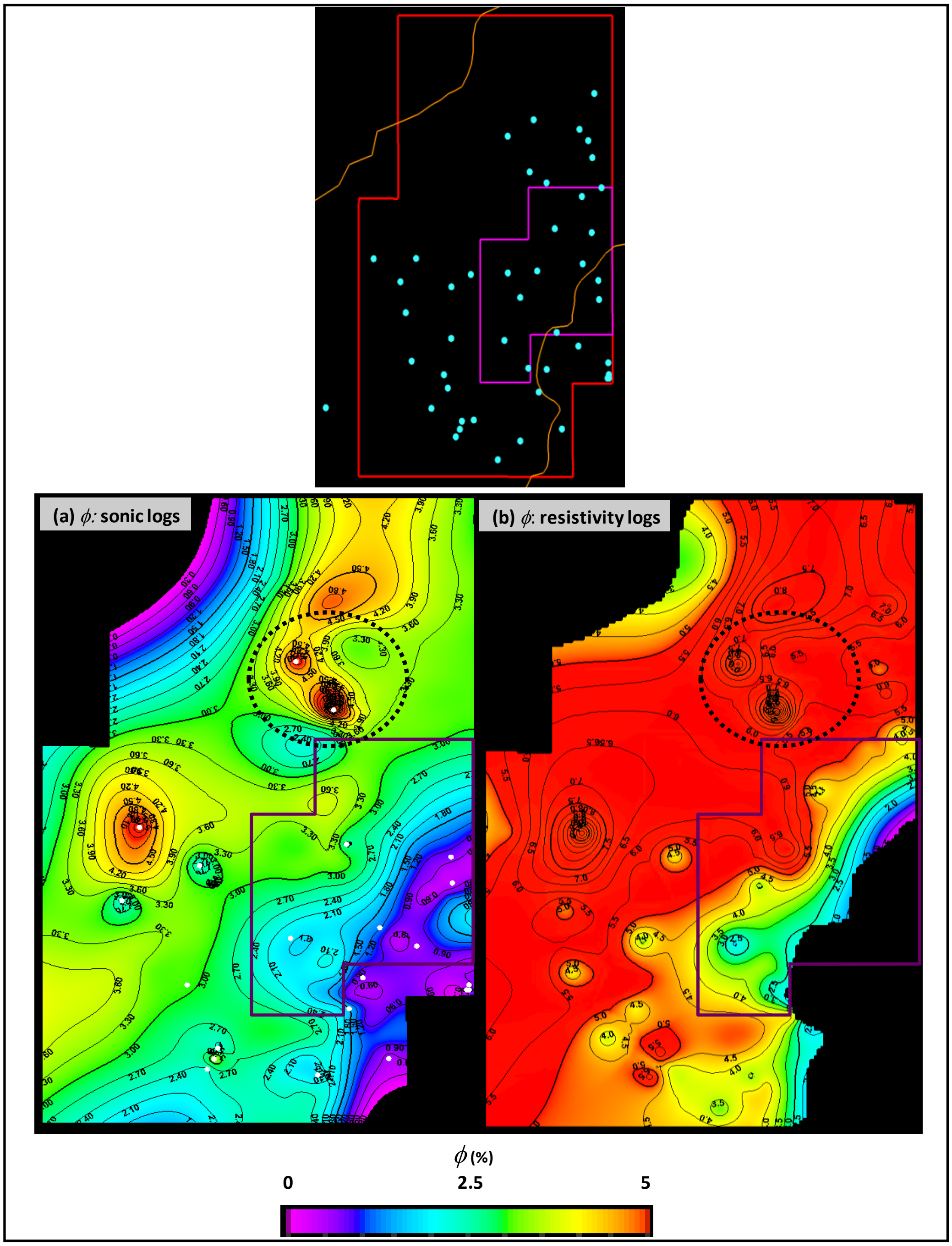

Figure 4-34: Bulk porosity of the Nisku Formation as estimated from (a) sonic logs, and (b) resistivity logs. The map on top shows the distribution of deep resistivity and conductivity logs in the WASP regional-scale (red polygon) and local-scale (violet polygon) study areas. The dashed ellipse outlines a zone of high porosity and permeability shown in the previous and next figures (Figure 4-33 and Figure 4-35). After Eisinger and Jensen (2009).

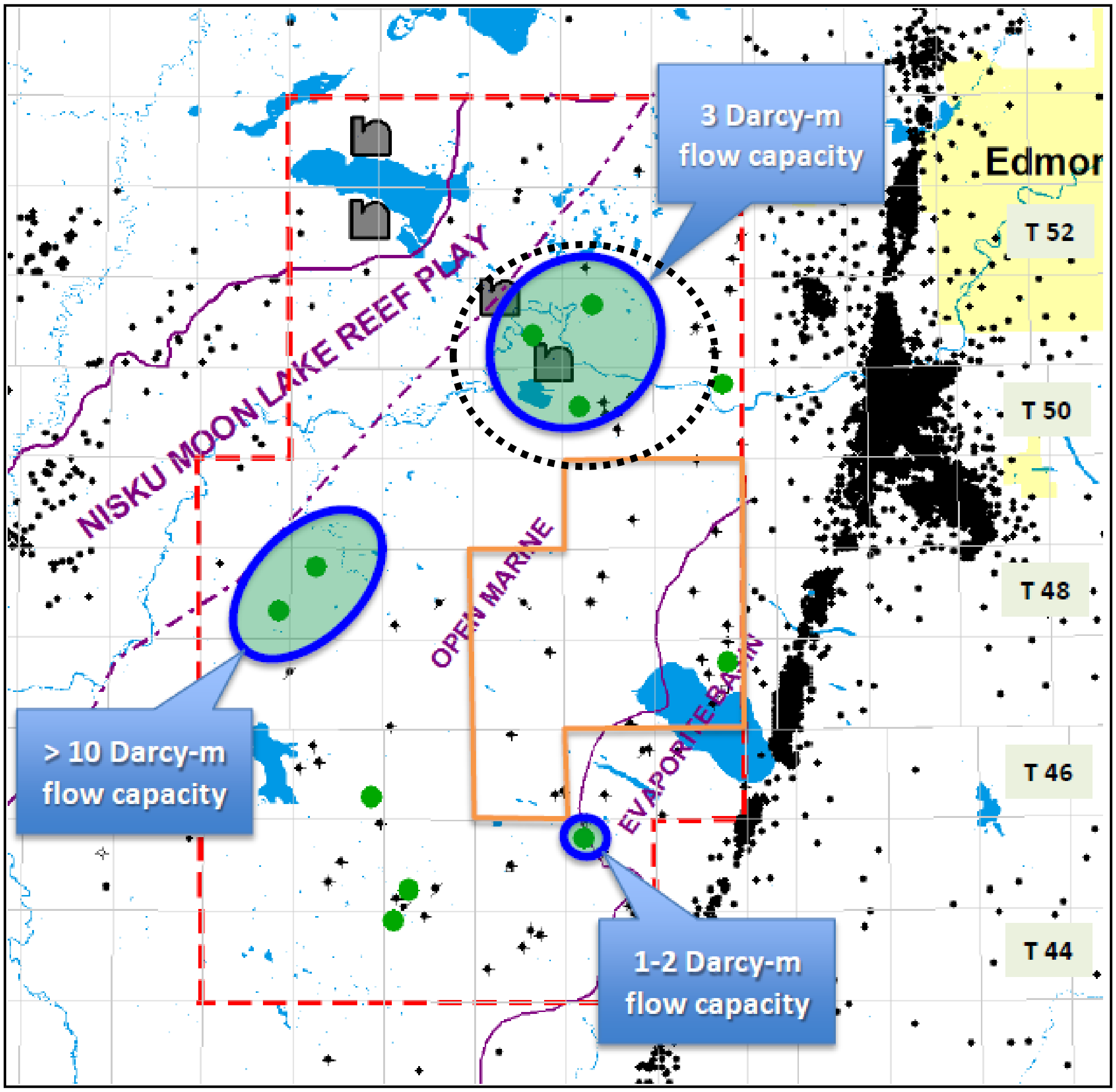

Figure 4-35: Potential high permeability zones of the Nisku Formation in the WASP study area. The dashed polygon outlines the boundary of the regional-scale study area wheras the orange polygon outlines the local-scale study area. The dashed ellipse outlines a zone of high porosity and permeability shown in the previous figures (Figure 4-33 and Figure 4-34). After Eisinger and Jensen (2009).

4.7 Discussion

Although data *calibration* and *normalization* were successful in reconciling the differences between the vintage data, only 3-D data were reliable when it came to the detailed interpretation. The 2-D data, on the other hand, was useful in delineating the long-wavelength structure of the Nisku Formation (Figure 4-5, Figure 4-6, Figure 4-7 and Figure 4-8). The interpreted time structure map of the Nisku Formation (Figure 4-10) is rather smooth and consistent with the regional NE-SW dip and is almost featureless except for a few subtle anomalies induced by the discontinuities in the overlying strata. The NRMS amplitude (Figure 4-12 and Figure 4-19) and acoustic impedance (Figure 4-31 and Figure 4-32) maps, on the other hand, show strong variations across the local-scale study area. These anomalies are interpreted to be either discontinuity induced or lithology or porosity driven. Furthermore, by correlating these attributes with the edge detection attribute (Figure 4-21 and Figure 4-22), it is feasible to isolate those anomalies associated with discontinuity footprints due to dissolution and karsting in the overlying Wabamun Formation and Pre-Cretaceous unconformity from other anomalies.

Likewise, the amplitude thickness of the peak (ATP) revealed an interesting Nisku pattern that is not captured by the other attributes (Figure 4-20). Unfortunately, there are no wells that penetrate the Nisku within that feature but, in general, variations in the ATP are interpreted to be driven by changes in lithology. Furthermore, by examining the ATP attribute in conjunction with the other seismic attributes, a favourable zone of the Nisku Formation was identified in the north of the local-scale study area (ellipse in Figure 4-31 and Figure 4-32). This zone, also, seems to have relatively high bulk porosity (Figure 4-33). Moreover, the estimated bulk porosity derived from seismic inversion correlates fairly well with that estimated independently from sonic and resistivity logs (Figure 4-34). In addition, core analysis indicates that this zone of the Nisku Formation exhibits high permeability (Figure 4-35).

Throughout this chapter, it is presumed that the seismic response of the Nisku event is primarily driven by lithology or porosity variations within the Nisku Formation. The presumption that these, rather than tuning effects are responsible for the amplitude and acoustic impedance variations were tested[51] against a good quality brine-bearing zone of the Nisku Formation near the southern corner of the local-scale study area, which exhibits excellent reservoir characteristics. The seismic data around this water source well show significant variations in the NRMS amplitude but data from neighbouring wells suggest only a negligible variation in the Nisku Formation thickness. However, differentiation between acoustic impedance changes caused by enhanced porosity and those associated with a possible increase in shale content based on the seismic data alone remains tenuous.

In conclusion, the seismic characterization of the Nisku Formation in the WASP study area has revealed two major groups of anomalies: one is associated with geological discontinuity footprints, primarily induced by dissolution in the overlying Wabamun Formation, while the other is interpreted to be a result of lithological or porosity changes within the Nisku Formation. Even though discontinuity footprints do not necessarily reflect physical discontinuities within the Nisku Formation itself, they should be taken into consideration in any future CO_2 sequestration program in the area. Conversely, a favourable zone of the Nisku Formation has been identified in the seismic data that correlates with a favourable zone based on the analysis of independent information by other WASP team members (Eisinger and Jensen, 2009). Such a locality could be adopted for any prospective CO_2 sequestration program in the WASP study area.

4.8 Summary

- In this chapter, the seismic site characterization for the Wabamun Area CO_2 Sequestration Project (WASP) was undertaken.
- The initial step was the calibration and normalization of the legacy seismic data in the WASP study area.
- Following that, regional 2-D lines were used for indentifying long-wavelength Nisku character.

---

[51] The modeling and its results will be presented and discussed in the next chapter (Chapter 5) but, for now, only the findings are invoked.

- Conversely, high resolution 3-D volumes were exploited in the detailed mapping and quantitative interpretation.
- In addition to time, depth and NRMS amplitude maps, several seismic attributes were invoked: acoustic impedance, amplitude thickness of the peak and edge detection.
- Two main categories of anomalies were revealed through the seismic characterization of the Nisku Formation.
- The first group consists of anomalies interpreted to be footprints of geological discontinuities induced by dissolution in the overlying strata, primarily in the Wabamun Formation. No signs of faulting were observed in the regional and local-scale study areas.
- Even though there is no evidence to indicate that the integrity of the Nisku Formation has been compromised, such geologic discontinuities should be taken into consideration if CO_2 were to be injected into the Nisku Formation.
- The second group of anomalies outlines contrasts in NRMS amplitude and acoustic impedance caused by lateral changes in lithology and/or porosity of the Nisku Formation.
- The analysis has revealed a favourable low impedance, potentially high porosity, zone of the Nisku Formation just north of the focus area that is interpreted to be favourable as a potential injection site.
- Finally, the high-porosity derived from seismic inversion correlates fairly well with a high porosity and permeability zone derived, independently, from resistivity logs and core analysis, respectively.

CHAPTER 5: WASP SEISMIC SITE CHARACTERIZATION II - NUMERICAL MODELLING

5.1 Introduction

In the previous chapter (Chapter 4), seismic characterization of the Nisku Formation was undertaken using post-stack legacy P-wave data in the Wabamun Area CO_2 Sequestration Project (WASP) study area. In arriving at some of the conclusions, only some of the findings of the numerical modelling regarding the behaviour of the seismic response of the Nisku Formation were invoked. In this chapter, a detailed account of the numerical modelling is presented with two main objectives:

1. Revisit and strengthen some of the interpretation in Chapter 4, and
2. Investigate the feasibility of time-lapse surface seismic for delineating a hypothetical CO_2 plume using fluid substitution and offset-dependent seismic reflectivity modelling.

5.2 WASP Interpretation Revisited

5.2.1 Approach

In Chapter 4, considerable emphasis was placed, directly and indirectly[52], on the seismic amplitude in characterizing the Nisku Formation. Therefore, a better understanding of how it behaves in the WASP local-scale study area is crucial in delineating the Nisku Formation seismic character and, eventually, making the interpretation results more conclusive. In the present context, the seismic amplitude response of the Nisku event is proportional to the following entities:

$$\text{Seismic Amplitude} \ \alpha \ \mathrm{F}\left(\text{thickness}\right)+\mathrm{F}\left(\text{impedance}\right)+\mathrm{F}\left(\text{wavelet}\right)+\mathrm{F}(\text{noise}) \quad (9.1)$$

where F(thickness) represents the change in the Nisku Formation thickness, F(impedance) represents the change in its acoustic impedance, F(wavelet) is the seismic wavelet, F(noise) is the noise present in the data, and F denotes some general form of functional relationship. Prior to undertaking the modelling, these entities were examined

---

[52] Indirectly in the sense that seismic attributes, such acoustic impedance, are essentially derived from the seismic amplitude.

to understand the role each one plays in the observed seismic amplitude. Furthermore, taking into consideration the data calibration and normalization in addition to the constraint imposed by the well control in the study area, the following were observed:

1. The Nisku Formation thickness within and near the focus area varies between 40 and 80 m and, thus, thickness should be taking into consideration as a primary element in the modelling to investigate the tuning effect.
2. The Nisku acoustic impedance (I_p) is another critical parameter that has to be included in the modelling. However, by examining the well control, it was found that the Nisku event impedance is mainly driven by variations in the average interval P-wave speed rather than density:

$$\Delta I_p = \Delta\alpha \times \Delta\rho \approx \Delta\alpha \tag{9.2}$$

where α is the P-wave speed in m/s and ρ is the density in kg/m^3. The average interval P-wave speed (α_{avg}) of the Nisku Formation was found to vary by more than 15% whereas the average density (ρ_{avg}) was found to vary by less than 4% only. Thus, variation in density was considered to be insignificant.

3. The waveform is assumed to be stationary; this follows from the data calibration.
4. The noise is assumed to be random; therefore it contributes insignificantly to the observed amplitude in the post-stack seismic data.

Based on these observations and after testing some sensitivity analyses, it was found that thickness and average interval P-wave speed are the primary parameters affecting the seismic response of the Nisku Formation. Subsequently, normal-incidence synthetic seismograms were generated by convolving (Section 3.5.5) the reflectivity series from well 100-10-05-52-2W5 (Figure 5-1) with a 30 Hz Ricker[53] wavelet (Figure 5-2) to further understand the effect of these two parameters on the Nisku event amplitude and some of the attributes derived. Note that the discontinuity footprint effect

[53] Ricker wavelet is a zero-phase wavelet obtained by taking the second derivative of the Gaussian function (Sheriff, 2002).

on the Nisku event amplitude will not be investigated thoroughly but it will be briefly probed later in this chapter as part of the exploding reflector finite-difference (ERFD) modelling in Section 5.3.3.2.

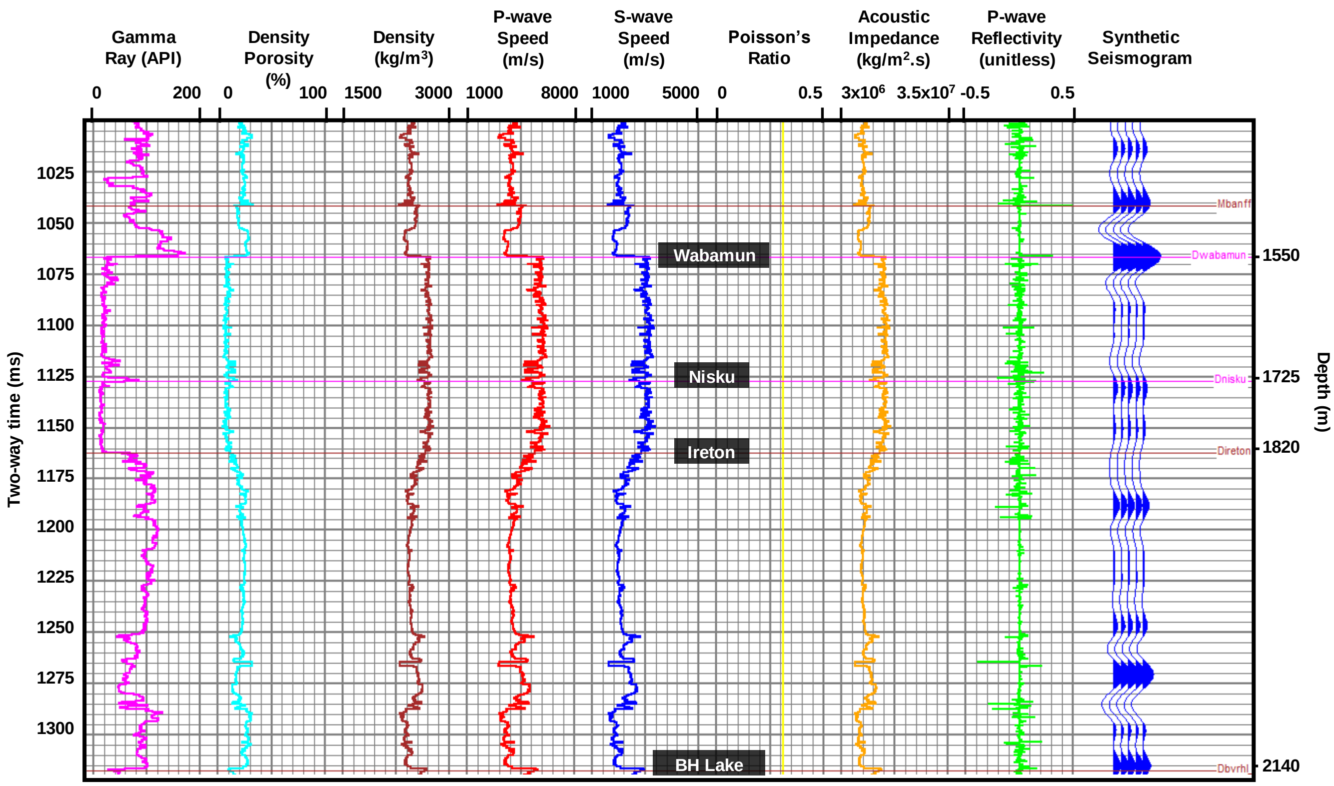

Figure 5-1: Display of the various log types of well 100-10-05-52-2W5. The reflectivity series was exploited alongside the 30 Hz Ricker wavelet in Figure 5-2 in generating the synthetic seismogram in Figure 3-1. The same wavelet was used in generating the synthetic seismogram shown here in blue (right-most panel). See, also, the stratigraphic model in Figure 2-9.

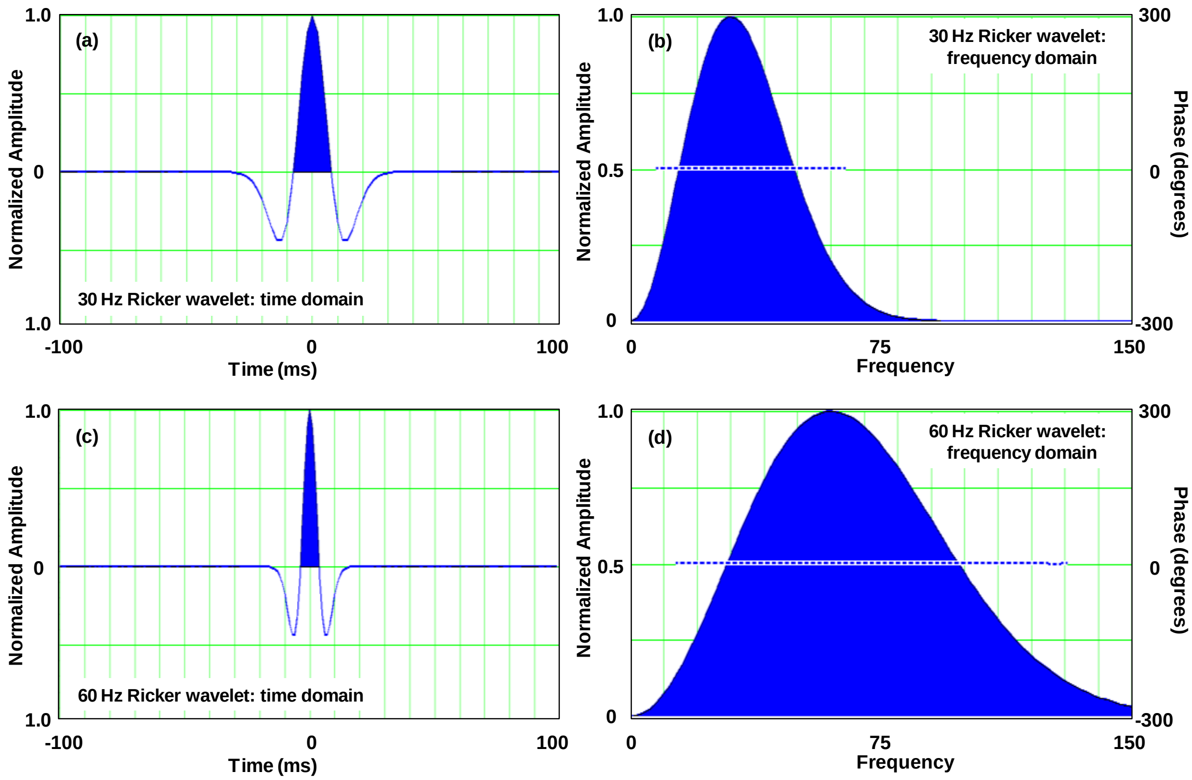

Figure 5-2: (a) time and (b) frequency-domain display of 30 Hz Ricker wavelet; (c) time and (d) frequency-domain display of 60 Hz Ricker wavelet. The 30 Hz Ricker wavelet was used in conjunction with the reflectivity series in Figure 5-1 to generate the synthetic seismogram in Figure 3-1. The 60 Hz Ricker wavelet is invoked in Section 5.3.3.1 and is shown here - in advance - for convenience and comparison with the 30 Hz wavelet. Dashed horizontal blue line in (b) and (d) depicts the wavelet phase.

5.2.2 Results

Figure 3-1 is a sequential display of synthetic seismograms illustrating the effect of thickness and average interval P-wave speed on the traveltime and amplitude of the Nisku and the underlying Ireton event. In order to better discern the individual effects, the time and amplitude associated with these two events were picked using the peak amplitude (~ 1130 ms) for the Nisku event and the underlying trough (~ 1170 ms) for the Ireton event. For the Nisku event, the modelling results (Figure 5-4) suggest that the amplitude variations (Figure 5-5) in the study area, excluding those associated with discontinuity footprints, are most likely due to variability in the average acoustic impedance (mainly average interval P-wave speed) rather than thickness. For instance, an increase in the average interval wavespeed (along the vertical axis in Figure 5-4 (b)) causes over 60% relative change in the Nisku event amplitude whereas variation in the thickness (along the horizontal axis in Figure 5-4 (b)) corresponds to about an 8% relative change in amplitude. The highest amplitude effect is observed for a high average interval P-wave speed regardless of the thickness (Figure 5-5). The results also suggest that there would be a small time shift at which the Nisku event is predicted.

Figure 5-6 illustrates the footprint effect on the Ireton event as a result of changes in the thickness and average interval P-wave speed of the Nisku Formation. As expected, the maximum time delay in the Ireton event time is associated with low average interval Nisku P-wave speed, whereas the highest amplitude change correlates with high average interval Nisku P-wave speed. In all the modelling results, the conclusion is that the highest sensitivity in the seismic amplitude and traveltime is associated with changes in the average interval P-wave speed rather than thickness.

In addition to seismic amplitude, the amplitude thickness of the peak (ATP) of the Nisku event was revisited using the same synthetic seismogram in Figure 3-1. The results suggest that the ATP attribute response is rather complicated and suffers from some non-uniqueness as depicted in Figure 5-7. Nonetheless, the result from the synthetic model seems to indicate that the magnitude of the ATP attribute is, in general, inversely proportional to the average interval P-wave speed. Furthermore, the thickness effect is non-unique except over the expected Nisku Formation thickness range (~ 40-80 m) where there seems to be a binary effect where the separation occurring around the average interval P-wave speed corresponding to the dominant wavelength Figure 5-7. The fact that a prominent trend was observed in the ATP attribute map (Figure 4-20) over the expected range of the Nisku Formation average interval P-wave speeds and thicknesses indicate that those anomalies are most likely impedance-derived, perhaps due to change in lithology as discussed in Section 4.6.2. It is difficult to extract any useful information at thicknesses smaller or larger than the expected Nisku thickness range.

Finally, in order to relate variations in the acoustic impedance (Figure 4-31 and Figure 4-32) to the two primary physical parameters of interest, i.e. thickness and average interval P-wave speed, the acoustic impedance model for the synthetic seismogram in Figure 3-1 was reconstructed using the two inversion schemes employed in Chapter 4

(Section 4.6.4), namely recursive inversion (Figure 5-8 (a)) and model-based inversion (Figure 5-8 (b)). As with the amplitude modelling, variations in the average interval P-wave speed seems to be the primary factor influencing the estimated acoustic impedance of the Nisku Formation in Section 4.6.4. Furthermore, the same scaling difference between RI and MBI is, also, observed in the results from synthetic model. However, this should not be of major concern as it is only realistic, in the current context, to interpret the estimated acoustic impedance in terms of relative rather than absolute change due mainly to the sparse and limited data available through well control.

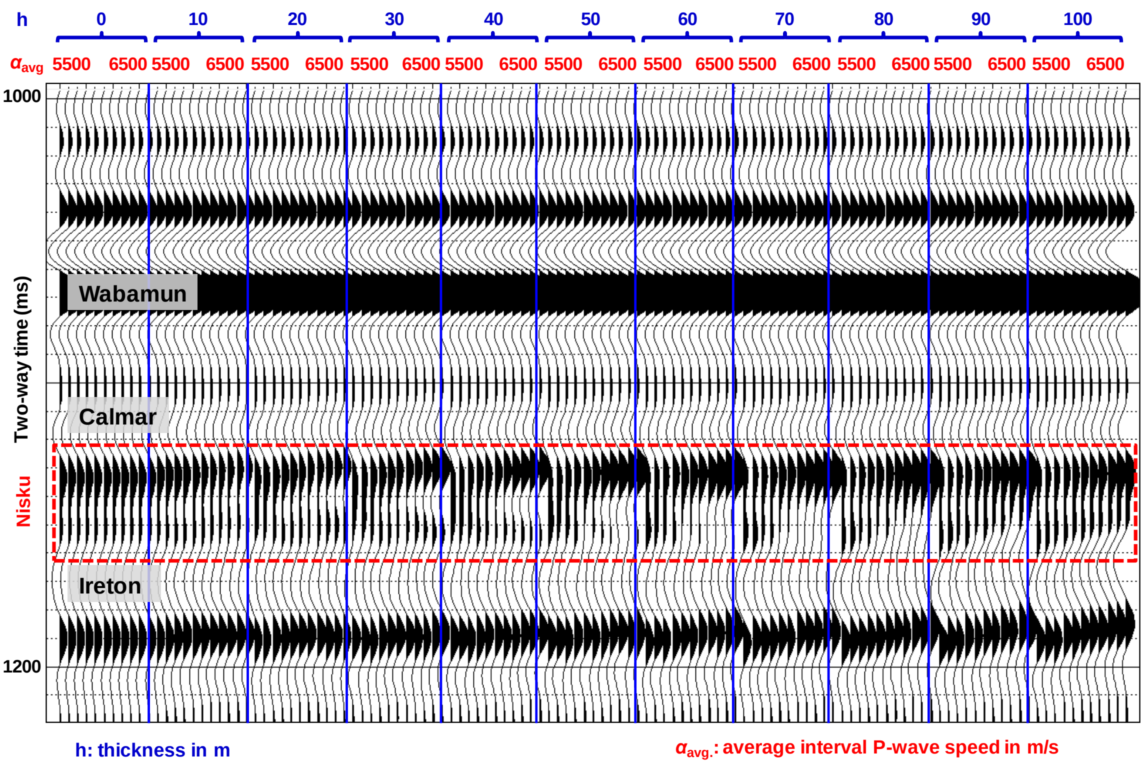

Figure 5-3: Sequential display of the normal incidence synthetic seismogram in which the Nisku event amplitude is modelled as function of thickness and average P-wave speed. The dashed red rectangle encloses the Nisku event whereas its top is identified as the peak at approximately 1130 ms. In each blue bracket (thickness effect), there are 11 traces, each representing the seismic amplitude associated with that thickness and an average Nisku P-wave speed increasing from 5500 m/s to 6500 ms/ at an increment of 100 m/s. The modelling was performed using the convolutional model with a 30 Hz Ricker wavelet and the reflectivity series computed from the logs of well 100-10-05-52-2W5.

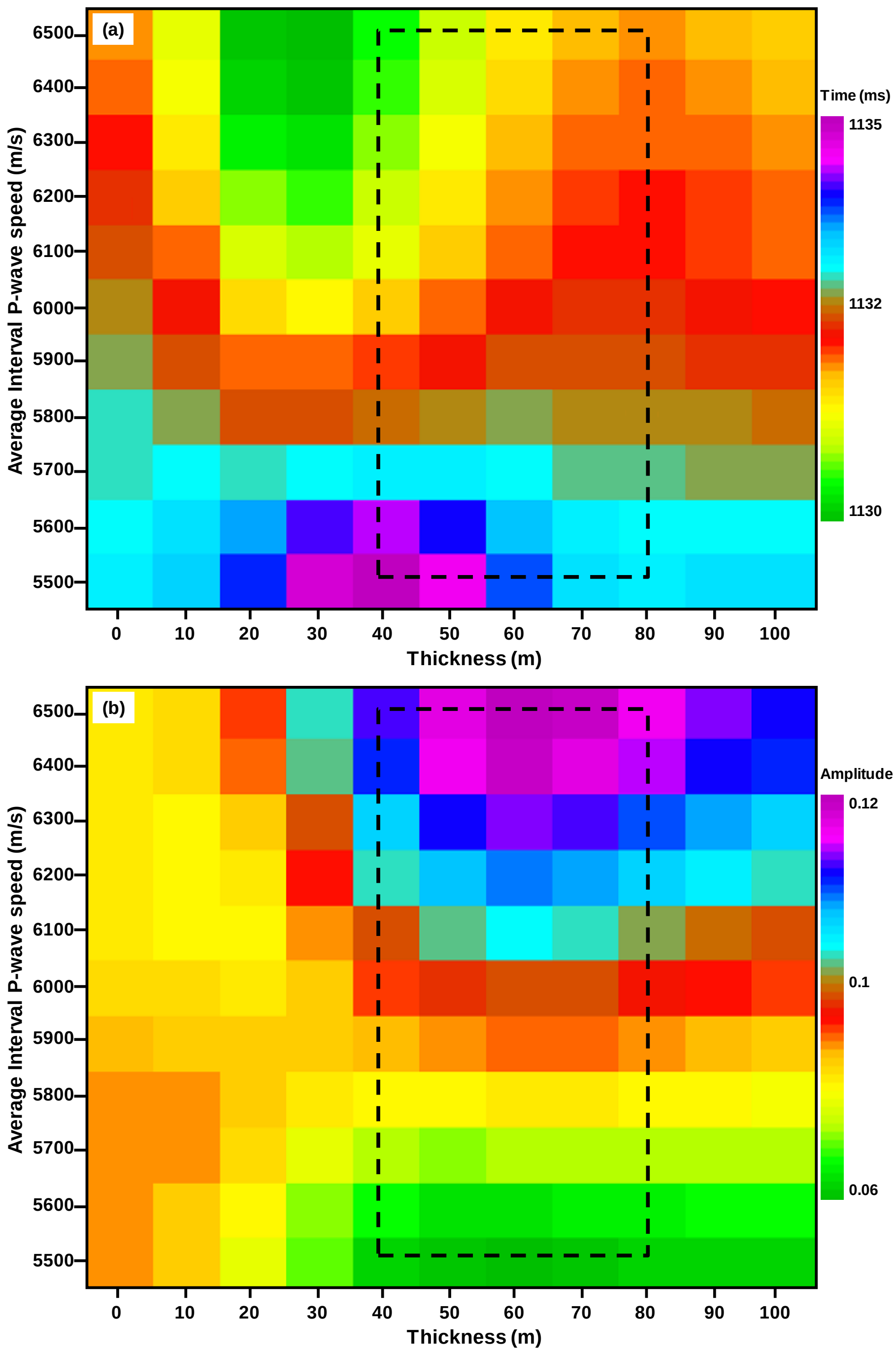

Figure 5-4: Nisku event time (a) and amplitude (b) as a function of thickness and average interval P-wave speed. The maps represent the Nisku amplitude and time horizons that were constructed by picking the peak amplitude corresponding to the Nisku event in Figure 3-1. The black dashed rectangle outlines the observed Nisku thickness and average interval P-wave speed values within the local-scale study area based on well control.

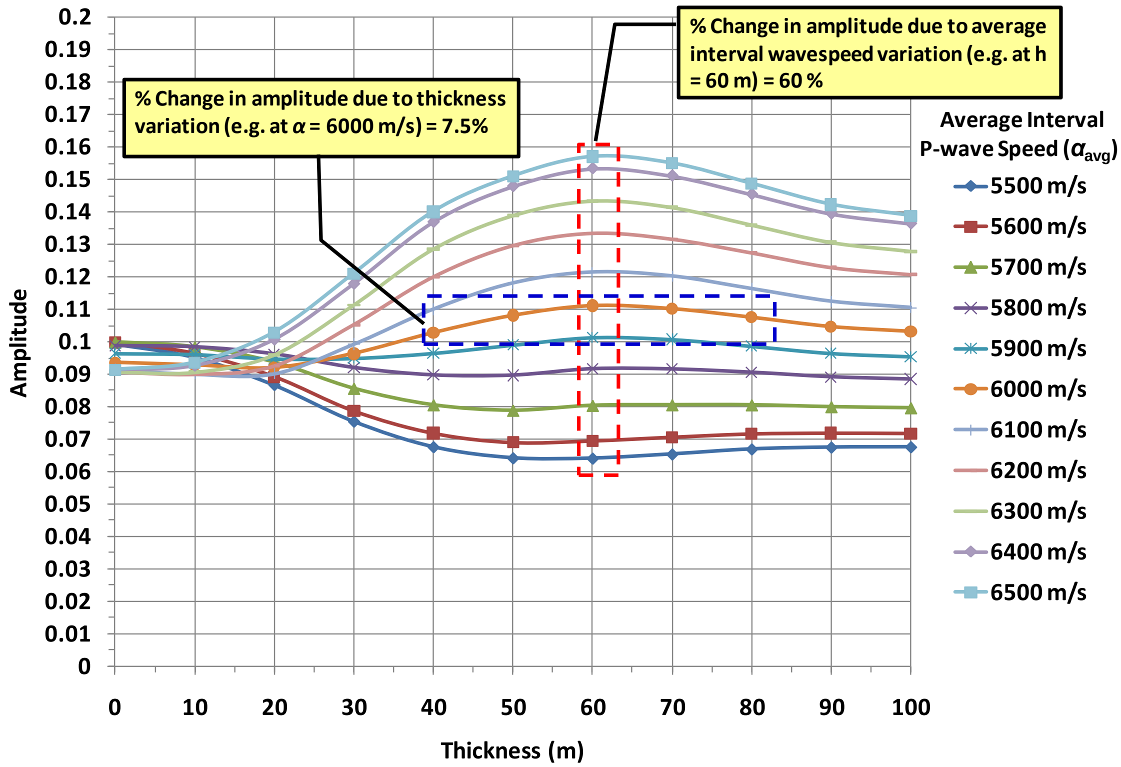

Figure 5-5: Nisku amplitude modelling result in which the difference between the thickness and average interval P-wave speed effect on the Nisku event amplitude is shown.

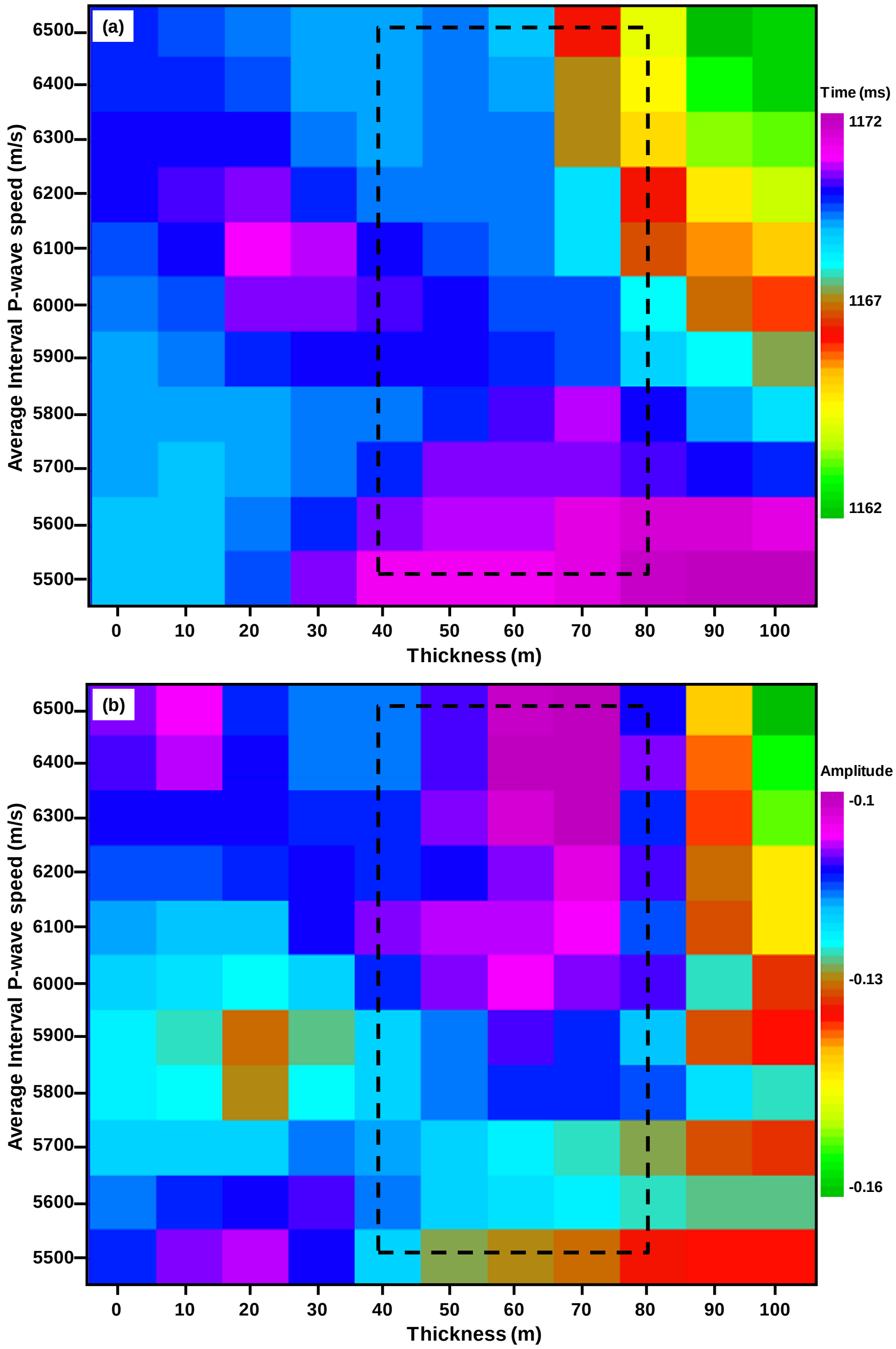

Figure 5-6: Ireton event time (a) and amplitude (b) as a function of the Nisku thickness and average interval P-wave speed. The maps represent the Ireton amplitude and time horizons that resulted from picking the trough amplitude corresponding to the Ireton event in Figure 3-1. The black dashed rectangle outlines the most likely Nisku thickness and average interval P-wave speed values within the local-scale study area based on well control.

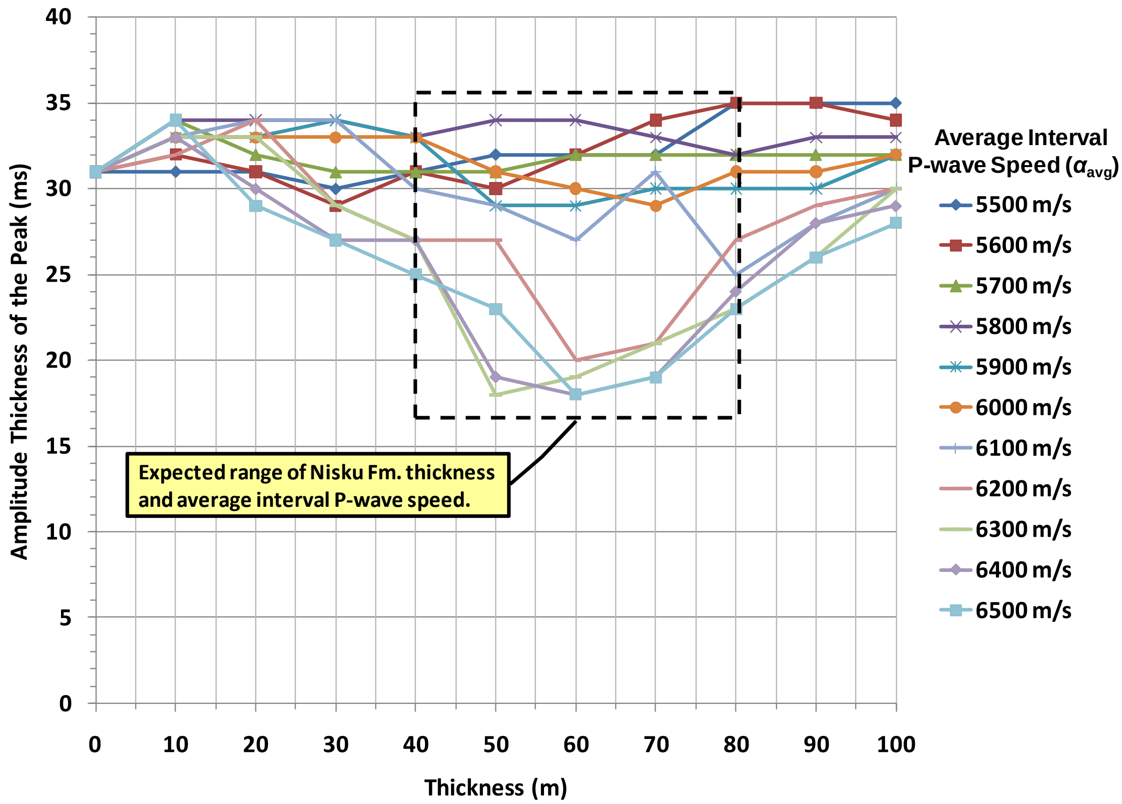

Figure 5-7: Nisku amplitude thickness of the peak (ATP) computed using the synthetic seismogram in Figure 3-1.

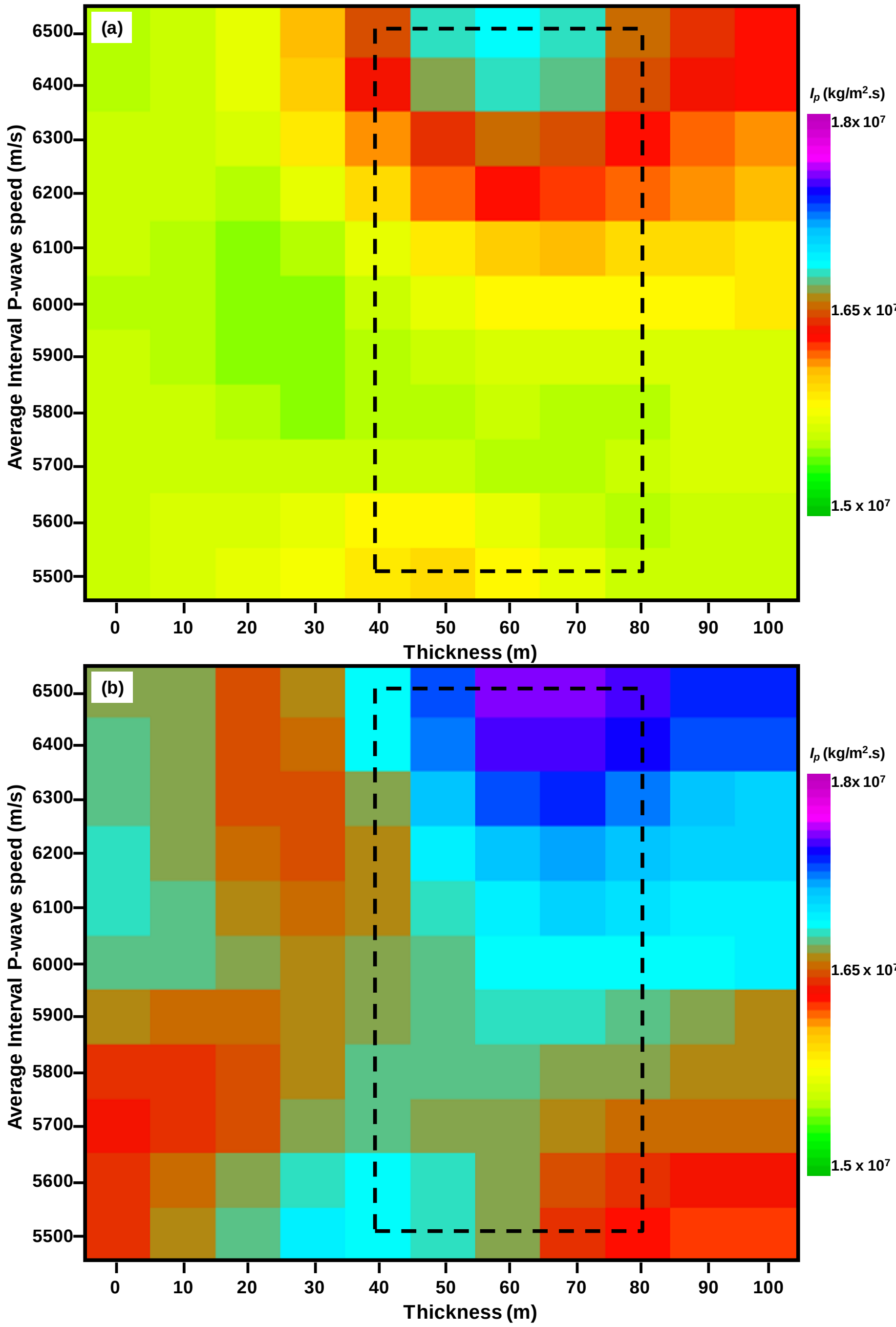

Figure 5-8: Acoustic impedance (I_p) of the synthetic seismogram in Figure 3-1 reconstructed using (a) recursive, and (b) model-based inversion schemes. The black dashed rectangle outlines the most likely Nisku thickness and average interval P-wave speed values within the local-scale study area based on well control.

5.3 Time-lapse Seismic Monitoring Feasibility Analysis

5.3.1 Approach

Figure 4-2 depicts the approach adopted in investigating the feasibility of time-lapse reflection seismology in delineating a CO_2 plume after injection. The individual steps and the results are discussed in more detail in the corresponding sections within Section 5.3. The objective behind the rock physics and fluid substitution modelling is to predict if the CO_2 replacement of in-situ fluid will produce a sufficient contrast in the physical properties of the aquifer that could be detected and delineated by time-lapse surface seismic surveys.

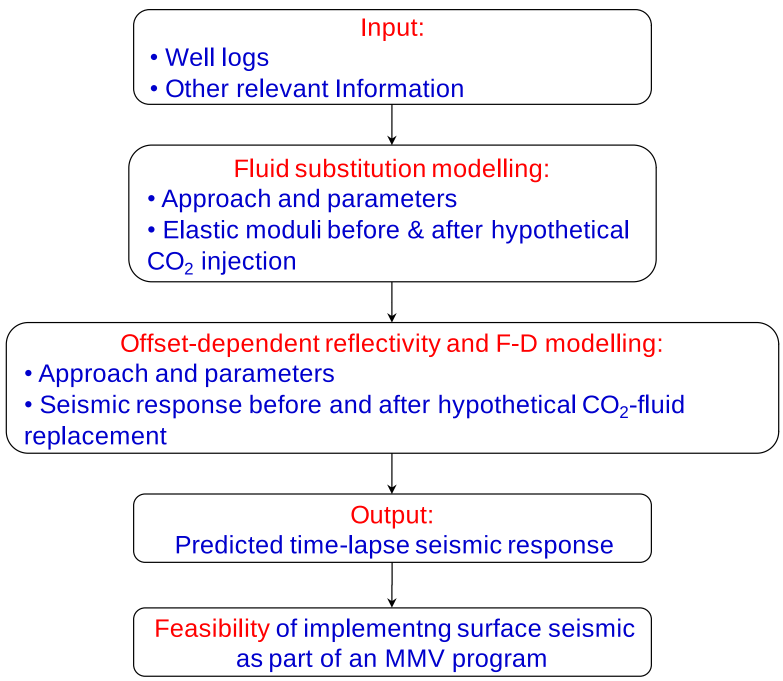

Figure 5-9: Flowchart outlining the major steps followed in the feasibility analysis of time-lapse seismology in delineating a hypothetical CO_2 plume. MMV: monitoring, measurements, and verification.

5.3.2 Rock Physics and Fluid Substitution Modelling

Understanding the seismic response to fluid changes within the Nisku Formation is crucial to the success of any time-lapse seismic monitoring that may be implemented as part of a monitoring, measurement and verification (MMV) program associated with any future CO_2 sequestration project in the study area. In this section, the fluid replacement modelling (FRM) method and approach are discussed. The objective is to predict changes in the elastic moduli that would result if the original pore-filling fluid (i.e. brine) is replaced with another fluid, namely supercritical CO_2. The FRM is fundamentally based on Gassmann relation (1951), which was introduced along with some references in Section 3.5.9. In particular, Berryman (1999) discusses the theoretical aspects of the Gassmann relation whereas Smith et al. (2003) give an excellent review of the Gassmann fluid substitution and some of the pertinent considerations and common pitfalls.

5.3.2.1 The Gassmann Formulation

Essentially, the Gassmann equation relates the bulk modulus of a fluid saturated rock to that of the porous rock frame through the following formula:

$$K_{\text{saturated}}^{\text{initial}} = K_{\phi} + \frac{\left(1 - \dfrac{K_{\phi}}{K_{\text{mineral}}}\right)^2}{\left(\dfrac{\phi}{K_{\text{fluid}}^{\text{initial}}} + \dfrac{(1-\phi)}{K_{\text{mineral}}} - \dfrac{K_{\phi}}{(K_{\text{mineral}})^2}\right)} \tag{9.3}$$

where:

$K_{\text{saturated}}^{\text{initial}}$ is the bulk modulus of the rock saturated with the “initial” in-situ fluid in GPa.

K_{ϕ} is the bulk modulus of the porous rock frame, or skeleton, in GPa.

K_{mineral} is the bulk modulus of the mineral comprising the rock matrix in GPa.

$K_{\text{fluid}}^{\text{initial}}$ is the bulk modulus of the “initial” in-situ pore-filling fluid in GPa.

ϕ is the porosity.

The bulk modulus of the rock in the initial saturation ($K_{\text{saturated}}^{\text{initial}}$), i.e. in-situ, state is given by:

$$K_{\text{saturated}}^{\text{initial}} = \rho_{\text{saturated}}^{\text{initial}} \left[\left(\alpha_{\text{saturated}}^{\text{initial}} \right)^2 - \frac{4}{3} \left(\beta_{\text{saturated}}^{\text{initial}} \right)^2 \right] \tag{9.4}$$

where $\alpha_{\text{saturated}}^{\text{initial}}$, $\beta_{\text{saturated}}^{\text{initial}}$, and $\rho_{\text{saturated}}^{\text{initial}}$ are the P-wave speed, S-wave speed, and density of the in-situ saturated rock. Recall that the S-wave speed is related to the shear modulus ($\mu_{\text{saturated}}^{\text{initial}}$) through:

$$\mu_{\text{saturated}}^{\text{initial}} = \rho_{\text{saturated}}^{\text{initial}} \left(\beta_{\text{saturated}}^{\text{initial}} \right)^2 \Rightarrow \beta_{\text{saturated}}^{\text{initial}} = \sqrt{\frac{\mu_{\text{saturated}}^{\text{initial}}}{\rho_{\text{saturated}}^{\text{initial}}}} \tag{9.5}$$

The porosity can, for instance, be estimated using porosity-density relation:

$$\phi = \frac{\left(\rho_{\text{saturated}}^{\text{initial}} - \rho_{\text{mineral}} \right)}{\left(\rho_{\text{mineral}} - \rho_{\text{fluid}}^{\text{initial}} \right)} \tag{9.6}$$

where ρ_{mineral} and $\rho_{\text{fluid}}^{\text{initial}}$ are the densities of the mineral and initial fluid present in the rock in kg/m^3.

One of the key aspects of the Gassmann formulation is that bulk modulus of the porous rock frame (K_ϕ) remains unchanged regardless of the fluid with which the rock is saturated. Thus, the next major step is to re-arrange Equation (9.3) to solve for (K_ϕ):

$$K_\phi = \frac{K_{\text{saturated}}^{\text{initial}} \left(\frac{\phi K_{\text{mineral}}}{K_{\text{fluid}}^{\text{initial}}} + 1 - \phi \right) - K_{\text{mineral}}}{\left(\frac{\phi K_{\text{mineral}}}{K_{\text{fluid}}^{\text{initial}}} + \frac{K_{\text{saturated}}^{\text{initial}}}{K_{\text{mineral}}} - 1 - \phi \right)} \tag{9.7}$$

Once K_ϕ is known, then it is possible to saturate the system with a replacement fluid ($K_{\text{fluid}}^{\text{new}}$) and thus calculate the new bulk modulus ($K_{\text{saturated}}^{\text{new}}$):

$$K_{\text{saturated}}^{\text{new}} = K_\phi + \frac{\left(1 - \frac{K_\phi}{K_{\text{mineral}}} \right)^2}{\left(\frac{\phi}{K_{\text{fluid}}^{\text{new}}} + \frac{(1-\phi)}{K_{\text{mineral}}} - \frac{K_\phi}{\left(K_{\text{mineral}} \right)^2} \right)} \tag{9.8}$$

where

$K_{\text{saturated}}^{\text{new}}$ is the bulk modulus of the rock saturated with the new fluid in GPa.

$K_{\text{fluid}}^{\text{new}}$ is the bulk modulus of the pore-filling (new) fluid GPa.

Alternatively, the step in which K_ϕ is computed in Equation (9.7) can be eliminated and the new saturation can be directly related to the initial saturation (Mavko et al., 2003):

$$\frac{K_{\text{saturated}}^{\text{new}}}{K_{\text{mineral}} - K_{\text{saturated}}^{\text{new}}} - \frac{K_{\text{fluid}}^{\text{new}}}{\phi\left(K_{\text{mineral}} - K_{\text{fluid}}^{\text{new}}\right)} = \frac{K_{\text{saturated}}^{\text{initial}}}{K_{\text{mineral}} - K_{\text{saturated}}^{\text{initial}}} - \frac{K_{\text{fluid}}^{\text{initial}}}{\phi\left(K_{\text{mineral}} - K_{\text{fluid}}^{\text{initial}}\right)} \quad (9.9)$$

Another important assumption in the Gassmann FRM is that the shear modulus is assumed to be insensitive to fluid change and therefore:

$$\mu_{\text{saturated}}^{\text{initial}} = \mu_{\text{saturated}}^{\text{new}} \quad (9.10)$$

Subsequently, the bulk and shear moduli of the new system are used to calculate the new P-wave ($\alpha_{\text{saturated}}^{\text{new}}$) and S-wave ($\beta_{\text{saturated}}^{\text{new}}$) speeds:

$$\alpha_{\text{saturated}}^{\text{new}} = \sqrt{\frac{K_{\text{saturated}}^{\text{new}} + \frac{4}{3}\mu_{\text{saturated}}^{\text{new}}}{\rho_{\text{saturated}}^{\text{new}}}} \quad (9.11)$$

$$\beta_{\text{saturated}}^{\text{new}} = \sqrt{\frac{\mu_{\text{saturated}}^{\text{new}}}{\rho_{\text{saturated}}^{\text{new}}}} \quad (9.12)$$

where $\rho_{\text{saturated}}^{\text{new}}$ is the density of the rock saturated with the new fluid. The new wavespeeds and density are then used to calculate the new acoustic and shear impedances:

$$I_p^{\text{new}} = \alpha_{\text{saturated}}^{\text{new}}\rho_{\text{saturated}}^{\text{new}} \quad (9.13)$$

$$I_s^{\text{new}} = \beta_{\text{saturated}}^{\text{new}}\rho_{\text{saturated}}^{\text{new}} \quad (9.14)$$

As with any mathematical model, the Gassmann formulation has a set of underlying assumptions (Berryman, 1999; Mavko et al., 2003; Smith et al., 2003):

- Low frequency, i.e. the seismic wavelength is much larger than grain or pore scale. This implies that pore-induced pressure must have time to equilibrate (i.e. become relaxed) during the passage of the seismic wave.
- The pore space is connected and the fluid-bearing rock is fully saturated. Thus, it is assumed that the fluid can flow fast enough to equilibrate the pore-induced disturbance caused by the seismic wave.
- The rock is isotropic and homogenous.

- The rock matrix is composed of single mineralogy. Alternatively, all minerals should have the same bulk and shear moduli.
- No interaction is taking place between the fluid(s) and the rock matrix.

Although some of the former assumptions are occasionally violated, the Gassmann formulation, interestingly, still yields reasonable results (Avseth et al., 2005; Calvert, 2005; Chopra, 2005; Sharma et al., 2006). Of course, in such cases, the Gassmann results may somewhat overestimate or underestimate actual observations. However, one has to keep in mind that many of these observed phenomena are based on laboratory measurements which are, normally, performed at ultrasonic frequencies (Sharma et al. 2006; Vega et al., 2007, Verwer et al., 2008). On the other hand, of the many developed rock physics formulations, such as the Biot relations (Biot, 1955a and 1955b), Hudson's model (Hudson et al., 1996) and Kuster and Toksöz relations (Kuster and Toksöz, 1974a and 1974b), only the Gassmann-based formulations are suitable for in-situ seismic frequencies[54]. Moreover, some of the limitations in the novel Gassmann formulation can be alleviated as will be discussed in the next section. So, those mitigations in addition to the geologic setting and the nature of the available data make it the most attractive formulation to be implemented in this dissertation.

---

[54] With the exception of the Biot's relation which at low frequency is equivalent to the Gassmann formulation. Other relations, also, exist such as Brown and Korringa (1975), and Berryman and Milton (1991). In addition, some of the limitations outlined above are not exclusive to the Gassmann relation.

5.3.2.2 Approach, Data and Parameters

The FRM approach implemented in this dissertation is depicted in Figure 5-10 whereas the parameters selected in performing the FRM in the WASP study area are given in Table 5-1. Some of the necessary parameters ($\alpha_{\text{saturated}}^{\text{initial}}$, $\beta_{\text{saturated}}^{\text{initial}}$, $\rho_{\text{saturated}}^{\text{initial}}$, and ϕ) required to perform the FSM were estimated using well data from selected wells (Figure 5-8). These wells were selected because of one or combination of the following: (i) the quality of the well data (e.g. minimum invaded zone effect), (ii) core (Eisinger and Jensen, 2009) and fluid (Shevalier et al., 2009) information, and (iii) representation of the Nisku Formation at the water source and in the northern part of the study area where the good 3-D seismic coverage is (Section 4.2).

Unfortunately, none of the wells used in the FSM had dipole sonic log, which is required to calculate the S-wave speed. Therefore, the empirical relation given by Greenberg and Castagna (1992) for carbonate rocks was investigated in estimating the S-wave (β) speed from the P-wave speed (α):

$$\beta = 0.532(\alpha) - 0.0777;\ \text{in km/s} \tag{9.15}$$

but, eventually, an α/β of 1.9 was used (Pickett, 1963).

The bulk density was supplied from density log or it was estimated from the sonic log using the empirical relation given by Gardner et al. (1974):

$$\rho = a\alpha^{m} \tag{9.16}$$

where a is 0.31, m is 0.25, and α is the P-wave speed in m/s. However, a local version of the Gardner et al. (1974) was derived, when necessary, using density logs in the study area. For the Nisku Formation, the average value of a and m were 0.815 and 0.134, respectively.

The clay content was estimated from core data (Michael et al., 2008; Nygaard, 2009a; Shevalier et al.; 2009) and from gamma ray log by using the Dresser Atlas (1979) gamma-ray index (GRI) empirical relation:

$$\%\ \text{Clay} = 100 \times \left(\frac{GR_{\text{reservoir}} - GR_{\text{clean}}}{GR_{\text{clay-shale}} - GR_{\text{clean}}} \right) \tag{9.17}$$

where $GR_{reservoir}$, $GR_{clean\text{-}shale}$ and $GR_{clean\text{-}carbonate}$ are the gamma ray (GR) measured in API in the reservoir, in clean shale and clean carbonate, respectively.

The Nisku aquifer temperature and pressure were provided by Michael et al. (2008). The choice of the mineral constituents was based on core analysis (Michael et al., 2008; Eisinger and Jensen, 2009; SCG, 2009) and reservoir mineralogy (Shevalier et al., 2009). Analysis on reservoir fluid samples by Shevalier et al. (2009) helped establishing the fluid composition, water salinity and gas-water ratio (GWR). With this information available, the bulk modulus ($K_{mineral}$) and density ($\rho_{mineral}$) of the individual minerals were obtained from laboratory measurements (Nygaard, 2009a) or published data (Mavko et al., 2003). As for the density and incompressibility of the various fluids, they were estimated using CREWES Fluid Property Calculator (Ursenbach, 2009). This interactive software applet is based on some empirical relations (Batzle and Wang, 1992; see Appendix B.1) and the Peng-Robinson (1976) equation of state (EOS)[55] (see Appendix B.2). The density (ρ_{gas}) and incompressibility (K_{gas}) of the various gases were determined using Peng-Robinson EOS whereas the empirical relations provided by Batzle and Wang (1992) were invoked in predicting ρ_{water} and K_{water}.

The approach implemented requires K_ϕ to be estimated. Once that was achieved, the system was then saturated with fluid(s) representative of those present in the reservoir, in this case 100% brine, prior to the fluid replacement process. Then, the saturation of the replacement fluid, i.e. CO_2, was gradually increased until the reservoir became fully saturated with the new fluids[56]. In the next section, the effect of the various parameters will be examined closely and only the FSM results corresponding to those parameters representatives of the in-situ condition will be adopted in the subsequent offset-dependent reflectivity (ODR) and exploding reflector finite-difference (ERFD) modelling.

[55] An equation of state describes how a material volume and density behave as function of temperature and pressure (Serway and Jewett, 2004).
[56] Of course, in reality, it is not possible to achieve saturation higher than about 50% (USDOE, 2008).

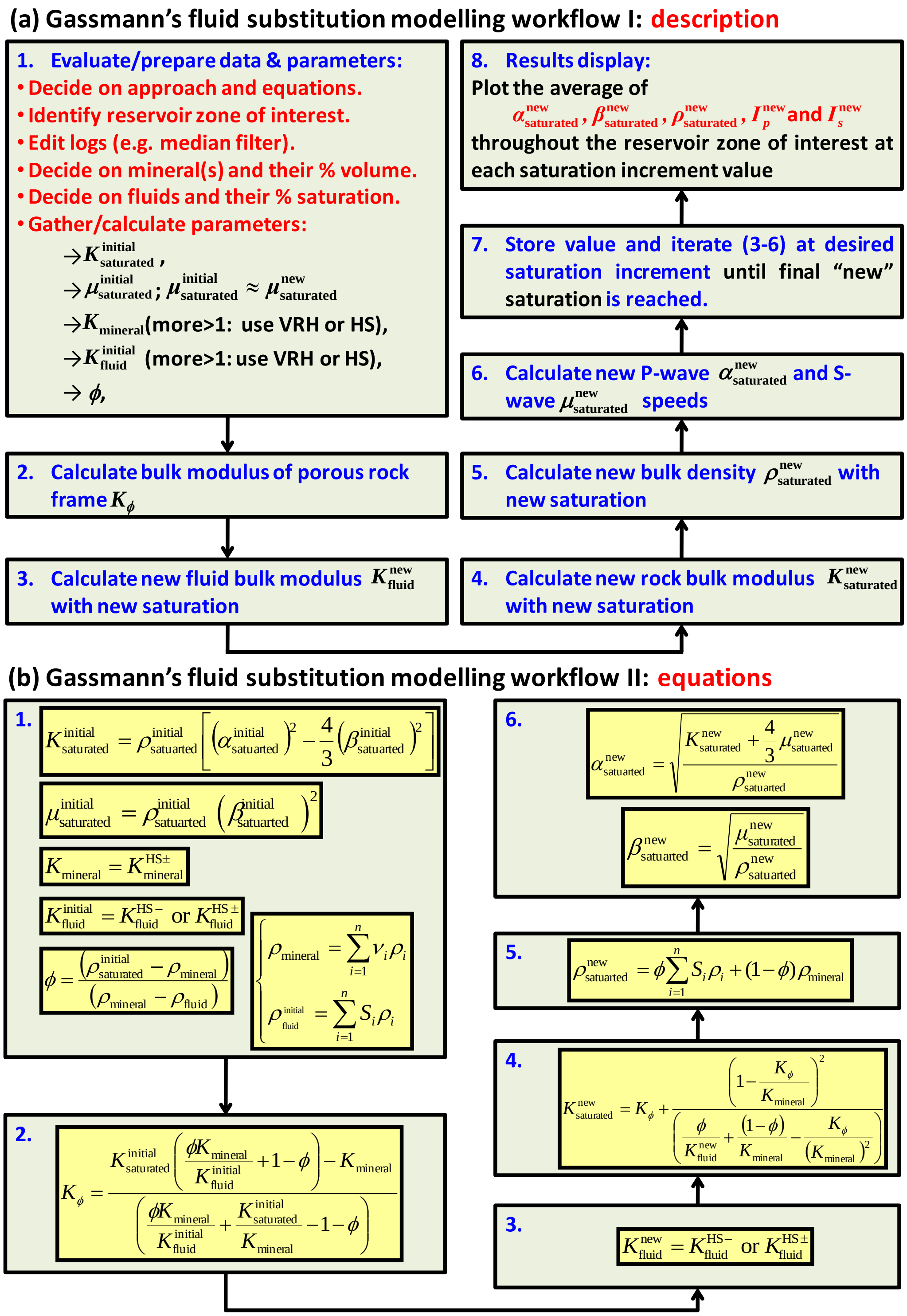

Figure 5-10: The FRM approach implemented in this dissertation illustrated using logical and mathematical expressions. The symbols and equations are discussed in the text (Sections 5.3.2.1 through 5.3.2.5). VRH: Voigt-Reuss-Hill average; HS±: Hashin-Shtrikman average.

Table 5-1: Information pertaining to physical and chemical properties that were invoked in the Nisku Formation FRM. There is no significant variation in pressure and temperature between the wells. The fluids properties reflect the in-situ values. The data was compiled using the following references (see text for data-reference association): Mavko et al. (2003), Michael et al. (2008), Nygaard (2009a), Shevalier et al. (2009), Ursenbach (2009), and Engineering ToolBox (2011). Also, see the study areas geology chapter; in particular Section 2.3 of Chapter 2. * See Figure 5-11.

Wells*	(a) 1F1-11-29-45-2W5 (b) 100-10-21-50-2W5 (c) 100-10-05-52-2W5
Target Aquifer/Formation	Nisku
Primary Lithology	Dolostone
Reservoir Bearing Fluid	Water (brine)
Other Reservoir Fluid	Gas
Reservoir Depth (d)	(a) 2200 m (b) 1815 m (c) 1730 m
Reservoir Thickness (h)	(a) 55 m (b) 65 m (c) 90 m
Reservoir Pressure (P)	15 MPa
Reservoir Temperature (T)	50.3 C^o
CO_2 Phase at the Reservoir	Supercritical
Gas-Water Ratio (GWR)	4 (insignificant)
Average Porosity (ϕ)	(a) 8.2% (b) 7.4% (c) 7.2%
Average Water Salinity (l)	115 g/l
Primary Reservoir Mineral	Dolomite (80%)
Secondary Reservoir Mineral	Calcite (18%)
Tertiary Reservoir Mineral	Clay (2%)
Primary Reservoir Gas	Methane (50%); volume insignificant
Secondary Reservoir Gas	Hydrogen sulphide (50%); volume insignificant
Density of Primary Mineral ($\rho_{dolomite}$)	2840 kg/m^3

Continued next page

Bulk Modulus of Primary Mineral ($K_{dolomite}$)	94 GPa
Shear Modulus of Primary Mineral ($\mu_{dolomite}$)	45 GPa
Density of Secondary Mineral ($\rho_{calcite}$)	2750 kg/m^3
Bulk Modulus of Secondary Mineral ($K_{calcite}$)	74 GPa
Shear Modulus of Secondary Mineral ($\mu_{calcite}$)	35 GPa
Density of Tertiary Mineral (ρ_{clay})	2580 kg/m^3
Bulk Modulus of Tertiary Mineral (K_{clay})	25 GPa
Shear Modulus of Tertiary Mineral (μ_{clay})	10 GPa
Density of Water (ρ_{water})	1118 kg/m^3
Bulk Modulus of Water (K_{water})	3.28 GPa
Density of Primary Gas (ρ_{CH4})	105 kg/m^3
Bulk Modulus of Primary Gas (K_{CH4})	0.025 GPa
Density of Secondary Gas (ρ_{H2S})	796 kg/m^3
Bulk Modulus of Secondary Gas (K_{H2S})	0.404 GPa
Density of Supercritical CO_2 (ρ_{CO2})	653 kg/m^3
Bulk Modulus of Supercritical CO_2 (K_{CO2})	0.081 GPa
Initial Water Saturation (S_{water})	Cases I, II and III: 100% Case IV: 95%
Initial Gas Saturation (S_{CH4}, S_{H2S})	Cases I, II and III: 0% CH_4, 0% H_2S Case IV: 2.5% CH_4, 2.5% H_2S
Initial CO_2 Saturation (S_{CO2})	Cases I, II and III: 0% Case IV: 0%
Final Water Saturation (S_{water})	Cases I, II and III: 0% Case IV: 0%
Final Gas Saturation (S_{CH4}, S_{H2S})	Cases I, II and III: 0% CH_4, 0% H_2S Case IV: 0% CH_4, 0% H_2S
Final CO_2 Saturation (S_{CO2})	Cases I, II and III: 100% Case IV: 100%
Comments	• Case I: FSM assuming uniform saturation • Case II: FSM assuming patchy-like saturation • Case III: FSM assuming uniform saturation but with effective minerals moduli softened. • Case VI: FSM same as I + in-situ gases

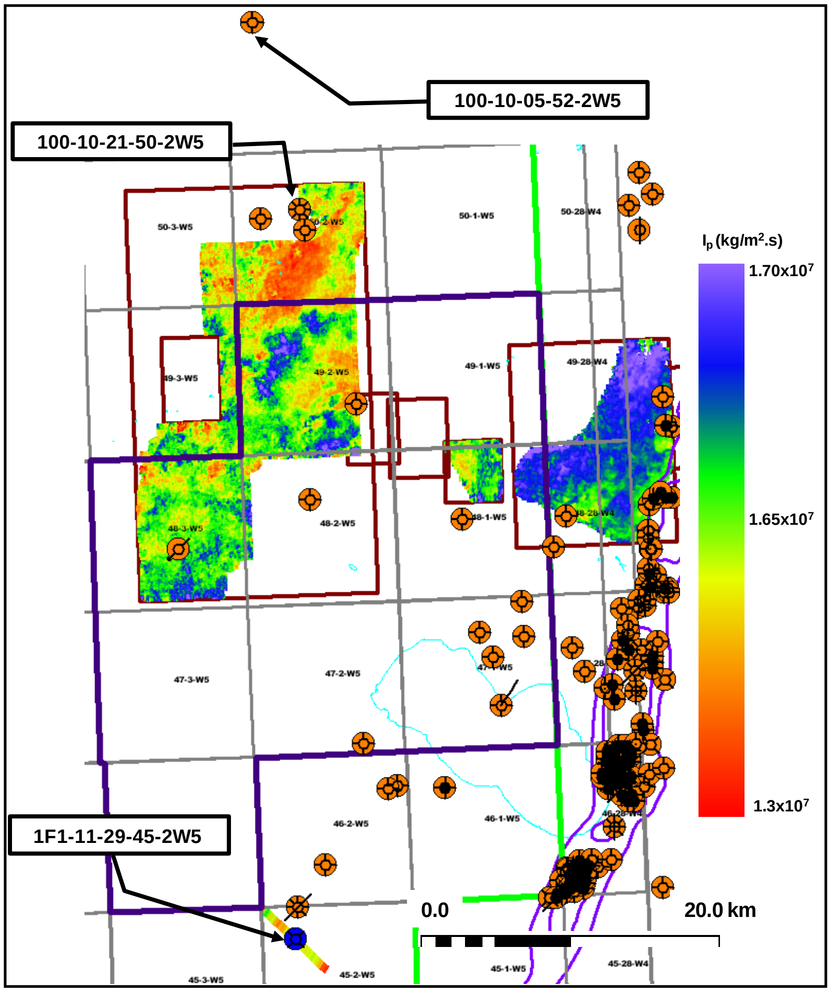

Figure 5-11: Acoustic impedance map of the Nisku Formation showing the location of the wells invoked in the FRM. See the base map (Figure 4-1) in Chapter 4 for legends and relative position with respect to large-scale study area.

5.3.2.3 Effective Moduli of Minerals Mixture

As outlined in Section 5.3.2.1, the original Gassmann formulation assumes that the rock is comprised of a single mineral. For a material composed of multi-mineral, the limitation on the effective elastic moduli can be alleviated by using an average of the elastic bounds which can be computed using either Voigt-Reuss-Hill (VRH) or Hashin-Shtrikman (HS) averages of effective moduli. The VRH average ($K_{\mathrm{mineral}}^{\mathrm{VRH}}$) can be written as (Hills, 1952; Mavko et al., 2003):

$$K_{\mathrm{mineral}}^{\mathrm{VRH}} = \frac{K_{\mathrm{mineral}}^{\mathrm{V}} + K_{\mathrm{mineral}}^{\mathrm{R}}}{2} \tag{9.18}$$

where $K_{\text{mineral}}^{\text{V}}$ is the Voigt average (Voigt, 1928; Mavko and Mukerji, 1998):, which gives the upper bound on the elastic moduli[57]:

$$K_{\text{mineral}}^{\text{V}} = \sum_{i=1}^{n} \nu_i K_i \tag{9.19}$$

Similarly, a lower bound ($K_{\text{mineral}}^{\text{R}}$) exists that is given by the Reuss average (Reuss, 1929; Smith et al., 2003):

$$K_{\text{mineral}}^{\text{R}} = \left[\sum_{i=1}^{n} \frac{\nu_i}{K_i} \right]^{-1} \tag{9.20}$$

ν_i and K_i are the volume fraction and bulk modulus (in GPa) of the i^{th} mineral constituent, respectively. The effective shear modulus can be computed in the same manner by exchanging K_i with μ_i. Although the VRH average has been observed to yield adequate results, the narrowest bounds can rather be computed using the Hashin-Shtrikman (HS) bounds of effective moduli (Hashin and Shtrikman, 1963). The bounds on the effective bulk modulus ($K_{\text{mineral}}^{\text{HS}\pm}$) can be expressed using the following notation[58] (Berryman, 1995):

$$K_{\text{mineral}}^{\text{HS}\pm} = \begin{cases} K_{\text{mineral}}^{\text{HS}+} = \left\{ \left[\sum_{i=1}^{n} \dfrac{\nu_i}{\left(K_i + \Lambda_{\max} \right)} \right]^{-1} - \Lambda_{\max} \right\}; \ \Lambda_{\max} = \dfrac{4}{3} \mu_{\max} \\ K_{\text{mineral}}^{\text{HS}-} = \left\{ \left[\sum_{i=1}^{n} \dfrac{\nu_i}{\left(K_i + \Lambda_{\min} \right)} \right]^{-1} - \Lambda_{\min} \right\}; \ \Lambda_{\min} = \dfrac{4}{3} \mu_{\min} \end{cases} \tag{9.21}$$

Likewise, the bounds corresponding to the effective shear modulus ($\mu_{\text{mineral}}^{\text{HS}\pm}$) can be written as:

---

[57] The numerical subscript is used throughout this section for mathematical convenience. In applying the formulae, the numerical subscript should be replaced by the mineral or fluid phase (e.g. dolomite or water) and the respective volume fraction or saturation.

[58] The notation has been modified from that given by Berryman (1995) to better fit the theme of this section.

$$\mu_{\text{mineral}}^{\text{HS}\pm}=\begin{cases}\mu_{\text{mineral}}^{\text{HS+}}=\left\{\left[\sum_{i=1}^{n}\frac{\nu_i}{\left(\mu_i+\Gamma_{\max}\right)}\right]^{-1}-\Gamma_{\max}\right\};\ \Gamma_{\max}=\frac{\mu_{\max}}{6}\left(\frac{9K_{\max}+8\mu_{\max}}{K_{\max}+2\mu_{\max}}\right)\\ \mu_{\text{mineral}}^{\text{HS}-}=\left\{\left[\sum_{i=1}^{n}\frac{\nu_i}{\left(\mu_i+\Gamma_{\min}\right)}\right]^{-1}-\Gamma_{\min}\right\};\ \Gamma_{\min}=\frac{\mu_{\min}}{6}\left(\frac{9K_{\min}+8\mu_{\min}}{K_{\min}+2\mu_{\min}}\right)\end{cases}\tag{9.22}$$

where $K_{\max}$, $\mu_{\max}$ and $K_{\min}$, $\mu_{\min}$ are the bulk and shear moduli (in GPa) of the stiffest and softest constituents, respectively. $K_{\text{mineral}}^{\text{HS+}}$ and $\mu_{\text{mineral}}^{\text{HS+}}$ are the HS upper bounds whereas $K_{\text{mineral}}^{\text{HS-}}$ and $\mu_{\text{mineral}}^{\text{HS}-}$ designate the lower HS bounds. The effective moduli of the medium matrix are then taken to be as the average:

$$K_{\text{mineral}}^{\text{HS}\pm}=\frac{K_{\text{mineral}}^{\text{HS+}}+K_{\text{mineral}}^{\text{HS}-}}{2};\ \mu_{\text{mineral}}^{\text{HS}\pm}=\frac{\mu_{\text{mineral}}^{\text{HS+}}+\mu_{\text{mineral}}^{\text{HS}-}}{2}\tag{9.23}$$

Figure 5-12 and Figure 5-13 illustrate the difference in the computed effective elastic moduli using the VRH and HS formulations when the rock matrix is composed of: (1) dolomite and calcite, and (2) dolomite and clay. Note that the VRH and HS formulations yield comparable results when the constituents are alike in terms of their elastic moduli (Figure 5-12 (a) and Figure 5-13 (a)). However, the separation between the VRH and HS bounds become larger as the constituents become more elastically different (Figure 5-12 (b) and Figure 5-13 (b)). The VRH and HS averages of the effective moduli as well as the density of the mineral mixture (Table 5-1) are shown in Figure 5-14. Obviously, the difference between the VRH (Figure 5-14 (a)) and HS (Figure 5-14 (b)) is insignificant for the amount of available pore space and the chosen mineral mixture and their respective volume fraction.

(a) Voigt-Reuss bounds and VRH averages of minerals: dolomite vs. calcite

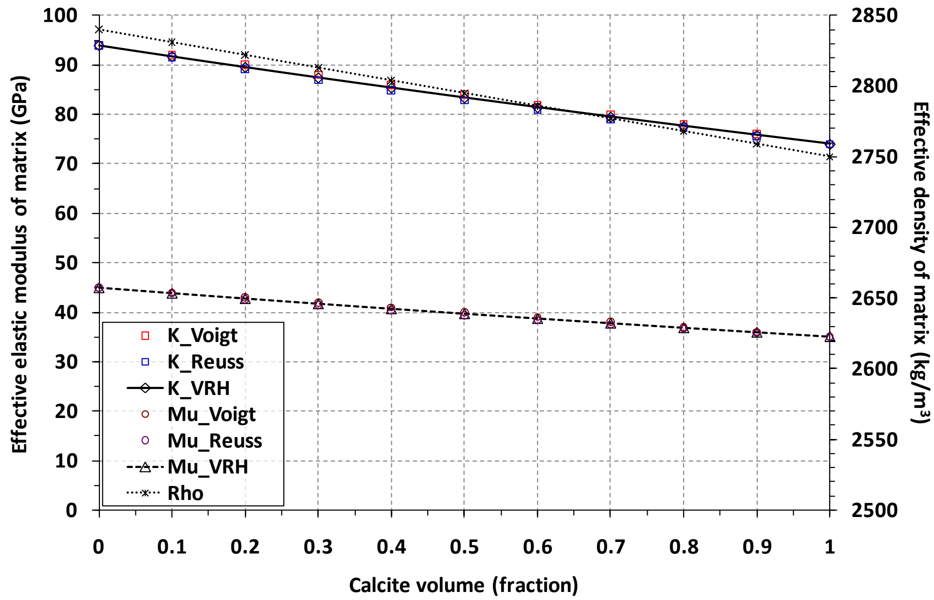

(b) Voigt-Reuss bounds and VRH averages of minerals: dolomite vs. clay

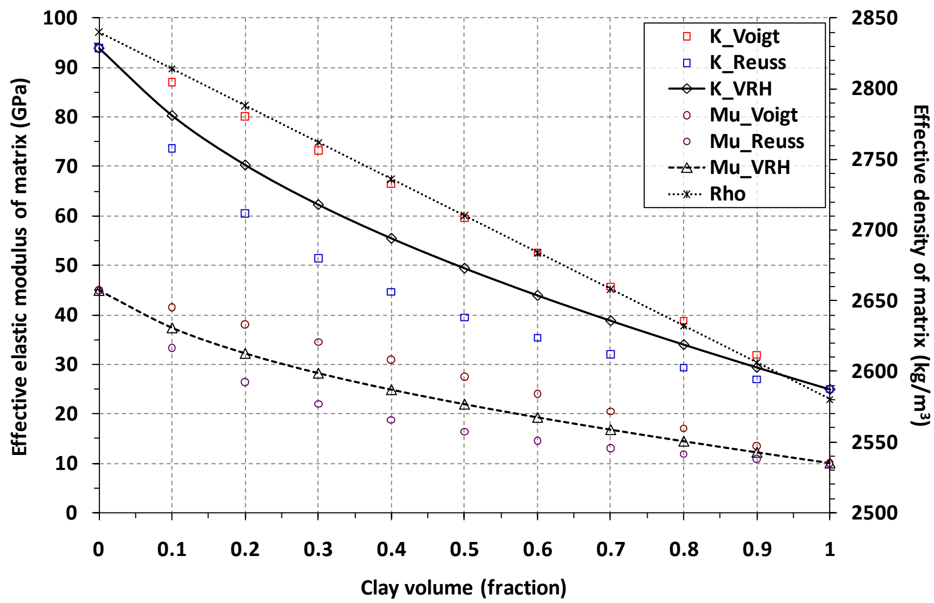

Figure 5-12: Upper and lower bounds on effective elastic moduli and their average of minerals mixture using Voigt-Reuss-Hill (VRH) formulations when the constituent minerals are: (a) dolomite and calcite and (b) dolomite and clay. Voigt gives the upper bound whereas Reuss yields the lower bound; Voigt-Reuss-Hill (VRH) is the average of the two. K: bulk modulus (GPa), Mu: shear modulus (GPa), Rho: density (kg/m^3).

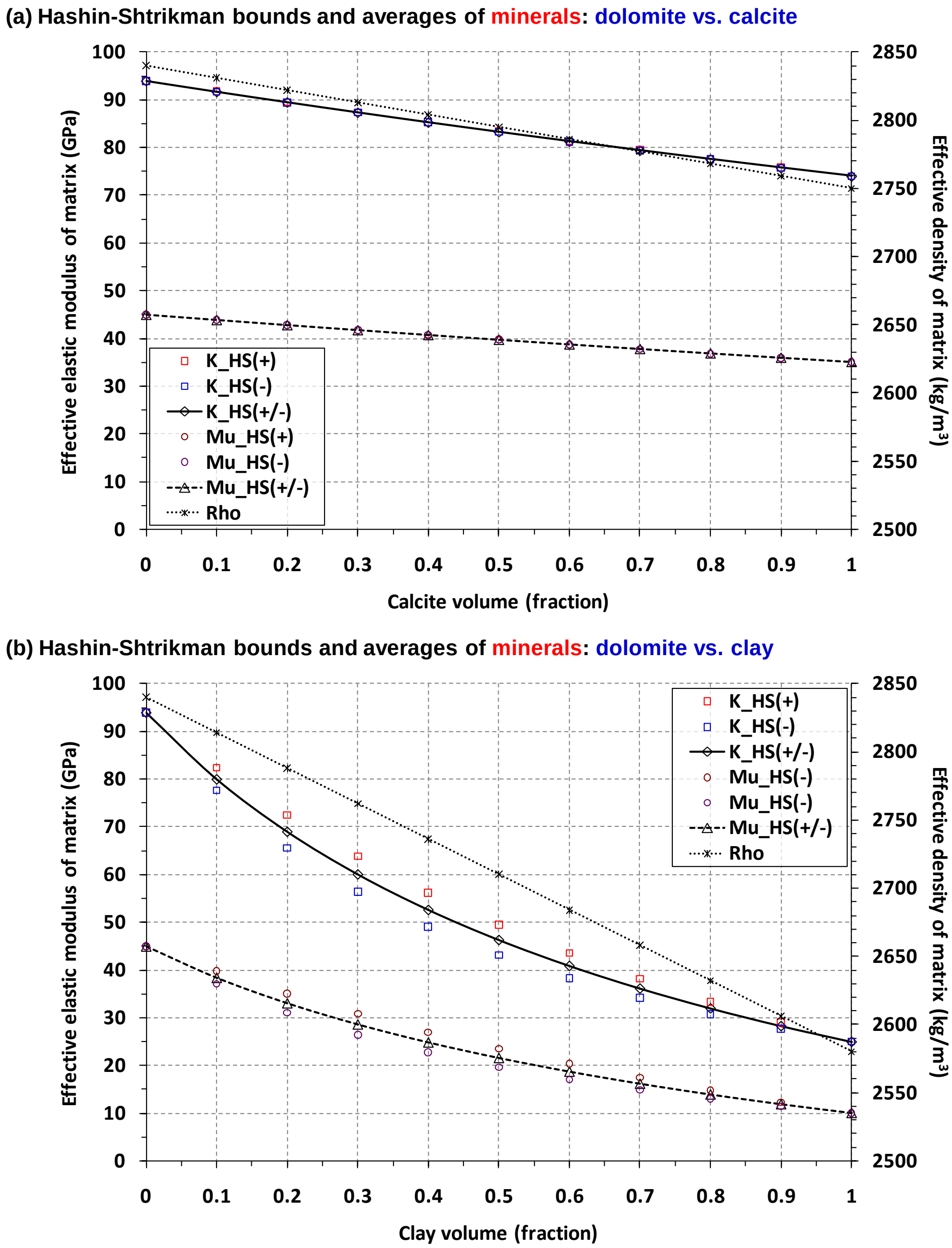

Figure 5-13: Upper and lower bounds on effective elastic moduli and their average of minerals mixture using Hashin-Shtrikman (HS) formulations when the constituent minerals are: (a) dolomite and calcite and (b) dolomite and clay. HS(+) refers to the upper bound while HS(-) designates the lower bound; HS(+/-) is the average of the two. K: bulk modulus (GPa), Mu: shear modulus (GPa), Rho: density (kg/m^3).

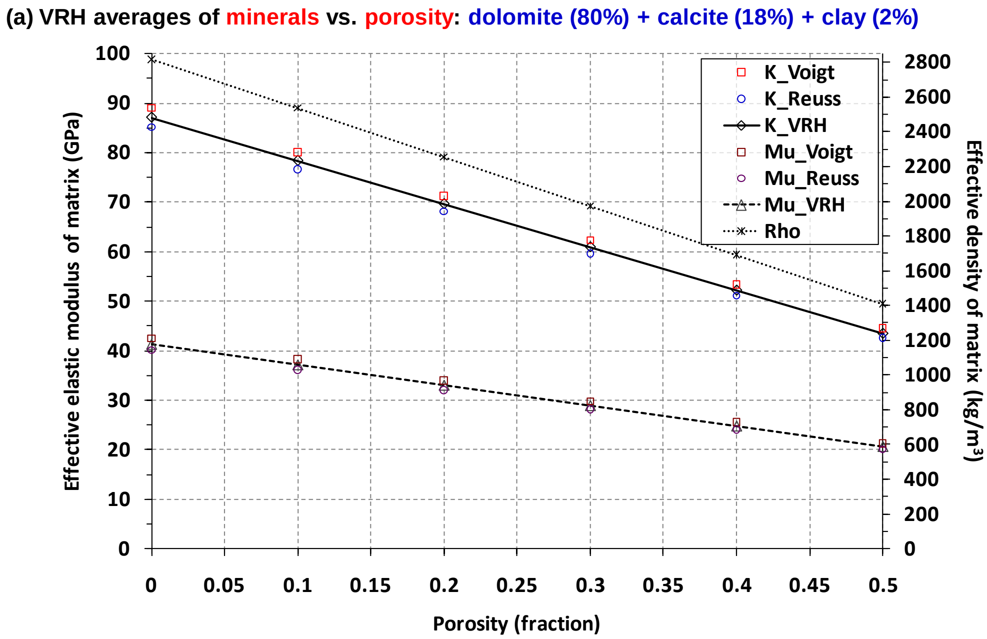

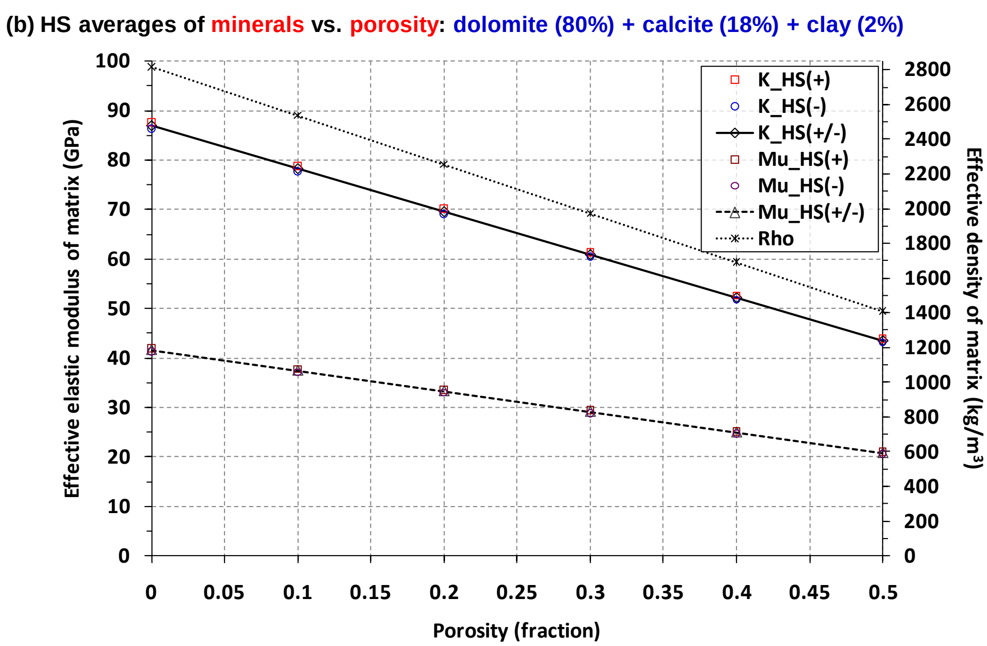

Figure 5-14: (a) Voigt-Reuss-Hill (VRH) and (b) Hashin-Shtrikman (HS) averages of effective moduli of the mineral mixture as a function of porosity. The respective volume fractions were estimated from core analysis and well logs (see Table 5-1). K: bulk modulus (GPa), Mu: shear modulus (GPa), Rho: density (kg/m^3). Note the similarity between the bounds and averages in (a) and (b) as the main constituents (dolomite and calcite) which make up 98% of the rock matrix are elastically alike.

5.3.2.4 Effective Modulus of a Mixture of Fluids

As for the multi-phase fluids and saturation distribution limitations within the Gassmann formulation, these can be mitigated by assuming that the effective fluid modulus (K_{fluid}) is a weighted average of the fluid mixture present in the system. In the case of uniform saturation, Reuss's arithmetic average gives the effective bulk modulus of multi-phase fluid mixture when all phases have the same pore-induced pressure (Reuss, 1929; Smith et al., 2003):

$$K_{\text{fluid}}^{\text{R}} = \left[\sum_{i=1}^{n} \frac{S_i}{K_i} \right]^{-1} \tag{9.24}$$

where S_i and K_i are the saturation and the bulk modulus (in GPa) corresponding to the i^{th} fluid phase. Once more, the HS bounds (Hashin and Shtrikman, 1963) can be used to compute the effective bulk modulus of the fluid mixture by exchanging the bulk modulus and the volume fraction (v_i) of the mineral in Equation (9.21) with the bulk modulus and saturation (S_i) of the individual fluid. Then, the HS average of the fluid mixture can be written as:

$$K_{\text{fluid}}^{\text{HS}\pm} = \frac{K_{\text{fluid}}^{\text{HS}+} + K_{\text{fluid}}^{\text{HS}-}}{2} \tag{9.25}$$

Equation (9.24) or (9.26) can be used to compute the effective bulk modulus of the multi-phase fluid mixture in the initial ($K_{\text{fluid}}^{\text{initial}}$) and new saturation ($K_{\text{fluid}}^{\text{new}}$) state by using the appropriate K_i and S_i that reflect the bulk modulus of the individual fluid and its respective saturation.

If the wave-induced pore pressure does not have time to equilibrate during the passage of the seismic wave, thus generating a pressure gradient, then the saturation becomes more like a patchy saturation (Avseth et al., 2005). In such case, the bulk modulus of the effective fluid can be approximated by Voigt's harmonic average (Voigt, 1928; Mavko and Mukerji, 1998):

$$K_{\text{fluid}}^{\text{V}} = \sum_{i=1}^{n} S_i K_i \tag{9.26}$$

where S_i and K_i are the saturation and the bulk modulus (in GPa) corresponding to the i^{th} fluid phase. However, the effective bulk modulus of fluid mixture rarely lie along the

Voigt's upper bound (Mavko et al., 2003) and a more lenient representation of patchy saturation could be approximated by Hill's equation (Hill, 1963) which stems from the Hashin-Shtrikman relation introduced in the previous section:

$$K_{\text{effective}} = \left[\sum_{i=1}^{n} \frac{w_i}{\left(K_i + \Lambda\right)} \right]^{-1} - \Lambda \tag{9.27}$$

where $K_{\text{effective}}$ is the effective bulk modulus of the rock with variant bulk modulus (K_i). Note that because shear modulus (μ) of the rock is invariant; $\Lambda_{\text{min}} = \Lambda_{\text{max}}$ in Equation (9.21) and, therefore, the upper ($K^{+\text{HS}}$) and lower ($K^{-\text{HS}}$) bounds collapse into $K_{\text{effective}}$; w_i is the volume fraction of the i^{th} constituent. Another empirical relation that could be used to approximate patchy saturation is given by Brie et al. (1995):

$$K_{\text{fluid}}^{\text{Brie}} = \left(K_{\text{liquid}} - K_{\text{gas}}\right)\left(1 - S_{\text{gas}}\right)^{e} + K_{\text{gas}} \tag{9.28}$$

where $K_{\text{fluid}}^{\text{Brie}}$ is the bulk modulus of the fluid mixture (in GPa), $K_{\text{liquid}}^{\text{R}}$ is the Reuss bulk modulus (in GPa) of the water other liquids if present (e.g. oil), K_{gas} and S_{gas} are the bulk modulus (in GPa) and saturation of the gas. The empirical coefficient e governs the level of "patchiness"; $e = 1$ gives the patchy saturation upper bound whereas $e = \infty$ reduces Equation (9.28) into the Reuss's average, i.e. Equation (9.24). Avseth et al. (2005) found values of $e \approx 3$ better fit laboratory and modelled patchy behaviours.

Figure 5-15 show the effective bulk modulus of multi-phase fluid as a function of CO_2 saturation using two fluid mixture scenarios[59] (see Table 5-1): (1) H_2O, CO_2, and (2) H_2O, CH_4, H_2S, CO_2. Note the strong effect of the presence of in-situ gas (i.e. CH_4 or H_2S) on the effective bulk modulus of the fluid mixture. The presence of these and similar gases in large concentration would effectively undermine the CO_2 effect to the extent that the magnitude of the time-lapse response due to CO_2 fluid replacement is effectively diminished, arguably to null.

---

[59] Although the amount of gases present in the reservoir is negligible, the objective behind including Case III is to demonstrate the immense effect of the presence of in-situ gas on the time-lapse seismic response.

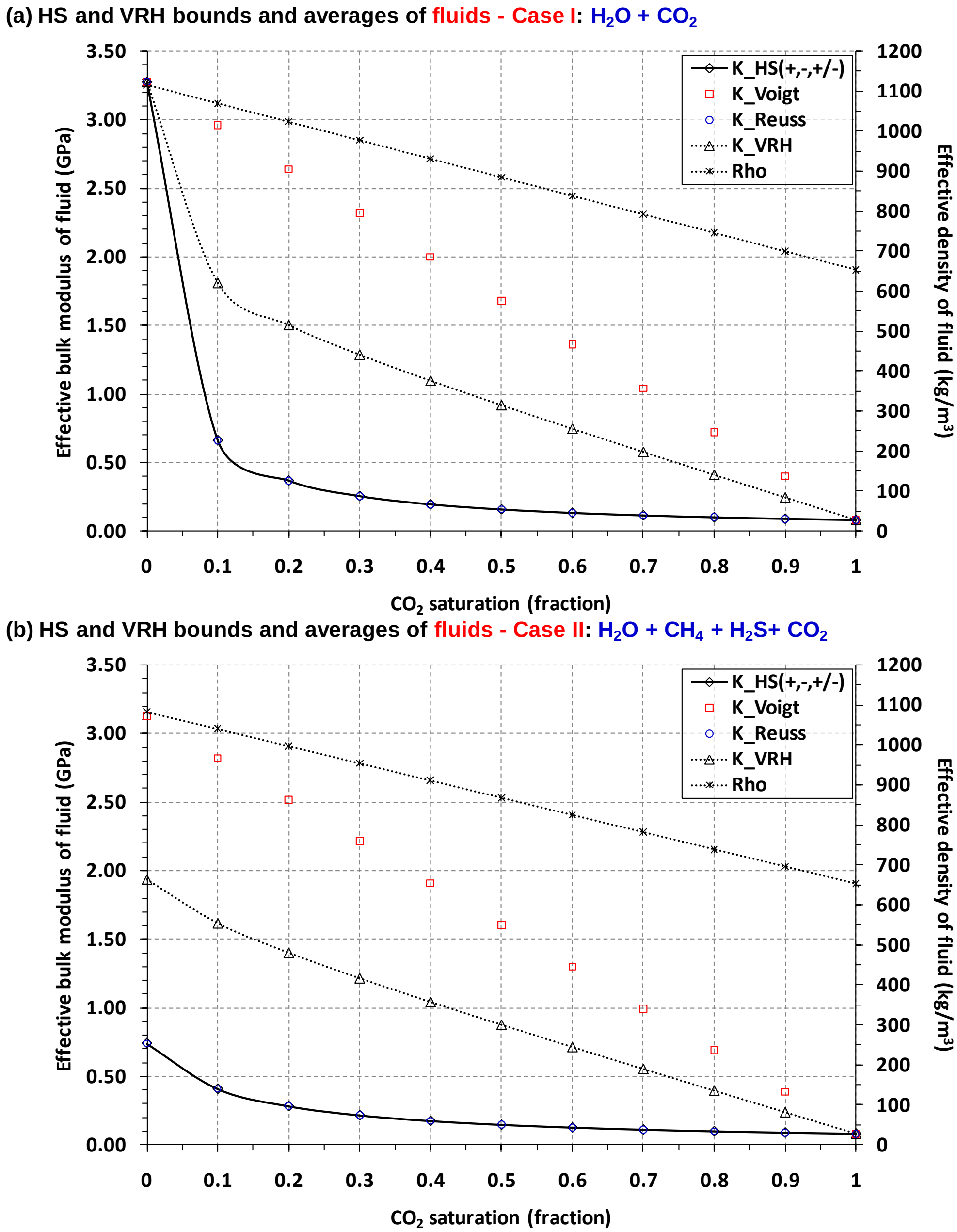

Figure 5-15: Effective bulk modulus (K) of multi-phase fluid as a function of CO_2 saturation using Hashin-Shtrikman bounds and averages, Voigt-Reuss bounds, and Voigt-Reuss-Hill average illustrated using two cases (see Table 5-1): (a) two-phase fluid mixture (H_2O and CO_2), and (b) four-phase fluid mixture (H_2O, CH_4, H_2S and CO_2). In Case I (a), the initial and final saturations are 100% H_2O, 0% CO_2 and 0% H_2O, 100% CO_2. In Case II (b), the initial and final saturations are 95% H_2O, 2.5% CH_4, 2.5% H_2S, 0% CO_2 and 0% H_2O, 0% CH_4, 0% H_2S, and 100% CO_2. Note that the HS bounds and averages are exactly equal to the Reuss bound.

Furthermore, the effective bulk modulus of the fluid (Case I) was modelled as a function of CO_2 saturation and pore space to examine the effect of these two parameters using the Reuss, HS and Voigt averages and the results are illustrated in Figure 5-16. Note that for fluid mixture, the HS average is exactly equal to the Reuss bound and they both describe the effective bulk modulus of fluid mixture when the saturation is uniform. Voigt average, on the other hand, can be used as a proxy to the effective bulk modulus of fluid mixture in the case of patchy saturation. Patchy saturation, as approximated by the Voigt average in Figure 5-16 (b), results in a stiffer fluid mixture and therefore weaker time-lapse change at low and intermediate CO saturation. Note, however, that the Reuss, HS and Voigt averages are exactly equal at 0% and 100% CO_2 saturation.

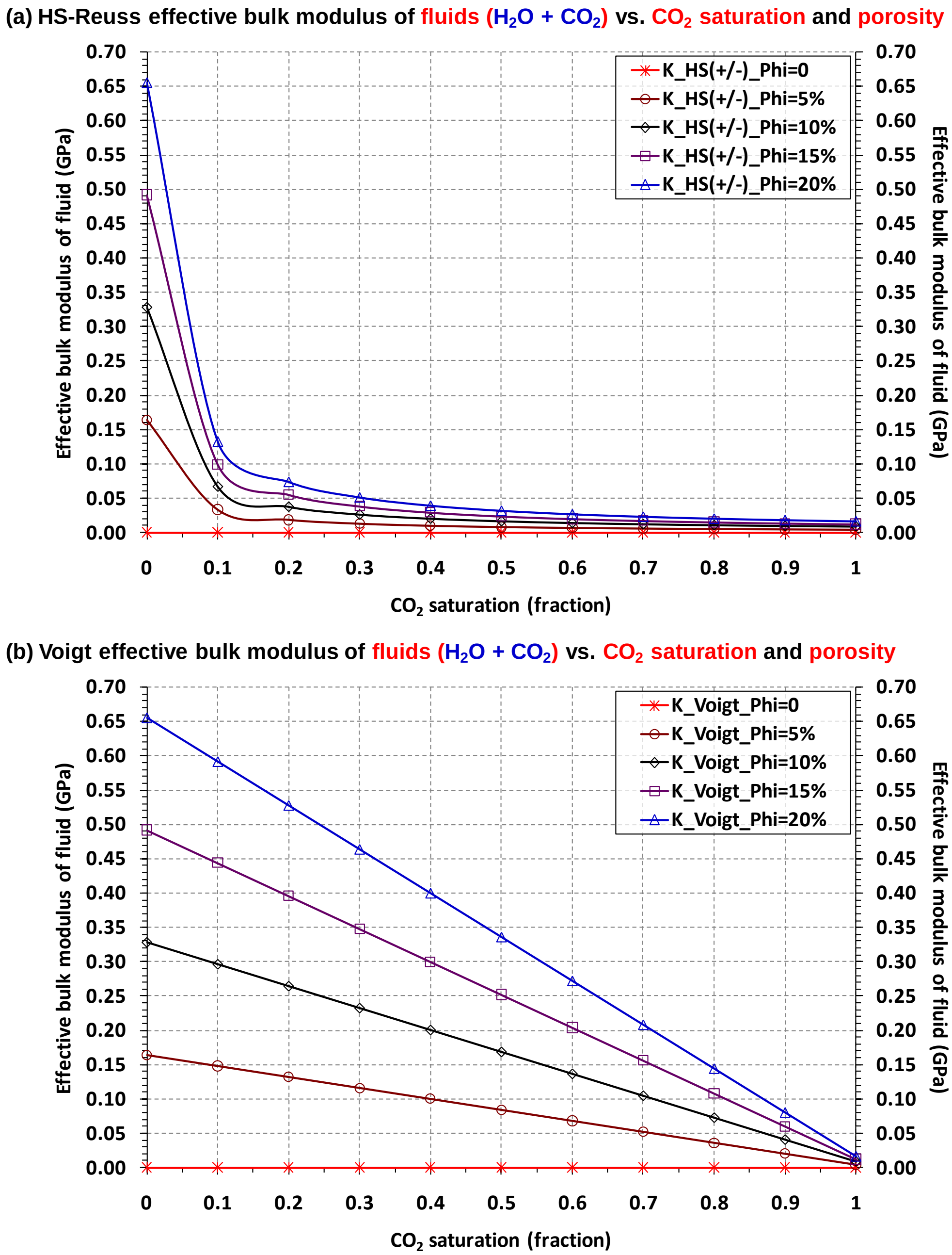

Figure 5-16: Effective bulk modulus (K) of multi-phase fluid (Case I in Table 5-1) as a function of CO_2 saturation and porosity (Phi) using: (a) Reuss and Hashin-Shtrikman averages, and (b) Voigt average. Note that the HS average is exactly equal to the Reuss bound

5.3.2.5 Effective Density of Minerals and Fluids Mixtures

The bulk density of a medium is a function of its constituents, i.e. the type of minerals and fluids present in the system. It can be calculated using an arithmetic average of the separate constituents as dictated by mass balance through the following relation (Batzle and Wang, 1992):

$$\rho_{\text{saturated}} = (1-\phi)\rho_{\text{mineral}} + \phi\rho_{\text{fluid}} \tag{9.29}$$

where the mineral density (ρ_{mineral}) is given by:

$$\rho_{\text{mineral}} = \sum_{i=1}^{n} \nu_i \rho_i \tag{9.30}$$

Similarly, the density of the pore fluids (ρ_{fluid}) can be calculated using (Batzle and Wang, 1992):

$$\rho_{\text{fluid}} = \sum_{i=1}^{n} S_i \rho_i \tag{9.31}$$

where ν_i is the volume fraction of the i^{th} mineral constituent, S_i is the saturation corresponding to the i^{th} fluid phase, and ρ_i is the density of the i^{th} mineral (Equation (9.30)) or i^{th} fluid (Equation (9.31)) in kg/m^3. Equation (9.29) can be used to compute the effective bulk density of the system in its initial ($\rho_{\text{fluid}}^{\text{initial}}$) and new saturation ($\rho_{\text{fluid}}^{\text{new}}$) status by using the appropriate volume (ν_i) and saturation (S_i) fractions as well as density (ρ_i) that reflect the type of minerals, fluids and their respective fraction. Figure 5-17 illustrates that the inverse proportionality between the density of the multi-phase mineral-fluid mixture on one hand and the porosity and CO_2 saturation on the other.

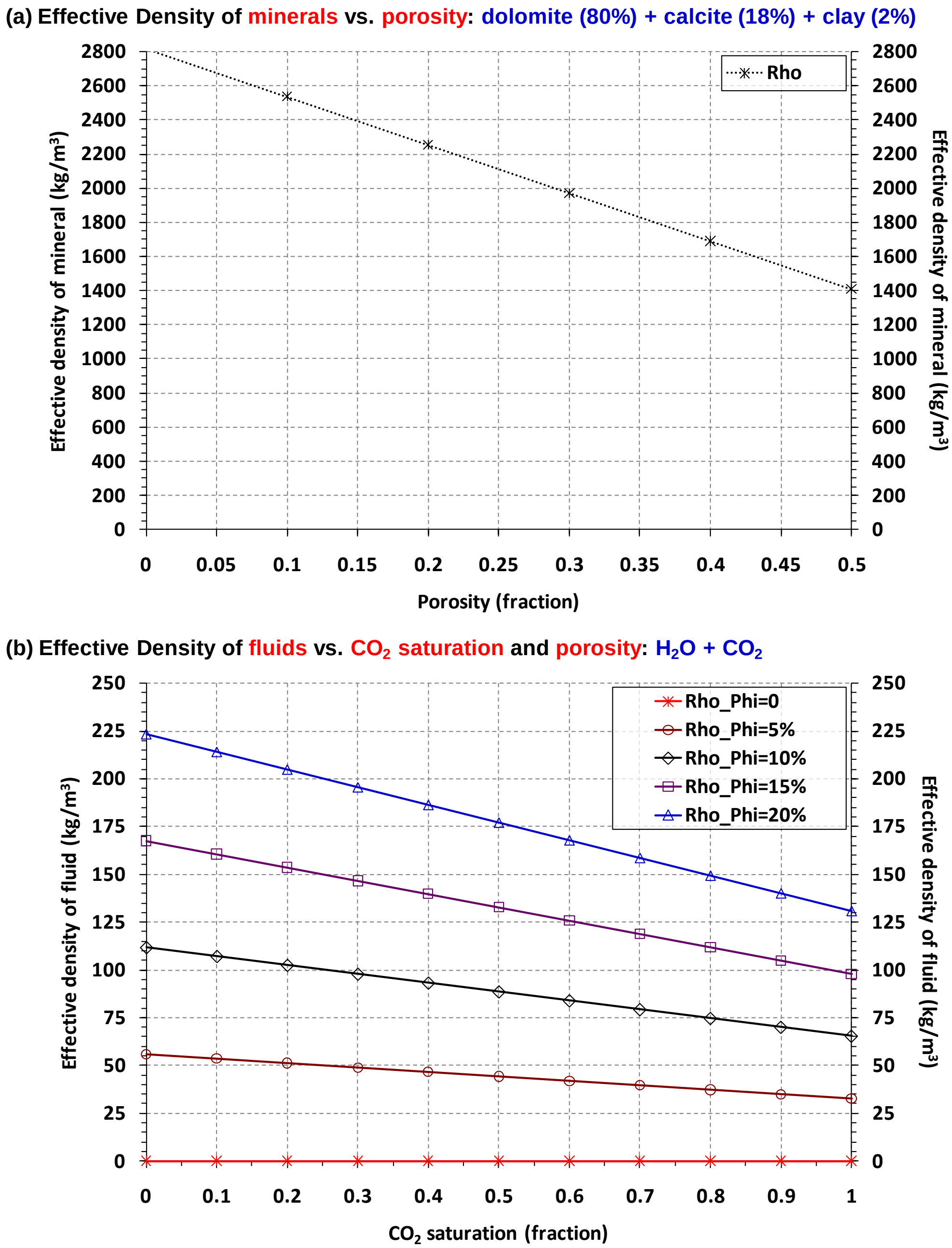

Figure 5-17: Effective density (Rho) of (a) multi-phase mineral as a function of porosity (Phi) and, (b) multi-phase fluid (Case I in Table 5-1) as a function of CO_2 saturation and porosity.

5.3.2.6 Effective Moduli of Minerals and Fluid Mixtures: Heuristic Approach

Now that the mineral and fluid components were independently investigated, the next step would be to predict how the effective elastic moduli and density of the mineral-fluid mixture would be affected by the CO_2 replacement of the in-situ fluid using the Gassmann formulation. But first, the effective moduli and density were modelled in terms of CO_2 saturation and porosity using the Hashin-Shtrikman formulae and the results are displayed in Figure 5-18 and Figure 5-19, respectively.

As for the bulk modulus, the upper bound shows little sensitivity whereas the lower bound exhibits larger response to CO_2 replacement (Figure 5-18 (a)). Furthermore, the bounds and their average are affected by the first 20-30% increase in porosity after which they appear to have reached a plateau. The shear modulus, on the other hand is sensitive to the fraction of pore space, i.e. porosity, but not to the change in fluid saturation, i.e. CO_2 replacement[60] (Figure 5-18 (b)). This observation holds for the upper and lower bounds as well as their average. The estimated change in the effective density of the mineral-fluid mixture shows a gradual decrease with an increase in both CO_2 saturation and porosity (Figure 5-19). Of course, the Hashin-Shtrikman modelling discussed here is purely theoretical. Nonetheless, it seems to provide a glimpse of the complex nature of the rock-fluid interaction and the many possible forms it might manifest itself in.

[60] This follows from the fact that the shear modulus of fluid is 0. Thus, the shear modulus is often referred to as lithology index whereas the bulk modulus, which is sensitive to both lithology and fluid, is called fluid index.

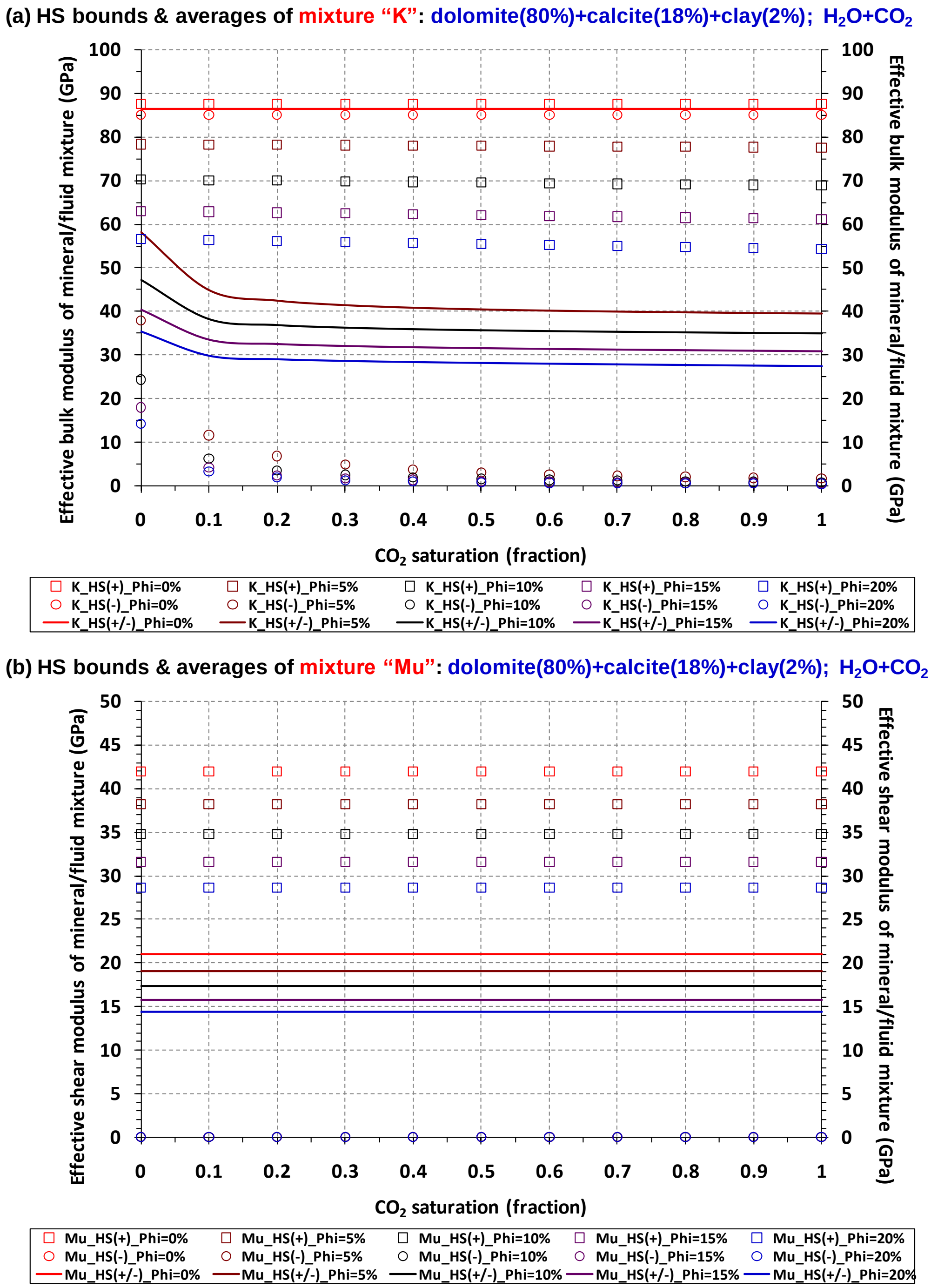

Figure 5-18: Effective (a) bulk and (b) shear moduli of the mineral-fluid mixture as a function of CO_2 saturation and porosity using Hashin-Shtrikman bounds and averages. HS(+) refers to the upper bound while HS(-) designates the lower bound, which is associated with uniform saturation; HS(+/-) is the average of the two. K: bulk modulus (GPa), Mu: shear modulus (GPa). The associated change in density is illustrated in the next figure.

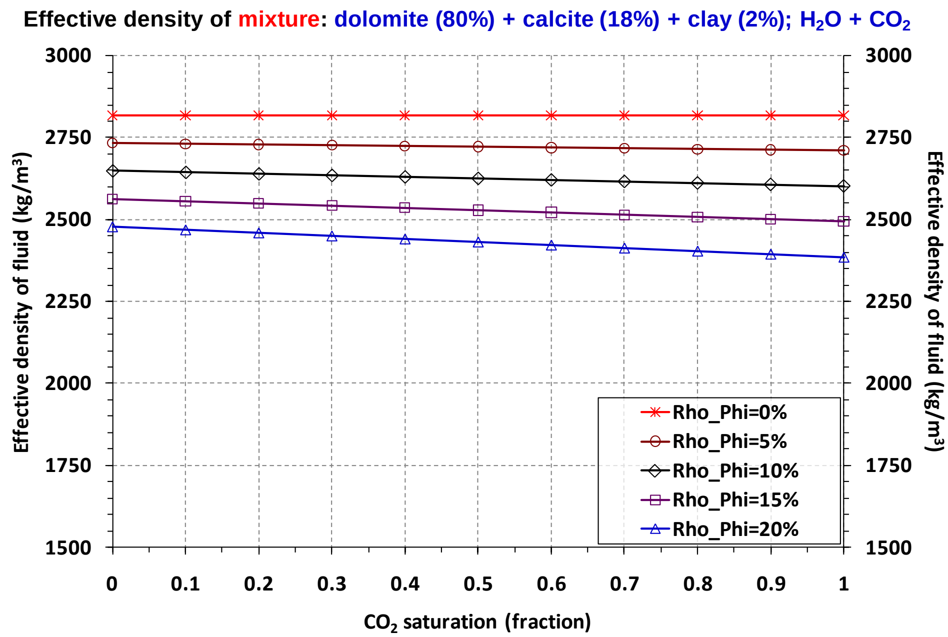

Figure 5-19: Effective density (Rho) of the mineral-fluid mixture as a function of CO_2 saturation and porosity.

5.3.2.7 Gassmann FSM Results

The final step in the implementation of the adopted FSM was to predict the change in the P-wave speed, S-wave speed and density of the Nisku Formation by incorporating the data from the three chosen wells (Table 5-1). Figure 5-20, Figure 5-21 and Figure 5-22 show results associated with the FSM on the water source well (1F1-11-29-45-2W5), well 100-10-21-50-2W5 and well 100-10-05-52-2W5 assuming uniform saturation, i.e. Case I in Table 5-1. In each case, the P-wave speed (α), S-wave speed (β), density (ρ), acoustic impedance (I_p) and shear impedance (I_s) are modelled as a function of CO_2 saturation in the Nisku Formation. In addition, the change in some of the elastic properties, namely Poisson's ratio (σ), α/β, Lambda-Rho ($\lambda\rho$) and Mu-Rho ($\mu\rho$), is displayed in the accompanying table. Interestingly, the change in the elastic properties at the water source well as a result of CO_2-brine replacement is rather small even though it suggested that the reservoir quality is good. The results from the other two wells, on the other hand, are very much alike and suggest a stronger response to the CO_2-brine fluid substitution process.

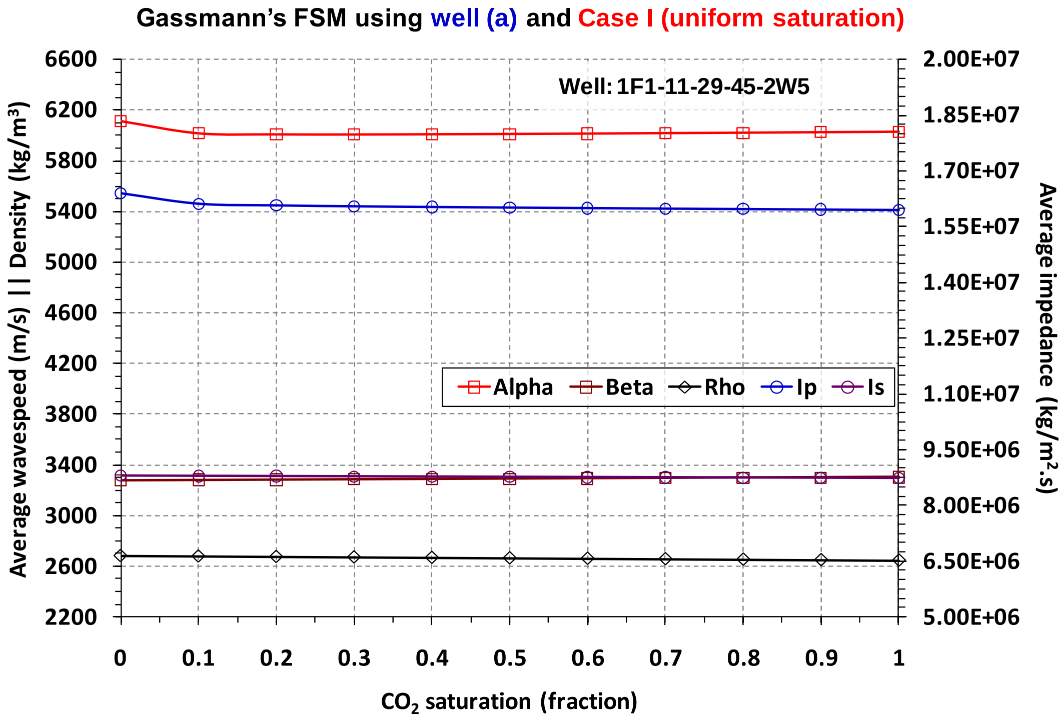

S_{CO2}	$\Delta\rho$ (%)	$\Delta\alpha$ (%)	$\Delta\beta$ (%)	$\Delta(\alpha/\beta)$	$\Delta\sigma$ (%)	ΔI_p (%)	ΔI_s (%)	$\Delta\lambda\rho$(%)	$\Delta\mu\rho$ (%)
0	0	0	0	0	0	0	0	0	0
10	-0.14	-1.57	0.07	-1.63	-3.23	-1.70	-0.07	-7.76	-0.14
20	-0.28	-1.70	0.14	-1.84	-3.66	-1.98	-0.14	-8.84	-0.28
30	-0.42	-1.72	0.21	-1.92	-3.82	-2.12	-0.21	-9.34	-0.42
40	-0.55	-1.69	0.28	-1.96	-3.91	-2.23	-0.28	-9.66	-0.55
50	-0.69	-1.65	0.35	-1.99	-3.97	-2.33	-0.35	-9.91	-0.69
60	-0.83	-1.60	0.42	-2.01	-4.01	-2.42	-0.42	-10.11	-0.83
70	-0.97	-1.54	0.49	-2.02	-4.03	-2.50	-0.49	-10.30	-0.97
80	-1.11	-1.48	0.56	-2.03	-4.05	-2.57	-0.56	-10.47	-1.11
90	-1.25	-1.42	0.63	-2.04	-4.07	-2.65	-0.62	-10.63	-1.25
100	-1.38	-1.36	0.70	-2.04	-4.08	-2.73	-0.69	-10.79	-1.38

Figure 5-20: The result of the FSM on the water source well (1F1-11-29-45-2W5) showing the average P-wave speed (α), S-wave speed (β), density (ρ), the acoustic impedance (I_p), and shear impedance (I_s) of the Nisku Formation as a function of CO_2 saturation (S_{CO2}). The accompanying table shows the numerical values of the percentage change (Δ%) in these and other elastic parameters, namely α/β wavespeeds ratio, Poisson's ratio (σ), Lambda-Rho ($\lambda\rho$) and Mu-Rho ($\mu\rho$). The modelling parameters and the well location are displayed in Table 5-1 and Figure 5-11, respectively.

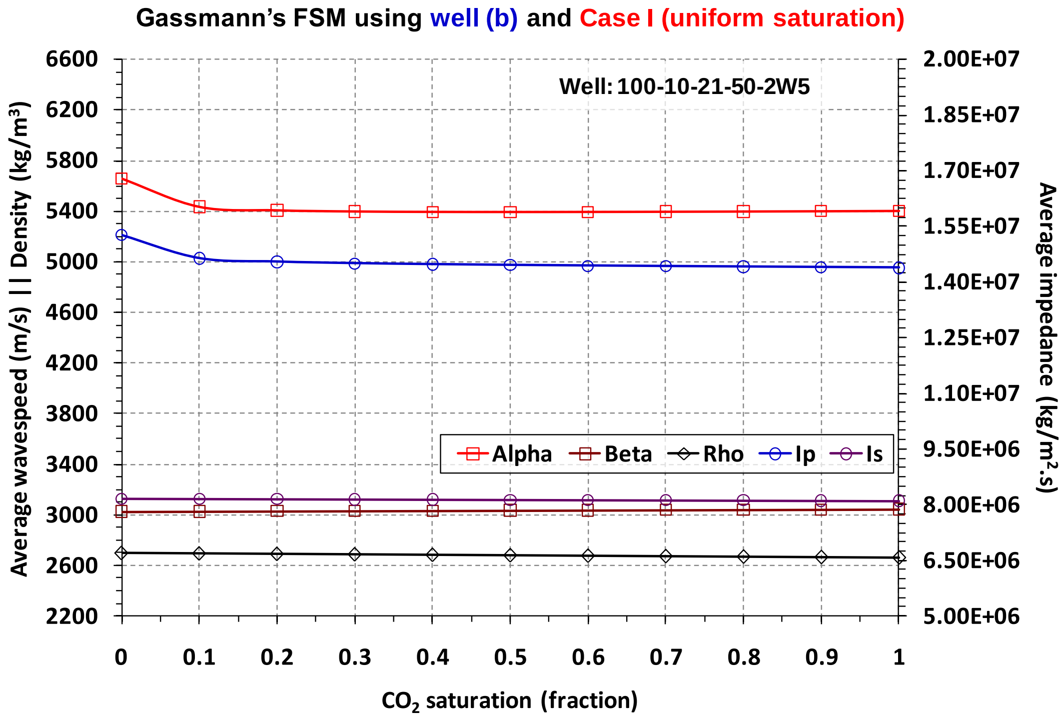

S_{CO2}	$\Delta\rho$ (%)	$\Delta\alpha$ (%)	$\Delta\beta$ (%)	$\Delta(\alpha/\beta)$	$\Delta\sigma$ (%)	ΔI_p (%)	ΔI_s (%)	$\Delta\lambda\rho$(%)	$\Delta\mu\rho$ (%)
0	0	0	0	0	0	0	0	0	0
10	-0.12	-3.96	0.06	-4.02	-8.28	-4.08	-0.06	-18.51	-0.12
20	-0.25	-4.46	0.12	-4.57	-9.55	-4.69	-0.12	-21.06	-0.25
30	-0.37	-4.61	0.19	-4.79	-10.06	-4.97	-0.19	-22.13	-0.37
40	-0.50	-4.67	0.25	-4.91	-10.34	-5.15	-0.25	-22.75	-0.50
50	-0.62	-4.69	0.31	-4.98	-10.51	-5.28	-0.31	-23.17	-0.62
60	-0.74	-4.68	0.37	-5.03	-10.63	-5.39	-0.37	-23.48	-0.74
70	-0.87	-4.65	0.44	-5.07	-10.72	-5.48	-0.43	-23.74	-0.87
80	-0.99	-4.62	0.50	-5.10	-10.78	-5.57	-0.50	-23.95	-0.99
90	-1.12	-4.58	0.56	-5.12	-10.84	-5.65	-0.56	-24.14	-1.12
100	-1.24	-4.54	0.63	-5.14	-10.88	-5.73	-0.62	-24.32	-1.24

Figure 5-21: The result of the FSM on well 100-10-21-50-2W5 showing the average P-wave speed (α), S-wave speed (β), density (ρ), the acoustic impedance (I_p), and shear impedance (I_s) of the Nisku Formation as a function of CO_2 saturation (S_{CO2}). The accompanying table shows the numerical values of the percentage change (Δ%) in these and other elastic parameters, namely α/β wavespeeds ratio, Poisson's ratio (σ), Lambda-Rho ($\lambda\rho$) and Mu-Rho ($\mu\rho$). The modelling parameters and the well location are displayed in Table 5-1 and Figure 5-11, respectively.

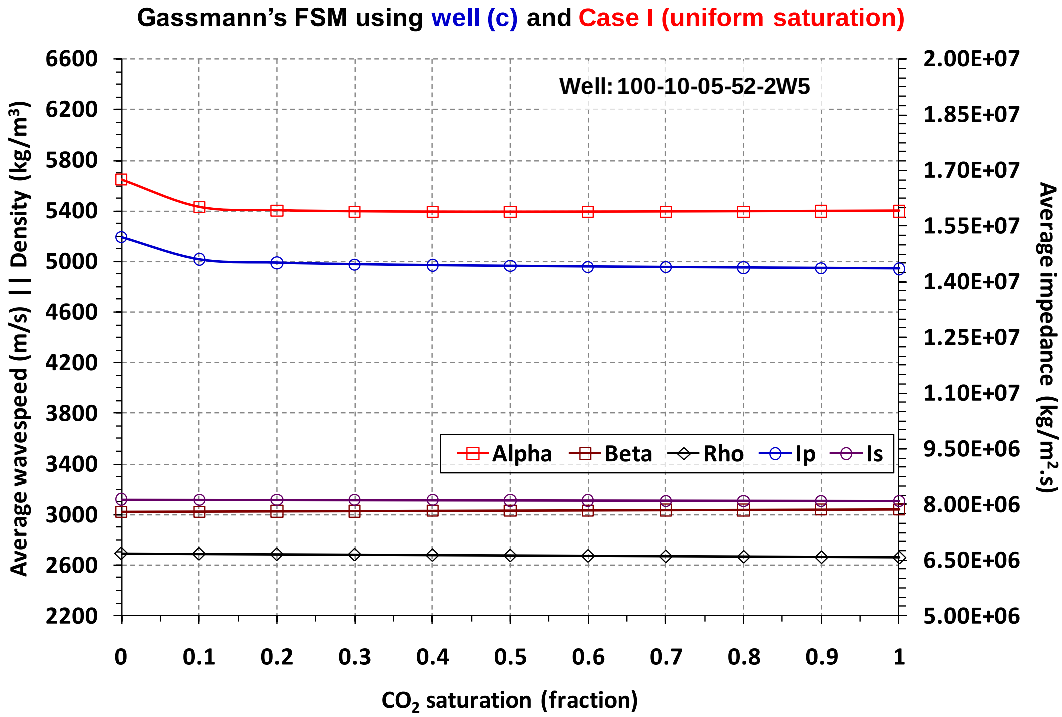

S_{CO2}	$\Delta\rho$ (%)	$\Delta\alpha$ (%)	$\Delta\beta$ (%)	$\Delta(\alpha/\beta)$	$\Delta\sigma$ (%)	ΔI_p (%)	ΔI_s (%)	$\Delta\lambda\rho$(%)	$\Delta\mu\rho$ (%)
0	0	0	0	0	0	0	0	0	0
10	-0.13	-3.91	0.06	-3.97	-8.18	-4.03	-0.06	-18.29	-0.13
20	-0.26	-4.39	0.13	-4.51	-9.42	-4.64	-0.13	-20.81	-0.26
30	-0.38	-4.55	0.19	-4.73	-9.92	-4.91	-0.19	-21.87	-0.38
40	-0.51	-4.60	0.26	-4.84	-10.19	-5.09	-0.26	-22.47	-0.51
50	-0.64	-4.61	0.32	-4.92	-10.36	-5.22	-0.32	-22.89	-0.64
60	-0.77	-4.60	0.38	-4.96	-10.48	-5.33	-0.38	-23.21	-0.77
70	-0.89	-4.57	0.45	-5.00	-10.56	-5.42	-0.45	-23.46	-0.89
80	-1.02	-4.54	0.51	-5.03	-10.62	-5.51	-0.51	-23.68	-1.02
90	-1.15	-4.50	0.58	-5.05	-10.68	-5.59	-0.58	-23.87	-1.15
100	-1.28	-4.45	0.64	-5.07	-10.72	-5.67	-0.64	-24.04	-1.28

Figure 5-22: The result of the FSM on well 100-10-05-52-2W5 showing the average P-wave speed (α), S-wave speed (β), density (ρ), the acoustic impedance (I_p), and shear impedance (I_s) of the Nisku Formation as a function of CO_2 saturation (S_{CO2}). The accompanying table shows the numerical values of the percentage change (Δ%) in these and other elastic parameters, namely α/β wavespeeds ratio, Poisson's ratio (σ), Lambda-Rho ($\lambda\rho$) and Mu-Rho ($\mu\rho$). The modelling parameters and the well location are displayed in Table 5-1 and Figure 5-11, respectively. The results presented here show the first of the four FSM realizations on this well (Table 5-2).

There are several general observations that can be made:

- The largest change in the elastic properties and, therefore, the highest sensitivity corresponds to the first 20-30% increase in CO_2 saturation. This follows from the change in the effective bulk modulus of the fluids mixture.
- After ~ 30% CO_2 saturation, the absolute magnitude of the relative change in the elastic properties (ρ, β, α/β, σ, I_p, I_s, $\lambda\rho$, $\mu\rho$) reaches a plateau and continues to only gradually increase as the CO_2 saturation is increased.
- The only exception is the P-wave speed (α) where the absolute magnitude actually starts to decrease at about 50% CO_2 saturation. This pattern is observed by many authors (Avseth et al., 2005; Lumley et al., 2008; Vanorio et al., 2010) and is attributed to the rate at which the bulk modulus and density change as a function of CO_2 saturation where the decrease in the bulk modulus dominates at low to intermediate CO_2 saturation whereas the change in density tends to dominate at intermediate to high saturation.
- The results suggest that in order to achieve an optimum amplitude-based seismic interpretation, one should consider the coupled wavespeed-density effect, i.e. impedance, as the seismic wavefield responds to change in both properties. $\lambda\rho$ shows higher sensitivity but, eventually, the strongest relative change is associated with the cross-product of $\lambda\rho$ and $\mu\rho$.
- As for time-based interpretation, the results show what has already been observed through various studies (Smith et al., 20003; Han and Batzle, 2004; Avseth et al., 2005) that the P-wave speed is far more sensitivity to the CO_2-brine replacement than the S-wave speed.
- The lesser sensitivity of S-wave speed follows from the fact that the shear modulus (μ) is sensitive to lithology and pore space but not to the type of fluid present. Since μ is assumed to be invariant during the FSM while density gradually decreases, this results in the observed diminutive increase in β. Hence, a better indication of time-change is obtained by coupling the P-wave speed and S-wave speed changes through their ratio, i.e. α/β.

- Poisson's ratio (σ) is a good gas indicator and, thus, exhibits a strong level of sensitivity toward the CO_2 saturation.

In order to achieve a better understanding of and account deterministically for the effects of some of the main variables influencing the Gassmann FSM. Four realizations were constructed using well (c), 100-10-05-52-2W. These four realizations are designated as cases and are summarized in Table 5-2. The first realization corresponds to the uniform saturation (Case I) that was shown in Figure 5-22. The results from Case I exhibit a modest yet - in principle - detectable change.

The magnitude and relative percentage change in the elastic properties at the final CO_2 saturation corresponding to the patchy-like saturation "Case II" depicted in the second realization (Figure 5-23) is smaller to that of the uniform saturation "Case I". However, they differ in the trajectory they take from the initial to the final saturation. Case I shows a sudden and large relative change at low CO_2 saturation that reaches a plateau rapidly whereas the relative change in Case II is more subtle and gradual but has a consistent monotonic trend over the full saturation range. Obviously, Case II poses a formidable challenge in time-lapse seismic monitoring whether using the surface seismic or VSP methods, especially when taking into account that it is implausible to saturate the reservoir with more than about 50% CO_2. Nonetheless, it should be noted that the patchy-like saturation was modelled using the Voigt average (Section 5.3.2.4), which gives the stiffest possible effective modulus of the fluid mixture (Mavko et al., 2003).

The results from the third FSM realization (Case III), which investigates the effect of the stiffness of the mineral constituents on the predicted elastic properties, might at first might seem imperceptive as one would expect that softening the minerals constituents would cause the effect of the CO_2-brine replacement to be more sensible. However, the results appear to concur with the modelling results presented earlier in this section (Figure 5-12 and Figure 5-13). An inference that can be drawn from those results is that there is a relationship between the magnitude of the change in the effective moduli and density of the medium and how elastically different the constituents are. In other words, it seems that both the absolute magnitude and relative percentage change in the effective elastic properties decrease as the difference in the elastic properties between the individual constituents comprising the mineral and fluid mixtures becomes smaller. This should not be confused with the stiffness of the porous rock frame (K_ϕ) where a stiffer rock exhibits little sensitivity to the CO_2-fluid replacement in contrast to softer skeleton. Case III presents an example of what some authors might call internal inconsistency in the Gassmann FSM due to improper choice of the minerals constituents.

The effect of in-situ gas on the FSM is illustrated in the fourth realization "Case IV" where even a small quantity of native gas could substantially reduce the already small magnitude of the absolute and relative percentage change in the elastic properties (Figure 5-25).

Obviously, only the first realization corresponding to uniform saturation without any significant amount of in-situ gas "Case I" (Figure 5-22) seems to produce a discernable time-lapse anomaly that should be detectable by the surface seismic and VSP methods at realistic CO_2 saturations.

Table 5-2: Outline of four realizations of the Gassmann FSM using the water source well (100-10-05-52-2W5). The results are shown in the corresponding figures. See Table 5-1 for the modelling parameters and Figure 5-11 for the well location. The seismic response associated with the Cases I and II will be investigated in the next Section using offset-dependent reflectivity modelling.

Realization	Description	Comment
Case I: uniform saturation	Data as presented in Table 5-1. The effective moduli of mineral and fluid mixture were, independently, calculated using $HS^{\pm}$ average.	Small time-lapse change. See Figure 5-22.
Case II: Patchy-like saturation	Data as presented in Table 5-1. The effective moduli of mineral were calculated using $HS^{\pm}$ average whereas the Voigt average was invoked in deducing the effective modulus of fluid mixture.	Same as above but change is gradual. See Figure 5-23 .
Case III: uniform saturation with minerals softened	Data as presented in Table 5-1, i.e. similar to Case I except that the effective moduli and density of the minerals were reduced by 20% and 5%, respectively.	Smaller change than Case I. See Figure 5-24.
Case IV: uniform saturation with in-situ gas	Data as presented in Table 5-1. The effective moduli of mineral and fluid mixture were, independently, calculated using $HS^{\pm}$ average.	Very small time-lapse change. See Figure 5-25.

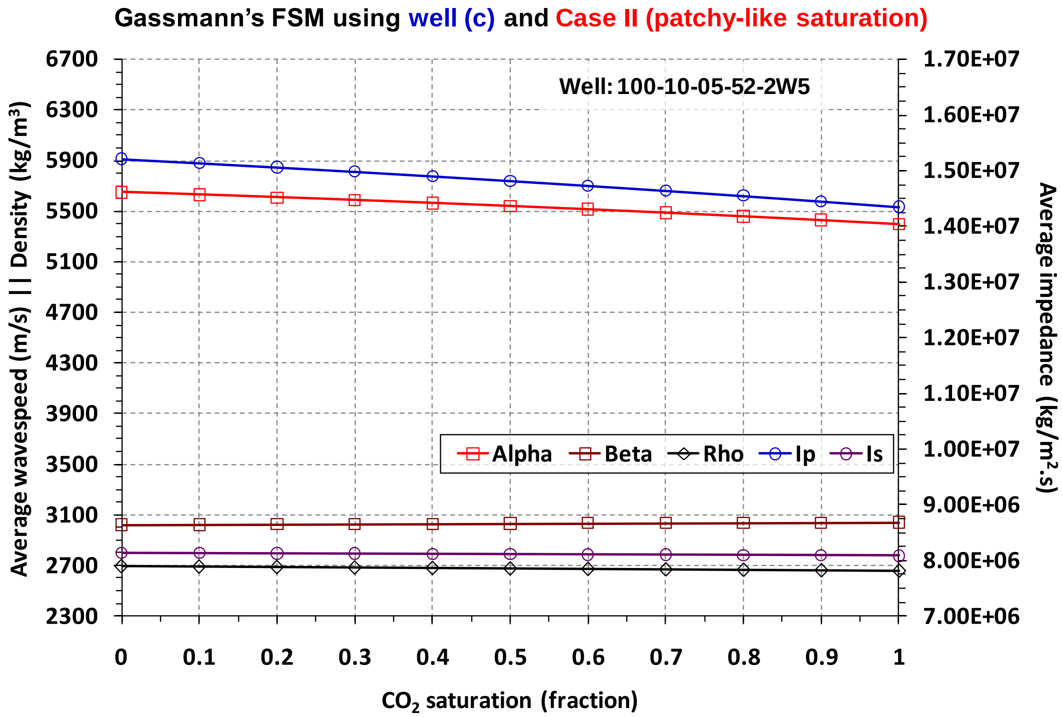

S_{CO2}	$\Delta\rho$ (%)	$\Delta\alpha$ (%)	$\Delta\beta$ (%)	$\Delta(\alpha/\beta)$	$\Delta\sigma$ (%)	ΔI_p (%)	ΔI_s (%)	$\Delta\lambda\rho$(%)	$\Delta\mu\rho$ (%)
0	0	0	0	0	0	0	0	0	0
10	-0.12	-0.36	0.06	-0.42	-0.80	-0.48	-0.06	-2.08	-0.12
20	-0.25	-0.74	0.12	-0.86	-1.64	-0.98	-0.12	-4.24	-0.25
30	-0.37	-1.13	0.19	-1.32	-2.54	-1.50	-0.19	-6.46	-0.37
40	-0.50	-1.55	0.25	-1.79	-3.49	-2.04	-0.25	-8.75	-0.50
50	-0.62	-1.98	0.31	-2.29	-4.52	-2.59	-0.31	-11.12	-0.62
60	-0.74	-2.44	0.37	-2.81	-5.61	-3.17	-0.37	-13.57	-0.74
70	-0.87	-2.93	0.44	-3.35	-6.78	-3.77	-0.43	-16.11	-0.87
80	-0.99	-3.44	0.50	-3.92	-8.04	-4.39	-0.50	-18.75	-0.99
90	-1.12	-3.97	0.56	-4.51	-9.40	-5.05	-0.56	-21.48	-1.12
100	-1.24	-4.54	0.63	-5.14	-10.88	-5.73	-0.62	-24.32	-1.24

Figure 5-23: The result of the second FSM realization (Table 5-2) on well 100-10-05-52-2W5 showing the average of the P-wave speed (α), S-wave speed (β), density (ρ), the acoustic impedance (I_p), and shear impedance (I_s) of the Nisku Formation as a function of CO_2 saturation (S_{CO2}). The accompanying table shows the numerical values of the percentage change (Δ%) in these and other elastic parameters, namely α/β wavespeeds ratio, Poisson's ratio (σ), Lambda-Rho ($\lambda\rho$) and Mu-Rho ($\mu\rho$). The modelling parameters and the well location are displayed in Table 5-1 and Figure 5-11, respectively.

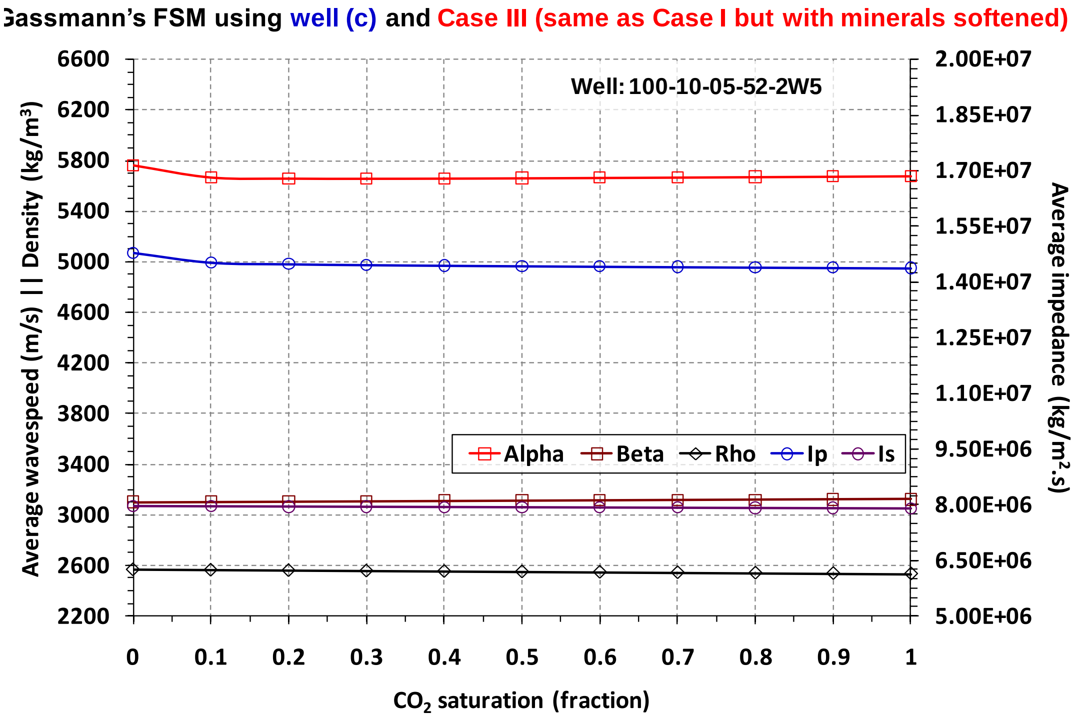

S_{CO2}	$\Delta\rho$ (%)	$\Delta\alpha$ (%)	$\Delta\beta$ (%)	$\Delta(\alpha/\beta)$	$\Delta\sigma$ (%)	ΔI_p (%)	ΔI_s (%)	$\Delta\lambda\rho$(%)	$\Delta\mu\rho$ (%)
0	0	0	0	0	0	0	0	0	0
10	-0.13	-1.59	0.07	-1.65	-3.33	-1.71	-0.07	-7.91	-0.13
20	-0.26	-1.73	0.13	-1.86	-3.78	-1.99	-0.13	-9.02	-0.26
30	-0.39	-1.75	0.20	-1.94	-3.96	-2.14	-0.20	-9.52	-0.39
40	-0.52	-1.73	0.26	-1.99	-4.05	-2.24	-0.26	-9.85	-0.52
50	-0.65	-1.70	0.33	-2.02	-4.11	-2.34	-0.33	-10.09	-0.65
60	-0.78	-1.65	0.39	-2.03	-4.15	-2.42	-0.39	-10.30	-0.78
70	-0.91	-1.60	0.46	-2.05	-4.18	-2.50	-0.46	-10.48	-0.91
80	-1.04	-1.54	0.53	-2.06	-4.20	-2.57	-0.52	-10.64	-1.04
90	-1.17	-1.49	0.59	-2.07	-4.22	-2.64	-0.59	-10.80	-1.17
100	-1.30	-1.43	0.66	-2.07	-4.24	-2.71	-0.65	-10.95	-1.30

Figure 5-24: The result of the third FSM realization (Table 5-2) on well 100-10-05-52-2W5 showing the average of the P-wave speed (α), S-wave speed (β), density (ρ), the acoustic impedance (I_p), and shear impedance (I_s) of the Nisku Formation as a function of CO_2 saturation (S_{CO2}). The accompanying table shows the numerical values of the percentage change (Δ%) in these and other elastic parameters, namely α/β wavespeeds ratio, Poisson's ratio (σ), Lambda-Rho ($\lambda\rho$) and Mu-Rho ($\mu\rho$). The modelling parameters and the well location are displayed in Table 5-1 and Figure 5-11, respectively.

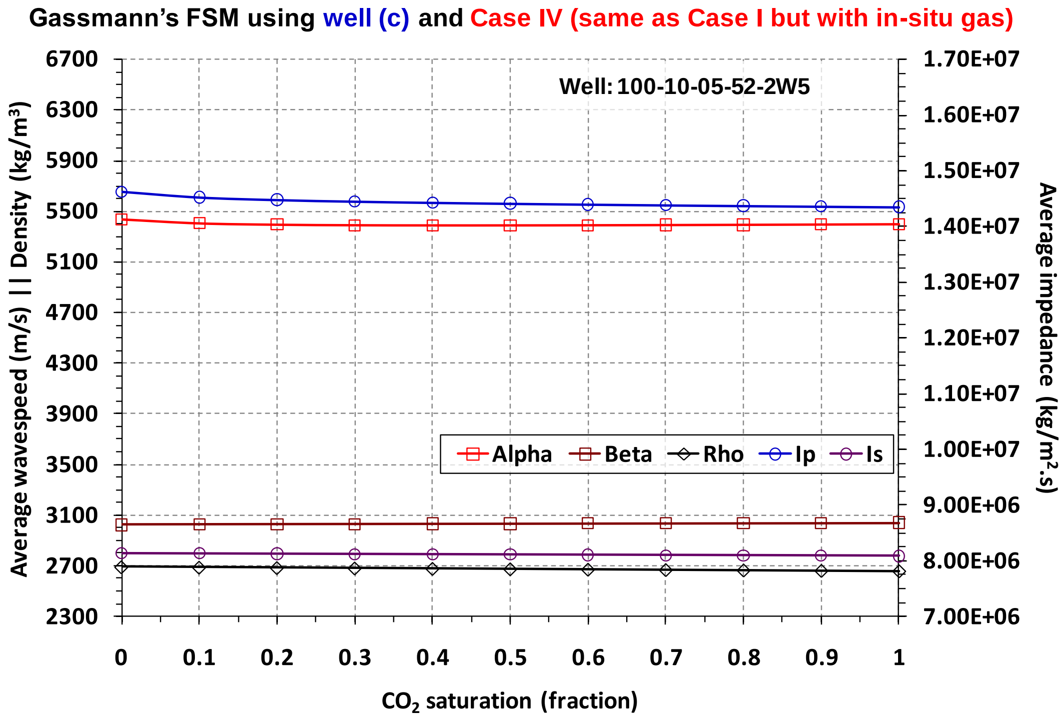

S_{CO2}	$\Delta\rho$ (%)	$\Delta\alpha$ (%)	$\Delta\beta$ (%)	$\Delta(\alpha/\beta)$	$\Delta\sigma$ (%)	ΔI_p (%)	ΔI_s (%)	$\Delta\lambda\rho$(%)	$\Delta\mu\rho$ (%)
0	0	0	0	0	0	0	0	0	0
10	-0.12	-0.58	0.06	-0.64	-1.53	-0.70	-0.06	-3.46	-0.12
20	-0.23	-0.78	0.12	-0.89	-2.14	-1.01	-0.12	-4.88	-0.23
30	-0.35	-0.86	0.17	-1.03	-2.48	-1.20	-0.17	-5.69	-0.35
40	-0.46	-0.88	0.23	-1.11	-2.69	-1.34	-0.23	-6.23	-0.46
50	-0.58	-0.88	0.29	-1.17	-2.83	-1.45	-0.29	-6.64	-0.58
60	-0.69	-0.87	0.35	-1.21	-2.93	-1.55	-0.35	-6.96	-0.69
70	-0.81	-0.84	0.41	-1.24	-3.01	-1.64	-0.40	-7.23	-0.81
80	-0.92	-0.81	0.46	-1.27	-3.07	-1.72	-0.46	-7.47	-0.92
90	-1.04	-0.77	0.52	-1.29	-3.12	-1.80	-0.52	-7.68	-1.04
100	-1.15	-0.73	0.58	-1.30	-3.16	-1.87	-0.58	-7.87	-1.15

Figure 5-25: The result of the fourth FSM realization (Table 5-2) on well 100-10-05-52-2W5 showing the average of the P-wave speed (α), S-wave speed (β), density (ρ), the acoustic impedance (I_p), and shear impedance (I_s) of the Nisku Formation as a function of CO_2 saturation (S_{CO2}). The accompanying table shows the numerical values of the percentage change (Δ%) in these and other elastic parameters, namely α/β wavespeeds ratio, Poisson's ratio (σ), Lambda-Rho ($\lambda\rho$) and Mu-Rho ($\mu\rho$). The modelling parameters and the well location are displayed in Table 5-1 and Figure 5-11, respectively.

Table 5-3 shows a comparison of the in-situ elastic properties as well as K_ϕ and ϕ from the three wells used in the Gassmann FSM (Table 5-1). The data suggests that there is a high level of similarity between these wells. Moreover, there is clearly a direct proportionality between the magnitude of the elastic moduli and ϕ (and K_ϕ) which agrees with the theoretical aspects of the Gassmann relation (Berryman, 1999; Smith et al., 2003). Nonetheless, a question that emerges is why the FSM results suggest a smaller change at the water source well although it has a slightly higher porosity and seems to exhibit good reservoir quality?

It is uncertain whether this small response is due to intrinsic reservoir properties or is a result of the rough well condition and its effect on the quality of the measured logs and the derived density. Another observation that follows from the previous discussion is the direct proportionality between the magnitude of the elastic moduli and porosity. Furthermore, discussions with the WASP petrophysical team indicate that the high permeability rather than high porosity could be responsible for the observed high production volume of brine, thus, causing the well to be designated as good quality water source well. In any case, the small changes in the elastic properties at the water source well predicted through the FSM seem to reflect the stiffness of the in-situ saturated bulk modulus and the derived K_ϕ.

Table 5-3: Comparison between the elastic moduli (K and μ), density (ρ) and porosity (ϕ) as estimated from the well logs reflective of in-situ conditions before the fluid substitution modelling. The comment column indicates, qualitatively, the magnitude of the time-lapse change after the CO_2 fluid replacement. The quantitative results are shown in the corresponding figures. See Section 5.3.2.1 for definition of these parameters and Figure 5-11 for the wells location.

Well	$K^{\text{in-situ}}_{\text{saturated}}$ (GPa)	$\mu^{\text{in-situ}}_{\text{saturated}}$ (GPa)	$\rho^{\text{in-situ}}_{\text{saturated}}$ (kg/m^3)	K_ϕ (GPa)	ϕ (%)	Comment
(a) 1F1-11-29-45-2W5	65.64	28.83	2679	57.59	8.2	Very small time-lapse change. See Figure 5-20.
(b) 100-10-21-50-2W5	55.96	24.58	2693	44.44	7.4	Modest time-lapse change. See Figure 5-21.
(c) 100-10-05-52-2W5	56.20	24.68	2697	44.53	7.2	Similar to Well (b) above. See Figure 5-22.

In general, the shear modulus is sensitive to changes in lithology, whether it is caused by variation in lithofacies (e.g. shale content) or the volume of pore space (i.e. porosity). However, based on information provided by other WASP team members, it is thought that enhanced aquifer conditions as demonstrated by production (Lavoie, 2009) and other data (Eisinger and Jensen, 2009; SCG, 2009; Shevalier et al., 2009) is the main dynamic shaping the magnitude of the elastic moduli. Furthermore, there is an inclination toward extending this observation to the rest of the focus area since there is no evidence to suggest a sudden and significant variation in the shale content within and nearby the local-scale study area. In contrast, diagenetic processes, such as dissolution and magnesium replacement, are quite common in the area (SCG, 2009). Such processes are known to increase the volume of the pore space.

5.3.2.8 Considerations

Recall that three parameters are required in order to predict the effective elastic moduli of a mixture: (1) the elastic moduli of the individual constituents, (2) their volume fraction, and (3) the geometry describing how these constituents are arranged with respect to each other. In the current study, only two parameters could be estimated, namely the elastic moduli and their volume fraction. Thus, only the average of the upper and lower bounds (Figure 5-14 and Figure 5-16) was used in the FSM. Furthermore, in order to mitigate the other limiting aspects of the Gassmann, e.g. anisotropy and anelasticity, additional information and mathematical models are required that incorporate knowledge about entities such as the pore structure and the saturation distribution among other things. Unfortunately, such data were not available. Nonetheless, it could be argued that the implemented approach would provide a practical understanding of the anticipated changes in the elastic properties investigated.

One of the most important arguments arising in the implementation of the Gassmann relation is whether or not the shear modulus is dynamically changing as a result of interaction between supercritical CO_2 and the host rock. This is particularly important in carbonate rocks. Interestingly, the results from the geochemical modelling undertaken by the WASP geochemistry team (Shevalier et al., 2009) indicate that chemical reaction between supercritical CO_2 and the main minerals (i.e. dolomite and calcite) comprising about 98% of the Nisku Formation rock matrix is negligible. This is based on the aquifer conditions in the WASP study area over the simulated time shown in Figure 5-26 (a) and (b). Furthermore, any change in porosity due to such chemical reaction is insignificant as well over the first 50 years of CO_2 injection (Figure 5-26 (c)).

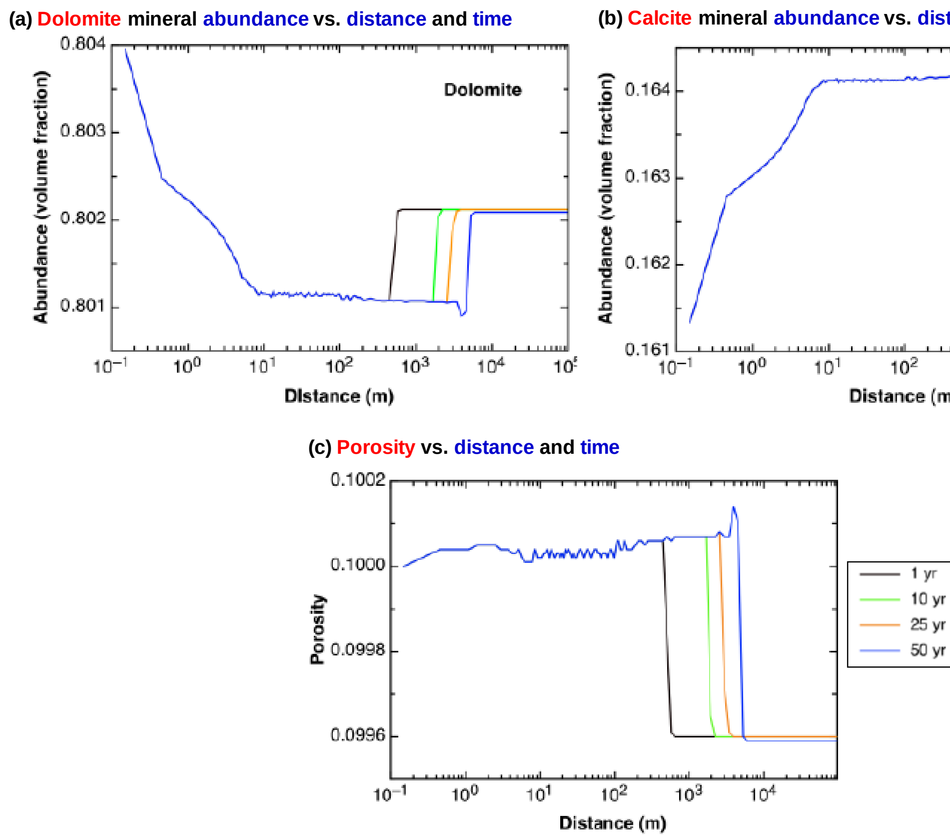

Figure 5-26: Change in (a) dolomite mineral abundance, (b) calcite mineral abundance, and (c) porosity as a function of radial distance and time following the commencement of CO_2 injection at a rate of 1 Mt/year. Couresty of Shevalier et al. (2009). Further information on the modelling parameters can be found in their WASP geochemical analysis report.

The results obtained using the parameters and the fluid substitution method discussed throughout Section 5.3.2 suggest that changes in the average acoustic impedance is - in principle – detectable[61] whereas changes in the shear impedance as a function of increasing CO_2 saturation is insignificant. Furthermore, the approach implemented, and hence the derived results, herein attempts at addressing but not

[61] Based on Case I, i.e. uniform saturation with no in-situ gases.

necessarily solving the many uncertainties and limitations involved in the Gassmann FSM. In order to minimize the errors caused by uncertainties in porosity, water saturation, fluid properties, or lithology, the data/parameters were derived, whenever possible, from the geological (Michael et al., 2008; SCG, 2009), petrophysical (Eisinger and Jensen, 2009), geochemical (Shevalier et al., 2009), and geomechanical (Nygaard, 2009a) analyses which were undertaken by other team members as part of WASP. This was followed by investigating the effect of the individual entities independently and collaboratively using numerical forward modelling. In addition, several realizations of the Gassmann FSM were synthesized.

In the succeeding forward ODR and ERFD modelling, only the time-lapse seismic response corresponding to Case I (uniform saturation) and Case II (patchy saturation) will be investigated as Case III (softened minerals) and Case IV (uniform saturation with in-situ gas) are considered to be unlikely scenarios. As for Case IV, geochemical analysis of fluid samples (Shevalier et al., 2009) did not show that a significant amount of in-situ gas is present in the Nisku aquifer. Furthermore, given the aquifer maturity, the relatively low porosity and negligible amount of gas, all these lead to the speculation that patchy saturation is unlikely to occur in a significant form (Sengupta, 2000; Smith et al., 2003). Smith et al. (2003) outlines the assumptions under which patchy saturation can be modelled whether using Voigt (1928), Hill (1963), or Brie et al (1995) relations. In summary, the assumptions are:

1. The fluids are distributed in patches that are much smaller than the seismic wavelength.
2. The patches do not allow the wave-induced pore pressure to equilibrate during the passage of the seismic wave.
3. The shear modulus is invariant and independent of the pore fluids.

Further discussion on patchy saturation can be found in Dvorkin and Nu (1998) and Mavko et al. (2003). In addition, Avseth et al. (2005) present a dimensional relation that could be used to draw a distinction between the uniform and patchy saturation based on the bulk modulus and viscosity of the most viscous fluid as well as permeability and seismic frequency.

5.3.3 Numerical Forward Seismic Modelling

The forward seismic modelling undertaking is divided into two sections: (1) offset-dependent reflectivity (ODR), and (2) exploding reflector finite-difference (ERFD) modelling. The first investigates the forward AVO response of the Nisku reflection through ray tracing and the Zoeppritz equations. This provided a localized yet a detailed understanding of the fundamental change in the seismic response due to CO_2-brine replacement as well as the CO_2 saturation and frequency effects. The second modelling scheme rendered a broader image that in a way resembles post-stack time-migrated 2-D seismogram. In the current context, "baseline" refers to the seismic response of the Nisku Formation when there is no CO_2, i.e. 0% CO_2 and 100% H_2O. The "monitor" refers to any of the saturation levels when CO_2-brine replacement had occurred in any proportion, i.e. 10-100% CO_2. In all the modelling schemes and scenarios, the simulated wavefield was assumed to be noise-free.

As illustrated by the FSM results under Section 5.3.2.7, it is evident that the change in the P-wave speed is the principle factor dictating whether or not a CO_2-induced time-lapse change is detectable or not in the current investigation. This holds for time-based attributes, i.e. P-wave speed induced time shift, and amplitude-based attributes, i.e. I_p and $\lambda\rho$, as demonstrated by the results from the first FSM realization on well 100-10-05-52-2W5 (Figure 5-22). The extremely small change in the PS-wave response seems only to complement that of the P-wave. Therefore, the forward modelling herein is dedicated to predicting the P-wave seismic response only.

5.3.3.1 Offset-dependent Reflectivity (ODR) Modelling

The variation in seismic amplitude with offset (AVO) of the Nisku reflection due to CO_2-brine replacement (in well 100-10-05-52-2W5) was modelled using a ray tracing algorithm (Section 3.5.4) employing the Zoeppritz equations (Section 3.3). Table 5-4 outlines the modelling parameters, the objectives, the various experiments and other relevant information. First, the frequency dependence of the AVO response was investigated using Ricker wavelets with two dominant frequencies: 30 Hz and 60 Hz. Then, the stacked responses corresponding to these dominant frequencies as well as that associated with patchy-like saturation using the 30 Hz Ricker wavelet were closely examined using amplitude and time-based seismic attributes. The responses were stacked to resemble that of a post-stack seismogram at a given CO_2 saturation. In all the experiments, the synthetic AVO traces were normal moveout (NMO) corrected to account for the difference in the reflection time due to the source-receiver offset.

The top panel in Figure 5-27 (a) illustrates the AVO response as a function of increasing CO_2 saturation in the case of uniform saturation (Figure 5-22) and the 30 Hz seismic wavelet. The corresponding seismic amplitude is plotted alongside in the bottom panel (blue curve). Clearly, there is proportionality between the seismic amplitude, or reflectivity, and offset which in this example is reciprocal. Moreover, AVO gradient analysis suggests that the AVO anomaly in this instance is designated as Class I (Rutherford and Williams, 1989; Castagna and Backus, 1993) as depicted in Figure 5-28. The same observation could be extended to the relationship between seismic amplitude and CO_2 saturation but since the seismic amplitude was predicted by the Gassmann FSM (Figure 5-22), it appears to have reached a plateau shortly following the onset of CO_2 saturation (10-20%). The difference between the baseline (0% CO_2 saturation) and monitor surveys (10%-100% CO_2 saturation) is displayed in the top panel of Figure 5-27 (b).

The AVO response associated with the 60 Hz seismic wavelet as well as the difference between the baseline (0% CO_2 saturation) and monitors (10%-100% CO_2 saturation) are shown in Figure 5-29 (a) and (b). Obviously, there is a difference in the AVO response from the 30 Hz wavelet experiment as demonstrated by the departure in the seismic amplitude (blue curve) in the bottom panel of Figure 5-29 (a) from that previously shown at the bottom panel of Figure 5-27 (a). At 0% CO_2 saturation, the seismic amplitude corresponding to the 30 Hz wavelet attains higher magnitudes than those associated with the 60 Hz wavelet. In contrast, the seismic amplitude values associated with the 60 Hz appears to consistently increase as the CO_2 saturation is increased - a rather counterintuitive trend - as depicted by the blue curves in the bottom panel of Figure 5-29 (a). This seems to be due to the combined effect of the seismic wavelet and tuning effect involving the Graminia (shale), Calmar (shale) and Nisku events (see Figure 2-9). These observations suggest that the seismic response to CO_2-brine replacement is non-unique and is frequency-dependent.

Table 5-4: Outline of the main offset-dependent reflectivity forward seismic modelling parameters and other pertinent information.

Simulation method	Ray tracing (Section 3.5.4) employing the Zoeppritz equations (Section 3.3)
Seismic Wavelet	Zero-phase Ricker wavelet (Figure 5-2)
Frequency	30 Hz (Figure 5-2 (a) and (b)); 60 Hz (Figure 5-2 (c) and (d))
Seismogram Sampling Rate	1 ms
Minimum Offset	0 m
Maximum Offset	1500 m (maximum angle of incidence is ~ 35^o)
Offset Spacing	150 m
Target Depth and Thickness	1730 m; 90 m
Well	100-10-05-52-2W5 (Figure 5-1)
Objective	Investigating seismic reflectivity change as a function of offset, seismic frequency and CO_2 saturation in the Nisku Formation.
Comments	I. AVO Experiments: • Experiment 1: uniform saturation and 30 Hz wavelet (Figure 5-27). • Experiment 2: uniform saturation and 60 Hz wavelet (Figure 5-29). II. Post-stack Experiments: • Experiment 1: uniform saturation and 30 Hz wavelet (Figure 5-30). • Experiment 2: uniform saturation and 60 Hz wavelet (Figure 5-32). • Experiment 3: patchy-like saturation and 30 Hz wavelet (Figure 5-33).

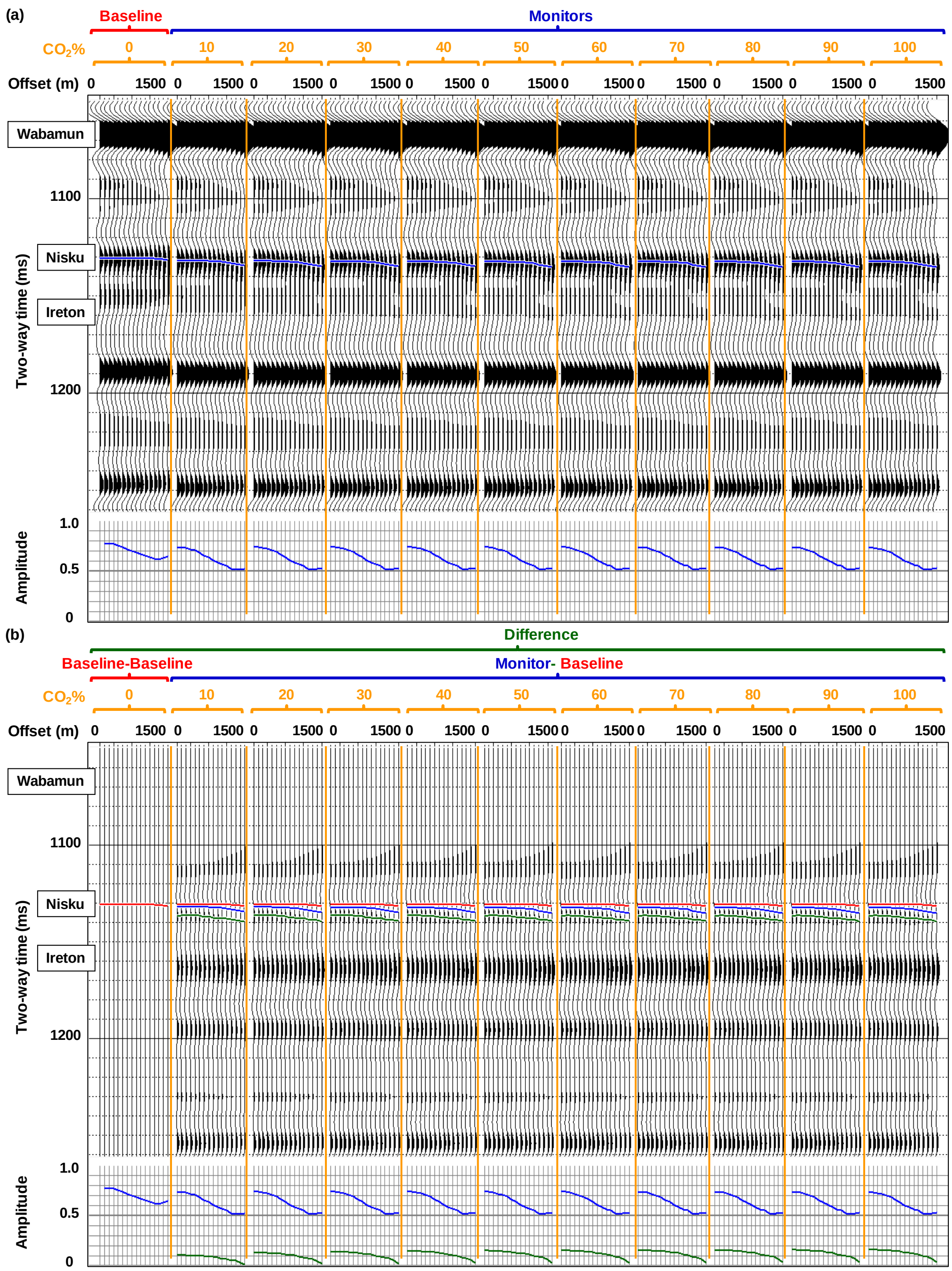

Figure 5-27: Sequential display of the NMO-corrected synthetic AVO response of the Nisku event showing (a) the baseline and monitors, and (b) the difference between the two as a function of offset and CO_2 saturation. The corresponding amplitude values are plotted in the bottom panel. Red: baseline amplitude; blue: monitor amplitude; dark green: difference amplitude. Note that the baseline and monitor picks are equivalent at 0% CO_2 saturation. The gathers were generated using the first realization (Case Iu) of the FSM on well 100-10-05-52-2W5 (Figure 5-22) alongside the 30 Hz Ricker wavelet displayed in Figure 5-2.

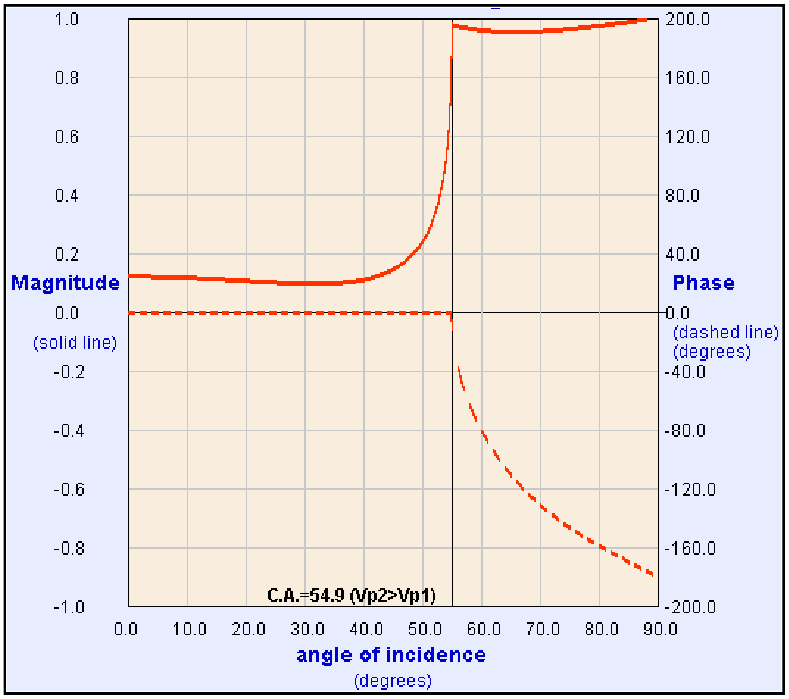

Figure 5-28: Reflection coefficient (amplitude magnitude) and phase of the Nisku event as a function of angle of incidence. The curves are based on the Zeoppritz equations and were genearted using the CREWES Zoeppritz Explorer 2.2 (Ursenbach, 2010).

Note that the difference amplitude in the bottom panel (dark green curve) of Figure 5-27 (b) and Figure 5-29 (b) should be negative but a peak was chosen to facilitate better picking. Furthermore, the amplitude appears to increase as CO_2 saturation is increased regardless of the frequency but this could be a result of picking the Nisku event as a peak in the difference seismograms. However, the same pattern persisted even when the preceding trough was picked instead. This illustrates that picking events on the difference seismogram could lead to misleading conclusions and, therefore, should be avoided. In order to compute the difference in seismic attributes between a baseline and a monitor, one should always extract the desired attribute(s) from the individual seismograms and then compute the difference.

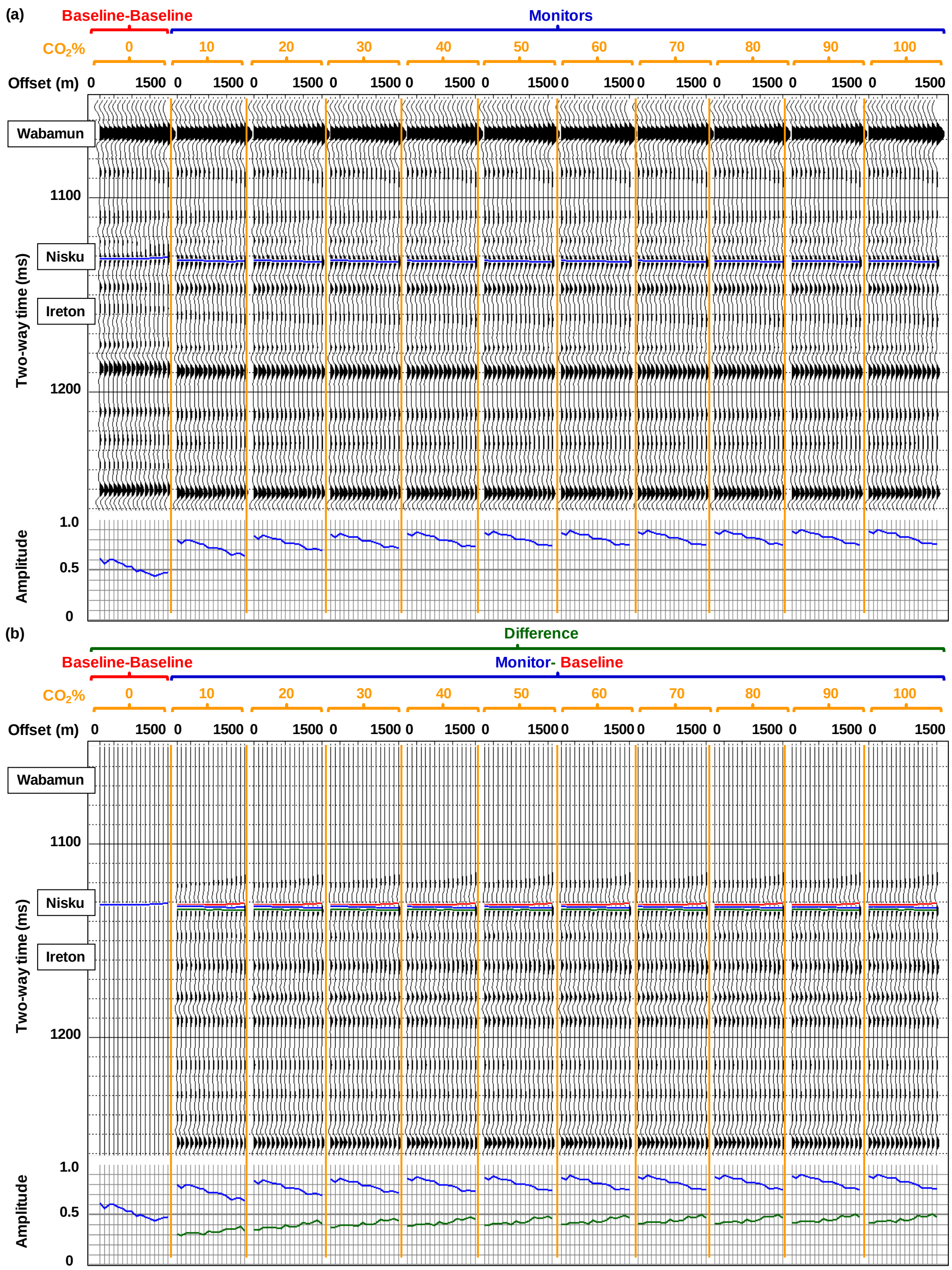

Figure 5-29: Sequential display of the NMO-corrected synthetic AVO response of the Nisku event showing (a) the baseline and monitors, and (b) the difference between the two as a function of offset and CO_2 saturation. The corresponding amplitude values are plotted in the bottom panel. Red: baseline amplitude; blue: monitor amplitude; dark green: difference amplitude. Note that the baseline and monitor picks are equivalent at 0% CO_2 saturation. The gathers were generated using the first realization (Case Iu) of the FSM on well 100-10-05-52-2W5 (Figure 5-22) alongside the 60 Hz Ricker wavelet displayed in Figure 5-2.

As outlined in Table 5-4, three experiments were investigated for the stacked response: (1) uniform saturation with 30 Hz Ricker wavelet (Figure 5-30), (2) uniform saturation with 60 Hz Ricker wavelet (Figure 5-32), and (3) patchy-like saturation with 30 Hz Ricker wavelet (Figure 5-33). In each experiment, four quantitative seismic attributes were generated to aid in the investigation. These are: (i) Nisku event cross-correlation, (ii) Wabamun-Beaverhill Lake isochron[62] difference, (iii) Nisku event predictability (PRED), and (iv) Nisku event normalized root-mean squares (NRMS). The first two are time-based attributes which are sensitive to changes in the P-wave speed as a result of the CO_2-brine replacement. The cross-correlation should detect any time shift in the onset of the Nisku reflection whereas the isochron difference should delineate the induced time-delay in observed traveltime of the deeper Beaverhill Lake event. PRED and NRMS are considered to be standard measures of repeatability and were introduced in Section 3.6.3. The latter has been observed to be sensitive to the seismic amplitude (Kragh and Christie, 2002; Calvert, 2005) and, thus, should provide a quantitative measure of the change in the magnitude of the seismic reflection, which is indicative of acoustic impedance change. For Experiment 1 shown in Figure 5-30, the cross-plot of the seismic amplitude from the baseline and monitors are displayed in Figure 5-31.

The results from the first experiment (Figure 5-30) suggest a small time-shift due to the CO_2-brine replacement. For instance, the Nisku event cross-correlation time shift displayed in Figure 5-30 (a) suggests a maximum delay of around 1.5 ms in the Nisku reflection. The Wabamun-Beaverhill Lake isochron difference depicted in Figure 5-30 (b) also exhibits a maximum increase in the two-way traveltime of about 1.5 ms. Since the time shift is small and given the fact that the synthetic seismogram is noise-free, the PRED metric shows very small change as demonstrated by the high predictability, which is around 95% or higher. The NRMS, on the other hand, exhibits a strong response to the fluid substitution, around 40% NRMS at 100% CO_2 saturation, due to its sensitivity to the seismic amplitude[63]. Furthermore, the sensitivity of seismic amplitude to the CO_2-brine

---

[62] An isochron is measure of the interval traveltime between two seismic events.
[63] Recall that under ideal circumstances and if there had been no fluid substitution procedure, the PRED and NRMS would be 100% and 0%, respectively. See Section 3.6.3.

replacement is evident in Figure 5-31, which shows a cross-plot of the seismic amplitude of the 30 Hz experiment. Figure 5-31 (a) delineate the so-called background trend whereas Figure 5-31 (b) depicts the change due to the CO_2 saturation effect, which is quite obvious in this case.

Once more, the frequency-dependence is demonstrated by comparing the results from the second experiment, i.e. 60 Hz, (Figure 5-32) with that from the 30 Hz experiment (Figure 5-30). The absolute magnitude of the Nisku event cross-correlation time shift illustrated in Figure 5-32 (b) is smaller than in the 30 Hz wavelet experiment (Figure 5-30 (b)) by approximately 0.5 ms. However, the NRMS magnitude appears to be almost 20% higher in the 60 Hz experiment (Figure 5-32 (e)) in comparison to the 30 Hz wavelet (Figure 5-30 (e)). Interestingly, the amount of time delay in the onset of the Beaverhill Lake reflection seems to be frequency independent as demonstrated by the similarity in Wabamun-Beaverhill Lake isochron difference between Figure 5-30 (b) and Figure 5-32 (b).

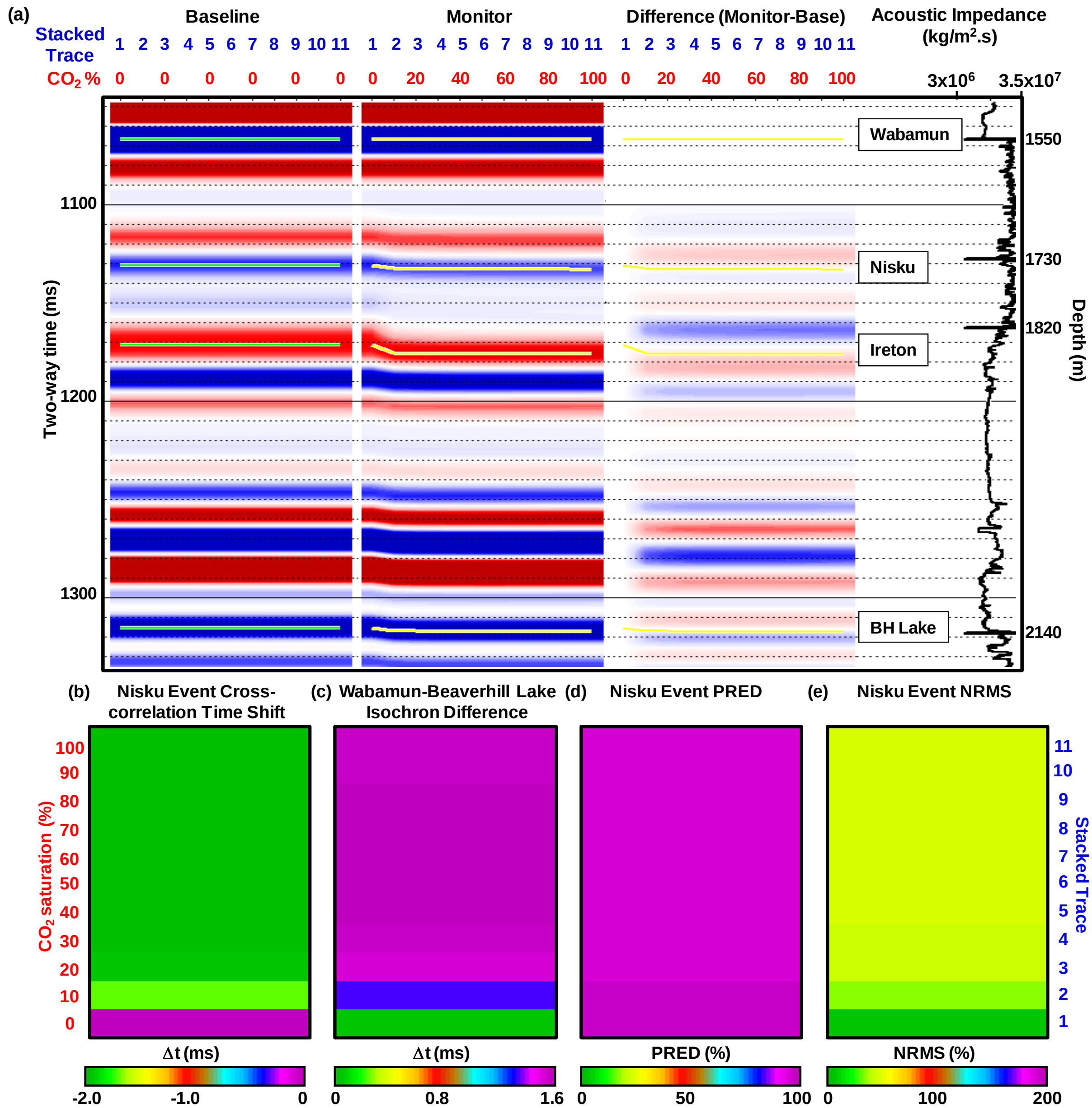

Figure 5-30: (a) Synthetic seismograms (baseline, monitor and their difference) in which the Nisku reflection is modelled as function of CO_2 saturation using the first realization of the FSM (uniform saturation; Figure 5-22) on well 100-10-05-52-2W5 (Figure 5-1) and the 30 Hz Ricker wavelet displayed in Figure 5-2. The monitor picks (yellow) are shown in the difference section in (a) as well as the acoustic impedance of the baseline. The bottom panel (b through c) shows a mosaic display of selected time and amplitude-based attributes; (b), (d) and (e) were computed using 100 ms window centered at the Nisku event. Note that each trace represents the stacked response of the NMO-corrected CDP gathers shown in Figure 5-27 at the given saturation. BH Lake: Beaverhill Lake.

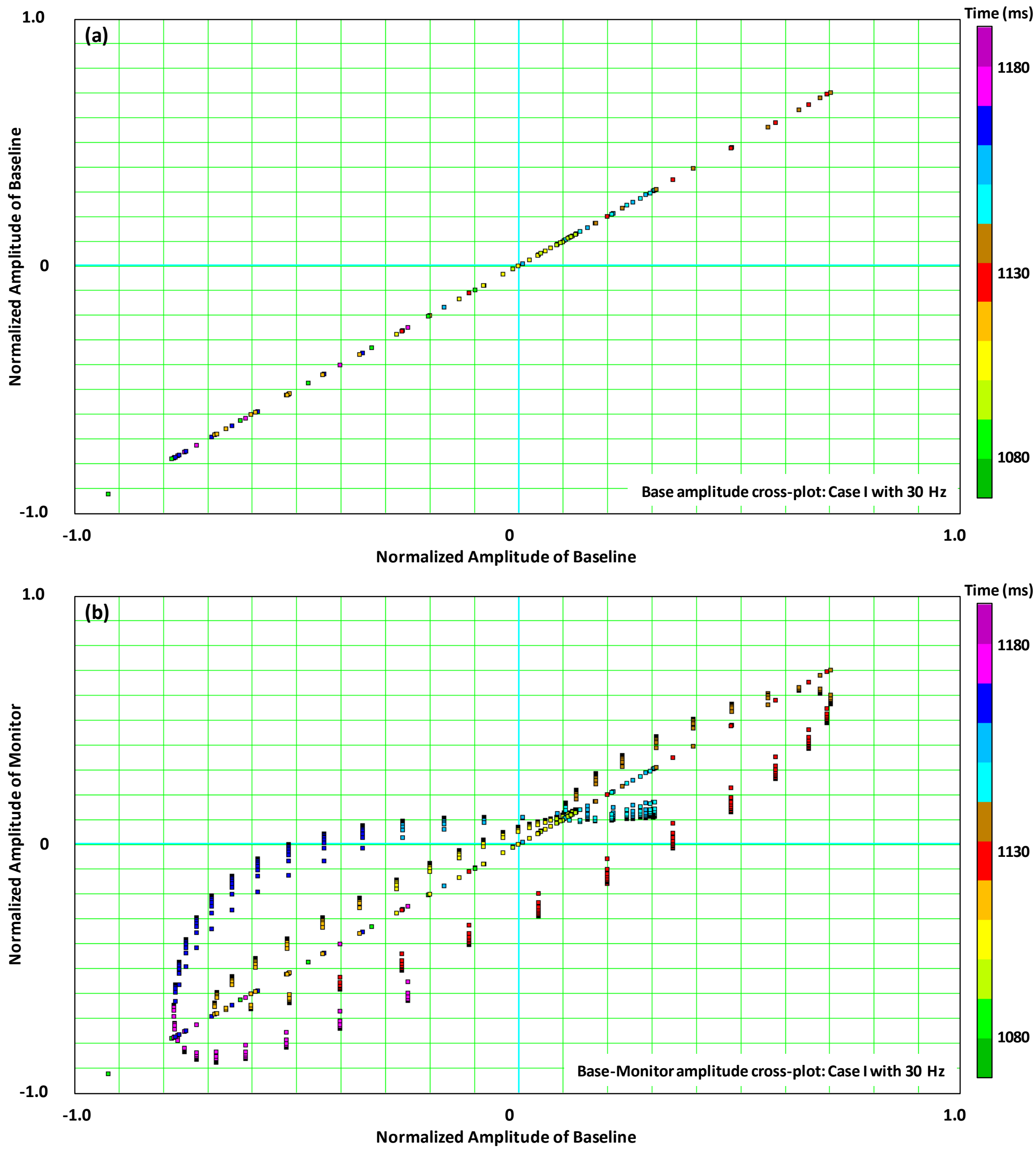

Figure 5-31: Seismic amplitude cross-plot of (a) baseline versus baseline (background trend), and (b) baseline versus monitors corresponding to the Nisku event shown in Figure 5-30.

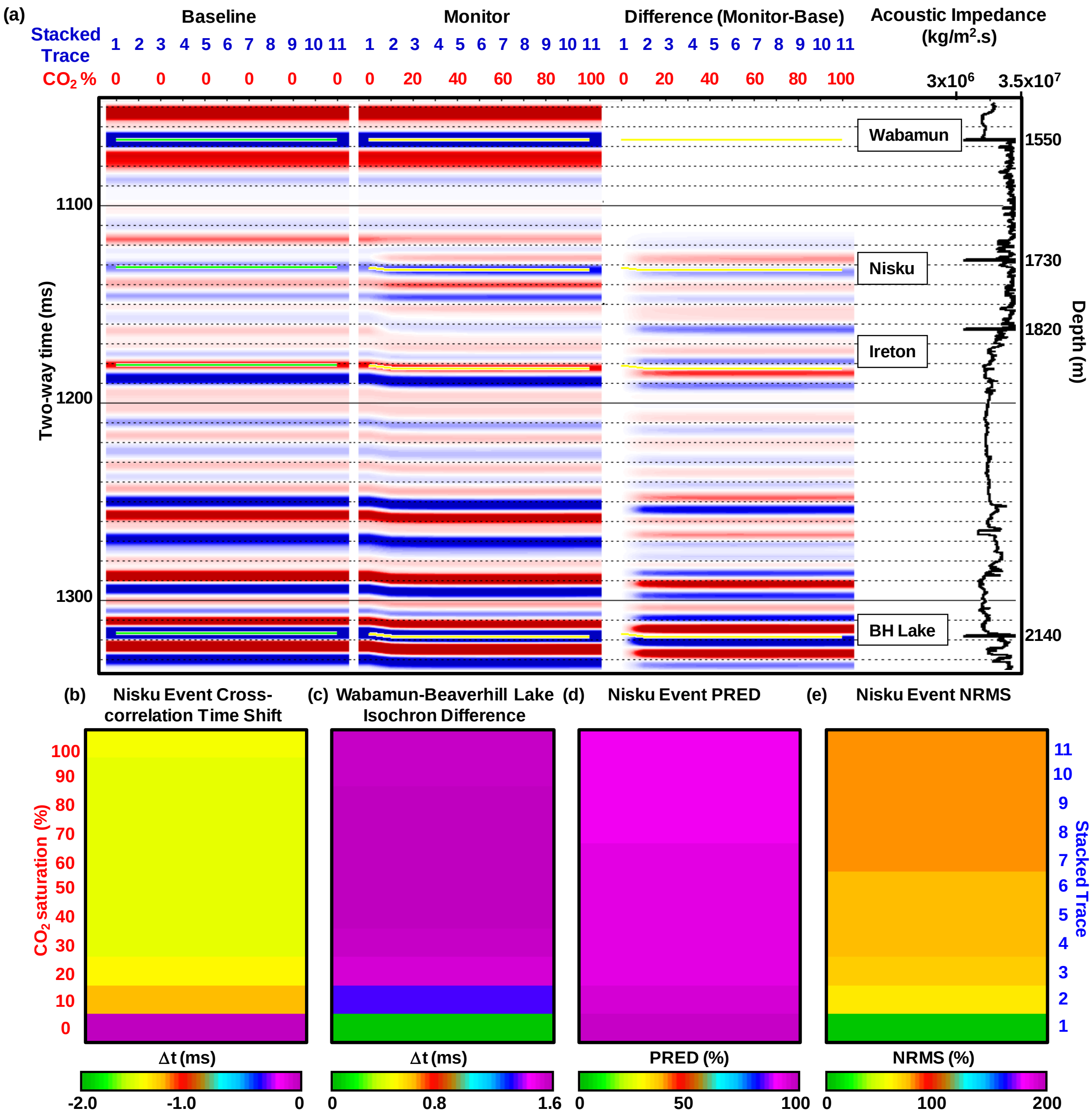

Figure 5-32: (a) Synthetic seismograms (baseline, monitor and their difference) in which the Nisku reflection is modelled as function of CO_2 saturation using the first realization of the FSM (uniform saturation; Figure 5-22) on well 100-10-05-52-2W5 (Figure 5-1) and the 60 Hz Ricker wavelet displayed in Figure 5-2. The monitor picks (yellow) are shown in the difference section in (a) as well as the acoustic impedance of the baseline. The bottom panel (b through c) shows a mosaic display of selected time and amplitude-based attributes; (b), (d) and (e) were computed using 100 ms window centered at the Nisku event. Note that each trace represents the stacked response of the NMO-corrected CDP gathers shown in Figure 5-27 at the given saturation. BH Lake: Beaverhill Lake.

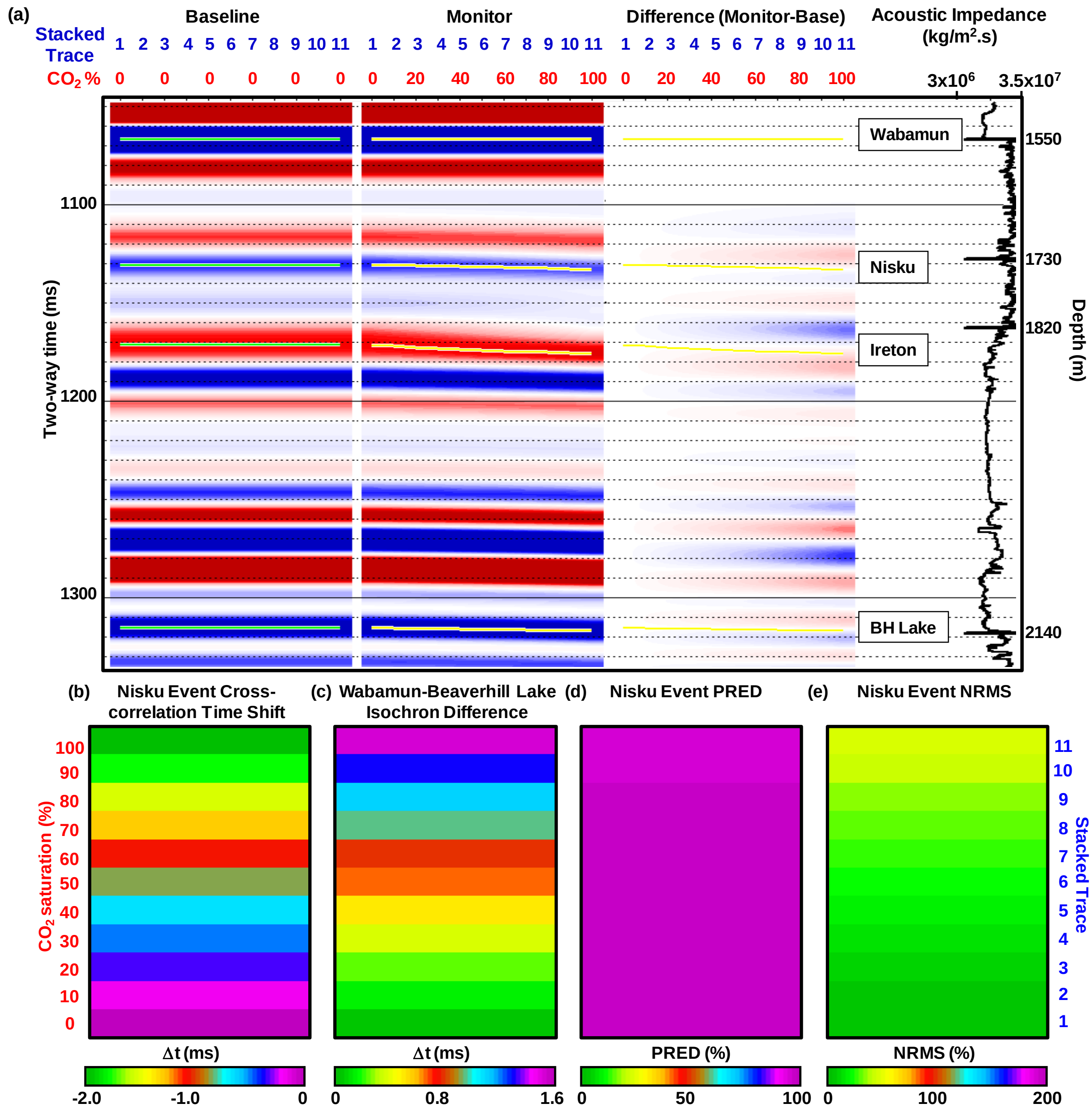

Figure 5-33: (a) Synthetic seismograms (baseline, monitor and their difference) in which the Nisku reflection is modelled as function of CO_2 saturation using the second realization of the FSM (patchy-like saturation; Figure 5-23) on well 100-10-05-52-2W5 (Figure 5-1) and the 30 Hz Ricker wavelet displayed in Figure 5-2. The monitor picks (yellow) are shown in the difference section in (a) as well as the acoustic impedance of the baseline. The bottom panel (b through c) shows a mosaic display of selected time and amplitude-based attributes; (b), (d) and (e) were computed using 100 ms window centered at the Nisku event. Note that each trace represents the stacked response of the NMO-corrected CDP gathers similar to those shown in Figure 5-27 at the given patchy-like saturation. BH Lake: Beaverhill Lake.

The results from the patchy-like saturation using the 30 Hz wavelet are depicted in the third experiment (Figure 5-33). Although the values of the four seismic attributes in Figure 5-33 (b) through (e) are identical to those observed in the first “uniform saturation” experiment (Figure 5-30 (b) through (e)) at the initial and final saturation, the response is rather monotonic and gradual. Small change in Nisku event cross-correlation time shift and NRMS as well as Wabamun-Beaverhill Lake isochron would not start to surface until around 50% CO_2 saturation.

In terms of sensitivity to CO_2 saturation, all experiments reflect what have been observed previously in Section 5.3.2.7. For instance, the highest relative change in experiments 1 and 2 is associated with first 10-20% increase in the CO_2 saturation following which a plateau is reached before the relative change starts to slightly decrease (Figure 5-22). This pattern is subtle but can be seen most clearly in the Wabamun-Beaverhill Lake isochron difference Figure 5-30 (b) and Figure 5-32 (b) where the time delay increases until about 60% CO_2 saturation and then starts to decrease toward the final saturation of 100% CO_2. The results from the patchy-like saturation has profound ramification on the feasibility of time-lapse seismic monitoring since small changes start to emerge at about 50% CO_2 saturation as predicted by the second FSM realization (Figure 5-23). However, as outlined previously in Section 5.3.2.7, studies suggest that it is unfeasible to reach CO_2 saturation higher than about 50% given in-situ conditions (Baviere, 2007; USDOE, 2008).

5.3.3.2 Exploding Reflector Finite-Difference (ERFD) Modelling

The main ERFD modelling parameters alongside the objectives and the various scenarios investigated are outlined in Table 5-5. Note that the exploding reflector model (ERM) (Appendix B.3) was chosen to simulate the acoustic wavefield. Hence, the synthesized seismograms can rather be described as pseudo 2-D as they are largely equivalent to zero-offset sections (ZOS). Furthermore, since the acoustic wavefield was simulated using the ERM, only one key processing step, namely migration, was required before interpreting the synthetic seismograms. For this purpose, a Kirchhoff-based time migration algorithm was employed (Appendix B.4).

Table 5-5: Outline of the main ERFD modelling parameters and other pertinent information.

Simulation method	Finite-difference using an explicit solution (Section 3.5.3) to the acoustic wave-equation (Section 3.1)
Source Type	Exploding reflector
Boundary Type	Absorbing
Seismic Wavelet and Frequency	30 Hz Ricker wavelet (see Figure 5-2 (a) and (b))
Time Increment	0.1 ms
Minimum Offset	0 m
Maximum Offset	4000 m
Position of First Receiver	0 m
Position of Last Receiver	4000 m
Bin spacing	2 m
Maximum Model Depth	2200 m
Target Depth and Thickness	1730 m; 90 m (see Figure 5-34)
Objectives	• Corroborate the ray tracing modelling results in investigating seismic reflectivity change as a function of offset and CO_2 saturation in the Nisku Formation using the first (uniform) realization (Figure 5-22) of the FSM on well 100-10-05-52-2W5 (Figure 5-1). • Investigate sensitivity to upward migration of fraction of hypothetically injected CO_2 into shallow aquifer, namely Belly River Formation. • Revisit the discontinuity footprint interpretation (in Chapter 4).
Comments	• Scenario I: 40% uniform CO_2 saturation in the Nisku Formation. Wabamun karsting is portrayed as an effective uniform medium. • Scenario II: 40% and 5% uniform CO_2 saturation in the Nisku Formation and the shallow Belly River aquifer, respectively. Wabamun karsting is portrayed as an effective uniform medium. • Scenario III: no CO_2 saturation. Similar to baseline model (Figure 5-34) but with the Wabamun karsting depicted as a collapse feature. • See Figure 5-34 for the acoustic geologic model.

The 2-D acoustic geologic model used in simulating the wavefields association with Scenarios I and II is depicted in Figure 5-34. Since no particular area of WASP has been identified as a target for Phase II of the project (Table 4-1), the model was constructed by cooperating information from the overall WASP study area geology as well as the seismic data discussed in Chapter 4. Nonetheless, the 2-D model was based largely on well 100-10-05-52-2W5 given the detailed stratigraphic model and the amount of geologic information available (Michael et al., 2008) as well as the fact that the 3-D seismic interpretation and petrophysical data show favourability toward the northern part of the WASP local-scale study area (Section 4.6.5 and Section 4.7).

Figure 5-35 shows the results corresponding to Scenario I, which assumes 40% uniform CO_2 saturation in the Nisku Formation (Figure 5-22). The Nisku reflection is observed at ~ 1180 ms in the baseline seismogram as indicated by the green arrow in Figure 5-22 (a). Although no appreciable change is visible between the baseline and monitor seismic sections as portrayed in Figure 5-22 (a) and (b), the difference between the two which is displayed in Figure 5-22 (c) exhibits a small yet supposedly detecatble change.

Sensitivity to upward migration of hypothetically injected CO_2 is illustrated in the seismograms associated with Scenario II (Figure 5-36). In this scenario, the CO_2 saturation in the Nisku Formation is identical to Scenario I, i.e. uniform 40% saturation. The departure, however, is in the proposition that a certain amount of CO_2 had migrated into the shallow Belly River aquifer (Figure 2-9) in such a way that it became uniformly saturated with a small amount of, i.e. 5% CO_2. Note that at the Belly River aquifer depth (~ 500 m), the CO_2 will be either in gas or liquid phase depending on the temperature and pressure (Bachu et al., 2000). In the FSM that was undertaken using well 100-10-05-52-2W5, to predict the change in the elastic properties of the Belly River aquifer due to CO_2 migration, the temperature and pressure were assumed to be 27 ^{o}C and 7 MPa, respectively. At uniform 5% CO_2 and 95% water saturations, the P-wave speed and density in the Belly River aquifer changed by 10% and -1%, respectively.

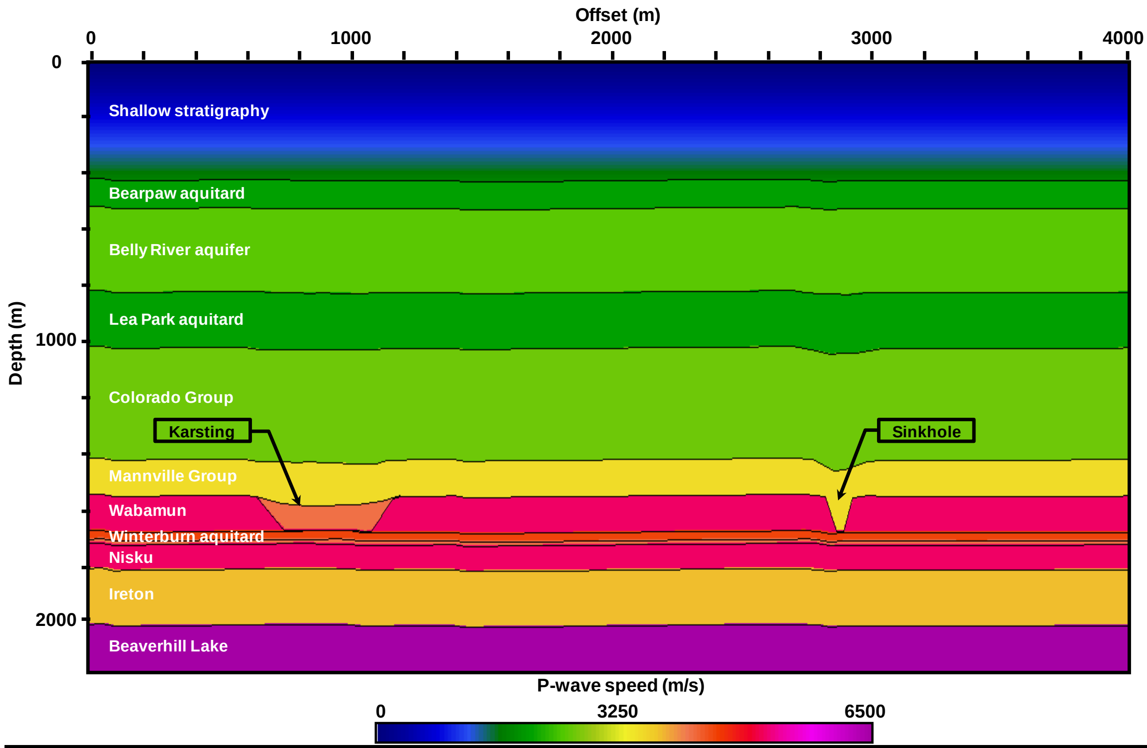

Layer	Average Depth[1] (m)	Average Thickness (m)	Average Acoustic Properties	
			P-wave speed (m/s)	Density (kg/m^3)
Shallow stratigraphy	0.0	425	2700	2225
Bearpaw aquitards	425	100	3000	2300
Belly River aq.: before CO_2	525	300	3200	2350
Belly River aq.: after CO_2	525	300	2880	2325
Lea Park aquitard	825	200	3000	2410
Colorado Group	1025	400	3300	2500
Mannville Group	1425	130	4000	2580
Wabamun Formation	1555	130	5900	2700
Winterburn Group	1685	30	4700	2650
Calmar Formation (aquitard)	1715	14	4500	2580
Nisku Fm.: before CO_2	1730	90	5500	2690
Nisku Fm.: after CO_2	1730	90	5280	2560
Ireton Fm. (Woodbend Group)	1820	200	4200	2500
Beaverhill Lake Group	2020	180	6200	2700
Karsting	1555	125	4500	2500

Figure 5-34: 2-D acoustic model depicting the overall geology in the WASP study area in a rather simplified way. The accompanying table shows the name and average physical properties of the various layers. There are 13 layers including the Wabamun karsting, which is depicted here as an effective uniform medium. The color scale depicts the P-wave speed in the model before CO_2-brine replacement. See the geologic cross-section in Figure 2-7 and the stratigraphic model in Figure 2-9. [1] Average depth to layer top. Fm.: Formation; aq.: aquifer.

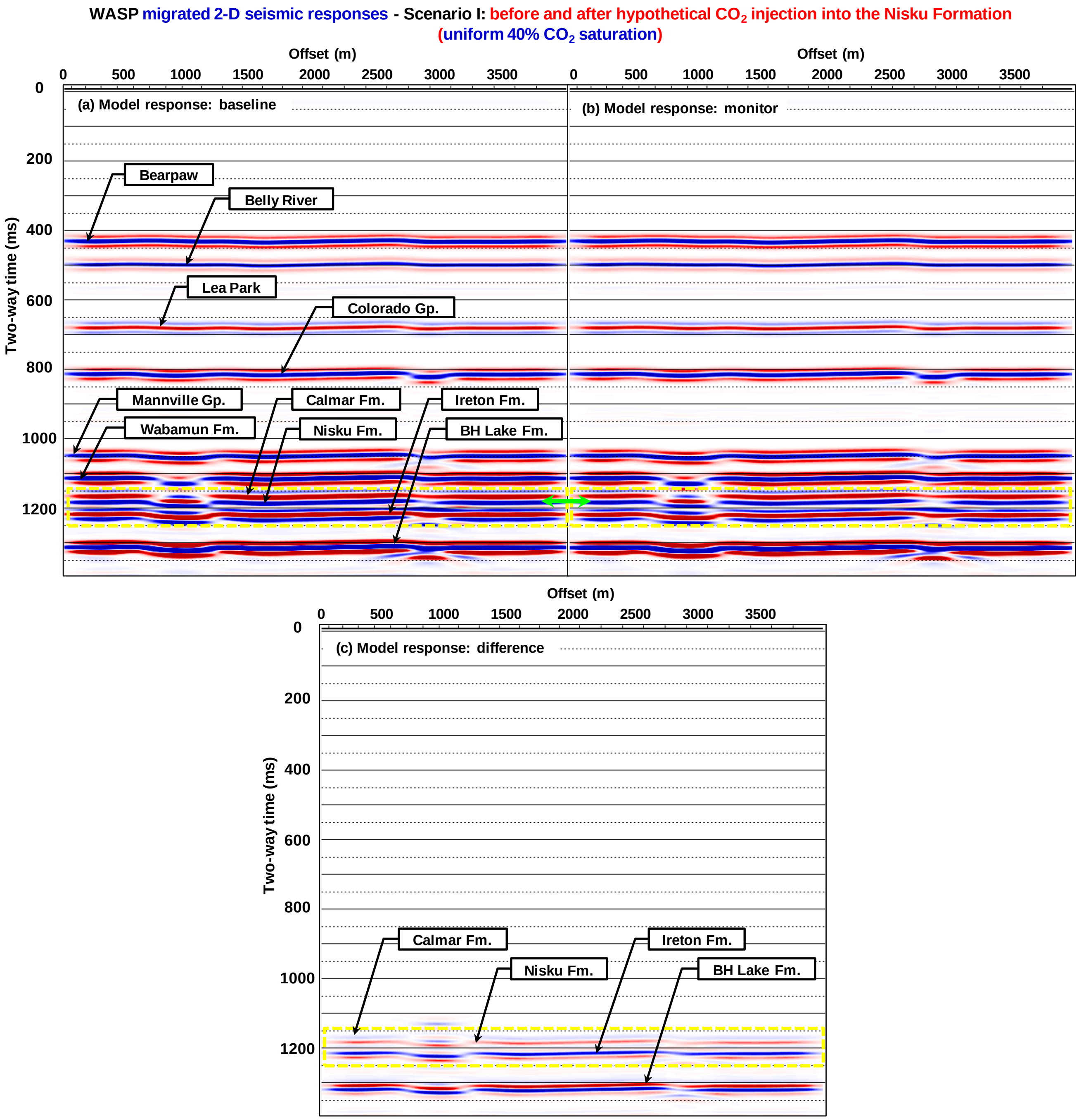

Figure 5-35: The model response of the 2-D model in Figure 5-34 (a) before, and (b) after CO_2-brine replacement (40% uniform CO_2 saturation) in the Nisku Formation. The difference between (a) and (b) is shown in (c). The callout shapes point to the seismic events corresponding to the top of the layers listed in the table in Figure 5-34. The dashed yellow rectangle encloses the Winterburn Group, Calmar, Nisku Formation, and Ireton Formation. The double-sided green arrow traversing the vertical line separating (a) and (b) identifies the Nisku event. Gp.: group; Fm.: formation; BH Lake: Beaverhill Lake. The amplitude scale is the same in these and subsequent seismograms.

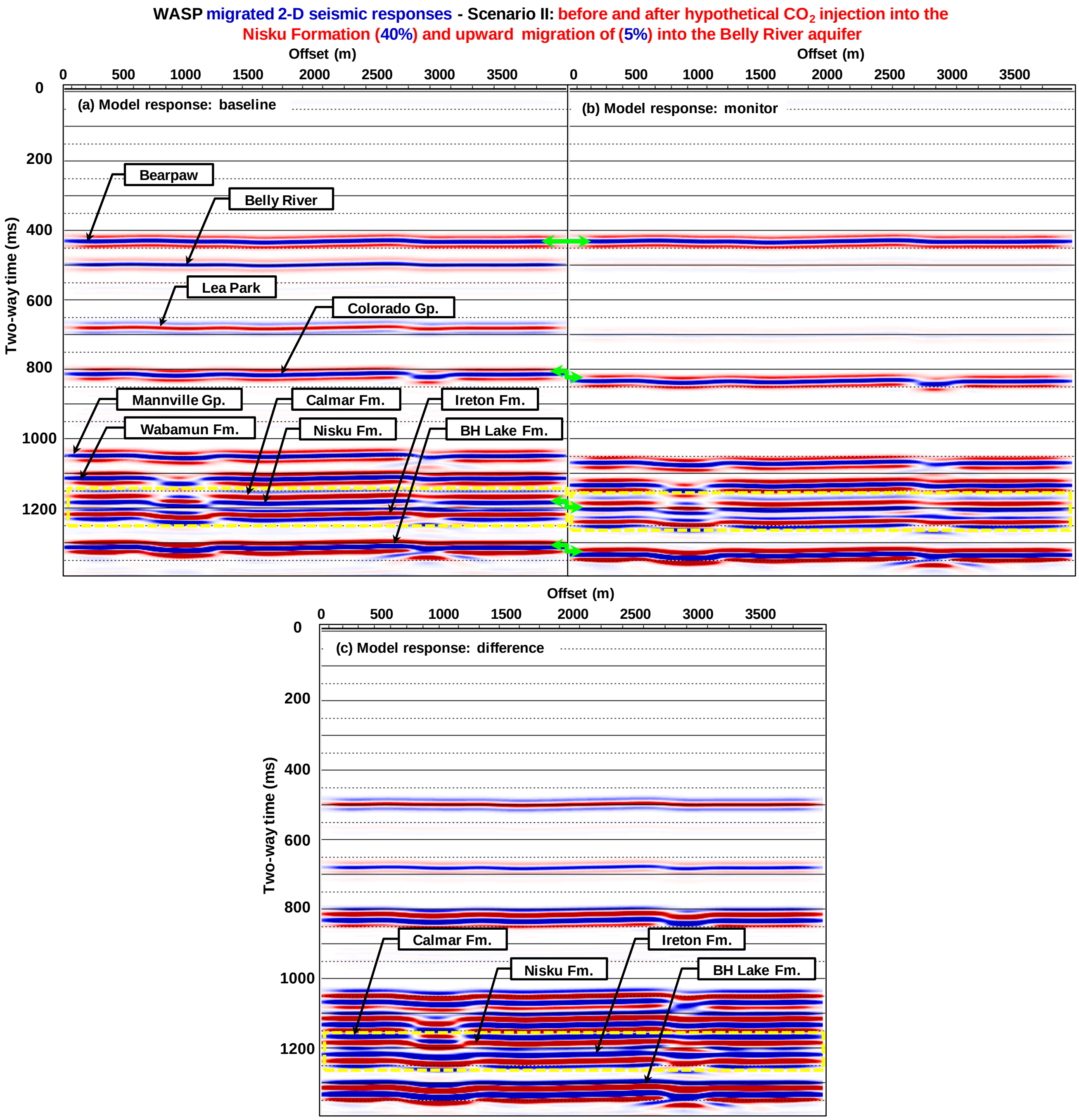

Figure 5-36: The model response of the 2-D model in Figure 5-34 (a) before, and (b) after CO_2-brine replacement (40% CO_2 saturation in Nisku Formation and 5% in the shallow Belly River sandstone aquifer). The difference between (a) and (b) is shown in (c). The callout shapes point to the seismic events corresponding to the top of the layers listed in the table in Figure 5-34. The dashed yellow rectangle encloses the Winterburn Group, Calmar, Nisku Formation, and Ireton Formation. The double-sided green arrows traversing the vertical line separating (a) and (b) identify the Bearpaw, Colorado Group and Nisku events. Gp.: group; Fm.: formation; BH Lake: Beaverhill Lake.

The results depicted in Figure 5-36 suggest a very high sensitivity in the seismic response to this hypothetical upward migration as the seismic energy associated with the reflections from the top (~ 500 ms) and bottom (~ 680 ms) of the Belly River event seems to have disappeared. In fact, there has been a subtle reversal in these reflections as the one at the top went from being a small positive event to an extremely weak negative event. Similarly, the reflection from the bottom of the Belly River aquifer has experienced the same effect but in an opposite fashion. The time shift effect is clearly seen starting at the Colorado Group reflection which experienced about 20 ms delay. The consequences of the 5% CO_2 saturation in the Belly River on the succeeding seismic events is profound as can be seen in the difference seismogram shown in Figure 5-36 (c).

In the previous discussions, the results from the first and second scenarios were considered in a rather qualitative way. A more encompassing interpretation could be achieved by looking at the results in a quantitative style as attempted through the repeatability depicted in Figure 5-37. Table 5-6 summarizes the change in the magnitude of the repeatability attributes. In addition, the change in the Bearpaw-Beaverhill Lake isochron in both Scenarios is plotted in Figure 5-38.

Table 5-6: Comparison of the average repeatability corresponding to Scenarios I and II (Table 5-5) shown in Figure 5-37 and Figure 5-38.

Seismic Event	Scenario I		Scenario II	
	NRMS (%)	PRED (%)	NRMS (%)	PRED (%)
Belly River	00.00	100.0	173.4	99.93
Nisku	34.66	93.61	154.9	1.825
Complete Window	24.85	94.48	150.4	1.821

In Scenario I, the magnitude of the Nisku event NRMS is modest (~ 34%) but should be detectable; at least in principle. The magnitudes of PRED (> 93%) and isochron time shift (~ 1.48 ms), on the other hand, are very small which suggests that these might not be reliable indicators. As depicted in the difference seismogram in Figure 5-36 (c), Scenario II exhibits a change in the NRMS of the individual events as well as the whole survey; all of which are one order of magnitude higher than in Scenario I (> 150%). Similarly, the Bearpaw-Beaverhill Lake isochron difference in Scenario II is substantial (~ 21.8 ms) in comparison to Scenario I (~ 1.48 ms). Note that because the

Belly River event is anti-correlated, the PRED gives the almost the same values in both Scenarios (Section 3.6.3).

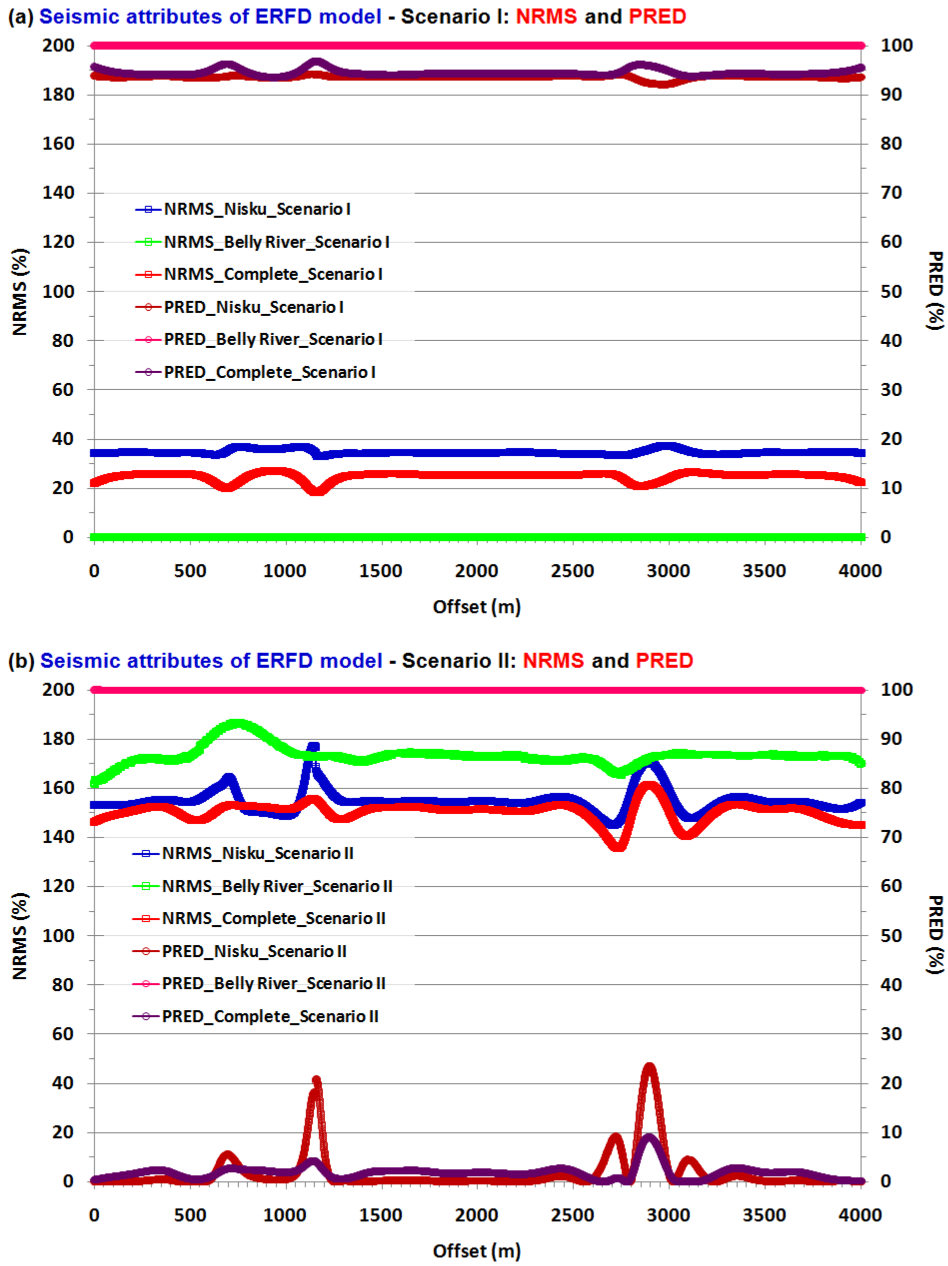

Figure 5-37: Repeatability of the ERFD synthetic seismograms corresponding to (a) Scenario I, and (b) Scenario II. NRMS and PRED were computed using three widnows. Two are 100 ms long windows encompassing the Nisku and Belly River evets while the third comprises the entire trace (Complete).

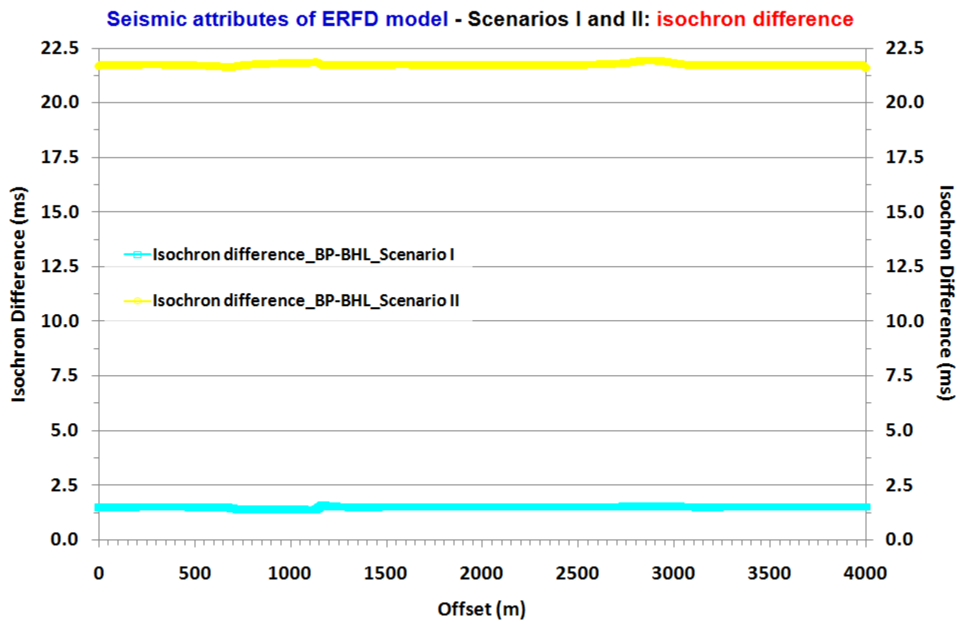

Figure 5-38: Time shift in the Bearpaw-Beaverhill Lake isochron associated with Scenarios I and II. BP: Bearpaw event; BHL: Beaverhill Lake event.

In Scenarios I and II, the Wabamun karsting is portrayed as an effective uniform medium and its footprint in terms of time shift, in particular on the Beaverhill Lake event, is visible in Figure 5-35 and Figure 5-36 but, perhaps, most evident in the repeatability plots in Figure 5-37. However, the amplitude footprint is less obvious. Similarly, the Wabamun sinkhole seems to induce a time shift that is smaller in magnitude than that associated with the karsting. In addition, the migration algorithm seems to have a difficulty in collapsing the diffractions associated with the sinkhole. In order to look into the effect of more realistic karsting geometry, the acoustic wavefield was simulated in Scenario III with the Wabamun karsting depicted as a collapse feature (Figure 5-39). However, no major differences are observed between the migrated response in Figure 5-39 (c) and those in which the karsting was depicted as effective uniform medium, namely Figure 5-35 (a) and Figure 5-36 (a).

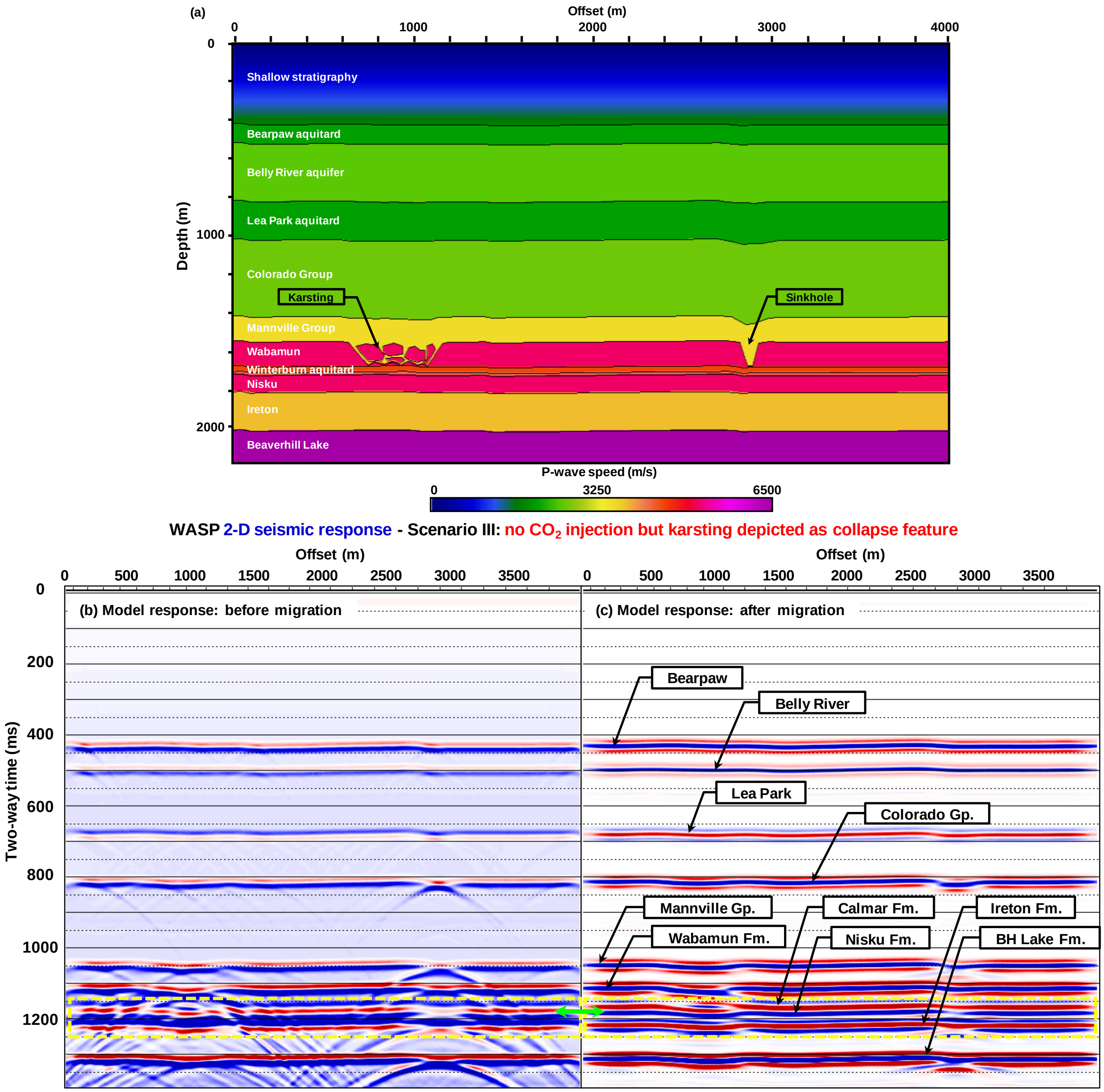

Figure 5-39: (a) 2-D acoustic model similar to that shown in Figure 5-34 except that the Wabamun karsting is portrayed as a collapse feature with blocks properties similar to the Wabamun Formation. The background properties are of the overlying Mannville Group; (b) and (c) show the model response before and after post-stack time migration, respectively. The callout shapes in (c) point to the seismic events corresponding to the top of the layers listed in the table in Figure 5-34. The dashed yellow rectangle encloses the Winterburn Group, Calmar, Nisku Formation, and Ireton Formation. The double-sided green arrow traversing the vertical line separating (a) and (b) identifies the Nisku event.

5.4 Discussion

The forward numerical seismic modelling undertakings in this chapter can be divided into two categories. The first examined the seismic response in an interpretation framework to revisit some of the conclusions of the WASP seismic site characterization discussed in Chapter 4. The second investigated the feasibility of time-lapse reflection seismology in delineating a hypothetical CO plume to assess its role being one of the principle monitoring, measurements and verification (MMV) techniques.

As for the first category, numerical modelling suggests that the differential tuning effect on the seismic amplitude of the Nisku event is insignificant based on the thickness values range encountered in the study area (Figure 5-4). On the other hand, the effect of impedance contrast, in terms of P-wave speed variation, on the seismic response of the Nisku reflection is quite substantial (Figure 5-5). This suggests that anomalies observed in the seismic attribute maps in Chapter 4 are mostly caused by change in the lithology rather than thickness. Of course, excluding those associated with discontinuity footprints.

The second modelling category consists of two components: (1) rock physics and Gassmann fluid substitution modelling (FSM), and (2) forward seismic modelling. The FSM was undertaken to predict the change in the elastic properties prior to simulating the synthetic acoustic wavefield. Although the assumptions underlying Gassmann formulation were not all satisfied, different cases were investigated and the results presented in Section 5.3.2.7 should provide a broad range of the effect of the CO_2-brine replacement on the time-lapse seismic response. The Gassmann FSM results (Figure 5-22) suggest a modest change in the P-wave speed (~ -4%) at reasonable CO_2 saturations (20-40%) whereas the change in the S-wave speed and density at the same saturation range were much smaller, 0.5% and -0.3%, respectively.

Since the predicted change in the elastic properties was modest, this was reflected on the acoustic wavefield simulated using offset-dependent reflectivity (ODR) and exploding reflector finite-difference (ERFD) modelling schemes. First, several ODR modelling experiments (Section 5.3.3.1) were examined in an effort to deterministically account for some of the uncertainty in a rather unpretentious style. Interestingly, the ODR modelling shows a non-unique frequency-dependent seismic response toward the hypothetical CO_2 plume (Figure 5-27 and Figure 5-29). Furthermore, the results from the stacked responses corresponding to uniform CO_2 saturation (Figure 5-30 and Figure 5-32) suggest that the CO_2-induced change should be detectable under ideal circumstances. On the other hand, the results from the patchy-like saturation experiment (Figure 5-33) indicate that the seismic response may not be able to detect the CO_2 plume.

Similarly, two ERFD scenarios (Section 5.3.3.2) were considered to corroborate the ODR modelling results (Scenario I; Figure 5-35) and assess the seismic response sensitivity to upward migration of CO_2 into the relatively shallow Belly River aquifer (Scenario II; Figure 5-36). In the first scenario where no upward migration of the hypothetical CO_2 plume is proposed, the results (Figure 5-35) are strikingly similar to those associated with the first experiment of the stacked response under the ODR modelling section (Figure 5-30). As for the second scenario, the results suggest a profound change in the seismic response should an upward migration of CO_2 had occurred and that the shallow Belly River aquifer became saturated even with a small amount of CO_2.

Simple time and amplitude-based seismic attributes were computed for each experiment (Section 5.3.3.1) or scenario (Section 5.3.3.2) to quantitatively aid in the interpretation of the forward seismic modelling results. For the uniform saturation experiments and scenario with no upward migration of CO_2, the magnitude of the NRMS repeatability metric (~ 34%) occurs within the typical NRMS range of onshore time-lapse surface seismic surveys (Kragh and Christie, 2002). Thus, it could be difficult indeed to extract useful information about the CO_2 plume in reality due, for instance, to non-repeatable noise whether its acquisition or processing related. Furthermore, it should be noted that the effects of pore pressure and anisotropy were not considered in this investigation. These can constitute parts of future work as data becomes available although it is suggested that the effect of the former may not be significant at low level of CO_2 saturation.

In the CO_2 upward migration scenario and as depicted in the difference seismogram in Figure 5-36, there has been a substantial change in the NRMS of the individual events as well as the whole survey; all of which are one order of magnitude higher (~ 150%) than in the no upward migration scenario (~ 34%). Similarly, the Bearpaw-Beaverhill Lake isochron difference in the upward migration scenario is substantial (~ 21.8 ms) in comparison to the no upward migration scenario (~ 1.48 ms). Aside from the predictability, the results from Scenario II indicates that the seismic would be successful in detecting upward migration of CO_2 into shallow aquifers even if the uniform CO_2 saturation is very small; in this case 12.5% of that present in the target aquifer (Nisku Formation). Of course, sensitivity to upward migration is dependent on many factors including the depth, thickness and lithology of the host.

5.5 Summary

- The numerical seismic modelling results indicate that the tuning effect is insignificant and that variations in acoustic impedance, predominately in the form of P-wave speed contrast, is the primary influence on the seismic amplitude of the Nisku reflection in the WASP study area.
- The results from the Gassmann FSM suggest a modest change - in the best case scenario of uniform saturation - in the elastic properties of the Nisku Formation due to CO_2-brine replacement.
- The FSM results indicate that the seismic response is sensitive to small to intermediate CO_2 saturation, which are within the attainable saturation range - given in-situ conditions - of typically around or less than 50%.
- The results from the best case scenario indicate that as far as the individual elastic parameters are concerned, the P-wave speed exhibits the most sensitivity toward the CO_2-brine replacement (~ -4%). This sensitivity is manifested in the form of induced time shift on deeper events, in this case the Beaverhill Lake event (~ 1.48%).
- The acoustic impedance which combines the change in P-wave speed with the change density results in an amplitude change that is stronger in magnitude and, therefore, more discernable and reliable than time shift.
- A stronger response is captured by coupling the change in Lamé's elastic parameters with the change in density through LR. The cross-product of LR and

MR gives an even more prominent response. However, extracting reliable LR and MR from seismic data could be very difficult in actual circumstances.

- The predicted changes in the elastic properties associated with the least favourable scenarios, namely patchy-like saturation and in the case of the presence of in-situ gas, are interpreted to be seismically undetectable.
- The forward AVO modelling invoking the FSM results from the best case scenario show that the Nisku event, modestly, exhibits the characteristics of Class I AVO anomalies.
- In addition to sensitivity to offset and CO_2 saturation, the AVO modelling results suggest frequency-dependent seismic amplitude as demonstrated by the AVO responses constructed using the 30 Hz and 60 Hz seismic wavelets.
- The stacked responses corresponding to these AVO responses show modest NRMS magnitude of ~ 35% in the 30 Hz experiment and a stronger NRMS magnitude (~ 50%) in the 60 Hz experiment at uniform 40% CO_2 saturation.
- The corresponding magnitudes of the PRED are almost identical (~ 95% and 93%) whereas the Wabamun-Beaverhill Lake isochron difference is very small (~ 1.48 ms) and is frequency independent.
- The results from a third experiment, which was constructed using the 30 Hz seismic wavelet and the FSM corresponding to patchy-like saturation, demonstrates the imperceptibility of the seismic response associated with patchy-like saturation at feasible CO_2 saturation.
- The results from Scenario I of the ERFD corroborates the ODR results and show striking similarity in the magnitudes of the NRMS, PRED and isochron difference.
- The results from Scenario II, in which the seismic sensitivity to upward migration of CO_2 was investigated, suggest a profound change in the seismic wavefield (> 150% NRMS and ~ 21 ms time shift).
- The discontinuities footprint is evident in terms of induced time shift but less obvious when it comes to amplitude footprint.

CHAPTER 6: PCEP TIME-LAPSE SEISMIC ANALYSIS I - FIELD DATA

6.1 Introduction

The second venture investigated in this dissertation pertains to the time-lapse seismic monitoring of the Cardium Formation for the Pembina Cardium CO_2-Enhanced Oil Recovery Pilot Project (PCEP). The project was introduced in Chapter 1 in which the motivations and objectives underlying the seismic monitoring of PCEP were outlined in Sections 1.4 and 1.5, respectively, whereas Section 2.3 discussed the geology of the PCEP study area. Recall that the main objectives were:

5. To undertake the interpretation of the time-lapse surface seismic and vertical seismic profiling data (VSP) using qualitative and quantitative seismic interpretation methods in an effort to detect the injected supercritical CO_2.
6. To perform feasibility analysis of time-lapse seismic monitoring using rock physics and numerical modelling to predict how the seismic response of the Cardium Formation would be affected by the CO_2 injection, and understand whether the implemented time-lapse seismic program was capable of delineating the CO_2 plume within reservoir and detecting any upward plume migration.

In the current chapter, the discussion is focused on achieving the first objective through the seismic analysis of the field data whereas objective 2 along with other modelling aspects of PCEP are discussed in Chapter 7. Table 4-1 gives an overview of PCEP and the disciplines involved as well as the various phases of the project. In depth discussion of the project and the various disciplines involved can be found in the project final report (Hitchon, 2009). Nonetheless, this dissertation combined with previous work by Lawton et al. (2005), Chen (2006) and Couëslan (2007) provides a far more comprehensive discussion of the seismic component of the monitoring, measurements and verification (MMV) program.

Table 6-1: PCEP overview.

Motivation	CO_2-EOR and storage (~20 Kt/year)
Location	PennWest CO_2-EOR Pilot Site, Violet Grove, Alberta
Target Formation	Upper Cretaceous Cardium sandstone
Formation Type	Oil reservoir
Disciplines Involved	Geology, geophysics, geochemistry, geomechanics (and wellbore integrity), reservoir engineering, and environmental monitoring
Phases	Phase I (2004-2005): • Regional characterization, site selection and baseline measurements • Design and construction of pilot facilities and MMV program Phase II (2005-2008): • Pilot operation (injection of > 1 Kt/month) • Implementation of MMV program Phase III (2008-2009): • Second seismic monitoring survey • Conclusion of pilot operation after the injection of > 50 Kt of CO_2
Project Status	Completed

6.2 Data and Seismic MMV Program

A brief introduction to the source of the seismic and well data was given in Section 1.6 and one can refer to Lawton (2005), Lawton et al. (2005) and Lawton et al. (2009) for more discussion of the design of the whole seismic MMV program. Figure 6-1 shows a base map outlining the distribution of the seismic and well data and Table 6-2 gives a brief summary of the various phases and the pertinent seismic data. In brief, the seismic monitoring program can be summarized as follows:

- Phase I: acquisition of the baseline multi-component surface seismic survey and fixed-array VSP data in March of 2005. The objective was to image the Cardium reservoir before the CO_2 injection and provide the necessary baseline measurements for the monitoring activity that came later in the program.
- Phase II: the first monitoring survey acquired in December 2005, i.e. nine months after the CO_2 injection activity began. The primary objectives were to detect the CO_2 plume, identify any CO_2 leakage and delineate possible changes within the

reservoir using multi-component surface seismic and vertical seismic profile data[64].

- Phase III: the second, and final, monitoring survey acquired in March 2007; two years after the commencement of the program. The main objectives remain similar to that of Phase II. In this phase, a new 2D seismic line was added into the program. In addition, a high resolution 16-level VSP survey was simultaneously acquired (in the western injector) in addition to the surface seismic in order to provide improved image of the target[65].

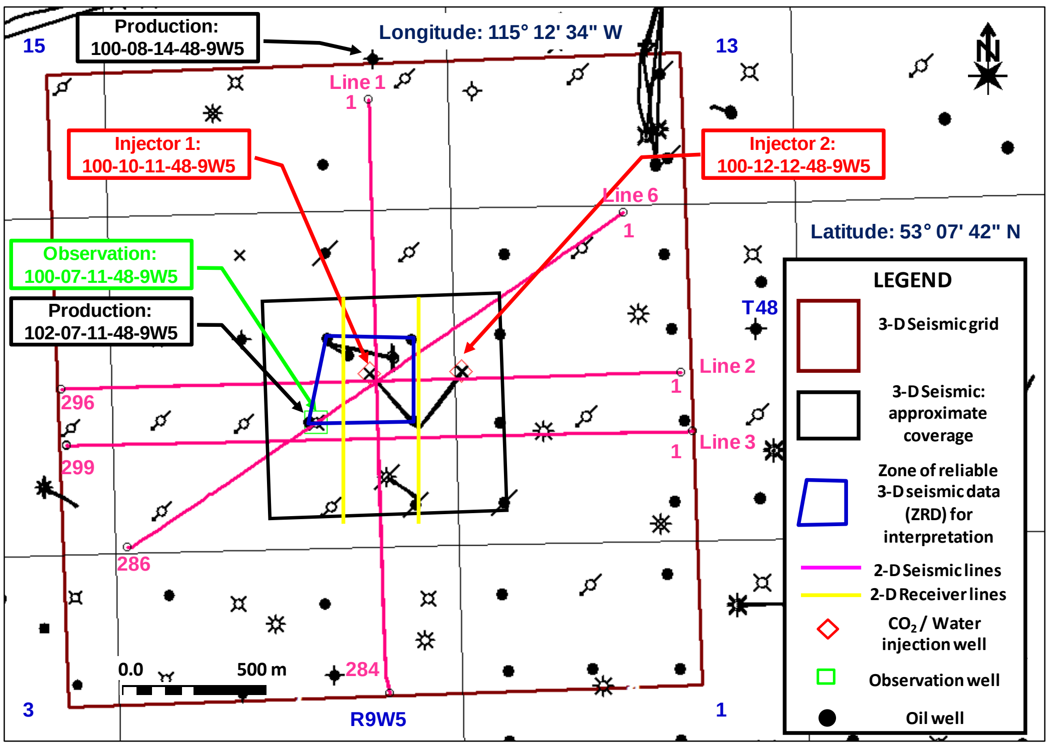

Figure 6-1: Base map showing the distribution of the 2-D and 3-D seismic data as well as the injection and observation wells in the local-scale study areas. Note the injection wells are deviated and the annotations in red point to the location of the bottom holes. See Figure 6-2 for a vertical schematic of the observation well (100-07-11-48-9W5). T: township, R: range, W: west of the meridian reference. The numbers in blue represent the section number within the corresponding township and range. See Figure 2-13 for definition of the rest of the well symbols.

[64] See theses by Chen (2006) for surface seismic and Couëslan (2007) for VSP interpretation.

[65] Since these additional data has no baseline measurements, they are not incorporated into the time-lapse analysis in this dissertation. More information on this data can be found in Lawton et al. (2009).

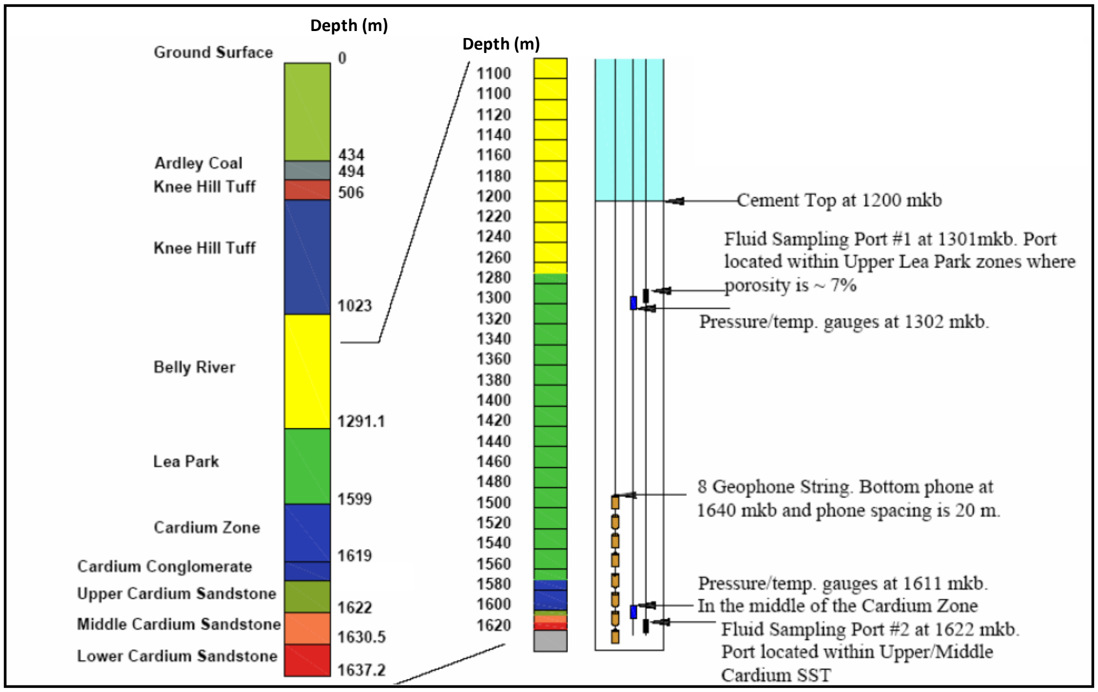

Figure 6-2: Schematic display illustrating the layout of the seismic instrumentation within the observation well (100-07-11-48-9W5) in Figure 6-1; mkb: measured from kelly bushing. Schematic by Rick Chalaturnyk (retrieved from Shevalier et al., 2007).

Table 6-2: Summary and some comments regarding the seismic component of the MMV program at the Pembina Cardium CO_2-EOR Pilot Project (PCEP) site. Kt: kilo-tonne.

Project Status	Seismic Data	Amount of CO_2 Injected
Phase I (March 2005)	- 2-D: Line 1 (north-south); Lines 2 and 3 (east-west) - 3-D: Sparse/limited - VSP: Fixed geophone array (8 geophones)	0
Phase II (December 2005)	- 2-D: Line 1 (north-south); Lines 2 and 3 (east-west) - 3-D: Sparse/limited - VSP: Fixed geophone array (8 geophones)	~ 20 Kt
Phase III (March 2007)	- 2-D: Line 1 (north-south); Lines 2 and 3 (east-west) - 3-D: Sparse/limited - VSP: Fixed geophone array (7 geophones)	~ 50 Kt
Comments	• Phase I and Phase III data were acquired at the same time of the year, i.e. March, but that did not guarantee that the near-surface conditions were identical. • The same types of source and receiver were used in acquiring the time-lapse data but that did not guarantee the preclusion of acquisition and instrument-related noises. • Similarly, the same processing flows were used in processing the individual time-lapse datasets but that as well did not guarantee the impediment of non CO_2-related variations. • In the context of this dissertation (from here forward), baseline and monitor refer to the Phase I (March 2005) and Phase III (March 2007) surveys. Difference refers to the baseline (2005) subtracted from the monitor (2007).	

Well 102-07-11-48-9W5 (Figure 6-1) contains the density, sonic and dipole sonic logs that were used in generating the synthetic seismograms (Section 6.4) as well as in the fluid substitution modelling (Chapter 7). However, since this well and, therefore, the logs terminate at the top of the Blackstone Formation below the Cardium Formation, it was decided to splice the logs from another production well, namely 100-08-14-48-9W5 (Figure 6-1) which penetrates into the top of Paleozoic Banff Formation (see table of formations in Section 2.3). This well has sonic and density logs but no dipole sonic log. Therefore, an S-wave log was synthesized using a local mudrock line[66] derived from 102-07-11-48-9W5. The P-wave and PS-wave synthetic seismogram generated using the hybrid logs, which for convenience was named after and placed at the observation well (100-07-11-48-9W5), provided a means of correlating important reflections in the seismic data that arrive after the Cardium reflection, in particular the Viking reflection. The relevance of this event will become clear as the reader progresses through this chapter. Further discussion on the local mudrock line and the utilization of the hybrid well logs is provided under the fluid substitution modelling in the next chapter.

The surface seismic dataset is comprised of two parallel, multi-component east-west 2-D lines that are 400 m apart and one orthogonal multi-component north-south 2-D line (Figure 6-1). These three lines were approximately 3 km long each with a receiver interval of 20 m, a source interval of 40 m, and a 2 kg dynamite source at a depth of 15 m (Lawton et al., 2005). In addition, 8 multi-component geophones were cemented at 20 m intervals into an observation well (100-07-11-48-9W5) at depths between 1498 m and 1640 m (Figure 6-1 and Figure 6-2). The deepest geophone was located at the bottom of the reservoir. All surface and borehole receivers were active throughout each survey (Lawton et al., 2009). Thus, the surface seismic data was recorded as sparse/limited 3-D while the VSP data was recorded as a walk-way VSP (Lawton et al., 2009). Hence, the surface seismic program provided low-fold 3-D subsurface coverage of the pilot site in addition to the relatively high-fold 2-D coverage. The borehole seismic data, on the other

---

[66] Mudrock line is an equation that relates the P-wave and S-wave speeds in siliclastic rocks using linear regression. Local means that the equation was derived using local data which is likely to produce an equation with sets of parameters different from those obtained by using the global mudrock line by Castagna et al. (1985).

hand, provided high-resolution images of the target reservoir locally around the observation well (Lawton et al., 2009). Note that the seismic MMV program was designed in such a way to maximize the coverage near the main injection (injector 1) and observation wells.

During Phase III of the project, a new southwest-northeast trending 2-D line (Line 6) and a retrievable multi-level VSP (recorded in the western injector) were added to the seismic program (Lawton et al., 2009). However, by the time of the second monitoring survey, i.e. Phase III, the program has already lost nearly 20% of the baseline shots due to additional infrastructure development that took place at the site (Lawton et al., 2009). Furthermore, and to due quality issues and failure[67] of some of the 8 cemented multi-component receivers in the observation well during Phase III, the converted-wave data corresponding to the VSP surveys were not incorporated into this dissertation. As far as the PS-wave surface seismic data is concerned, only the sparse 3-D was processed from time-lapse perspective and, therefore, incorporated in the interpretation[68].

The time-lapse multi-component surface seismic data were acquired and processed by CGGVeritas®. The 2-D P-wave surface seismic data from Phase I and Phase III were also, independently, processed by Divestco®. In all the processing vintages, the surface seismic datasets were processed using a standard flow through to post-stack time migration (Lawton et al., 2009). Identical flows were used for the baseline and monitor surveys after all non-repeated shots were first removed from the datasets. The 2-D lines were initially processed, independently, and this was followed by a sparse 3-D processing flow since all receivers were active during all shots (Lawton et al., 2009). The main data acquisition parameters are summarized in Appendix C.1. The 2-D and 3-D processing flows implemented contractor 1 (CGGVeritas®) are given in Appendix C.2.1 whereas the

[67] In particular, the second receiver cemented at 1520 m which failed by the time of Phase III. Therefore, the receivers were re-numbered in this dissertation from 1 to 7 instead from 1 to 8, where receiver 7 corresponds to 8 in the original baseline numbering scheme. In addition, the signals corresponding to the PS-wave component of two other receivers (4 at 1558 and 6 at 1599) in the original naming scheme were corrupted.

[68] Not only the 2-D PS-wave data was not processed in a time-lapse framework but, also, non-repeated shots were not removed from the base survey (2005) and, therefore, meaningful time-lapse interpretation could not be achieved using both dataset. These are in addition of the poor data quality.

2-D processing flows implemented by contractor 2 (Divestco®) are displayed in Appendix C.2.2. Likewise, the VSP data from all phases was processed by Schlumberger® (see Appendix C.3.1) although in-house processing (see Appendix C.3.2) was undertaken during the third phase of the project.

6.3 Previous Analysis

As outlined in Sections 1.4 and 1.5, two graduate theses were published as part of the seismic MMV program during first two phases of the Pembina Cardium CO_2-EOR Pilot Project. Chen (2006) discussed the interpretation of the time-lapse multi-component surface seismic data from Phase II. The work performed by Chen (2006) included some fluid substitution modelling, AVO and 2-D post-stack acoustic impedance inversion. For elaborate discussion, the reader is referred to the thesis by Chen (2006) but below is an outline of some of the main conclusions:

- On the seismic data, the Cardium event correlated with a weak reflection, which is quite typical of this formation in the central plains of Alberta.
- The fluid substitution modelling results produced by Chen (2006) indicated that the P-wave speed would decrease by approximately 5% whereas the S-wave speed would increase by 1% after the reservoir was 99% saturated with CO_2. This corresponded to a small amplitude change and about 1 ms time shift between baseline and monitoring observations.
- Several time-lapse seismic interpretation methods were invoked in the interpretation of the surface seismic data. Those were time and amplitude differencing, α/β, AVO inversion and acoustic impedance inversion.
- Chen (2006) observed subtle changes on the intercept-gradient AVO attribute sections as well as on the acoustic impedance difference maps estimated using the P-wave surface seismic data from Line 1 but nothing conclusive, especially when considering the remaining 2-D data.
- However, Chen (2006) reported that no anomalies were observed above the reservoir, which indicated that no CO_2 leakage was occurring by at time of the

first monitoring survey. Furthermore, the data seemed to indicate that CO_2 was confined to a thin layer within the reservoir.

The second thesis was published by Couëslan (2007), whom had undertaken the time-lapse processing and interpretation of the baseline and first monitor multi-component VSP data recorded using the fixed-array geophones in the observation well (Figure 6-1). The processing involved some analysis pertaining to the anisotropy that was attributed to a shallow shale formation in the study area. The 1-D vertical traverse isotropic (VTI) model velocity model developed through Couëslan's (2007) work was later used in the time migration of the VSP data. The key findings in Couëslan (2007) thesis could be summarized as follows:

- Couëslan (2007) reported that there is a high degree of similarity between the baseline (Phase I) and the first monitoring (Phase II) surveys, i.e. data repeatability is high.
- Couëslan (2007) observed a small reflectivity increase at the reservoir in the P-wave data. This is accompanied by small time shift of 0.2 ms at the base of the reservoir on one of the walkaway lines. She reported that these changes were in agreement with those predicted by the fluid substitution modelling of Chen (2006).
- Couëslan (2007) indicated that the PS-wave (converted-wave) VSP data showed some inconsistency and, therefore, the results derived from it were inconclusive.
- Couëslan (2007) interpreted that the small changes she observed (time shift and reflectivity increase) were caused by the CO_2 plume. Moreover, she concluded that the plume is moving southwest from the injector wells, i.e. along the dominant fracture trend in the region (NE-SW), at a rate of 47.5 m per month.

In summary, the data quality was good in both studies but no concrete conclusions could be drawn in regard to the CO_2 plume and its distribution in the reservoir. Moreover, both authors proposed that a more profound 4-D seismic response should be observed after the acquisition and processing of the data from Phase III of the project. Besides the two theses mentioned above, several pertinent publications were contributed throughout the life span of the project by many authors in the CREWES project. These include passive seismic monitoring (Bland et al., 2006), comparisons of multi-component geophones and accelerometer (Lawton et al., 2006; Hons, 2008), 2-D and 3-D data processing (Lu et al., 2005), hypocenter location errors of microseismic events (Chen and Stewart, 2006), Borehole geophone repeatability experiment (Gagliardi and Lawton, 2010), and spectral ratio analysis (Hasse et al., 2010).

6.4 Data Calibration

Although the data acquisition parameters and processing flow were consistent between the various phases of the project, subtle changes still occurred between the time-lapse surveys due, for instance, to variation in near-surface conditions or acquisition-related issues as described by many authors including Naess (2006) and Pevzner et al. (2010). Therefore, the next crucial undertaking, prior to qualitative and quantitative interpretation, was data calibration. This consisted primarily of the design and application of shaping filter to the monitoring data (Section 3.6.1). When necessary, two additional steps were incorporated into the calibration process, namely cross-correlation time shift and cross-normalization. The former calculates the cross-correlation between the baseline and monitor datasets and then applies any necessary time shift to the monitor data whereas the latter normalizes the amplitude of the monitor data with respect to the baseline by calculating an RMS-based scalar (in a concept similar to that described in Section 3.6.1 using both surveys and then applies such scalar to the monitor data. Figure 6-3 outlines the data calibration scheme while Table 6-3 summarizes the main calibration parameters.

As illustrated in Figure 6-3, the calibration was preceded by seismic-to-well tie. A process by which seismic data is correlated with corresponding geologic formations using synthetic seismograms generated by utilizing edited well logs and the convolutional model (see Section 3.5.5). The reason the seismic-to-well tie was included as part of the calibration workflow was because it provided a better understanding of the seismic data that helped in guiding and assessing the calibration process. Figure 6-4 shows the seismic-to-well tie using the 3-D P-wave and PS-wave data and well logs at the observation well. The gamma ray, density, P-wave speed (α), S-wave speed (β), α/β, P-wave reflectivity series, S-wave reflectivity series as well as the P-wave and PS-wave synthetic seismograms are plotted in Figure 6-4.

The Cardium event (reservoir) is visible at about 1050 ms in the P-wave (Figure 6-4 (a)) and 1710 ms in the PS-wave (Figure 6-4 (b)) seismic data. In the well logs, the Cardium Formation is characterized by a subtle increase in both P-wave speed and S-wave speed, and in density logs accompanied with a rather strong decrease in the gamma-ray response. In addition to the Cardium event, two prominent reflections were also identified which correspond to the Ardley Zone and Viking Formation (see Section 2.3). The Ardley is part of the upper Scollard Formation and it consists of series of shallow coals that are observed at traveltime of about 360 ms and 660 ms in the P-wave (Figure 6-4 (a)) and PS-wave (Figure 6-4 (b)) seismic data, respectively. The Viking Formation gives rise to a strong reflection at about 1230 ms in P-wave section (Figure 6-4 (a)) and 1970 ms in PS-wave section (Figure 6-4 (b)) as a result of a shale-sandstone interface. The Ardley and Viking are of particular interest because they exhibit strong and consistent reflections in the seismic data throughout the study area. Thus, the former provided a shallow marker whereas the latter was used as an indicator to monitor any anomalies induced by changes in the overlying Cardium reservoir due to CO_2 injection.

Once these key horizons had been identified, calibration commenced by designing and applying a shaping filter to the individual monitoring surveys to account for any difference in the waveform between the time-lapse surveys. The theory underlying the shaping filter, known as Wiener-Levinson algorithm, used in the calibration process was discussed in Section 3.6.1. In each case, the baseline was chosen as the reference and the shaping filter was designed using both baseline and monitoring surveys. In the case of the multi-component surface seismic data, different design windows were tested but ultimately a design window of 700 ms and 1400 ms above the reservoir were selected for the P-wave and PS-wave data, respectively. Selecting a design window above the reservoir provided good results for the surface seismic but not for the VSP data since the seismic image only starts at the reservoir level. Therefore, a 1000 ms design window was used below the reservoir for the VSP data calibration. Different operator lengths and (pre-whitening) noise levels were tested as well. Quality control measures, such as cross-correlation, were computed in each trial and these were accompanied by visual inspection[69]. If the calibrated data exhibited good visual and numerical correlation, then the data calibration proceeded to the next step (Figure 6-3). Otherwise, the shaping filter was re-designed and applied again until a satisfactory result was obtained.

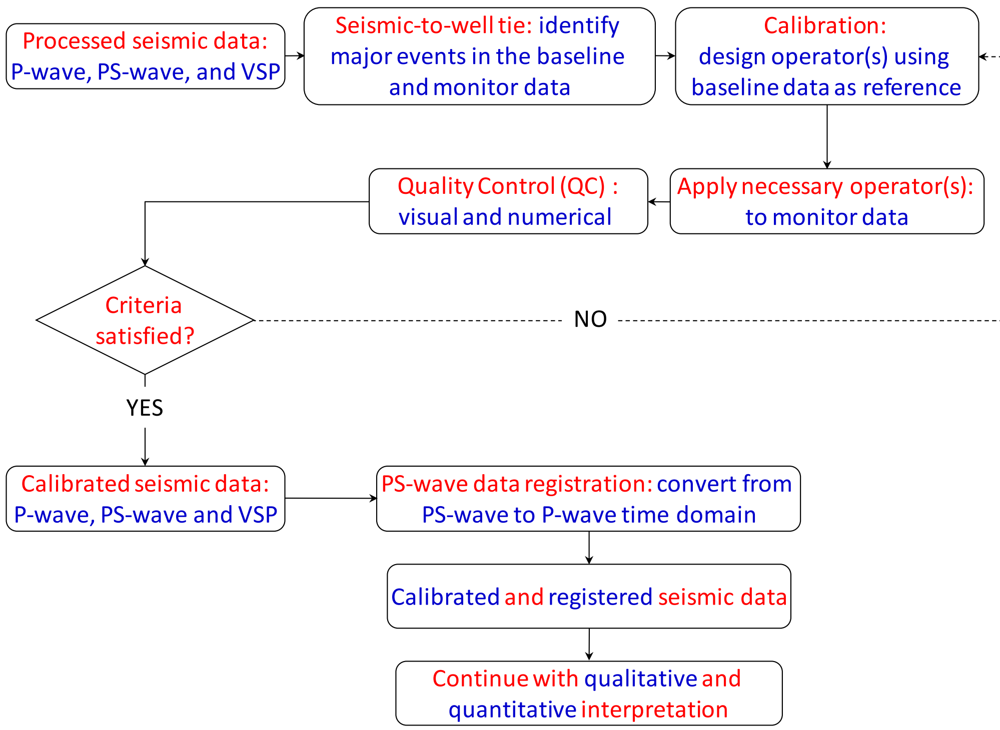

Figure 6-3: Workflow outlining the main calibration processes. Note that the criteria would be satisfied if a good visual and numerical correlation is achieved.

Table 6-3: Main data calibration parameters used in the calibration.

Design Window (P-wave surface seismic)	700 ms (above the reservoir); others tested
Design Window (PS-wave surface seismic)	1400 ms (above the reservoir); others tested
Design Window (VSP)	1000 ms (below the reservoir); others tested
Operator Length (shaping filter)	75 ms; others tested
Pre-whitening (shaping filter)	0.001%; others tested

[69] To avoid redundancy, repeatability metrics, namely NRMS and PRED, which serves as quality control measures will be discussed in the next section (Section 6.5.1).

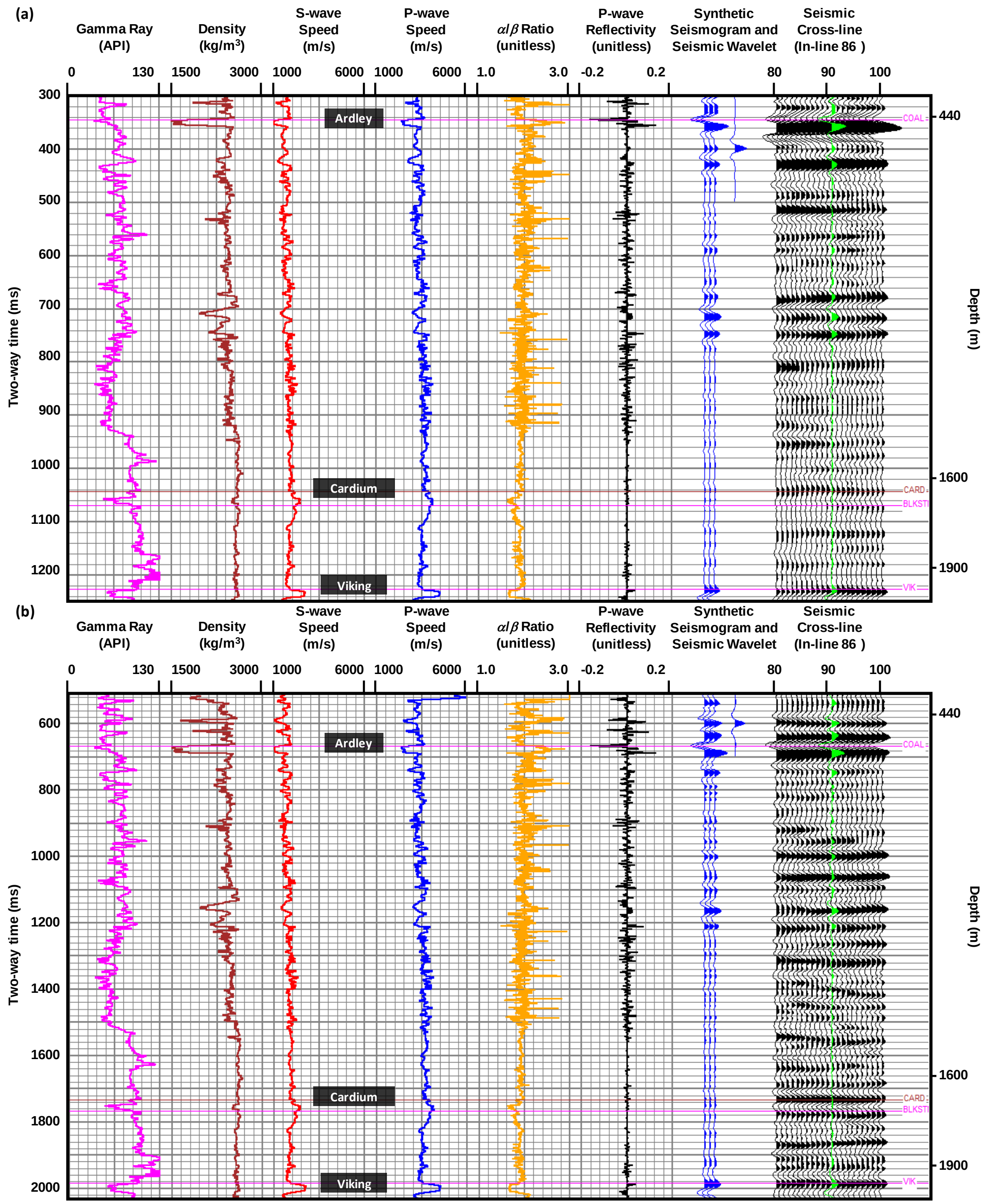

Figure 6-4: Seismic-to-well tie at the observation well (100-07-11-48-9W5) using the baseline (a) 3-D P-wave, and (b) 3-D PS-wave surface seismic data. The location of the well is shown in the base map (Figure 6-1). The blue and green traces depict the synthetic seismograms whereas the black traces represent the seismic data at and near the well location. The correlation coefficients of the P-wave and PS-wave well-tie are 0.87 and 0.70, respectively. The three major events discussed in the section are identified. The wavelets were statistically extracted from the corresponding seismic volumes. Figure 6-52 shows representations of the amplitude spectra of these wavelets. See Figure 7-3.

6.5 Qualitative and Quantitative Interpretation

Following the data calibration, the various datasets were examined and compared. Although the calibration process had reconciled what was considered to be non-CO_2 related differences, it was clear that some of the data did not exhibit the necessary signal to noise ratio (S/N) quality to aid in achieving the objectives outlined earlier in this dissertation (Section 6.1). Nonetheless, it was perceived that qualitative scrutinizing alone was not sufficient. Hence, repeatability metrics were invoked in gauging the data quality as well as in making decisions as whether a given dataset would to be included in the qualitative and quantitative interpretation. Consequently, the first quantitative method to be explored in this section is repeatability. It, also, has another important application pertaining to the CO_2 plume detection as outlined in Section 3.6.3. Once the data selection has been completed, the interpretation proceeded by looking at some direct and conventional attributes, such as amplitude, as well as a portfolio of more vigorous seismic attributes. However, before proceeding with the qualitative and quantitative interpretation, a brief discussion is presented that reviews the nature of the expected seismic response.

6.5.1 Predicted Changes in the Seismic Response at the PCEP Site[70]

Initially, it was important to relate the expected changes caused by the injection of supercritical CO_2 and the seismic response being analyzed. In this study, the magnitude of time shift and isochron difference is predicted to be very small, i.e. a time shift of ~ 0.3 ms in the P-wave data and half of that in the case of the PS-wave data[71]. Furthermore, CO_2 injection should cause the amplitude of the multi-component, i.e. P-wave and PS-wave, seismic data to decrease as a result of the decrease in the acoustic and shear impedances. Therefore, the difference in the seismic amplitude of the P-wave data is

---

[70] Besides the corroboration provided by the cited literature in Chapter 1, the statements made here were substantiated by the results from the fluid substitution and the offset-dependent reflectivity seismic modelling, which will be discussed in the next chapter.
[71] Based on the modelling results in Chapter 7.

expected to decrease by ~ 5% whereas that of the PS-wave data would decrease as well but by smaller magnitude (~ 2.5%)[72].

As for the seismic signal repeatability, it is predicted[73] that CO_2 injection would cause the NRMS to be around 5%, predominantly due to the decrease in the seismic amplitude as the contribution by time shift is insignificant. Similarly, the PRED of the time-lapse surveys is expected to be approximately 99%[74]. Since, the predicted magnitude change in all the aforementioned attributes is very small, any non-repeatable noise, whether related to acquisition or processing, would most likely obscure any time-lapse change induced by the CO_2 plume. Despite that, the analysis and discussion were conducted in an objective and unbiased fashion. As outlined in thesis objectives, the effects of anisotropy and pore pressure were not investigated in the time-lapse analysis[75].

6.5.2 Repeatability

Repeatability metrics, namely normalized root-mean squares (NRMS) and predictability (PRED), play an important role in quantifying the consistency between the time-lapse seismic surveys and, hence, the reliability of the data involved in the time-lapse seismic analysis. The underlying mathematical formulations were discussed in the methods chapter (Section 3.6.3). First, source repeatability is examined followed by that of the various time-lapse seismic datasets.

6.5.2.1 Sources and Receivers

Figure 6-5 and Figure 6-6 show the lateral and vertical positions of the dynamite shots in the baseline (2005) and the monitor (2007) whereas the corresponding difference and NRMS of Line 1, Line 2 and Line 3 are plotted in Figure 6-7, Figure 6-8, and Figure 6-9, respectively. Obviously, source repeatability is very good except for the vertical position, i.e. shots depth, which exhibit poor repeatability as indicated by the high NRMS

---

[72] Predicted through seismic modelling in Chapter 7.

[73] See footnote 9.

[74] Recall that NRMS is sensitive time shift as well as amplitude change whereas PRED is sensitive to noise-level (see discussion under Section 3.6.3).

[75] In particular, the effect of pore pressure was not considered due to compromised quality of the PS-wave data.

values. This could be attributed to ground conditions and difficulties in placing the dynamite charge at the desired depth. However, the difference is relatively small and studies (Pevzner et al., 2010) suggest that variation in source depth is small and not as significant as the effect of variation in source strength and type. As far as receiver repeatability is concerned, geophones in the observation well were cemented and, hence, the coordinates and depth remained unchanged throughout the MMV program. For the surface receivers, there is no evidence to suggest that they are of lesser repeatability than that of the sources, especially since the surface receivers were much easier to reposition than dynamite shots.

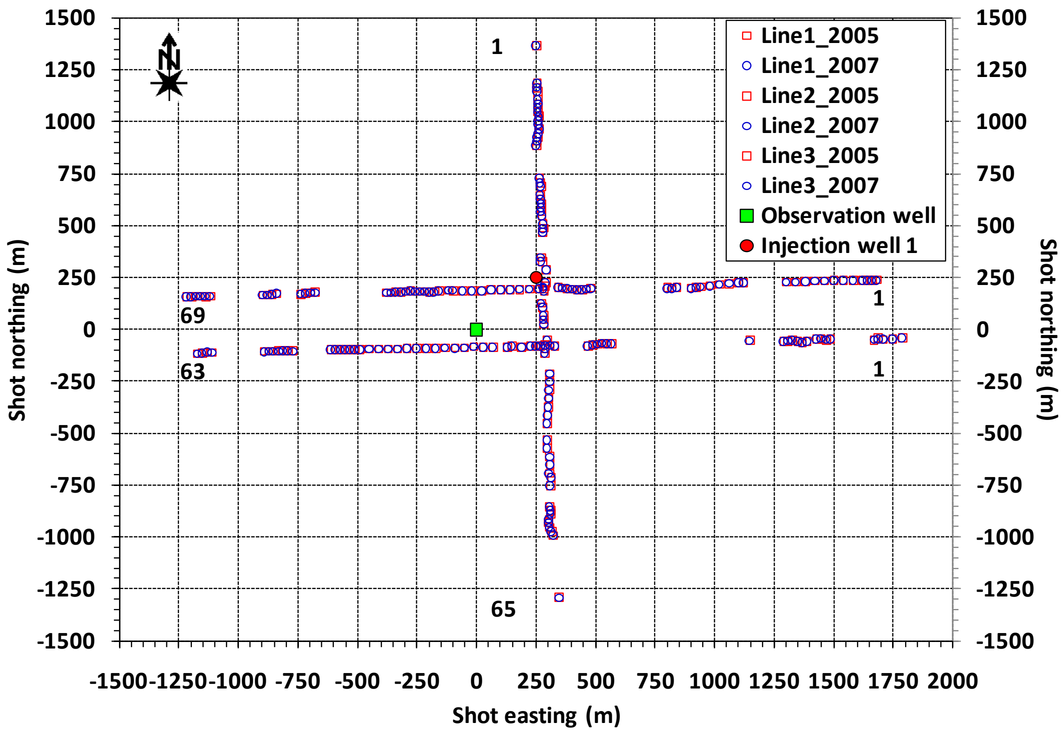

Figure 6-5: Lateral position of sources in the baseline (2005) and monitor (2007). Note that non-repeated shots were removed and that northing and easting are relative to the observation well.

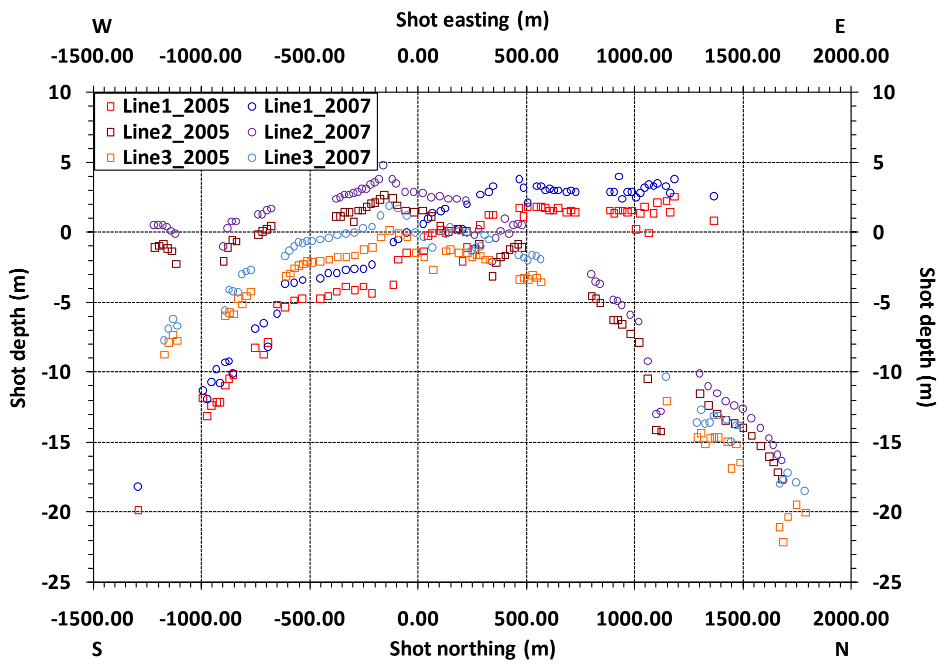

Figure 6-6: Vertical position of sources (Figure 6-5) in the baseline (2005) and monitor (2007). Note that northing and easting are relative to the observation well whereas the depth is with respect to the surface well-head of to injector 1 (883.6 m).

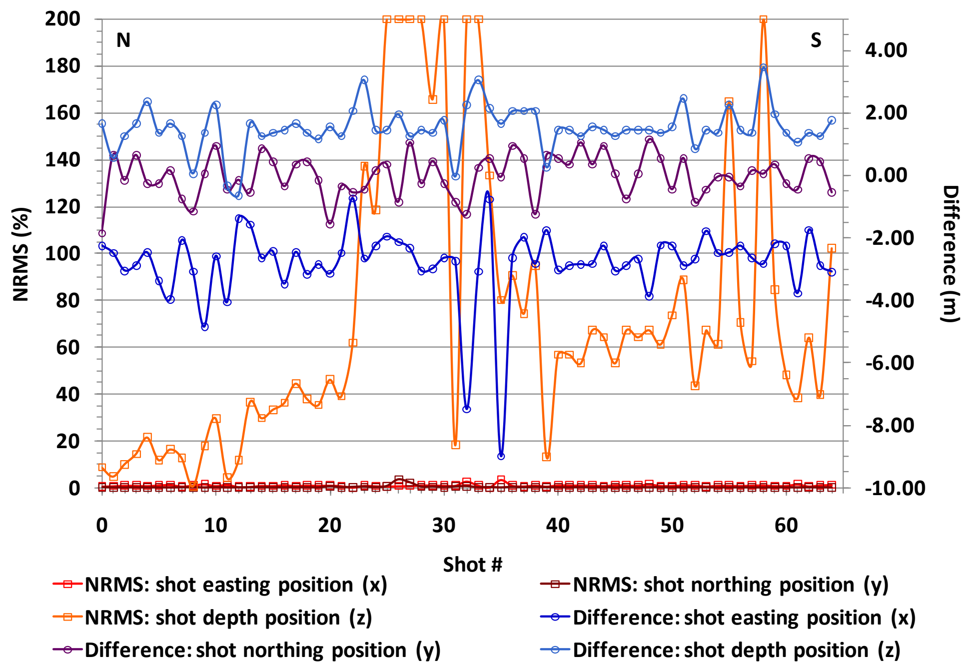

Figure 6-7: Source position NRMS (left-hand axis) and difference (right-hand axis) of Line 1. Note the excellent repeatability of the source lateral position as illustrated by the low NRMS values. The vertical position repeatability, on the other hand, is not as good.

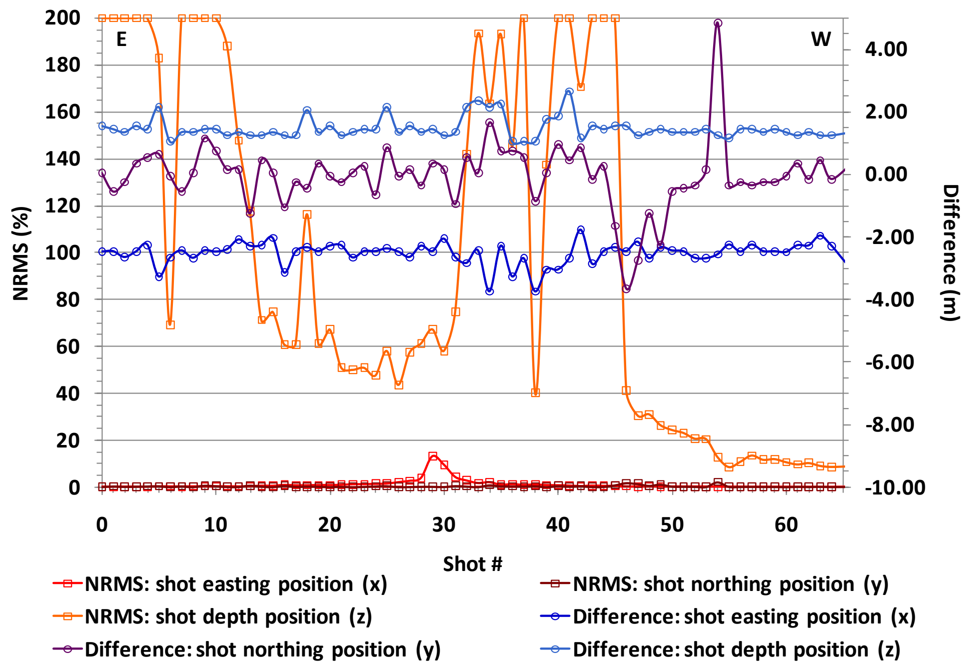

Figure 6-8: Source position NRMS (left-hand axis) and difference (right-hand axis) of Line 2. Repeatability of the source lateral position is excellent except for the easting position anomaly near shot # 30. Like that of Line 1, the vertical position repeatability is poor.

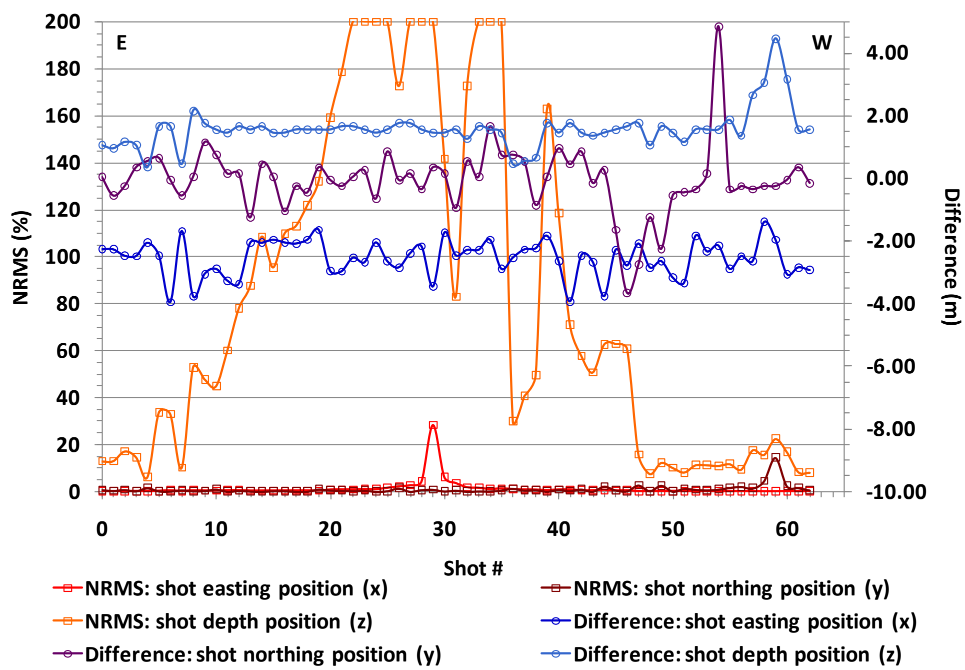

Figure 6-9: Source position NRMS (left-hand axis) and difference (right-hand axis) of Line 3. Lateral repeatability is excellent except for the easting and northing anomalies near shots # 30 and # 60, respectively. Once more, vertical position repeatability is poor.

6.5.2.2 VSP Data

Figure 6-10 shows the repeatability of the raw VSP data from Lines 1, 2 and 3, respectively, before and after the calibration process. The repeatability metrics were computed using a vertical window encompassing samples from each full trace, although other window lengths were investigated as well. Interestingly, the raw VSP repeatability is actually good but data calibration was necessary in this case and significant improvements were made after calibration. These can be seen in terms of the decrease in the NRMS and the increase in PRED magnitude. For example, note the suppression of the spurious observations caused by either gaps in the shots (see Figure 6-5) or the so-called edge effect at both ends of each profile as can be seen above and below the tips of the arrows in Figure 6-10. Nonetheless, the calibration was not so aggressive in the sense that subtle changes between the time-lapse surveys were preserved.

The NRMS (~ 10%) and PRED (~ 98%) of the calibrated raw VSP are excellent and consistent across the various lines except for the 4^{th} receiver (R4 at 1578 m) between traces 190 and 250 which exhibits lower PRED compared to the other receivers (Landrø, 1999; O'Brien et al., 2004). The fact that the NRMS does not show any significant variation at this receiver suggests that the cause behind the observed anomaly is noise-related, probably due to some mechanical issues with this receiver or the cables.

The repeatability of the migrated VSP sections from Lines 1, 2 and 3 are shown in Figure 6-11. These were computed using a long window encompassing the Cardium, Ardley and deeper reflections although shorter windows were investigated as well. Clearly, Line 1 attains the best NRMS repeatability (~ 23%) whereas no distinctive superiority could be established in terms of the PRED (~ 92%) of the various lines. Furthermore, there seems to be an interesting repeatability anomaly in the migrated VSP section of Line 1 (Figure 6-11) where there is an increase in the magnitude of the NRMS and a decrease in the magnitude of the PRED near the observation well (between traces 170 and 190). Such change is what one would expect to see due to the CO_2 injection. However, the repeatability of Line 2 and Line 3 (Figure 6-11) at the same zone only slightly improves from neighbouring traces.

Since it is suggested by some experts[76] in the field of borehole geophysics that sometimes the migration of VSP data introduce artefacts that might suppress subtle anomalies associated with CO_2 injection, it was decided to also investigate the repeatability of the common-depth point (CDP) transformed VSP data as well (Figure 6-12). Overall, the repeatability of the CDP-transformed lines (NRMS ~ 30% and PRED ~ 88%) is not as good as that corresponding to the migrated VSP (NRMS ~ 23% and PRED ~ 92%) although the NRMS of Line 3, in particular, in Figure 6-12 is poorer than the other lines. However, no additional information, in regard to the CO_2 plume distribution, could be inferred from the repeatability of the CDP-transformed VSP data.

Table 6-6 shows simple statistics comparisons of the VSP data repeatability. Aside from the CO_2 plume delineation, it is intriguing to observe that the repeatability of the raw VSP data is superior to that of the migrated and CDP-transformed VSP data. This provoked the plot in Figure 6-13 which looks closer at the raw traces corresponding to the first (and shallowest) receiver from Line 1. By examining the repeatability of this receiver as well as the rest of the receivers from the raw VSP in addition to the migrated and CDP-mapped VSP data, there does not seem to be any prominent and consistent anomaly that could be attributed to the CO_2 injection activity.

Finally, the repeatability analysis indicates that the observed variations in the magnitude of the NRMS and PRED metrics are most likely driven and dominated by non CO_2-related differences due to variations in the near-surface ground conditions in addition to the effects of the gaps in the shot line and processing noise. Recall that NRMS and PRED values predicted through the modelling results (Chapter 7) are ~ 10% and 99%, respectively, whereas those belonging to the migrated and CDP-transformed VSPs are 23% - 92% and 30% - 88%. Furthermore, the lack of a clear CO_2-related repeatability anomaly in the VSP data, in particular the raw data, might have ramifications for the presence of such an anomaly in the repeatability of the surface seismic data (following sections). The is because the VSP data is thought to suffer less from the near-surface effects in addition to the fact that the position of the receivers in the observation well are

[76] In particular, through personal communication with Mr. Tom Daley of Lawrence Berkeley National Laboratory.

exactly repeatable since they are permanently cemented in the borehole. Of course, the types of source and receiver were maintained although some other aspects, primarily source depth and charge weight, could not be completely sustained between the two surveys. But, as mentioned under the source and receiver repeatability (Section 6.5.2.1), the effect of small variations in these parameters, as the case in this project, is expected to be insignificant.

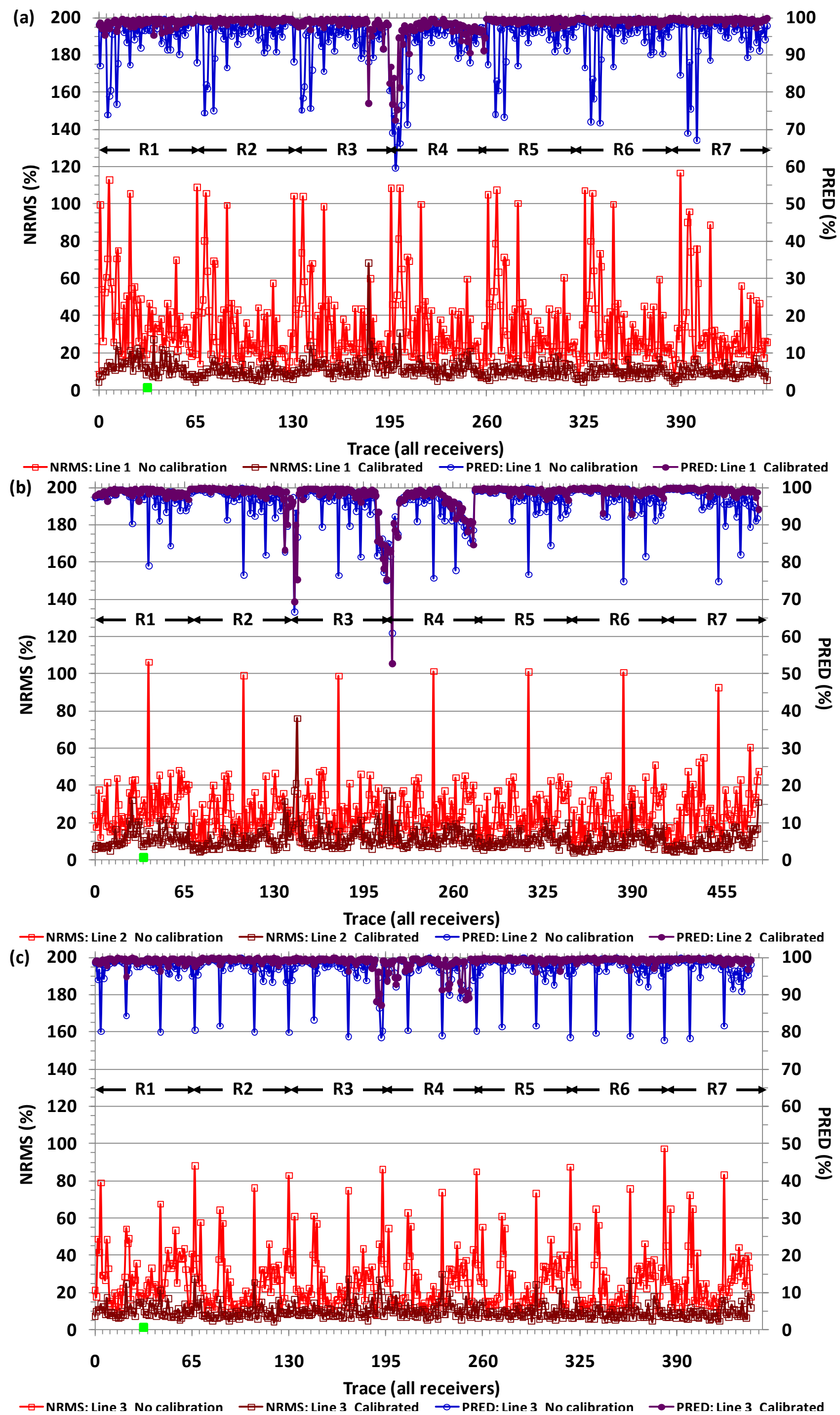

Figure 6-10: Repeatability of the raw VSP data from (a) Line 1, (b) Line 2, and (c) Line 3 before and after calibration. R1: 1st and shallowest receiver at 1498 m; R7: 7th and deepest receiver at 1640 m. The double-sided arrows at the left and right-hand sides in the middle of the plot show the extent of the traces belonging to the 1st and 7th receivers, respectively. The location of the observation well corresponds approximately to the midpoint of the traces belonging to each receiver as demonstrated by the green square.

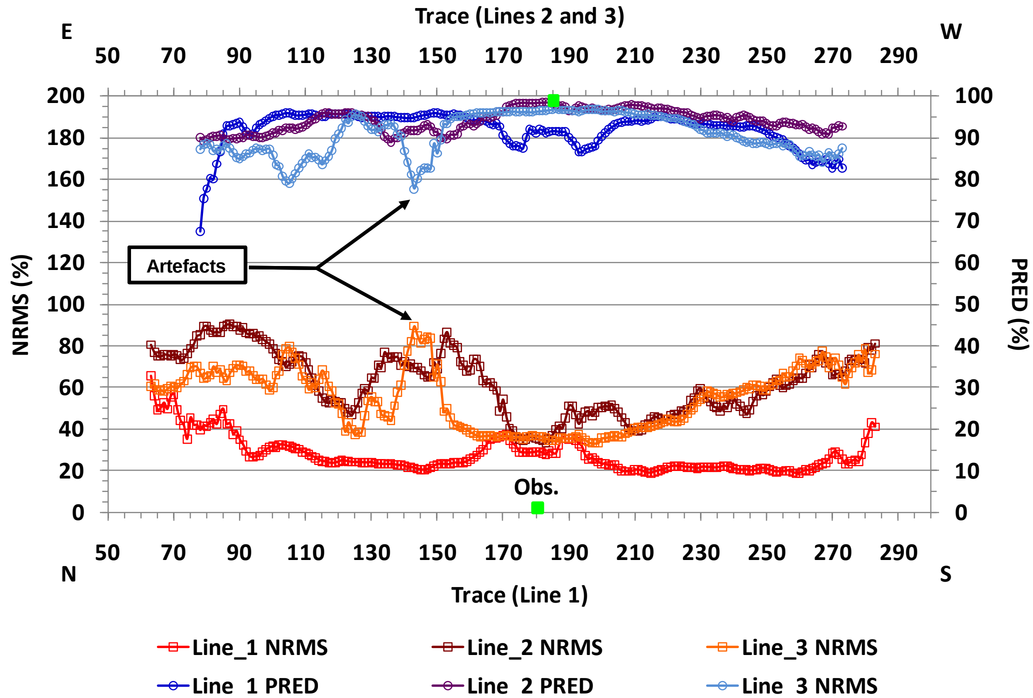

Figure 6-11: Repeatability of the calibrated and migrated VSP data from Lines 1, 2 and 3. The approximate projected location of the observation well is shown by the green square. Note how the artefacts correlate with the source gaps in Figure 6-5.

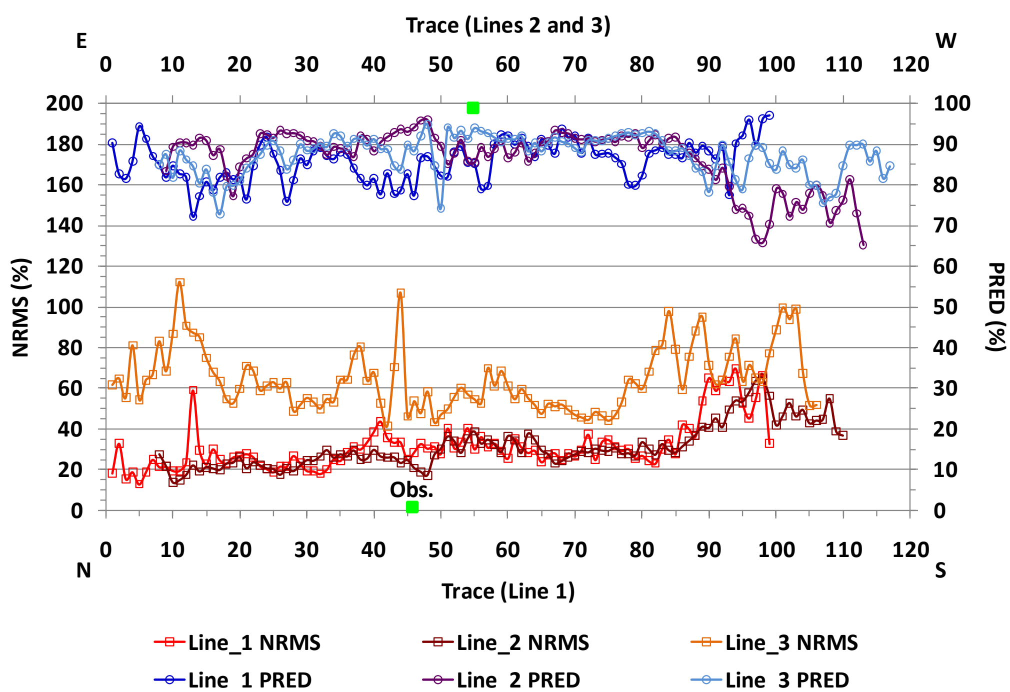

Figure 6-12: Repeatability of the calibrated and CDP-mapped VSP data from Lines 1, 2 and 3. The approximate projected location of the observation well is shown by the green square.

Table 6-4: Comparisons of the repeatability of the calibrated VSP data. Std. Dev.: standard deviation.

2-D Line	Vintage	Average NRMS	NRMS Std. Dev.	Average PRED	PRED Std. Dev.
Line 1	Raw	10.94	4.63	98.39	2.90
	CDP-transformed	31.46	11.82	85.88	4.95
	Migrated	30.45	12.56	86.07	15.03
Line 2	Raw	10.88	5.81	97.92	4.13
	CDP-transformed	32.76	12.75	84.39	12.03
	Migrated	36.42	16.98	90.24	11.13
Line 3	Raw	9.73	3.78	98.89	1.64
	CDP-transformed	32.16	7.55	86.94	6.64
	Migrated	29.88	11.86	88.11	10.21

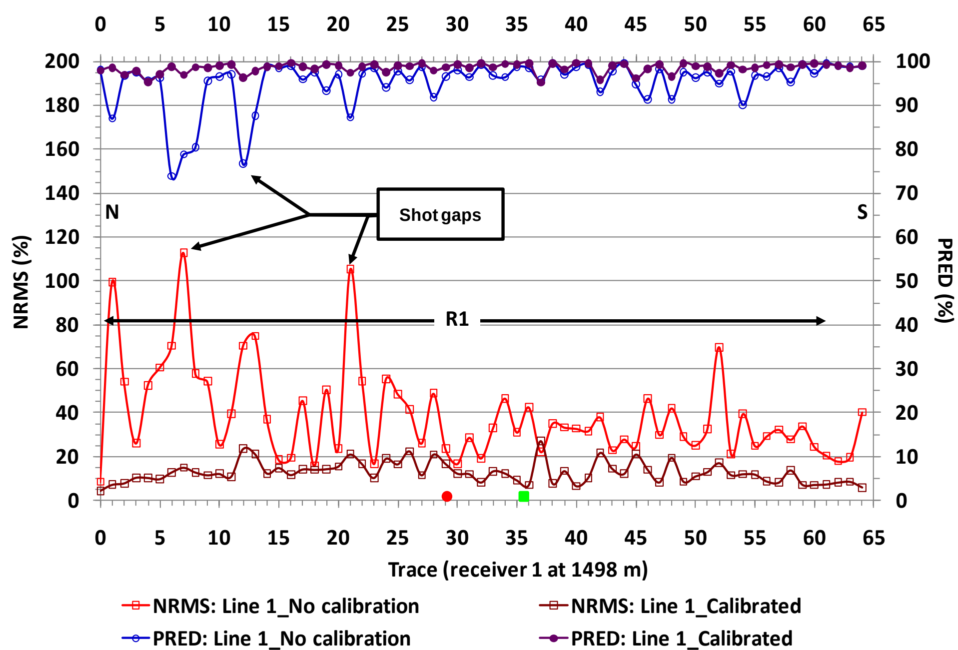

Figure 6-13: Repeatability of the first receiver (R1) of the raw VSP data from Line 1 before and after calibration (see Figure 6-10). The approximate projected location of the injection (red circle) and observation (green square) wells are shown on the primary horizontal axis.

6.5.2.3 2-D Surface Seismic Data

The repeatability of the various calibrated vintages corresponding to the 2-D surface seismic data from Line 1, Line 2 and Line 3 are plotted in Figure 6-14, Figure 6-15 and Figure 6-16, respectively. In these plots, the NRMS and PRED were computed using a wide window enclosing the Ardley, Cardium and Viking events (Figure 6-4 (a)) although other windows were investigated as well. The repeatability of the data processed by the 2nd contractor show a rather poor and sometimes erratic pattern between the various lines. For instance, the “fmig” and “fstr” versions exhibit average NRMS and PRED of about 85% both which seems to be caused by processing inconsistency, probably due to scaling and noise attenuation variance. In the case of Lines 2 and 3, the NRMS of the processing vintages by the 2nd contractor show more resemblance to that of the 1st contractor whereas the PRED pattern is still somewhat erratic. Table 6-6 gives statistical comparisons of the repeatability of the various 2-D lines.

In particular, the data processed by the 1st contractor exhibits better repeatability than that processed by the 2nd contractor. This is most clearly seen in the relatively low-NRMS, high-PRED values of the “fsmig” and “unufmig” versions of Line 1 in Figure 6-14 and Table 6-6. Moreover, of all the processing vintages, the filtered, scaled and migrated (fsmig) version by the 1st contractor attains the best repeatability. Although it is hard to draw a distinction concerning the repeatability of the data processed by the 1st contractor, it seems that the NRMS and PRED values are associated with Line 1 followed by Lines 2 and 3, respectively. This seems to be primarily due to the continuity in the positioning of the shots in the case of Line 1 (Figure 6-5). Interestingly, there appears to be no relationship between fold and repeatability. However, the direct correlation between poor repeatability and acquisition footprint, i.e. gaps in the shot positions, is evident. For example, the repeatability of Line 3 deteriorates between traces 60 and 120 (Figure 6-16). Obviously, this zone corresponds to the wide gap in the eastern segment of Line 3 (Figure 6-5).

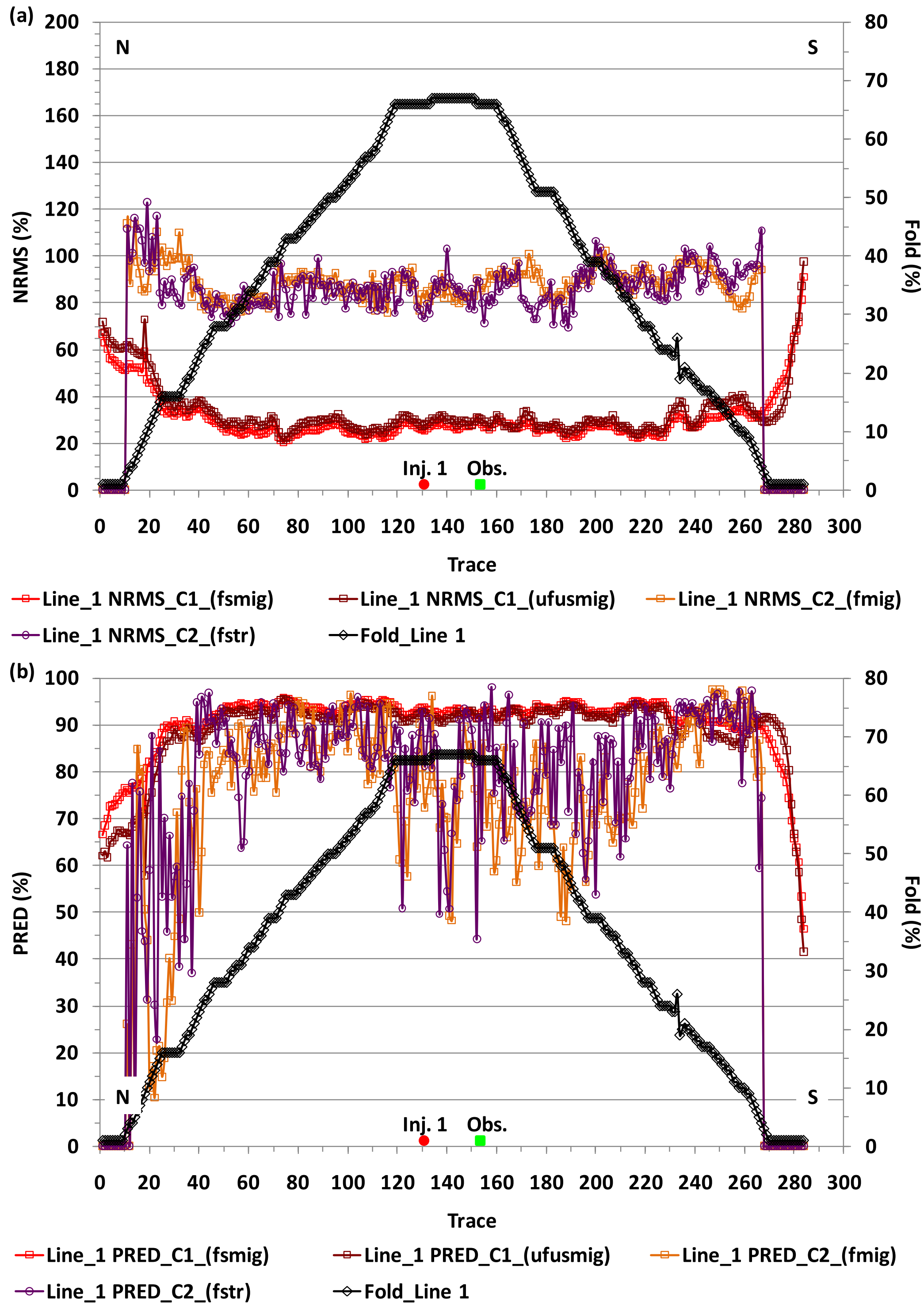

Figure 6-14: (a) NRMS, and (b) PRED repeatability of Line 1 after calibration. C1: contractor 1; C2: contractor 2. The characters inside the parentheses refer to the processing vintage (See Table 6-5). The approximate projected location of the injector (Inj. 1) and observation (Obs.) wells are indicated by the red circle and the green square, respectively.

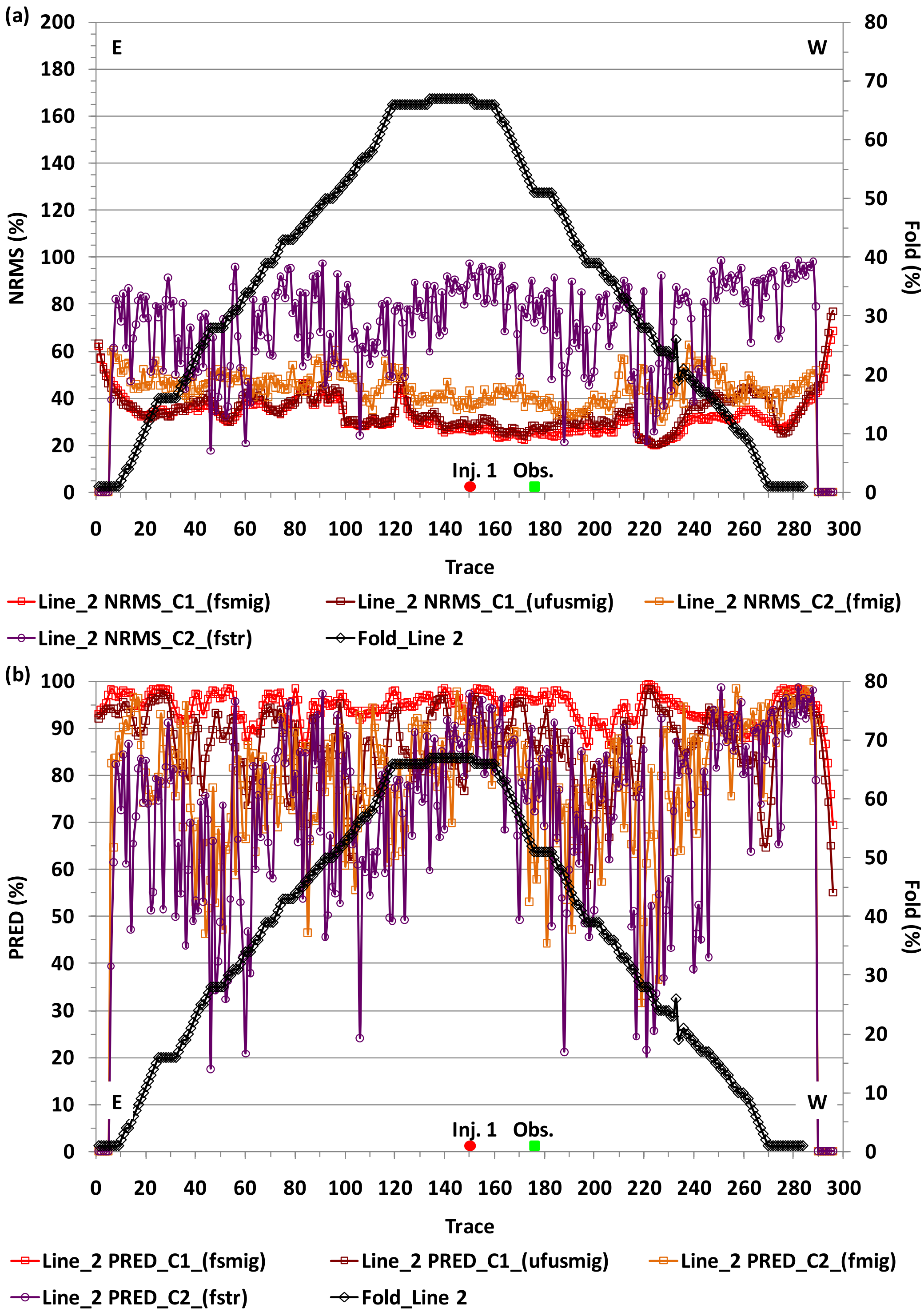

Figure 6-15: (a) NRMS, and (b) PRED repeatability of Line 2 after calibration. C1: contractor 1; C2: contractor 2. The characters inside the parentheses refer to the processing vintage (See Table 6-5). The approximate projected location of the injector (Inj. 1) and observation (Obs.) wells are indicated by the red circle and the green square, respectively.

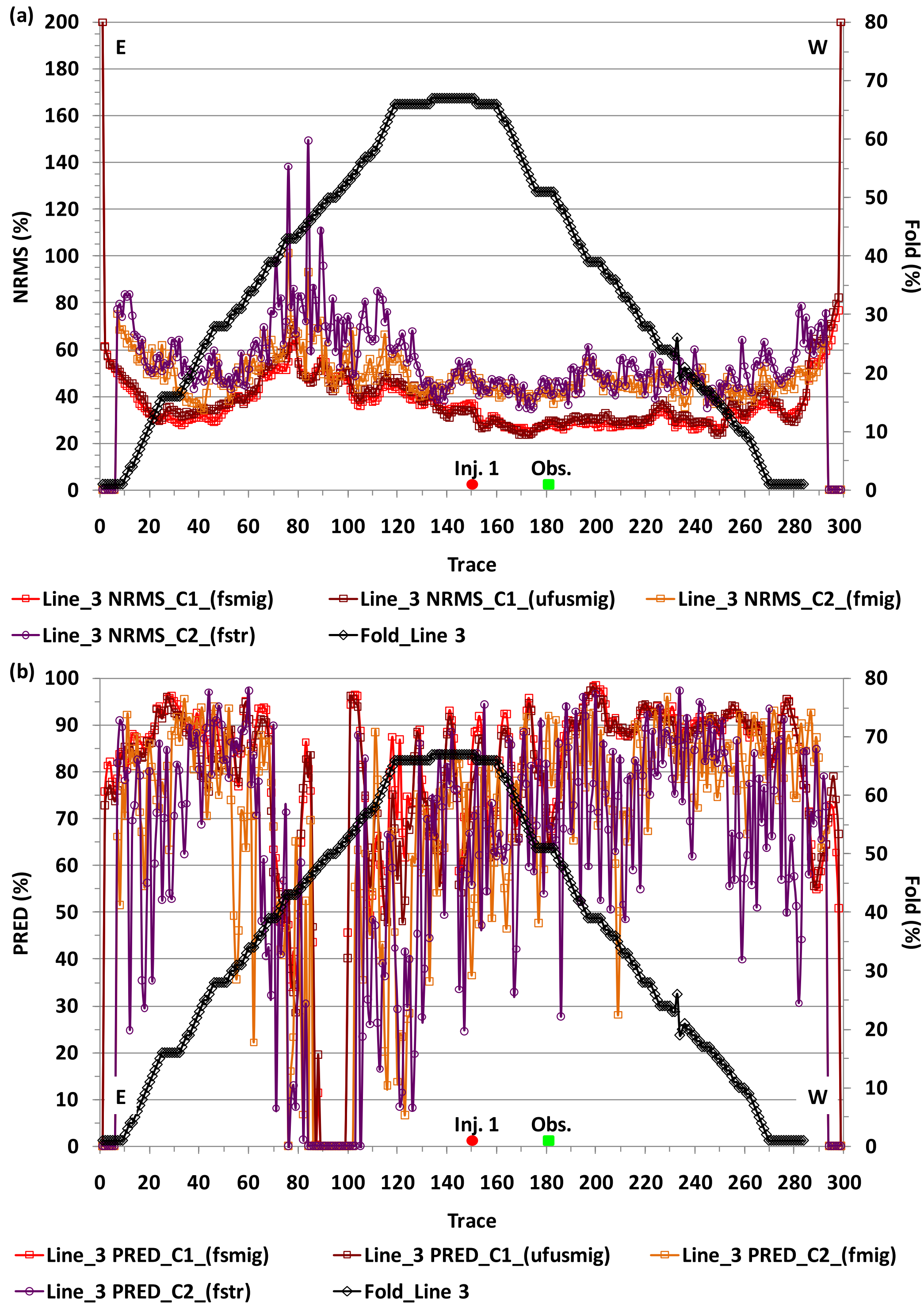

Figure 6-16: (a) NRMS, and (b) PRED repeatability of Line 3 after calibration. C1: contractor 1; C2: contractor 2. The characters inside the parentheses refer to the processing vintage (See Table 6-5). The approximate projected location of the injector (Inj. 1) and observation (Obs.) wells are indicated by the red circle and the green square, respectively.

The results indicate that the overall repeatability of the 2-D surface seismic data (NRMS ~ 30% and PRED ~ 91%) is reasonably good for land data (Tura et al., 2005; Zadeh et al., 2010). However, there does not appear to be any consistent trend or prominent anomaly that could be ascribed to the CO_2 plume (see discussion in the last paragraph of Section 6.5.2.2). It seems that the low magnitude of CO_2-induced NRMS and PRED anomalies predicted through numerical modelling (Section 6.5.1 and Chapter 7) is overwhelmed by the interference from non CO_2-related causes. Due to some qualitative and quantitative privileges, only the “fsmig” vintage will be incorporated into the 2-D surface seismic interpretation (Section 6.5.4).

Table 6-5: Nomenclature and comments regarding the 2-D data processing vintages.

fsmig	Filtered, scaled and migrated	Contractor 1. See Figure F-1 in Appendix F.2.1. Only this vintage will be incorporated into the subsequent analysis
ufusmig	Unfiltered, unscaled and migrated	Contractor 1. See Figure F-1 in Appendix F.2.1
fmig	Filtered and migrated	Contractor 2. See Figure F-4 in Appendix F.2.2
fstr	Filtered and structured	Contractor 2. See Figure F-4 in Appendix F.2.2

Table 6-6: Comparisons of the average and median of the repeatability of the calibatred 2-D vintages. Std. Dev.: standard deviation.

2-D Line	Vintage	Average NRMS	NRMS Std. Dev.	Average PRED	PRED Std. Dev.
Line 1	fsmig	31.00	10.11	90.41	7.08
	ufusmig	33.52	11.32	88.90	8.35
	fmig	88.76	6.89	76.30	17.62
	fstr	87.35	8.89	80.86	15.33
Line 2	fsmig	32.26	7.45	94.48	3.56
	ufusmig	34.64	7.99	86.40	8.15
	fmig	44.60	6.38	79.57	12.35
	fstr	49.44	9.02	72.71	17.98
Line 3	fsmig	37.80	16.60	78.02	22.01
	ufusmig	39.50	17.13	76.70	21.79
	fmig	48.41	9.10	67.76	25.30
	fstr	55.55	14.83	62.47	27.22

Figure 6-17 shows a comparison of the NRMS and PRED magnitudes from Line 1 which were computed using different statistical windows encompassing the three events introduced under Section 6.4 in addition to the entire samples at each trace. As indicated under Section 3.6.3 and illustrated under Section 5.3.3.2, the computation is sensitive to the statistical analysis window. For instance, the lowest repeatability is associated with Cardium event since it is comprises the reservoir zone whereas the highest repeatability corresponds to the entire samples at each trace. Nonetheless, the modelling results (Section 7.2.3.1.2 and 7.2.3.1.3) suggest both reservoir-specific and long windows should provide a good indication of time-lapse change. For instance, the high repeatability of the Ardley event suggests that no upward migration of the injected CO_2 was taking place during the monitoring activities.

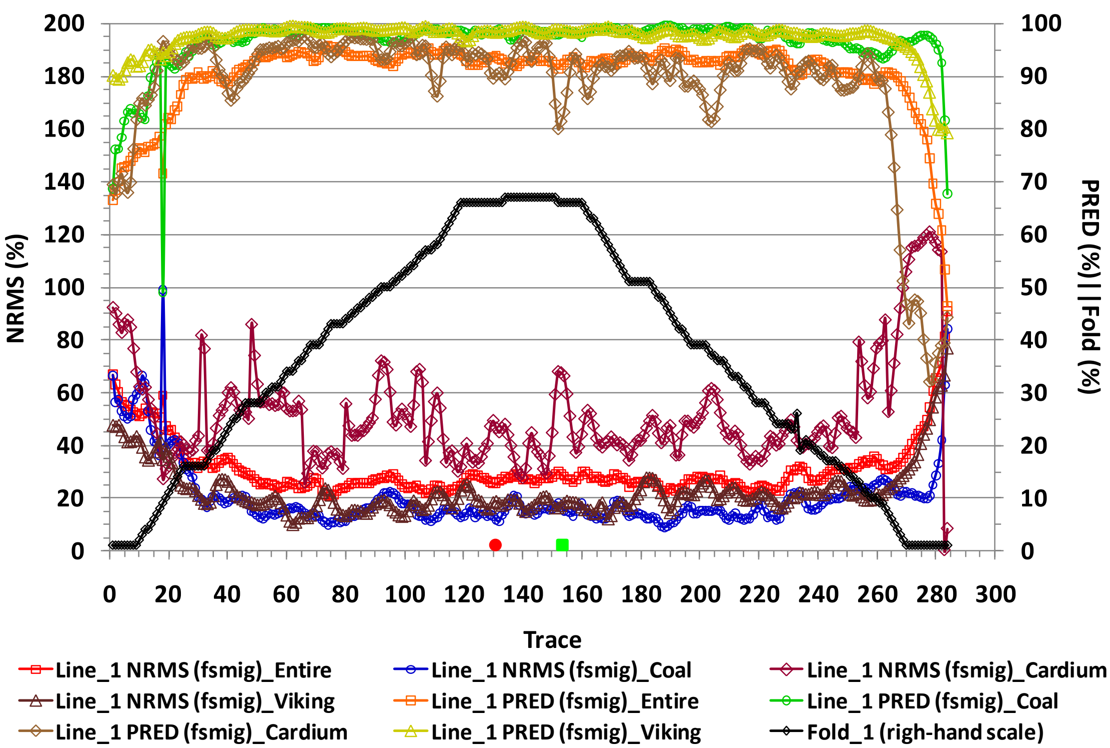

Figure 6-17: Comparison of the NRMS and PRED of Line 1 after calibration using different statistical windows. The characters inside the parentheses in the legend refer to the processing vintage (filtered, scaled and migrated) and the event invoked in the computation. The repeatability was computed using a 100 ms window centered at the indicated event with exception of the “Entire” which was computed over the full trace. The approximate projected location of the injector (Inj. 1) and observation (Obs.) wells are indicated by the red circle and the green square, respectively.

6.5.2.4 3-D Surface Seismic Data

Figure 6-18 and Figure 6-19 demonstrate the repeatability of the P-wave and PS-wave 3-D surface seismic data while the 3-D and 4-D fold are displayed in Figure 6-20. Analogous to the 2-D repeatability, several analysis windows were inspected and the repeatability maps in Figure 6-18 and Figure 6-19 were generated using a broad window encompassing the Ardley, Cardium and Viking events (Figure 6-4 (a)). For the sake of context and consistency, a zone of reliable data (ZRD) is defined for the 3-D seismic data interpretation from here onward. This zone is enclosed by the blue polygon connecting the four wells surrounding the western injector in Figure 6-1. The zone is characterized by the best fold, most continuous coverage, and least interference caused by the gaps in shot positions and processing noise. Furthermore, the ZRD surrounds the western injector which is the main injection well, i.e. injection hotspot. In other words, the ZRD would be the zone to look at where the CO_2 anomaly, if detectable using 3-D surface seismic data, should be most prominent.

Apart from the artefacts near the edges, the maps in Figure 6-18 show that P-wave data has a very good repeatability as the vast majority (~ 90%) of the NRMS and PRED values cluster between 15-25% and 90-95%, respectively. In contrast, the PS-wave data exhibits poorer repeatability as over three-quarters of the NRMS and PRED values lie between 60-100% and 45-70%, respectively. This inferior repeatability of the 3-D PS-wave data could be a result of lower data quality or processing issues but it is difficult to associate this poor repeatability with a specific cause. The repeatability of the 3-D P-wave and PS-wave data (Figure 6-18 and Figure 6-19) show a decrease in the NRMS and an increase in the PRED near the first injector. This observed response contradicts what one would expect as the magnitude of the former would increase and that of the latter would decrease near the CO_2 injector. One possible speculation is that this improvement is caused by the relative increase in the 3-D fold (Figure 6-20). However, the NRMS and PRED are not necessarily sensitive to fold as was illustrated in the repeatability of the 2-D surface seismic (Section 6.5.2.3).

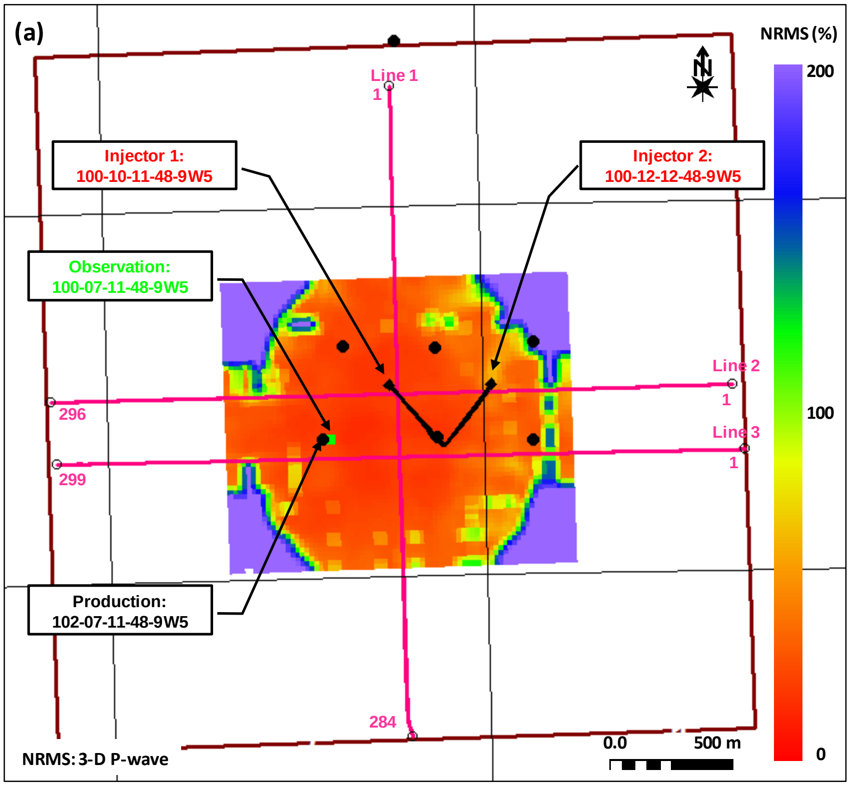

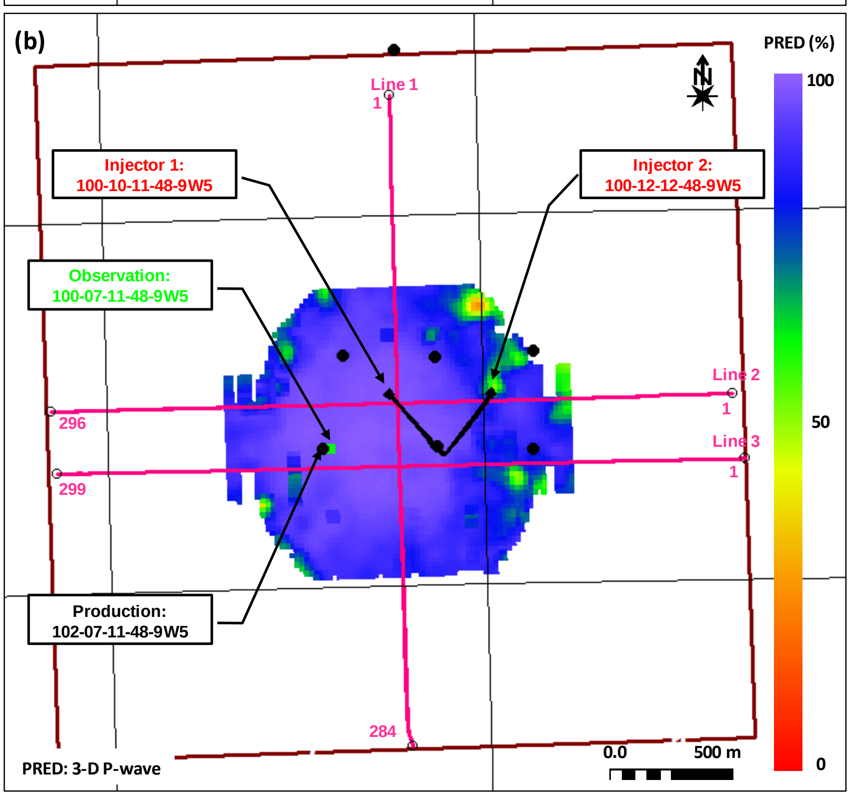

Figure 6-18: (a) NRMS, and (b) PRED of the 3-D P-wave surface seismic data.

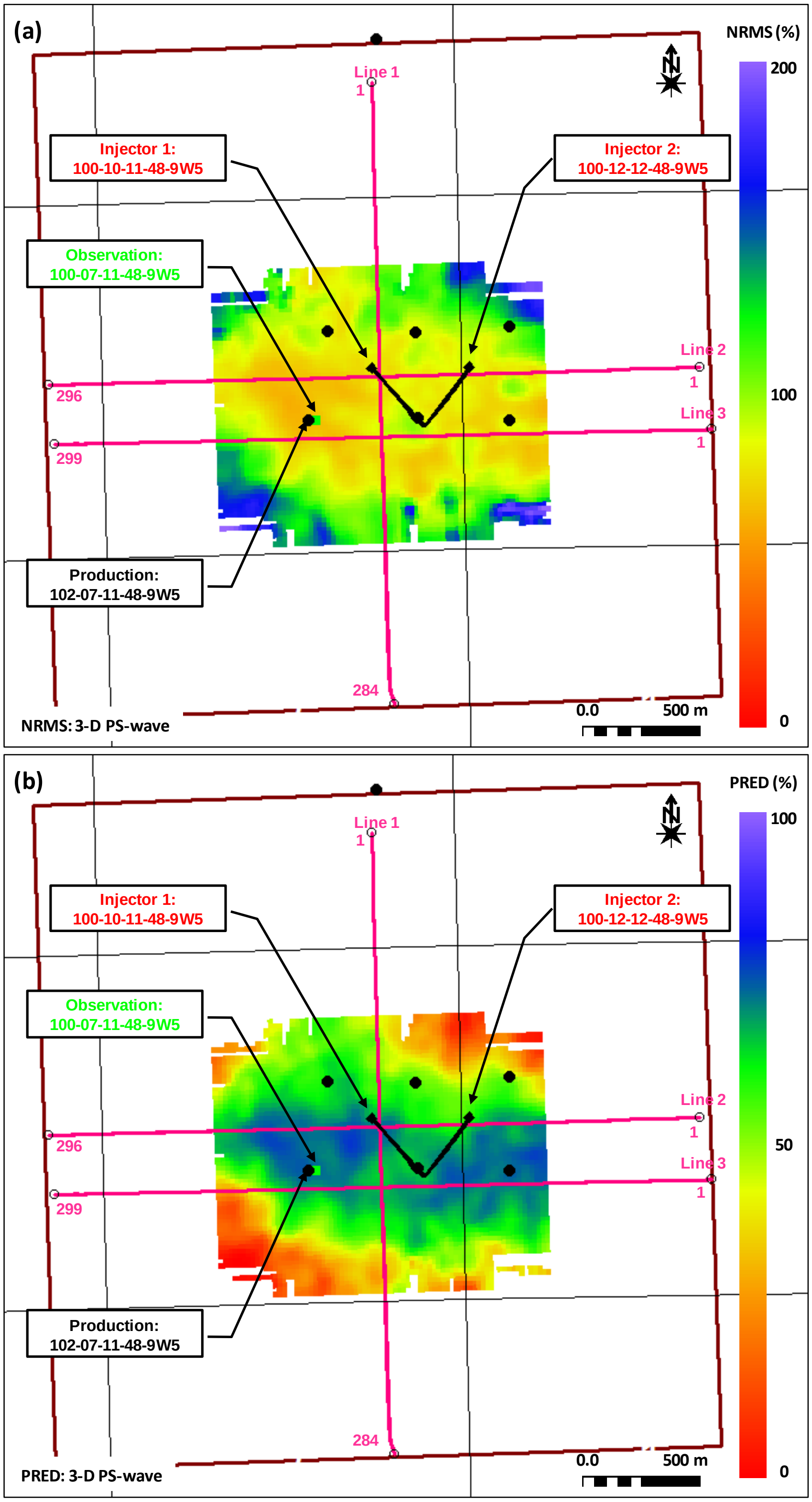

Figure 6-19: (a) NRMS, and (b) PRED of the 3-D PS-wave surface seismic data.

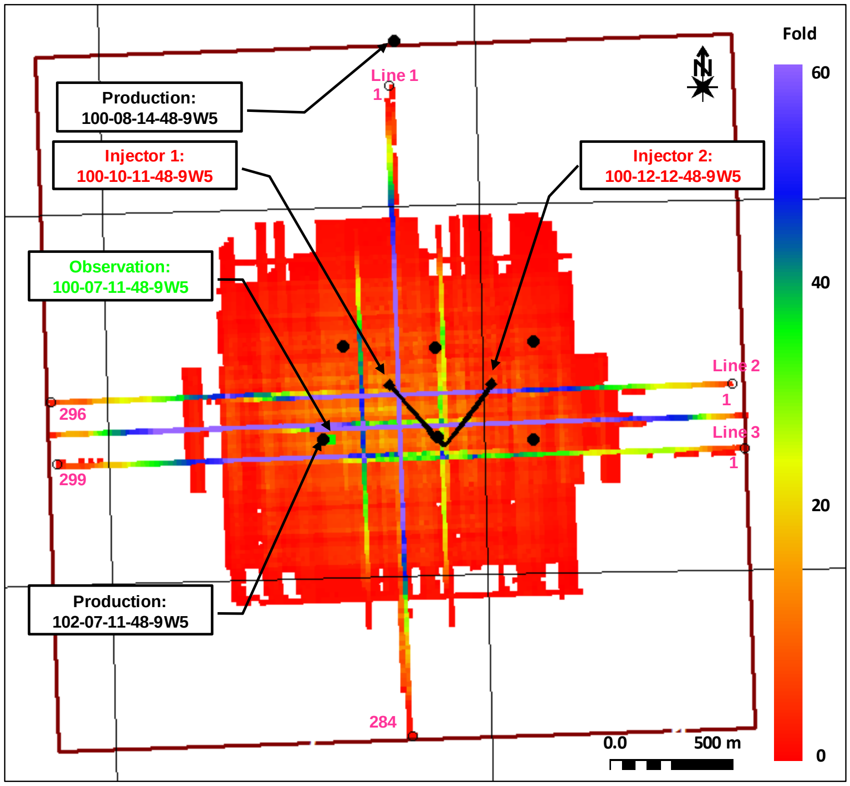

Figure 6-20: 3-D (along 2-D lines) and 4-D (between lines) fold of the P-wave surface seismic data.

Given it is broader perspective and good quality, the 3-D P-wave data were exploited further by computing the NRMS and PRED repeatability of three individual events: Ardley, Cardium and Viking. The computation utilized a 100 ms analysis window centered at the corresponding reflections. In the case of the Cardium event, the computation was, also, performed on the PS-wave data. The repeatability of the Cardium event corresponding to the 3-D P-wave data exhibits a subtle increase in NRMS (Figure 6-21 (a)) and, arguably, a small decrease in PRED (Figure 6-21 (b)), around the western injector within the ZRD. This subtle pattern could be indicative of changes within or near the reservoir. The repeatability of the Cardium event in the PS-wave data (Figure 6-22) is less consistent and, therefore, could not be interpreted with confidence although there seems to be an intriguing PRED anomaly north of the western injector (see discussion in the first paragraph of this Section).

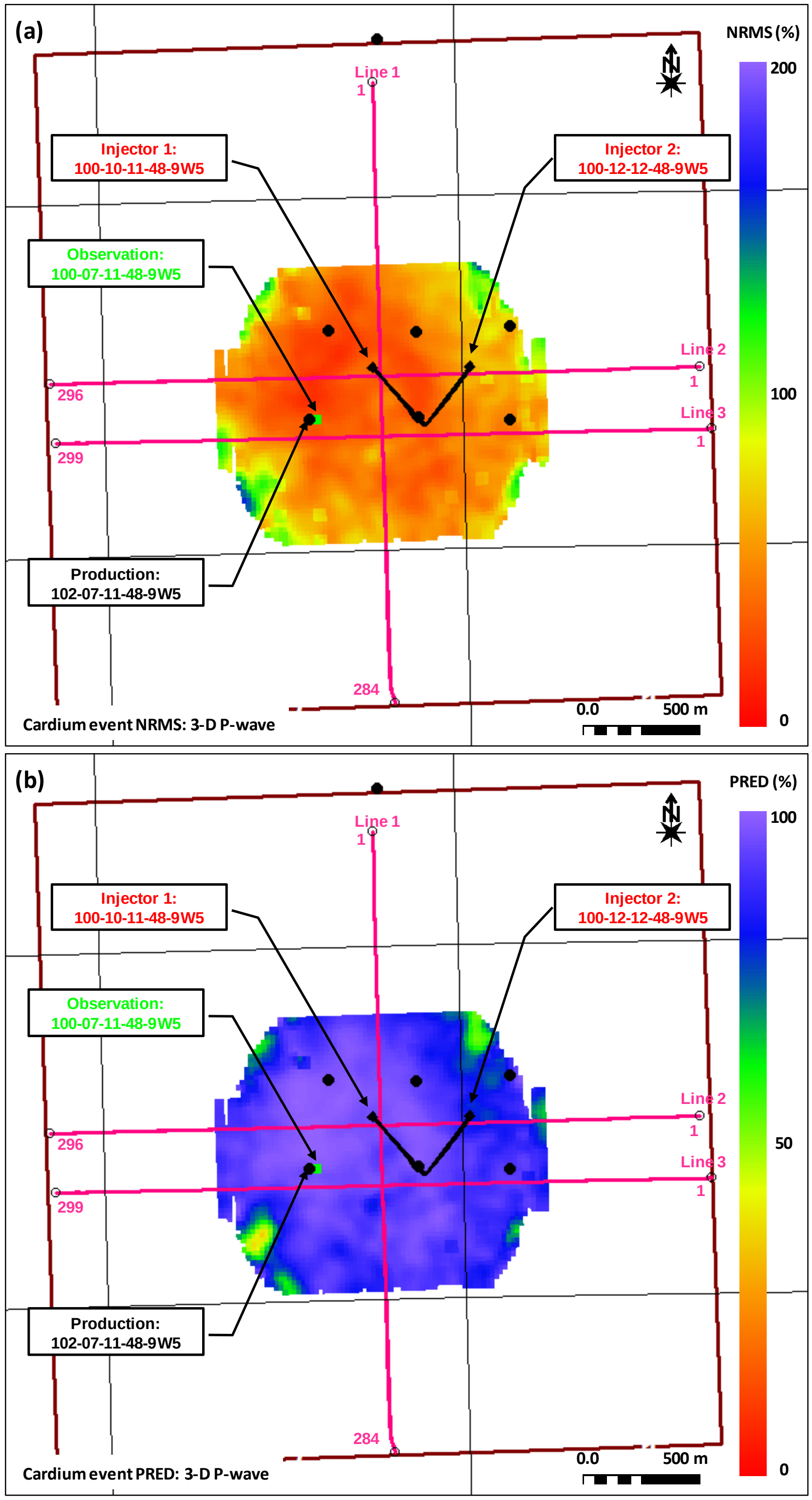

Figure 6-21: Cardium event (a) NRMS, and (b) PRED computed from the 3-D P-wave surface seismic data using a 100 ms window.

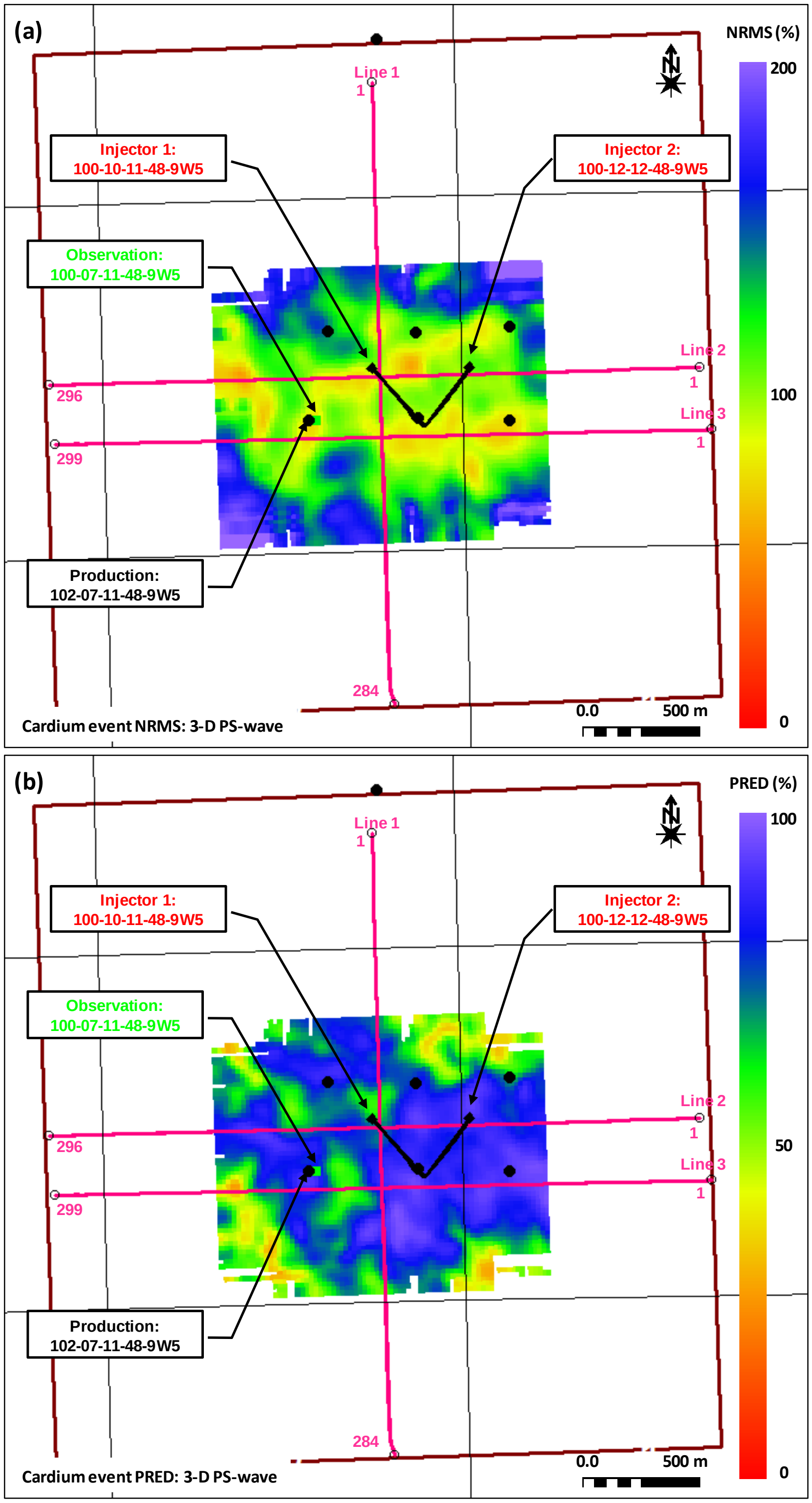

Figure 6-22: Cardium event (a) NRMS, and (b) PRED computed from the 3-D PS-wave surface seismic data using a 100 ms window.

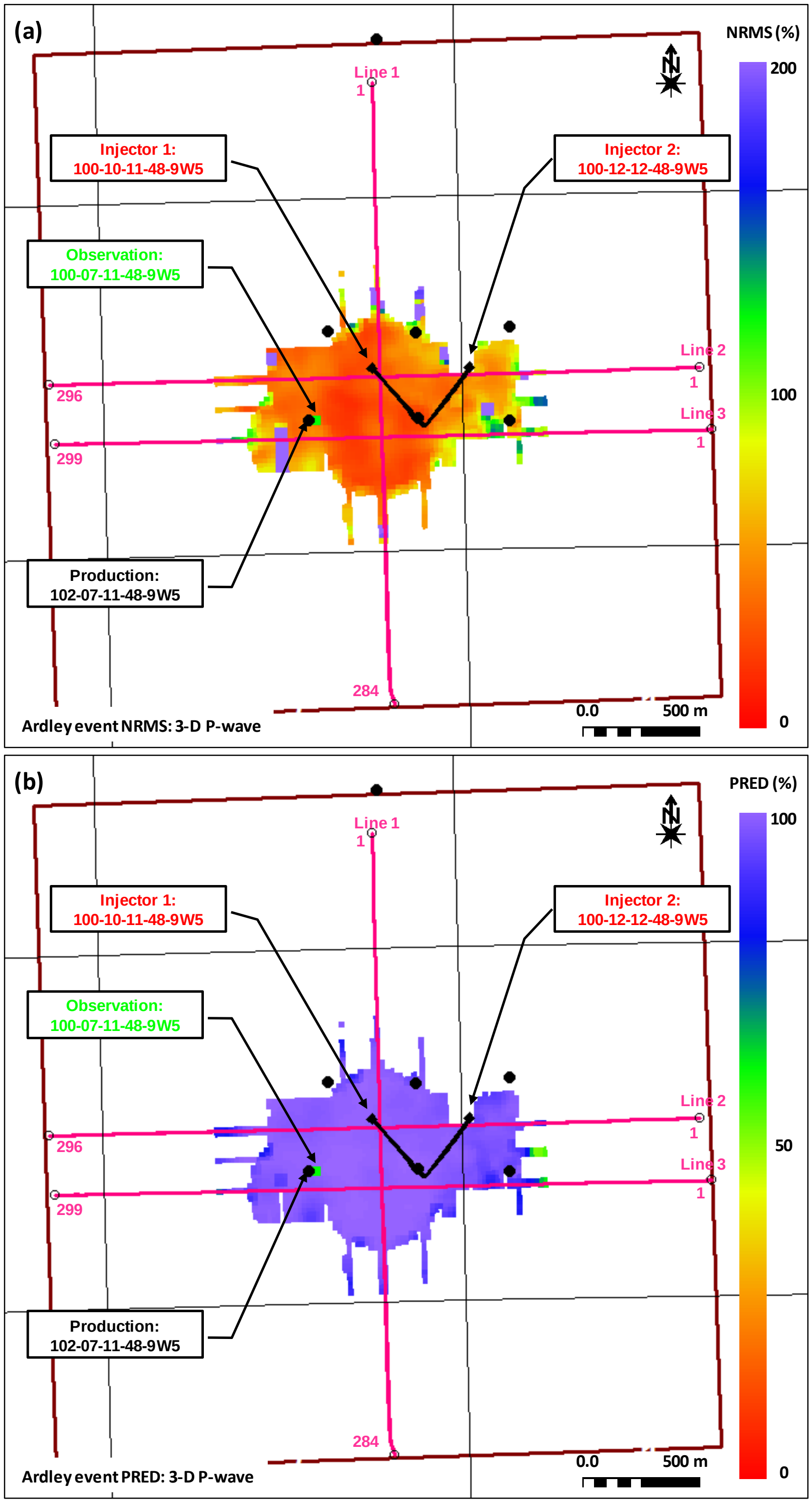

Figure 6-23: Ardley event (a) NRMS, and (b) PRED computed from the 3-D P-wave surface seismic data using a 100 ms window.

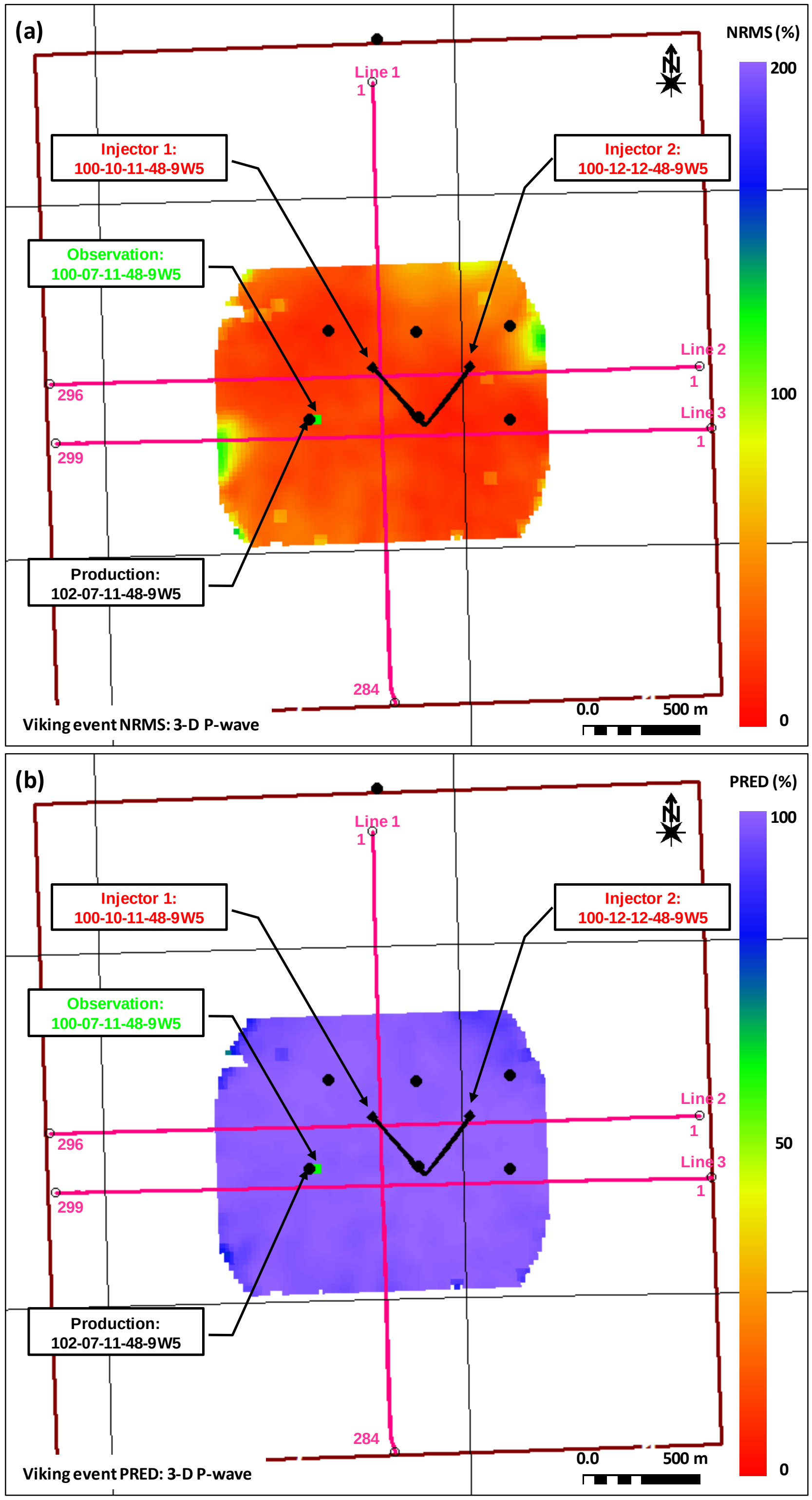

Figure 6-24: Viking event (a) NRMS, and (b) PRED computed from the 3-D P-wave surface seismic data using a 100 ms window.

Computing the NRMS and PRED of the Ardley and Viking events helped in gaining better understanding of the repeatability of the 3-D P-wave data above and below the reservoir given that it is a sparse 3-D and the potential effect of coverage variability. Both events demonstrate excellent repeatability as depicted by the low NRMS (~ 15%) and high PRED (~ 98%) values in Figure 6-23 and Figure 6-24, respectively. The high repeatability of the Viking event, in particular PRED, is consistent with the modeling results, suggesting a very small time shift in the Cardium event that would induce a small anomaly in the PRED and NRMS maps of the Viking event. On the other hand, the high repeatability of the Ardley event suggests that no upward migration of the injected CO_2 was taking place during the monitoring activities.

In summary, NRMS and PRED attributes in the 3-D P-wave data are similar to that of the 2-D (see discussion in the last paragraph of Section 6.5.2.3). Furthermore, the observations pertaining to the repeatability of the VSP and 2-D surface seismic suggest that what is being seen in the repeatability of the 3-D P-wave surface seismic data is likely not CO_2-related. Despite all of this, the credibility of the apparent Cardium repeatability anomaly in the 3-D P-wave data (mentioned in the previous paragraph) remains to be substantiated by looking at some of the other seismic attributes that will follow in this chapter.

6.5.3 Vertical Seismic Profile (VSP) Interpretation

Figure 6-25 and Figure 6-26 show the baseline (2005) and monitor (2007) as well the as the difference sections belonging to the CDP-transformed and migrated VSP data, respectively, from Line 1 while the corresponding amplitude spectra are displayed in Figure 6-27. Unfortunately, the lateral image of the Cardium Formation in the VSP data is limited to approximately 100 m due to the depth and limited vertical aperture of the geophone array in the observation well. Nonetheless, data quality of the baseline and monitor CDP-transformed and migrated VSP sections are quite good.

There is a laterally consistent residual amplitude near the Cardium event in the difference section of the CDP-transformed VSP in Figure 6-25 (c). This could be a result of the CO_2 injection or simply due to changes in the near-surface condition as the zone enclosing the reservoir was not included in designing the calibration operators (Section 6.4). The difference section of the migrated VSP in Figure 6-26 (c), on the other hand, shows residual amplitude of similar magnitude that is not localized to the Cardium and visible all over the section. Therefore, it is even more ambiguous to associate any residual amplitude in this case with the CO_2 injection.

The difference in Cardium event normalized amplitude and Cardium-Viking isochron between the baseline (2005) and the monitor (2007) of Line 1 are plotted in Figure 6-28. The difference in these two attributes corresponding to the CDP-transformed VSP in Figure 6-28 (a) demonstrates two trends: (1) north of the observation well where the difference in the normalized amplitude is positive while the isochron difference is positive, and (2) south of the observation well where the trend reverses. The difference in the case of the migrated VSP Figure 6-28 (b) exhibit a somewhat monotonic trend in the sense that the former is always negative and the latter is always positive with small variations near the observation well.

Since the main injector is to the north of the observation well and, therefore, one would expect the CO_2 injection to induce a more prominent effect in its vicinity. Unfortunately, the main injector is not captured in the VSP sections. In addition to the narrow image of the Cardium, the VSP image deteriorates rapidly away from the observation well, thus, hindering the confidence of the interpretation. Thus, neither of the results in Figure 6-28 (a) and (b) seems to produce a persuasive assertion of the CO_2 plume distribution and, arguably, the amplitude residual in Figure 6-25 (c) remains as the most credible CO_2-induced anomaly.

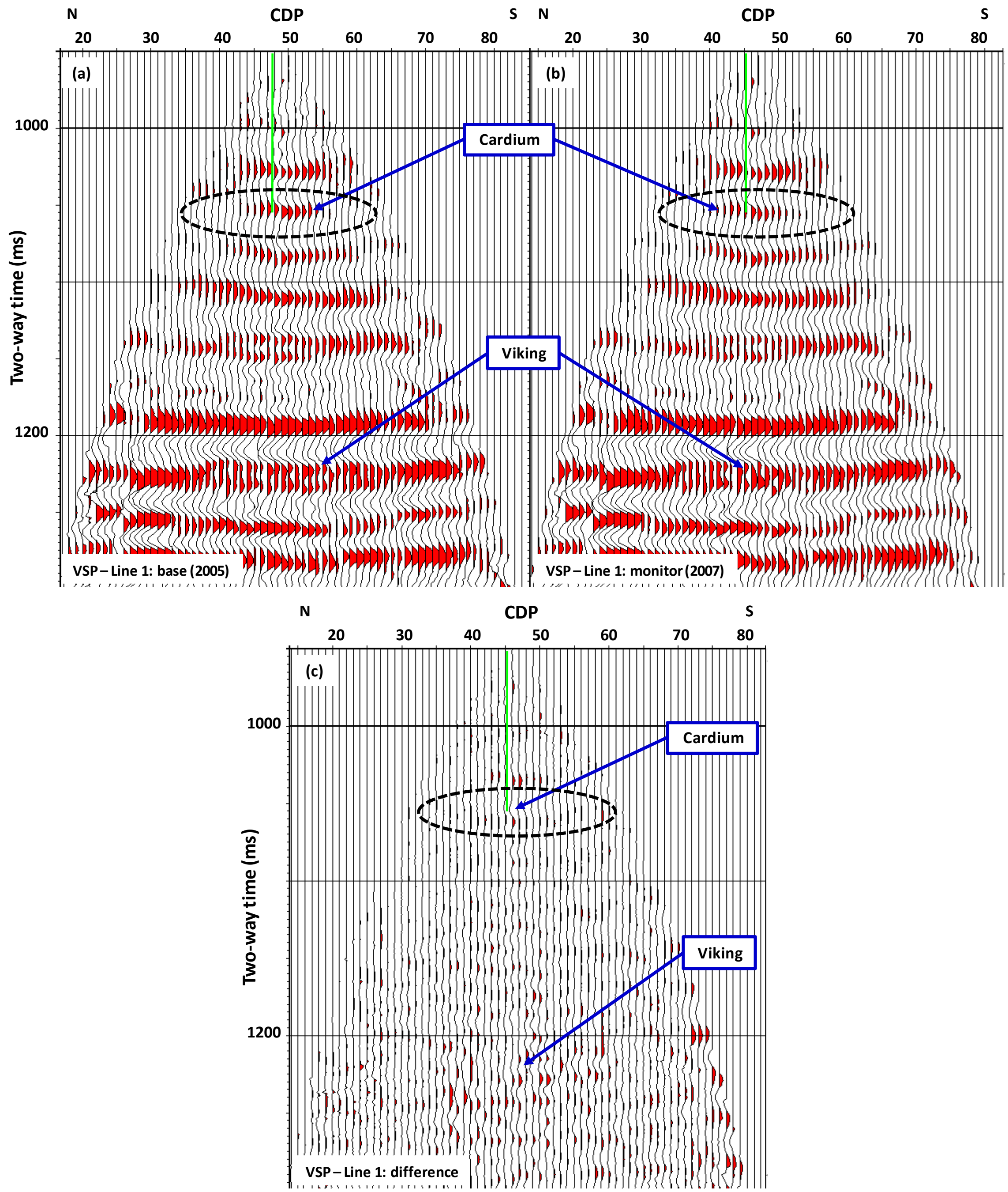

Figure 6-25: Display of the calibrated, CDP-transformed VSP from Line 1 showing (a) the baseline data, (b) the monitor data, and (c) the difference between the two. The green line shows the trajectory of the observation well. CDP: common-depth point.

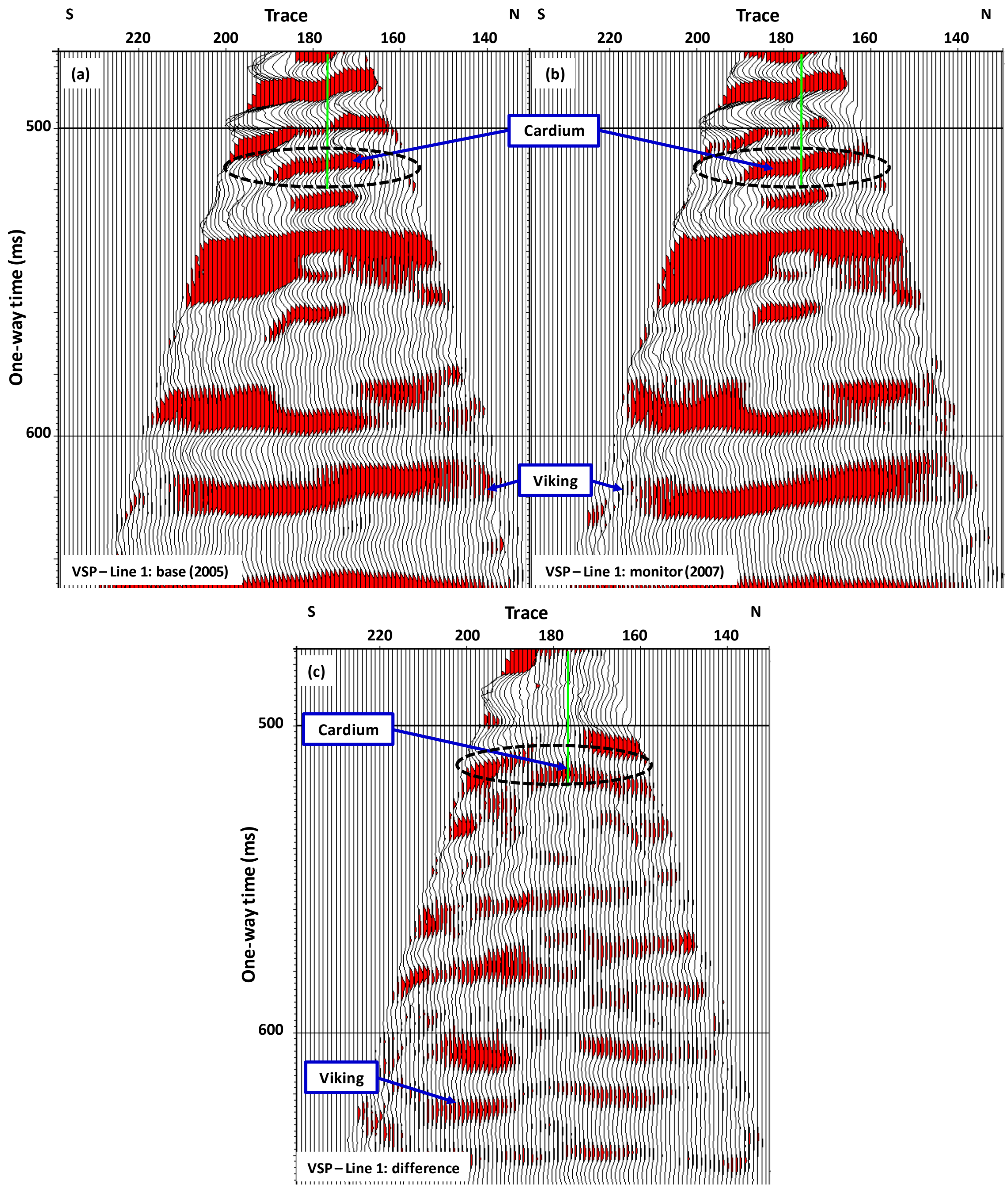

Figure 6-26: Display of the calibrated, migrated VSP from Line 1 showing (a) the baseline data, (b) the monitor data, and (c) the difference between the two. The green line shows the trajectory of the observation well.

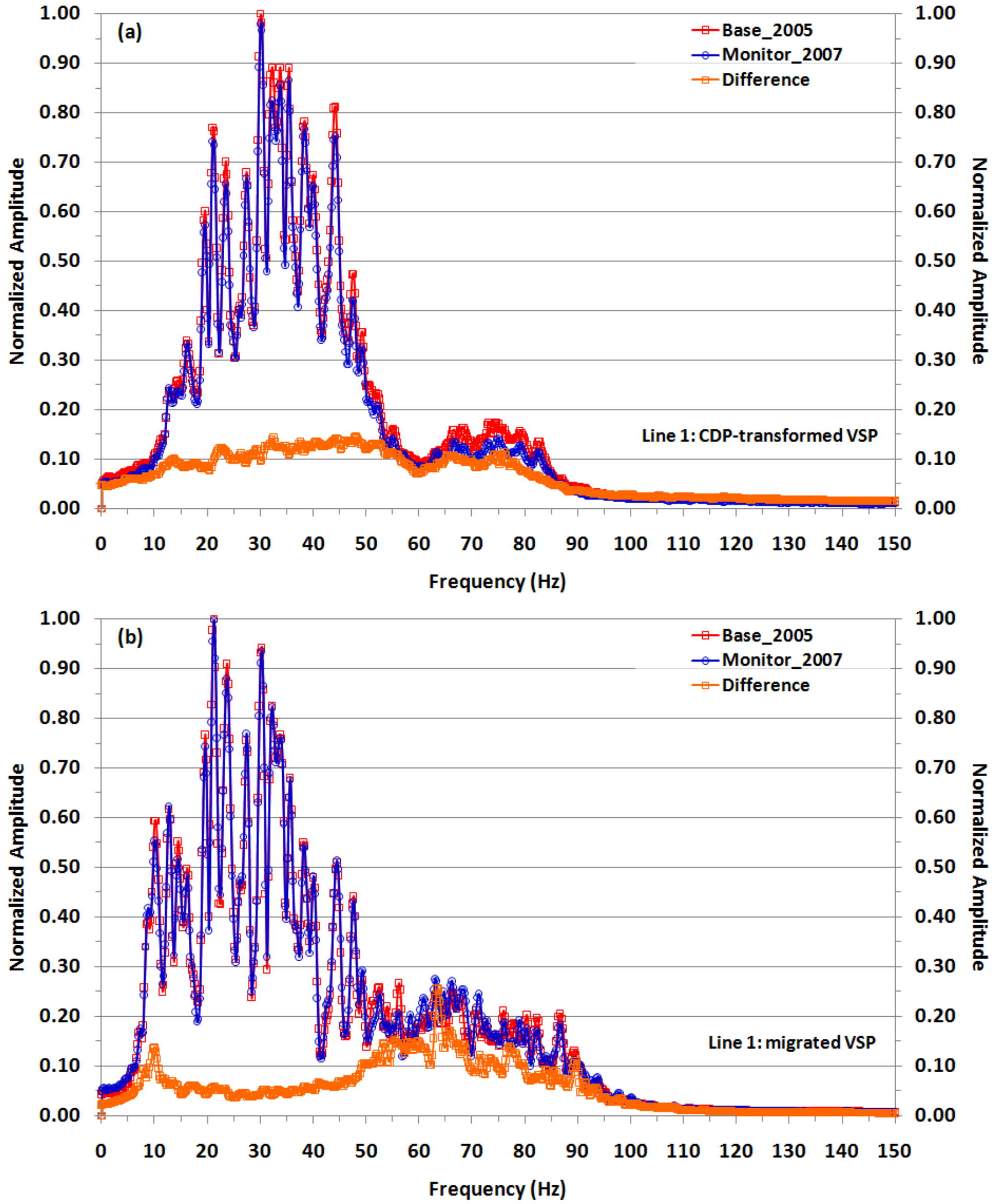

Figure 6-27: Average amplitude spectra of the calibrated (a) CDP-transformed, and (b) migrated VSP from Line 1 (see Figure 6-25 and Figure 6-26). Note that the difference spectrum is computed from the difference section not by taking the difference of the baseline and monitor spectra shown here and that all spectra are normalized with respect to maximum of the baseline.

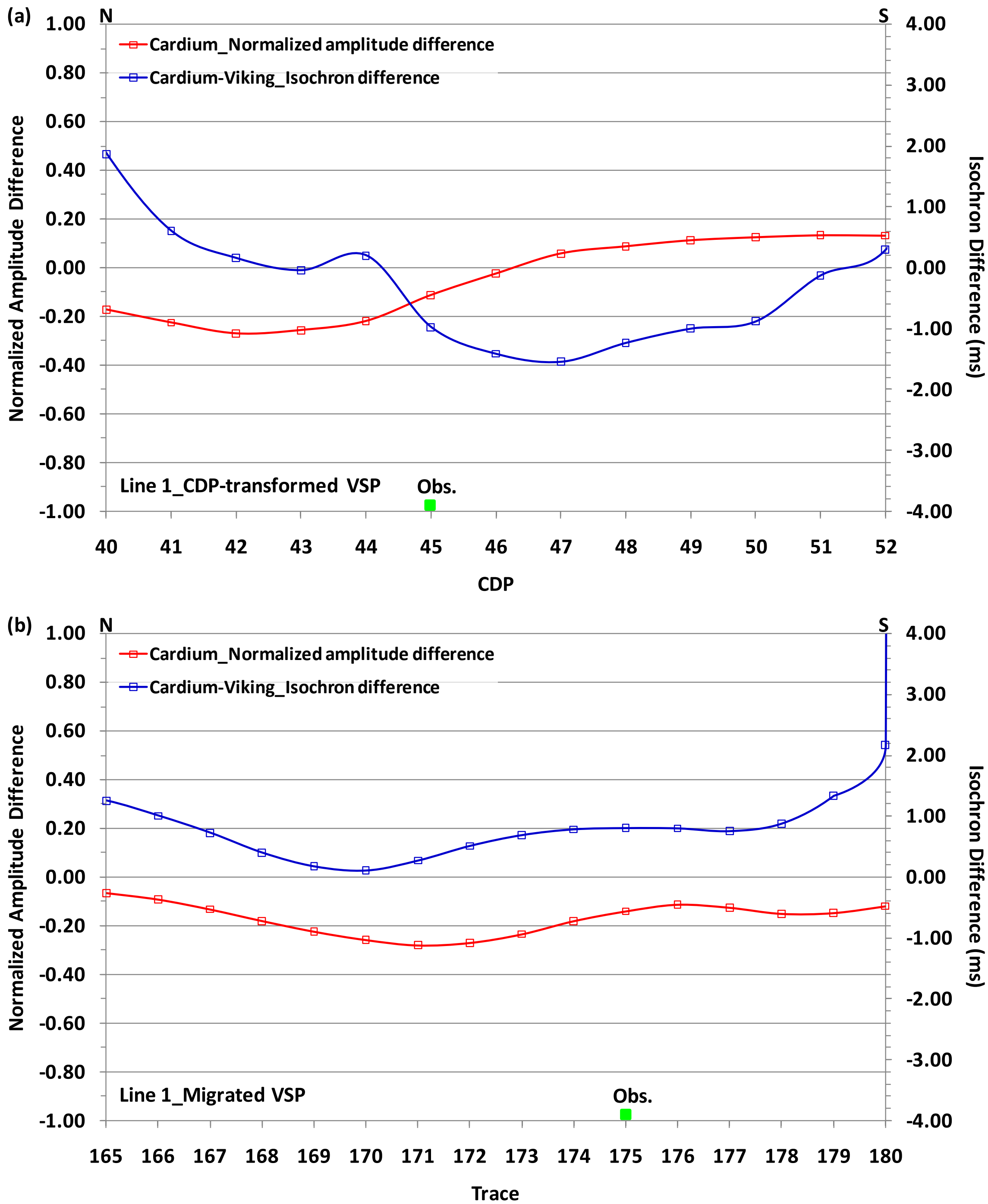

Figure 6-28: Differences in the normalized amplitude of the Cardium and the Cardium-Viking isochron between the baseline (2005) and monitor (2007) computed using (a) the CDP-transformed VSP, and (b) the migrated VSP from Line 1. The approximate projected location of the observation well is depicted by the green square.

The CDP-transformed and migrated VSP sections corresponding to Line 2 along with the accompanying amplitude spectra, normalized Cardium event amplitude difference and Cardium-Viking isochron difference plots are displayed in similar fashion to that of Line 1 in Figure 6-29 through to Figure 6-32, respectively. Similarly, those associated with Line 3 are presented in Figure 6-33 through to Figure 6-36, respectively. The difference plots of the CDP-transformed VSP sections from Lines 2 (Figure 6-29 (c)) and 3 (Figure 6-33 (c)), respectively, do not show coherent residual amplitude near the Cardium event as that of Line 1 (Figure 6-25 (c)). The gaps in shot positions effect is clearly visible to the west of the observation well in the migrated VSP difference section from Line 2 (Figure 6-30 (c)). Figure 6-34 (c), on the other hand, exhibits a rather coherent pattern that resembles, in terms of continuity, that of Line 1.

The magnitude of Cardium normalized amplitude and Cardium-Viking isochron from the CDP-transformed VSP section along Line 2 show increases in both parameters to the west of the observation well Figure 6-32 (a). The observed trend is rather unexpected as the main injector is located to the northeast of the observation well and, therefore, the anomaly induced by the CO_2 plume should be observed along the closest principle direction, i.e. east of the observation well in the case of Line 2. Furthermore, although the increase in the Cardium-Viking isochron is in agreement with what is predicted, the magnitude of the normalized amplitude of the Cardium event, on the other hand, is expected to decrease rather than increase as a result of the CO_2 plume migration toward the observation well, which is not the case observed. The former observations, combined with the fact that Line 2 suffers the most from gaps in the shot line makes it difficult to draw and useful conclusions concerning any data derived from this line. Furthermore, the Cardium normalized amplitude and Cardium-Viking isochron plots corresponding to the migrated VSP section from Line 2 (Figure 6-32 (a)) are not reliable as the gaps in the shot line seems to have leaked significantly into the data (see Figure 6-30).

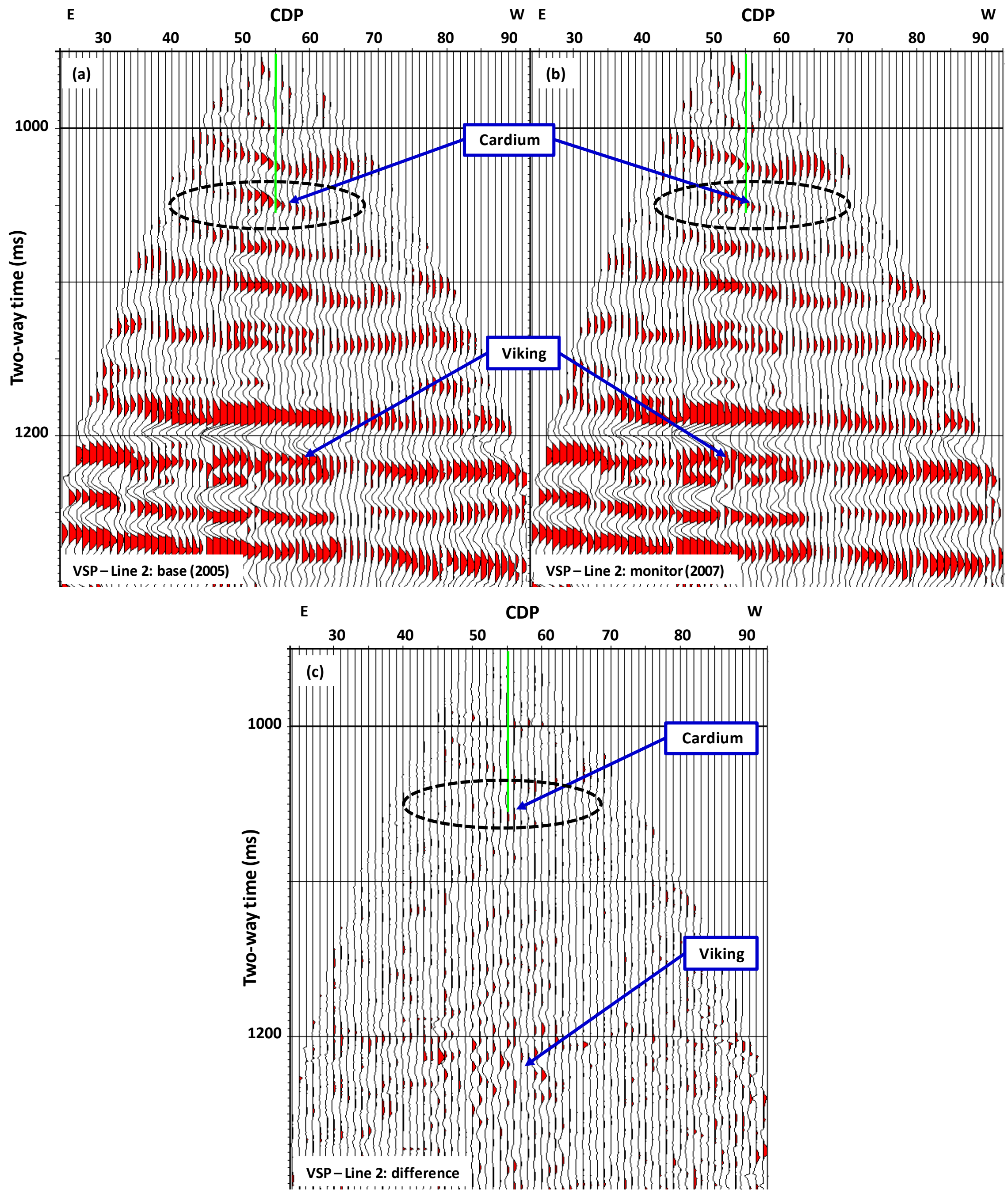

Figure 6-29: Display of the calibrated CDP-transformed VSP from Line 2 showing (a) the baseline data, (b) the monitor data, (c) the difference between (a) and (b). The green line shows the trajectory of the observation well.

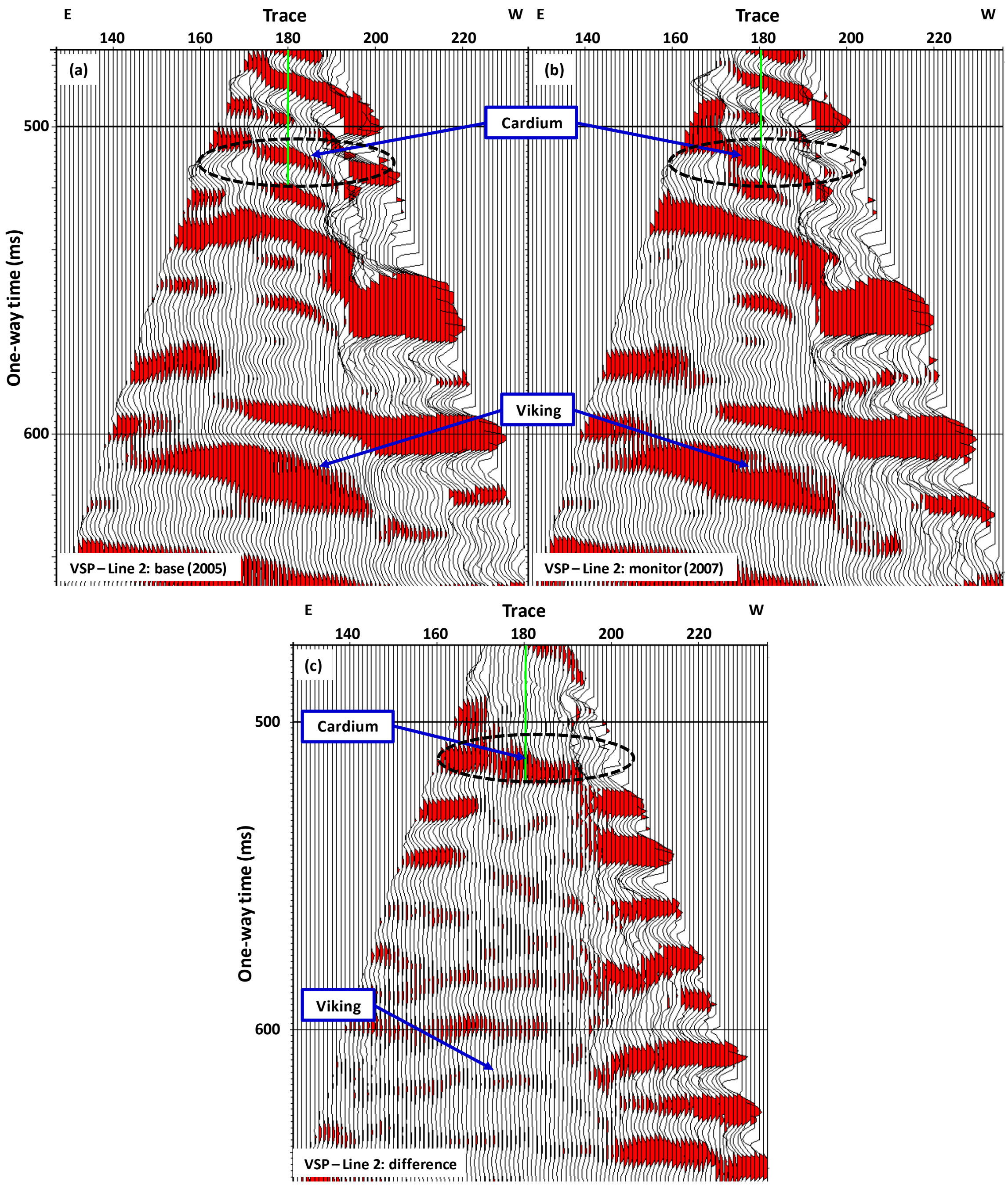

Figure 6-30: Display of the calibrated, migrated VSP from Line 2 showing (a) the baseline data, (b) the monitor data, and (c) the difference between the two. The green line shows the trajectory of the observation well.

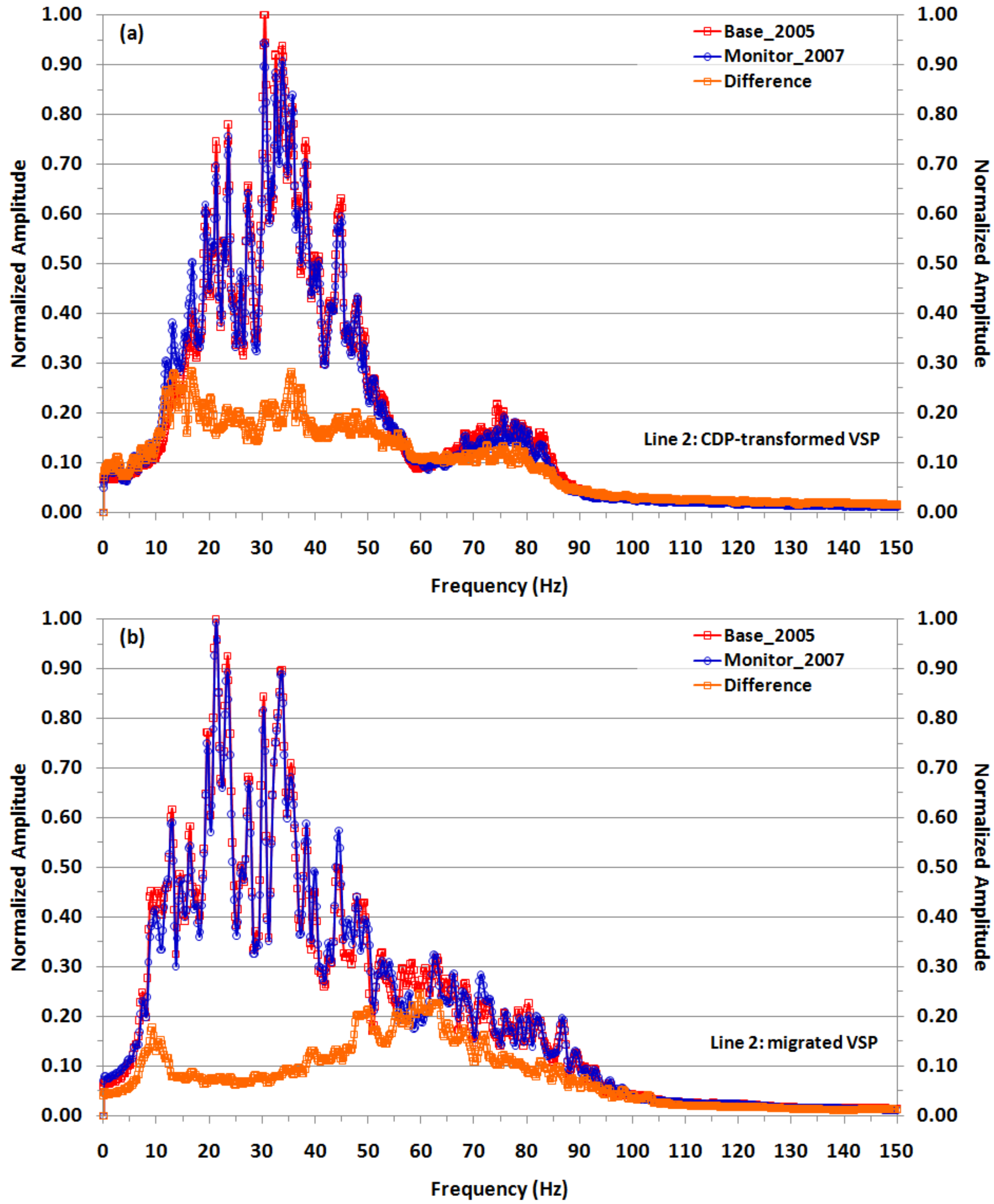

Figure 6-31: Average amplitude spectra of the calibrated (a) CDP-transformed, and (b) migrated VSP from Line 2 (see Figure 6-33 and Figure 6-34). Note that the difference spectrum is computed from the difference section not by taking the difference of the baseline and monitor spectra shown here and that all spectra are normalized with respect to maximum of the baseline.

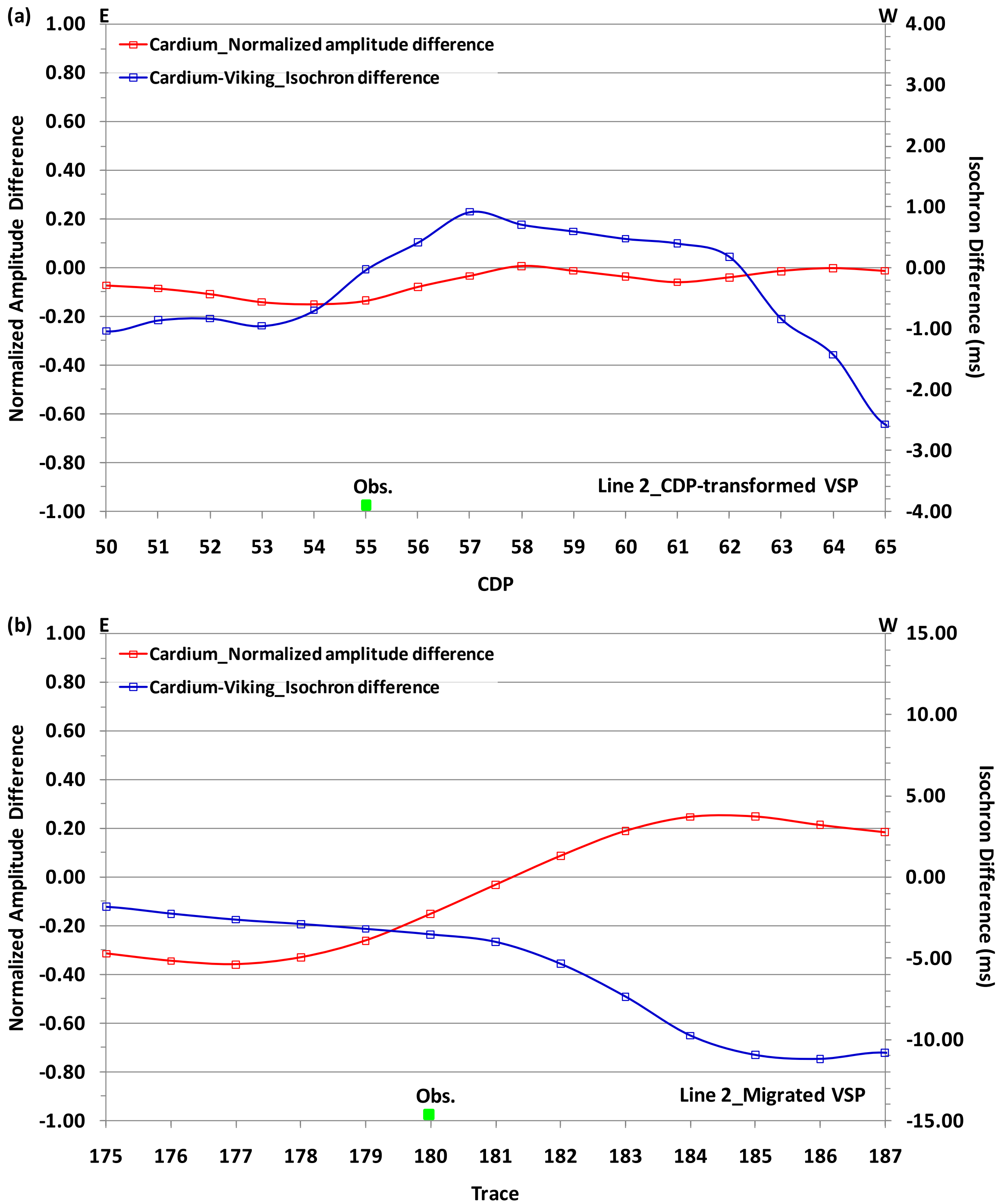

Figure 6-32: Differences in the normalized amplitude of the Cardium and the Cardium-Viking isochron between the baseline (2005) and monitor (2007) computed using (a) the CDP-transformed VSP, and (b) the migrated VSP from Line 2. The approximate projected location of the observation well is depicted by the green square.

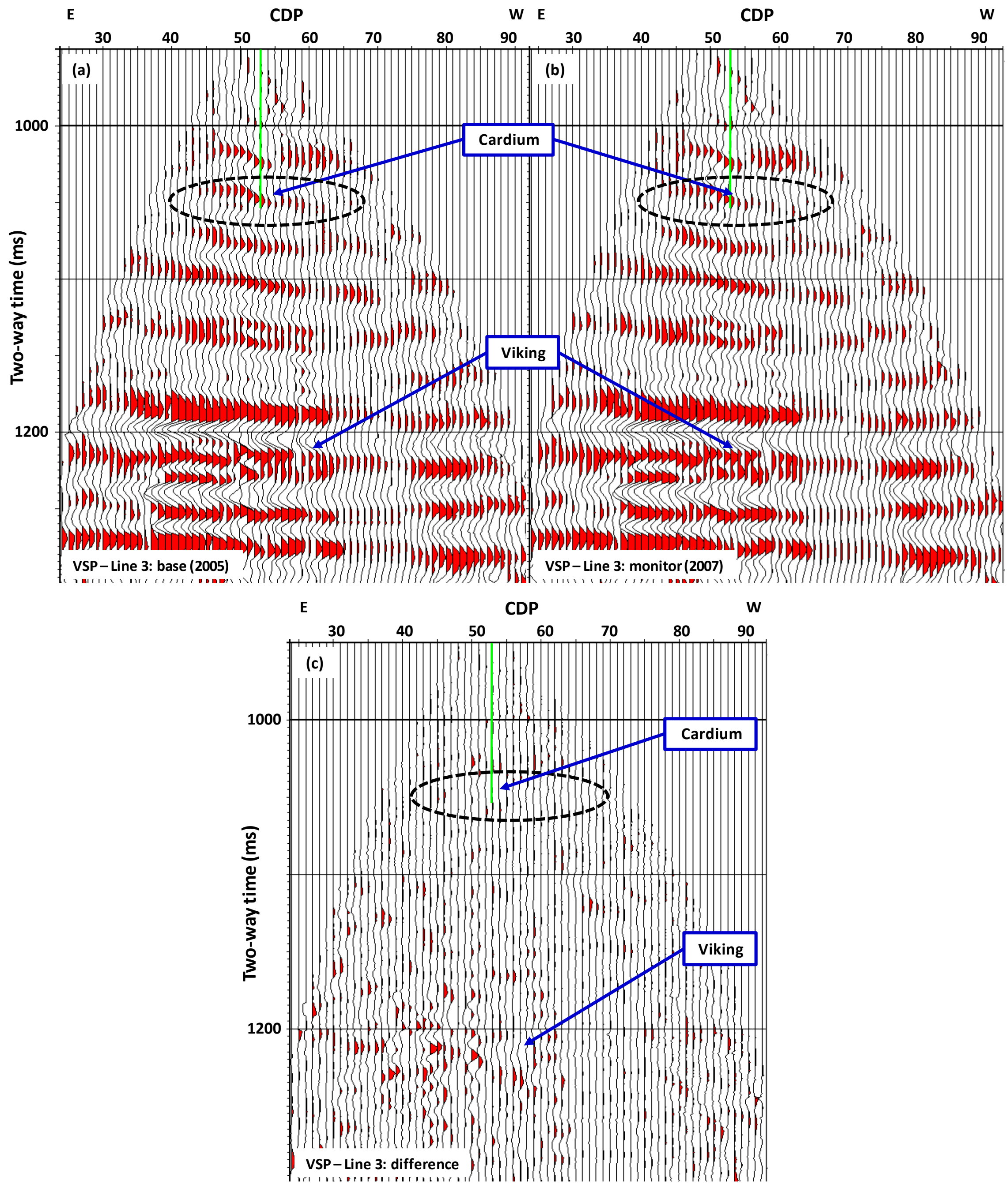

Figure 6-33: Display of the calibrated CDP-transformed VSP from Line 3 showing (a) the baseline data, (b) the monitor data, (c) the difference between (a) and (b). The green line shows the trajectory of the observation well.

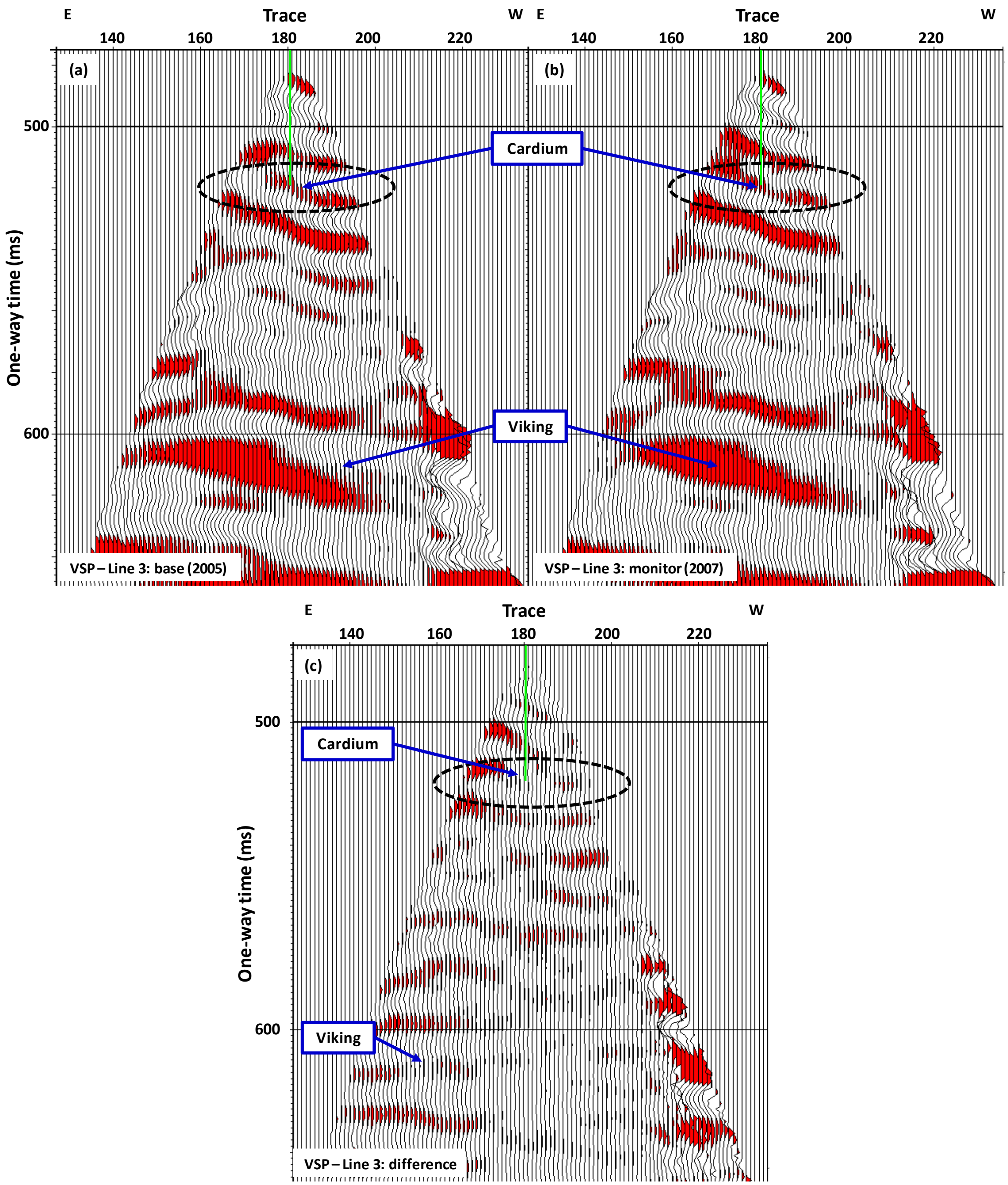

Figure 6-34: Display of the calibrated, migrated VSP from Line 3 showing (a) the baseline data, (b) the monitor data, and (c) the difference between the two. The green line shows the trajectory of the observation well.

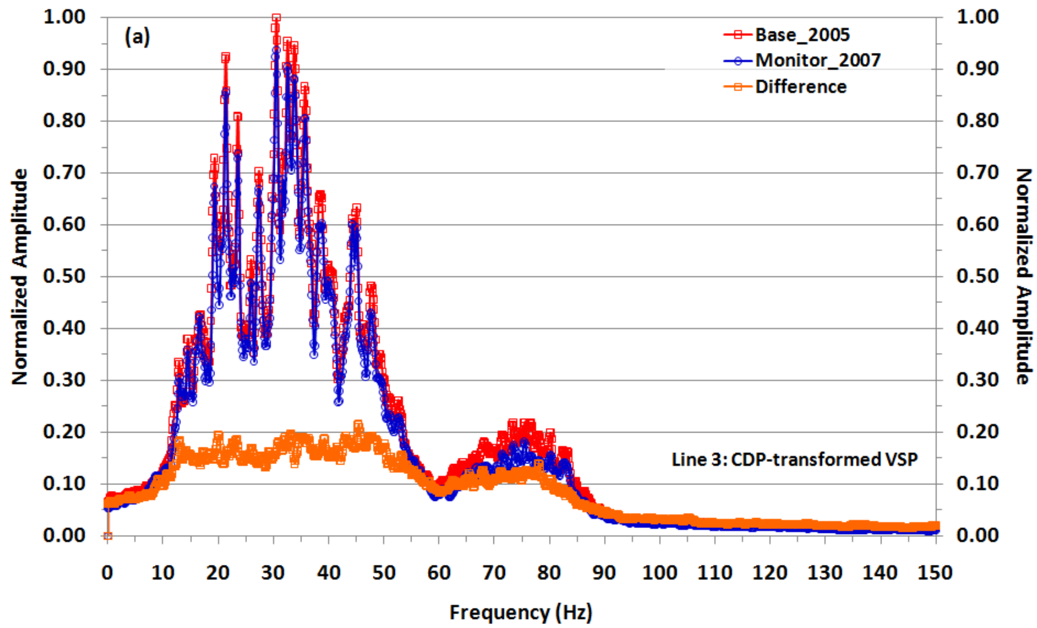

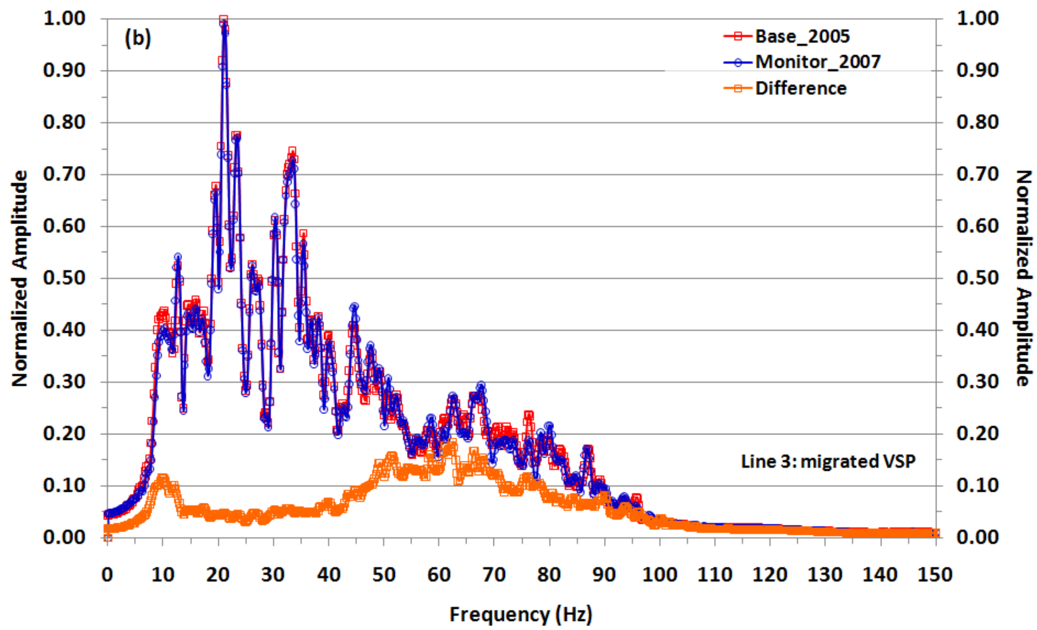

Figure 6-35: Average amplitude spectra of the calibrated (a) CDP-transformed, and (b) migrated VSP from Line 3 (see Figure 6-38 and Figure 6-39). Note that the difference spectrum is computed from the difference section not by taking the difference of the baseline and monitor spectra shown here and that all spectra are normalized with respect to maximum of the baseline.

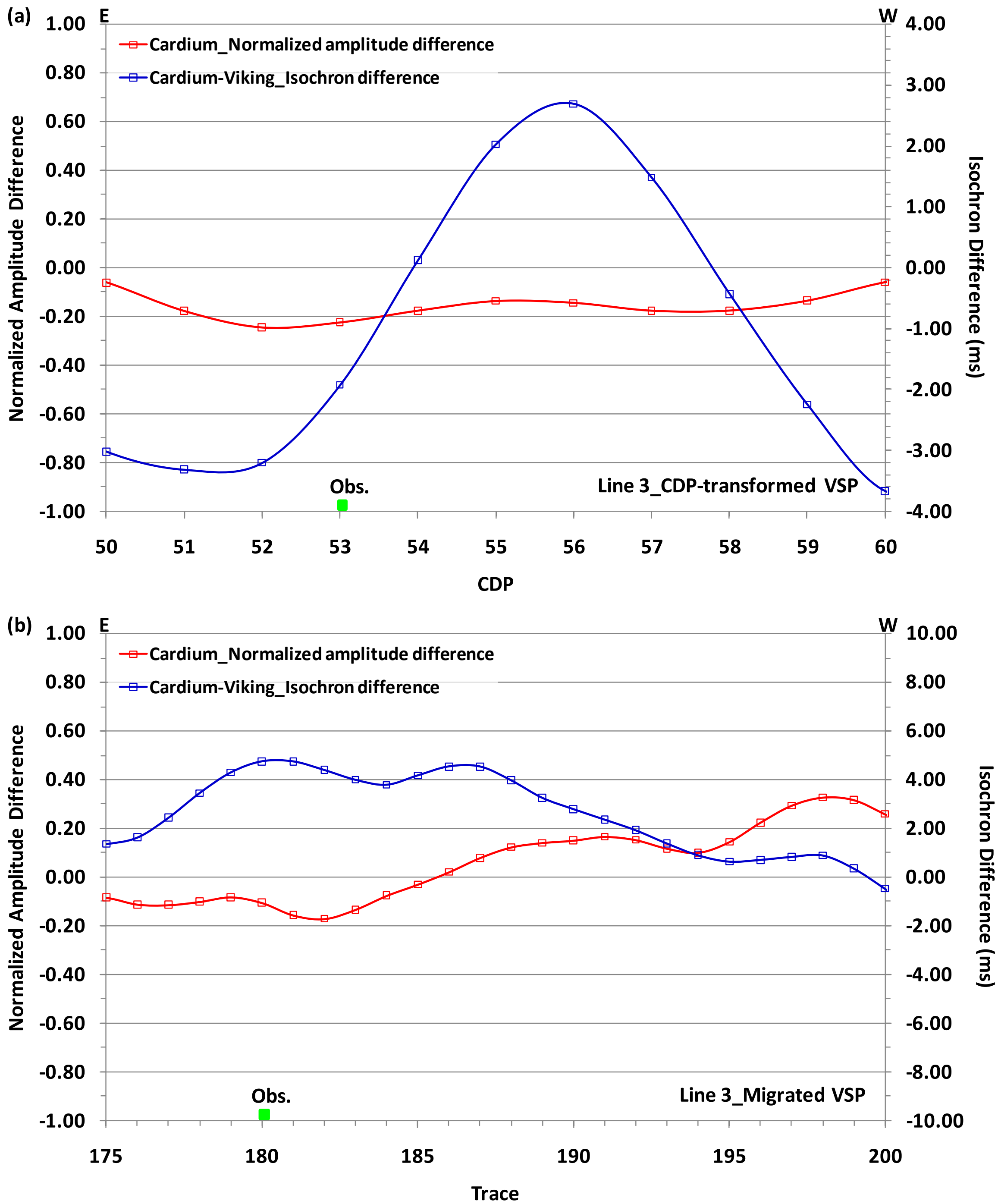

Figure 6-36: Differences in the normalized amplitude of the Cardium and the Cardium-Viking isochron between the baseline (2005) and monitor (2007) computed using (a) the CDP-transformed VSP, and (b) the migrated VSP from Line 3. The approximate projected location of the observation well is depicted by the green square.

The difference in Cardium event normalized amplitude from the CDP-transformed VSP sections of Line 3 (Figure 6-36 (a)) show the expected response, i.e. small negative magnitude. However, the difference in the Cardium-Viking isochron (Figure 6-36 (b)) exhibits a rather unrealistic bell-shaped response where the observed difference (~ 3 ms) is much higher than that predicted by the fluid substitution modelling (~ 0.1 ms). Although the difference in the Cardium event normalized amplitude derived from the migrated VSP sections (Figure 6-36 (b)) seem reasonable in terms of magnitude and plume migration, the magnitude of the corresponding increase in the isochron difference (Figure 6-36 (b)) deemed to be implausible.

By analyzing the various VSP sections and the corresponding Cardium event normalized amplitude and Cardium-Viking isochron difference sections, it is clear that there are no consistent and reliable trends that could be attributed to the CO_2 injection. Even when the difference section corresponding to the CDP-transformed VSP from Line 1 (Figure 6-25 (c)) seem to show an intriguing anomaly, the associated attributes, i.e. Cardium event normalized amplitude difference and Cardium-Viking isochron difference (Figure 6-28 (a)) exhibit rather inconclusive trends that undermine the credibility of this anomaly. As mentioned previously, Lines 2 and 3 have inferior acquisition in terms of the source distribution and, therefore, it was not possible to extract a consistent and reliable pattern from difference VSP section as well as the normalized amplitude and isochron difference plots of these lines. Overall, the lack of a distinct and consistent difference signature could be attributed to the depth and limited vertical aperture of the geophone array in the observation, as well as effects of the gaps in the shot line. Also, the amplitude spectra of the individual VSP section demonstrate that the frequency bandwidth is not sufficiently high.

Given the good repeatability of the VSP data, it was enticing to look at the response from the calibrated raw VSP data in an attempt to gain a better understanding of the credibility of the time-lapse difference seen, for instance, in Figure 6-25 (c). Figure 6-37, Figure 6-38 and Figure 6-39 show examples of the common-receiver gathers (CRG) from Line 1 that demonstrate the response of the baseline, monitor and difference of data collected at the shallowest receiver (1498 m) of the array as well as the receiver at the top of the reservoir (1620 m) and the receiver at the bottom of the reservoir (1640 m), respectively. There is always appreciable amount of residual amplitude immediately following the first arrival. This being most visible in the case of the shallowest receiver (Figure 6-37 (c)), It is hard to conclude whether this residual amplitude trend is caused by seismic wave attenuation due, for instance to CO_2 attenuation, or because the corresponding interval enclosing the Cardium event was excluded from the calibration process.

The ambiguity concerning the nature of the amplitude residual in the CRG difference sections was alleviated to some extent by looking at spectral ratios, which was undertaken by Dr. Arnim Hasse[77] (Hasse et al., 2010) as part of the pertinent research outlined in Section 6.3. In computing the spectral ratio, the signal recorded by the receiver at the top of the reservoir (R6 at 1620 m) was used as the reference whereas that registered by the receiver at bottom of the reservoir (R7 at 1640 m) was considered as the perturbed signal. More discussion on how the computation was performed can be found in Hasse et al. (2010) whereas some relevant background pertaining to spectral ratio theory was introduced in Section 3.6.6. Figure 6-40 show the spectral ratio plots of the baseline and monitor for each of the three VSP lines using the downgoing wavefield. Obviously, there is a consistent trend of a reduction in the magnitude of the spectral ratio of the monitor data. The trend is most prominent at and near the dominant frequency of the data (25-35 Hz). The only departure from the trend is in the case of spectral ratio of Line 2 data (Figure 6-40 (b)) where there is a cross-over at 50 Hz. Although the observed spectral decrease trend is intriguing, it is uncertain whether the magnitude reduction is a result of intrinsic attenuation, i.e. due to CO_2 injection, or extrinsic attenuation, e.g. near-surface effect.

---

[77] Dr. Arnim Hasse was a member of the CREWES project.

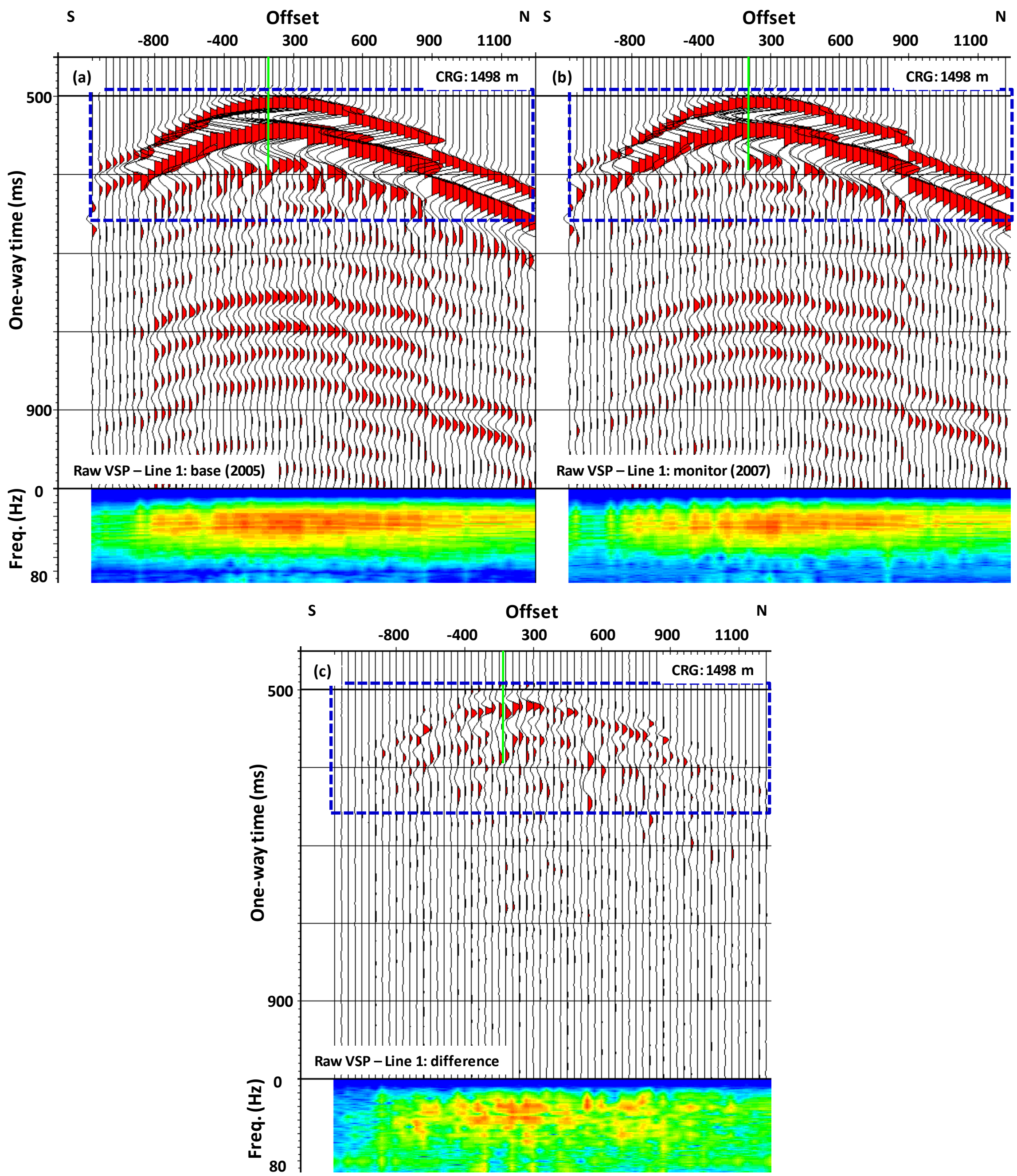

Figure 6-37: Common-receiver gather (CRG) from the calibrated raw VSP data of the shallowest receiver (R1 at 1498 m) from Line 1 showing (a) the baseline, (b) the monitor, and (c) the difference. The green line shows the approximate trajectory of the observation well. Note that the Cardium Formation sets in the area enclosed by the dashed blue rectangle, which shows some residual amplitude after the subtraction. The color scale plot at the bottom of each section shows the corresponding amplitude spectrum. Warm color: high amplitude; cool color: low amplitude. Freq.: frequency.

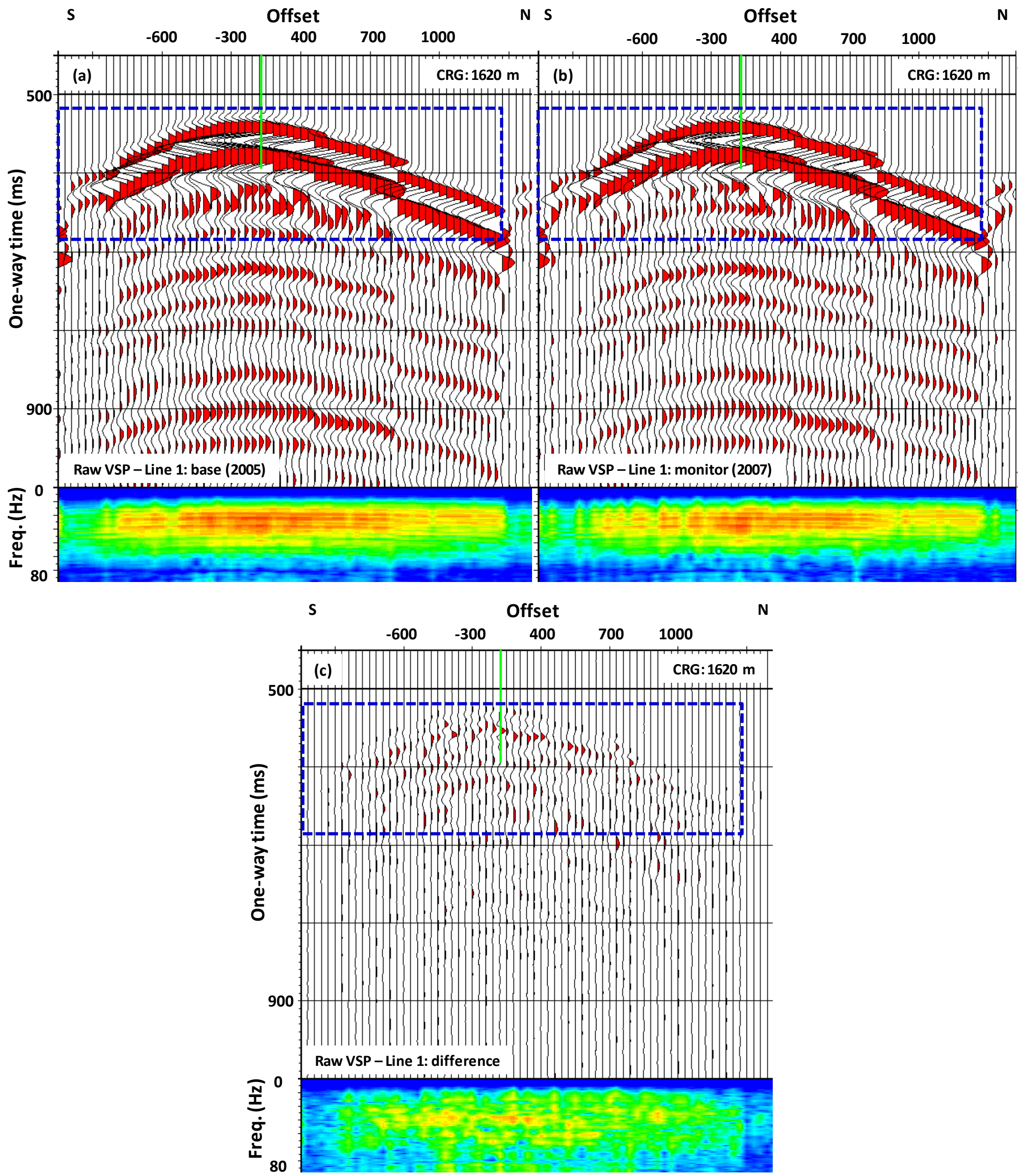

Figure 6-38: Common-receiver gather (CRG) from the calibrated raw VSP data of the receiver at the top of the reservoir (R6 at 1620 m) from Line 1 showing (a) the baseline, (b) the monitor, and (c) the difference. The green line shows the approximate trajectory of the observation well. Note that the Cardium Formation sets in the area enclosed by the dashed blue rectangle, which shows some residual amplitude after the subtraction. The color scale plot at the bottom of each section shows the corresponding amplitude spectrum. Warm color: high amplitude; cool color: low amplitude. Freq.: frequency.

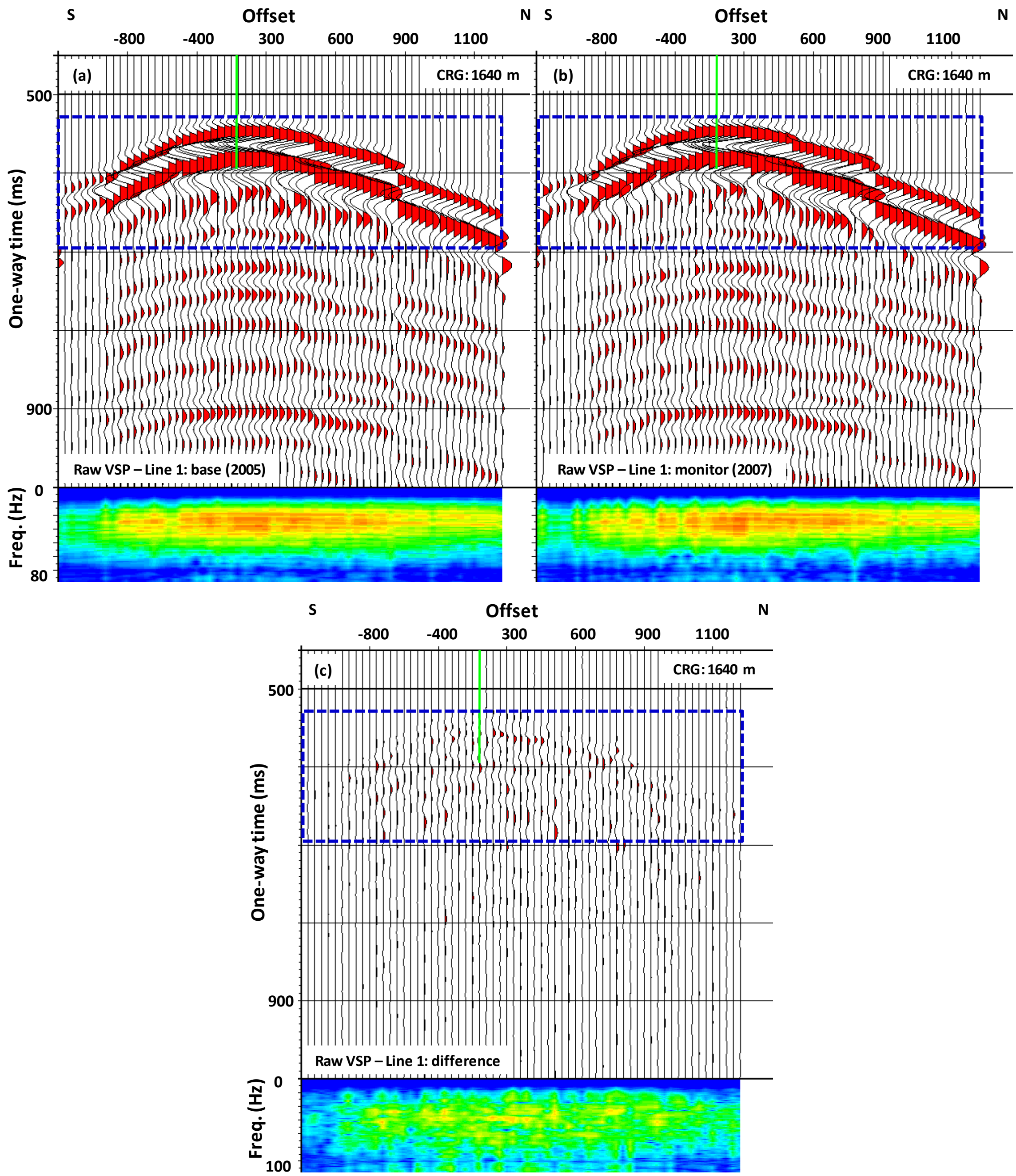

Figure 6-39: Common-receiver gather (CRG) from the calibrated raw VSP data of the deepest receiver at the bottom of the reservoir (R7 at 1640 m) from Line 1 showing (a) the baseline, (b) the monitor, and (c) the difference. The green line shows the approximate trajectory of the observation well. Note that the Cardium Formation sets in the area enclosed by the dashed blue rectangle, which shows some residual amplitude after the subtraction. Freq.: frequency. The color scale plot at the bottom of each section shows the corresponding amplitude spectrum. Warm color: high amplitude; cool color: low amplitude. Freq.: frequency.

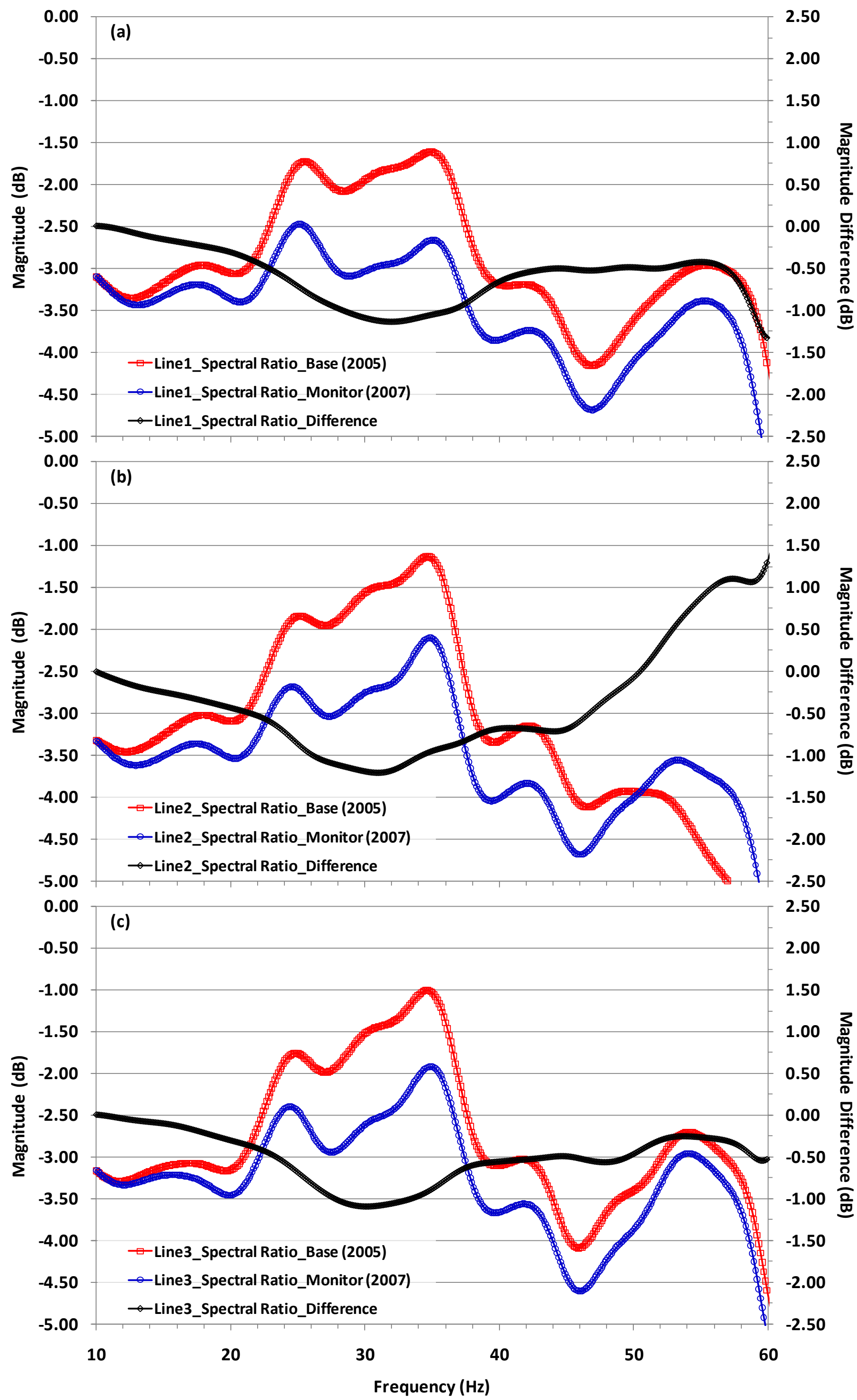

Figure 6-40: Spectral ratio of the baseline (2005) and monitor (2007) computed using the downgoing wavefield from the raw VSP data of (a) Line 1, (b) Line 2, and (c) Line 3. The ratio was computed using the signal recorded at R6 at the top of the Cardium (1620 m) as the reference and the one recorded at R7 at the bottom of the Cardium (1640 m) as the perturbed signal. Data courtesy of Dr. Arnim Hasse.

6.5.4 2-D Surface Seismic Interpretation

Figure 6-41, Figure 6-42, and Figure 6-43 show the baseline, monitor and difference from the calibrated 2-D surface seismic of Lines 1, 2 and 3, respectively. The corresponding amplitude spectra are plotted in Figure 6-44. Data quality is very good, and coherent high-amplitude reflections associated with the Ardley Formation (shallow marker at ~ 360 ms) and the Viking Formation (deep marker at ~ 1230 ms) are clearly visible on the baseline and monitor sections. The reflection from the Cardium Formation (~ 1050 ms), on the other hand, is not as prominent since it is a low-impedance reservoir.

The difference sections from all the lines do not display any distinct or consistent anomalies at the Cardium or Viking events. Furthermore, the difference sections are remarkably featureless except for small low-amplitude residual associated primarily with processing noise. The most enticing residual amplitude packet is the one seen at Cardium time east of the main injector in the difference section of Line 3 (Figure 6-43 (c)). Although tempting to associate this with the CO_2 plume, it could be caused by the wide gap in the source distribution of Line 3 (Figure 6-5). Moreover, this anomaly was not visible the other lines, in particular Line 1 which is closer to the main CO_2 injector and is along the up-dip CO_2 plume migration pathway[78].

In order to assess the former observations regarding the lack of CO_2-induced anomaly, the Cardium event was investigated more vigorously using a suite of seismic attributes shown in Figure 6-45 through Figure 6-49. The cross-plots of the seismic amplitude from the baseline and monitor from all the 2-D lines plotted in Figure 6-45 do not exhibit any anomalous trend. Similarly, the difference in the Cardium event time structure and the Cardium-Viking isochron between the baseline and monitor surveys do not reveal any consistent trend. This lack of discernible time shift is anticipated as outlined previously in Section 6.5.1 but the absence of distinct and consistent amplitude anomaly given the continuity and wide aperture of the 2-D surface seismic stimulated the generation of the subsequent amplitude-based attributes using all three lines. The basic

---

[78] This statement is supported by independent reservoir and geochemical data that will be briefly discussed in Section 6.7.

theories underlying some of these attributes were discussed in Chapter 3 and some were invoked in the interpretation pertaining to WASP in Chapter 4.

Figure 6-47 shows the normalized difference between the baseline and monitor surveys of three seismic attributes: seismic amplitude, root-mean squares (RMS) amplitude, and amplitude thickness of the peak (ATP). The normalized difference in the amplitude envelope and average amplitude spectrum are plotted in Figure 6-48. In addition to these, Figure 6-49 illustrates difference in the acoustic impedance between the baseline and monitor derived using seismic inversion[79]. Unfortunately, no distinctive anomaly is observed by the examining the difference in any of these attributes. Furthermore, the curves are of oscillatory nature, which suggest that the CO_2-induced time-lapse anomaly - if detectable - is at or below the lower threshold of the detection limit.

The most intriguing trend is the change in the average amplitude spectrum shown in Figure 6-48, which is consistently negative for all the 2-D lines. This is expected as the amplitude spectra in Figure 6-44 show a small decrease between the baseline and monitor surveys. Recall that the spectral ratio derived from the VSP data (previous section) displayed a similar pattern. The fact that similar decrease is also observed in the 2-D surface seismic data might indicate that some other phenomenon besides intrinsic attenuation, i.e. CO_2 injection inside the reservoir, is responsible for the observed decrease in the frequency bandwidth. As discussed in Section 6.5.3, this phenomenon is thought to be associated with extrinsic attenuation, most likely due to near-surface variation and perhaps acquisition and processing causes as well. More discussion on the absence of a discernible CO_2-related anomaly will follow under Section 6.6.

---

[79] For theoretical review, see the discussion under Sections 3.5.6 and 3.5.7. Acoustic impedance inversion was, also, invoked as one of the quantitative interpretation methods in the WASP site characterization (Chapter 4). Section 4.6.4 offers a detailed account of the acoustic impedance inversion approach implemented in this dissertation. The same approach was adopted in undertaking the shear impedance inversion as well.

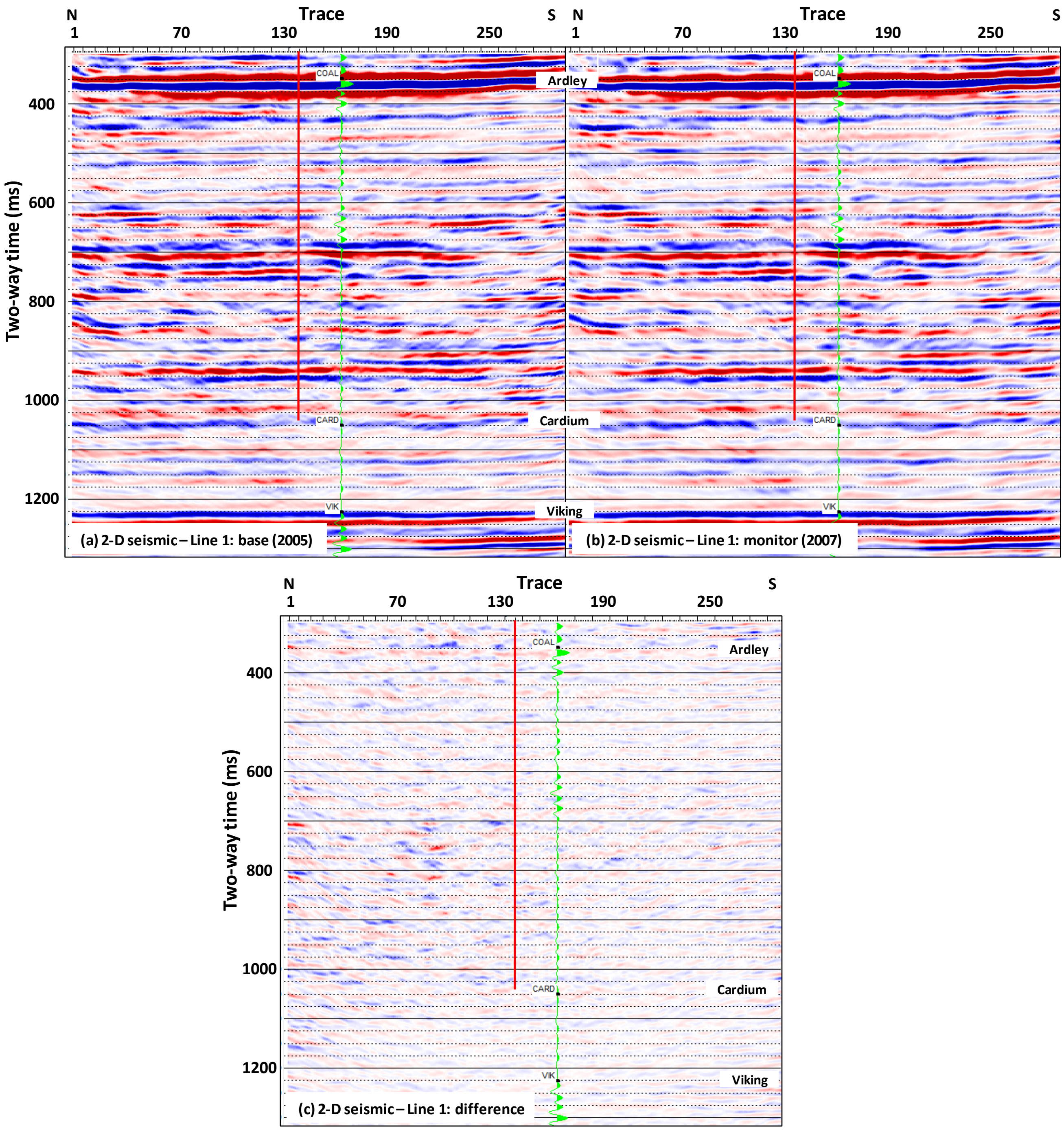

Figure 6-41: Calibarted 2-D surface seismic from Line 1 showing the baseline data (2005), (b) the monitor data (2007), and (c) the difference between (a) and (b). The green trace shows the synthetic seismogram along the trajectory of the observation well while the red line shows the approximate trajectory of the injection well (injector 1). Blue: positive amplitude, red: negative amplitude.

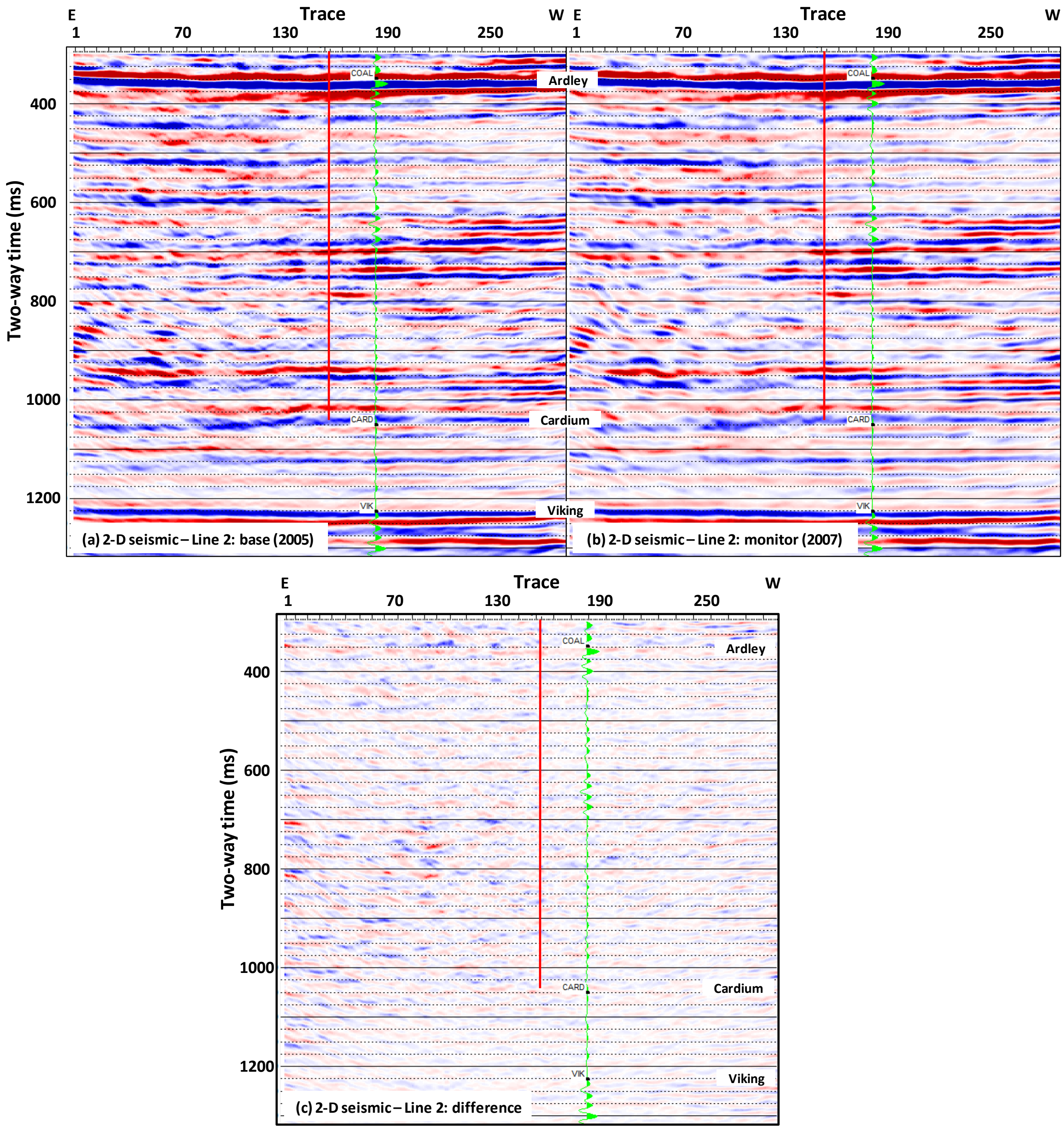

Figure 6-42: Calibarted 2-D surface seismic from Line 2 showing the baseline data (2005), (b) the monitor data (2007), and (c) the difference between (a) and (b). The green trace shows the synthetic seismogram along the trajectory of the observation well while the red line shows the approximate trajectory of the injection well (injector 1). Blue: positive amplitude, red: negative amplitude.

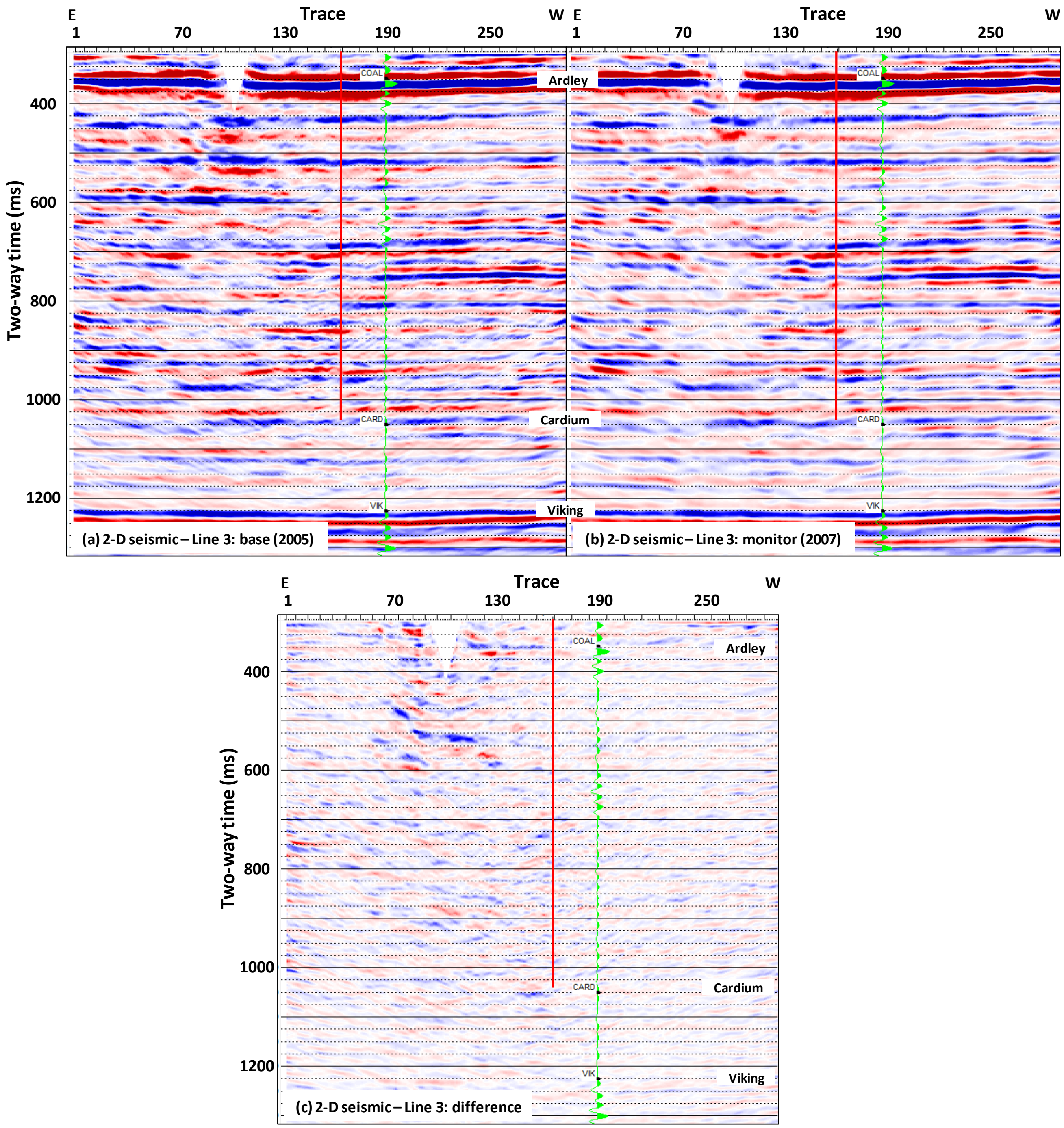

Figure 6-43: Calibarted 2-D surface seismic from Line 3 showing the baseline data (2005), (b) the monitor data (2007), and (c) the difference between (a) and (b). The green trace shows the synthetic seismogram along the trajectory of the observation well while the red line shows the approximate trajectory of the injection well (injector 1). Blue: positive amplitude, red: negative amplitude.

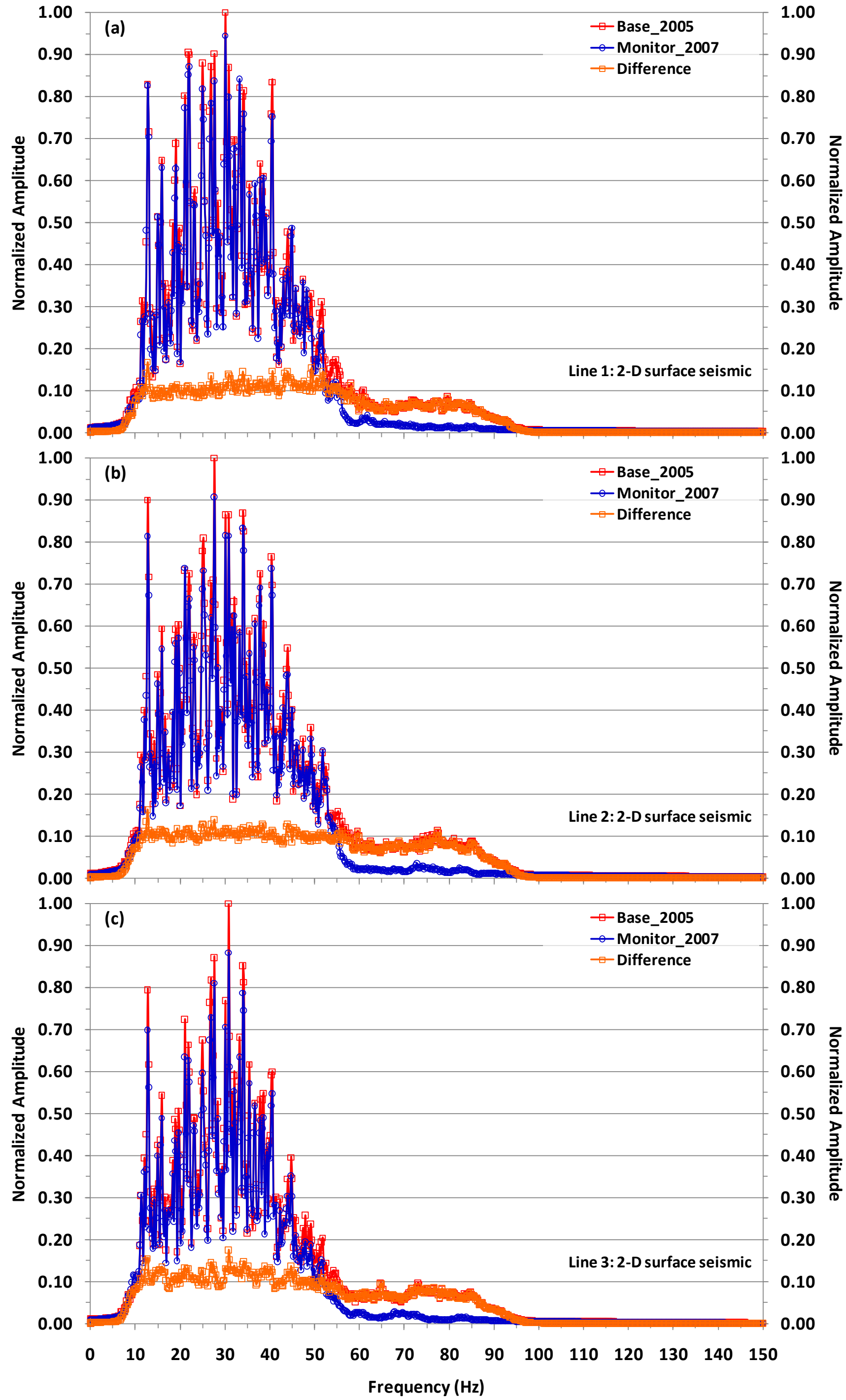

Figure 6-44: Average amplitude spectra of the calibrated 2-D P-wave surface seismic data from (a) Line 1, (b) Line 2, and (c) Line 3 computed over a long window encompassing the Ardley, Cardium and Viking formations. Note that the difference spectrum is computed from the difference section not by taking the difference of the baseline and monitor spectra shown here and that all spectra for each line are normalized with respect to the maximum of the baseline data.

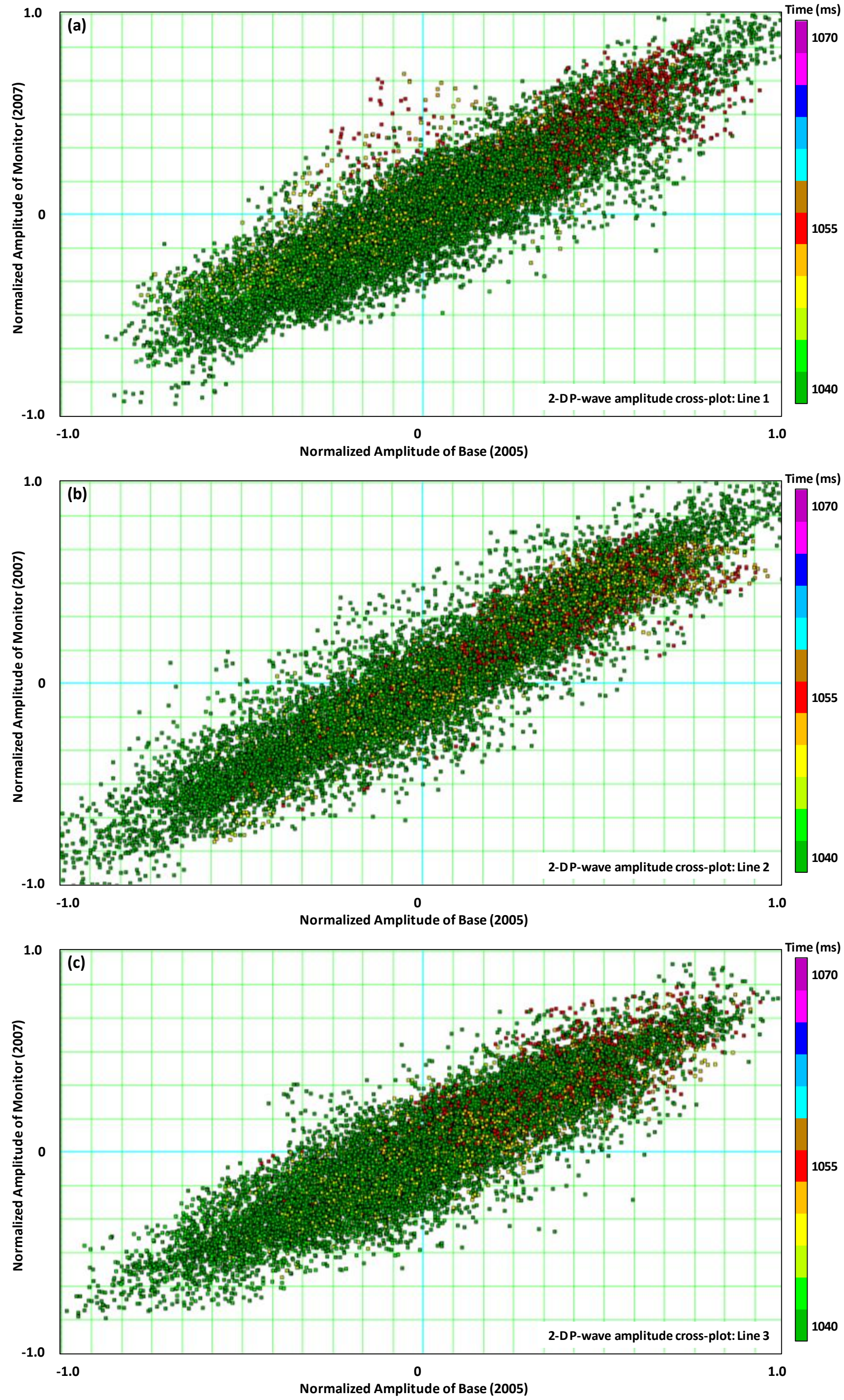

Figure 6-45: Cross-plot of the seismic amplitude of the baseline (2005) and monitor (2007) of the Cardium interval from (a) Line 1, (b) Line 2, and (c) Line 3 computed over a 30 ms window.

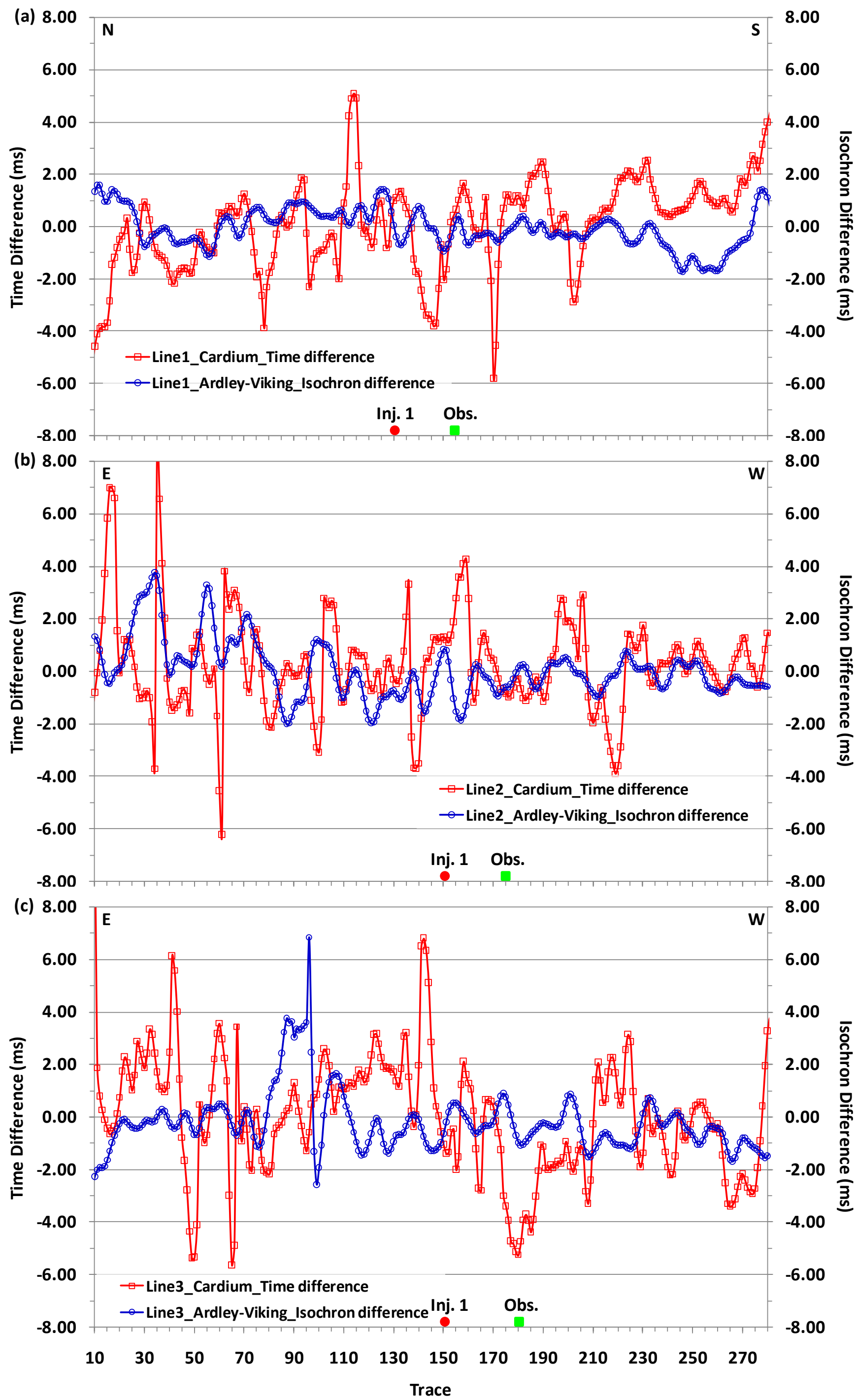

Figure 6-46: Difference in the Cardium event time and the Ardley-Viking isochron, and between the baseline (2005) and monitor (2007) from (a) Line 1, (b) Line 2, and (c) Line 3. The approximate projected location of the injector (Inj. 1) and observation (Obs.) wells are indicated by the red circle and the green square, respectively

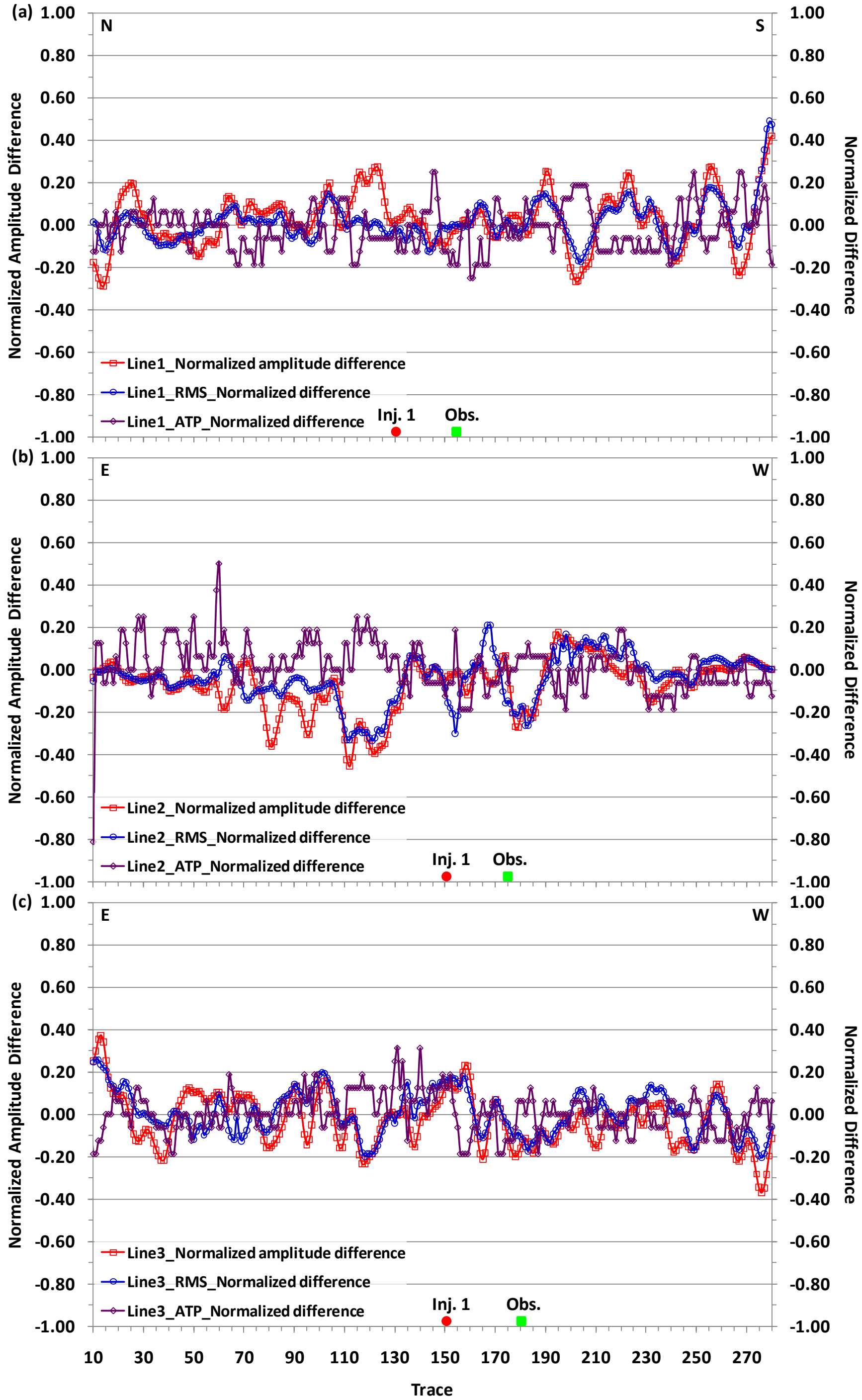

Figure 6-47: Difference in some of the Cardium seismic zone attributes between the baseline (2005) and monitor (2007) from (a) Line 1, (b) Line 2, and (c) Line 3. These attributes were averaged over a 30 ms window centered at the Cardium event and then subtracted. RMS: root-mean squares amplitude; ATP: amplitude thickness of the peak. The values in were normalized with respect to maximum of the baseline to facilitate better plotting. The approximate projected location of the injector (Inj. 1) and observation (Obs.) wells are indicated by the red circle and the green square, respectively.

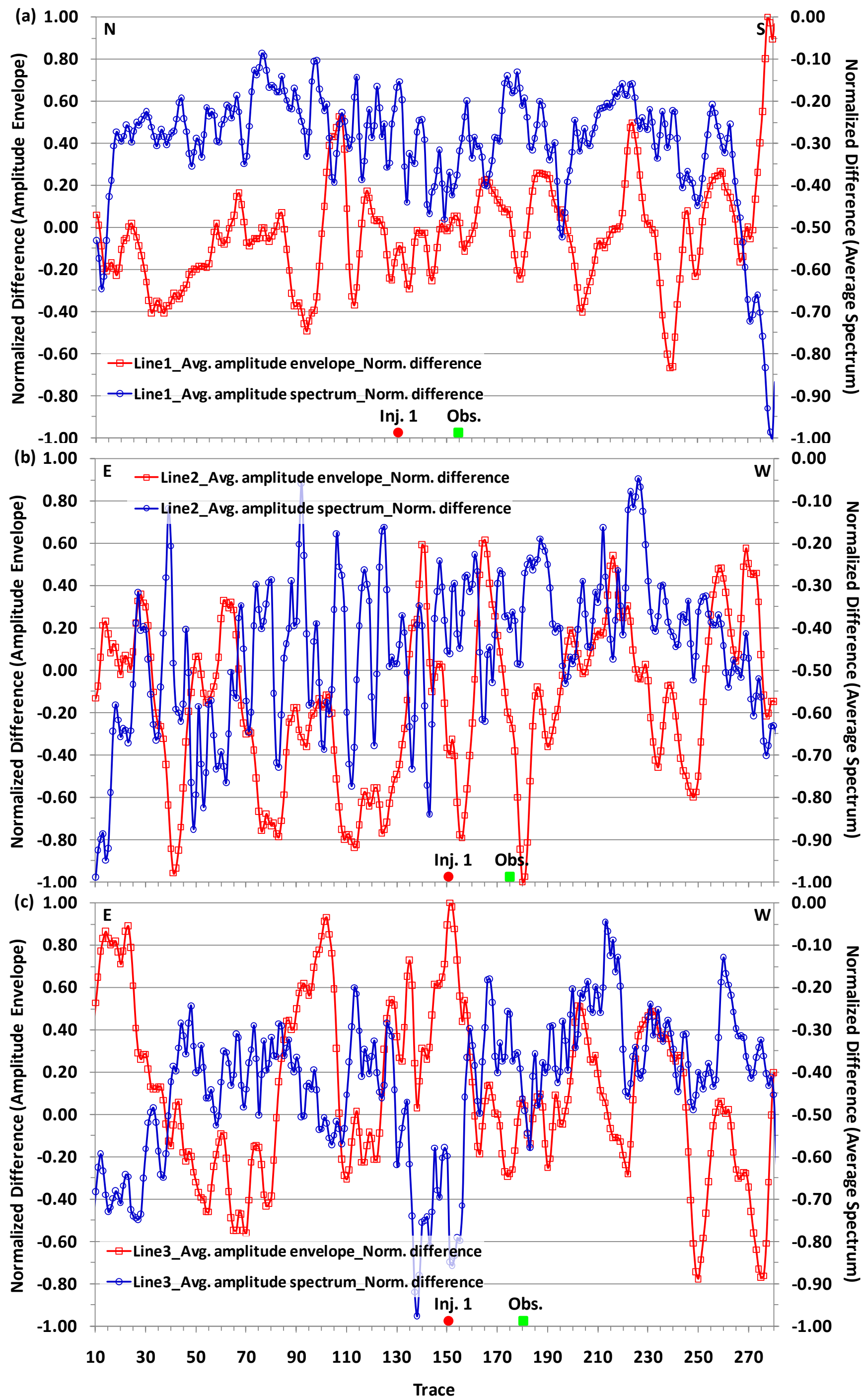

Figure 6-48: Differences in the averagedamplitude of the envelope and the averaged amplitude spectrum and of the Cardium event between the baseline (2005) and monitor (2007) from (a) Line 1, (b) Line 2, and (c) Line 3. These attributes were individually averaged over a 30 ms window centered at the Cardium event then subtracted. Norm.: normalized; avg.: average. The approximate projected location of the injector (Inj. 1) and observation (Obs.) wells are indicated by the red circle and the green square, respectively.

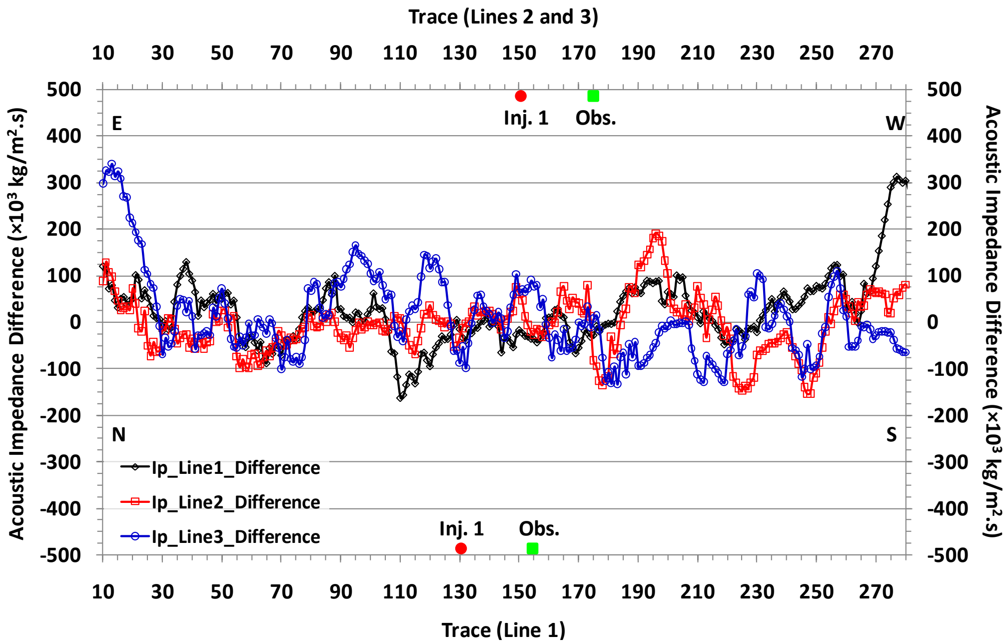

Figure 6-49: Difference in the acoustic impedance (I_p) of the Cardium between the baseline (2005) and monitor (2007) estimated using model-based inversion of (a) Line 1, (b) Line 2, and (c) Line 3. The impedance values were averaged over a 30 ms window centered at the Cardium event. The approximate projected location of the injector (Inj. 1) and observation (Obs.) wells are indicated by the red circle and the green square, respectively.

6.5.5 3-D Surface Seismic Interpretation

Figure 6-50 and Figure 6-51 show SW-NE sections that depict a typical seismic response from the baseline, monitor and difference corresponding to the 3-D P-wave and PS-wave surface seismic data. The diagonal line, also, traverses the western injection well in addition to the observation well. The dataset attain typical frequency bandwidth as demonstrated by the corresponding amplitude spectra plotted in Figure 6-52. The spectrum of the baseline P-wave data separates from that of the monitor beyond 60 Hz, probably due to processing variance. Another observation is the large magnitude associated with the amplitude spectrum of the difference PS-wave data. This in addition to the PS-wave data character difference as seen in Figure 6-51 along with the poor repeatability (Section 6.5.2.4) places unreliability on the PS-wave difference interpretation.

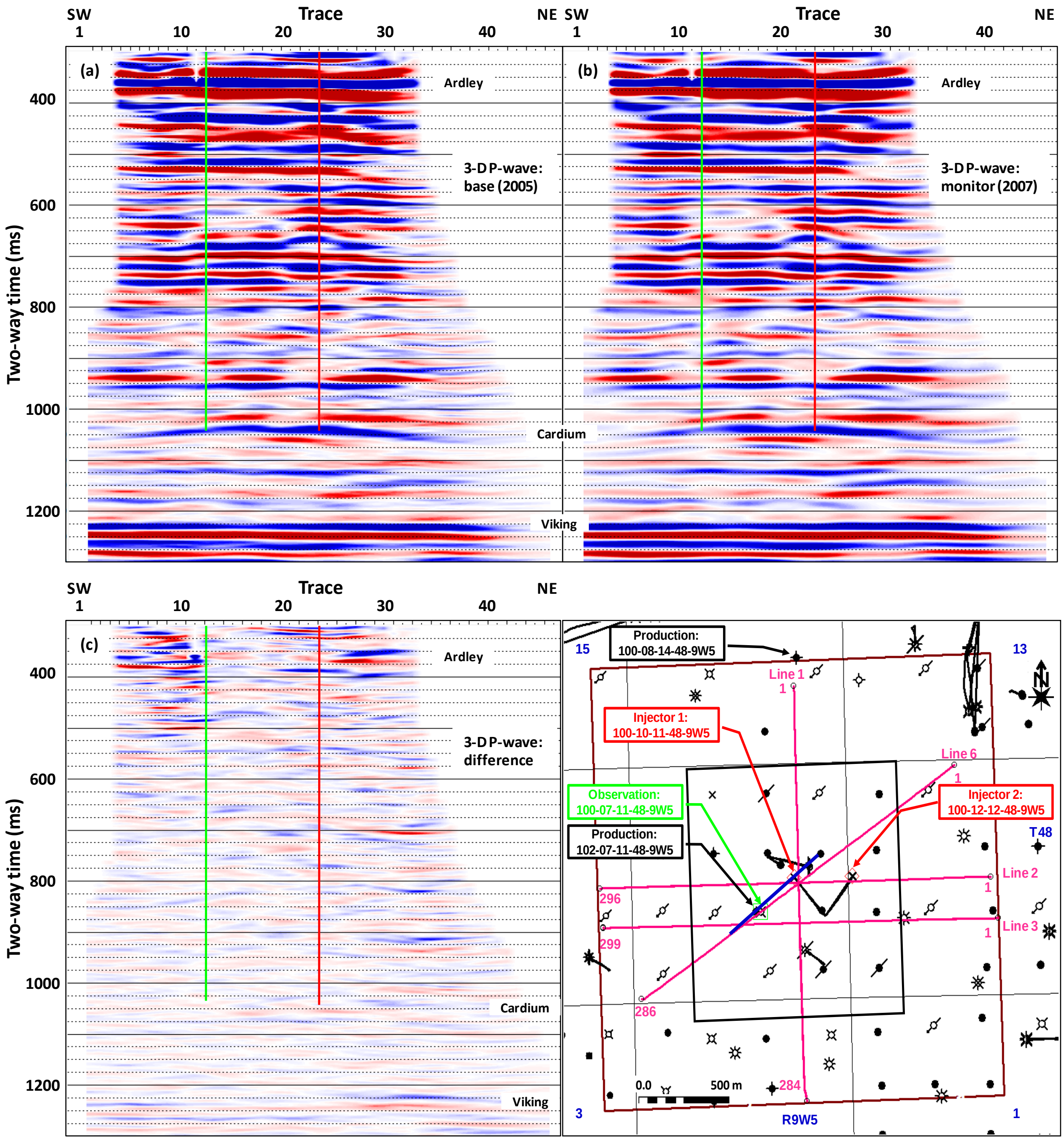

Figure 6-50: Display of the calibrated 3-D P-wave surface seismic from showing the baseline data (2005), (b) the monitor data (2007), and (c) the difference between (a) and (b). The green and red lines show the approximate trajectory of the of the observation and injection (injector 1) wells. The location of the seismic section is shown by the NE-SW blue line traversing the observation and injection wells in the base map (lower-right corner). Blue: positive amplitude, red: negative amplitude.

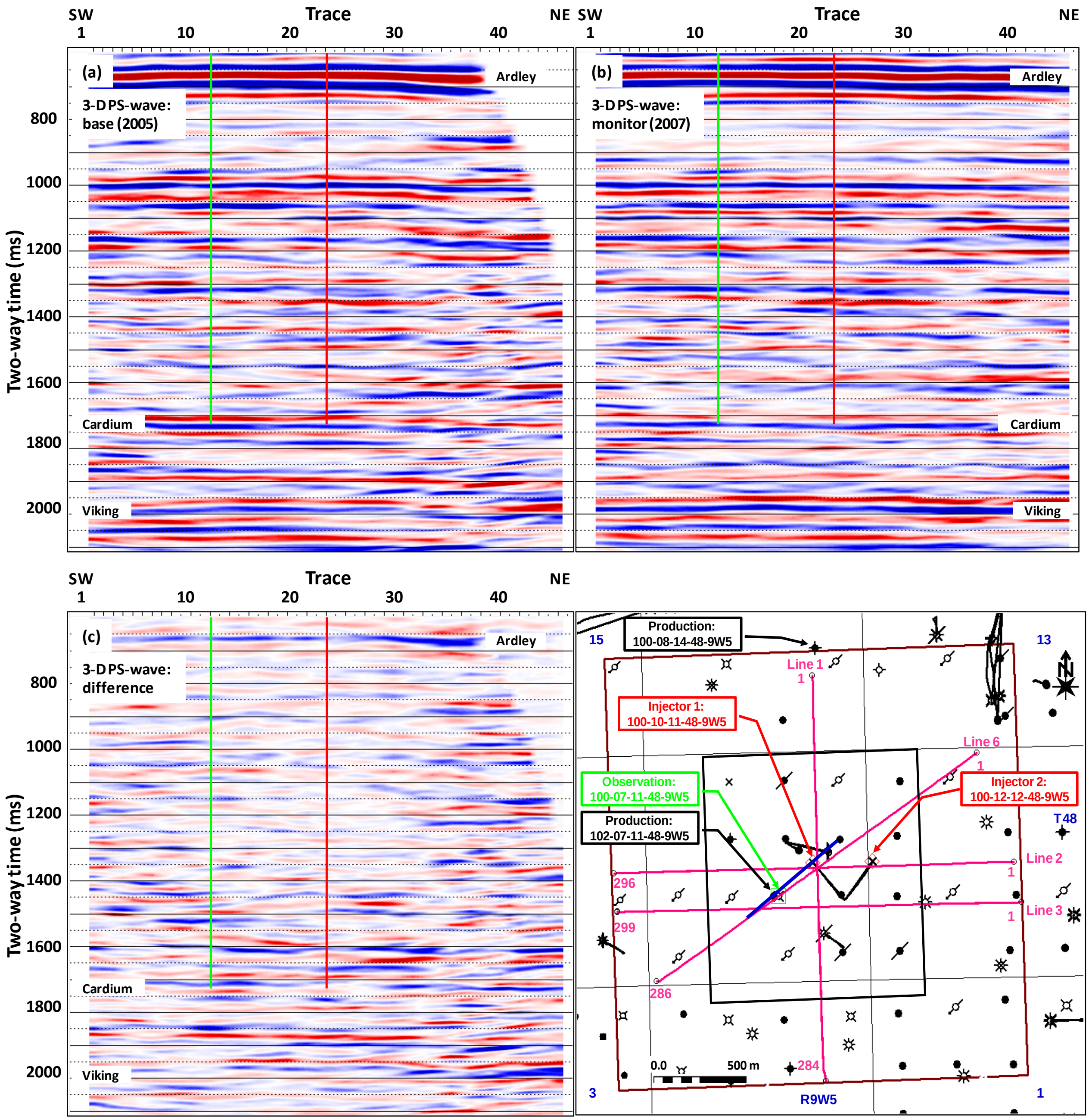

Figure 6-51: Display of the calibrated 3-D PS-wave surface seismic from showing the baseline data (2005), (b) the monitor data (2007), and (c) the difference between (a) and (b). The green and red lines show the approximate trajectory of the of the observation and injection (injector 1) wells. The location of the seismic section is shown by the NE-SW blue line traversing the observation and injection wells in the base map (lower-right corner). Blue: positive amplitude, red: negative amplitude.

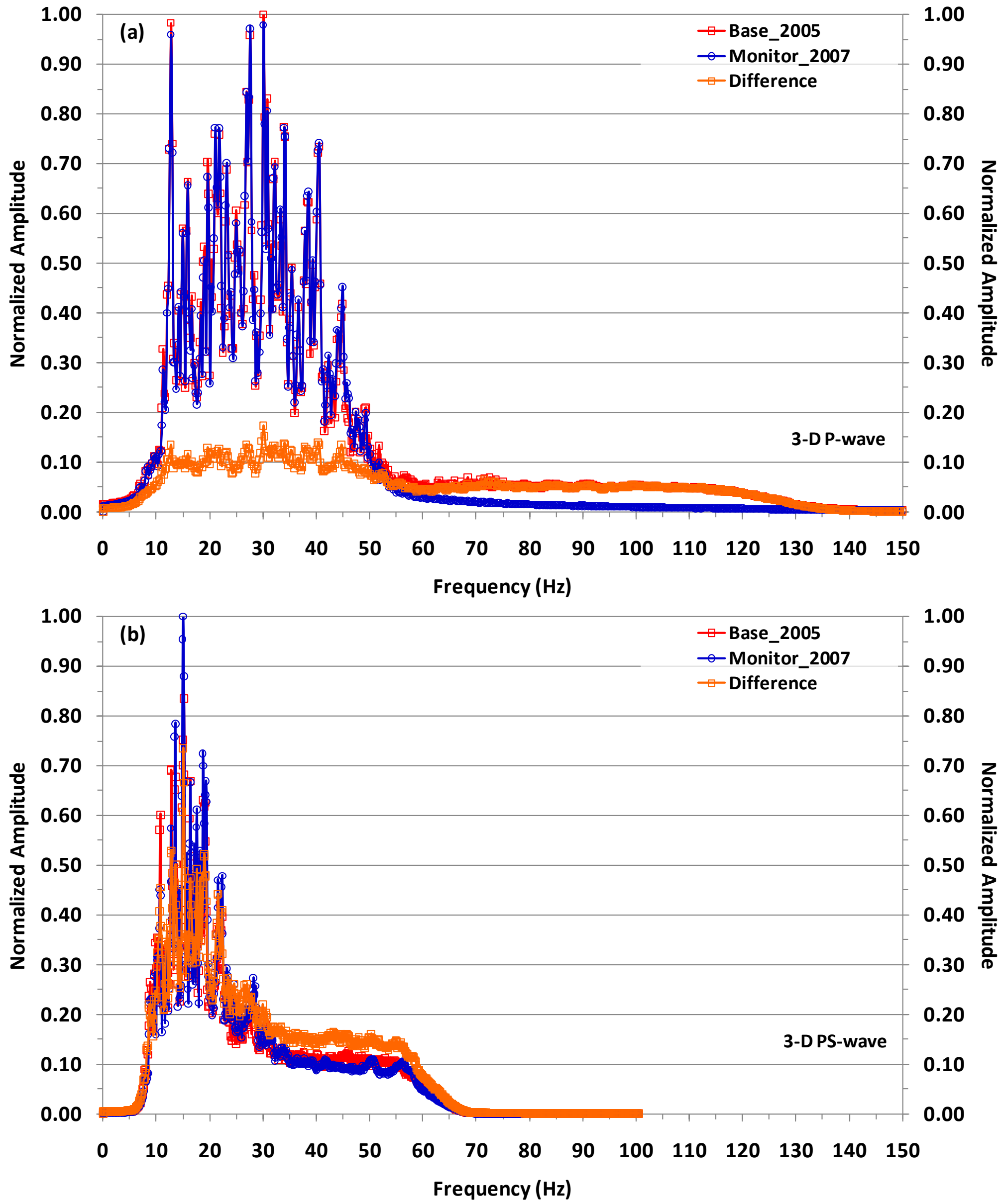

Figure 6-52: Average amplitude spectra of the calibrated 3-D surface seismic data (a) P-wave, and (b) PS-wave from the baseline and monitoring surveys. Note that the spectra in each plot are normalized with respect to the maximum of the baseline data.

The difference section from the 3-D P-wave data (Figure 6-50 (c)) resembles difference in the 2-D surface seismic, i.e. only residual amplitudes of small magnitude are visible, especially in the near-surface due to ground condition changes and near the edges. The difference section corresponding to the PS-wave data (Figure 6-51 (c)), on the other hand, shows a substantial amount of residual amplitude packets that are observed randomly in the 3-D volume. As denoted in the repeatability discussion of the PS-wave data (Section 6.5.2.4), the reason behind this could be difficulty in converted-wave data processing and low signal to noise ratio (S/N).

3-D visualization of the Ardley (shallow marker), Cardium (reservoir) as well as the Viking (deep marker) events from the P-wave and PS-wave volumes is displayed in Figure 6-53. The reasons the former and the latter events are being emphasized were presented in Section 6.4 and will even be more appreciated in the isochron and interval α/β analyses that follow shortly. Cross-plots of the seismic amplitude from the baseline and monitor surveys from the P-wave and PS-wave data are displayed Figure 6-54. In the case of the P-wave (Figure 6-54 (a)), the pattern is similar to that of the 2-D surface seismic, i.e. no distinctive pattern is discerned. The PS-wave amplitude cross-plot (Figure 6-54 (b)) does not exhibit any distinct pattern either but rather exhibits a significant level of variability, which could be attributed to the reasons mentioned in the previous paragraph.

Figure 6-55 and Figure 6-56 demonstrate the difference in the Cardium event time and peak amplitude corresponding to the P-wave and PS-wave data, respectively. In the case of the P-wave data (Figure 6-56), there seems to be a small negative time shift (Figure 6-56 (a)) accompanied by amplitude decrease (Figure 6-56 (b)) near the western injector inside the ZRD[80]. The area around the eastern injector show similar pattern that is associated with larger magnitude in these two entities, i.e. more negative time shift and amplitude differences, but that is outside the ZRD and is known to be spurious due to picking issues concerning the Cardium event in that area. In the case of the PS-wave data, there is a rather “false” circular anomaly suggesting an increase in the Cardium event

[80] Zone of Reliable Data (ZRD). See the first paragraph under the 3-D surface seismic repeatability (Section 6.5.2.4).

traveltime around the western injector whereas the amplitude difference (Figure 6-55 (b)) exhibits a negative north-south trend.

It is difficult to extract reliable time shift information by taking the time difference at the reservoir itself. Hence, the difference in the Ardley-Viking isochron between the baseline and monitor was computed using the 3-D P-wave and PS-wave data and the results are shown in Figure 6-57. The difference corresponding to the P-wave data (Figure 6-57 (a)) suggests an increase in the Ardley-Viking interval traveltime north and south of the western injector and a decrease elsewhere. The difference corresponding to the PS-wave data (Figure 6-57 (b)) exhibits an increase east of the western injector and a decrease elsewhere. The north-south increase pattern in the case of the P-wave data (Figure 6-57 (a)) and the elsewhere decrease between the lines in the case of the PS-wave data (Figure 6-57 (b)) seem to agree in principle with the modelling results (Chapter 7) although the difference magnitude observed in the field data is much higher.

However, by looking at the isochron difference maps over the entire ZRD, there appears to be a lack of a consistent and a coherent pattern, in general, and between the P-wave and PS-wave, in particular, which undermines the credibility of these individual anomalies. Moreover, it seems that the difference maps are reflecting the lower threshold of the dynamic range of the data. In other words, the variations being seen are dominated by the noise-level whether caused by the gaps in the shot line, processing noise or some other culprits. Furthermore, and as mentioned earlier, the fluid substitution and seismic modelling (Chapter 7) indicate that the amount of time shift is extremely small (~ 0.1 ms) and is below seismic detection at least in this case.

Another time-based attribute, namely the P/S wavespeeds ratio (α/β)[81], was calculated as well using the multi-component data and the difference in this attribute between the baseline and monitor surveys is displayed in Figure 6-58. The α/β difference map indicates that there is an increase east of the western injector and a decrease elsewhere. The elsewhere decrease pattern seems to be in agreement with the modelling results (Chapter 7). However, due to the issues outlined in the first two paragraphs of this

[81] See Section 3.5.9.

Section with regard to the quality and character of the PS-wave data, it is deemed that any results derived from the PS-wave data pertaining to the CO_2 plume is unreliable. As a result, the effort in the subsequent analysis was primarily dedicated toward presenting and discussing the attributes derived from the P-wave data as it is proven to be a more robust indication of fluid changes, such as those associated with CO_2 injection (see literature review in Chapter 1 and modelling results in Chapter 7). The difference maps of the seismic attributes to follow were obtained by computing the designated attribute in the baseline and monitor volumes, individually, over optimally selected windows[82] to better capture any time-lapse change associated with the CO_2 injection and then taking the difference. Furthermore, the following analysis focuses on the ZRD and on delineating the most likely CO_2-induced anomaly within the ZRD.

Figure 6-59 shows the difference in the RMS and median amplitude of the Cardium event; both of which show a decrease pattern in a roughly northern semicircle around the western injector within the ZRD. The difference in the amplitude envelope and ATP (Figure 6-60) exhibits similar “decrease” trend north and east of the western injector inside this zone. A rather intriguing and consistent pattern is shown in Figure 6-61 (a) which depicts the difference in the amplitude spectrum of the P-wave data which extends beyond the ZRD. This pattern seems to resemble that of the 2-D surface seismic data and the credibility of such pattern was discussed in the last paragraph under Section 6.5.4. Figure 6-62 depicts the dominant frequency of the P-wave, which suggest very small changes in the case of the P-wave data except for the isolated packets, such as the one shown west and south of the western injector within the ZRD (Figure 6-62). Figure 6-63 demonstrates the difference of two frequency components, i.e. 25 Hz and 35 Hz, computed using spectral decomposition (SD)[83]. The difference images corresponding to the P-wave data show a rational negatively-dominated responses but no distinct pattern that could be attributed to the CO_2 injection.

---

[82] That is a 30 ms window centered at the Cardium event. The only deviation from this window length is in the case of the spectral decomposition computation where a 100 ms window was used instead.
[83] See Section 3.6.4 for a brief theoretical review of SD.

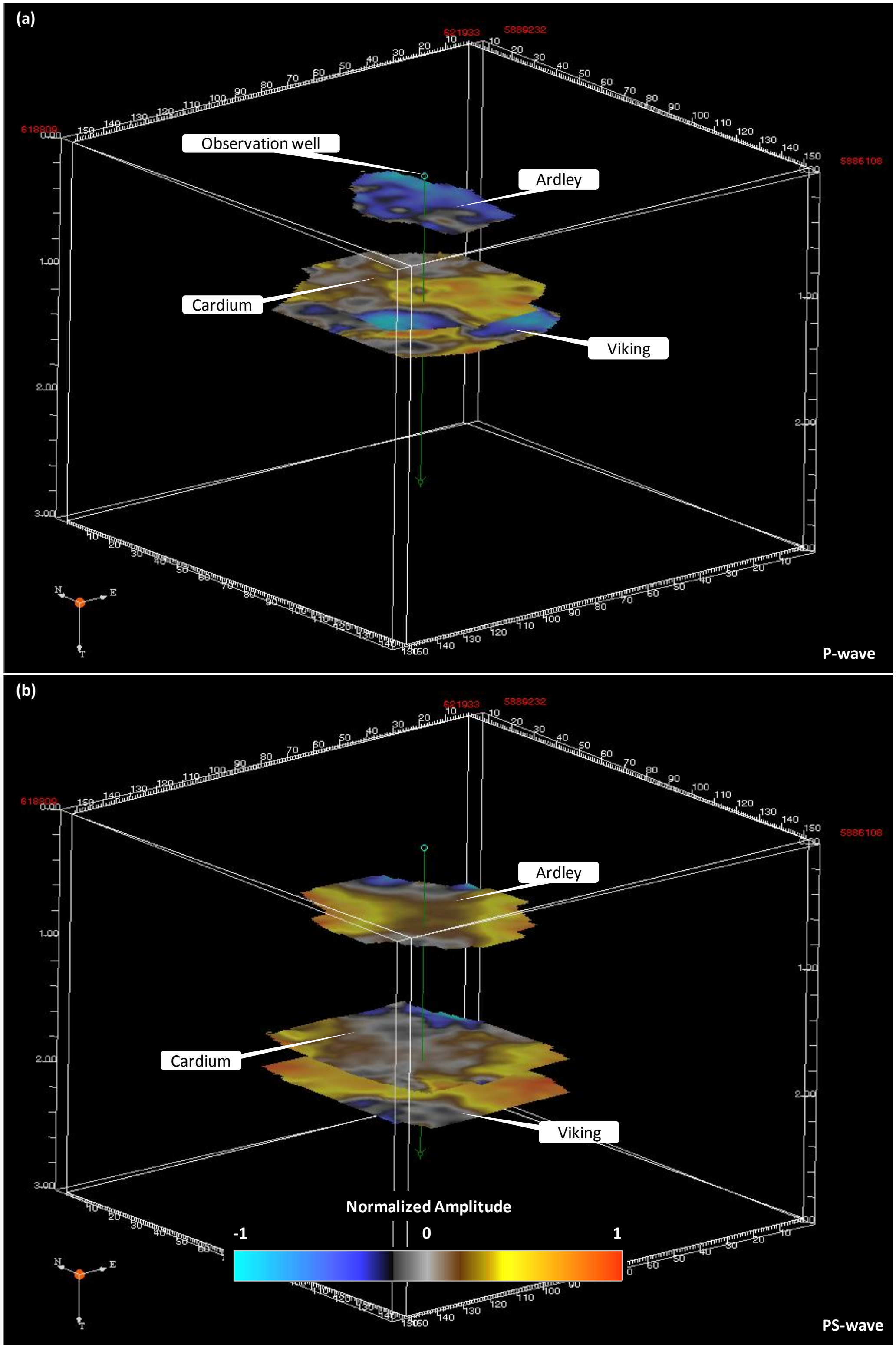

Figure 6-53: 3-D visualization of the Ardley, Cardium and Viking events showing the seismic amplitude from (a) P-wave data, and (b) PS-wave data. The trajectory of the observation well is shown by the green line.

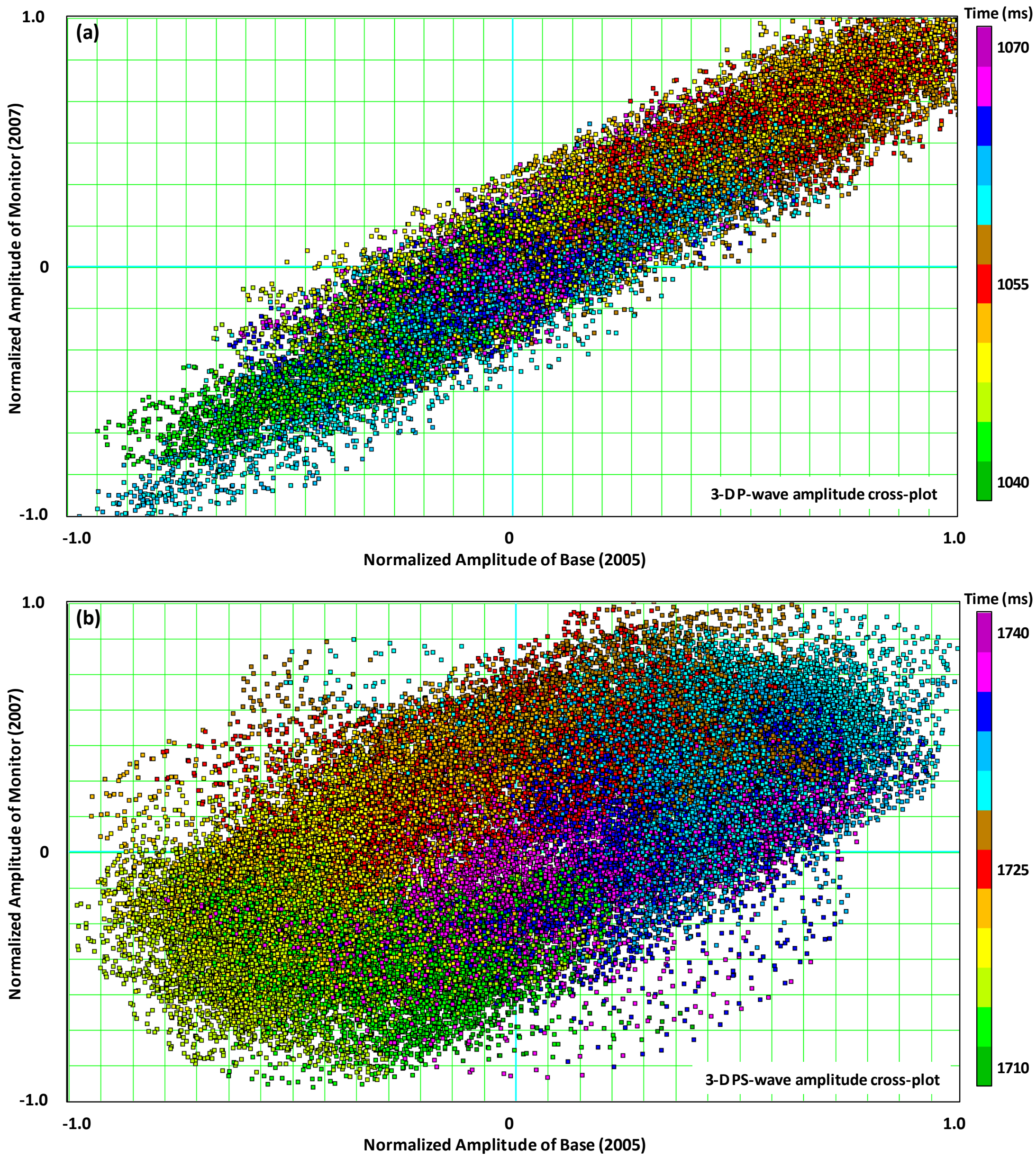

Figure 6-54: Cross-plot of the seismic amplitude of the baseline (2005) and monitor (2007) of the Cardium interval from (a) 3-D P-wave, and (b) 3-D PS wave volumes computed over a 30 ms window.

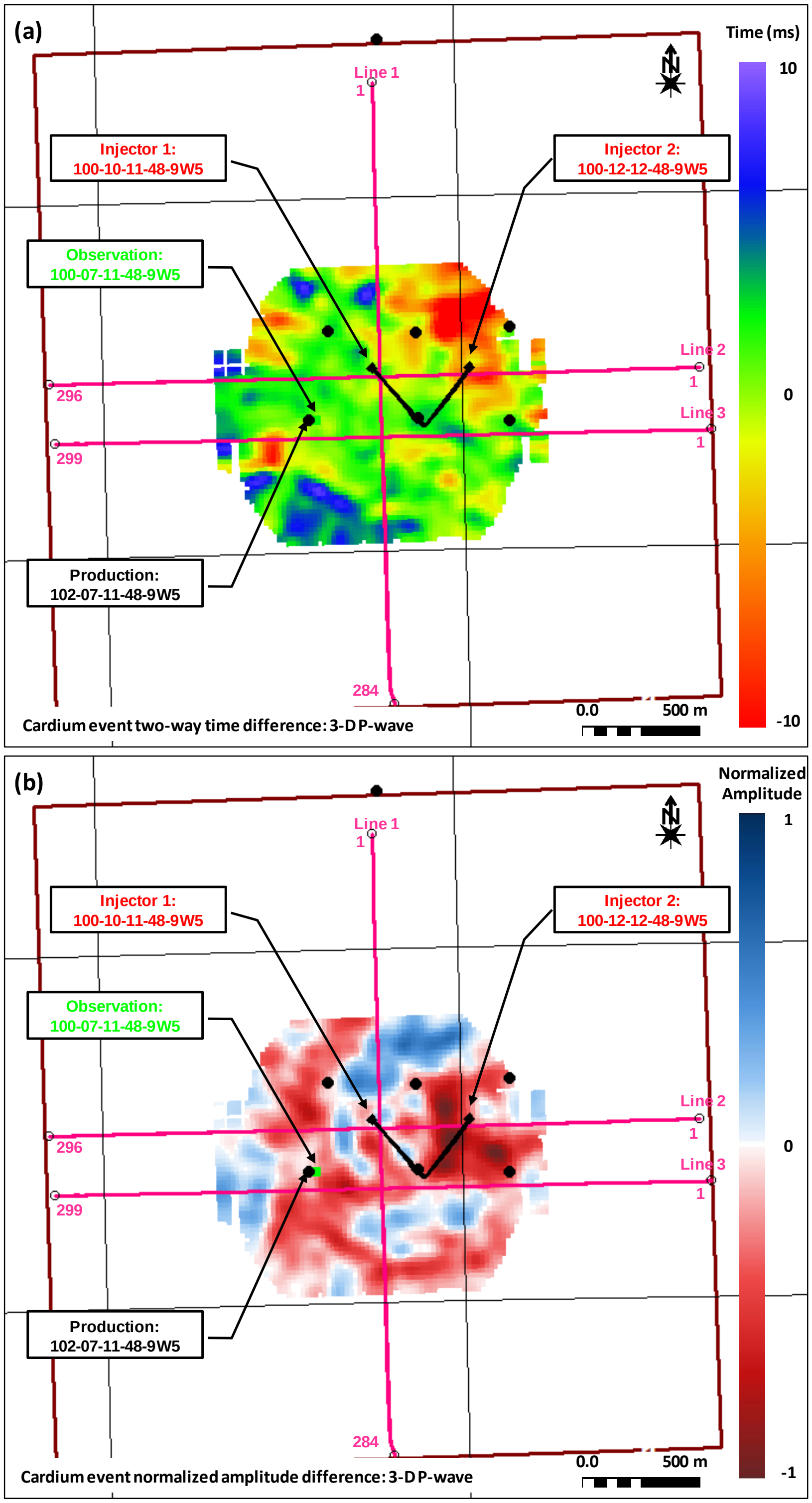

Figure 6-55: Difference in the Cardium event (a) two-way time, and (b) peak amplitude between the baseline (2005) and monitor (2007) corresponding to the 3-D P-wave surface seismic data. The difference amplitude in (b) was normalized by the maximum of the baseline.

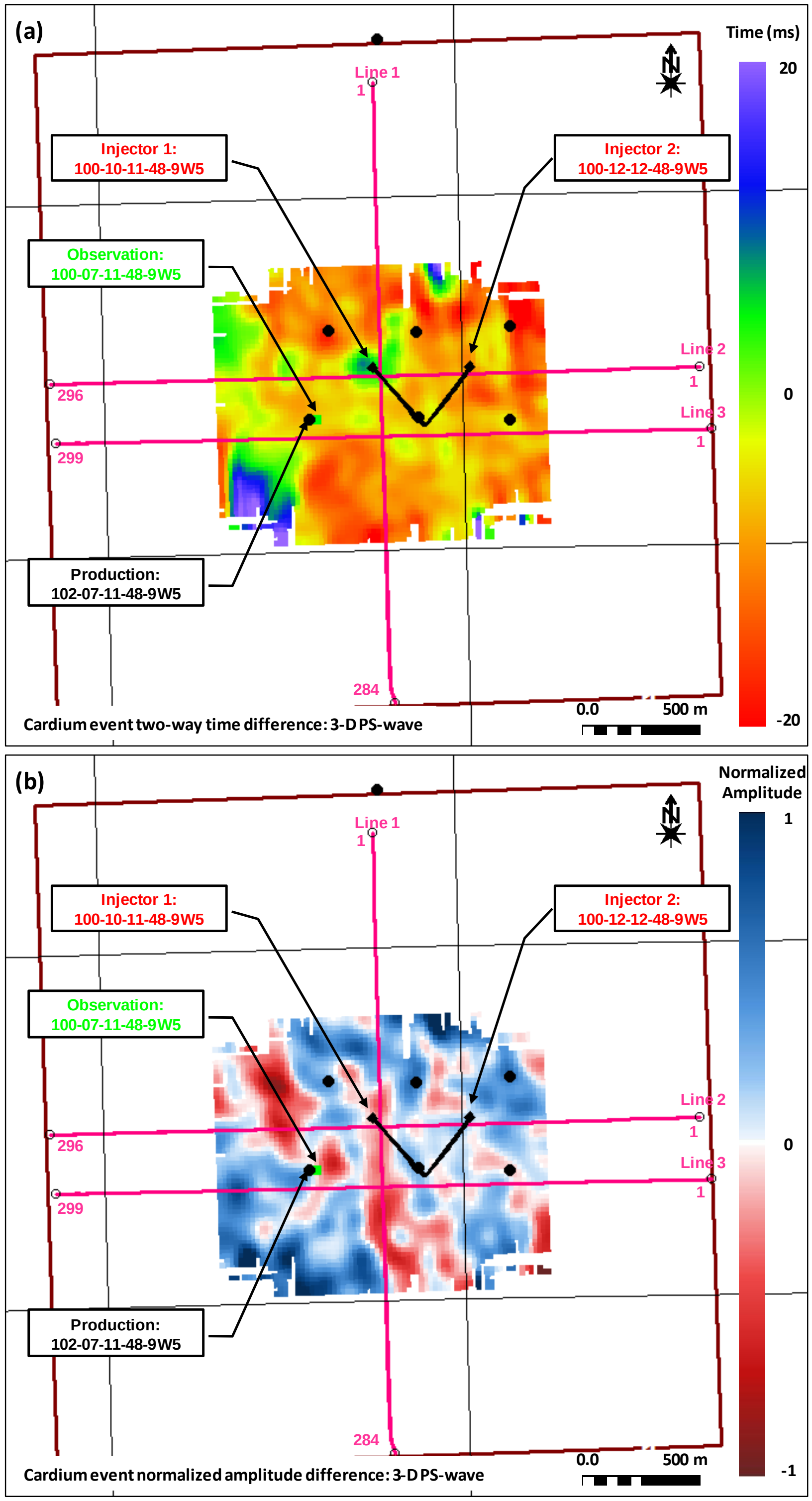

Figure 6-56: Difference in the Cardium event (a) two-way time, and (b) peak amplitude between the baseline (2005) and monitor (2007) corresponding to the 3-D PS-wave surface seismic data. The difference amplitude in (b) was normalized by the maximum of the baseline.

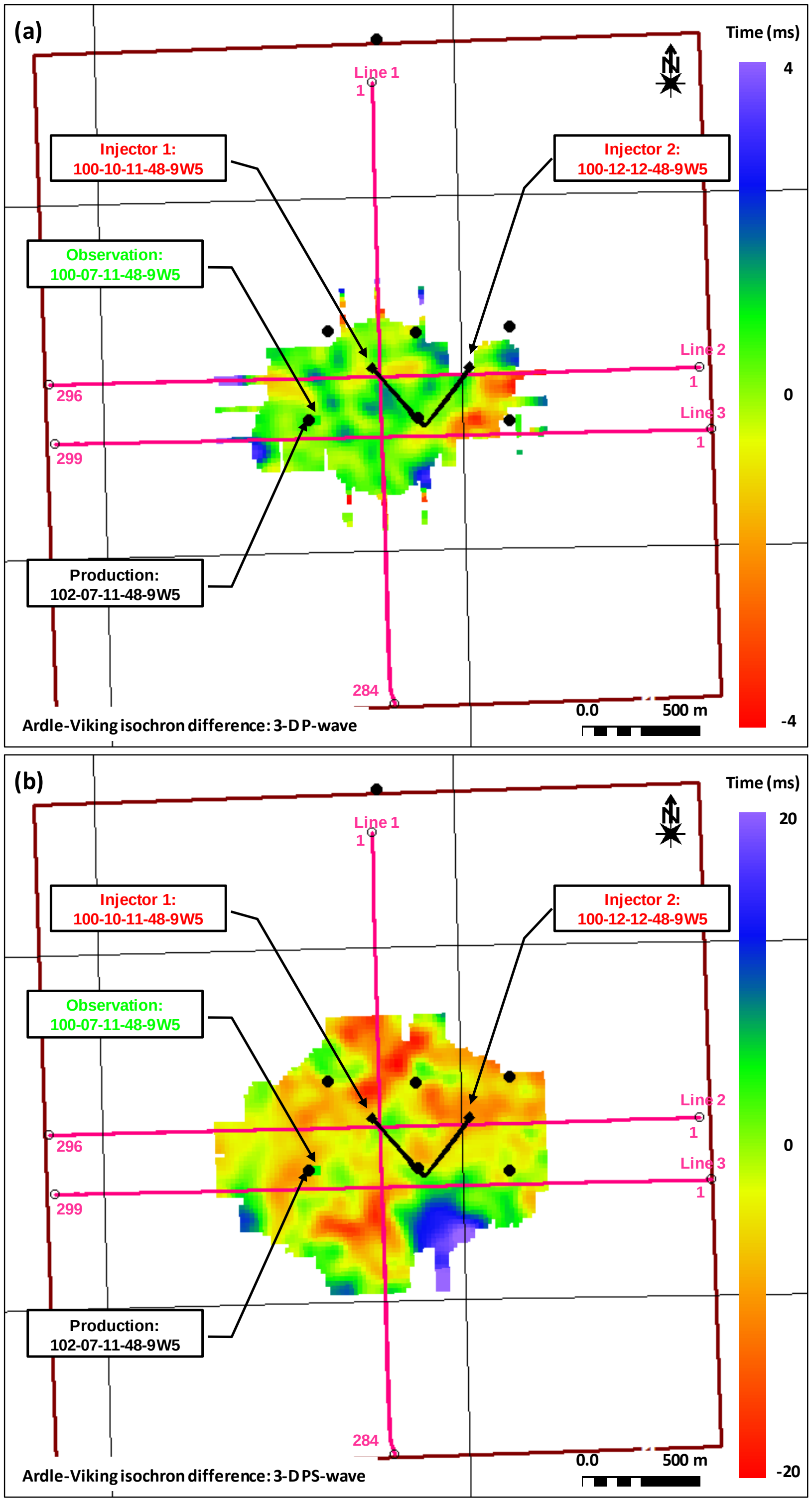

Figure 6-57: Difference in the Ardley-Viking isochron between the baseline (2005) and monitor (2007) from (a) 3-D P-wave, and (b) 3-D PS-wave surface seismic.

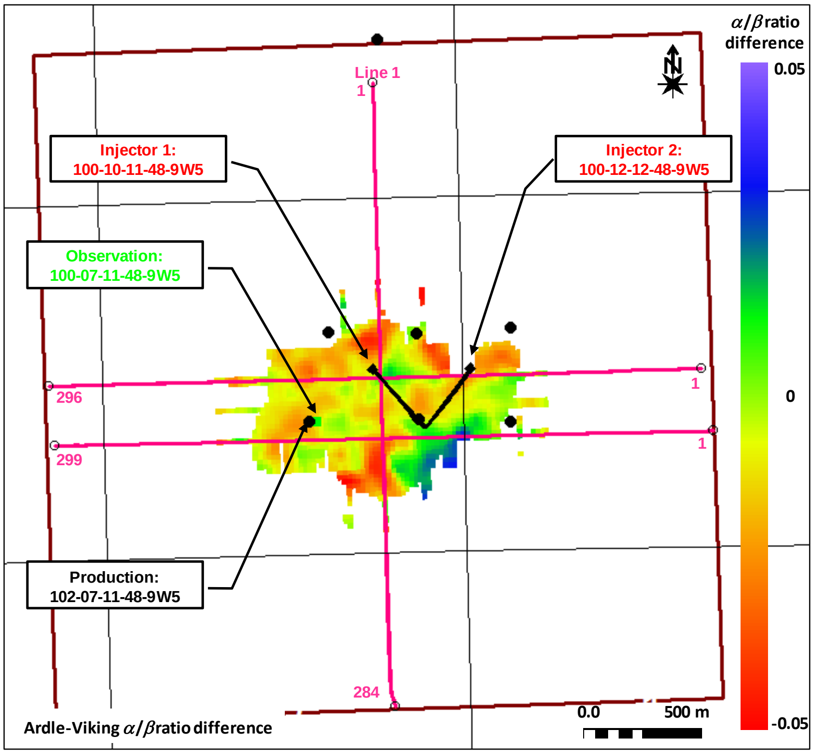

Figure 6-58: Difference in the Ardley-Viking interval α/β between the baseline (2005) and monitor (2007) computed using the 3-D multi-component surface seismic data.

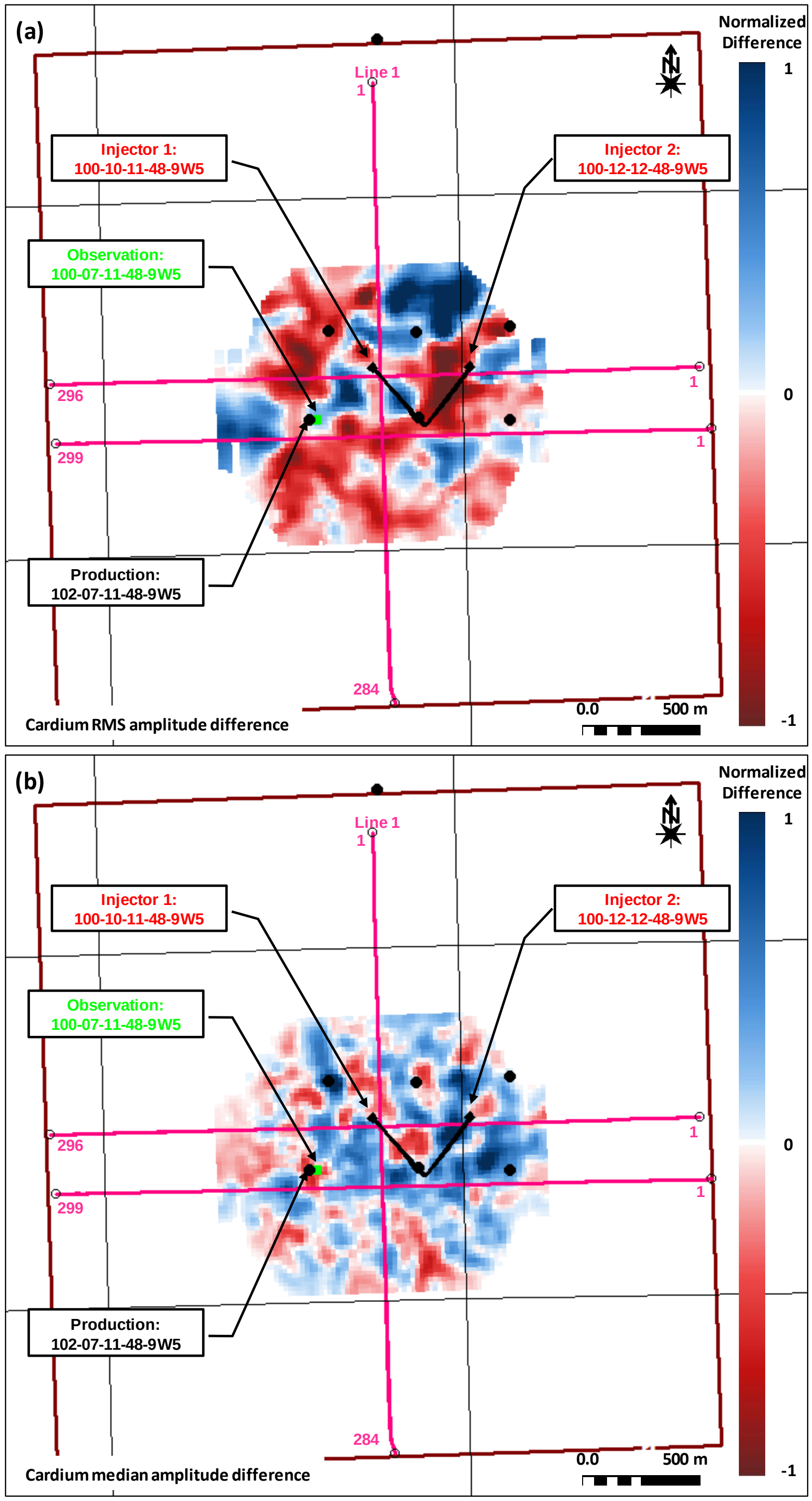

Figure 6-59: Difference in the Cardium (a) RMS amplitude, and (b) median amplitude between the baseline (2005) and monitor (2007) corresponding to the 3-D P-wave surface seismic data. The difference amplitude in (a) and (b) was normalized by the maximum of the baseline.

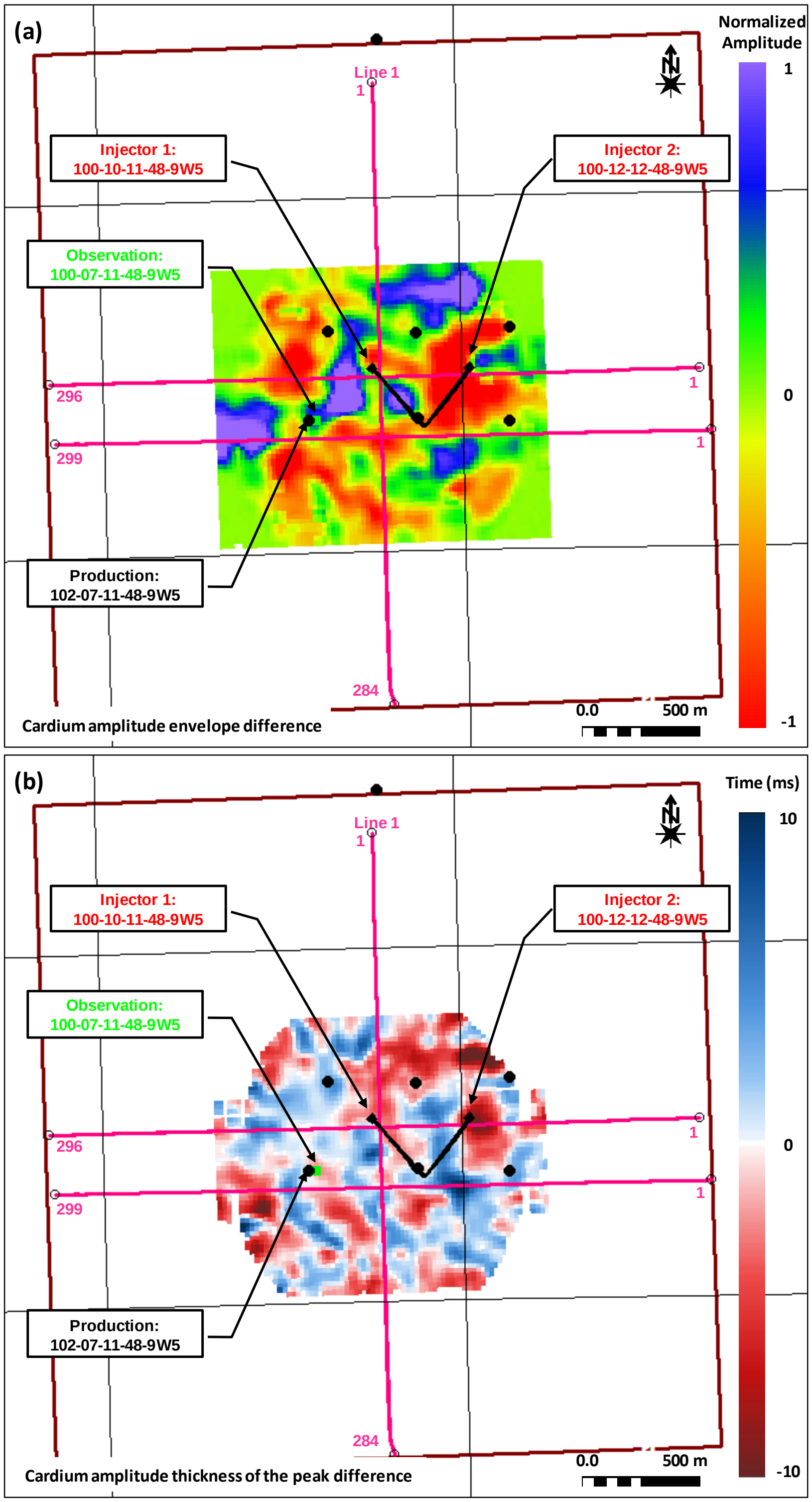

Figure 6-60: Difference in the Cardium (a) amplitude envelope, and (b) ATP between the baseline (2005) and monitor (2007) corresponding to the 3-D P-wave surface seismic data. The difference amplitude in (a) was normalized by the maximum of the baseline.

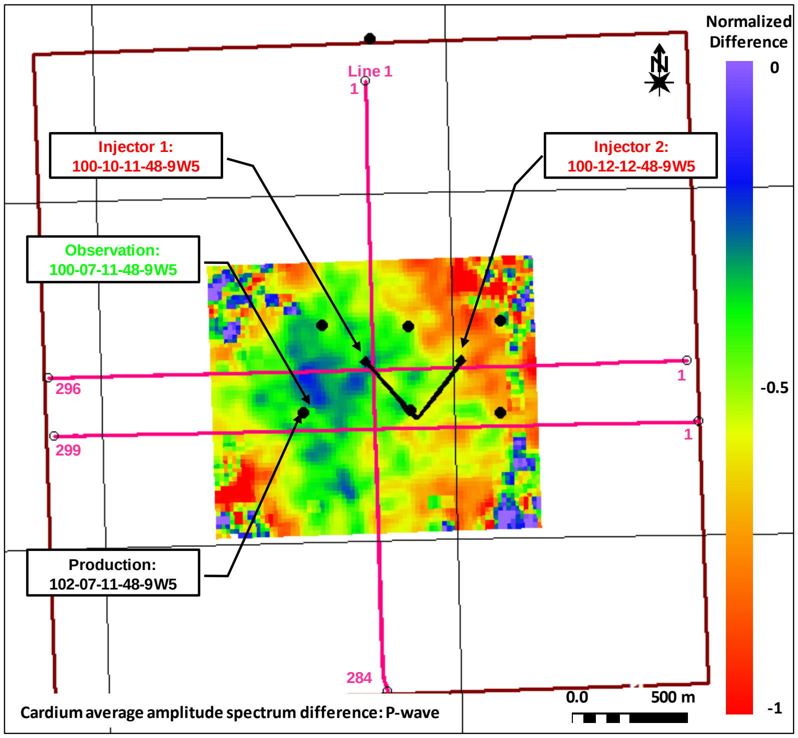

Figure 6-61: Difference in the average amplitude spectrum between the baseline (2005) and monitor (2007) surveys of the 3-D P-wave surface seismic data. The difference amplitude was normalized by the maximum of the baseline.

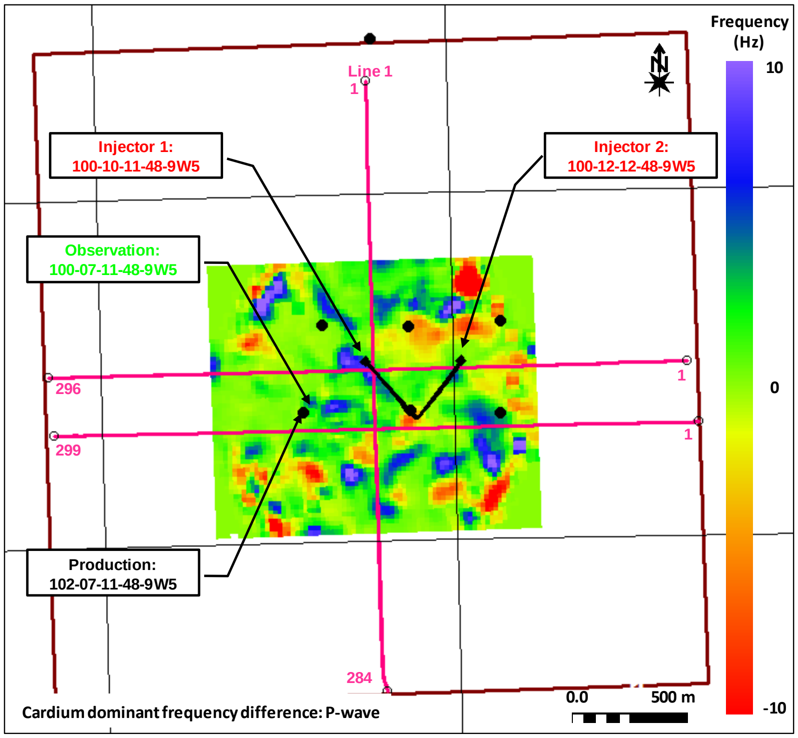

Figure 6-62: Difference in the dominant frequency between the baseline (2005) and monitor (2007) surveys of the 3-D P-wave surface seismic data.

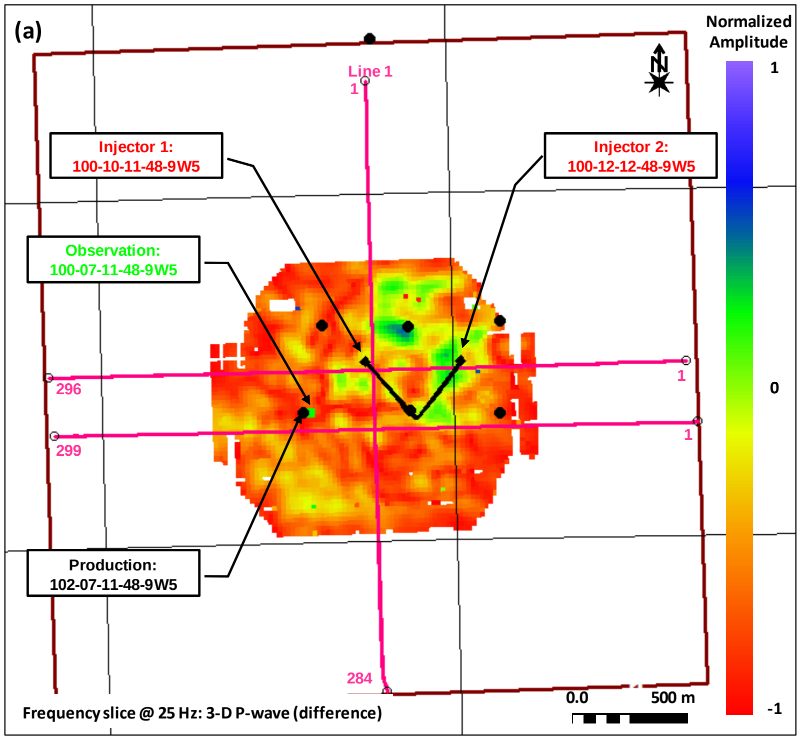

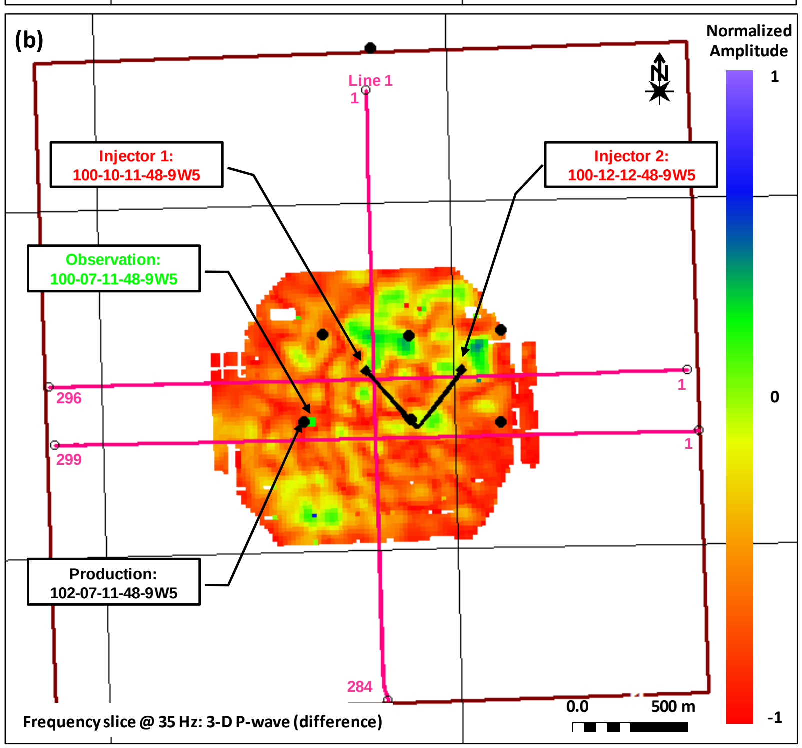

Figure 6-63: Spectral decomposition images of the difference between the baseline (2005) and monitor (2007) corresponding to the 3-D P-wave surface seismic data at (a) 25 Hz and (b) 35 Hz. The images were constructed by computing SD in the individual volumes over a 100 ms window centered at the Cardium event and then taking the difference. The difference amplitude was normalized by the maximum of the baseline.

The results from another category of seismic attributes are shown Figure 6-64 through Figure 6-66. Figure 6-64 displays the difference in the acoustic impedance (see footnote 16 under Section 6.5.4). The acoustic impedance (Figure 6-64 (a)) appears to have decreased around the western injector predominantly within the ZRD but no distinct pattern is observed. Proceeding with the Lambda-Mu-Rho (LMR) transformation[84], one can also obtain the difference in Lambda-Rho (LR) shown in Figure 6-65 as well as the difference in LR×MR (Figure 6-66). Unfortunately, none of the LMR difference maps show any prominent anomaly pertaining to the CO_2 injection. The inconclusiveness of the results derived from LMR is most likely due to the issues with PS-wave data.

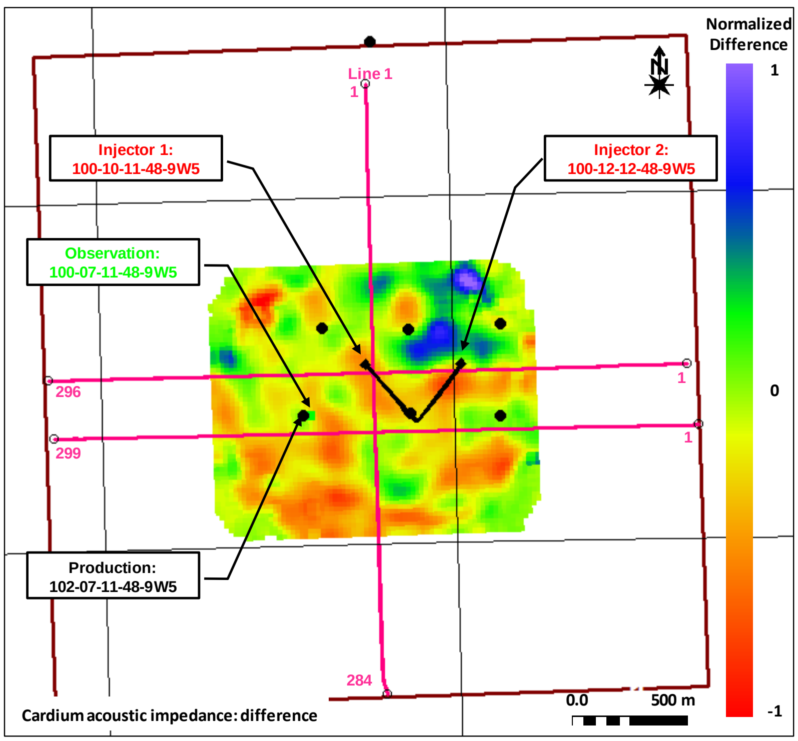

Figure 6-64: Impedance slice showing the difference in the acoustic impedance of the Cardium between the baseline (2005) and monitor (2007) surveys using MBI method. The difference amplitude was normalized by the maximum of the baseline.

[84] The main concept underlying Lambda-Mu-Rho (LMR) was briefly discussed in Section 3.6.2.

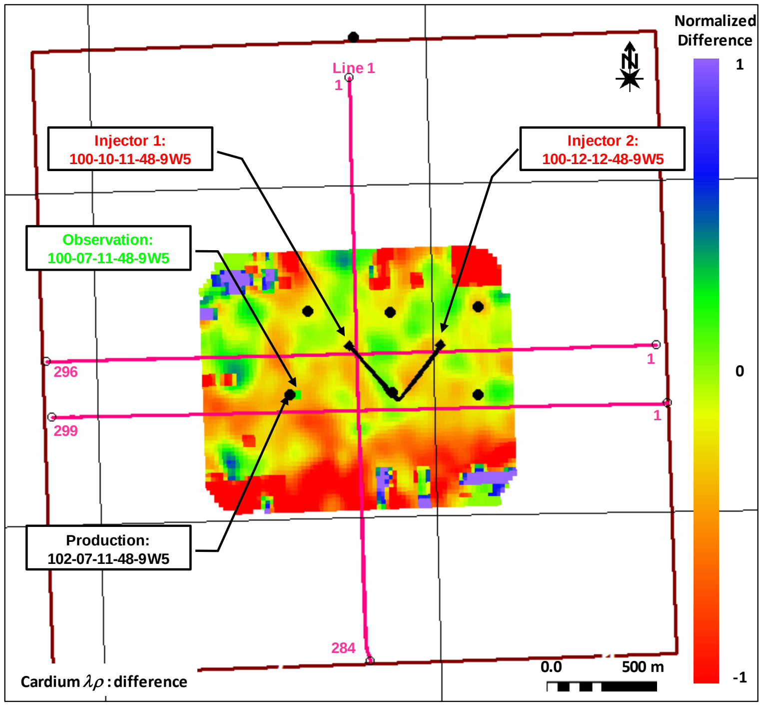

Figure 6-65: Slice showing the difference in the Cardium Lambda-Rho map of the Cardium between the baseline (2005) and monitor (2007) surveys using MBI method. The difference amplitude was normalized by the maximum of the baseline.

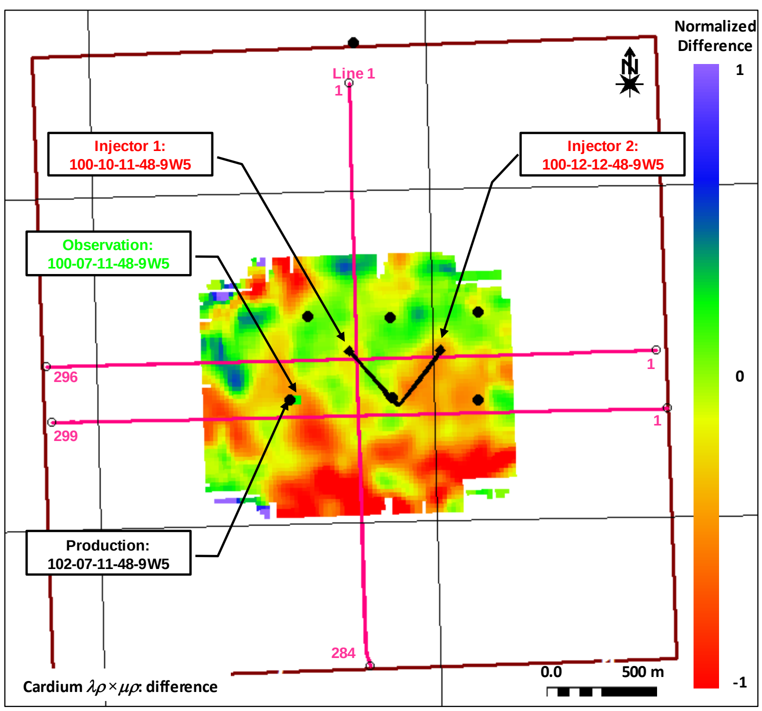

Figure 6-66: Slice showing the difference in the Cardium Lambda-Rho×Mu-Rho ($\lambda\rho\times\mu\rho$) between the baseline (2005) and monitor (2007) surveys using MBI method. The difference amplitudewas normalized by the maximum of the baseline.

6.6 Discussion

By examining the various seismic datasets and the attributes derived from them, it is clear that none offer a credible account of the CO_2 plume. The repeatability metrics indicate that data quality, in particular P-wave data, is very good but still provides no conclusive information about the location of the CO_2 plume. Furthermore, the time shift and amplitude-based attributes deduced from the calibrated VSP, 2-D and 3-D surface seismic also seem to give inconclusive results.

Given the sensitivity to various perpetrators, such as gaps in the shots line, it seems that repeatability metrics, i.e. NRMS and PRED, might not be robust indicators for detecting changes due to CO_2 injection in this case. Attributes based on time shift, i.e. isochron and α/β differences, are considered to be unreliable indicators in this study because of the reasons discussed under Section 6.5.1 and under the interpretation of the VSP and 2-D surface seismic data (Sections 6.5.3 and 6.5.4). These are essentially due to the very small magnitude of time shift and the limited quality of the PS-wave data. Amplitude-based attributes involving PS-wave data, namely shear impedance and LMR, are not considered to be reliable either due to the poor character and quality issues with the PS-wave data (Sections 6.5.2.4 and 6.5.5). This leaves the amplitude-based attributes extracted from the P-wave which, unfortunately, do not convey any compelling message in regard to the CO_2 plume and its distribution.

The lack of a discernible CO_2-induced anomaly in the repeatability as well as time and amplitude-based attributes within the reservoir could be attributed to the following reasons:

1. The low contrast in the physical properties between the in-situ fluid, i.e. hydrocarbon/water, and the injected supercritical CO_2, thus giving rise to a small time-lapse anomaly.
2. The reservoir architecture; the Cardium Formation is a thin, tight and low-impedance reservoir.
3. The indications that flow seems to be confined preferentially to the thin reservoir unit, i.e. upper sandstone unit within the reservoir.

Other less profound reasons include gaps in the shot line, processing noise, and possible interference by multiples originating from the shallow Ardley coals. A particular reason in the case of the VSP is the limited vertical aperture of the geophone array in the observation well. The analysis performed in this chapter corroborated by the modelling results that will be presented in next chapter indicates that the reasons outlined here rather than the incompetency of the implemented seismic attributes are the bases for the lack of a discernible CO_2-related time-lapse anomaly.

Although the analysis in this chapter has been primarily focused on the CO_2 plume delineation within the reservoir, the results from the 2-D and 3-D surface seismic data suggest that no upward migration of CO_2 was taking place between the time-lapse surveys. The sensitivity to CO_2 plume upward migration was investigated in Chapter 6 whereas (1), (2) and (3) will be investigated in Chapter 7. The next section will shed some light on these aspects as well but in the framework of independent data. Finally, it should be noted that the effects of pore pressure and anisotropy were not investigated in this dissertation due to the poor quality of the PS-wave data. Nonetheless, it is suggested that the effect of the pore pressure is not significant at the current level of CO_2 saturation.

6.7 Independent Data

As outlined in the previous section, the absence of a seismically-identifiable CO_2 anomaly within the reservoir in the data is, essentially, attributed to the architecture of the reservoir. As described under Section 2.3, the Cardium reservoir consists of a major flow unit which is the upper sandstone in addition to two secondary flow units. These are the overlying conglomerate and underlying middle sandstone units. The thickness of the individual flow units could be as low as 0 m and could reach a maximum of 4 m. Figure 6-67 show the net pay thickness[85] of the individual units in addition to the lower sandstone unit. Insights into the rather nontrivial[86] flow within these units could be inferred by looking the porosity (ϕ-h) and permeability-thickness (k-h) maps in Figure

[85] The net pay thickness is defined as the thickness of reservoir-quality interval or lithology of a reservoir, typically determined from well logs (Sheriff, 2002).
[86] In the sense that the flow is not exactly in the NE along the regional up-dip direction or reflect the net pay thickness.

6-68. Combined all together, it seems that the variability in the net pay thickness, ϕ-h and k-h as well as the limited bandwidth[87] of the seismic data result in an extremely difficult environment to monitor supercritical CO_2 using seismic methods in general.

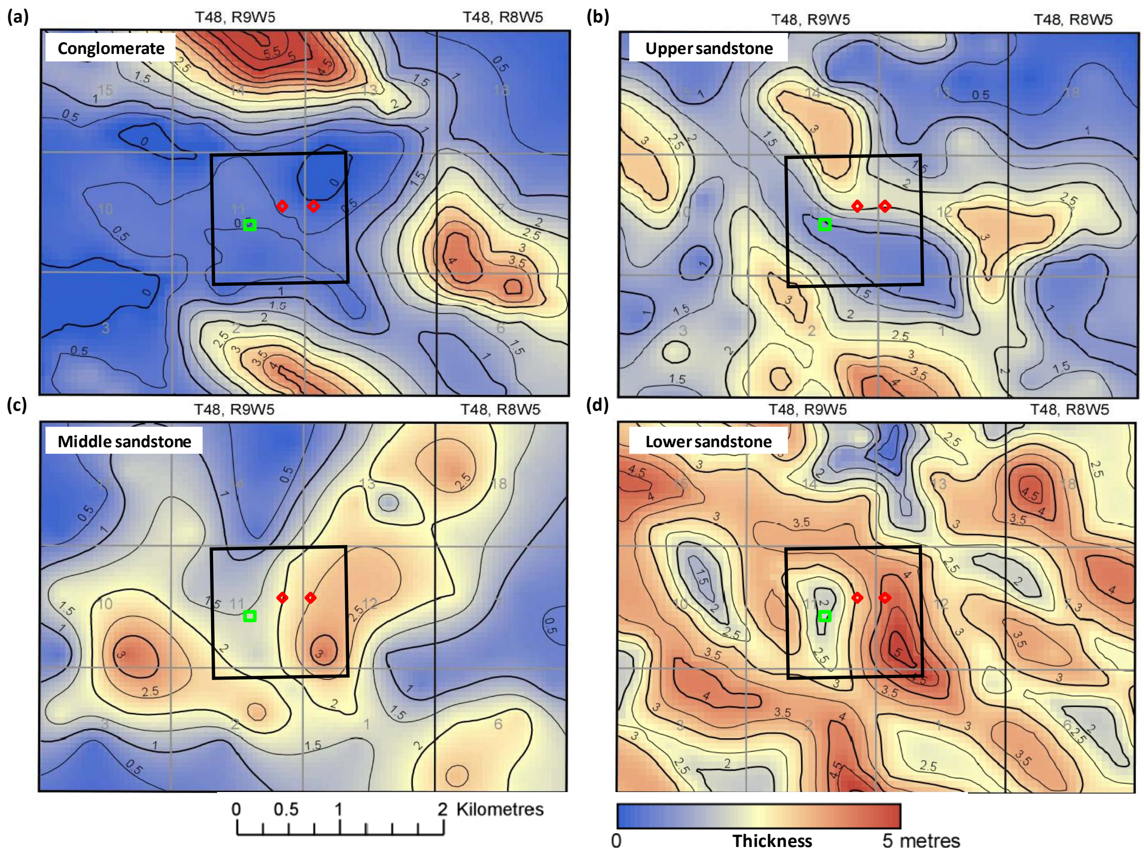

Figure 6-67: Net pay thickness maps of the Cardium (a) conglomerate, (b) upper sandstone, (c) upper shale, and (d) middle sandstone units. The approximate seismic coverage (black rectangle), the injection (red diamond), and observation wells (green square) are shown by the respective shapes. After Dashtgard et al. (2006).

[87] Further reduced by the shallow Ardley coalbeds.

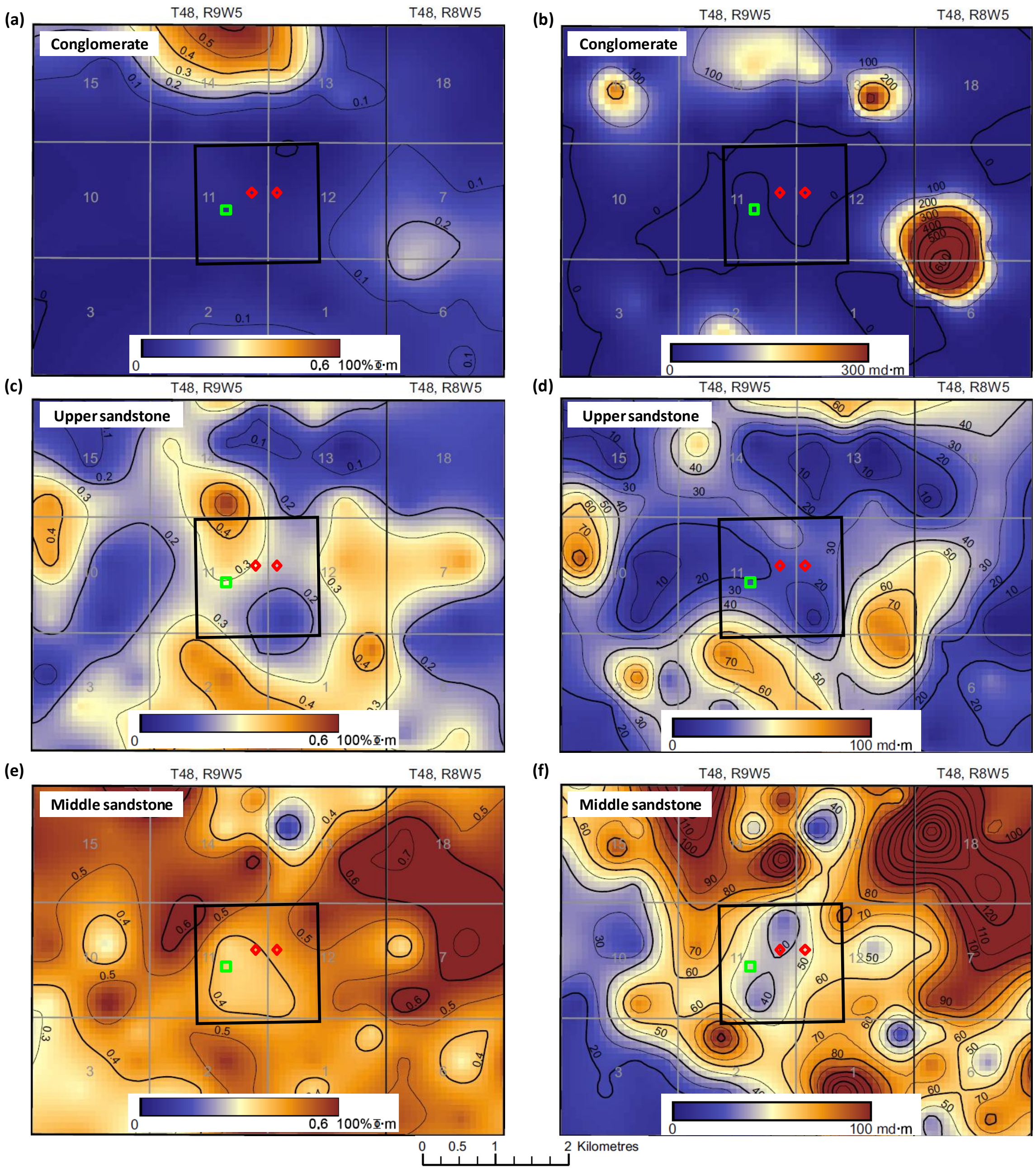

Figure 6-68: Geological maps showing (a) porosity and (b) permeability thickness of the Cardium conglomerate unit; (c) porosity and (d) permeability thickness of the Cardium upper sandstone unit; (e) porosity and (f) permeability thickness of the Cardium middle sandstone unit. The contour interval (CI) of the porosity thickness maps is 0.1 ϕ.m, where 1 m of thickness equals to 1 m thickness of 100% porosity. The CI of the permeability thickness is 10 mD.m, with the exception of the conglomerate (b) which has a CI of 100 mD.m. The approximate seismic coverage (black rectangle), the injection (red diamond), and observation wells (green square) are shown by the respective shapes. After Dashtgard et al. (2006).

Reservoir data, primarily, in the form of fluid composition through geochemical monitoring (Shevalier et al., 2007; Lim and Gunter, 2008; Nightingale et al, 2008; Johnson, 2010) indicate the CO_2 is confined to three porous and permeable zones in the Cardium Formation. These are: the conglomerate, the upper sandstone and middle sandstone with the highest saturation occurring in the main reservoir unit, i.e. upper sandstone (Figure 6-69). In the previous section it was stated the seismic data suggests that there is no upward migration of the CO_2 plume. The seismically-driven statement is corroborated by environmental monitoring, namely air emissions, subsurface gas and groundwater monitoring which show no indication of leakage of the injected CO_2 into the atmosphere, soil or shallow groundwater system (van Everdingen et al., 2008).

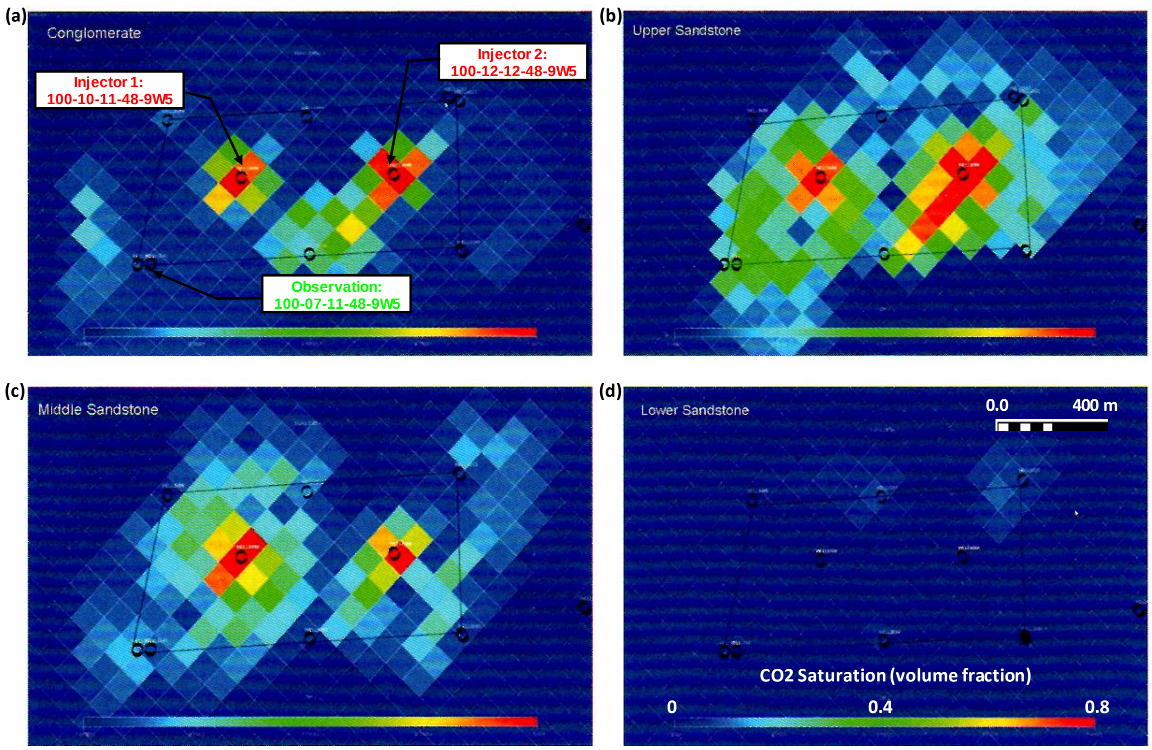

Figure 6-69: Distribution of CO_2 in the Cardium (a) conglomerate, (b) upper sandstone, (c) middle sandstone, and (d) lower sandstone during Phase III (March 2007) of the PCEP project obtained. The pixels depict the CO_2 saturation (color scale) derived using production rates and produced fluid composition (Lim and Gunter, 2008). The location of the injection wells, observation well and the producers are shown by the black circles.

6.8 Summary

- The VSP and surface seismic data quality and repeatability were very good, with exception of the converted-wave data which was considered to be less reliable.
- The time-lapse analysis invoked a suite of statistical as well as time and amplitude-based seismic attributes.
- None of the seismic data and the attributes derived provided a distinct, consistent, corroborative, or conclusive account of the injected CO_2 even though the modelling results (next chapter) predict a discernible NRMS magnitude change of ~ 40%. The magnitude of time shift (~ 0.1 ms) is considered to be below the lower threshold of seismic detection under the current conditions.
- The results suggest that the seismic component of the MMV program at the PCEP site was not successful in delineating the CO_2 plume in the Cardium Formation after the injection of ~ 50 Kt between Phase I (2005) and Phase III (2007).
- There most likely reason for the inconclusiveness of the results derived from the time-lapse seismic data is the confinement of supercritical CO_2 to the thin upper sandstone unit within the Cardium reservoir.
- Interference caused by the small amount of non-repeatable noise, whether induced by gaps in the shot line, processing noise, or multiples made it unfeasible to extract any useful time-lapse signal.
- Due to the lack of a discernible CO_2-related time-lapse anomaly in the reservoir, the seismic data could not be correlated with and independent data, which suggest that the CO_2 plume is predominantly moving up-dip in a NE-SW trend.
- Importantly, the lack of a 4-D seismic change above the reservoir indicates that the injected CO_2 is not migrating upward through the caprock into shallower formations as the seismic response would be more sensitive to such migration.
- The “no-leakage’ notion was confirmed by the independent environmental monitoring data, which shows no indication of CO_2 presence at the surface or in the shallow groundwater system in the study area.

CHAPTER 7: PCEP TIME-LAPSE SEISMIC ANALYSIS II - NUMERICAL MODELLING

7.1 Introduction

In Chapter 6, the time-lapse seismic analysis of multi-component surface seismic and the P-wave vertical seismic profile (VSP) data revealed no conclusive information about the injected CO_2. In this chapter, fluid substitution modelling (FSM) and forward numerical seismic modelling were undertaken to investigate the lack of an unambiguous 4-D response in the seismic data. The investigation estimated the magnitude of change in the elastic properties due to CO_2-fluid replacement given the in-situ conditions in the Pembina-Cardium CO_2-EOR Pilot Project (PCEP) study area. Then, the numerical forward seismic response was synthesized based on the FSM results to assess the the actual seismic response observed as part of the implemented seismic MMV program.

Important to note is that seismic response sensitivity toward upward migration of CO_2 into, for instance, shallow aquifers was not investigated in this chapter since it has already been considered under the WASP modelling chapter (Section 5.3.3.2). Furthermore, given the fact that the PCEP and WASP study areas coexist within the same sedimentary basin and in close proximity to each other and share to great extent the shallow stratigraphy, it was deemed redundant to repeat the same investigation.

7.2 Time-lapse Seismic Response: Numerical Modelling Investigation

7.2.1 Approach

The approach implemented in investigating the time-lapse seismic response in the PCEP study area is depicted in Figure 4-2, which is fairly similar to that shown in Figure 5-9. Note, however, the incorporation of ray trace VSP modelling since VSP was one of the seismic methods comprising the implemented seismic monitoring program. Nonetheless, there is a considerable level of similarity between the approach presented here and that discussed under the WASP modelling chapter (Section 5.3). Therefore, only individual steps and the PCEP-specific results are discussed in relevant detail throughout this chapter. Furthermore, the results and conclusions of the WASP modelling were be invoked when appropriate and the reader is referred to Chapter 5 accordingly.

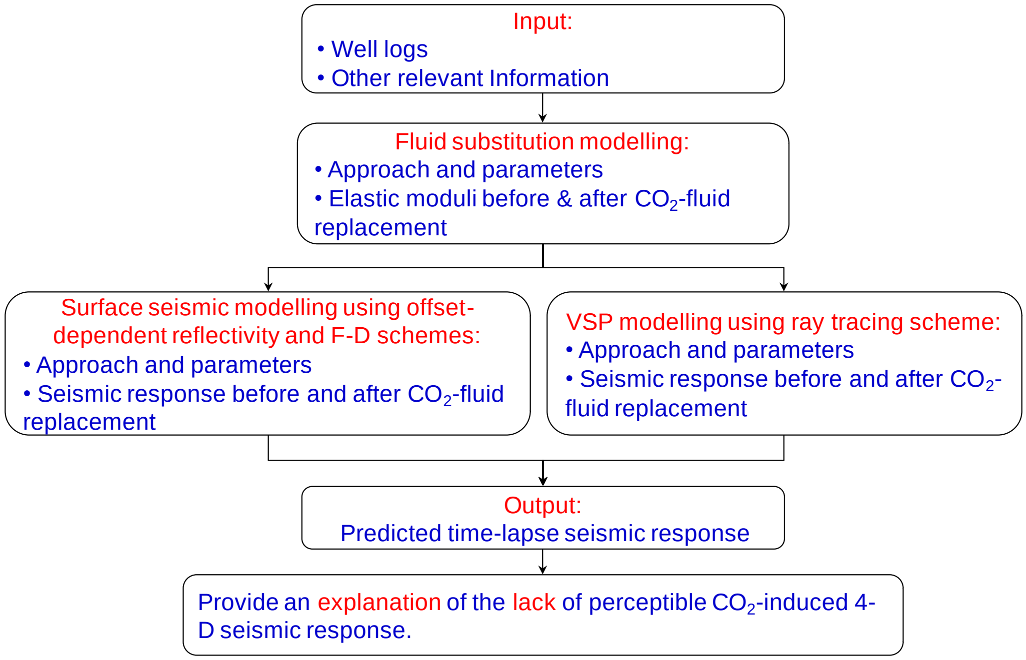

Figure 7-1: Flowchart outlining the key steps followed in investigating the time-lapse seismic response at the PCEP study area as part of the monitoring, measurements and verification (MMV) program.

7.2.2 Rock Physics and Fluid Substitution Modelling (FSM)

7.2.2.1 Approach, Data and Parameters

Recall that the objective behind the rock physics and FSM was to predict if the CO_2 replacement of in-situ fluid would produce a sufficient contrast in the physical properties of the Cardium reservoir that could be detected and delineated by time-lapse seismology. Detailed discussion of the FSM approach implemented in this dissertation including a brief review of the Gassmann formulation along with the methods of parameters estimation was given under Section 5.3.2.

The FSM in the PCEP framework was undertaken using two wells: 100-07-11-48-9W5[88] and 102-08-14-48-9W5 (Figure 5-11). Figure 7-3 illustrates the response of the various log curves from the observation well (100-07-11-48-9W5). The main FSM parameters as well as the various cases investigated and other relevant information are summarized in Table 7-1. The values of the in-situ P-wave speed ($\alpha^{\text{initial}}_{\text{saturated}}$), S-wave

---

[88] Refer to the discussion under Section 6.2 where the well data and the naming scheme were described.

speed ($\beta^{\text{initial}}_{\text{saturated}}$), bulk density ($\rho^{\text{initial}}_{\text{saturated}}$), and porosity ($\phi$) were estimated using well logs for each well accordingly. Fortunately, one of the wells (100-07-11-48-9W5) has dipole sonic log. Therefore, a local linear empirical relation (mudrock line) was constructed to estimate the S-wave (β) speed from the P-wave speed (α) for the other well (102-08-14-48-9W5):

$$\beta = 0.5097(\alpha) - 270.89;\ \text{in km/s} \tag{7.1}$$

In addition, two other means of S-wave speed estimation, namely constant α/β ratio (1.9) and Castagna et al. (1993), were attempted and compared with the one derived locally (Figure 7-4). Interestingly, a constant α/β ratio of 1.9 yielded better results than Castagna et al. (1993). So, one possible recommendation is to use this constant scalar for estimating the S-wave speed for clastic reservoir with small shale content in the Pembina Oil Field area if a dipole sonic is not available.

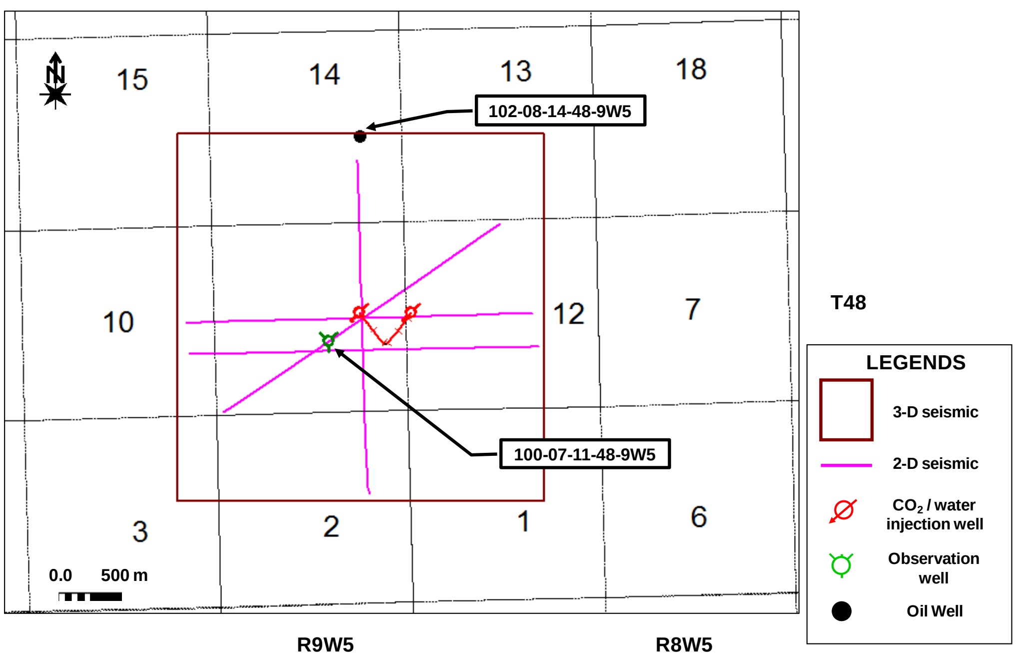

Figure 7-2: Base map showing the location of the wells used in the FSM. See the base map (Figure 6-1) in Chapter 6 for legned and relative position with respect to large-scale study area.

The temperature and pressure were estimated using sensors installed in the observation well. Some of the physical properties, namely the reservoir mineralogy, fluid composition, oil gravity, GOR and water salinity were estimated from rock and fluid samples (Shevalier et al., 2007; Nightingale et al., 2008). Once the type of minerals was established, the bulk modulus (K_{mineral}) and density (ρ_{mineral}) of the individual constituents were obtained from published data (Mavko et al., 2003). Similarly, the density and incompressibility of the individual fluids were estimated, once they were delineated, using CREWES Fluid Property Calculator (Ursenbach, 2009; see Section 5.3.2.2). In the PCEP FSM context, the density and bulk modulus of the various gases were determined using Peng-Robinson EOS (Appendix B.2) whereas the seismic properties of the water and oil were estimated using the empirical relations given by Batzle and Wang (1992). The latter are summarized in Appendix B.1.

One departure from the Nisku Formation FSM is that the Cardium aquifer is an oil-bearing reservoir. So, once K_ϕ is estimated (Section 5.3.2.2), the system was then saturated with fluid(s) representative of those present in the reservoir, in this case 50% brine and 50% oil, before the fluid replacement process. Then, the saturation of the replacement fluid, i.e. CO_2, is gradually increased until the reservoir becomes fully saturated with the new fluids.

Figure 7-5 demonstrate the effective elastic moduli of the multi-phase mineral constituents as well as the corresponding effective bulk density as function porosity (Table 7-1). Note that the effective elastic moduli of the minerals mixture were computed using Hashin-Shtrikman (HS) bounds and averages which were discussed under Section 5.3.2.3. The effective bulk modulus of the multi-phase fluid mixture was computed using the various methods introduced in Section 5.3.2.4 and the results are presented in Figure 7-6 (a). Note that the density was computed using a simple mass balance relation as was discussed under Section 5.3.2.5. Recall that the HS bounds and averages are exactly equal to the Reuss average and, therefore, they are all observed on the same trajectory. Also, note the great degree of similarity between Voigt (1928) and Hill (1963) averages. The corresponding effective density calculated as dictated by mass balance and is displayed as a function of 5 discrete porosity values in Figure 7-6 (b).

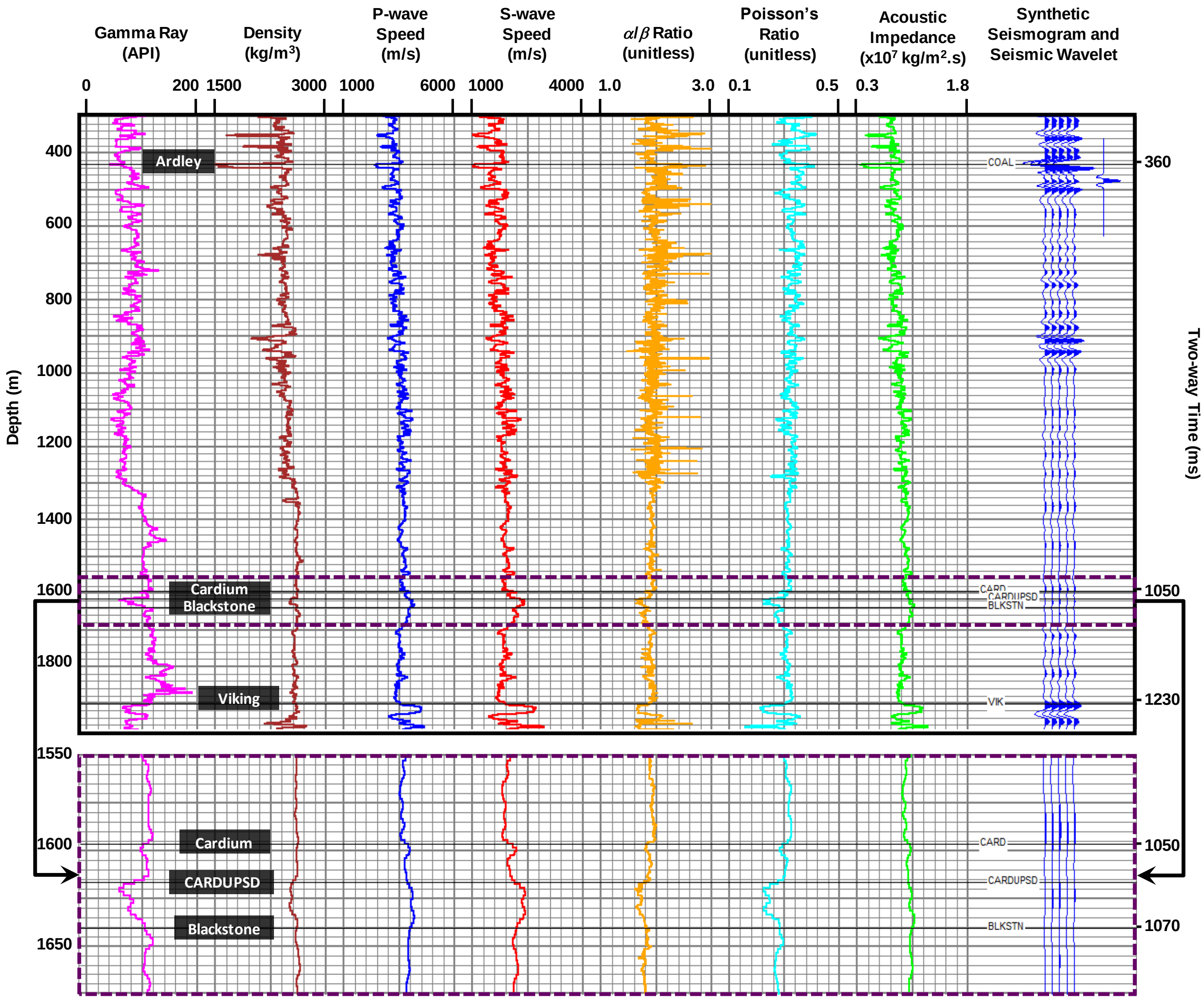

Figure 7-3: Display of the various log types from the observation well (100-07-11-48-9W5). The P-wave synthetic seismograms shown in blue (right-most panel) was constructed using the convolutional model (Section 3.5.5) invoking the 30 Hz Ricker wavelet shown in Figure 5-2 (a) and (b). The zone enclosing the Cardium Formation is enlarged as indicated by the dashed violet rectangle. The three major events frequently referred to in Chapter 6 are identified. The location of the well is shown in the base map (Figure 6-1). See Figure 6-4 for a broader perspective and seismic-to well tie using both P-wave and PS-wave data. See, also, the stratigraphic model in Figure 2-16. CARDUPSD: Cardium upper sandstone unit.

Table 7-1: Information pertaining to physical and chemical properties that were invoked in the Cardium Formation FRM. The data was compiled using the following references (see text for data-reference association): Mavko et al. (2003), Dashtgard et al. (2006), Shevalier et al. (2007), Nightingale et al., (2007), Ursenbach (2009), and Engineering ToolBox (2011). [1] See Figure 6-1.[2] of well (a).[3, 5] Including all three reservoir units (third row; see text as well).[4] Depth to the top of the upper sandstone unit (Section 2.3).

Wells[1]	(a) 100-07-11-48-9W5 (b) 102-08-14-48-9W5
Target Formation /Reservoir	Cardium Formation
Reservoir Units and Their Thickness[2]	Main: upper sandstone (3 m) Secondary: conglomerate (2) and middle sandstone (4 m)
Primary Lithology	Sandstone
Reservoir Bearing Fluid	Oil
Other Reservoir Fluid	Water (brackish) and gas
Reservoir Depth[3] (d)	(a) 1616 m (b) 1605 m
Reservoir Thickness[4] (h)	(a) 9 m (formation thickness = 43 m) (b) 10 m (formation thickness = 26 m)
Reservoir Pressure (P)	18.5 MPa
Reservoir Temperature (T)	50 C^{o}
CO_2 Phase at the Reservoir	Supercritical
Average Porosity[4] (ϕ)	(a) 9.0% (b) 8.5%
Primary Reservoir Mineral	Quartz (85%)
Secondary Reservoir Mineral	Clay (10%)
Tertiary Reservoir Mineral	Muscovite (5%)
Primary Reservoir Gas	Methane (50%); volume insignificant
Secondary Reservoir Gas	Nitrogen (50%); volume insignificant
Gas-Oil Ratio (GOR)	4
Oil Gravity	40 API
Specific Gravity of Oil	0.81
Specific Gravity of Primary Gas	0.56
Specific Gravity of Secondary Gas	0.97
Specific Gravity of CO_2	1.52
Average Water Salinity (l)	7.5 g/l
Density of Primary Mineral (ρ_{quartz})	2650 kg/m^3
Bulk Modulus of Primary Mineral (K_{quartz})	40 GPa

Continued next page

Shear Modulus of Primary Mineral (μ_{quartz})	44 GPa
Density of Secondary Mineral (ρ_{clay})	2580 kg/m^3
Bulk Modulus of Secondary Mineral (K_{clay})	25 GPa
Shear Modulus of Secondary Mineral (μ_{clay})	10 GPa
Density of Tertiary Mineral ($\rho_{muscovite}$)	2790 kg/m^3
Bulk Modulus of Tertiary Mineral ($K_{muscovite}$)	60 GPa
Shear Modulus of Tertiary Mineral ($\mu_{muscovite}$)	40 GPa
Density of Water (ρ_{water})	1001 kg/m^3
Bulk Modulus of Water (K_{water})	2.50 GPa
Density of Oil (ρ_{oil})	812 kg/m^3
Bulk Modulus of Oil (K_{oil})	1.44 GPa
Density of Primary Gas (ρ_{CH4})	129 kg/m^3
Bulk Modulus of Primary Gas (K_{CH4})	0.0332 GPa
Density of Secondary Gas (ρ_{N2})	186 kg/m^3
Bulk Modulus of Secondary Gas (K_{N2})	0.0323 GPa
Density of CO_2 (ρ_{CO2})	737 kg/m^3
Bulk Modulus of CO_2 (K_{CO2})	0.117 GPa
Initial Water Saturation (S_{water})	Case Iu and Case Ip: 50% Case IIu and Case IIp: 50% Case III: 50%
Initial Oil Saturation (S_{oil})	Case Iu and Case Ip: 50% Case IIu and Case IIp: 50% Case III: 45%
Initial Gas Saturation (S_{CH4}, S_{N2})	Case Iu and Case Ip: 0% CH_4, 0% H_2S Case IIu and Case IIp: 0% CH_4, 0% H_2S Case III: 2.5% CH_4, 2.5% H_2S
Initial CO_2 Saturation (S_{CO2})	Case Iu and Case Ip: 0% Case IIu and Case IIp: 0% Case III: 0%
Final Water Saturation (S_{water})	Case Iu and Case Ip: 0% Case IIu and Case IIp: 0% Case III: 0%
Final Gas Saturation (S_{CH4}, S_{N2})	Case Iu and Case Ip: 0% CH_4, 0% H_2S Case IIu and Case IIp: 0% CH_4, 0% H_2S Case III: 0% CH_4, 0% H_2S
Final CO_2 Saturation (S_{CO2})	Case Iu and Case Ip: 100% Case IIu and Case IIp: 100% Case III: 100%
Comments	• Case I: FSM on upper sandstone unit only • Case II: FSM on effective reservoir units • Case III: FSM same as II + in-situ gases • u: uniform saturation • p: patchy-like saturation

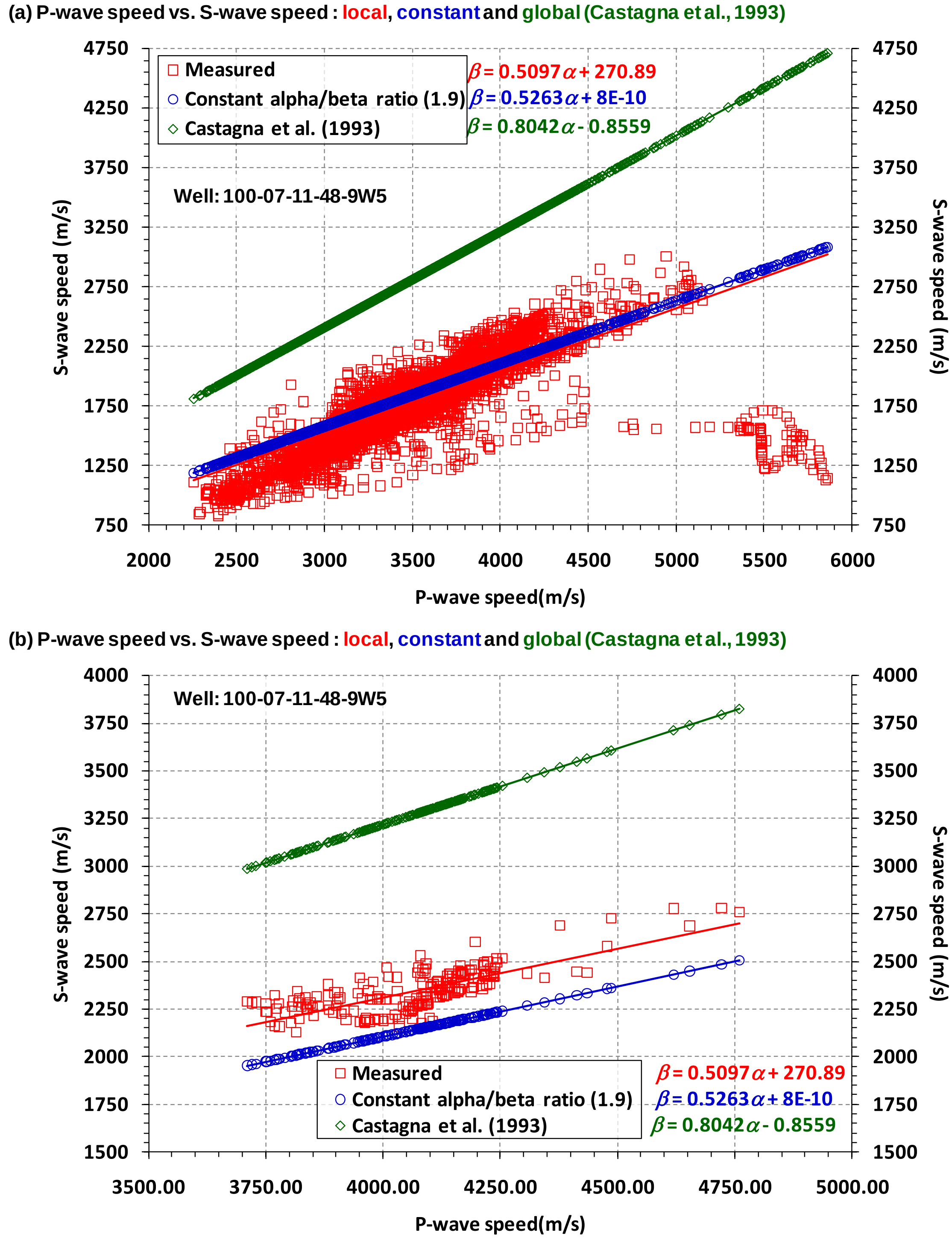

Figure 7-4: α-β cross-plot (a) over the entrie logged interval, and (b) over the zone of interest, i.e. Cardium Formation. The results from three different approaches are compared. Red: the one derived locally; blue: the one derived using constant α/β of 1.9; dark green: the global mudrock line given by Castagna et al. (1993). The best-fit linear regression relations are displayed in correspodnig colors.

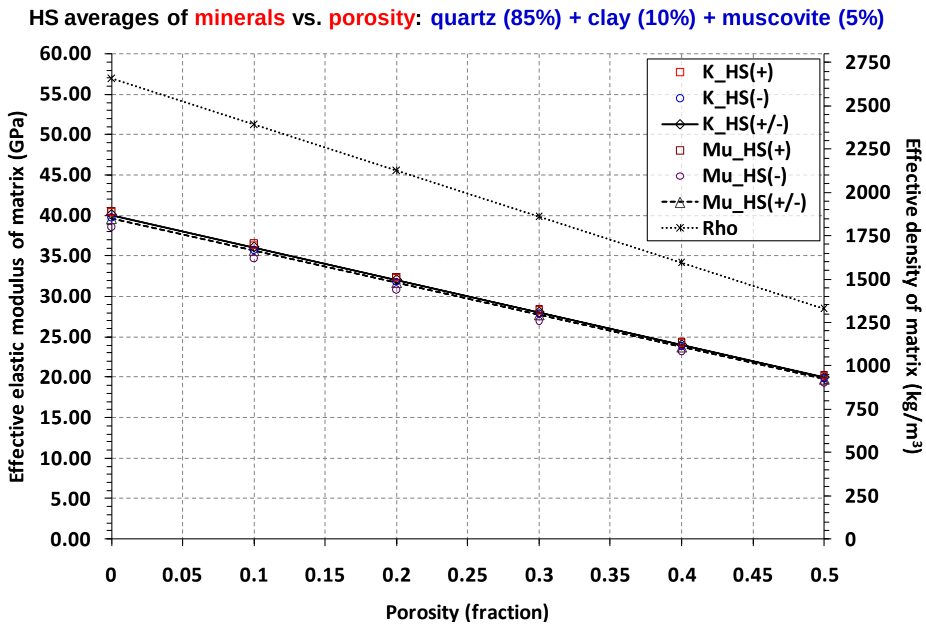

Figure 7-5: Hashin-Shtrikman (HS) averages of effective moduli as well as the corresponding effective density of the mineral mixture as a function of porosity (Phi). The respective volume fractions were estimated from core analysis and well logs (see Table 7-1). K: bulk modulus (GPa), Mu: shear modulus (GPa), Rho: density (kg/m^3).

In undertaking the FSM, two main cases were investigated: Case I and Case II. In the former, the FSM was restricted to the main reservoir unit, i.e. upper sandstone unit, whereas three reservoir units were integrated as an effective medium in the latter. Beside the upper sandstone, these are the overlying conglomerate and the underlying middle sandstone units (see Section 2.3). Furthermore, two different saturation schemes were considered in each case: uniform (u) and patchy-like (p). Case II emerges from the geological characterization (Dashtgard et al., 2006) as well as the reservoir data (Lim and Gunter, 2008) which suggest that the interstitial shale separating the upper and lower sandstone units might not always be an effective permeability barrier. Similarly, the unconformity separating the upper sandstone unit from the overlying Cardium conglomerate might not always constitute an impermeable layer. Therefore, it was deemed appropriate to investigate this case as well. In addition to Cases I and II, a third case was considered that examined the effect of the presence of in-situ or native gases on the FSM (Case III). The results from Case III are strikingly similar to those presented under the WASP FSM (Section 5.3.2.7) and, therefore, are not presented here.

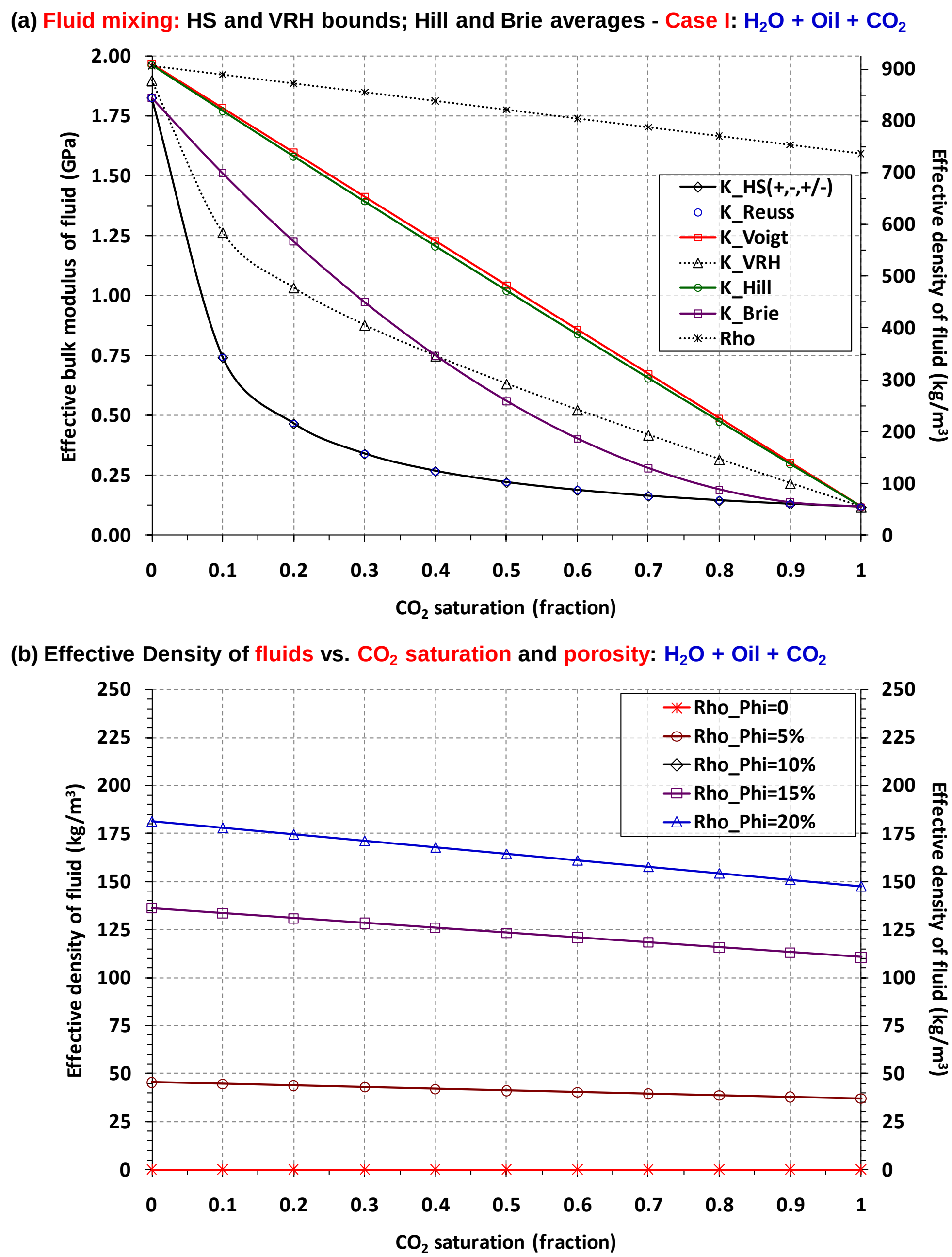

Figure 7-6: (a) Effective bulk modulus (K) of the multi-phase fluid mixture (Case I in Table 7-1) as a function of CO_2 saturation using Hashin-Shtrikman bounds (+,-) and averages (+/-), Voigt bound, Reuss bound, Voigt-Reuss-Hill average, Hill average and Brie et al. mixing equation (e = 3); (b) effective density (Rho) of this multi-phase fluid mixture as a function of CO_2 saturation and porosity. The initial and final saturations were 50% H_2O, 50% oil, 0% CO_2 and 0% H_2O, 0% oil, 100% CO_2, respectively.

7.2.2.2 Gassmann FSM Results

Table 7-2 outlines the results of the main FSM realizations in the PCEP framework using the parameters summarized in Section 7.2.2.1. Figure 7-7 and Figure 7-8 show the results of the FSM on the observation well assuming uniform CO_2 saturation in the upper sandstone unit (Case Iu) and the effective reservoir units (Case IIu), respectively. The FSM results from the patchy-like saturation (Case IIp) based on Brie et al. (1995) formula with e = 3 is displayed in Figure 7-9. For quality control purposes, the FSM was undertaken for well (b) as well assuming Case IIu and the results are illusrated in Figure 7-10. All the general observations discussed under the WASP FSM results in Section 5.3.2.7 are still being observed here with one minor variance. Note that in all the uniform saturation realizations in Section 5.3.2.7, there is a subtle inflection point at around 50% CO_2 saturation, where the absolute magnitude of relative change in the P-wave speed reaches its maximum before starting to decrease again. In the PCEP FSM uniform saturation cases, however, the absolute magnitude of relative change in the P-wave speed is monotonic in the sense that it continually increases from the onset of CO_2 saturation until the reservoir is fully saturated with CO_2. The reason for the observed phenomenon is the coupled effect of changes in the bulk modulus and density as discussed under Section 5.3.2.7.

Table 7-2: Outline of four realizations of the Gassmann FSM using observation well (100-07-11-48-9W5). See Table 7-1 for the modelling parameters and Figure 5-11 for the well location.

Realization	Description	Comment
Case Iu: uniform saturation in the upper sandstone unit	Data as presented in Table 7-1. The effective moduli of mineral and fluid mixture were, independently, calculated using HS± average.	Modest time-lapse change. See Figure 7-7.
Case IIu: uniform saturation in the effective reservoir unit	Data as presented in Table 7-1. The effective moduli of mineral and fluid mixture were, independently, calculated using HS± average.	Modest time-lapse change (~ 1% lower than in Case Iu). See Figure 7-8.
Case IIp: Patchy-like saturation in the effective reservoir unit	Data as presented in Table 7-1. The effective moduli of mineral were calculated using HS± average whereas the Brie average (e = 3) was invoked in deducing the effective modulus of fluid mixture.	Same as above but change is gradual. See Figure 7-9.
Case III: uniform saturation & in-situ gas	Data as presented in Table 7-1. The effective moduli of mineral and fluid mixture were, independently, calculated using HS± average.	Indiscernible time-lapse change. Not shown.

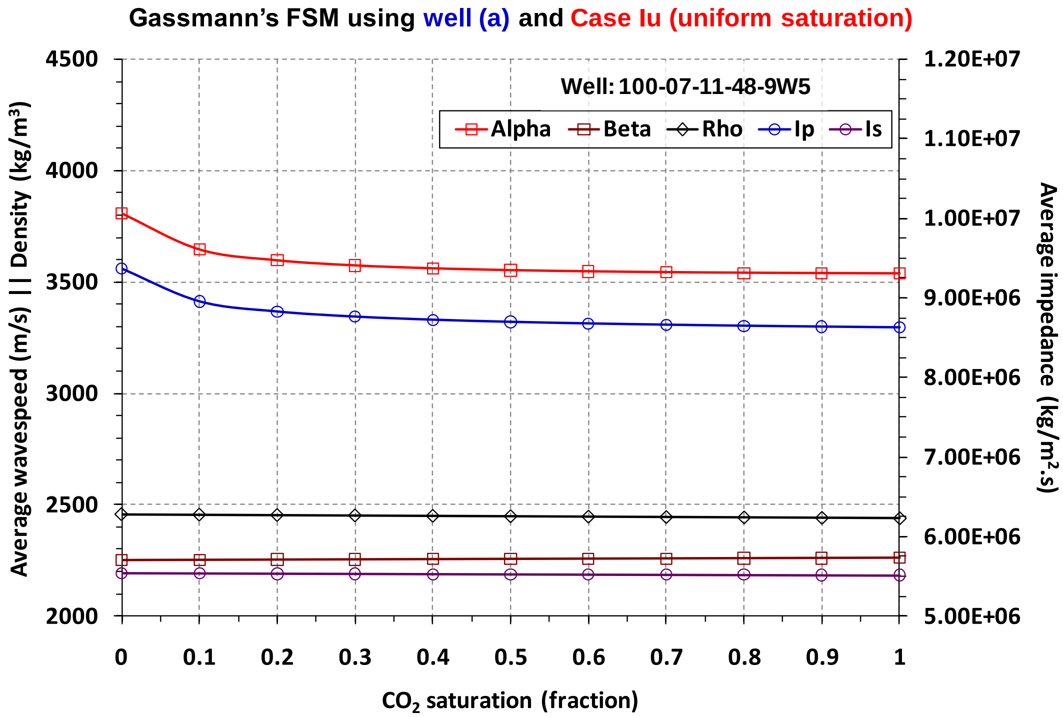

S_{CO2}	$\Delta\rho$ (%)	$\Delta\alpha$ (%)	$\Delta\beta$ (%)	$\Delta(\alpha/\beta)$	$\Delta\sigma$ (%)	ΔI_p (%)	ΔI_s (%)	$\Delta\lambda\rho$(%)	$\Delta\mu\rho$ (%)
0	0	0	0	0	0	0	0	0	0
10	-0.08	-4.31	0.04	-4.35	-17.41	-4.38	-0.04	-28.26	-0.08
20	-0.15	-5.61	0.08	-5.68	-23.64	-5.75	-0.08	-36.68	-0.15
30	-0.23	-6.22	0.11	-6.32	-26.83	-6.43	-0.11	-40.73	-0.23
40	-0.30	-6.56	0.15	-6.70	-28.78	-6.84	-0.15	-43.13	-0.30
50	-0.38	-6.78	0.19	-6.95	-30.09	-7.13	-0.19	-44.72	-0.38
60	-0.46	-6.92	0.23	-7.13	-31.03	-7.34	-0.23	-45.85	-0.46
70	-0.53	-7.02	0.27	-7.26	-31.74	-7.51	-0.27	-46.71	-0.53
80	-0.61	-7.09	0.30	-7.37	-32.29	-7.65	-0.30	-47.38	-0.61
90	-0.68	-7.13	0.34	-7.45	-32.74	-7.77	-0.34	-47.92	-0.68
100	-0.76	-7.16	0.38	-7.52	-33.10	-7.87	-0.38	-48.37	-0.76

Figure 7-7: The result of the FSM (Case Iu) on well 100-11-07-48-9W5 showing the average P-wave speed (α), S-wave speed (β), density (ρ), the acoustic impedance (I_p), and shear impedance (I_s) of the Cardium reservoir units as a function of CO_2 saturation (S_{CO2}). The accompanying table shows the numerical values of the percentage change (Δ%) in these and other elastic parameters, namely α/β wavespeeds ratio, Poisson's ratio (σ), Lambda-Rho ($\lambda\rho$) and Mu-Rho ($\mu\rho$). The modelling parameters and the well location are displayed in Table 7-1 and Figure 6-1, respectively. The results presented here show the results pertaining to the uniform saturation using HS (+/-) average and the upper sandstone unit only (Table 7-2).

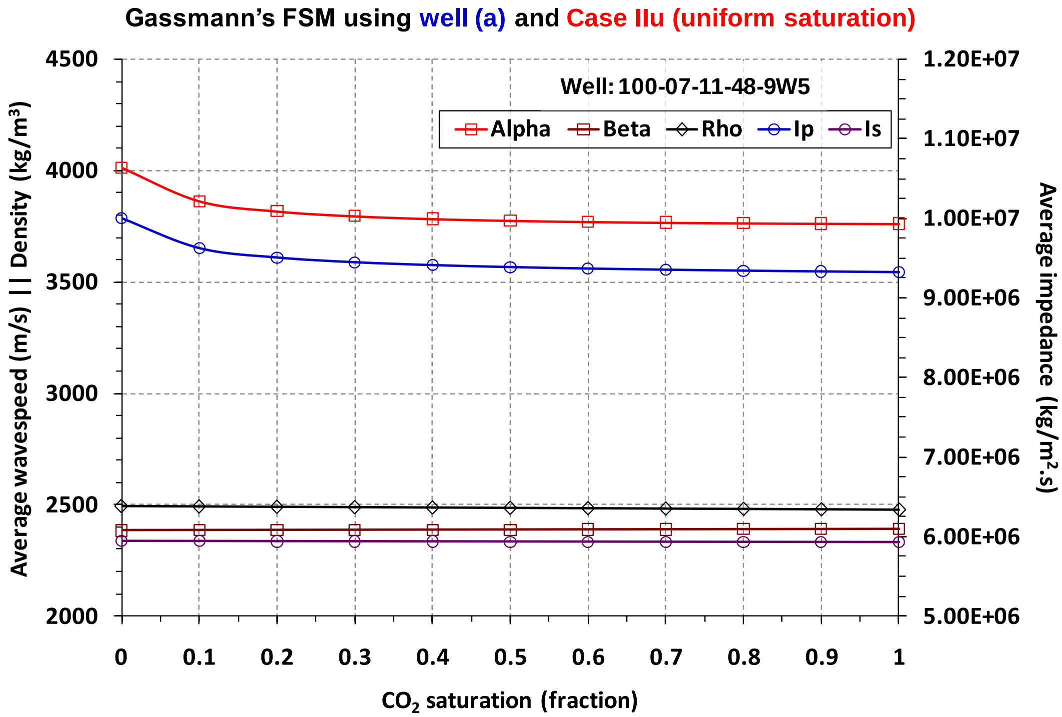

S_{CO2}	$\Delta\rho$ (%)	$\Delta\alpha$ (%)	$\Delta\beta$ (%)	$\Delta(\alpha/\beta)$	$\Delta\sigma$ (%)	ΔI_p (%)	ΔI_s (%)	$\Delta\lambda\rho$(%)	$\Delta\mu\rho$ (%)
0	0	0	0	0	0	0	0	0	0
10	-0.06	-3.71	0.03	-3.74	-15.39	-3.77	-0.03	-25.04	-0.06
20	-0.12	-4.84	0.06	-4.90	-20.84	-4.96	-0.06	-32.62	-0.12
30	-0.18	-5.38	0.09	-5.47	-23.63	-5.55	-0.09	-36.30	-0.18
40	-0.24	-5.68	0.12	-5.80	-25.33	-5.91	-0.12	-38.48	-0.24
50	-0.31	-5.88	0.15	-6.02	-26.47	-6.16	-0.15	-39.93	-0.31
60	-0.37	-6.00	0.18	-6.18	-27.29	-6.35	-0.18	-40.96	-0.37
70	-0.43	-6.09	0.21	-6.29	-27.90	-6.50	-0.21	-41.74	-0.43
80	-0.49	-6.15	0.25	-6.38	-28.38	-6.61	-0.25	-42.35	-0.49
90	-0.55	-6.20	0.28	-6.46	-28.77	-6.72	-0.28	-42.85	-0.55
100	-0.61	-6.23	0.31	-6.52	-29.09	-6.80	-0.31	-43.26	-0.61

Figure 7-8: The result of the FSM (Case IIu) on well 100-07-11-48-9W5 showing the average P-wave speed (α), S-wave speed (β), density (ρ), the acoustic impedance (I_p), and shear impedance (I_s) of the Cardium reservoir units as a function of CO_2 saturation (S_{CO2}). The accompanying table shows the numerical values of the percentage change (Δ%) in these and other elastic parameters, namely α/β wavespeeds ratio, Poisson's ratio (σ), Lambda-Rho ($\lambda\rho$) and Mu-Rho ($\mu\rho$). The modelling parameters and the well location are displayed in Table 7-1 and Figure 6-1, respectively. The results presented here show the results pertaining to the uniform saturation using HS (+/-) average and the effective reservoir units (Table 7-2).

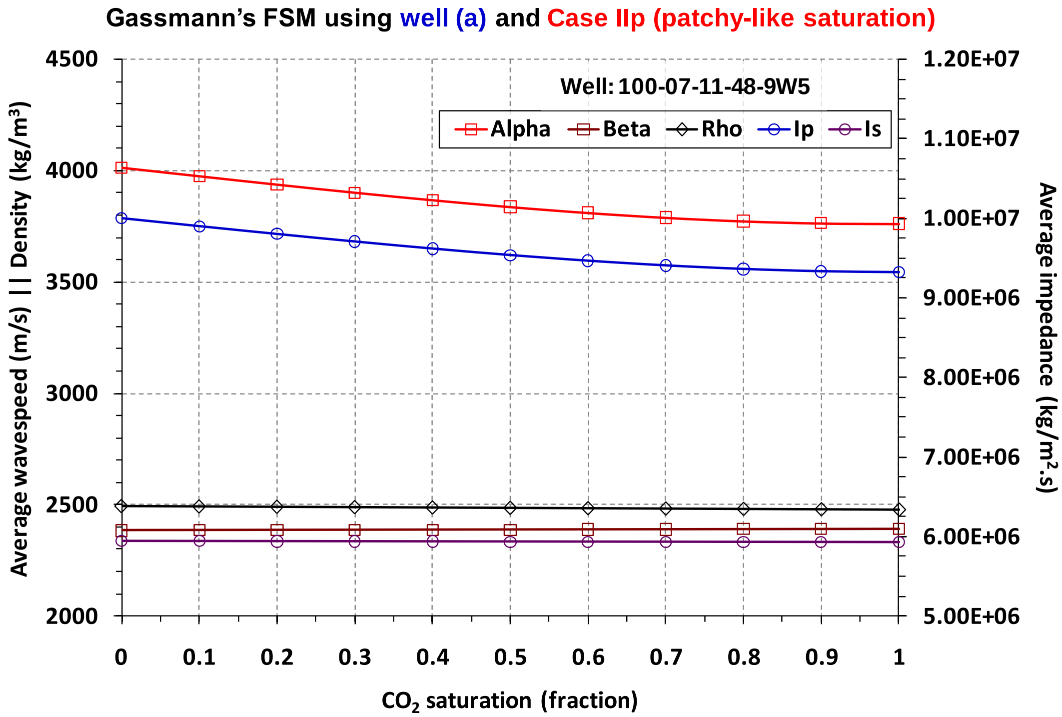

S_{CO2}	$\Delta\rho$ (%)	$\Delta\alpha$ (%)	$\Delta\beta$ (%)	$\Delta(\alpha/\beta)$	$\Delta\sigma$ (%)	ΔI_p (%)	ΔI_s (%)	$\Delta\lambda\rho$(%)	$\Delta\mu\rho$ (%)
0	0	0	0	0	0	0	0	0	0
10	-0.06	-0.94	0.03	-0.97	-3.71	-1.00	-0.03	-6.66	-0.06
20	-0.12	-1.87	0.06	-1.93	-7.55	-1.99	-0.06	-13.12	-0.12
30	-0.18	-2.76	0.09	-2.85	-11.43	-2.94	-0.09	-19.27	-0.18
40	-0.24	-3.59	0.12	-3.71	-15.25	-3.83	-0.12	-24.99	-0.24
50	-0.31	-4.35	0.15	-4.50	-18.90	-4.64	-0.15	-30.14	-0.31
60	-0.37	-5.01	0.18	-5.18	-22.22	-5.36	-0.18	-34.61	-0.37
70	-0.43	-5.54	0.21	-5.75	-25.06	-5.95	-0.21	-38.25	-0.43
80	-0.49	-5.94	0.25	-6.17	-27.23	-6.40	-0.25	-40.97	-0.49
90	-0.55	-6.17	0.28	-6.43	-28.61	-6.69	-0.28	-42.66	-0.55
100	-0.61	-6.23	0.31	-6.52	-29.09	-6.80	-0.31	-43.26	-0.61

Figure 7-9: The result of the FSM (Case IIp) on well 100-07-1148-9W5 showing the average P-wave speed (α), S-wave speed (β), density (ρ), the acoustic impedance (I_p), and shear impedance (I_s) of the Cardium reservoir units as a function of CO_2 saturation (S_{CO2}). The accompanying table shows the numerical values of the percentage change (Δ%) in these and other elastic parameters, namely α/β wavespeeds ratio, Poisson's ratio (σ), Lambda-Rho ($\lambda\rho$) and Mu-Rho ($\mu\rho$). The modelling parameters and the well location are displayed in Table 7-1 and Figure 6-1, respectively. The results presented here show the results pertaining to the patchy-like saturation using Brie et al. (1995) formula with empirical coefficient e = 3 and the effective reservoir units (Table 7-2).

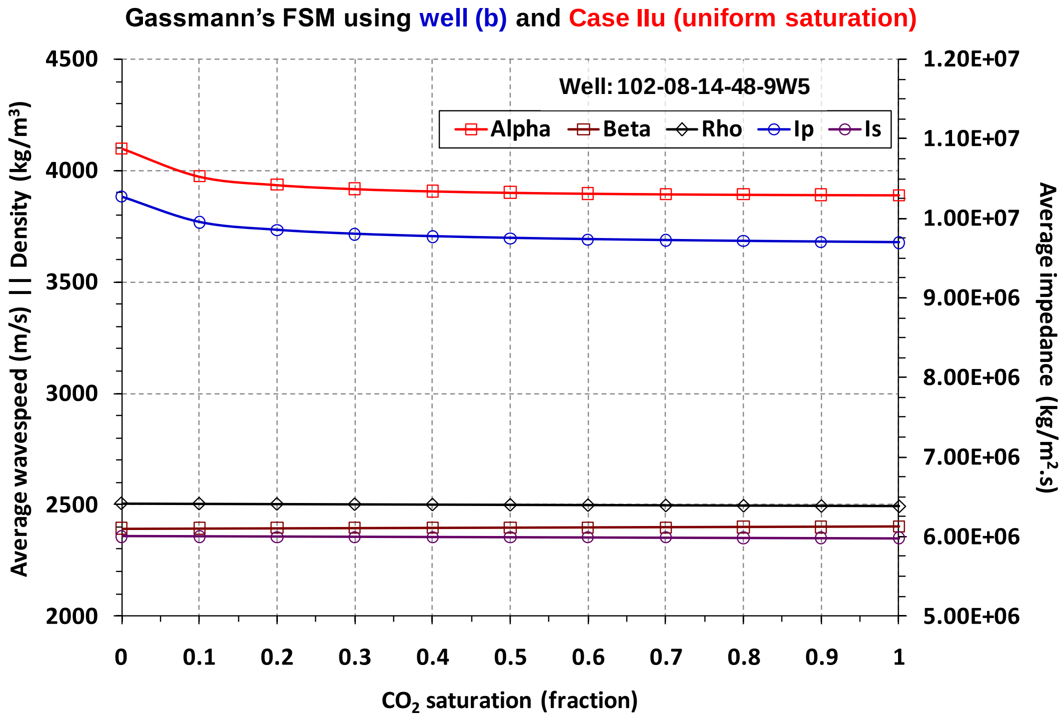

S_{CO2}	$\Delta\rho$ (%)	$\Delta\alpha$ (%)	$\Delta\beta$ (%)	$\Delta(\alpha/\beta)$	$\Delta\sigma$ (%)	ΔI_p (%)	ΔI_s (%)	$\Delta\lambda\rho$(%)	$\Delta\mu\rho$ (%)
0	0	0	0	0	0	0	0	0	0
10	-0.06	-3.07	0.03	-3.09	-10.91	-3.12	-0.03	-19.19	-0.06
20	-0.11	-3.99	0.06	-4.04	-14.63	-4.10	-0.06	-24.98	-0.11
30	-0.17	-4.42	0.08	-4.50	-16.51	-4.58	-0.08	-27.78	-0.17
40	-0.22	-4.67	0.11	-4.77	-17.65	-4.88	-0.11	-29.45	-0.22
50	-0.28	-4.82	0.14	-4.95	-18.40	-5.09	-0.14	-30.56	-0.28
60	-0.34	-4.92	0.17	-5.08	-18.95	-5.24	-0.17	-31.36	-0.34
70	-0.39	-4.99	0.20	-5.18	-19.35	-5.36	-0.20	-31.96	-0.39
80	-0.45	-5.04	0.22	-5.25	-19.67	-5.46	-0.22	-32.43	-0.45
90	-0.50	-5.07	0.25	-5.31	-19.92	-5.55	-0.25	-32.82	-0.50
100	-0.56	-5.09	0.28	-5.36	-20.13	-5.62	-0.28	-33.14	-0.56

Figure 7-10: The result of the FSM (Case IIu) on well 102-08-14-48-9W5 showing the average P-wave speed (α), S-wave speed (β), density (ρ), the acoustic impedance (I_p), and shear impedance (I_s) of the Cardium reservoir units as a function of CO_2 saturation (S_{CO2}). The accompanying table shows the numerical values of the percentage change (Δ%) in these and other elastic parameters, namely α/β wavespeeds ratio, Poisson's ratio (σ), Lambda-Rho ($\lambda\rho$) and Mu-Rho ($\mu\rho$). The modelling parameters and the well location are displayed in Table 7-1 and Figure 6-1, respectively. The results presented here show the results pertaining to the uniform saturation using HS (+/-) average and the effective reservoir units (Table 7-2).

Note that as predicted in Figure 7-6 (a), the results from Case IIp utilizing Brie average show slightly more compliance, in terms of the change in the elastic properties, towards the CO_2 saturation than Voigt or Hill averages. Aside from these minor differences, the absolute magnitude of relative changes in the P-wave speed (α) and acoustic impedance (I_p) appear to be detectable; based on Cases Iu, IIu and, perhaps, Case IIp as well at intermediate and high saturation (~ 50%). Table 7-3 summarizes some of the elastic properties from the two wells employed in the FSM.

Table 7-3: Comparison between the elastic moduli (K and μ), density (ρ) and porosity (ϕ) as estimated from the well logs reflective of in-situ conditions before the fluid substitution modelling. The comment column indicates the zone over which these elastic proeprties were computed.

Well	$K^{\text{in-situ}}_{\text{saturated}}$ (GPa)	$\mu^{\text{in-situ}}_{\text{saturated}}$ (GPa)	$\rho^{\text{in-situ}}_{\text{saturated}}$ (kg/m^3)	K_ϕ (GPa)	ϕ (%)	Comment
(a) 100-07-11-48-9W5	20.12	12.46	2498	15.74	11.4	Upper sandstone unit. See Figure 7-7.
(b) 102-08-14-48-9W5	18.89	11.65	2433	12.87	13.5	Upper sandstone unit
(a) 100-07-11-48-9W5	22.43	14.17	2515	15.74	9.0	Effective reservoir units See Figure 7-8.
(b) 102-08-14-48-9W5	24.37	14.36	2506	18.20	8.5	Effective reservoir units. See Figure 7-10.

As far as the two wells (a) and (b) are concerned, it seems that the observation well (100-07-11-48-9W5) shows, to some extent, more sensitivity towards the CO_2-fluid replacement as can been seen, for instance, in terms of the absolute relative change of P-wave speed at 50% CO_2 saturation where the former attains a value of -5.88% versus -4.82% at well 102-08-14-48-9W5. Furthermore, and as observed under the WASP FSM modelling (Section 5.3.2.7), the changes in the shear elastic properties, for instance β and I_s are insignificant. Hence, multi-component modelling was not incorporated into the subsequent numerical modelling.

The considerations and uncertainties associated with the Gassmann FSM were discussed under (Section 5.3.2.8). Once more, regarding the shear modulus, the geochemical simulations undertaken by the PCEP geochemistry team indicates that no significant interaction was taking place between the injected supercritical CO_2 and the Cardium reservoir rock matrix (Shevalier et al., 2008; Nightingale et al., 2008; Talman and Perkins, 2008). In the subsequent offset-dependent reflectivity (ODR) and VSP modelling, only Case Iu and Case IIu were investigated whereas only Case IIu was invoked in exploding reflector finite-difference (ERFD) modelling scheme.

7.2.3 Numerical Forward Seismic Modelling

The scope of the forward seismic modelling is divided into two categories: (1) surface seismic modelling, and (2) borehole seismic modelling. In the former, two schemes were employed: offset-dependent reflectivity (ODR) and exploding reflector finite-difference (ERFD) modes. In the case of the second category, vertical seismic profile (VSP) ray tracing scheme was exploited which invokes geometric ray theory (GRT). For the same reasons discussed under the WASP numerical modelling (Section 5.3.3), only the seismic response associated with the compressional wavefield (P-wave) was modelled.

7.2.3.1 Surface Seismic Modelling

7.2.3.1.1 Offset-Dependent Reflectivity (ODR) Modelling

The ODR modelling parameters and the various experiments investigated are summarized in Table 7-4. In a similar manner to that of the WASP numerical modelling (Section 5.3.3), all the noise-free synthetic seismograms were NMO-corrected. In Experiment 0 which is depicted in Figure 7-11, the AVO response of the Cardium events is modelled as a function of offset and CO_2 saturation based on Case Iu (Table 7-2). Figure 7-12 shows an enlarged display of the AVO response at 0 and 40% uniform CO_2 saturation. Obviously, the Cardium event is a low impedance reflection. Furthermore, AVO gradient analysis indicates that it mostly belongs to Class II AVO anomalies (Rutherford and Williams, 1989; Castagna and Backus, 1993) as depicted in Figure 7-13. As observed in the AVO response of Experiment 2 under the WASP ODR modelling in Section 5.3.3.1, the seismic amplitude seems to decrease with offset but slightly increases with CO_2 saturation before reaching a plateau at around 40% CO_2 saturation. As outlined in Section 5.3.3.1, this behaviour seems to be due to the combined effect of the seismic wavelet and tuning effect. In order to avoid redundancy, the frequency effect will be considered as part of the VSP modelling (Section 7.2.3.1.3). Overall, the results suggest that the response associated with Case Iu seems to be very weak at a dominant frequency of 30 Hz.

Table 7-4: Outline of the main ODR forward seismic modelling parameters and other pertinent information.

Simulation method	Ray tracing (Section 3.5.4) and employing the Zoeppritz equations (Section 3.3)
Seismic Wavelet	Zero-phase Ricker wavelet (Figure 5-2)
Frequency	30 Hz (Figure 5-2 (a) and (b))
Seismogram Sampling Rate	1 ms
Minimum Offset	0 m
Maximum Offset	1500 m
Offset Spacing	150 m
Target Depth and Thickness	• Case Iu (upper sandstone unit): 1616 m and 3 m • Case IIu (effective reservoir unit): 1614 m and 9 m
Well	100-07-11-48-9W5 (Figure 7-3)
Objective	Investigating seismic reflectivity change as a function of offset and CO_2 saturation in the Cardium Formation reservoir units.
Comments	• Experiment 0: AVO response based on Case Iu (see Table 7-2). • Experiment 1: Post-stack AVO response based on Case Iu (see Table 7-2). • Experiment 2: Post-stack AVO response based on Case IIu (see Table 7-2).

Figure 7-14 illustrates the results corresponding to Experiment 1. The maximum changes in the Cardium event cross-correlation time shift (~ -0.07 ms) as well as the Ardley-Viking isochron difference (~ 0.05 ms) are insignificant. Similarly, the maximum change in the magnitude of the PRED (~ 99%) suggests no sensitivity in the seismic response toward the CO_2-fluid replacement. The NRMS exhibits a modest change of ~ 17%. As anticipated, the maximum change in the magnitudes of PRED (~ 90%) and NRMS (~ 60%) over the same saturation range corresponding to Experiment 2 are higher due to the increase in the CO_2 saturation thickness column. On the contrary, the magnitude of the Cardium event cross-correlation time shift and Ardley-Viking isochron difference are still insignificant, i.e. ~ -0.43 ms and 0.27 ms, respectively. The observations pertaining to Experiments 2 and 3 have striking similarity to their counterparts presented under the WASP numerical modelling (Section 5.3.3.1).

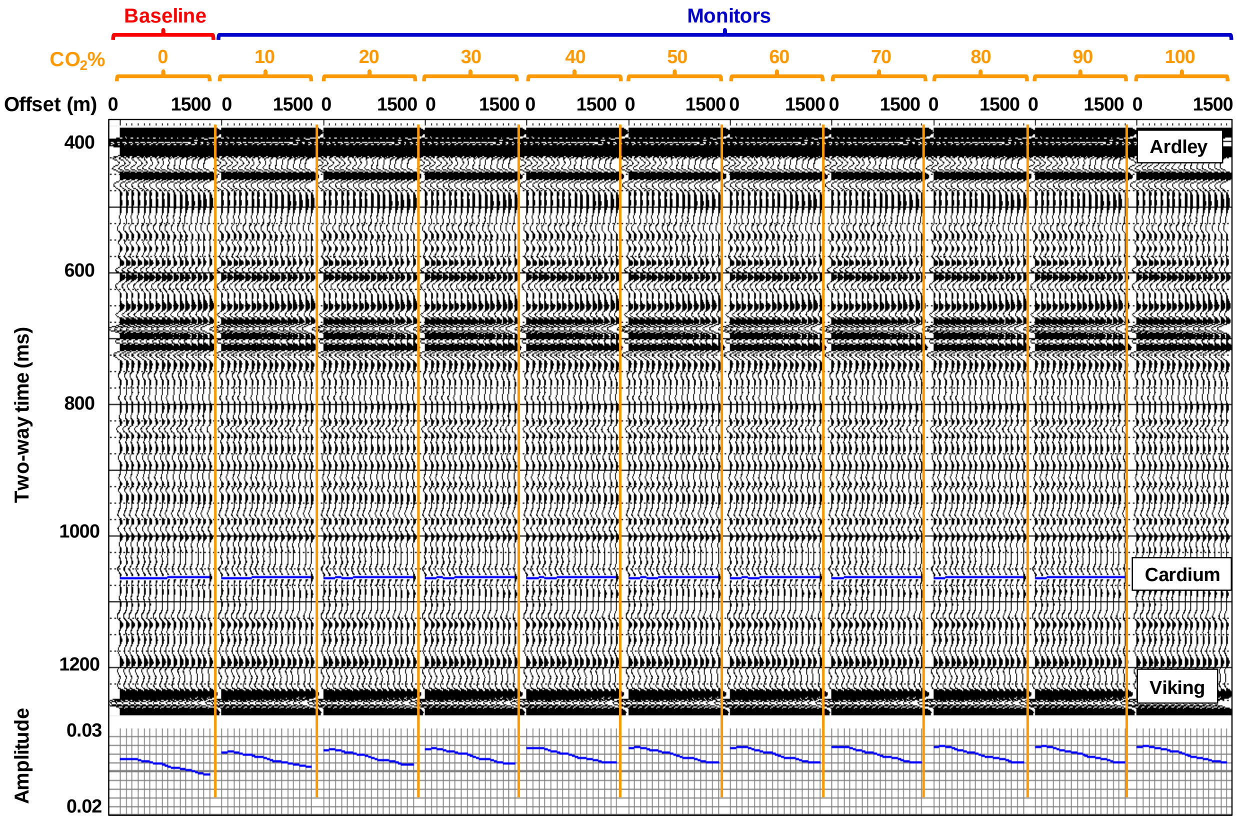

Figure 7-11: Broad sequential display of the NMO-corrected synthetic AVO response of the Cardium event showing the baseline and the various monitors. The corresponding amplitude values are plotted (blue curve) in the bottom panel. The gathers were generated using Case Iu (uniform saturation) of the FSM on well 100-07-11-48-9W5 alongside the 30 Hz Ricker wavelet displayed in Figure 5-2. Figure 7-12 shows a blown up display over the Cardium event at 0 and 40% CO_2 saturation.

The difference in the seismic amplitude as a function of CO_2 saturation corresponding to Experiments 2 and 3 is portrayed in the form of seismic amplitude cross-plot in Figure 7-16 (a) and (b), respectively. There appears to be no distinction in the seismic amplitude before and after CO_2-fluid replacement in Experiment 1 (Case Iu). However, the separation between the so-called background trend and the anomalous (i.e. CO_2-induced) trend is fairly discernible in the case of Experiment 2 (Case IIu).

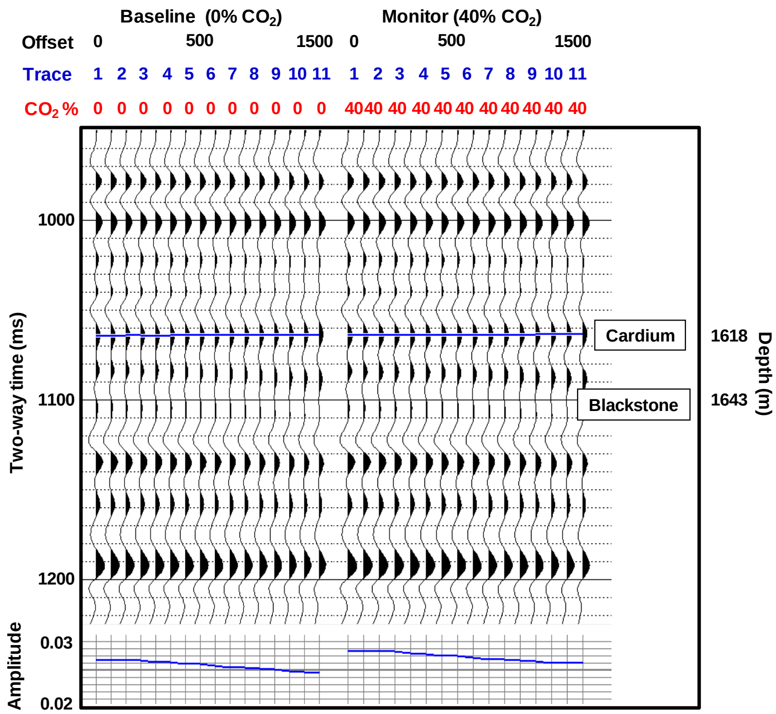

Figure 7-12: Enlarged display of the NMO-corrected AVO response shown in Figure 7-11 over the Cardium event at 0% CO_2 (left panel) and 40% CO_2 (right panel). Trace 1 is at 0 m offset; trace 11 is at 1500 m offset. Trace increment is 150 m.

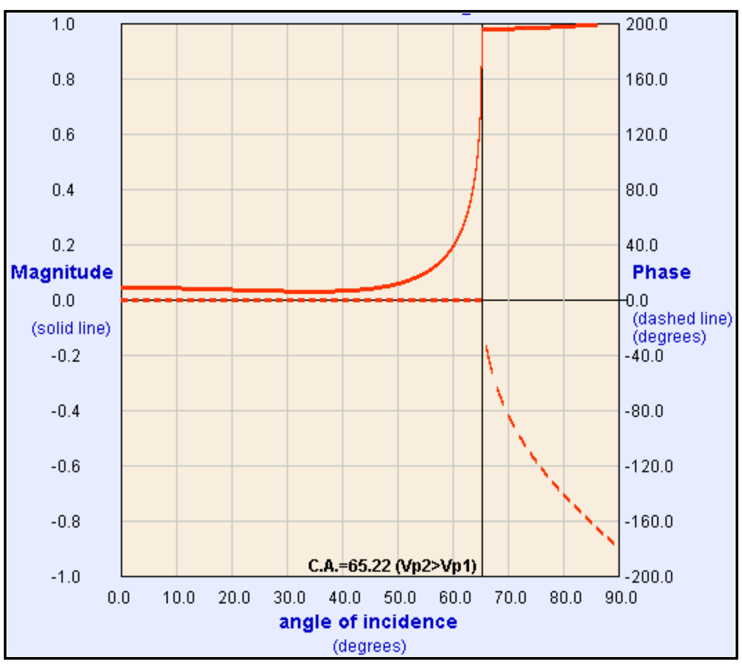

Figure 7-13: Reflection coefficient (amplitude magnitude) and phase of the Cardium event as a function of angle of incidence. The curves are based on the Zoeppritz equations and were geneарted using the CREWES Zoeppritz Explorer 2.2 (Ursenbach, 2010).

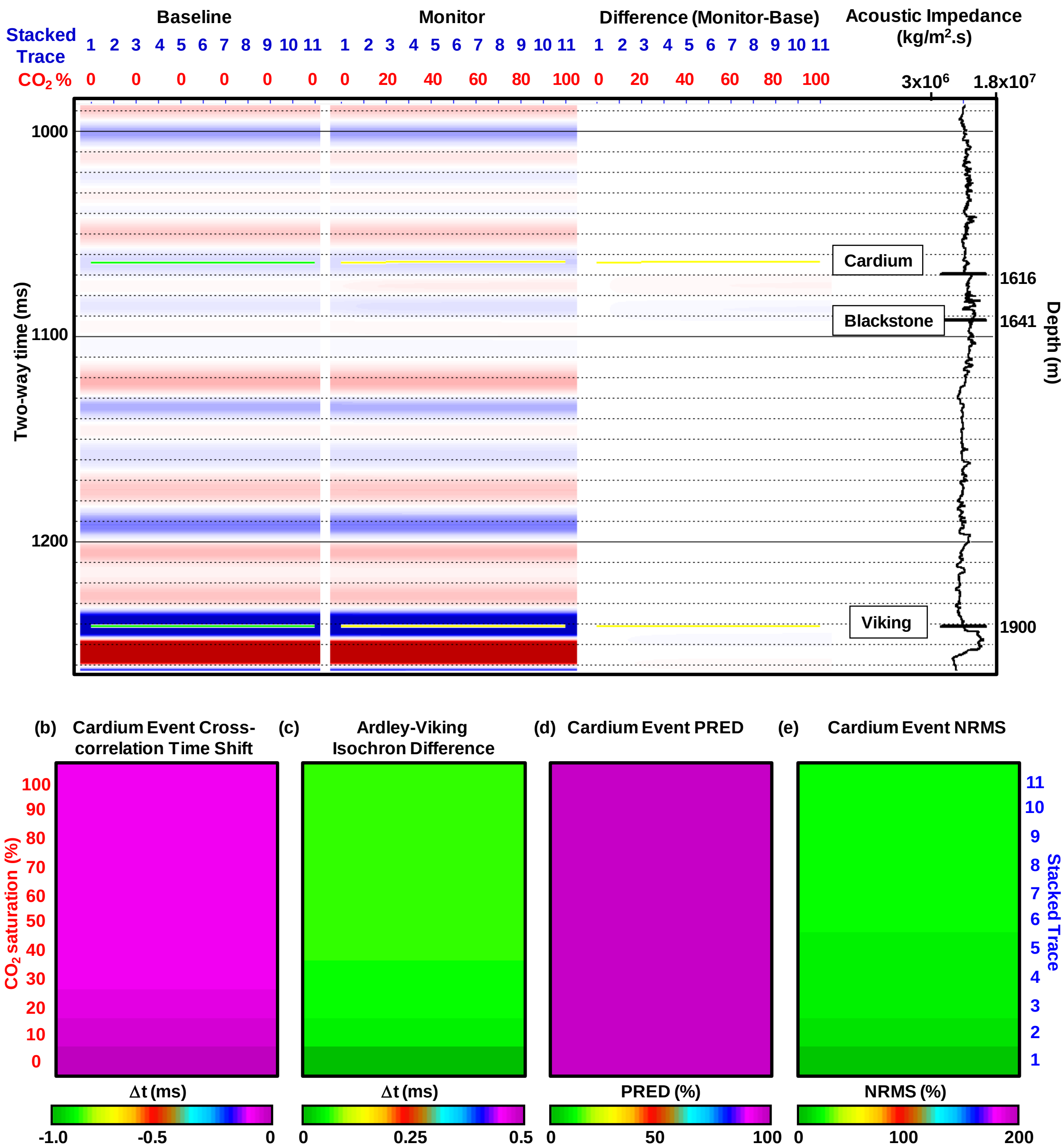

Figure 7-14: (a) Synthetic seismograms (baseline, monitor and their difference) corresponding to Experiment 1 in which the Cardium reflection is modelled as function of CO_2 saturation employing Case Iu on the observation well and the 30 Hz Ricker wavelet displayed in Figure 5.2. The monitor picks (yellow) are shown in the difference section in (a) as well as the acoustic impedance of the baseline. The bottom panel (b through c) shows a mosaic display of selected time and amplitude-based attributes; (b), (d) and (e) were computed using 100 ms window centered at the Cardium event. Note that each trace represents the stacked response of the NMO-corrected CDP gathers shown in Figure 7-11 at the given saturation.

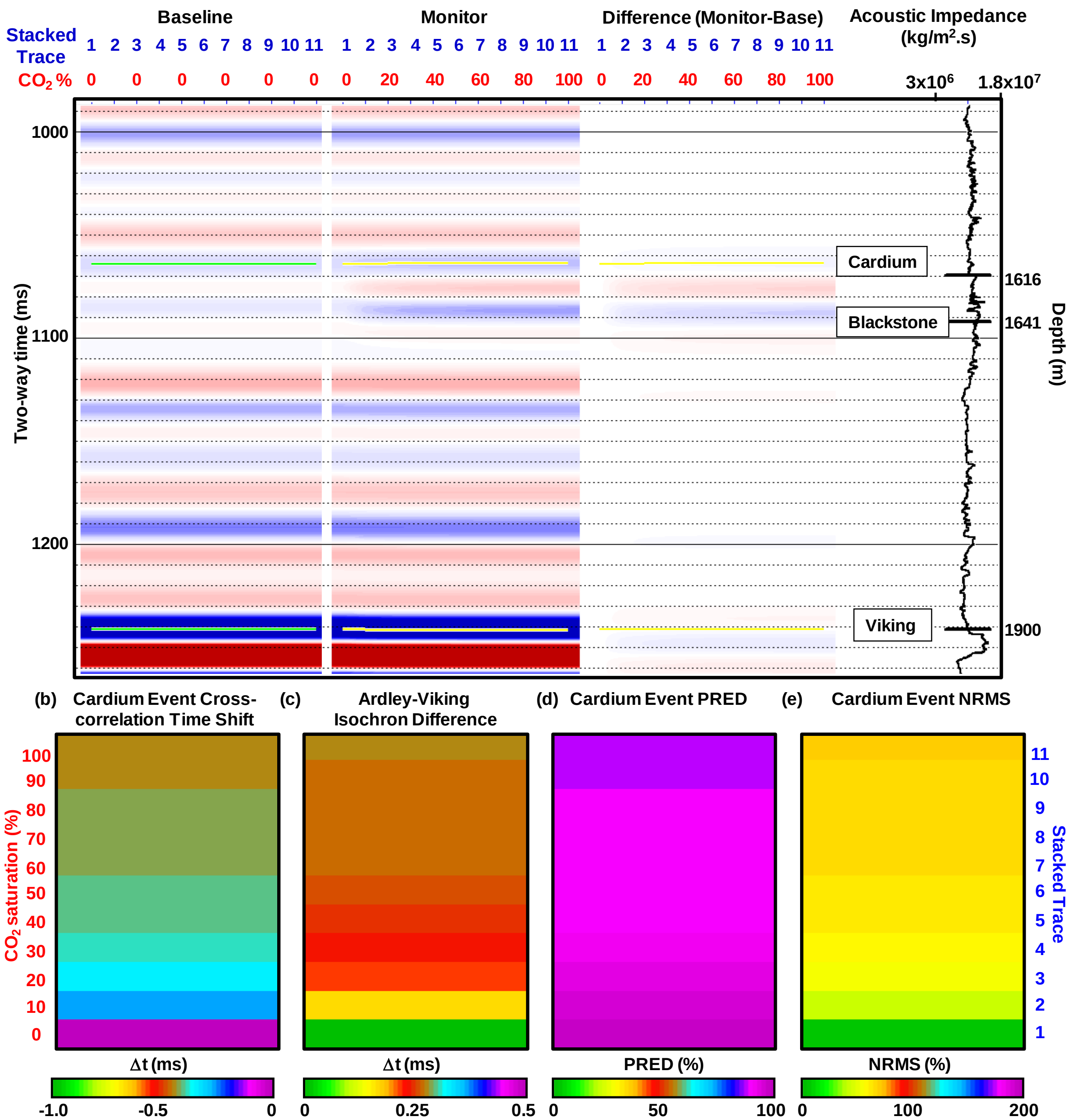

Figure 7-15: (a) Synthetic seismograms (baseline, monitor and their difference) corresponding to Experiment 2 in which the Cardium reflection is modelled as function of CO_2 saturation employing Case IIu on the observation well and the 30 Hz Ricker wavelet displayed in Figure 5.2. The monitor picks (yellow) are shown in the difference section in (a) as well as the acoustic impedance of the baseline. The bottom panel (b through c) shows a mosaic display of selected time and amplitude-based attributes; (b), (d) and (e) were computed using 100 ms window centered at the Cardium event. Note that each trace represents the stacked response of the NMO-corrected CDP gathers similar to those shown in Figure 7-11 at the given saturation.

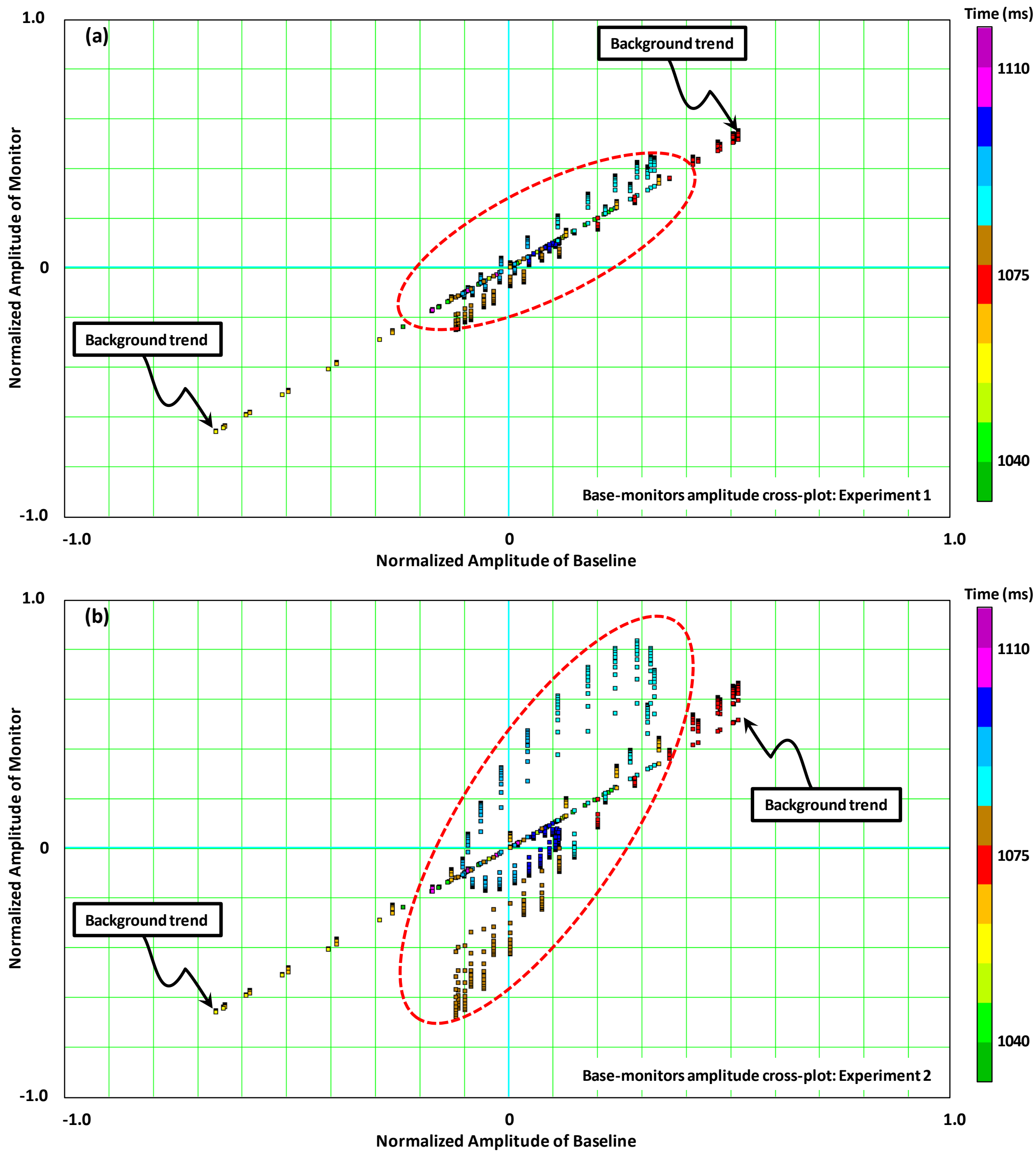

Figure 7-16: Seismic amplitude cross-plot of the baseline versus monitors corresponding to the Cardium event from (a) Experiment 1 (Figure 7-14), and (b) Experiment 2 (Figure 7-15). Note that the background trend is the straight line traversing the origin as indicated by the arrows at both ends. The dashed red ellipse shows the location and extent of the 4-D anomaly associated with the CO_2-fluid replacement.

7.2.3.1.2 Exploding Reflector Finite-Difference (ERFD) Modelling

The ERFD modelling parameters are outlined in Table 7-5. Figure 7-17 depicts the 2-D acoustic geologic model which was constructed using information provided by the seismic data, primarily Line 1 (Section 6.5.4), as well as the geologic cross-section shown in Figure 2-14 and the stratigraphic model in Figure 2-15. In addition, the logs from well 100-07-11-48-9W5 were used for estimating the acoustic properties and thickness of the individual layers. Note that although the Cardium Formation is comprised of 8 units (see Figure 2-17), the formation was divided into three effective units (Figure 7-17) based on the following assumptions:

- The Cardium shale comprising the Cardium Zone was assumed to be a single unit.
- The conglomerate, upper sandstone, upper shale and middle sandstone units were combined into an effective flow unit. Hence, it is called the effective reservoir unit. The acoustic properties, i.e. P-wave speed and density, of this unit were assigned the average of the three constituent units.
- Similarly, the middle shale, lower sandstone and lower shale units were combined into a single layer with its acoustic properties equivalent to the average of the three units. This layer is designated as the lower Pembina River unit.

The seismic response before and after the CO_2-fluid replacement as well as the difference between the two are displayed in Figure 7-17. The difference section shown in Figure 7-17 (c) exhibits a weak time-lapse response due to the CO_2-fluid replacement in the effective reservoir unit. The corresponding time and amplitude-based attributes, which offer a quantitative means of assessing the 4-D effect, are plotted in Figure 7-19. The repeatability metrics, namely PRED and NRMS, shown in Figure 7-19 (a) were computed for three seismic events as well as the entire trace at each offset and the corresponding averages are given in Table 7-6. Chronologically, the seismic events are: Ardley, Cardium and Viking reflections.

As frequently emphasized in Chapter 6, the Ardley reflection offers as shallow marker whereas the Viking reflection provide a deep marker. Under ideal conditions, the Ardley event should not exhibit any change as a results of the CO_2-fluid replacement in the Cardium Formation and, thus, should be exactly repeatable. Clearly, this is the case as demonstrated by the PRED and NRMS magnitudes of 100% and 0%, respectively. Under the same ideal conditions, the change in the repeatability of the Viking event will depend primarily on the CO_2-induced effect, which in this case is extremely small resulting in PRED and NRMS magnitudes of approximately 99.97% and 5.30%, respectively.

Table 7-5: Outline of the main ERFD modelling parameters and other pertinent information.

Simulation method	Finite-difference using an explicit solution (Section 3.5.3) to the acoustic wave-equation (Section 3.1)
Source Type	Exploding reflector
Boundary Type	Absorbing
Seismic Wavelet and Frequency	30 Hz Ricker wavelet (Figure 5-2 (a) and (b))
Time Increment	0.1 ms
Minimum Offset	0 m
Maximum Offset	3000 m
Position of First Receiver	0 m
Position of Last Receiver	3000 m
Bin spacing	2 m
Maximum Model Depth	2000 m
Target Depth and Thickness	1616 m; effective units: 9 m
Objectives	Collaborate the ODR ray trace modelling results in investigating seismic reflectivity change as a function of offset and CO_2 saturation in the Cardium Formation using Case IIu of the FSM on well 100-07-11-48-9W5 (Figure 7-3).
Comments	• See Section 5.3.3.2 and Figure 5-35 for sensitivity to upward plume migration. In the PCEP context, the shallow aquifer would be the Edmonton Group aquifer instead of the Belly River Group aquifer in the WASP investigation. • See Figure 7-17 for the acoustic geologic model.

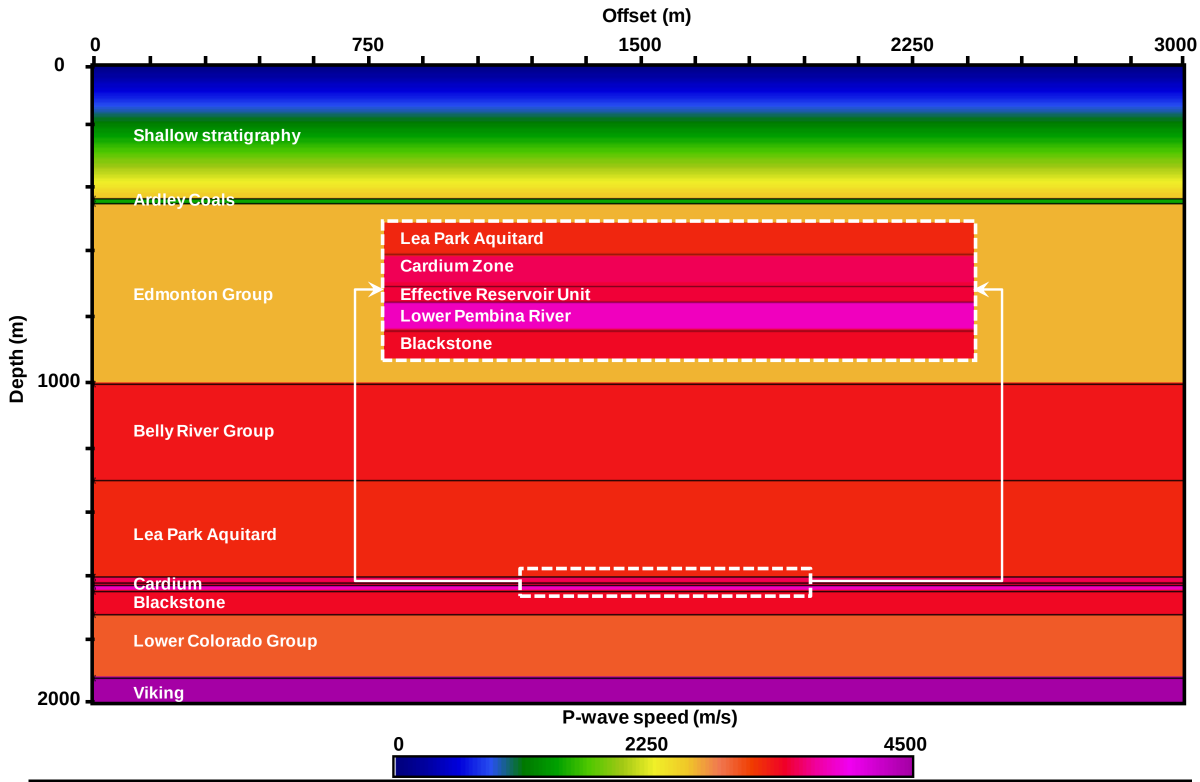

Layer	Average Depth[1] (m)	Average Thickness (m)	Average Acoustic Properties	
			P-wave speed (m/s)	Density (kg/m^3)
Shallow stratigraphy	0.0	430	3000	2262
Ardley Formation (coals)	430	15.0	2470	1582
Edmonton Group	445	555	3250	2415
Belly River Group	1000	300	3680	2460
Lea Park Group	1300	298	3650	2580
Cardium Formation	1598	43.0	3990	2550
Cardium Zone (shale)	1598	16.0	3820	2600
Effective Reservoir Unit (before CO_2)	1614	9.00	4018	2553
Effective Reservoir Unit (after CO_2)	1614	9.00	3790	2546
Lower Pembina River	1623	18.0	4008	2533
Blackstone Formation	1641	74.0	3730	2590
Lower Colorado Group	1715	195	3485	2560
Viking Formation	1910	90.0	4500	2600

Figure 7-17: 2-D acoustic model depicting the geology in the PCEP local-scale study area. There are 11 effective layers. The accompanying table shows the name and average acoustic properties of the various layers. Note that the Cardium Formation was divided into three effective units (see text). The color scale depicts the P-wave speed in the model before CO_2-fluid replacement. [1] Average depth to layer top.

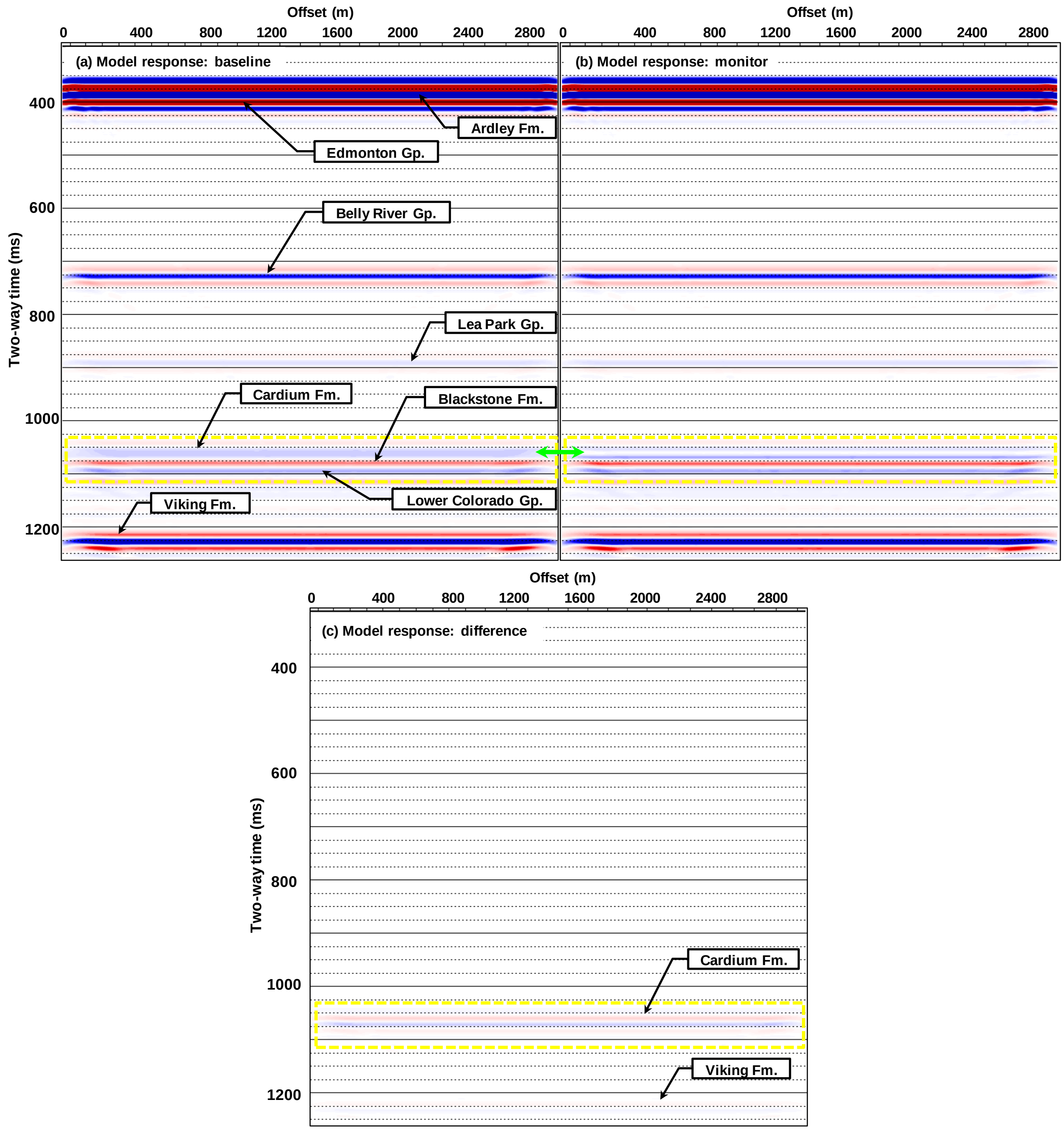

Figure 7-18: The model response of the 2-D model in Figure 7-17 (a) before, and (b) after CO_2-fluid replacement (40% uniform CO_2 saturation) in the effective reservoir unit of the Cardium Formation. The difference between (a) and (b) is shown in (c). The callout shapes point to the seismic events corresponding to the top of the layers listed in the table in Figure 7-17. The dashed yellow rectangle encloses the Cardium Formation and the overlying Lea Park and underlying Blackstone aquitards. The double-sided green arrow traversing the vertical line separating (a) and (b) identifies the Cardium event. Fm.: formation; Gp.: group. The seismograms share the same amplitude scale.

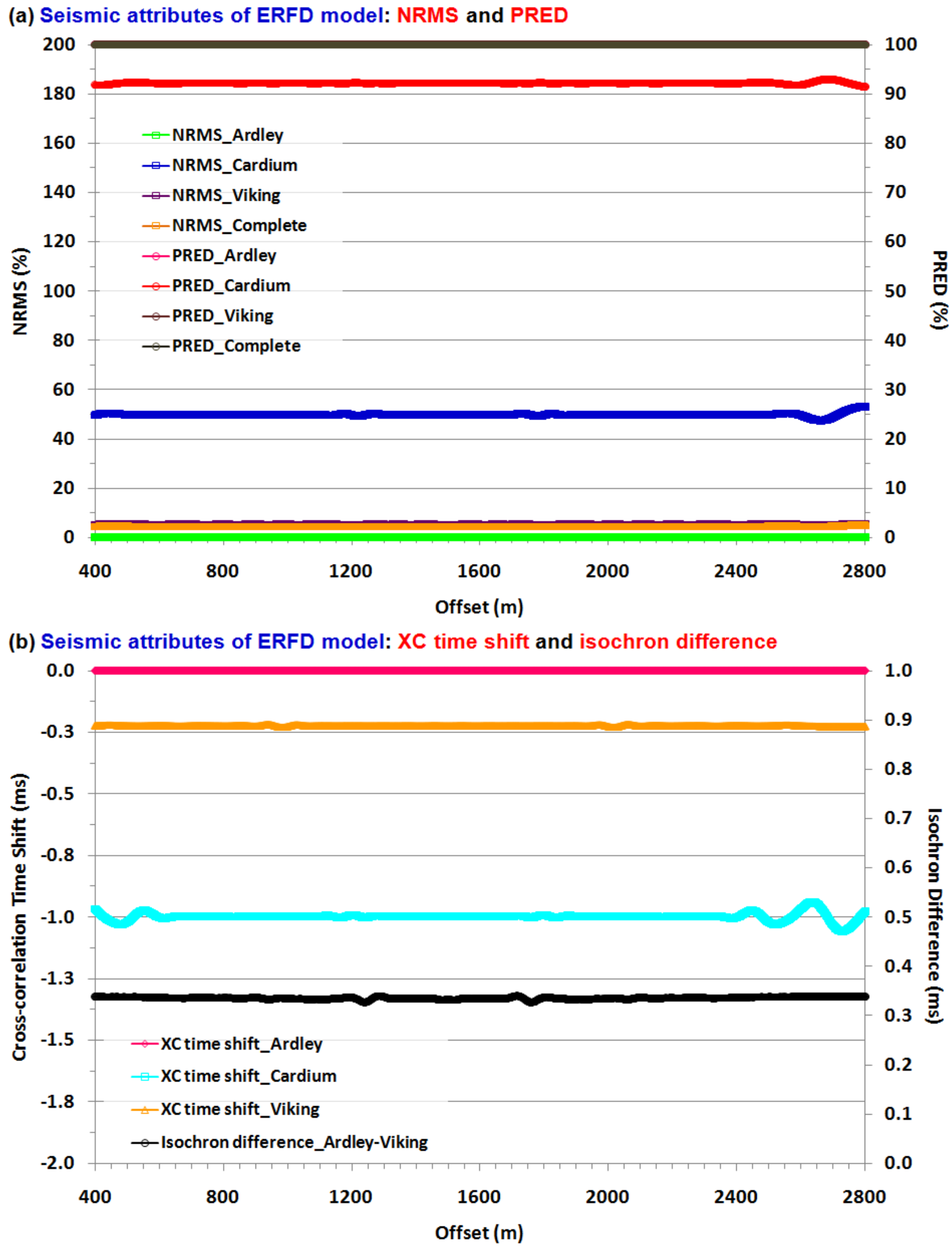

Figure 7-19: (a) Repeatability of the some of the relevant events as well as the entire traces associated with synthetic seismograms shown in Figure 7-18. For the seismic events, the NRMS and PRED were computed using a 100 ms enclosing these events; (b) cross-correlation (XC) time shift of the same events in (a) in addition to the difference in the Ardley-Viking isochron of the same synthetic seismogarms. Note that the PRED curves in (a) are overlapping, except that corresponding to the Cardium event, as can be clearly seen in see Table 7-6.

In contrast to the deep markers, the repeatability of the reservoir (Cardium event), where the CO_2-fluid replacement is taking place, is more prominent. This is most obvious in terms of the NRMS which attains an average magnitude of ~ 50%. The magnitude of the PRED is not as large since the seismograms are noise-free and the amount of time shift is small as discussed in the next paragraph. Furthermore, the magnitude of the PRED and NRMS appears to largely agree with that associated with the ODR modelling in Figure 7-15 (d) and (e).

The cross-correlation time shift of the three seismic events invoked in the repeatability analysis in addition to the Ardley-Viking isochron difference are plotted in Figure 7-19 (b). The average cross-correlation time shift corresponding to Ardley, Cardium and Viking reflections is listed in Table 7-6. Obviously, the magnitude of time shift is insignificant even in the case of the Cardium event (~ -1 ms). Unlike the repeatability metrics, there appears a small difference in the magnitude of the Cardium event cross-correlation time shift between the ODR in Figure 7-15 (b) and the ERFD in Figure 7-19 (b). This could be attributed to the minor artefacts associated with F-D modelling, e.g. numerical dispersion. In the WASP ERFD modelling, such artefacts were not significant but since the Cardium reflection is a weak impedance contrast, it tends to susceptible to the smallest F-D artefacts. Regardless, the time-based attributes are considered to be less reliable, in this investigation, than amplitude-based attributes for the same reasons mentioned under Section 5.3.3 and Section 7.2.3.1.1.

Table 7-6: Comparison of the average repeatability and cross-correlation time shift of the three seismic events discussed in the text and the entire traces corresponding to ERFD synthetic seismograms shown in Figure 7-18.

Seismic Event	Average PRED (%)	Average NRMS (%)	Cross-correlation Time Shift (ms)
Ardley	100.0	0.00	0.00
Cardium	92.10	49.85	-0.98
Viking	99.97	5.30	-0.28
Entire Trace	99.90	4.36	-

7.2.3.1.3 Borehole Seismic Modelling: VSP

Table 7-7 summarizes the main VSP modelling parameters and the various scenarios investigated. As outlined in Table 7-7, two scenarios were considered: Scenario I and Scenario II. The former invokes the FSM results pertaining to Case Iu (Figure 7-7) whereas the latter is based on those corresponding to Case IIu (Figure 7-8). Recall that both cases were investigated as part of the ODR modelling scheme presented in Section 7.2.3.1.1 (see Figure 7-14 for Case Iu and Figure 7-15 for Case IIu). In addition, the seismic response associated with Case IIu was examined using the ERFD modelling scheme in the previous sub-sub-subsection. Hence, the 2-D acoustic geologic model utilized in Scenario II (Figure 7-17) including the data used in constructing the model as well as the underlying assumptions were already discussed in Section 7.2.3.1.2. As for the 2-D acoustic geologic model corresponding to Scenario I (Figure 7-20), the same seismic well logs data were invoked with one major distinction; the Cardium Formation was divided into five effective units instead of three as follows:

- As in Scenario II, the Cardium shale comprising the Cardium Zone was assumed to be a single unit.
- The conglomerate and upper sandstone were designated as separate units.
- The upper shale and middle sandstone units were considered as single unit, which was named the middle Pembina River unit. The acoustic properties, i.e. P-wave speed and density, of this unit were assigned the average of the two constituent units.
- In a similar manner to Scenario II, the middle shale, lower sandstone and lower shale units were combined into a single layer with its acoustic properties equivalent to the average of the three units. This layer was designated as the lower Pembina River unit.

In processing the synthetic VSP data, a standard flow was used similar to that employed in processing the field VSP data in Chapter 6 (see Figure F-6 in Appendix F).

Table 7-7: Outline of the main VSP ray trace modelling parameters and other pertinent information

Simulation method	Ray tracing (Section 3.5.4) employing the geometric ray theory (Section 3.1)
Seismic Wavelet and Frequency	60 Hz zero-phase Ricker wavelet (see Figure 5-2 (c) and (d))
Sampling Rate	1 ms
Minimum Offset	0 m
Maximum Offset	3000 m
Position of First Source	0 m
Position of Last Source	3000 m
Source Spacing	40 m
Borehole Position	1500 m
Depth of First Receiver	1500 m
Depth of Last Receiver	1640 m
Receiver Spacing	20 m
Maximum Model Depth	2000 m
Target Depth and Thickness	• Case Iu (upper sandstone unit): 1616 m and 3 m • Case IIu (effective reservoir unit): 1614 m and 9 m
Objectives	Collaborate the ODR and ERFD modelling results in investigating the change in the seismic response change due to CO_2-fluid replacement in the Cardium Formation using Case Iu and Case IIu of the FSM on well 100-07-11-48-9W5 (Figure 7-3).
Comments	• Scenario I (based on Case Iu): see Figure 7-17 for the acoustic geologic model and Figure 7-7 for the FSM results. Also, compare with Experiment 1 of the ODR modelling scheme (Figure 7-14). • Scenario II (based on Case IIu): see Figure 7-20 for the acoustic geologic model and Figure 7-8 for the FSM results. Also, compare with Experiment 2 of the ODR modelling scheme (Figure 7-15).

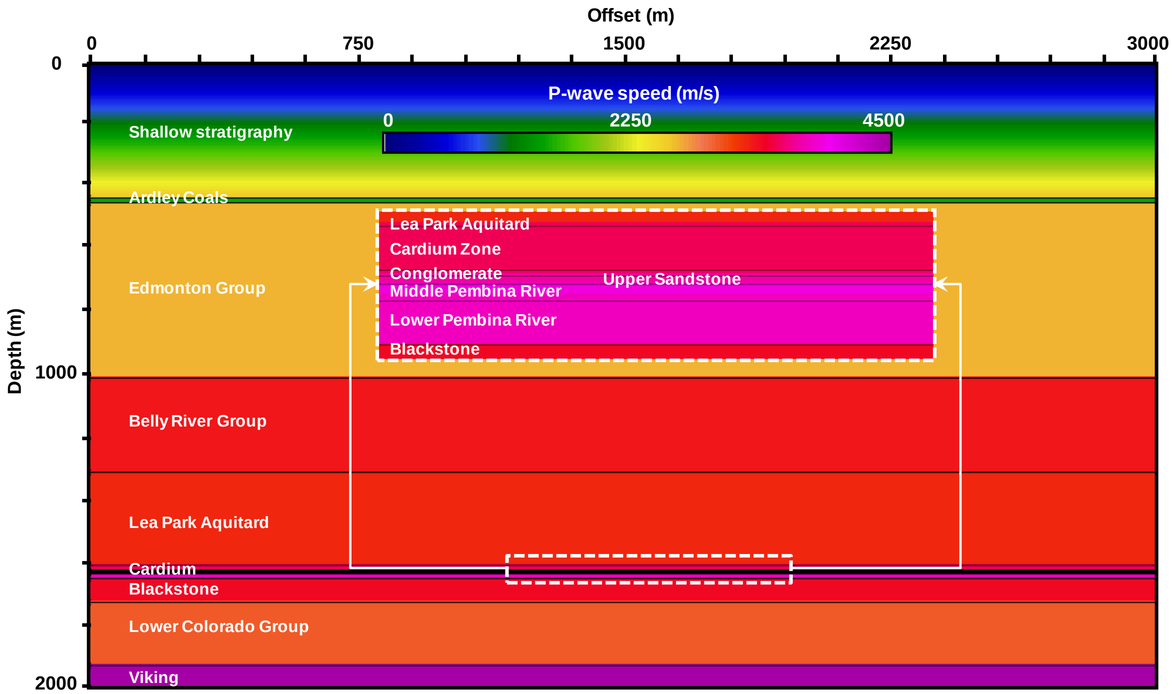

Layer	Average Depth[1] (m)	Average Thickness (m)	Average Acoustic Properties	
			P-wave speed (m/s)	Density (kg/m^3)
Shallow stratigraphy	0.0	430	3000	2262
Ardley Formation (coals)	430	15.0	2470	1582
Edmonton Group	445	555	3250	2415
Belly River Group	1000	300	3680	2460
Lea Park Group	1300	298	3650	2580
Cardium Formation	1598	43.0	3990	2550
Cardium Zone (shale)	1598	16.0	3820	2600
Cardium Conglomerate	1614	2.00	3950	2580
Upper Sandstone Unit (before CO_2)	1616	3.00	4100	2510
Upper Sandstone Unit (after CO_2)	1616	3.00	3890	2504
Middle Pembina River	1619	4.00	4010	2560
Lower Pembina River	1623	18.0	4008	2533
Blackstone Formation	1641	74.0	3730	2590
Lower Colorado Group	1715	195.0	3485	2560
Viking Formation	1910	90.0	4500	2600

Figure 7-20: 2-D acoustic model depicting the geology in the PCEP local-scale study area. There are 13 effective layers. The accompanying table shows the name and average acoustic properties of the various layers. In contrast to the model in Figure 7-17, the Cardium Formation was divided into five effective units (see text). The color scale depicts the P-wave speed in the model before CO_2-fluid replacement. [1] Average depth to layer top.

The processed synthetic VSP seismograms corresponding to Scenario I are shown Figure 7-21. There seems to be a subtle difference between the baseline and monitor seismograms as demonstrated in Figure 7-21 (a) and (b), respectively. Furthermore, the difference between the two depicted in Figure 7-21 (c) suggests a small 4-D anomaly at the Cardium reflection. This is in contrast to the difference section corresponding to Experiment 1 (Figure 7-14 (a)) of the ODR modelling in which the difference is weak. This could be attributed to the higher bandwidth of the VSP data, i.e. dominant frequency of 60 Hz, in comparison to the 30 Hz employed in the ODR modelling. Note that aside from the Cardium event, the CO_2-fluid replacement effect on deeper seismic events, e.g. the Viking reflection also seems to be insignificant.

The 4-D anomaly is far more obvious in Figure 7-22 which depicts the processed synthetic VSP seismograms corresponding to Scenario II. The time-lapse anomaly is most clearly visible at the Cardium reflection in the difference section (Figure 7-22 (c)). The induced effect on the Viking events is, also, more prominent than in Scenario I. Once again, the higher frequency bandwidth seems to cause the 4-D anomaly to be more visible in the VSP sections than in those associated with the ODR (Figure 7-15) and the ERFD (Figure 7-18) modelling schemes.

The results from Scenarios I and II are simultaneously presented in a quantitative manner in Figure 7-23. The PRED and NRMS repeatability metrics of the Cardium event as well as the entire trace at each common-depth point (CDP) are plotted in Figure 7-23 (a) whereas the Cardium event cross-correlation time shift is given in Figure 7-23 (b). Table 7-8 summarizes the average value of these attributes. As previously noted under Section 7.2.3.1.1, Scenario II exhibits a stronger response towards the CO_2-fluid replacement in comparison to Scenario I as manifested in the form lower PRED magnitude and higher NRMS magnitude (Table 7-8). This is thought to be most likely due to the increased CO_2 saturation thickness column, i.e. the effective reservoir unit (9 m) versus the upper sandstone unit (3 m).

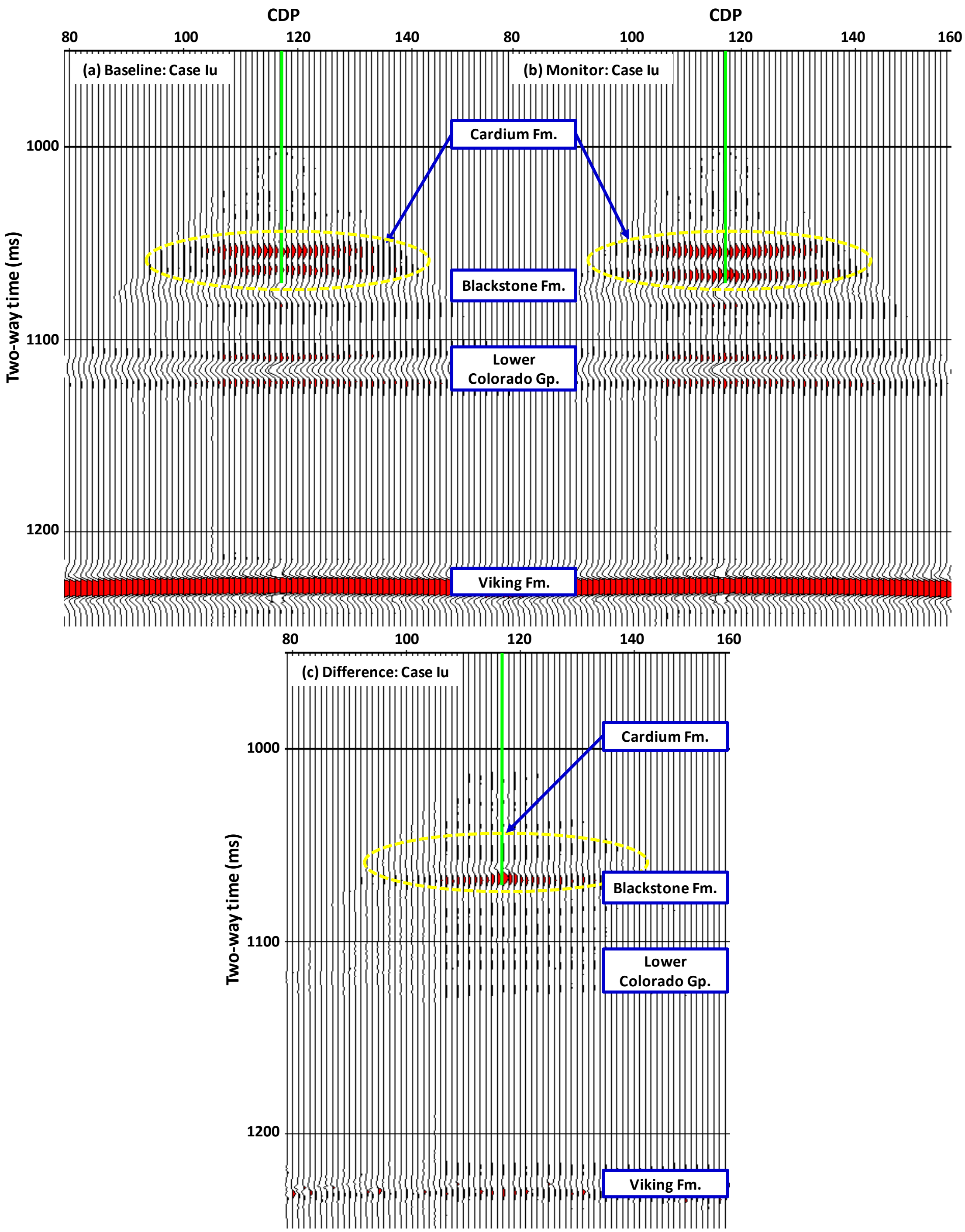

Figure 7-21: The VSP model response of the 2-D model in Figure 7-20 (a) before, and (b) after CO_2-fluid replacement assuming 40% uniform CO_2 saturation in the upper sandstone reservoir unit of the Cardium Formation (Case Iu). The difference between (a) and (b) is shown in (c). The dashed yellow ellipse encloses the Cardium Formation. The green line shows the location of the borehole. See Figure 7-17 for the 2-D acoustic geologic model. Gp.: group; Fm.: formation. The amplitude scale is the same in these and subsequent seismograms. 10 common-depth points (CDPs) = 50 m.

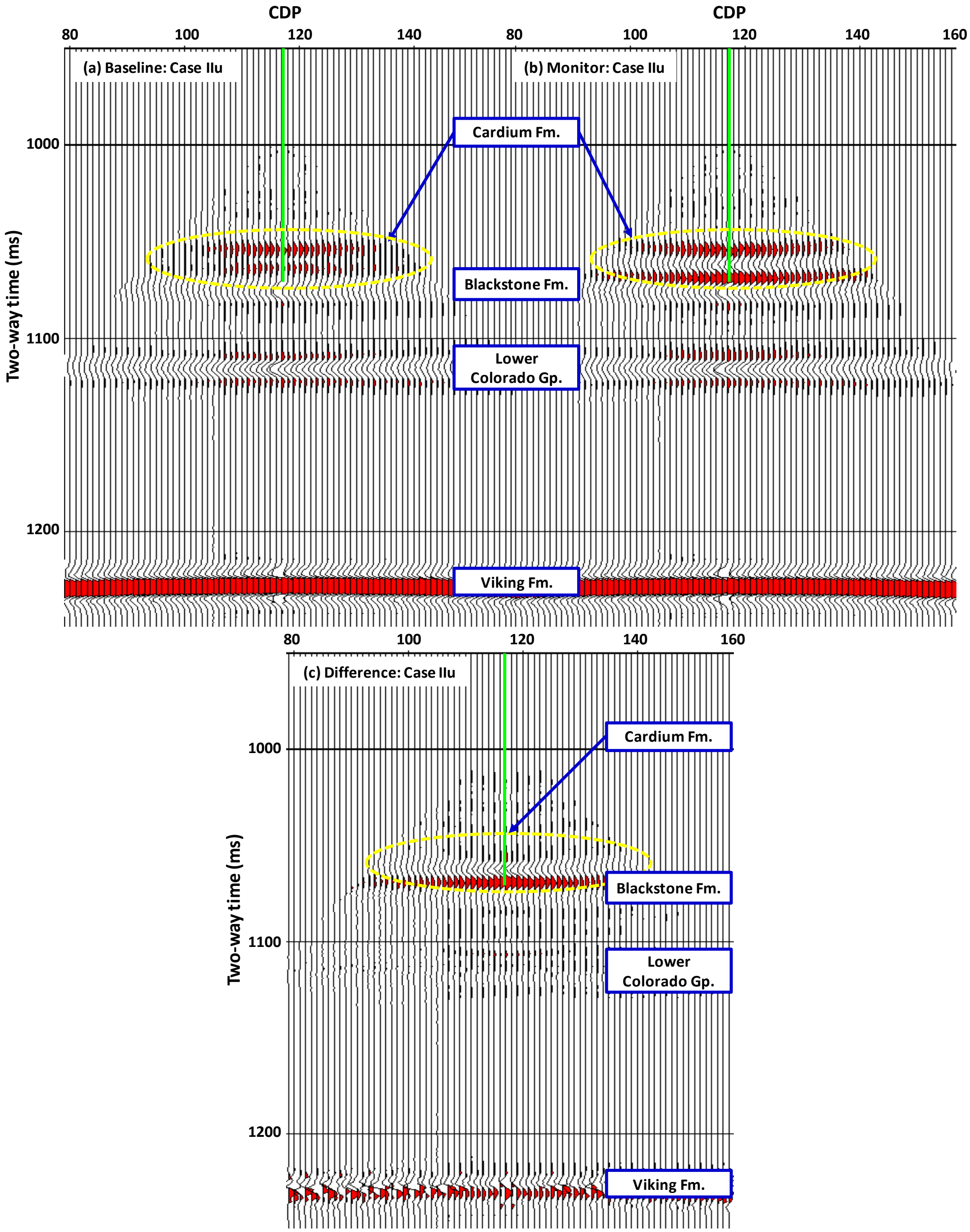

Figure 7-22: The VSP model response of the 2-D model in Figure 7-17 (a) before, and (b) after CO_2-fluid replacement assuming 40% uniform CO_2 saturation) in the effective reservoir unit of the Cardium Formation (Case IIu. The difference between (a) and (b) is shown in (c). The dashed yellow ellipse encloses the Cardium Formation. The green line shows the location of the borehole. See Figure 7-20 for the 2-D acoustic geologic model. Gp.: group; Fm.: formation. The amplitude scale is the same in these and subsequent seismograms. 10 common-depth points (CDPs) = 50 m.

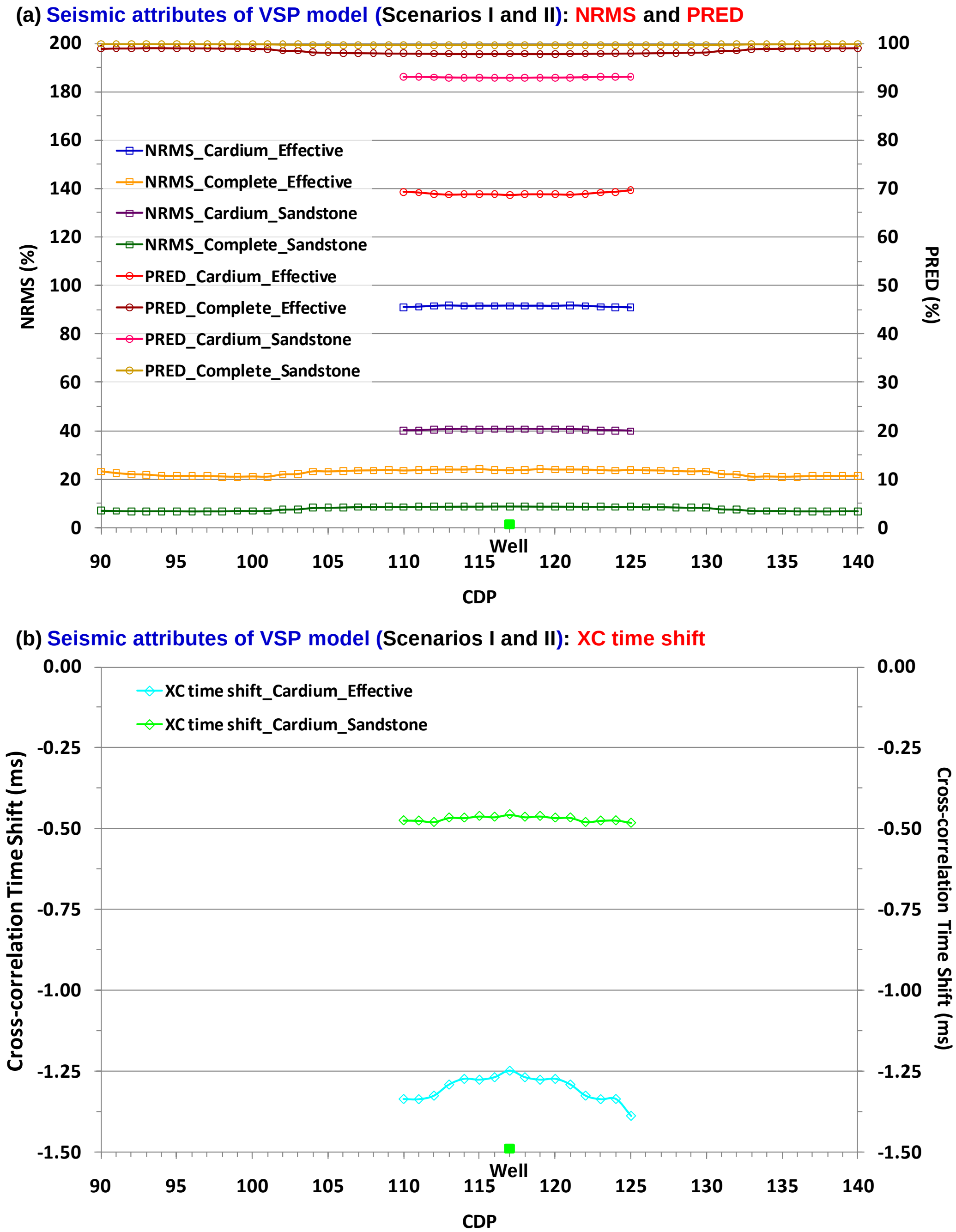

Figure 7-23: (a) Repeatability of the VSP synthetic seismograms shown in Figure 7-21 and Figure 7-22; (b) Cardium event cross-correlation (XC) time shift. NRMS and PRED were computed using two windows: a 100 ms enclosing the Cardium event and a long window encompassing the entire trace (Complete). Scenario I: FSM on sandstone unit (Case Iu); Scenario II: FSM on effective reservoir unit (Case IIu).

Table 7-8: Average PRED and NRMS of the Cardium and the entire trace corresponding to the VSP synthetic seismograms shown in Figure 7-21 and Figure 7-22.

Seismic Event	Scenario I		Scenario II	
	Average PRED (%)	Average NRMS (%)	Average PRED (%)	Average NRMS (%)
Cardium	93.12	39.88	69.43	90.56
Entire Trace	99.64	8.61	97.91	23.68

As for the Cardium event cross-correlation time shift, there are some differences between the VSP and the ODR modelling schemes; perhaps for the same reasons mentioned in the previous paragraph, i.e. difference in the frequency bandwidth. Nonetheless, the magnitude of time shift is small compared to the amplitude-based attributes, namely PRED and NRMS. Therefore, and as initially observed under the WASP ODR modelling in Section 5.3.3.1, the seismic response appears to be frequency-dependent as exhibited when comparing the repeatability of Scenarios I and II (Figure 7-23) with their counterparts, i.e. Experiments 2 (Figure 7-14) and 3 (Figure 7-15), in Section 7.2.3.1.1.

7.3 Discussion

As presented throughout Section 7.2.2.2, the FSM results from all the investigated realizations - with exception of Case III - show a reasonable change in the P-wave speed and acoustic impedance up until the 40% saturation where the frequently referred to plateau is reached. So, the notion of insufficiency in the contrast between the physical properties of the in-situ fluid and the injected supercritical CO_2 in the PCEP study area as postulated under Section 6.6 does not seem to be compelling. In addition to being discernible, there is a striking similarity in the magnitude of change in the acoustic properties between Case Iu (uniform saturation in the upper sandstone unit) and Case IIu (uniform saturation in the effective reservoir unit). However, the level of perceptibility might be dramatically diminished as the saturation moves towards patchy-like saturation or if the GOR ratio provided is not representative of the in-situ conditions.

The AVO response of the Cardium Formation presented in Section 7.2.3.1.1, which seems to belong to Class II AVO anomalies, is extremely weak (Figure 7-11 and Figure 7-12). This is rather anticipated as the Cardium reflection is a low-impedance contrast. Hence, this might emphasize the cause for the lack of a reliable AVO anomaly in the analysis undertaken by Chen (2006) when using pre-stack CDP gathers obtained from the field data. Furthermore, the AVO response seems to be affected by the thin-bed tuning as demonstrated under Experiment 0, where the seismic amplitude decreases with offset but rather appears to increase with CO_2 saturation.

The results from the stacked responses in Experiments 2 (Figure 7-14) and 3 (Figure 7-15) indicate that the effect of the CO_2 saturation thickness is profound. For instance, the repeatability metrics of Experiment 1 invoking Case Iu of the FSM suggest a very small change in the Cardium event PRED (~ 99%) and a very weak change in the NRMS (~ 17%). In contrast, the change is substantial when Case IIu of the FSM modelling was employed in the ODR modelling as demonstrated in Experiment 2. In this case, the NRMS high value of ~ 60% whereas the change in the PRED magnitude (90%) is less profound. The difference in the 4-D effect between Experiments 2 and 3 is, also, visible in the seismic amplitude cross-plot (Figure 7-16). In all the experiments, the time shift is low and, therefore, unreliable for delineating the CO_2 plume.

The analysis from Experiment 2 was further investigated using the ERFD modelling scheme (Figure 7-18) introduced in Section 7.2.3.1.2. The difference seismogram (Figure 7-18 (c)) in this modelling scheme exhibit a weak time-lapse anomaly between the baseline and monitor based on Case IIu of the FSM realizations. Recall that the ERFD modelling assumes a 40% uniform CO_2 saturation in the 9 m effective reservoir unit comprised of the Cardium conglomerate, upper sandstone, upper shale and middle sandstone units. As for the quantitative attributes, the repeatability metrics display what seems to be a significant change in magnitude (e.g. NRMS ~ 50%) when computed over a 100 ms window encompassing the Cardium reflection (Figure 7-19). However, when PRED and NRMS were computed over the deep marker (Viking event) and the entire traces, the magnitude of change became insignificant, i.e. maximum change in PRED and NRMS were ~ 100% and ~ 5%, respectively (Figure 7-19 and Table 7-6). Of course, the shallow marker (Ardley event), is above the Cardium reservoir and, therefore, is exactly repeatable as demonstrated by the PRED and NRMS of 100% and 0%, respectively. When compared with the results from Experiment 2 of the ODR modelling scheme at the same CO_2 saturation level (40%), the repeatability of the Cardium reflection in the ERFD modelling exhibits agreement, as shown by the similarity in the magnitudes of the PRED ~ 92% and NRMS ~ 50%.

In addition, the ODR and ERFD modelling schemes were complemented by the VSP ray trace modelling. In the VSP context, two scenarios were considered: Scenario I and Scenario II. Scenario I corroborated the results from the ODR modelling corresponding to Experiment 1, which invokes the results of Case Iu of the FSM realizations. Similarly, Scenario II served in substantiating the results from Experiment 2 which is based on the results from Case IIu of the FSM realizations. The VSP modelling, also, served in revisiting the frequency-dependence as first observed under the WASP ODR modelling in Section 5.3.3.1.

The difference VSP section corresponding to Scenario I show a weak time-lapse response (Figure 7-21 (c)) that, nonetheless, is more visible than that associated with Experiment 1 of the ODR modelling (Figure 7-14 (a)). Furthermore, the magnitude of the repeatability metrics of the Cardium event are higher in the VSP modelling scheme (Figure 7-23) than in the ODR modelling scheme (Figure 7-14 (d) and (e)). This is most visible in terms of the NRMS which seems to have increased by ~ 20% whereas the change in the magnitude of the PRED is not as much (~ 6% decrease) since the magnitude of Cardium cross-correlation time shift is still very small. The same observations in regard to the NRMS, PRED and cross-correlation time shift can be extended to the comparison between the results from Scenario II (Figure 7-22 and Figure 7-23) and Experiment 2 (Figure 7-15). However, a major distinction exists between Experiment 1/Scenario I on one hand and Experiment 2/Scenario II on the other in terms of the perceptibility. Clearly, the magnitudes of the amplitude and time-based attributes are far more prominent in Experiment 2/Scenario II, which assume uniform CO_2 saturation in the effective reservoir unit (Case IIu). For instance, see the comparison between Scenarios I and II in Table 7-8.

Combined together, the Cardium refection repeatability metrics and cross-correlation time shift show a very good agreement between the various numerical modelling schemes. The minor difference could be attributed to the difference in the frequency bandwidth between the ODR and ERFD modelling schemes on one hand and the VSP modelling scheme on another. Furthermore, some of the differences associated with the ERFD modelling scheme could be attributed to F-D artefacts, such as numerical dispersion, whereas the differences associated with VSP modelling scheme could be a result of the limited aperture at the reservoir. In both schemes, minor processing artefacts are not completely implausible.

As observed under the WASP ODR modelling, the seismic response seems to be frequency-dependent as can be seen by comparing the repeatability metrics of Experiment 1 (Figure 7-14) and Scenario I (Figure 7-23) or Experiment 2 (Figure 7-15) and Scenario II (Figure 7-23). In regard to the higher magnitude of PRED and NRMS when computed over the reservoir (Cardium event) in comparison to deeper events and the entire trace, this seems to be due to the PRED and NRMS sensitivity to the length of the window used in the statistical analysis, which tends to amplify the 4-D effect when restricted to the zone of change (reservoir). Therefore, it is thought to assess the repeatability magnitude at the zone of interest as well as the entire traces.

Throughout the numerical modelling undertaking in Section 7.2.3, the seismic responses of two FSM realizations were investigated. Unfortunately, no definite answer could be provided as which realization is more accurate even when invoking independent data, namely geological mapping (Dashtgard et al., 2006), geochemical monitoring (Johnson (2010) and reservoir data (Lim and Gunter, 2008). One could possibly reconcile both cases by postulating that Case IIu dominates locally at the injection wells whereas Case Iu takes over elsewhere in the local-scale study area. Such statement could be justified by the following:

- The discrete high-resolution reservoir fluid composition analysis at the injection wells (see Figure 6-69) which seems to suggest a very high CO_2 saturation at those locales.
- However, one has to keep in mind that results derived from reservoir fluid analysis are based on discrete control points. Furthermore, certain assumptions were made in estimating the CO_2 plume distribution away from

the control points and, therefore, the there is some level of uncertainty associated as one moves laterally away from the well location.

- As for Case Iu, it could be argued that buoyancy effect might drive the injected supercritical CO_2 toward preferential flowing in the upper sandstone unit away from the injection wells.

The results of the numerical simulations associated with Case IIu (Figure 7-18 and Figure 7-22) suggest a modest 4-D effect that - in principle - should be unambiguously detectable. In contrast, the extremely weak time-lapse response associated with the VSP simulation invoking Case Iu (Figure 7-21 (c)) resembles that observed in Line 1 of the field data (Figure 6-25 (c)). However, there are doubts as whether or not the observed true-like 4-D anomaly in Figure 6-25 (c) is credible as it could not be substantiated by results from any of the various seismic attributes invoked in the analysis Chapter 6.

There is non-uniqueness as to whether Case Iu or Case IIu is more dominant. For instance, the average NRMS of the CDP-transformed field VSP data (Figure 6-25 and Table 6-4) display an average of ~ 32% which is closer to that NRMS of Scenario II (~ 24%) rather than Scenario I (~ 9%) . In addition, the NRMS of the Cardium event corresponding to Line 1 of the 2-D surface seismic data (Figure 6-14) suggest an average magnitude of ~ 50%. Similarly, the average NRMS of the Cardium reflection corresponding to the favourable ERFD simulation invoking Case IIu suggest an average magnitude of ~ 50%. So, although the difference synthetic VSP seismogram associated with Scenario I in Figure 7-21 (c) seems to visually better resemble the field data, the repeatability metrics suggest otherwise. In any case, there are two important statements to be made:

- The notion that Scenario II (or Case IIu) is the most likely mechanism should not be taken for granted as one might question the effect of the gaps in the source positioning as well as the processing-related artefacts associated with the field data, which compromise the observations derived from the field data.

- Likewise, the results derived from the numerical simulations is not perfect either and are subject to many assumptions as discussed throughout Section 3.5.2.

The analysis undertaken in Chapter 7 combined with the observations presented throughout Chapter 6 suggests a lack of an unambiguously discernible 4-D anomaly pertaining to the injected supercritical CO_2 in the PCEP field data. This is interpreted to be due to the confinement of the injected supercritical CO_2 to the thin upper sandstone unit of the Cardium Formation. This is manifested in the numerical forward seismic modelling results based on Case Iu of the FSM realizations. That is, Experiment 1 in the case of the ODR modelling scheme and Scenario I in the VSP ray trace modelling scheme.

One argument that might emerge is that the results from the numerical simulations indicate that VSP data should be more robust in delineating the CO_2 plume. In that case, the lack of a prominent 4-D anomaly could be attributed to some additional reasons. Those being the limited receiver aperture alongside the gaps in the source positioning as discussed in Chapter 6. The effects of these acquisition-related factors as well as multiples were not considered and could constitute a component of future work.

7.4 Summary

- The results from the Gassmann FSM realizations (Cases Iu, IIu and IIp) suggest a discernible change (~ 5%) in the acoustic properties (predominantly in the P-wave speed) of the Cardium Formation due to CO_2-fluid replacement. The only exception being the unlikely realization corresponding to Case III which incorporates the effect of in-situ gases.
- The synthetic forward response of the amplitude variation with offset (AVO) of the Cardium Formation as a function of uniform CO_2 saturation in the 3 m upper sandstone unit (Case Iu) is extremely weak, which might explain the lack of a discernible 4-D anomaly in the AVO inversion undertaken previously by Chen (2006).

- The results from Experiment 1 of the stacked offset-dependent reflectivity (ODR) modelling schemes indicate that the time-lapse response is essentially undetectable under the current circumstances if the CO_2-fluid replacement is uniformly confined to the thin upper sandstone unit (Case Iu).
- The magnitude of the 4-D effect increased reasonably in the results corresponding to Experiment 2 of the ODR modelling in which the uniform CO_2 saturation was assumed in the effective 9 m reservoir unit (Case IIu) comprised of the Cardium conglomerate, upper sandstone, upper shale and middle sandstone units.
- The results from the exploding reflector finite-difference (ERFD) modelling scheme resembling the 2-D surface seismic experiment suggests a small time-lapse anomaly.
- The results from Scenario I of VSP simulations, which is based on Case Iu of the FSM realizations, exhibit a weak time-lapse anomaly. The results from Scenario II invoking Case IIu of the FSM seem to offer a better delineation of the CO_2 plume.
- In all the seismic modelling schemes, the magnitudes of the time-based attributes were found to be extremely small and, ultimately, not a reliable indicator of the CO_2 plume.
- The amplitude-based attributes, especially NRMS, show higher sensitivity toward the CO_2-fluid replacement. The NRMS magnitude tends to be highest when the analysis window is restricted to the reservoir zone, i.e. Cardium event, but long window should, also, be invoked in assessing the perceptibility of the 4-D anomaly.
- In addition to being frequency-dependent, the seismic response of the Cardium Formation is dominated by thin-bed tuning.
- Overall, there is a good agreement between the results derived from the various modelling schemes implemented, i.e. ODR, ERFD and VSP.
- Combining the observations in Chapters 6 and 7 seem to indicate that the lack of an unambiguously discernible delineation of the injected supercritical CO_2 could

be attributed to the plume being confined to the thin upper sandstone unit of the Cardium Formation.

CHAPTER 8: CONTRIBUTIONS, CONCLUSIONS, RECOMMENDATIONS AND FUTURE WORK

8.1 Contributions

Contributions achieved in this dissertation are summarized below:

1. Assessed the suitability and sustainability, in the framework of reflection surface seismic and vertical seismic profile (VSP) techniques, of the Cardium Formation at the Pembina-Cardium CO_2-EOR Pilot Project (PCEP) site and the Nisku Formation at the Wabamun Area CO_2 Sequestration Project (WASP) study area for CO_2 sequestration. Those are two geologic formations that are advocated to be major players in the implementation of the carbon capture and storage (CCS) technology in the Western Canadian Sedimentary Basin (WCSB) in west-central Alberta.
2. Investigated the effects of CO_2 saturation, rock composition and frequency on the time-lapse seismic response.
3. Arrived at a better understanding of the role and limitations of the reflection surface seismic and VSP techniques in CCS site characterization and time-lapse monitoring at the study areas in particular and the WCSB in general.
4. Developed and implemented of an approach for regional site characterization and time-lapse monitoring, which can also be used for prospective CCS projects in the WCSB in Alberta in particular and elsewhere in general.
5. Specifically to the PCEP are the followings:
   i. Demonstrated the containment of the injected CO_2 to the Cardium Formation.
   ii. Provided a better understanding of the lack of an unambiguous 4-D anomaly related to CO_2 plume by incorporating analysis of the field data, rock physics, numerical modelling and independent data.
   iii. Illustrated how the integration of geochemical and petrophysical data influences the results of the Gassmann fluid substitution modelling fluid (FSM) and, therefore, decisions related to the feasibility of time-lapse seismic monitoring.
6. In the case of WASP, the following contributions were achieved:

i. Mapped the Nisku Formation, delineating its character and identifying favourable injection zones.

ii. Identified geologic discontinuities, in the form of karsting and sinkholes, primarily in the Wabamun Formation and the associated footprint effect on the Nisku event.

iii. Estimated the magnitude of an induced time-lapse effect due to a hypothetical CO_2 injection and the feasibility of its detection using a surface seismic survey at different frequency bandwidth.

8.2 Conclusions

As for site characterizations and based on the WASP undertakings, the following conclusions can be made:

- Regional 2-D seismic data can be very useful in delineating long wavelength features and different paleogeographic environments. In the WASP case, the latter is depicted in the delineation of the transition from the Nisku continental shelf to the Nisku basin environments.
- In addition to mapping the local and regional continuity of Nisku Formation, the seismic data was shown to be extremely useful in identifying geologic discontinuities in the area, such as karsting and sinkholes, that could compromise CO_2 storage integrity.
- Seismic amplitude and attributes derived hereof, such as acoustic impedance, can provide significant information pertaining to favourable zones that could be developed for CO_2 sequestration projects.
- There is an element of an ambiguity in differentiating whether seismically derived pseudo-porosity is caused by increase the volume of pore space or lithology. Therefore, it is important to corroborate the results from the seismic characterization with that from petrophysical analysis. In the WASP study, a good qualitative correlation was observed between the seismically estimated pseudo-porosity and petrophysically derived porosity-permeability favourable zones. Thus, reducing the uncertainty.

- In terms of time-lapse monitoring, undertaking fluid substitution modelling (FSM) combined with numerical forward seismic modelling is extremely important. In the WASP case, the results suggest a small CO_2-related 4-D anomaly that is at the threshold of seismic detection limit using P-wave surface seismic survey. Of course, vertical seismic profile (VSP) technique should offer better detection locally around the VSP well.
- Converted-wave data was found to be less useful in mapping the hypothetical CO_2 plume based on the FSM results. The only exception is if Lamda-Mu-Rho (LMR) transformation was undertaken. However, obtaining good quality PS-wave data and then extracting reliable amplitude information from it, leave aside inverse modelling ambiguities, is difficult.
- Converted-wave data may play an important role in delineating pore pressure change due to CO_2 injection.

As for the PCEP time-lapse monitoring, the conclusions can be summarized as follows:

- Even with careful survey design and data acquisition, it was be difficult to obtain highly repeatable 4-D seismic signal as part of CCS MMV programs involving sites in developed oil fields due, for instance, to infrastructure developments.
- Obtaining an unambiguous 4-D CO_2 anomaly in depleted hydrocarbon (HC) reservoirs was not possible in part due to the many complex processes, such as CO_2-HC interaction.
- Time-based attributes, e.g. time shift, can be: (i) large as in Sleipner project, (2) small as in Weyburn CO_2-EOR project, or (iii) extremely small, i.e. below the detection limit, as in the PCEP case.
- Of all the time-based attributes, P/S wavespeeds ratio (α/β) seems to be very robust. In the PCEP study, α/β was not sufficiently reliable due to the poor quality of multi-component seismic data.
- Even in structurally simple geologic environments, it can be hard to obtain a reliable converted-wave seismic data. In the PCEP case, both time-based and

amplitude-based attributes derived from PS-wave data were extremely weak and, therefore, the results derived from it were inconclusive.

- Amplitude-based attributes, such as NRMS and acoustic impedance, are more sensitive than time-based attributes and, therefore, are considered more reliable in drawing conclusions about the injected CO_2.
- The seismic response of CO_2 can be affected by many factors. Some, e.g. CO_2 saturation effect, are more obvious than others, e.g. frequency and thin-bed tuning. In both cases, the associated response may be non-unique.
- The FSM and numerical modelling results can assist in substantiating the field observations. In the PCEP case, the modelling results indicate that CO_2 confinement to a thin layer within the reservoir due to preferential flow and buoyancy phenomena is the, perhaps, the primary cause for the lack of an unambiguous 4-D anomaly.
- The success of seismic techniques in CO_2 4-D monitoring depends largely on site-specific and reservoir conditions. In the PCEP study, the seismic component of the MMV program was deemed unsuccessful in identifying the injected CO_2 due to the lack of consistent and conclusive 4-D CO_2 anomaly at the Cardium reservoir in the seismic data.
- Seismic sensitivity to upward migration of injected CO_2 increases substantially as the plume moves towards the surface "leakage". Crucially in the PCEP case, there is no evidence of such migration in the surface seismic data. This observation was, independently, corroborated by data from the groundwater and environmental monitoring components of the MMV program.

In CO_2 sequestration projects, it is important to gain some perspective on the sensitivity towards the CO_2-induced time-lapse anomaly. Figure 8-1 offers an insight into the sensitivity of the 4-D seismic response corresponding to the two projects investigated in this dissertation as function dry rock and fluid compressibility contrast (Lumley, 2010). In addition, the 4-D sensitivity belonging to the two industrial examples presented in Section 1.3.5 is depicted in the diagram for comparison. Seismic methods have been used for decades in hydrocarbon exploration and reservoir monitoring and, therefore, are highly developed. However, as with any other technique, seismic methods have their inherited limitations. It is crucial to understand these limitations by gathering relevant information and then invoking fluid substitution and numerical modelling. When CO_2 monitoring is concerned, there must exist a sufficient contrast in the physical properties between the in-situ fluids and the injected CO_2 for seismic monitoring to be successful. This is manifested, primarily in the form of rock and fluids compressibility contrast. There are other factors as well that will be introduced in the next section.

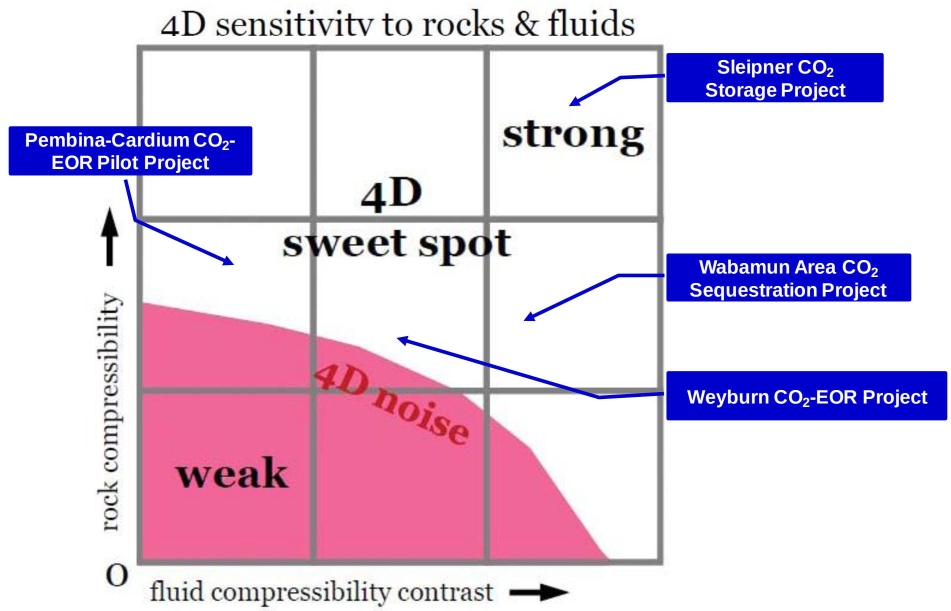

Figure 8-1: Sensitivity to the CO_2-induced 4-D response based on dry rock compressibility and fluid compressibility contrasts given by Lumley (2010). The shaded pink overlay represent the area dominated by non-repeatble 4-D noise. The 4-D sensitivity corresponding to the indutrial examples presented in Section 1.3.5 as well as those investigated in this dissertation is depicted by the blue callout shapes.

8.3 Considerations and Recommendations

The following recommendations can be made by corroborating the observations made in this dissertation with those obtained from other case histories in the literature:

- It is important to understand: (1) the physical properties of CO_2 at the reservoir/aquifer pressure and temperature (hydrodynamic and thermodynamic), and (2) the physiochemical interaction between CO_2 and the reservoir rock and fluids (rock physics and geochemistry).

- Rock physics and fluid substitution modelling (FSM) should be invoked in predicting changes in the elastic properties as a result of introducing CO_2 into the reservoir/aquifer. For in-situ seismic bandwidth (surface seismic, VSP and cross-well tomography), Gassmann-based approaches seem to be among the most suitable FSM formulations available based on literature review and personal communication with world-class rock physicists.
- Numerical seismic modeling should be integrated with rock physics using appropriate FSM schemes. In addition, deterministic or stochastic scenario approaches should be considered to alleviate the uncertainties involved.
- Reservoirs or aquifers with high porosity and low dry rock incompressibility are preferred for CO_2 monitoring perspective. For example, sedimentary geologic formations composed of unconsolidated sediments or containing significant fractures whether onshore or offshore. In contrast, reservoirs or aquifers that are made of stiff rock, such as tight carbonate, are less favourable.
- Depleted hydrocarbon (HC) reservoirs seem to pose serious challenges in 4-D seismic monitoring in comparison to saline aquifers due to difference in the nature of the reaction between CO_2-HC on hand and CO_2-brine on the other.
- Reservoirs with high gas-oil ratio (GOR) and saline aquifers with high gas-water ratio (GWR) offer poor environments for 4-D seismic monitoring and, therefore, are considered unfavourable.
- Results from industrial examples, such as the Sleipner project, seem to suggest that conventional 4-D P-wave surface seismic is more successful in CO_2 monitoring in saline aquifer. In particular, offshore geologic formations seem to be more sensitive to CO_2 injection due perhaps to the typically lower overburden pressure compared to onshore aquifers.
- Whether working in developed venues or new frontiers, one should always undertake CO_2 sequestration feasibility analysis using an appropriate workflow before commencing.

- Each CO_2 sequestration project has elements that are unique and the level of success of a given project will depend on many factors as presented throughout this section.
- Pertaining to seismic methods, one has to consider the following:
  - → Existence of detectable contrast between the injected CO_2 and the in-situ fluids as well as reservoir architecture.
  - → Survey design and data acquisition needs to be optimized, e.g. coverage versus cost.
  - → Adaptation of appropriate data processing approach in order to preserve the typically weak time-lapse CO_2 anomaly.
  - → Pertinent interpretation workflow using qualitative and quantitative attributes.
- Obtaining good quality multi-component seismic data is important in site characterization, e.g. delineation of lithology and anisotropy. In addition, the 4-D information provided by the multi-component data pertaining to identifying/tracking the injected CO_2 as well as in the differentiation between the change in differential pressure and CO_2 saturation may be substantial.
- When possible, corroboration of seismically driven data with independent data. For example, reservoir fluid composition can be used to corroborate CO_2 movement in the reservoir whereas near-surface and atmospheric monitoring can be used to assess potential upward migration of the CO_2 plume.
- Also, integration of geophysical and reservoir data should be considered where the former could serve in constructing 3-D geologic model that could be used by the latter in prediction and history matching involving injected CO_2 and pressure changes.
- CO_2 sequestration is a multi-disciplinary (Figure 1-5) undertaking and it is crucial to understand the effect of the various processes. This can be achieved by gathering the necessary information and involving the various relevant disciplines (team work) in order to better assess the role of processes, such as storage integrity, porosity, permeability, storage capacity, pressure regime, reservoir

architecture, migration paths, rock and fluids compressibility, and contribution of the various trapping mechanisms.

Figure 8-2 depicts a mosaic 4-D sensitivity diagram that incorporates some of the effects of the various CO_2 sequestration disciplines presented in Section 1.3.1. The premises for this sensitivity diagram emerge from some of the observations made while working on this dissertation. It is, also, motivated by the rock and fluids 4-D sensitivity diagram introduced by Lumley (2010) which was presented in the previous section (Figure 8-1). Crucial to understand is that the 4-D sensitivity diagram in Figure 8-2 is not all-encompassing and there are some processes that are not explicitly listed but may still play an important role in CO_2 sequestration. For instance, the reader is referred to the criteria pertaining to site selection and basin sustainability presented in Section 2.1 (Table 2-1 and Figure 2-4).

In Figure 8-2 (a), complexity refers to the presence processes that may originate in the overburden, such as multiples and scattering, or features, such as folds, faults, or embayment (in reef environments) that may constitute the reservoir/aquifer itself or the cap rock or exist in the overburden. These may affect CO_2 flow in the reservoir/aquifer itself and/or the reconstruction of the final processed image. The effect of the reservoir thickness was examined in the PCEP modeling in Section 7.2.3.1.1 in which the CO_2 thickness column and thin-bed tuning effects were denoted. Reservoir uniformity could refer to phenomena, such as homogeneity and isotropy, that may significantly affect the CO_2 flow as well as the imaging processing.

The diagram in Figure 8-2 (b) depicts what has been demonstrated in this dissertation as part of the rock physics and fluid substitution modeling (Section 5.3.2 and Section 7.2.3.1.1) and other studies as well, e.g. Avseth et al. (2005) and Lumley (2010), that the higher the contrast between the injected supercritical CO_2 and the in-situ fluids, the stronger the 4-D sensitivity. In addition, the 4-D sensitivity is directly proportional to the dry rock, or porous rock frame, compressibility as discussed under Section 5.3.2. One important phenomenon that is not depicted in the diagram is that the seismic signal might not differentiate between the multi-phase CO_2.

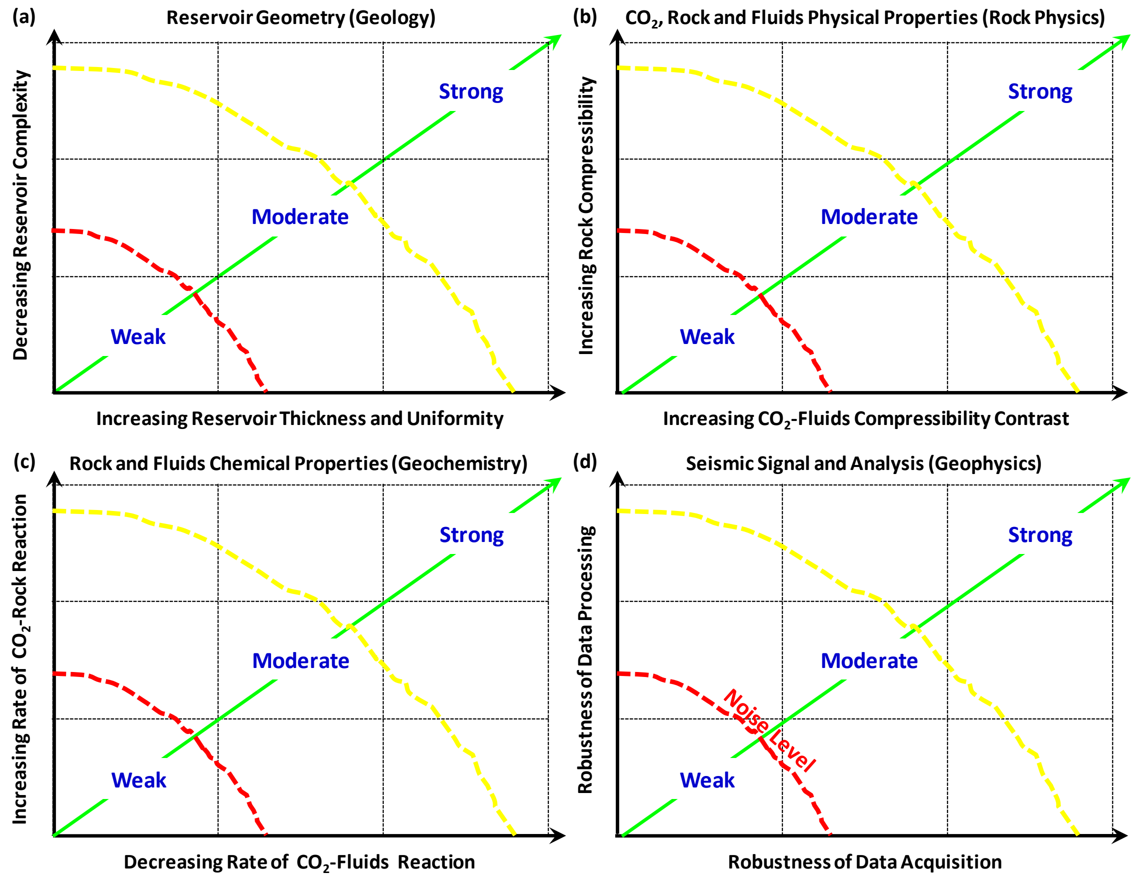

Figure 8-2: Mosiac diagram depicting, arbitrarily, the sensitivity of the CO_2-induced 4-D response to (a) reservoir geometry (geological component), (b) CO_2-rock and fluid interaction (rock physics component) which is modified after Lumley (2010), (c) CO_2-rock and fluid interaction (geochemical component), and (d) seismic signal and analysis (geophysical component). The green diagonl line indicates the direction of highest increase in 4-D sensitivity. Because of the uncertainity involved, the transitions between the senstivity zones and the noise level are depicted by a dashed, rough curve.

As for the 4-D sensitivity dependence on the geochemical component, it was illustrated in this dissertation by invoking the results from the simulation undertaken by WASP geochemistry team that chemical reaction between the injected CO_2 and carbonate rock over typical CCS projects operational timeframe is not always an issue (Section 5.3.2.8). Nonetheless each CO_2 sequestration site is different and it is important to keep in mind the complexity and non-uniqueness effects. For instance, the increasing rate of the CO_2-rock reaction as depicted in Figure 8-2 (c) could produce more pore space. However, whether or not that induced pore space contributes, constructively, to the overall reservoir porosity depends on where the precipitation, e.g. of calcium ions, occur within the reservoir. In other words, it makes a significant difference whether the precipitants accumulate in non-effective pore space or if they significantly “throttle” existing effective pore space. Furthermore, it is seems unlikely that the seismic signal would differentiate between the injected CO_2 and the in-situ fluids once the former is completely dissolved in the host fluids.

The role of robust 4-D seismic data acquisition and processing portrayed in Figure 8-2 (b) is of paramount importance. As demonstrated in more than one occasion in this dissertation (Chapters 5 and 7), the CO_2-induced 4-D anomaly is typically weak and, therefore, special care has to been taken into consideration in order to preserve the modest time-lapse response so that meaningful interpretation could be achieved. Examples of data acquisition and processing aspects that might fall under this category are given under Section 0. Other entities that might fall under the geophysical component include the type of the seismic experiment being implemented and the associated frequency bandwidth. The role of frequency bandwidth was illustrated in more than instance in this dissertation (Section 5.3.3.1 and Section 7.2.3).

When undertaking a CO_2 sequestration project, it is recommended to assess the validity of the observations - when appropriate - to avoid some of the pitfalls, such as those pertaining to internal inconsistency in the FSM. The reader might recall that the seismic response is very sensitivity to small to intermediate CO_2 saturation as suggested by the Gassmann FSM in this dissertation and other similar work. However, whether this is true or not seems to depend largely on variables, such as the saturation scheme (uniform versus patchy-like) and the reservoir/aquifer conditions. For instance, deducing the type of saturation can be important in deciding when and how frequently the seismic monitoring surveys should be undertaken. Therefore, gaining some perspective on the various processes involved is important in moving towards best practice CO_2 sequestration.

8.4 Challenges and Future Work

Below are some of the current challenges and areas of active/future research:

- Mitigating problems faced when working in developed operational sites where geophysical survey repeatability can be largely affected by infrastructure developments.
- Many complex physicochemical processes, such as CO_2 retention, capillary forces, CO_2-rock interaction, and CO_2-fluid interaction that may cause non-unique observations pertaining to CO_2 saturation in the reservoir/aquifer. In order to better define the effects of these process one need to better understand the role of rock physics, e.g. fluid flow using core measurements, and geochemistry, e.g. CO_2-rock-fluids interaction.
- Quantitative estimation of injected CO_2 through geophysical inversion poses many challenges due to many reasons including difficulties in accurately defining the CO_2 plume and the type of saturation in addition to the over-saturation of the seismic signal beyond ~ 40% CO_2. For instance, studies by Benson (2006), Hoversten et al. (2006) and White (2009) among others suggest that the CO_2-related time-lapse seismic response typically starts to emerge at approximately 3,000 to 5,000 metric tonnes. Other studies suggest that as little as 500 tonnes of supercritical CO_2 could be detected using seismic methods (Chadwick et al., 2006).
- Non-unique saturation response where uniform and patchy saturations could give rise to the same magnitude of change in the elastic properties of the rock. For example, in the PCEP rock physics modeling, the P-wave speed at 65% patchy saturation (Voigt average) is equivalent to that at 10% uniform saturation (Reuss average).
- Discerning a form of relationship between CO_2 saturation and change in elastic properties using laboratory measurements might not be always appropriate due to the frequency dependence, i.e. dispersion. Therefore, there is a need to devise an effective and accurate mechanism to calibrate laboratory and field observations.

- The relationship between CO_2 saturation and compressibility could be further complicated if the rate of chemical reaction between the injected CO_2 and the rock matrix composing the host geologic formation is both rapid and significant.
- In addition, differentiation between the pore pressure and CO_2 saturation is another challenge, especially when it is difficult to obtain good quality multi-component data
- Better understanding of the combined effects of CO_2 injection and anisotropy on the 4-D seismic monitoring is needed.
- Density estimation is, also, difficult because it requires high level of CO_2 saturation as well as high-quality and far-offset seismic reflections.
- Development of robust time-lapse acquisition and processing techniques is essential in order to detect and then extract useful time-lapse signal from multi-component seismic data.
    - → As for data acquisition, the final seismic image depends largely on the quality of the input raw data. Some of the aspects that warrant some consideration include: (i) achieving better source and receiver repeatability, (ii) mitigation of variations in near-surface conditions, (iii) increasing the signal bandwidth by implementing new technologies, e.g. low frequency receivers, and (iv) exploring novel monitoring techniques, such as quasi-real-time monitoring which invoke permanent sparsely-embedded sources and receivers.
    - → From data processing perspective, there are many phenomena that could affect the quality and reliability of seismic data, e.g. non-repeatable noise, internal scattering, wave-mode conversions, multi-pathing and inter-bed multiples. The future research scope could be broad but below are some examples: (i) development of adequately repeatable 4-D processing flow and true-amplitude preserving data processing algorithms, (ii) effective non-repeatable noise attenuation data processing techniques, (iii) imaging the sometimes complex wavefield, e.g. the premise of new imaging methods such as full waveform inversion, (iv) 4-D constrained inversion,

and (v) quantitative estimation of CO_2 which depends largely on the proper handling of all of the preceding processes.

- Although CO_2 sequestration projects may be influenced by the regulatory component of CO_2 sequestration, it is important to achieve a balance between the cost, frequency, and length of monitoring activities and data acquisition and processing cost. For instance, the scope the so-called quasi-real-time monitoring techniques.
- The seismic response can be non-linear and non-unique as emphasized throughout this chapter and as reported by Lumley (2010) among others. These problems can be alleviated by integrating seismic methods with other geophysical methods such as gravity, micro-seismic, electrical and electromagnetic (EM) methods and satellite-based techniques, such as interferometric synthetic aperture radar (inSAR).
- Also, corroboration of geophysical methods with non-geophysical methods, such as geochemical and reservoir simulation methods, is another approach that seems to improve the reliability of the information provided by the geophysical data.

APPENDIX A: INTRODUCTION

A.1. Canada's GHG Sources in 2004

The following pie chart shows Canada's greenhouse gases (GHG) emissions, in CO_2 equivalent, by sectors in 2004 (Environment Canada, 2008). See Section 1.2.

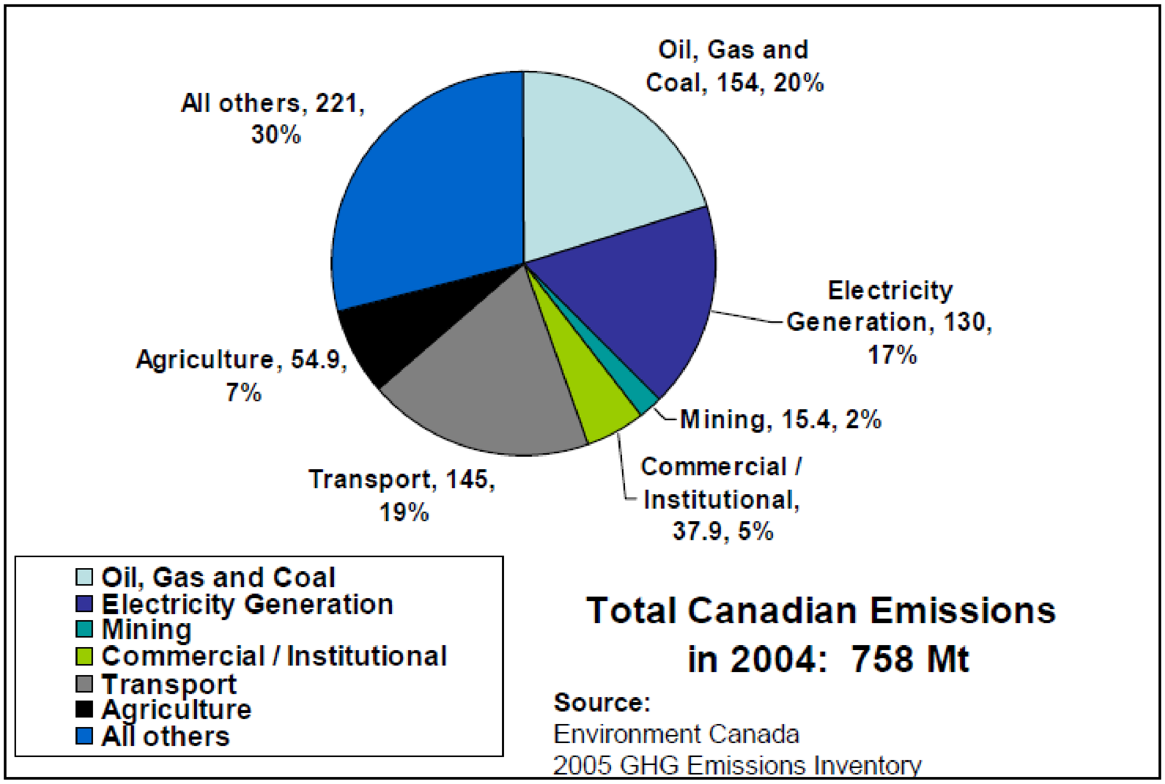

A.2. Alberta GHG Emissions by Sector in 1990 and 2004

The following table shows Alberta (AB) greenhouse gases (GHG) emissions, in CO_2 equivalent, by sectors in 1990 and 2004 (Environment Canada, 2008). See Section 1.2.

	AB
1990 GHG Emissions by Sector[1,2,3]	
Energy	146 000
Industrial Processes	8 080
Solvent and Other Product Use	38
Agriculture	13 000
Land Use, Land-Use Change and Forestry[4]	N/A
Waste	1 500
Total	**168 000**
2004 GHG Emissions by Sector[1,2,3]	
Energy	203 000
Industrial Processes	12 700
Solvent and Other Product Use	48
Agriculture	17 000
Land Use, Land-Use Change and Forestry[4]	N/A
Waste	2 200
Total	**235 000**
Absolute Change in Emissions (kt), 1990–2004	**66 300**
Relative Change in Emissions (%), 1990–2004	39%
Relative Contribution to Absolute Growth in Emissions (%)	43.2%
2004 GHG Emissions Per Capita[1,5,6] (tonnes GHGs/person)	**72.9**
2004 GHG Intensity of GDP[1,7,8] (kt CO_2 eq/$Million GDP)	1.83

Notes:

1 GHG Emissions: Environment Canada (2006), *National Inventory Report — Greenhouse Gas Sources and Sinks in Canada: 1990–2004*.

2 Due to confidentiality and rounding, individual values may not add up to totals (zero values may represent estimated quantities too small to display).

3 Emissions associated with the use of HFCs, PFCs, ammonia, limestone, and soda ash are reported in the national total.

4 All GHG emissions or removals in the LULUCF Sector are excluded from totals and reported only at the national level.

5 Population data: Statistics Canada (2003), *Demographic Statistics*, Catalogue No. 91-213-XIB.

6 National average: 23.39 tonnes per person.

7 GDP data: Informetrica Limited (2006), *Gross Domestic Product (Million 1997 Chained Dollars)*, January 11, 2006.

8 National value: 0.72.

9 GHG Intensity of GDP reported for total territories due to data availability.

kt: kilotonne; N/A: not applicable

APPENDIX B: WASP SEISMIC SITE CHARACTERIZATION II - NUMERICAL MODELLING

B.1. Summary of the Empirical Relations Given in Batzle and Wang (1992)[89]

B.1.1. Seismic Properties of Brine

Batzle and Wang (1992) used a modified version of a polynomial originally presented by Chou (1970) and data compiled by others (Zarembo and Fedorov, 1975; Potter and Brown, 1977) to describe the density of brine as:

$$\begin{aligned}\rho_{\text{brine}} &= \rho_{\text{pure water}} \\ &+ S\left\{0.668 + 0.44S + 10^{-6}\left[300P - 2400PS + T\left(80 + 3T - 3300S - 13P + 47PS\right)\right]\right\}\end{aligned} \quad \text{(I.1)}$$

where P is the pressure (in MPa), T is the temperature (in ^{o}C), S is the salinity (in fractions of parts per million), and $\rho_{\text{pure water}}$ is the density of pure water (in g/cm^3):

$$\begin{aligned}\rho_{\text{pure water}} &= 1 + 10^{-6} \\ &(-80T - 303T^2 + 0.00175T^3 + 489P - 2TP \\ &+ 0.016T^2P - 1.3\times10^{-5}T^3P - 0.333P^2 - 0.002TP^2)\end{aligned} \quad \text{(I.2)}$$

They define the P-wave speed of brine (α_{brine} in m/s) as (Chen et al., 1978; Batzle and Wang, 1992):

$$\begin{aligned}\alpha_{\text{brine}} &= \alpha_{\text{pure water}} \\ &+ S\left(1170 - 9.6S + 0.055T^2 - 8.5\times10^{-5}T^3 + 2.6P - 0.0029TP - 0.0476P^2\right) \\ &+ S^{1.5}\left(780 - 10P - 0.16P^2\right) - 1820S^2\end{aligned} \quad \text{(I.3)}$$

where $\rho_{\text{pure water}}$ is the density of pure water (in g/cm^3) given by Wilson (1959) and is defined as:

$$\alpha_{\text{pure water}} = \sum_{i=0}^{4}\sum_{j=0}^{3} w_{ij} T^i P^j \quad \text{(I.4)}$$

---

[89] Only the fundamental relations used in calculating the P-wave speed and density are presented. The reader is encouraged to refer to their paper for limitations and considerations. The notations used here do not necessarily follow that established under List of Symbols, Abbreviations and Nomenclature. Furthermore, the notations of Batzle and Wang (1992) will be followed in this appendix section except for the P-wave speed (α), density (ρ) and bulk modulus (K) for which the notation theme of the dissertation will be retained.

where the w_{ij} coefficients are given in Table B-1. Recall that the bulk modulus of a given fluid (K_{fluid}) is related to its acoustic wavespeed α_{fluid} and density ρ_{fluid} through the following relation:

$$K_{\text{fluid}} = \rho_{\text{fluid}} \alpha_{\text{fluid}}^2 \tag{I.5}$$

For temperature below 250 ^{o}C, they define the brine viscosity (η_{brine}) as (Kestin et al., 1981; Batzle and Wang, 1992):

$$\eta_{\text{brine}} = 0.1 + 0.333S + \left(1.65 + 91.9S^3\right) e^{-\left[0.42\left(S^{0.8}-0.17\right)^2+0.045\right]T^{0.8}} \tag{I.6}$$

Table B-1: Values of the w_{ij} coefficients for computing the P-wave speed of pure water as given by Batzle and Wang (1992).

w_{00}	1402.85	w_{22}	-2.135×10^{-6}
w_{01}	1.524	w_{23}	1.237×10^{-8}
w_{02}	3.437×10^{-3}	w_{30}	1.487×10^{-4}
w_{03}	-1.197×10^{-5}	w_{31}	-6.503×10^{-7}
w_{10}	4.871	w_{32}	-1.455×10^{-8}
w_{11}	-0.0111	w_{33}	1.327×10^{-10}
w_{12}	1.739×10^{-4}	w_{40}	-2.197×10^{-7}
w_{13}	-1.628×10^{-6}	w_{41}	7.987×10^{-10}
w_{20}	-0.04783	w_{42}	5.230×10^{-11}
w_{21}	2.747×10^{-7}	w_{43}	-4.614×10^{-13}

B.1.2. Seismic Properties of Gas

Batzle and Wang (1992) used a modified version of a relation given by Thomas et al. (1970) to define the gas density (ρ_{gas}) as:

$$\rho_{\text{gas}} = \frac{28.8GP}{ZRT_{\text{a}}} \tag{I.7}$$

where:

$$G = \frac{\rho_{\text{gas}}}{\rho_{\text{air}}} \tag{I.8}$$

$$T_r = \frac{T_a}{94.72 + 170.75G} \tag{I.9}$$

$$T_a = T + 273.15 \tag{I.10}$$

$$P_r = \frac{P}{4.892 - 0.4048G} \tag{I.11}$$

$$Z = aP_r + b + E \tag{I.12}$$

$$E = cd \tag{I.13}$$

$$a = 0.03 + 0.00527\left(3.5 - T_r\right)^2 \tag{I.14}$$

$$b = 0.642T_r - 0.007T_r^4 - 0.52 \tag{I.15}$$

$$c = 0.109\left(3.85 - T_r\right)^2 \tag{I.16}$$

$$d = e^{\frac{-P_r^{1.2}}{T_r}\left[0.45+8\left(0.56-\frac{1}{T_r}\right)^2\right]} \tag{I.17}$$

P and P_r are the pressure and pseudo-pressure (in MPa); T, T_a and T_r are the temperature (in ^{o}C), absolute temperature (in K) and pseudo-temperature (in K); R is the universal gas constant (8.31441 Joule/mole.Kelvin), and G is the gas gravity, or specific density of gas, and is a measure of the ratio of the gas density (ρ_{gas}) to that of air (ρ_{air}) at 15.6 ^{o}C and atmospheric pressure (0.101 MPa). For instance, the CO_2 and air densities at these temperature and pressure are 1.87 kg/m^3 and 1.23 kg/m^3, respectively (Engineering ToolBox, 2008).

The acoustic wavespeed of gas is related to the adiabatic[90] bulk modulus through Equation (I.5) and can be computed using the following relation (Batzle and Wang, 1992; Thomas et al., 1970):

$$K_{\text{gas}} = \frac{P\gamma}{1 - \frac{P_r}{Z}\frac{\partial Z}{\partial P_r}} \tag{I.18}$$

where:

$$\gamma = 0.85 + \frac{5.6}{P_r + 2} + \frac{27.1}{\left(P_r + 3.5\right)^2} - 8.7e^{-0.65(P_r+1)} \tag{I.19}$$

$$\frac{\partial Z}{\partial P_r} = cdm + a \tag{I.20}$$

---

[90] Adiabatic means that no heat is gained or lost with the surroundings.

$$m = -1.2\frac{P_r^{0.2}}{T_r}\left[0.45 + 8\left(0.56 - \frac{1}{T_r}\right)^2\right] \tag{I.21}$$

B.1.3. Seismic Properties of Oil

Batzle and Wang (1992) used a simplified form of a relation by Wang et al. (1988) to describe the acoustic wavespeed of oil with no dissolved gas, i.e. dead oil ($\alpha_{\text{dead oil}}$) as:

$$\begin{aligned}\alpha_{\text{dead oil}} &= 50{,}676\left(77.1 + \text{API}_{\text{dead oil}}\right)^{-0.5} - 3.7T \\ &+ 4.64P + 0.0115\left[0.36\left(\text{API}_{\text{dead oil}}\right)^{0.5} - 1\right]TP\end{aligned} \tag{I.22}$$

where P is the pressure (in MPa), T is the temperature (in ^{o}C), and API is the American Petroleum Institute oil gravity:

$$\text{API}_{\text{dead oil}} = \frac{141.5}{\rho_{\text{oil reference}}} - 131.5 \tag{I.23}$$

where $\rho_{\text{oil reference}}$ is the standard density of oil (in g/cm^3) measured at 15.6 ^{o}C and 0.101 MPa. Note the inverse proportionality between API and oil density. Thus, the denser the oil, the lower the API. Typical API values occur between 5 and 40 (Batzle and Wang, 1992). The density of dead oil ($\rho_{\text{dead oil}}$) at a given pressure is (Dodson and Standing, 1945; Batzle and Wang, 1992):

$$\rho_{\text{dead oil}} = \frac{\rho_P}{\left[0.972 + 3.81\times10^{-4}\left(T + 17.78\right)^{1.175}\right]} \tag{I.24}$$

where the pressure dependence of density (ρ_P) can be computed at a give pressure P (in MPa) using:

$$\begin{aligned}\rho_P &= \rho_{\text{oil reference}} + \left(0.00277P - 1.17\times10^{-3}P^3\right)\left(\rho_{\text{oil reference}} - 1.15\right)^2 \\ &+ 3.49\times10^{-4}P\end{aligned} \tag{I.25}$$

If the oil contains appreciable amount of dissolved gas, it is called live oil ($\alpha_{\text{live oil}}$) and its P-wave speed is calculated using Equation (I.22) but with a reduced API gravity:

$$\text{API}_{\text{live oil}} = \frac{\rho_{\text{oil reference}}}{B_{\text{oil reference}}} - \left[1 + 0.001\left(\text{GOR}\right)\right]^{-1} \tag{I.26}$$

where the gas-oil ratio (GOR) refers to the volume of released gas to that of oil (in litre/litre) at 15.6 ^{o}C and 0.101 MPa and is defined as:

$$\text{GOR} = 2.03G\left\{Pe^{\left[0.02878\left(\text{API}_{\text{live oil}}\right)-0.00377T\right]}\right\}^{1.205} \tag{I.27}$$

Then, $B_{\text{oil reference}}$ is calculated using the following relation (Standing, 1962):

$$B_{\text{oil reference}} = 0.972 + 0.00038\left[2.4\left(\text{GOR}\right)\left(\frac{G}{\rho_{\text{oil reference}}}\right)^{0.5} + T + 1.78\right]^{1.175} \tag{I.28}$$

The density of live oil ($\rho_{\text{live oil}}$ in g/cm^3) is computed using:

$$\rho_{\text{live oil}} = \frac{\left[\rho_{\text{oil reference}} + 0.0012\left(\text{GOR}\right)\right]}{B_0} \tag{I.29}$$

To describe dead oil viscosity ($\eta_{\text{dead oil}}$) as a function temperature and, independently, of pressure, they used the following relation (Beggs and Robinson, 1975):

$$\log_{10}\left(\eta^{T}_{\text{dead oil}} + 1\right) = 0.505y\left(17.8 + T\right)^{-1.163} \tag{I.30}$$

where the superscript T indicates temperature dependence only. The empirical parameter y is given by:

$$\log_{10}\left(y\right) = 5.693 - \frac{2.863}{\rho_{\text{oil reference}}} \tag{I.31}$$

At a given temperature (in ^{o}C), the viscosity of dead oil can be described as (Beal, 1946):

$$\eta_{\text{dead oil}} = \eta^{T}_{\text{dead oil}} + 0.145PI \tag{I.32}$$

where:

$$\log_{10}\left(I\right) = 18.6\left\{0.1\left[\log_{10}\left(\eta^{T}_{\text{dead oil}}\right)\right] + \left[\log_{10}\left(\eta^{T}_{\text{dead oil}}\right) + 2\right]^{-0.1} - 0.985\right\} \tag{I.33}$$

B.2. Peng-Robinson Equation of State (EOS)[91]

The Peng-Robinson EOS (1976) can be expressed in the following form:

$$P = \frac{RT_a}{V_m - b} - \frac{a\alpha}{V_m^2 - 2bV_m + b^2} \tag{I.34}$$

where:

$$a = \frac{0.45724 R^2 T_c^2}{P_c} \tag{I.35}$$

$$b = \frac{0.07780 RT_c}{P_c} \tag{I.36}$$

$$\alpha = \left[1 + \left(0.37464 + 1.54226\mathrm{E} - 0.26992\mathrm{E}^2\right)\left(1 - T_r^{0.5}\right)\right]^2 \tag{I.37}$$

$$V_m = \frac{V}{n} \tag{I.38}$$

$$T_r = \frac{T_a}{T_c} \tag{I.39}$$

where, P is the pressure (in Pa), P_c is the critical pressure (in Pa), T_a is the absolute temperature (Kelvin) defined in the previous section, T_c is the absolute critical temperature (Kelvin), T_r is the absolute reduced (or pseudo) temperature (Kelvin), V is the volume (m^3), V_m is the molar volume (m^3/mole), n is the number of moles of substance, R is the universal gas constant (8.31441 J/mole.K), and E is the acentric coefficient used in characterizing the substances by measuring the non-sphericity of the molecules (Wikipedia: equation of state, 2008). Further information can be found in the Peng-Robinson paper (1976). In general, predicting fluid properties through the Peng-Robinson EOS seem to yield robust results compared to other cubic EOSs (Wikipedia: equation of state, 2008).

---

[91]Similar fashion to that of Section B.1 is adopted here as well, i.e. only the fundamental relations used in calculating the P-wave speed and density are presented. The reader is encouraged to refer to their paper for limitations and considerations. The notations used here do not necessarily follow that established under List of Symbols, Abbreviations and Nomenclature. Furthermore, the notations in this section might be different from of that used in defining Batzle and Wang (1992) empirical relations.

B.3. Exploding Reflector Model (ERM)

The ERM concept devised by Loewenthal et al. (1976) is a direct form of wave-theory modeling in which the model layers are assumed to explode at time zero with explosive strengths proportional to the reflectivity (Section 3.2) at their boundaries (Wason et al., 1984). So, using the ERM means that starting at time t = 0, all points emitted from a reflector or diffractor are the starting point of a Huygen's elementary wave with amplitude proportional to the reflection coefficient for the normal incidence case (Sandmeier, 2009). The generated wavefield travels in the upward direction from what can be thought of as a common-depth point (CDP) on the interfaces separating the layers. Therefore, wavespeed (α_{ERM}) is cut in half so that the one-way traveltime to the surface equals the two-way traveltime for coincident source-receiver pairs at the surface (Gazdag and Sguazzero, 1985).

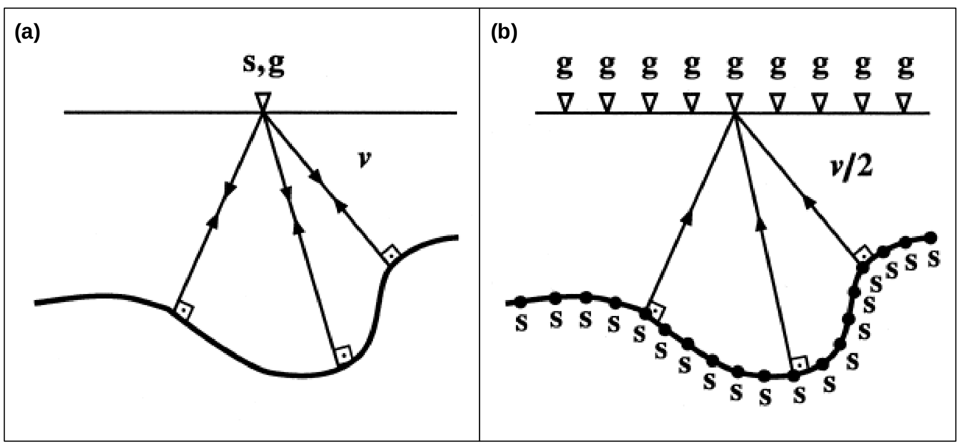

Figure B-1: Schematics illustrating (a) the geometry of a zero-offset section, and (b) the exploding reflector model concept. After Clarebout (1976).

The acoustic (scalar) ERM wavefield can be written as (Margrave, 2007):

$$\nabla^2\psi(x,z,t) = \frac{1}{\alpha_{\mathrm{ERM}}}\frac{\partial^2\psi(x,z,t)}{\partial t^2} \tag{I.40}$$

where:

$$\alpha_{\mathrm{ERM}} = \frac{\alpha_{\mathrm{real}}}{2} \tag{I.41}$$

The solution is given by (Yilmaz, 2001):

$$\psi(x, z=0, t) = \iint \psi(k_x, 0, \omega) e^{-ik_z z} e^{-i(k_x x - \omega t)} dk_x d\omega \tag{I.42}$$

where:

$$k_z = \frac{2\omega}{\alpha}\sqrt{1 - \frac{(\alpha k_x)}{2\omega}} \tag{I.43}$$

where z and x are depth and surface coordinates (in m), t is the two-way traveltime (s), ω is the angular frequency ($\omega = 2\pi f$ in rad/s), f is the frequency (in Hz), k_x and k_z are the horizontal and vertical wavenumbers ($k_x = 1/\Delta x$ and $k_z = 1/\Delta z$ in 1/m), Δx is the spatial sampling interval (in m), Δz is the depth step (in m), α is the P-wave speed, and i is the imaginary unit. Note that Equation (I.42) gives the recorded wavefield $\psi(x,z=0,t)$ whereas the migrated depth section $\psi(x,z,t=0)$ is provided when:

$$\psi(x, z, t=0) = \iint \psi(k_x, 0, \omega) e^{-i(k_x x + k_z z)} dk_x d\omega \tag{I.44}$$

The ERM allows the simulation of a zero-offset section (ZOS) in a single F-D simulation. In addition, it allows the simulation of the kinematic (traveltime) as well as dynamic amplitude and frequency (Sandmeier, 2009). The result of the simulation is a wavefield depending on the offset (x), depth (z) and time (t). With the implemented algorithm (Sandmeier, 2009), an explicit method is used (Subsection 3.5.3), i.e. the wavefield is calculated for a certain point of time with the values of the preceding point and so on.

There are a number of limitations associated with the ERM, which could be summarized as follows (Clarebout, 2000):

- The ERM is restricted to data recorded at zero-offset in which the upgoing and downgoing wavefields from a reflector are identical.
- It does not handle multiples, at least not properly.
- Multi-arrival paths caused by abrupt lateral wavespeed change, e.g. lens, or complex structure, e.g. salt diaper, are not be predicted by the ERM.
- Since the synthetic seismogram generated using the ERM resembles a CDP stacked section, it assumes hyperbolic normal-moveout.
- The concept may not be very useful in acquisition optimization and survey design.

Nonetheless, the ERM remains one of the most useful and most widely used concepts in post-stack wavefield migration (Clarebout, 2000; Margrave, 2007). Further discussion on the ERM can be found in Wason et al. (1984), Clarebout (1976), Yilmaz, (2001). Margarve (2007) gives an excellent discussion of the topic and relates it to post-stack seismic imaging including Kirchhoff migration which is introduced in the next section.

B.4. Kirchhoff Migration (KM):

KM is a method of seismic data migration that employs the integral solution to the wave-equation (WE) and the ray theory (Schneider, 1978; Docherty, 1991). In principle, reflector imaging is achieved through KM by performing a weighted summation along diffraction hyperbola constructed by ray tracing (Snell's law) involving the source, receive and the point to be imaged, e.g. reflector. Then, the computed image point (weighted sum) is assigned to the crest or apex, i.e. point of origin on the reflector. The process is repeated for each point on the reflector as if it was covered by elementary, or diffraction, points sources as postulated by Huygen's principle.

Based on the far-field approximation to the Kirchhoff integral solution to the WE (Yilmaz, 2001) and continuing with the ERM concept in the previous section (Margrave, 2007), the migrated acoustic (pressure) wavefield (ψ_{migrated}) in 2-D can be written as (Berkhout, 1980; Gazdag and Sguazzero, 1985):

$$\psi_{\text{migrated}}(x,z,t=0) \approx \int_{-x}^{+x} \frac{\cos\theta}{\sqrt{\pi\alpha_{\text{rms}} r}} \frac{\partial^{1/2}}{\partial t} \psi_{\text{unmigrated}}(x_0, z_0, t = 2r/\alpha_{\text{rms}}) dx_0 \tag{I.45}$$

where r is the distance between the observation point and the source location:

$$r = \sqrt{\left(x - x_0\right)^2 + \left(z - z_0\right)^2} \tag{I.46}$$

where z_0 and x_0 are the depth and surface coordinates, z and x are the coordinates of the subsurface point to be migrated, t is the two-way traveltime computed by ray tracing, $\cos\theta$ and $\alpha_{\text{rms}} r$ are the obliquity and spherical divergence scaling factors which are required to obtain the correct amplitude, θ is the angle of propagation, α_{rms} is the root-mean squares P-wave speed, $\psi_{\text{unmigrated}}$ is the input (unmigarted) image, the operator $\partial^{1/2}/\partial t$ is the half time derivative and is equivalent to $\sqrt{i\omega}$ in the frequency domain where

ω is the angular frequency and i is the imaginary unit (Gazdag and Sguazzero, 1985). The integration is performed over what is called the migration aperture ($-x$ to $+x$), whose center coincides with the location of the apex of the hyperbola. The differential operator inside the integral applies amplitude and phase (wavelet shaping) correction factor (Yilmaz, 2001), the phase correction operator which in 2-D is equivalent to applying 45 phase shift to the data (Margrave, 2007). Implementation of Kirchhoff migration in practice requires consideration of the aperture width, maximum dip to migrate and migration velocity (Yilmaz, 2001). Further discussion on the classical Kirchhoff migration theory can be found in Schneider (1978), Clarebout (1976), Gazdag and Sguazzero (1985), Docherty (1991), and Yilmaz (2001).

APPENDIX C: PCEP TIME-LAPSE SEISMIC ANALYSIS I - FIELD DATA

C.1. Data Acquisition

Table C-1: List of the main acquisition parameters.

Source Type	Dynamite (2.0 kg)
Source Spacing	40 m
Source Depth	15-20 m
Receiver Type	Sercel DSU 3C
Receiver Spacing	20 m
VSP: number of fixed geophones levels	8
VSP: geophone\level spacing	20 m
VSP: shallowest level	1598 m
VSP: deepest level	1640 m
Sampling Rate	1.0 ms
Total Record Length	4.0 s

C.2. Data Processing: Surface Seismic

C.2.1. Contractor 1: CGGVeritas®

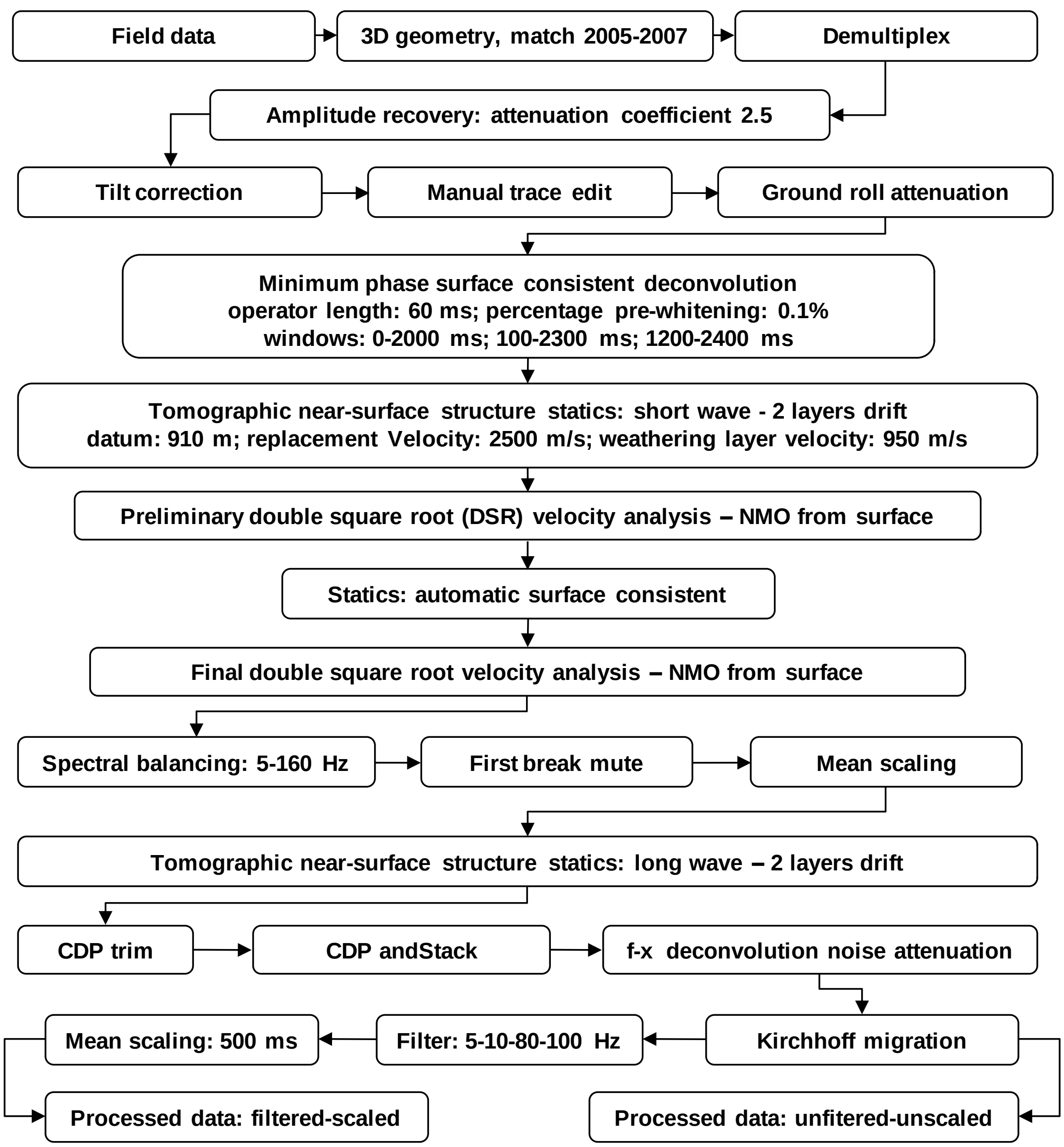

Figure F-1: Processing flow for the 2-D P-wave surface seismic data as implemented by the contractor.

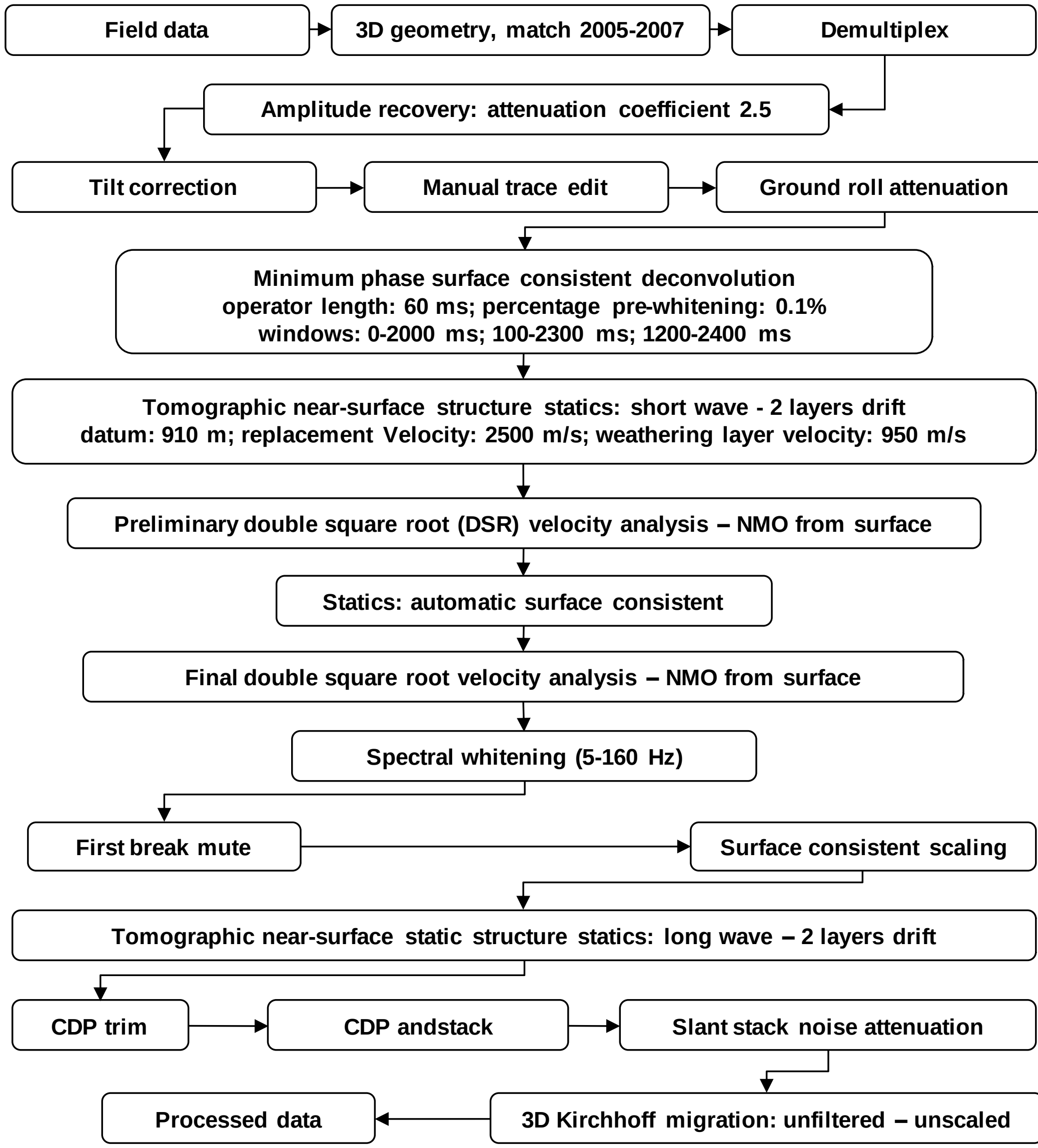

Figure F-2: Processing flow for the 3-D P-wave surface seismic data as implemented by the contractor.

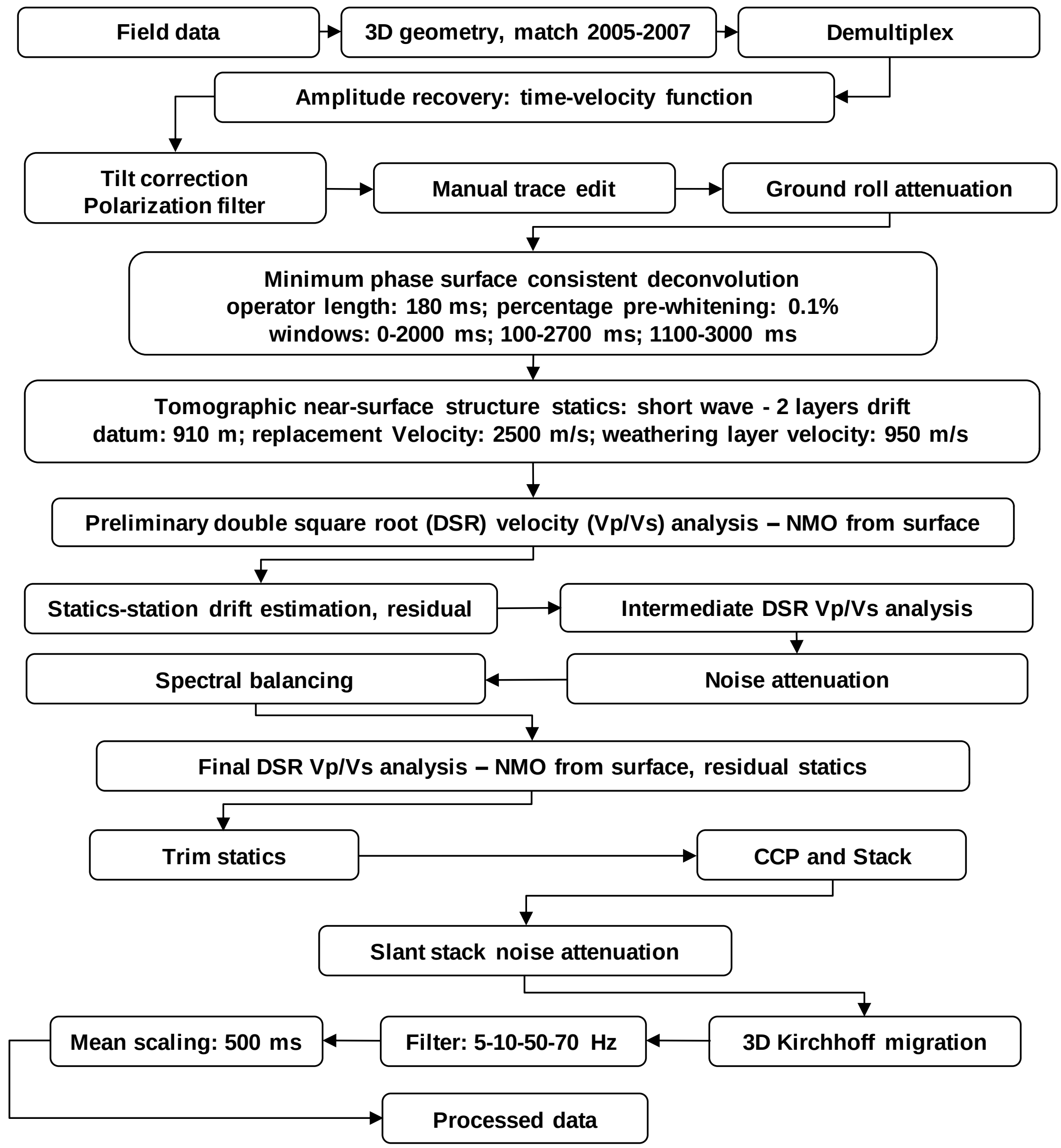

Figure F-3: Processing flow for the 3-D PS-wave surface seismic data as implemented by the contractor.

C.2.2. Contractor 2: Divestco®

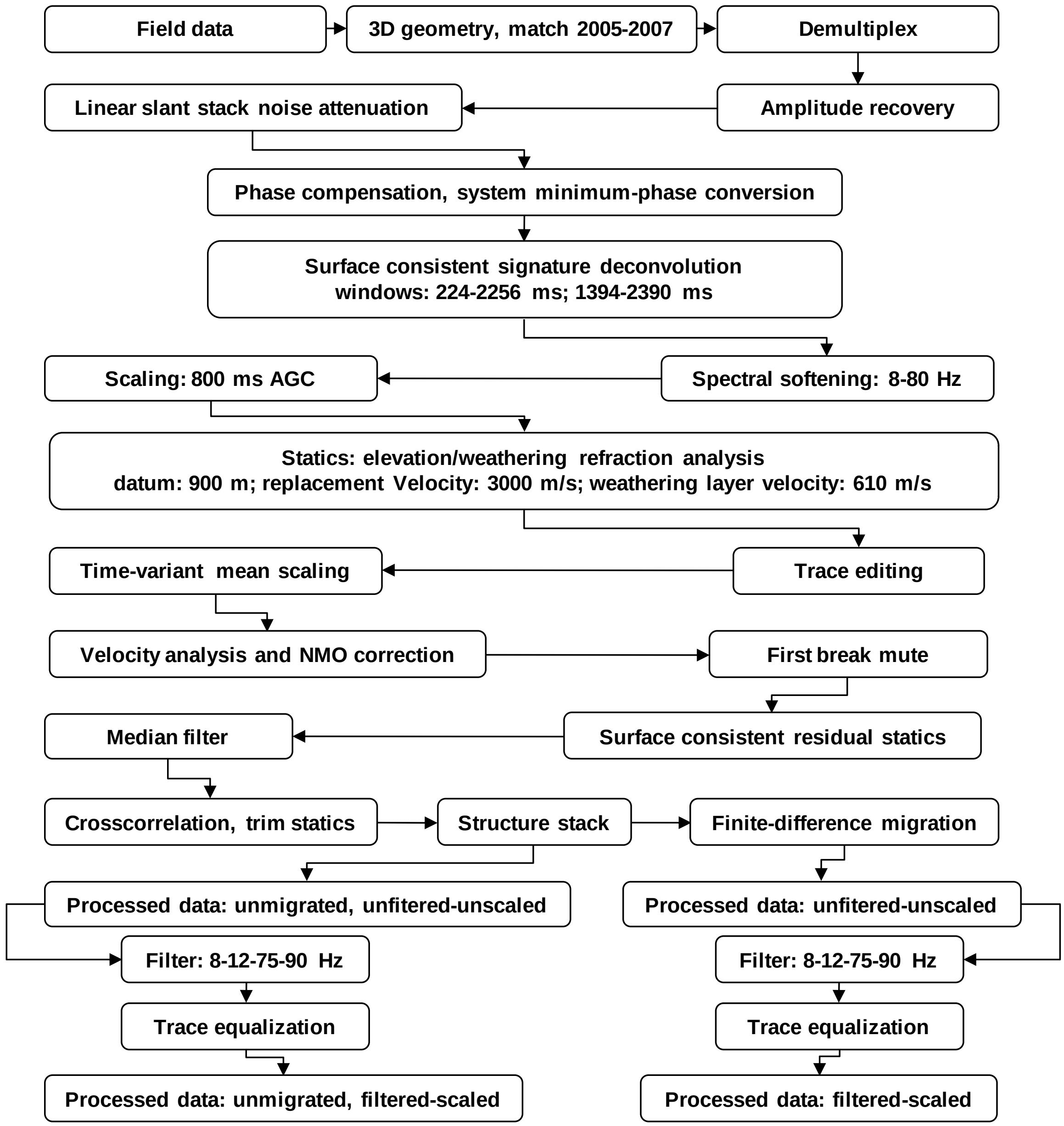

Figure F-4: Processing flow for the 2-D P-wave surface seismic data as implemented by the contractor.

C.3. Processing Flow: Vertical Seismic Profile

C.3.1. Contractor: Schlumberger®

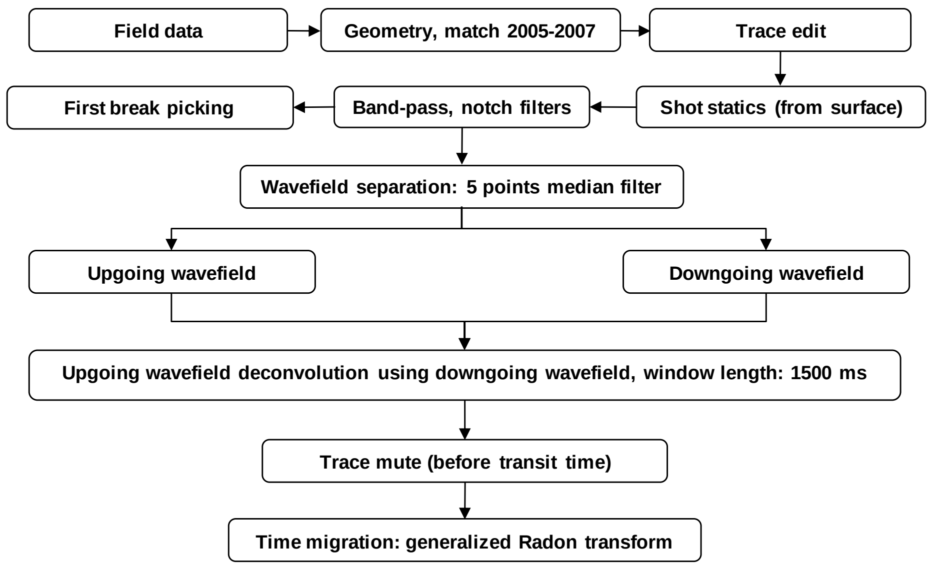

Figure F-5: Processing flow for the walkaway VSP P-wave data as implemented by the contractor.

C.3.2. University of Calgary

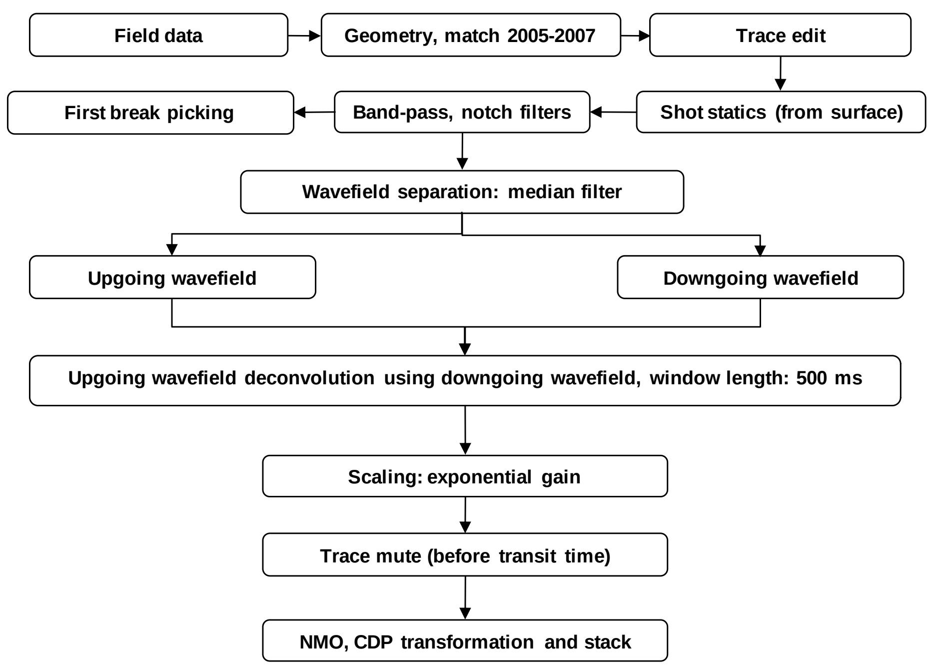

Figure F-6: Processing flow for the walkaway VSP P-wave data implemented as part of this dissertation.

References

Abriel, W. (2008). Reservoir Geophysics: Applications. Society of Exploration Geophysicists/European Association of Geoscientists & Engineers: Distinguished Lecture Series (No. 10).

Aki, K., & Richards, P. (2002). Quantitative seismology: Theory and Methods (2nd ed.). San Francisco: University Science Books.

Alberta Energy and Utilities Board. (2009). Table of Formations. Retrieved January 31, 2010, from Alberta Energy and Utilities Board: www.ercb.ca/docs/products/catalog/TOF.pdf

Alberta Geologic Survey. (2008, March 1). Alberta and Canada's CO2 Emissions Profile in 1999. Retrieved August 31, 2010, from Alberta Geologic Survey: http://www.ags.gov.ab.ca/co2_h2s/figure1.html

Allen, P., & Allen, J. (2005). Basin analysis: principles and applications. Oxford: Blackwell Publishing.

Ames, W. (1992). Numerical Methods for Partial Differential Equations. Academic Press.

Angerer, E., Crampin, S., Li, X.-Y., & Davis, T. (2000). Time-lapse seismic changes in a CO2 injection process in a fractured reservoir. Expanded Abstract of the 70th Annual International SEG Meeting, (pp. 1532–1535). Calgary.

Archie, G. (1942). The electrical resistivity log as an aid in determining some reservoir characteristics. American Institute of Mining and Metallurgical Engineers Transactions , 146, 54-62.

Arts, R., & Winthaegen, P. (2005). Monitoring Options for CO2 Storage. In S. Benson (Ed.), Carbon Dioxide Capture for Storage in Deep Geologic Formations (Vol. II, pp. 1001-1013). Amsterdam: Elsevier.

Arts, R., Eiken, O., Chadwick, A., Zweigel, P., Meer, L., & Zinszner, B. (2002). Monitoring of CO2 injected at Sleipner using time lapse seismic data. Abstract of the 6th international conference on greenhouse gas control technology (GHGT-6). Kyoto, Japan: International Energy Agency.

Avseth, P., Mukerji, T., & Mavko, G. (2005). Quantitative Seismic Interpretation: Applying Rock Physics Tools to Reduce Interpretation Risk (1st ed.). Cambridge University Press.

Bachu, S. (2001). Screening and Ranking of Hydrocarbon Reservoirs for CO2 Storage in the Alberta Basin, Canada. National Conference on Carbon Sequestration. US Department of Energy – National Energy Technology Laboratory.

Bachu, S. (2002). Sequestration of CO2 in Geological Media Criteria and Approach for Site Selection in Response to Climate Change. Energy Conversion and Management , 43, 87-102.

Bachu, S. (2003). Screening and ranking of sedimentary basins for sequestration of CO2 in geological media in response. Environmental Geology , 44, 277–289.

Bachu, S., & Adams, J. (2003). Sequestration of CO2 in geological media in response to climate change: capacity of deep saline aquifers to sequester CO2 in solution. Energy Conversion and Management , 44, 3151-3175.

Bachu, S., & Bennion, B. (2009, May 30). Effects of In-situ Conditions on Relative Permeability Characteristics of CO2-Brine System. Retrieved August 31, 2010, from http://www.gwpc.org/elibrary/documents/co2/LBNL%20CO2%20Effects%20of%20Insitu%20Conditions%20on%20Permeability.pdf

Bachu, S., & Shaw, J. (2005). CO2 storage in oil and gas reservoirs in Western Canada: effect of aquifers, potential for CO2-flood enhanced oil recovery and practical capacity. In E. Rubin, D. Keith, & C. Gilboy (Eds.), Abstract of the 7th International Conference on Greenhouse Gas Technologies (pp. 361-369). Amsterdam: International Energy Agency.

Bachu, S., & Stewart, S. (2002). Geological sequestration of anthropogenic carbon dioxide in the Western Canada Sedimentary Basin: suitability analysis. Canadian Journal of Petroleum Technology , 41, 32-40.

Bachu, S., Brulotte, M., Grobe, M., & Stewart, S. (2000). Suitability of the Alberta subsurface for carbon-dioxide sequestration in geologic media. Alberta Geological Survey, Earth Sciences Report. Edmonton: Alberta Energy and Utilities Board.

Bachu, S., Gunter, W., & Perkins, E. (1994). Aquifer disposal of CO2: hydrodynamic and mineral trapping. Energy Conversion and Management , 35, 269-279.

Bamberger, A., Chavent, G., Hemon, C., & Lailly, P. (1982). Inversion of normal incidence seismograms. Geophysics , 47, 757-770.

Barnes, A. (2007). A tutorial on complex seismic trace analysis. Geophysics , 72, W33-W44.

Bath, M. (1974). Spectral analysis in geophysics. In M. Bath (Ed.), Developments in Solid Earth Geophysics (Vol. 7). Amsterdam: Elsevier.

Batzle, M., & Wang, Z. (1992). Seismic properties of pore fluids. Geophysics , 57, 1396-1408.

Baviere, M. (2007). Basic Concepts in Enhanced Oil Recovery Processes. London: Elsevier .

Bell, J., & Bachu, S. (2003). In-situ stress magnitude and orientation estimates for Cretaceous coal-breaing strata beneath the plains area of central and southern Alberta. Bulletin of Canadian Petroleum Geology , 51 (1), 1-28.

Benson, S. (2005). Overview of Geologic Storage of CO2. In D. Thomas, & S. Benson (Eds.), Carbon Dioxide Capture for Storage in Deep Geologic Formations (Vol. II, pp. 665-671). Amsterdam: Elsevier.

Benson, S. (2006). Monitoring Carbon Dioxide Sequestration in Deep Geological Formations for Inventory Verification and Carbon Credits. Proceedings of the 2006 Annual Technology Conference and Exhibition (pp. 1-14). San Antonio, Texas: Society of Petroleum Engineers.

Berkhout, A. (1987). Applied seismic wave theory: Advances in exploration geophysics . Amsterdam: Elsevier.

Berkhout, A. (1980). Seismic migration. Amsterdam: Elsevier.

ical Constants (pp. 205-228). Washington, D.C.: American Geophysical Union.

Berryman, J., & Milton, G. (1991). Exact results for generalized Gassmann's equation in composite porous media with two constituents. Geophysics , 56, 1950–1960.

Berrymay, J. (1999). Origin of Gassmann’s equations. Geophysics , 64, 1627–1629.

Biot, M. (1955a). Theory of Propagation of Elastic Waves in a Fluid-Saturated Porous Solid I. Low-Frequency Range. The Journal of the Acoustical Society of America , 28, 168-178.

Biot, M. (1955b). Theory of Propagation of Elastic Waves in a Fluid-Saturated Porous Solid II. High-Frequency Range. The Journal of the Acoustical Society of America , 28, 179-191.

Bland, H., Lawton, D., Chalaturnyk, R., & Soderberg, H. (2006). Passive seismic monitoring at a CO2 injection site, Violet Grove, Alberta, Canada. Passive Seismic: Exploration and Monitoring Applications (pp. 1-5). Dubai: European Association of Geoscientists and Engineers.

Bracewell, R. (1986). The Fourier Transform and its Applications (3rd ed.). McGraw Hill.

Brie, A., Pampuri, F., Marssala, A., & Meazza, O. (1995). Shear sonic interpretation in gas-bearing sands. Society of Petroleum Engineering Annual Technical Conference. Society of Petroleum Engineering.

Brown, A. (2004). Interpretation of three-dimensional seismic data (6th ed.). Society of Exploration Geophysicists: Investigations in Geophysics.

Brown, L., Davis, T., & Batzle, M. (2002). Integration of rock physics, reservoir simulation, and time-lapse seismic data for reservoir characterization at Weyburn Field, Saskatchewan. Expanded Abstract of the 76th Annual International SEG Meeting (pp. 1708-1711). Society Of Exploration Geophysicists.

Brown, R., & Korringa, J. (1975). On the dependence of the elastic properties of a porous rock on the compressibility of the pore fluid. Geophysics , 40, 608–616.

Bullen, K. (1987). Seismic Ray Theory. Geophysical Journal of the Royal Astronomical Society , 4, 93-105.

Bullen, K., & Bolt, B. (1985). An introduction to the theory of seismology. Cambridge : Cambridge University Press.

Calvert, R. (2005). Insights and Methods for 4D Reservoir Monitoring and Characterization. Distinguished Instructor Short Course . Society of Exploration Geophysicists/European Association of Geoscientists & Engineers: Distinguished Instructor Series (No. 8).

Carcione, J., Herman, G., & ten Kroode, A. (2002). Y2K review article: Seismic modeling. Geophysics , 67, 1304-1325.

Castagna, J. (1993). Petrophysical imaging using AVO. The Leading Edge , 12, 172.

Castagna, J., & Backus, M. (Eds.). (1993). Offset Dependent Reflectivity-Theory and Practice of AVO (1st ed.). Tulsa: Society of Exploration Geophysicists: Investigations in Geophysics (No. 8).

Castagna, J., Batzle, M., & Eastwood, R. (1985). Relationship between compressional and shear-wave velocities in clastics silicate rocks. Geophysics , 63, 948-956.

Castagna, J., Batzle, M., & Kan, T. (1993). Rock physics-the link between rock properties and AVO response. In J. Castagna, & M. Backus (Eds.), Offset-dependent reflectivity-theory and practice of AVO analysis (1st ed., pp. 131–171). Society of Exploration Geophysicists.

Castagna, J., Swan, H., & Foster, D. (1998). Framework for AVO gradient and intercept interpretation. Geophysics , 63, 948-956.

Červený, V. (2001). Seismic Ray Theory (1st ed.). Cambridge: Cambridge University Press.

Chadwick, A., Arts, R., Eiken, O., Williamson, P., & Williams, G. (2006). Geophysical Monitoring of CO2 Plume at Sleipner, North Sea. Advances in the Geologic Storage of Carbon Dioxide: NATO Science Series , 65, 303-314.

Chadwick, A., Noya, D., Artsb, R., & Eikenc, O. (2009). Latest time-lapse seismic data from Sleipner yield new insights into CO2 plume development. Energy Procedia , 2103-2110.

Chadwick, R., Holloway, S., & Riley, N. (2001). Deep subsurface CO2 sequestration - a viable greenhouse mitigation strategy. Geoscientist , 11, 4-5.

Chapman, C. (2004). Fundamentals of seismic wave propagation (1st ed.). Cambridge: Cambridge University Press.

Chapman, M., Zatsepin, S., & Crampin, S. (2000). Time-lapse seismic changes in a CO2 injection process in a fractured reservoir. Expanded Abstract of the 76th Annual International SEG Meeting (pp. 1536-1539). Society Of Exploration Geophysicists.

Chen, F. (2006). Interpretation of Time-lapse Surface Seismic Data at a CO2 Injection Site, Violet Grove, Alberta. M. Sc. Thesis . Calgary, Alberta, Canada: University of Calgary.

Chen, Z., & Stewart, R. (2006). Hypocenter location errors of microseismic events located by using a 3-C VSP downhole geophone array at Violet Grove. CREWES research report, Volume 18.

Chopra, S. (2005). Expert Answers - Gassmann's Equation. CSEG Recorder , 8-12.

Chopra, S., & Marfurt, K. (2007). Seismic Attributes for Prospect ID and Reservoir Charcaterization (1st ed.). Society of Exploration Geophysicists: Geophysical Developments (No. 11).

Clarebout, J. (2000, December 13). Basic Earth Imaging. Retrieved January 15, 2011, from Jon Claerbout's Classroom: http://sepwww.stanford.edu/sep/prof/bei/toc_html/index.html

Clarebout, J. (1976). Fundamentals of geophysical processing (1st ed.). New York: McGraw-Hill Book Co.

Cooke, D., & Schneider, W. (1983). Generalized linear inversion of reflection seismic data. Geophysics , 48, 665-676.

Couëslan, M. (2007). Processing and Interpretation of Time-lapse Vertical Seismic Profile Data from the Penn West CO2 Monitoring Project. M. Sc. Thesis . Calgary, Alberta, Canada: University of Calgary.

Daley, T., Myer, L., Hoversten, G., & Peterson, J. (2006). Borehole Seismic Monitoring of Injected CO2 at the Frio Site. Abstract of the 8th International Conference on Greenhouse Gas Control Technologies. Trondheim, Norway: International Energy Agency.

Dashtgard, S., Buschkuehle, M., Berhane, M., & Fairgrieve, B. (2006). Local-Scale Baseline Geological Report for the Pembina-Cardium CO2-Enhanced Oil Recovery Site. Alberta Geological Survey. Edmonton: Alberta Energy and Utilities Board.

Dashtgard, S., Buschkuelel, M., Fairgrieve, B., & Berhane, M. (2008). Geological characterization and potential for carbon dioxide (CO2) enhanced oil recovery in the Cardium Formation, central Pembina, Alberta. In B. Hitchon (Ed.), Pembina Cardium CO2 Monitoring Pilot, a CO2-EOR Project, Alberta, Canada. Geoscience Publishing.

Davis, T., Terrell, M., Cardona, R., Kendall, R., & Winarsky, W. (2003). Multi-component seismic characterization and monitoring of the CO2 flood at Weyburn Field, Saskatchewan. The Leading Edge , 22, 696-697.

Davison, J., Freund, P., & Smith, A. (2001). Putting Carbon Back Into The Ground. IEA Greenhouse Gas R & D Programme (p. 32). International Energy Agency.

del Pino, S., Levinson, R., & Larsen, J. (2006). Hot Climate, Cool Commerce: A Service Sector Guide to Greenhouse Gas Management.

Downton, J. (2005). Seismic parameter estimation from AVO inversion. M. Sc. Thesis . Calgary, Alberta, Canada.

Dresser Atlas. (1979). Log interpretation charts. Houston: Dresser Industries Inc.

Dvorkin, J., & Nur, A. (1998). Acoustic Signatures of Patchy Saturation. International Journal of Solid Structure , 35, 4803-4810.

Eisinger, C., & Jensen, J. (2009). Data Integration, Petrophysics, and Geomodeling – Wabamun Area CO2 Sequestration Project (WASP). University of Calgary, Institute for Sustainable Energy, Environment and Economy (ISEEE): Energy and Environmental Systems Group.

Engineering ToolBox. (2008, August 31). Gases - Specific Gravities. Retrieved January 25, 2011, from Engineering ToolBox: http://www.engineeringtoolbox.com/specific-gravities-gases-d_334.html

Environment Canada. (2008, November 30). Canada's Greenhouse Gas Emissions: Understanding the Trends, 1990-2006. Retrieved August 31, 2010, from Environment Canada: http://www.ec.gc.ca/pdb/ghg/inventory_report/2008_trends/trends_eng.cfm

Environment Canada. (2009, April 17). National Inventory Report Greenhouse Gas Sources and Sinks in Canada 1990–2007. Retrieved August 31, 2010, from Environment Canada: http://unfccc.int/files/national_reports/annex_i_ghg_inventories/national_inventories_submissions/application/zip/can_2009_nir_17apr.zip

Gagliardi, P., & Lawton, D. (2010). Borehole geophone repeatability experiment. CREWES research report, Volume 22.

Gale, J., & Freund, P. (2001). Coal-Bed Methane Enhancement with CO2 Sequestration Worldwide Potential. Environmental Geosciences , 8, 210-217.

Gardner, G., Gardner, L., & Gregory, A. (1974). Formation Velocity and Density - The Diagnostic Basics for Stratigraphic Traps. Geophysics , 39, 770-780.

Gassmann, F. (1951). Uber die elastizitat poroser medien. Verteljahrss-chrift der Naturforschenden Gesellschaf , 23, 1-23.

Ghaderi, S., & Leonenko, Y. (2009). Reservoir Modeling of the Nisku Formation in the WASP area. University of Calgary, Institute for Sustainable Energy, Environment and Economy (ISEEE): Energy and Environmental Systems Group.

Gjøystdal, H., Iversen, E., Laurain, R., Lecomte, I., Vinje, V., & Åstebøl, K. (2002). Review of Ray Theory Applications in Modelling and Imaging of Seismic Data. Studia Geophysica et Geodaetica , 46, 113-164.

Goodarzi, S., & Settari, A. (2009). Wabamun Area CO2 Sequestration Project (WASP) Geoemchanical modeling and analysis. University of Calgary, Institute for Sustainable Energy, Environment and Economy (ISEEE): Energy and Environmental Systems Group.

Goodway, W., Chen, T., & Downton, J. (1997). Improved AVO fluid detection and lithology discrimination using Lame petrophysical parameters; "λρ", "μρ", & "λ/μ fluid stack", from P and S inversions. Expanded Abstract of the 67th Annual International SEG Meeting, (pp. 183-186).

Greenberg, M., & Castagna, J. (1992). Shear-wave velocity estimation in porous rocks: Theoretical formulation, preliminary verification and applications . Geophysical Prospecting , 195-209.

Gubbins, D. (2004). Time Series Analysis and Inverse Theory for Geophysicists. Cambridge : Cambridge University Press.

Gunter, W., Perkins, E., & Hutcheon, I. (2000). Aquifer disposal of acid gases: modelling of water-rock reactions for trapping of acid wastes. Applied Geochemistry , 15, 1085-1095.

Gunter, W., Perkins, E., & McCann, T. (1993). Aquifer disposal of CO2-rich gases: reaction design for added capacity. Energy Conversion and Management , 34, 941-948.

Hampson-Russell. (2009). Hampson-Russell Assistant. Hampson-Russell Software Documentation . Hampson-Russell, A CGGVERTIAS Company.

Han, D., & Batzle, M. (2004). Gassmann's equation and fluid-saturation effects on seismic velocities. Geophysics , 69, 398-405.

Hardage, B. (2000). Vertical seismic profile: Principle. In K. Helbig, & S. Treitel (Eds.), Handbook of Geophysical Exploration: Seismic Exploration (3rd ed., Vol. 14). Amsterdam: Pergamon.

Hashin, Z., & Shtrikman, S. (1963). A variational approach to the theory of the elastic behaviour of multiphase materials. Journal of the Mechanics and Physics of Solids , 11, 127-140.

Hasse, A., Lawton, D., & Alshuhail, A. (2010). Spectral ratios for the Pembina Cardium formation computed with virtual sources. CREWES research report, Volume 22.

Herawati, I. (2002). The use of time-lapse P-wave impedance inversion to monitor CO2 flood at Weyburn Field, Saskatchewan, Canada. M. Sc. Thesis . Golden, Colorado, USA: Colorado School of Mines.

Hill, R. (1963). Elastic properties of reinforced solids: Some theoretical principles. Journal of the Mechanics and Physics of Solids , 11, 357–372.

Hilterman, F. (2001). Seismic Amplitude Interpretation. Society of Exploration Geophysicists/European Association of Geoscientists & Engineers: Distinguished Instructor Series (No. 4).

Hilterman, F., Sherwood, J., Schellhorn, R., Bankhead, B., & Devault, B. (1998). Identification of lithology in the Gulf of Mexico. The Leading Edge , 17, 215-222.

Hinds, R., Anderson, N., & Kuzmiski, R. (1996). VSP Interpretive Processing: Theory and Practice. (B. Hardage, Ed.) Tulsa: Society of Exploration Geophysicists: Geophysical References.

Hitchon, B. (Ed.). (2009). Pembina Cardium CO2 Monitoring Pilot, a CO2-EOR Project, Alberta, Canada. Geoscience Publishing.

Hofmann, R., Xu, X., Batzle, M., Prasad, M., Furre, A.-k., & Pilliterri, A. (2005). Effective pressure or what is the effect of pressure? The Leading Edge , 24, 1256-1260.

Holloway, S., Chadwick, A., Lindeberg, E., Czernichowski-Lauriol, I., & Arts, R. (2004). Best Practice Manual from SACS - Saline Aquifer CO2 Storage Project. Appendix A Statoil, Research Center, N-7005 Trondheim, Norway.

Hons, M. (2008). Seismic sensing: Comparison of geophones and accelerometers using laboratory and field data. M. Sc. Thesis . Calgary, Alberta, Canada: University of Calgary.

Hoversten, G., Gasperikova, E., & Benson, S. (2006). Theoretical Limits for Seismic Detection of Small Accumulations of Carbon Dioxide in the Subsurface. Abstract of the 8th International Conference on Greenhouse Gas Control Technologies. Trondheim, Norway: International Energy Agency.

Hudson, J., Liu, E., & Crampin, S. (1996). The mechanical properties of materials with interconnected cracks and pores. Geophysical Journal International , 124, 105–112.

IPCC. (2007, July 30). IPCC Fourth Assessment Report: Climate Change 2007 . Retrieved August 31, 2010, from Intergovernmental Panel on Climate Change: http://www.ipcc.ch/publications_and_data/publications_and_data_reports.htm

IPCC. (2005). IPCC Special Report on Carbon Dioxide Capture and Storage. Prepared by Working Group III of the Intergovernmental Panel on Climate Change. (B. Metz, O. Davidson, H. de Coninck, M. Loos, & L. Meyer, Eds.) Cambridge, United Kingdom and New York, NY, USA: Cambridge University Press.

Japan Petroleum Exploration Co. Ltd. (JAPEX). (2008, March 31). CO2 Geological Sequestration. Retrieved August 31, 2010, from http://www.japex.co.jp/english/technology/co2.html

Johnson, G. (2010). Stable isotope approaches to monitoring and verification of injected CO2 at the Pembina Cardium CO2 monitoring pilot, Alberta, Canada. Ph. D. Thesis . Calgary, Alberta, Canada: University of Calgary.

Keith, D., & Lavoie, R. (2009). An overview of the Wabamun Area CO2 Sequestration Project (WASP). Energy Procedia , 1, 2817-2824.

Kelly, K., & Marfurt, K. (Eds.). (1990). Numerical modeling of seismic wave propagation. Tulsa: Society of Exploration Geophysicists.

Kelly, K., Ward, R. T., & Alford, R. (1976). Synthetic Seismograms: A finite-difference approach. Geophysics , 41, 2-27.

Kennett, P., Ireson, R., & Conn, P. (1980). Vertical Seismic Profiles: Their Applications in Exploration Geophysics. Geophysical Prospecting , 28, 676-699.

Knott, C. (1899). Reflexion and refraction of elastic waves with seismological applications. Philosophical Magazine , 48, 64-97.

Kragh, E., & Christie, P. (2002). Seismic repeatability, normalized rms, and predictability. The Leading Edge , 21, 640-647.

Krause, F., & Collins, H. (1984). Pembina Cardium recovery efficiency study: a geological and engineering synthesis. Petroleum Recovery Institute.

Krause, F., Collins, H., Nelson, D., Machemer, S., & French, P. (1987). Multi-scale anatomy of a reservoir: geological characterization of Pembina-Cardium Pool, west-central Alberta, Canada. American Association of Petroleum Geologists Bulletin , 71, 1233-1260.

Krebes, E. (2004). Seismic Forward Modeling. CSEG RECORDER , April, 28-39.

Kuster, G., & Toksöz, M. (1974a). Velocity and attenuation of seismic waves in two-phase media: Part I. Theoretical formulations. Geophysics , 39, 587–606.

Kuster, G., & Toksöz, M. (1974b). Velocity and attenuation of seismic waves in two-phase media: Part II. Experimental Results. Geophysics , 39, 607–618.

Lake, L. (2006). Review of enhanced oil recovery (EOR) technology. International Association for Mathematical Geology Distinguished Lecture Tour . International Association for Mathematical Geology.

Lakeman, B. (2009, October 15). Canadian CCS Opportunities and Challenges. Retrieved August 31, 2010, from National Energy Board: http://www.neb-one.gc.ca/clf-nsi/rnrgynfmtn/nrgyrprt/nrgyftr/cnslttnrnd3/brent_lakeman.pdf

Landrø, M. (1999). Repeatability issues of 3-D VSP data. Geophysics , 64, 1673-1679.

Lavoie, R. (2009). Aquifer Material Balance of the Nisku Formation in the WASP area. University of Calgary, Institute for Sustainable Energy, Environment and Economy (ISEEE): Energy and Environmental Systems Group.

Lawton, D. (2005). Seismic survey design for monitoring CO2 storage: integrated multi-component surface and borehole seismic surveys, Penn West Pilot, Alberta, Canada. The 8th international conference on greenhouse gas control technology (GHGT-8). Trondheim, Norway: International Energy Agency.

Lawton, D., Alshuhail, A., Couëslan, M., & Chabot, L. (2009). Pembina Cardium CO2 Monitoring Project: Time-lapse seismic analysis. In B. Hitchon (Ed.), Pembina Cardium CO2 Monitoring Pilot, a CO2-EOR Project, Alberta, Canada. Geoscience Publishing.

Lawton, D., Bertram, M., Margrave, G., & Gallant, E. (2006). Comparisons between data recorded by several 3-component coil geophones and a MEMS sensor at the Violet Grove monitor seismic survey. CREWES research report, Volume 18.

Lawton, D., Coueslan, M., Chen, F., Bland, H., Jones, M., Gallant, E., et al. (2005). Overview of the Violet Grove CO2 seismic monitoring project. CREWES research report, Volume 17.

Lay, T., & Wallace, T. (1995). Modern global seismology. San Diego: Academic Press.

Levenberg, K. (1944). A method for the solution of certain nonlinear Problems in least squares. Quarterly of Applied Mathematics , 2, 164-168.

Li, G. (2003). 4D seismic monitoring of CO2 flood in a thin fractured carbonate reservoir. The Leading Edge , 22, 690-695.

Lim, G., & Gunter, B. (2009). Reservoir Simulation Modelling for the Penn West Pembina CO2-EOR Site. In B. Hitchon (Ed.), Pembina Cardium CO2 Monitoring Pilot, a CO2-EOR Project, Alberta, Canada. Geoscience Publishing.

Lines, L., & Newrick, R. (2004). Fundamentals Of Geophysical Interpretation (2nd ed.). Society of Exploration Geophysicists: Geophysical Monographs Series.

Lines, L., & Treitel, S. (1984). A review of least-squares inversion and its application to geophysical problems. Geophysical Prospecting , 32, 159-186.

LITHOPROBE. (2010, March 15). Retrieved August 31, 2010, from Canada's LITHOPROBE Geoscience Project: http://www.lithoprobe.ca/

Lu, H., Hall, K., & Lawton, C. (2005). Violet Grove 2D and 3D data processing at CREWES. CREWES research report, Volume 17.

Lumley, D. (2010). 4D seismic monitoring of CO2 sequestration. The Leading Edge , 29, 150-155.

Lumley, D. (2004). Business and technology challenges for 4D seismic reservoir monitoring. The Leading Edge , 23, 1166-1168.

Lumley, D., Adams, D., Wright, R., Markus, D., & Cole, S. (2008). Seismic monitoring of CO2 geo-sequestration: realistic capabilities and limitations. Expanded Abstract of the 78th Annual International SEG Meeting (pp. 2841-2845). Las vegas: Society of Exploration Geophysicists.

Luo, Y., Higgs, W., & Kowalik, W. (1996). Edge detection and stratigraphic analysis using 3D seismic data. Expanded Abstract of the 66th Annual International SEG Meeting (pp. 324-331). Society Of Exploration Geophysicists.

Margrave, G. (2007). Methods of Seismic Data Processing. Geophysics 557 course notes . University of Calgary.

Margrave, G. (2003, July 11). Numerical Methods of Exploration Seismology with algorithms in Matlab. Retrieved August 31, 2010, from CREWES: http://crewes.org/ResearchLinks/FreeSoftware/EduSoftware/NumMeth.pdf

Marquardt, W. (1963). An algorithm for least squares estimation of non-linear parameters. Journal of the Society of Industrial and Applied Mathematics , 11, 431-441.

Mavko, G., & Mukerji, T. (1998). Bounds on low-frequency seismic velocities in partially saturated rocks. Geophysics , 63, 918-924.

Mavko, G., Mukerji, T., & Dvorkin, J. (2003). The Rock Physics Handbook: Tools for Seismic Analysis of Porous Media (3rd ed.). Cambridge University Press.

Menke, W. (1989). Geophysical data analysis: discrete inverse theory. San Diego: Academic Press.

Michael, K., Bachu, S., Buschkuehle, B., Haug, K., & Talman, S. (2008). Comprehensive Characterization of a Potential Site for CO2 Geological Storage in Central Alberta, Canada. American Association of Petroleum Geologists Manuscript , 40.

Mitchell, A. (1969). Computational Methods in Partial Differential Equations. New York: Wiley.

Morgan, T. (1983). Foundations of Wave Theory for Seismic Exploration. Boston: International Human Resources Development Corporation.

Mossop, G.; Shetsen, I (comp.). (1994). Geological atlas of the Western Canada Sedimentary Basin. Retrieved August 31, 2010, from http://www.ags.gov.ab.ca/publications/wcsb_atlas/atlas.html

Naess, O. (2006). Repeatability and 4D seismic acquisition. Expanded Abstract of the 74th Annual International SEG Meeting (pp. 3300-3304). Society of Exploration Geophysicists.

Natural Resources Canada. (2008, March 31). Atlas of Canada - Alberta. Retrieved August 31, 2010, from Natural Resources Canada: http://atlas.nrcan.gc.ca/site/english/maps/reference/provincesterritories/alberta

Nightingale, M., Johnson, G., Shevalier, M., Mayer, B., & Perkins, E. (2008). Pembina Cardium CO2 Monitoring Project, Alberta, Canada: Imapct of Injected CO2 on Reservoir Mineralogy. In B. Hitchon (Ed.), Pembina Cardium CO2 Monitoring Pilot, a CO2-EOR Project, Alberta, Canada. Geoscience Publishing.

Nightingale, M., Shevalier, M., Mayer, B., & Perkins, B. (2007). Local Evaluation: Penn West CO2-EOR Pilot Project, Drayton Valley, Alberta: Reservoir Mineralogy. In B. Hitchon (Ed.), Pembina Cardium CO2 Monitoring Pilot, a CO2-EOR Project, Alberta, Canada. Geoscience Publishing.

NOAA (National Oceanic and Atmospheric Adiminstration). (2010, January 25). Retrieved August 31, 2010, from United States Global Change Research Program: http://www.globalchange.gov/HighResImages/1-Global-pg-17.jpg

Nygaard, R. (2009a). Geomechanical analysis of the Nisku Formation in the WASP area. University of Calgary, Institute for Sustainable Energy, Environment and Economy (ISEEE): Energy and Environmental Systems Group.

Nygaard, R. (2009b). Well design and well integrity. University of Calgary, Institute for Sustainable Energy, Environment and Economy (ISEEE): Energy and Environmental Systems Group.

O'Brien, J., Kilbride, F., & Lim, F. (2004). Time-lapse VSP reservoir monitoring. The Leading Edge , 23, 1178-1184.

OECD (Organisation for Economic Co-operation and Development). (2007). CO2 Emissions from Fuel Combustion: 1971 / 2005. Organisation for Economic Co-operation and Development Publications.

Parker, R. (1994). Geophysical Inverse Theory. Princeton: Princeton University Press.

Partyka, G., Gridley, J., & Lope, J. (1999). Interpretational applications of spectral decomposition in reservoir characterization. The Leading Edge , 18, 353-360.

Patterson, N., & Anderson, A. (1957). Geology of Pembina field, Alberta. American Association of Petroleum Geologist Bulletin , 41, 937-949.

Peng, D., & Robinson, D. (1976). A New Two-Constant Equation of State. Industrial and Engineering Chemistry: Fundamentals , 15, 59-64.

Petroleum Technology Research Centre. (2008, March 15). Weybrun-Midale CO2 Project. Retrieved August 31, 2010, from http://www.ptrc.ca/weyburn_overview.php

Pevzner, R., Shulakova, V., Kepic, A., & Urosevic, M. (2010). Repeatability analysis of land time-lapse seismic data: CO2CRC Otway pilot project case study. Geophysical Prospecting , 1-12.

Pickett, G. (1963). Acoustic character logs and their applications in formation evaluation. Journal of Petroleum Technology , 15, 650-667.

Pujol, J. (2007). The solution of nonlinear inverse problems and the Levenberg-Marquardt method. Geophysics , 72, W1-W16.

Reuss, A. (1929). Brechnung der fliessgrense von mischkristallen auf grund der plastizitatsbedinggung für einkristalle. Zeitschrift für Angewandle Mathematik und Mechanik , 9, 49-58.

Riddiford, F., Akretche, S., & Tourqui, A. (2003). Stoarge and Sequetsration of CO2 in the In Salah Gas Project. World Gas Conference. Tokyo, Japan.

Robinson, E., & Treitel, S. (2000). Geophysical Signal Analysis. Society of Exploration Geophysicists: General.

Ross, C. (1985). Effective AVO crossplot modeling: a tutorial. Geophysics , 65, 700-711.

Russell, B. (1988). Introduction to Seismic Inversion Methods. Society of Exploration Geophysicists: Course Notes.

Russell, B., & Lines, L. (2007). Applications of Geophysical Inversion and Imaging. SEG Continuing Education Week . Society of Exploration Geophysicists Professional Development.

Rutherford, S., & Williams, R. (1989). Amplitude-versus-offset variations in gas sands. Geophysics , 54, 680-688.

Sandmeier, K. (2009). Reflexw Software Manual. Sandmeier Scientific Software.

Sayers, C., & Wilson, T. (2010). An introduction to this special section: CO2 sequestration. The Leading Edge , 29, 148-149.

Scales, J., Smith, M., & Treitel, S. (2001). Introductory Geophysical Inverse Theory. Golden: Samizdat Press.

SCG. (2009). Stoakes Consulting Group Ltd.: personal communication.

Schneider, W. (1978). Integral formulation for migration in two and three dimensions. Geophysics , 43, 49-76.

Sheriff, R. (2002). Encyclopedic Dictionary of Applied Geophysics (4th ed.). Tulsa: Society of Exploration Geophysicists: Geophysical References.

Sheriff, R., & Geldart, L. (1995). Exploration Seismology (2nd ed.). New York: Cambridge University Press.

Shevalier, M., Nightingale, M., & Mayer, M. (2009). Geochemistry of the Nisku Formation in the WASP area. University of Calgary, Institute for Sustainable Energy, Environment and Economy (ISEEE): Energy and Environmental Systems Group.

Shevalier, M., Nightingale, M., Mayer, B., Johnson, G., & Perkins, E. (2008). Reservoir Geochemistry Monitoring of the Pembina Cardium CO2 Monitoring Project. In B.

Hitchon (Ed.), Pembina Cardium CO2 Monitoring Pilot, a CO2-EOR Project, Alberta, Canada. Geoscience Publishing.

Shevalier, M., Perkins, E., & Talman, S. (2007). Reservoir Geochemistry Monitoring of the Penn West CO2-EOR Site for the period ending March, 2007. Alberta Geologic Survey. Edmonton: Alberta Energy and Utilities Board.

Shuey, R. (1985). A simplification of the Zoeppritz equations. Geophysics , 50, 609-614.

Slawinski, M. (2003). Seismic Waves and Rays in Elastic Media. In K. Helbig (Ed.), Handbook Of Geophysical Exploration: Seismic Exploration (Vol. 34). Amsterdam: Elsevier.

Smith, G. (1985). Numerical solution of partial differential equations: finite difference methods (3rd ed.). Oxford: Oxford University Press.

Smith, T., Sondergeld, C., & Rai, C. (2003). Gassmann fluid substitutions: a tutorial. Geophysics , 68, 430-440.

Snieder, R., & Trampert, J. (1999). Inverse Problems in Geophysics. In A. Wirgin (Ed.), Wavefield Inversion (pp. 119-190). New York: Springer Verlag.

Stark, A. (2008). Seismic Methods and Applications: A Guide for the Detection of Geologic Structures, Earthquake Zones and Hazards, Resource Exploration, and Geotechnic. Boca Raton: BrownWalker Press.

Stephen, D. (2002, June 17). Ocean Drilling Program Publication Services: Texas Agricultural and Mechanical University. Retrieved September 28, 2010, from Chapter 2. Data Report Physical Properties Measurements in ODP Hole 735B: http://www-odp.tamu.edu/publications/176_SR/chap_02/chap_02.htm

STRATA. (2009). Hampson-Russell Assistant: STRATA Theory. Hampson-Russell Software.

Switzer, S., Holland, W., Christie, P., Graf, G., Hedinger, A., McAnley, R., et al. (1994). Devonian Woodbend - Winterburn strata of the Western Canada Sedimentary Basin. Geological Atlas of the Western Canada Sedimentary Basin . (G. Mossop, & I. Shetsen, Eds.) Canadian Society of Petroleum Geologists and Alberta Research Council.

Talman, S., & Perkins, E. (2008). Geochemical Analysis and Modelling of the Penn West Pembina Cardium CO2-EOR Site. In B. Hitchon (Ed.), Pembina Cardium CO2 Monitoring Pilot, a CO2-EOR Project, Alberta, Canada. Geoscience Publishing.

Taner, M., Koehler, F., & Sheriff, R. (1979). Complex seismic trace analysis. Geophysics , 44, 1041-1063.

Tarantola, A., & Valette, B. (1982). Inverse Problems - Quest for Information. Journal of Geophysics , 50, 159-170.

Telford, W., Geldart, L., & Sheriff, R. (1990). Applied Geophysics (2nd ed.). Cambridge: Cambridge University Press.

Terrell, M., Davis, T., Brown, L., & Fuck, R. (2002). Seismic monitoring of a CO2 flood at Weyburn field, Saskatchewan, Canada: demonstrating the robustness of time-lapse seismology. Expanded Abstract of the 72nd Annual International SEG Meeting (pp. 1673-1676). Society Of Exploration Geophysicists.

Todd, T., & Simmons, G. (1972). Effect of Pore Pressure on the Velocity of Compressional Waves in Low Porosity Rocks. Journal of Geophysical Research , 77, 3731-3743.

Tonn, R. (1991). The Determination of the Seismic Quality Factor Q from VSP data: A comparison of Different Computational Methods. Geophysical Prospecting , 39, 1-27.

Tura, A., Barker, T., Cattermole, P., Collins, C., Davis, J., Hatchell, P., et al. (2005). Monitoring primary depletion reservoirs using amplitudes and time shifts from high-repeat seismic surveys. The Leading Edge , 24, 1214-1221.

Udías, A. (1999). Principles of seismology. Cambridge: Cambridge University Press.

UNEP (United Nations Environment Programme). (2008, March 1). Canada Greenhouse Gas Emissions. Retrieved August 31, 2010, from GRID-Arendal: http://www.grida.no/Emissions.aspx?m=36&countryiso=CA

Ursenbach, C. (2009, September 10). Fluid Properties Calculator. Retrieved August 31, 2010, from CREWES Fluid Properties Calculator: http://crewes.org/ResearchLinks/ExplorerPrograms/FlProp/FluidProp.htm#

USDOE. (2009, March 1). Energy Information Administration. Retrieved August 31, 2010, from United States Department of Energy: http://www.eia.doe.gov/oiaf/1605/ggccebro/chapter1.html

USDOE. (2010, January 31). Energy Information Administration. Retrieved August 31, 2010, from US Department of Energy: http://www.eia.doe.gov/emeu/international/reserves.html

USDOE. (2008, February 8). Enhanced Oil Recovery/CO2 Injection. Retrieved August 31, 2010, from United States Department of Energy: http://www.fossil.energy.gov/programs/oilgas/eor/index.html

van Everdingen, D., Trottier, S., Birks, J., Gordon, S., & Mellor, A. (2008). Environmental Monitoring for the Penn West CO2-EOR Site. In B. Hitchon (Ed.), Pembina Cardium CO2 Monitoring Pilot, a CO2-EOR Project, Alberta, Canada. Geoscience Publishing.

Vanorio, T., Mavko, G., Vialle, S., & Spratt, K. (2010). The rock physics basis for 4D seismic monitoring of CO2 fate: Are we there yet? The Leading Edge , 29, 156-162.

Verwer, K., Eberli, G., Baechle, G., & Wege, R. (2010). Effect of carbonate pore structure on dynamic shear moduli. Geophysics , 75, E1-E8.

Vestrum, R., Lawton, D., & Schmid, R. (1999). Imaging structures below dipping TI media. Geophysics , 64, 1239-1246.

Vigrass, L. (2010, January 31). The Encyclopedia of Saskatchewan. Retrieved August 31, 2010, from University of Regina: http://esask.uregina.ca/entry/western_canada_sedimentary_basin.html

Voigt, W. (1928). Lehrbuch der kristallphysik. Leipzig: Teubner.

Wang, Z. (1997). Feasibility of time-lapse seismic reservoir monitoring: the physical basis. The Leading Edge , 16, 1327-1329.

Wang, Z. (2001). Fundamentals of seismic rock physics. Geophysics , 66, 398-412.

Wang, Z., & Nur, A. (2001). Seismic & Acoustic Velocities in Reservoir Rocks (Vol. III). Society of Exploration Geophysicists: Geophysics Reprints.

Wang, Z., Cates, M., & Langan, R. (1998). Seismic monitoring of a CO2 flood in a carbonate reservoir: A rock physics study. Geophysics , 63, 1604-1617.

Wason, C., Black, J., & King, G. (1984). Seismic Modeling and Inversion. Proceedings of the IEEE , 72, 1385-1393.

Waters, K. (1978). Reflection seismology. John Wiley and Sons.

Watts, N. (1987). Carbonate sedimentology and depositional history of the Nisku Formation in south-centra Alberta. In F. Krause, & O. Burrowes (Eds.), Devonian lithofacies and reservoir styles in Alberta (pp. 87-152). 2nd International Symposium of the Devonian System: 13th CSPG Core Conference.

White, D. (2009). Monitoring CO2 storage during EOR at the Weyburn-Midale Field. The Leading Edge , 28, 838-842.

White, R. (1980). Partial coherence matching of Synthetic Seismograms with Seismic Traces. Geophysical Prospecting , 28, 333-358.

White, R. (1991). Properties of instantaneous attributes. The Leading Edge , 7, 26-32.

Wikipedia: Equation of state . (2008, August 31). Retrieved from Wikipedia, the free encyclopedia: http://en.wikipedia.org/wiki/Equation_of_state.

Wright, G., M., M., & Potter, D. (1994). Structure and architecture of the Western Canada Sedimentary Basin. Geological Atlas of the Western Canada Sedimentary Basin . (G. Mossop, & I. Shetsen, Eds.) Canadian Society of Petroleum Geologists and Alberta Research Council.

Wuerdemann, H., Moeller, F., Kuehn, M., Heidug, W., Christensen, N., Borm, G., et al. (2010). CO2SINK-From site characterisation and risk assessment to monitoring and verification: One year of operational experience with the field laboratory for CO2storage at Ketzin, Germany. International Journal of Greenhouse Gas Control , 4, 938-951.

Wyllie, M., Gregory, A., & Gardner, L. (1956). Elastic wave velocities in heterogeneous and porous media. Geophysics , 21, 41-70.

Yilmaz, Ö. (2001). Seismic data analysis (Vol. I and II). Tulsa: Society of Exploration Geophysicists: Investigations in Geophysics (No. 10).

Yu, H., Zhou, G., Fan, W., & Ye, J. (2006). Predicted CO2 enhanced coalbed methane recovery and CO2 sequestration in China. International Journal of Coal Geology , 71, 345-357.

Zadeh, H., Srivastava, R., Vedanti, N., Landrø, & M. (2010). Seismic monitoring of in situ combustion process in a heavy oil field. Journal of Geophysical Engineering , 7, 16-29.

Zoeppritz, R. (1919). On the reflection and propagation of seismic waves. Göttinger Nachrichten , I, 66-84.

Zweigel, P., Arts, R., Bidstrup, T., Chadwick, A., Eiken, O., Gregersen, U., et al. (2001). Results and experiences from the first industrial-scale underground CO2 sequestration case (Sleipner Field, North Sea). Extended abstract the American Association of Petroleum Geologists annual meeting. Denver, USA: American Association of Petroleum Geologists.